The effect of Sn on the phase stability and oxidation behaviour of Nb silicide based alloys

By

Zhen Xu



Thesis submitted for the degree of Doctor of Philosophy

Department of Materials Science & Engineering

The University of Sheffield

December 2015

Summary

The manufacturers of future aero engines would need new ultra-high temperature alloys for blade applications with capabilities beyond those of Ni based superalloys to meet performance and environmental targets. The new alloys should meet property goals set by industry and would be expected to operate under conditions where turbine entry temperatures could be as high as 1800 °C and alloy surface temperatures ≥ 1300 °C. Ni based alloys cannot be used because of the melting temperature of Ni. Nb silicide based alloys are strong candidates for blade applications owing to their lower density and potential to offer a balance of properties that can satisfy property goals. The oxidation of the new alloys in service must be comparable with that of single crystal Ni based superalloys, such as CMSX4, at 1050°C. The oxidation of the new alloys is significantly improved by additions of Sn. However, to date it is not understood how Sn affects the oxidation of these alloys in the pest regime and high temperatures. The research described in this thesis attempts to understand how Sn on its own and in synergy with Al and Cr individually and simultaneously contributes towards improving the oxidation behaviour, how the stability of Nb_3Sn, Nb_{ss}, βNb_5Si_3 and αNb_5Si_3 and Laves phase in Nb silicide based alloys is affected by the addition of Sn in the alloys and what the role played by Sn is in the isothermal oxidation behaviour of alloys at 800 °C (in the pest regime) and 1200 °C.

Model Nb-Si ternary alloys with low and high concentrations of Sn and higher order model Nb-24Ti-18Si based alloys with 5 at.% of each Al and Cr added individually and simultaneously were studied in the cast and heat treated conditions (100 h at 1200 °C, 1500 °C or 1450 °C depending on alloy). The nominal compositions (at.%) of the alloys were Nb-14Si-3Sn (ZX1), Nb-12.5Si-7.5Sn (ZX2), Nb-24Ti-18Si-5Cr-2Sn (ZX3), Nb-24Ti-18Si-5Cr-5Sn (ZX4), Nb-24Ti-18Si-5Al-2Sn (ZX5), Nb-24Ti-18Si-5Al-5Sn (ZX6), Nb-24Ti-18Si-5Cr-5Al-2Sn (ZX7) and Nb-24Ti-18Si-5Cr-5Al-5Sn (ZX8). The thesis presents a brief review of relevant literature on Nb silicide based alloys and outlines a method for making Sn containing alloys with control of Sn losses during clean melting using arc melting. The microstructures of the alloys were studied using XRD, SEM, SEM-EDS, EPMA-WDS and TGA.

Tin suppressed the Nb_3Si. The $Nb_{ss} + \beta Nb_5Si_3$ metastable eutectic formed in all alloys except the alloy ZX8. Depending on alloy composition and solidification conditions transitions from anomalous to anomalous + normal to normal eutectics were observed from the bottom towards the bulk of ingots. Tin on its own increased the stability of the lamellar microstructure of the eutectic up to 1500 °C but the additions of Al and/or Cr had the opposite effect. Increasing the Sn content in the ternary alloys accelerated the $\beta Nb_5Si_3 \rightarrow \alpha Nb_5Si_3$ transformation during heat treatment. The latter was also enhanced during the solidification of the alloys with only Cr (ZX3, ZX4). The αNb_5Si_3 was stable in all the heat treated higher order alloys. Increasing the Sn content led to formation of Nb_3Sn in the cast microstructure. With the exception of alloy ZX3 (low Sn, only Cr) the A15 phase was stable at 1500 °C in all alloys. Aluminium on its own destabilised the Nb_{ss} in the heat treated alloy ZX6. Only in the alloy ZX3 (low Sn, only Cr) the Laves phase was not stable at 1500 °C.

Tin with Al and/or Cr suppressed pest oxidation. The scales formed on all alloys at 1200 °C spalled off. The "best" alloys at 800 °C and 1200 °C respectively were the alloys ZX4 and ZX6. All alloys at 1200 °C followed linear oxidation kinetics. Cr and the presence of Laves phase and Al and the absence of Laves phase were important for oxidation at 800 °C and 1200 °C, respectively. The oxide scales formed at 800 °C consisted of Nb rich and Nb and Si rich oxides. The same oxides plus Ti rich oxide were in the scales formed at 1200 °C in all alloys with the exception of the alloy ZX5. Ti rich oxide was also observed in the scale of the alloy ZX4 at 800 °C.

The improved oxidation behaviour of Sn containing alloys was attributed to Sn rich area(s) that formed below the scale/substrate interface in all alloys at 800 °C and 1200 °C, with the exception of the alloy ZX7 at 800 °C. The thickness of the Sn rich area increased with Sn concentration in the alloy and with temperature. In the Sn rich areas the Sn rich intermetallics Nb_3Sn, Nb_5Sn_2Si, $NbSn_2$ were formed. The

latter was absent in the alloys ZX5 (“best” low Sn alloy at 1200 °C) and ZX6 (“best” high Sn alloy at 1200 °C) and in the alloy ZX8.

In all the alloys all phases in the diffusion zone and bulk were contaminated by oxygen. In the diffusion zone the effect was very severe for the Nb_{ss}. In general the contamination of the Nb_{ss} by oxygen was worse than Nb_5Si_3. The oxygen concentration in the A-15 phase in the bulk did not change (≈ 6 at.%) with increasing Sn in the alloy, but its Sn content increased.

At 800 °C the contamination of the bulk of ZX4 and ZX8 by oxygen shifted the phase equilibria and in the former alloy made the Laves phase unstable and in the latter caused the formation of Nb_{ss} and Nb_{ss} + Nb_5Si_3 lamellar microstructure (the Nb_{ss} was absent in the cast alloy). The contamination of the bulk of the alloy ZX8 by oxygen at 1200 °C caused a shift in phase equilibria and led to the destabilisation of the Nb_{ss} in the microstructure.

Acknowledgements

First of all, I would like to express my sincere gratitude to my supervisor Prof. Panos, Tsakiropoulos for his unconditionally continuous support of my PhD research. His precision and enthusiasm in research will always inspire me in my future career and life. During my project, I have come cross a lot of difficulties both experimentally and in data analysis which obstructed me in moving forward. It was Prof. Tsakiroplous who would patiently advise and instruct me how to solve the problems. My gratitude for him is beyond words and I hope all the best for him.

I also would like to thank University of Sheffield, EPSRC and Rolls-Royce plc for their financial support of my PhD project. It is a great honour to work on the project that closely related with advanced industry company Rolls-Royce plc. Advice from Dr. Neil Jones and Dr Ian Edmonds of Rolls- Royce also inspired me in my research.

My thanks also to Dr Peter Kogual, Dr Peng Zeng, Dr. Le Ma, Dr Cheryl Shaw for training me on electron microscopes, Mr Kyle Arnold for the heat treatment experiments. Mr Michael Bell and Mr Richard Kangley for the sample preparation training.

Last but not least, I would like to express my huge gratitude to my family. The unconditional support and encouragement from my Mum and Dad helped me to work through my project. And also to my dearest husband Andrew Cunliffe for his love and support whilst I was writing my thesis.

Introduction to thesis

Ni based superalloys are used in the hottest parts of current gas turbine engines. The turbine entry temperature-TET (about 1550 °C) is higher than the melting point of Ni (1455 °C). In the high pressure turbine (HPT) the Ni superalloys used in the aerofoils (blades) have liquidus temperatures around 1350 °C. Operation of the aerofoils in such high temperature environment is possible owing to their internal cooling and coating systems that insulates the substrate from the hot gases. The surface temperature of the aerofoils reaches 1150 °C (homologous temperature ≈ 0.8) and this is probably very close to the highest temperature that Ni superalloys can operate. Increasing their temperature capability is limited by the melting point of Ni.

The manufacturers of aero engines are under enormous pressure to make their operation friendlier to the environment (reduction in emissions) and more efficient. To meet future emissions and performance targets the future aero engines must run hotter, with TET exceeding 1800 °C. This requires new ultra-high temperature alloys with capabilities beyond those of Ni superalloys.

The refractory metals Nb, Mo, Ta and W have melting temperatures higher than Ni. Only Nb has density lower than Ni and the latest generation Ni superalloys. Ta and W are "too heavy". Nb has a very low Ductile-brittle transition temperature-DBTT (in the range -200 °C to -150 °C) compared with the DBTT of Mo that is above room temperature. For the above reasons and the advantages offered by the Nb-Si phase equilibria for microstructure manipulation and solidification processing Nb silicide based alloys are currently considered as possible replacements of Ni superalloys in critical moving component applications in future aero engines.

The development of Nb silicide based alloys has identified oxidation behaviour as the area where more research is needed, so that the oxidation resistance of the new alloys can meet the target imposed by industry, specifically polycrystalline Nb based alloys with oxidation performance ≥ 1300 °C similar to that of single crystal CMSX-4 Ni superalloy at 1100 °C. Significant advances have been made and the oxidation behaviour of the latest generation of developmental Nb silicide based alloys is close to the target. This has become possible using alloying elements specifically to improve oxidation. Tin is one of these elements.

How Sn manages to have such a dramatic effect on the oxidation of Nb silicide based alloys in the pest oxidation regime (600 to 900 °C) and high temperatures (> 1100 °C) is not understood. This is the aims of the research described in this thesis. The objectives of the research are to understand how the concentration of Sn in Nb silicide based alloys affects phase stability and oxidation behaviour. The approach adopted to meet the aim and objectives was to consider model alloys based on Nb-24Ti-18Si with additions of 5 at.% each of Al and Cr added individually and simultaneously with low (2 at.%) and high (5 at.%) Sn concentrations. Given the limited phase equilibria data for Nb-Si-Sn and parallel research in the group to build up our own data base for Nb-Si-Sn and Nb-Si-Sn-X alloys, two model ternary Nb-Si-Sn alloys with different low and high Sn concentrations were selected to study only phase stability and phase transformations, as the oxidation of such ternary alloys is poor.

The structure of the thesis is as follows. Chapters 1 to 4 review relevant literature on high temperature structural materials, phase equilibria in Nb silicide based alloys, their oxidation and mechanical properties. The experimental techniques used in this research are described in chapter 5. The experimental results are presented in chapters 6 to 9, in groups of alloys depending on alloying additions and are compared in chapter 10. The conclusions and suggestions for future work are given in chapter 11.

Table of contents

Summary ..... **i**

Acknowledgements ..... **iii**

Introduction to thesis ..... **iv**

Table of contents ..... **vi**

Part I Literature Review

Chapter 1 High temperature structural materials **1**

1.1 Introduction 1

1.2 High temperature structural materials 1

1.2.1 Ni based superalloys 1

1.2.2 Ceramics and ceramic matrix composites (CMCs) 3

1.2.3 High temperature intermetallic compounds 4

1.2.4 High temperature refractory metal intermetallic composites 6

1.3 Processing methods 8

1.3.1 Directional Solidification: Float Zone Processing 8

1.3.2 Directional Solidification: Czochralski Method 9

1.3.3 Directional Solidification: Bridgman Methods 10

1.3.4 Vacuum Arc Melting 11

Chapter 2 Phase equilibria of Nb silicide based alloys **12**

2.1 Introduction 12

2.2 The Nb-Si binary system 13

2.3 Ti addition to the Nb-Si system 15

2.3.1 The Ti- Nb system 15

2.3.2 The Ti-Si system 16

2.3.3 The Nb-Si-Ti system 17

2.4 Cr addition to the Nb-Si system 20

2.4.1 The Nb-Cr binary system 20

2.4.2 The Cr-Si system 21
2.4.3 The Ti-Cr system 22
2.4.4 The Nb-Si-Cr system 22
2.4.5 The Nb-Si-Ti-Cr system 24
2.5 Al addition in Nb-Si binary alloys 25
2.5.1 The Nb-Al system 25
2.5.2 The Al-Si system 26
2.5.3 The Nb-Si-Al system 27
2.6 Sn addition in the Nb-Si binary alloys 29
2.6.1 The Nb-Sn system 29
2.6.2 The Si-Sn system 30
2.6.3 The Nb-Si-Sn system 31
Chapter 3 Oxidation of Nb silicide based alloys 34
3.1 Introduction 34
3.2 Effects of alloying on the oxidation behaviour of Nb-Si based alloys 35
3.2.1 The effect of Ti addition 35
3.2.2 The effect of Cr addition 36
3.2.3 The effect of Al addition 36
3.2.4 The effect of Sn addition 36
Chapter 4 Mechanical properties of the Nb silicide based alloys 38
4.1 Introduction 38
4.2 Creep 38
4.3 Fracture toughness 41
4.4 Strength 43
Part II Present Studies
Chapter 5 Experimental procedures 45
5.1 Introduction 45
5.2 Alloy selection 45
5.3 Alloy preparation 47

5.4 Specimen preparation and heat treatments 49
5.5 X-ray Diffraction (XRD) 50
5.6 Scanning Electron Microscopy (SEM) 50
5.6.1 Secondary electron and backscattered electron images 50
5.6.2 Quantitative EDS 50
5.6.3 Qualitative X-ray elemental maps and line scans 51
5.6.4 Electron probe microanalysis (EPMA) 51
5.7 Thermo-gravimetric analysis (TGA) 52
Chapter 6 The alloys Nb-14Si-3Sn (ZX1) and Nb-12.5Si-7.5Sn (ZX2) 53
6.1 Introduction 53
6.2 Results 53
6.2.1 Alloy Nb-14Si-3Sn (ZX1) 53
6.2.2 Alloy Nb-12.5Si-7.5Sn (ZX2) 64
6.3 Discussion 78
6.3.1 Alloy Nb-12.5Si-7.5Sn (ZX2) 78
6.3.2 Alloy Nb-14Si-3Sn (ZX1) 89
6.4 Summary 95
Chapter 7 The alloys Nb-24Ti-18Si-5Cr-2Sn (ZX3) and Nb-24Ti-18Si-5Cr-5Sn (ZX4) 96
7.1 Introduction 96
7.2 Results 96
7.2.1 Alloy Nb-24Ti-18Si-5Cr-2Sn (ZX3) 96
7.2.2 Alloy Nb-24Ti-18Si-5Cr-5Sn (ZX4) 105
7.3 Thermo-gravimetric analysis of the alloys ZX3 and ZX4 113
7.3.1 Oxidation kinetics of the alloys ZX3 and ZX4 at 800 °C and 1200 °C .. 114
7.3.2 Microstructures of the oxidised alloys ZX3 and ZX4 at 800 °C 116
7.3.3 Microstructure of the oxidised alloys ZX3 and ZX4 at 1200 °C 123
7.4 Discussion 131
7.4.1 Macrosegregation of Si 131

7.4.2 Phase stability in Nb-24Ti-18Si-5Cr-2Sn (alloy ZX3) 132
7.4.3 Macrosegregation of Si and Phase stability in Nb-24Ti-18Si-5Cr-5Sn (alloy ZX4) 137
7.4.4 Oxidation of alloys ZX3 and ZX4 at 800 °C 141
7.4.5 Oxidation of the alloys ZX3 and ZX4 at 1200 °C 144
7.5 Summary 146
Chapter 8 The alloys Nb-24Ti-18Si-5Al-2Sn (ZX5) and Nb-24Ti-18Si-5Al-5Sn (ZX6) 148
8.1 Introduction 148
8.2 Results 148
8.2.1 Alloy Nb-24Ti-18Si-5Al-2Sn (ZX5) 148
8.2.2 Alloy Nb-14Ti-18Si-5Al-5Sn (ZX6) 156
8.3 Thermo-gravimetric study of the alloys ZX5 and ZX6 164
8.3.1 Oxidation kinetics of the alloys at 800 °C and 1200 °C 165
8.3.2 Microstructures of the oxidised alloys ZX5 and ZX6 at 800 °C 166
8.3.3 Microstructure of the oxidised alloys ZX5 and ZX6 at 1200 ° C 175
8.4 Discussion 185
8.4.1 Macrosegregation of Si 185
8.4.2 Phase stability in the alloy Nb-24Ti-18Si-5Al-2Sn (ZX5) 187
8.4.3 Phase stability in the alloy Nb-24Ti-18Si-5Al-5Sn (ZX6) 189
8.4.4 Oxidation of the alloys ZX5 and ZX6 at 800 °C 193
8.4.5 Oxidation of the alloys ZX5 and ZX6 at 1200 °C 195
8.5 Summary 202
Chapter 9 The alloys Nb-24Ti-18Si-5Cr-5Al-2Sn (ZX7) and Nb- 24Ti -18Si -5Cr -5Al-5Sn (ZX8) 204
9.1 Introduction 204
9.2 Results 204
9.2.1 Alloy Nb-24Ti-18Si-5Cr-5Al-2Sn (ZX7) 204
9.2.2 Alloy Nb-24Ti-18Si-5Cr-5Al-5Sn (ZX8) 213

9.3 Thermo-gravimetric study of the alloys ZX7 and ZX8 223
9.3.1 Oxidation kinetics of the alloys ZX7 and ZX8 at 800 °C and 1200 °C .. 224
9.3.2 Microstructure of Oxidised alloys ZX7 and ZX8 at 800 °C 225
9.3.3 Microstructure of Oxidised alloys ZX7 and ZX8 at 1200 °C 235
9.4 Discussion 251
9.4.1 Introduction 251
9.4.2 Macrosegregation of Si 251
9.4.3 Phase stability in the alloy Nb-24Ti-18Si-5Al-5Cr-2Sn (ZX7) 253
9.4.4 Phase stability in the alloy Nb-24Ti-18Si-5Al-5Cr-5Sn (ZX8) 257
9.4.5 Oxidation of the alloys ZX7 and ZX8 at 800 °C 259
9.4.6 Oxidation of the alloys ZX7 and ZX8 at 1200 °C 261
9.5 Summary 262
Chapter 10 Comparison of the alloys 265
10.1 Macrosegregation in the alloys 265
10.2 Phase stability and transformations in the alloys with low Sn concentration 267
10.3 Phase stability and transformations in the alloys with high Sn concentration 272
10.4 Segregation of Sn in the scale/substrate interface 275
10.5 Comparison of the oxidation of the alloys at 800 °C 279
10.6 Comparison of the oxidation of the alloys at 1200 °C 287
Chapter 11 Conclusions and Suggestions for future work 297
11.1 Conclusions 297
11.2 Suggestions for future work 305
References 306

Part I
Literature Review

Chapter 1
High temperature structural materials

1.1 Introduction

The development of high temperature structural materials has made significant contributions to the aerospace industry. Ni-based superalloys have been successfully applied in aircraft engine components and land-based high temperature gas turbines. Casting technologies for Ni based superalloys supported the development from equi-axed polycrystalline microstructure to directional solidified and single crystal components. The developments of new alloys and casting technologies have increased the application temperature of blade components by about 125 °C in the last 30 years and nowadays the temperature of the hottest location on the airfoils is approaching 1150 °C [1]. However, further increasing the high temperature capability of the single crystal Ni based superalloys is difficult due to the limit imposed by the melting temperature of Ni. New high temperature alloys that have higher melting points than Ni based superalloys are required for advanced turbine engines.

1.2 High temperature structural materials

1.2.1 Ni based superalloys

Nickel-based superalloys can offer a balance of high temperature mechanical properties and corrosion resistance. This class of alloys has been used extensively in gas-turbine engines. In fact, 40-50% of the total weight of an aircraft engine is composed of Ni-based superalloys due to their stable behaviour when elevated temperature is maintained during engine operation [2]. The basic microstructure of the Ni based superalloys is composed of an $L1_2$ fcc gamma prime (γ') nickel aluminium titanium $Ni_3(Al,Ti)$ intermetallic phase embedded in a predominantly fcc gamma (γ) nickel solid solution phase. Many alloying additions have been made to the basic

composition to achieve various properties. Figure 1.1 shows a typical microstructure of a Ni based superalloy.

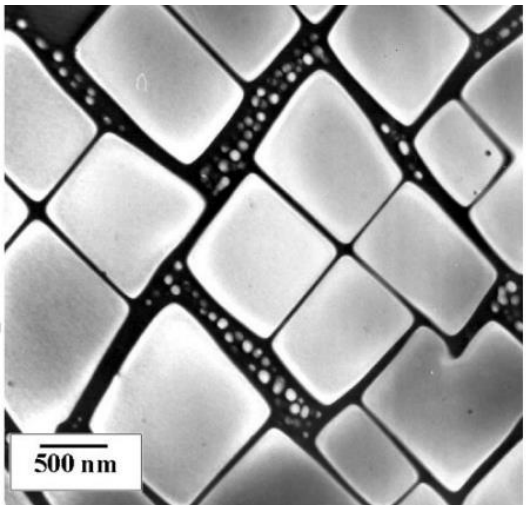


Figure 1.1 Microstructure of a Ni-based superalloy showing the bright contrast intermetallic Ni_3Al phase (gamma prime) and the dark contrast Ni rich solid solution containing some secondary gamma prime particles [3].

The blocky gamma prime phase has one characteristic which is almost unique to other materials. That is its strength increases up to a point with increasing temperature instead of decreasing, which is a normal phenomenon for most materials. In addition, the gamma phase is more resistant to deformation than it would be without the second phases and the second phase has high resistance to deformation.

Elements such as boron, carbon and hafnium were added to the Ni based superalloys to modify their grain boundaries with the intent of inhibiting creep at elevated temperatures. Besides the chemistry, processing techniques of the Ni based superalloys have also been developed significantly. In the early years, most blades were made by forging until investment casting was introduced to fabricate the blades. Later on, directional solidification was developed, which could produce grain boundaries that ran parallel to the axis of the blades. This eliminated the possibility of grain boundary sliding in the materials. The casting of single crystal turbine blades

became commercially attractive in the 80's and allowed the production of blades free of grain boundaries. Thus, alloying additions that were employed to control the grain boundaries were not required any more. This processing development simplified alloy compositions compared with the directionally solidified alloy compositions [3].

1.2.2 Ceramics and ceramic matrix composites (CMCs)

Ceramics are identified as a group of high temperature materials such as metal oxides and nitrides and are being used widely in industry. Ceramics are brittle materials that are prone to crack and spallation, which limit their application. Toughened ceramic materials have become important in recent years.

Toughened ceramics can use continuous ceramic fibres embedded in a ceramic matrix to form ceramic matrix composites (CMCs). Silicon carbide (SiC) CMCs reinforced by continuous-length, high preformation, small diameter, polycrystalline SiC fibres are considered enabling materials for many advanced applications [4]. The first generations of SiC/SiC CMCs with thermo structural capability to ~ 1250 °C are being introduced into the hot section components of gas turbine engines [5, 6]. To meet property goals, attention is focused on the interfacial bond of the fibres and matrix. If the bond strength is too high, the behaviour of the CMCs is brittle; if the bond strength is too low, the fibres are not able to cope with the load bearing process, and the result is brittle behaviour [3]. To obtain balanced interfacial bond strength, pyrolytic coatings have been applied on the fibres. Another problem occurs when the material used at elevated temperature, namely the fibres, can react with the matrix and alter the properties of the CMCs. No CMCs materials can currently operate above 1300 °C for over 1000 hours [3].

Research in the 70's and 80's put emphasis on developing Si_3N_4 and SiALONs (solid solutions based on Si_3N_4 formed by substitution of aluminium for silicon and oxygen

for nitrogen) for blade and rotor applications up to 60000 rpm and 1400 °C. The brittleness of the studied materials has not been overcome, and thus, the concept of a highly efficient, light weight ceramic gas turbine engine did not materialize. However, it is possible to use high temperature ceramics to replace a few ferrous cooling components in the engine such as the water pump, radiator and cooling fan, which improves the efficiency of the engine [3, 7].

1.2.3 High temperature intermetallic compounds

Intermetallic compounds are materials that have potential to be used in air-craft engines due to their promising strength properties at high temperatures. Intermetallic compounds generally have high melting temperatures, good strength and stiffness at high temperatures, but poor fracture toughness at room temperature. The brittleness of the intermetallic compounds at room temperature makes difficult the manufacture of components and thus has limited their utilization in aero- engine applications.

Considering melting temperatures above 1600 °C and binary intermetallic compounds formed between around 30 non-precious elements, one fifth of them have the A15 structure and can be alloyed [8]. The A15 cubic crystal structure has inherent isotropic thermal expansion which is beneficial for cyclic thermal applications. A15 compounds of transition elements can form with Al and Si.

The Nb_3Al and Cr_3Si intermetallic compounds have been extensively studied. Figure 1.2 shows the A15 crystal structure with A_3B stoichiometry. It consists of orthogonal chains of A atoms along <100> directions crisscrossing with the body centred cubic arrangement of B atoms [8]. The Nb_3Al attracted an interest as a base system due to its potential for alloying with a wide range of elements to improve properties. Indeed, the Nb_3Al intermetallic has a good solubility for many transition and refractory elements and simple metals and metalloids could replace Al atoms [8].

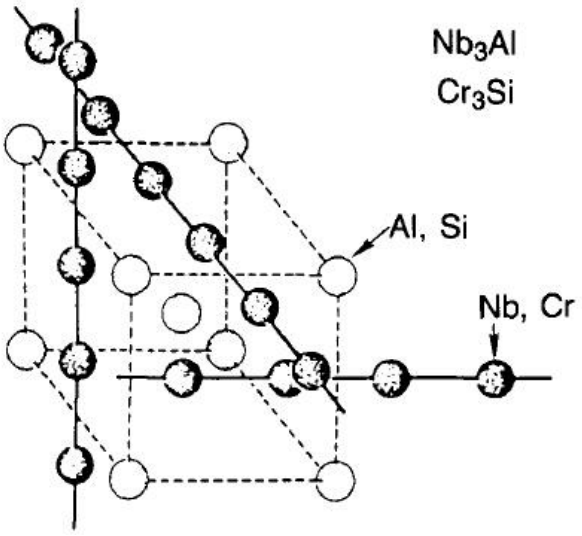


Figure 1.2 The A15 crystal structure with A_3B stoichiometry showing orthogonal chains of atoms crisscrossing the body centred cubic arrangement of B atoms [8].

Intermetallic compounds of the family of the topologically close packed intermetallic compounds, which are also known as TCP phases, have also attracted attention. The TCP compounds of AB_2 composition have solid solubility of the transition metal elements. Among the TCP compounds, the AB_2 Laves phases with cubic C14 structure, hexagonal C15 structure and di-hexagonal C36 structures offer the best combination of high melting point, low density and better oxidation resistance than other TCP phases [9]. Table 1.1 gives a list of Laves phases and their physical properties [10, 11].

Table 1.1 Summary of selected TCP phases and their properties [10, 11].

Compounds	Crystal Structure	Melting Point (°C)	Density($g \cdot cm^{-3}$)
Cr_2Nb	C14/C15	1720	7.7
Co_2Nb	C15	1520	9.0
Fe_2Nb	C14	1627	8.2
Cr_2Hf	C14/C15	1870	-
Fe_2Zr	C15	1645	7.7
Co_2Zr	C15	1560	8.2
Mo_2Hf	C36	2170	11.4

For oxidation and strength properties at temperatures above 1000 °C, silicides are another type of intermetallic compound that have been extensively researched in the

last twenty years. $MoSi_2$ has been studied extensively. The properties of $MoSi_2$ are compared with Si- based ceramics in Table 1.2 [13].

Table 1.2 Comparison between $MoSi_2$ and Si- based ceramics [13]

Property	$MoSi_2$	Ceramics
Low temperature toughness	Poor	Poor
High temperature toughness	Excellent	Poor
Creep	Very good	Excellent
Oxidation	Excellent	Excellent
Thermal shock	Excellent	Poor
Wear	Very good	Excellent
Machining	Electro-discharge machining	Diamond grinding
Density	6.3 g/cm^3	3.2 g/cm^3

Research has shown that alloying with Al significantly changes the room temperature slip behaviour of the $MoSi_2$ single crystals [14]. Addition of 2 at.% Al decreased the room temperature hardness of $MoSi_2$ by 25% compared with the un-alloyed $MoSi_2$.

The 5-3 Mo silicide Mo_5Si_3 has a higher melting point and better creep resistance than $MoSi_2$, but its oxidation resistance is lower than $MoSi_2$. Alloying with B improves its oxidation behaviour as B could form a protective borosilicate glass scale [15].

The 5-3 Nb silicide Nb_5Si_3 is another attractive intermetallic for temperature applications due to its high creep resistance. At room temperature, the fracture toughness of un-alloyed Nb_5Si_3 is low (~ 3 MPa$\sqrt{m}$). In-situ refractory metal composites were developed to achieve balanced properties used for high temperature applications [1]. The next section introduces the refractory metal intermetallic composites, which are also known as RMICs.

1.2.4 High temperature refractory metal intermetallic composites

A balance of oxidation resistance up to 1400 °C and high temperature strength are required for the new generation gas turbines [16, 17]. To increase the operating

temperature of airfoils above 1150 °C, refractory metal alloys have been considered to replace the Ni-based superalloys. Refractory metals have high melting points and some have low density.

Among the refractory metals, Nb and Mo offer the greatest potential to develop new ultra high temperature alloys. Both elements have a wide solid solubility for a number of strengthening alloying additions [17, 18]. Nb is ductile at room temperature and its density is lower than that of Ni. Mo, on the other hand, has a higher density and its ductility at room temperature is poor. The oxidation behaviour of both Nb and Mo is inferior to that of Ni.

The RMIC concept combines refractory metal and intermetallics in composites to achieve a balance of properties in the composite, where the refractory metal solid solution like, for example, Nb_{ss} toughens the brittle intermetallic compound [19]. The idea of developing "in-situ" two phases, a ductile refractory metallic phase and a brittle refractory intermetallic phase was adopted. The term "in-situ" was denoted here as the two phases were produced by the material during processing, which was different from particulate- or fibre-reinforced composites where the two phases are mechanically combined together [20, 21].

Nb-silicide based *in-situ* composites are considered to be most likely candidates for moving components in the new generation gas turbine engines as their melting temperature can be above 1750 °C, and their densities are low (6.6-7.2 g/cm^3). The Nb silicide based in situ composites consist of the metallic Nb solid solution and the Nb_5Si_3 and/or Nb_3Si intermetallic phases. The room temperature fracture toughness of Nb-silicide based in situ composite has been reported to be above 20 MPa$\sqrt{m}$ [1]. The mechanisms that control properties such as tensile strength, creep behaviour and oxidation behaviour need to be further investigated [1].

Alloys of the alloy system Nb-Ti-Hf-Si-Cr-Al-Sn that can have microstructures consisting of Nb solid solution, Nb_5Si_3 with or without C14 $NbCr_2$ based Laves phase have been investigated by Bewlay *et al* who reported that the Laves phase improved the oxidation resistance of the composites. Bewlay *et al* suggested that balanced properties of fracture toughness and oxidation resistance can be achieved with volume fraction of 40-45% Nb solid solution, 45-55% Nb_5Si_3 and 0-15% C14 Laves phase [17].

1.3 Processing methods

A variety of methods have been applied to manufacture Refractory Metal Intermetallic Composites (RMICs). These include arc melting and casting, physical vapour deposition [22] and directional solidification [23, 24]. The latter method has been mostly developed for manufacturing RMICs. Secondary processes such as forging [19] and extrusion [25] were also used for making RMICs. In this section, three directional solidification approaches are introduced, namely the float zone method, the Bridgeman method and the Czochralski method, followed by vacuum arc melting.

1.3.1 Directional Solidification: Float Zone Processing

Pope *et al* used the optical-imaging float zone (OIFZ) process to produce directionally solidified RMICs [26]. As seen in Figure 1.3, the heating source of the OIFZ system consisted of two 3.5kW tungsten halogen lamps (four lamps are used in the latest OIFZ system) in a double ellipsoidal water cooled copper chamber. A small volume of material in rod-shape charge is melted and the molten zone is then transferred along the rod. The molten zone is retained in position by surface tension between two collinear rods of the same material and thus the crucible is not required to retain the melt. Using this method, Pope *et al* produced a range of RMICs and monolithic intermetallic compounds. However, the small scale of the final products has limited the development of the OIFZ method [26].

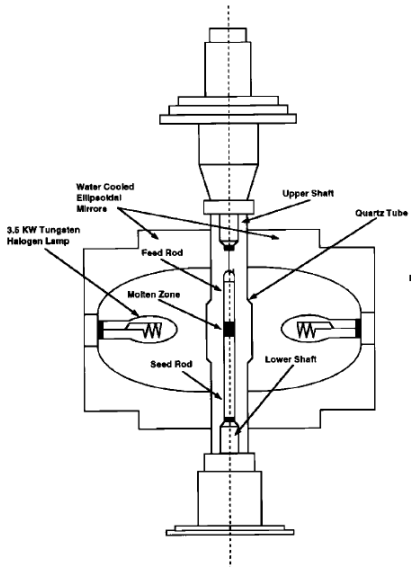


Figure 1.3 Schematic diagram of directional solidification using OIFZ [26].

1.3.2 Directional Solidification: Czochralski Method

The Czochralski method has been applied to produce high temperature alloys such as Nb-Si , Cr-Si, Cr-Nb, Mo-Si and their related high order alloys. This method provides excellent control of microstructure and composition in samples with low defect concentration and size [17].

High purity (> 99.99%) elements are used for preparing the alloys. As shown in Figure 1.4, the alloying elements are placed in a water cooled copper crucible and melted at least three times. A previously prepared seed of the same alloy that is to be directionally solidified is lowered into the melt and withdrawn at a controlled growth rate. The growth rate varies between 0.5 mm/min and 15 mm/min. A wide range of Nb-based RMICs have been produced using this method [17].

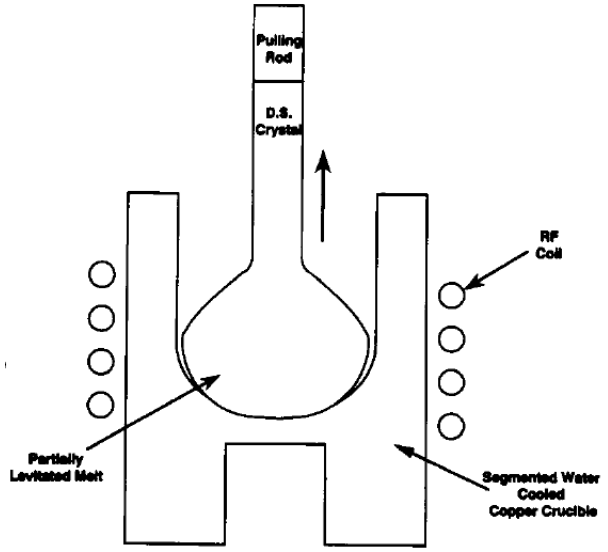


Figure 1.4 Schematic diagram of directional solidification of the Czochralski method [17]

1.3.3 Directional Solidification: Bridgman Methods

The Bridgeman directional solidification method has been applied for producing RMICs. A schematic diagram of this method is shown in Figure 1.5. Segmented water-cooled copper crucibles instead of ceramic crucibles are used for producing RMICs. The crucible is withdrawn in a controlled manner while an electromagnetic field is applied to melt the materials by induction levitation. According to Bewlay *et al*, this method could produce alloy ingots with diameter up to 50 mm [17].

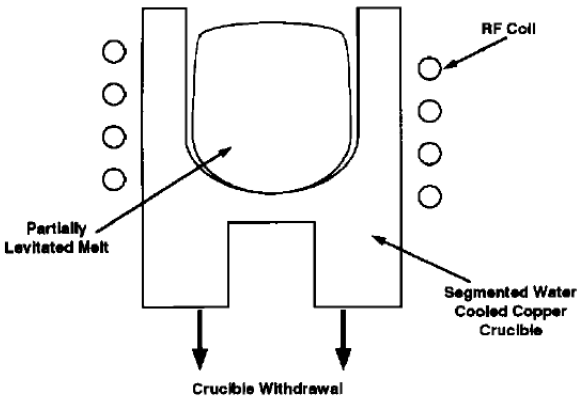


Figure 1.5 Schematic diagram of cold crucible Bridgman-type directional solidification [17]

1.3.4 Vacuum Arc Melting

Ingots of RMICs have been manufactured using vacuum arc melting. The technique can produce alloy ingots with diameter up to 75 mm and length up to 200 mm. Vacuum arc melting has been used to produce RMICs of Nb-Si binary alloys as well as higher order alloys containing Hf, Cr, Ti, Mo, Ta and Al.

Two or three phase Nb-Si based polycrystalline alloys have been produced depending on the alloying composition. In general, the microstructures of the alloys consist of a Nb based solid solution phase with one or two silicide phases, depending on alloying additions. However, it is hard to control the solidification of the alloys and composition homogeneity by using this method. Ingots produced by vacuum arc melting generally have large scale defects, especially in the last solidified area, and macrosegregation.

Chapter 2
Phase equilibria of Nb silicide based alloys

2.1 Introduction

The understanding of phase stability in Nb silicide based alloys is fundamental for developing this family of high temperature structural materials. Phase stability in binary Nb-Si alloys and ternary Nb-Si-X systems, where X is an alloying addition, has been studied.

The Nb-Si binary system was assessed by Schlesinger *et al.* in 1993 [27]. Alloying additions such as Ti, Cr, Al, Hf and Sn were added to the binary system; the related equilibrium of the ternary systems Nb-Si-Ti, Nb-Si-Cr, Nb-Si-Al, Nb-Si-Hf and Nb-Si-Sn were studied using the "diffusion multiple" method and/or CALPHAD. Zhao *et al.* studied the aforementioned first four ternary systems using "diffusion multiples" to map the phase diagrams [28]. Sun *et al* proposed isothermal sections of the ternary Nb-Si-Sn using CALPHAD and the data of other researchers' experimental works [29].

In this chapter, the Nb-Si binary system is introduced first, followed by the ternary Nb-Si-Ti system to examine the effect of the addition of Ti on phase stability in the ternary. The alloying additions of Al and Cr to the Nb-Si binary and Nb-Si-Ti ternary systems were investigated separately with emphasis on the Nb rich corner, as Al and Cr are not recommended to be added at concentrations exceeding 10 at.% to optimize the properties of the *in situ* composite [17]. The Nb-Si-Sn system is introduced separately in the last section of this chapter as Sn is one of the main alloying elements in the Nb silicide based alloys studied in this PhD research.

2.2 The Nb-Si binary system

The equilibrium phase diagram of the binary Nb-Si system is shown in Figure 2.1. The melting point of pure Nb is 2467 °C and Si has small solubility in Nb. Seven stable phases were reported in the binary system namely (1) the liquid (L); (2) the body centred cubic W-type terminal solid solution (Nb); (3) the tetragonal Ti_3P-type intermetallic Nb_3Si; (4) the tetragonal W_5Si_3-type intermetallic βNb_5Si_3; (5) the tetragonal Cr_5B_3-type intermetallic αNb_5Si_3; (6) the hexagonal $CrSi_2$-type intermetallic $NbSi_2$; (7) the diamond cubic terminal solid solution (Si); The equilibrium reactions of the binary system are summarized in Table 2.1 [27].

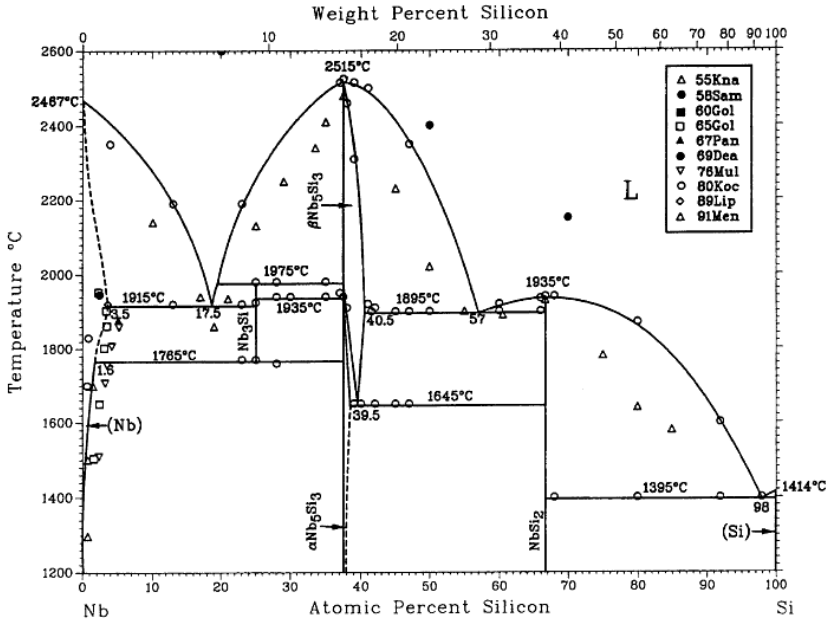


Figure 2.1 The Nb-Si phase diagram as assessed by Schlesinger *et al* [27].

Metastable intermetallics have also been reported in the Nb-Si binary system which can be stabilised by impurities such as Carbon [30]. The crystal structures of all the possible phases in the Nb-Si system are listed in Table 2.2 [27]. In Table 2.2 the phases listed below Si_{ss} are metastable.

Table 2.1 Characteristic reactions of the Nb-Si system [27]

Reaction with Si (at.%) of each phase	Temperature °C	Reaction Type
L → Nb_{ss}	2467	Melting
L (17.5%) → Nb_{ss} (3.5%) + Nb_3Si (25%)	1915	Eutectic
L (19.5%) + βNb_5Si_3 (37.5%) → Nb_3Si (25%)	1975	Peritectic
Nb_3Si (25%) → Nb_{ss} (1.6%) + αNb_5Si_3 (35.5%)	1765	Eutectoid
L (37.5%) → βNb_5Si_3 (37.5%)	2515	Melting
Nb_3Si (25%) + βNb_5Si_3 (37.5%) → αNb_5Si_3 (37.5%)	1935	Peritectoid
βNb_5Si_3 (39.5%) → αNb_5Si_3 (38.5%) + $NbSi_2$ (66.7%)	1645	Eutectoid
L (57%) → βNb_5Si_3 (40.5%) + $NbSi_2$ (66.7%)	1895	Eutectic
L (66.7%) → $NbSi_2$ (66.7%)	1935	Melting
L (98%) → $NbSi_2$ (66.7%) + Si_{ss} (100%)	1395	Eutectic
L (100%) → Si_{ss} (100%)	1414	Melting

Table 2.2 Crystal structures of equilibrium and metastable phases in the Nb-Si system [28].

Phase	Composition at.% Si	Pearson Symbol	Strukturbericht designation	Prototype
Nb_{ss}	0-3.5	cI2	A2	W
Nb_3Si	25	tP32	--	Ti_3P
αNb_5Si_3	36.7-39.8	tI32	D8l	Cr_5B_3
βNb_5Si_3	37.5-40.5	tI32	D8m	W_5Si_3
$NbSi_2$	64.9-68.8	hP9	C40	$CrSi_2$
Si_{ss}	100	cF8	A4	C(diamond)
Nb_7Si	8-13	c**	-	-
Nb_4Si	20	hP*	C6	ε- Fe_3Si
Nb_3Si-m	10-22	cF8	A15	Cr_3Si
Nb_3Si-m′	10-27	cF4	A1	Cu
Nb_3Si-m″	25	cP4	LI2	$AuCu_3$
Nb_3Si I	25	t**	-	-
γNb_5Si_3	37.5	hP16	$P6_3/mcm$	Mn_5Si_3

The eutectic reaction of L to Nb_{ss} and Nb_3Si occurs at 1915 °C where Si is around 17.5 at.%. Under equilibrium conditions, the tetragonal W_5Si_3-type βNb_5Si_3 has Si solubility from 37.5 to 40.5 at.%, depending on temperature. This high temperature stable βNb_5Si_3 is transformed to the lower temperature αNb_5Si_3 at 1935 °C. The

αNb_5Si_3 also forms via the eutectoid transformation $Nb_3Si \rightarrow Nb_{ss} + \alpha Nb_5Si_3$. This reaction has received particular attention as alloys with Si around 12 to 25 at.% i.e. hypoeutectic, eutectic, or hypereutectic alloys are expect to have this transformation under equilibrium conditions. However, according to Mendiratta and Dimiduk, the transformation kinetics of this eutectoid reaction is very sluggish and therefore heat treatment at 1500 °C for 100 hours is required to obtain the eutectoid reaction products. The line compound Nb_3Si is the other silicide of interest in the Nb-Si binary system with Si = 25 at.% [31].

2.3 Ti additions to the Nb-Si system

Titanium plays a key role in reducing the density, providing solid solution strengthening and improving oxidation resistance of Nb-silicide based alloys [28]. The Ti-Nb and Ti-Si binary systems and the Nb-Si-Ti ternary system are briefly studied to understand the effect of Ti on phase stability in Nb silicide based alloys.

2.3.1 The Ti- Nb system

The Ti-Nb equilibrium phase diagram is shown in Figure 2.2 [32]. Only two stable solid phases exist in this system, namely the hexagonal α Ti solid solution (Ti_{ss}) and the body centred cubic β Nb-Ti solid solution β(Nb,Ti). There are three fixed points on the stable Ti-Nb phase diagram, the Ti melting point T = 1670 °C; the Nb melting point T = 2469 °C and the allotropic transformation temperature of Ti at 882 °C. Above 882 °C, Nb and Ti are completely miscible [33].

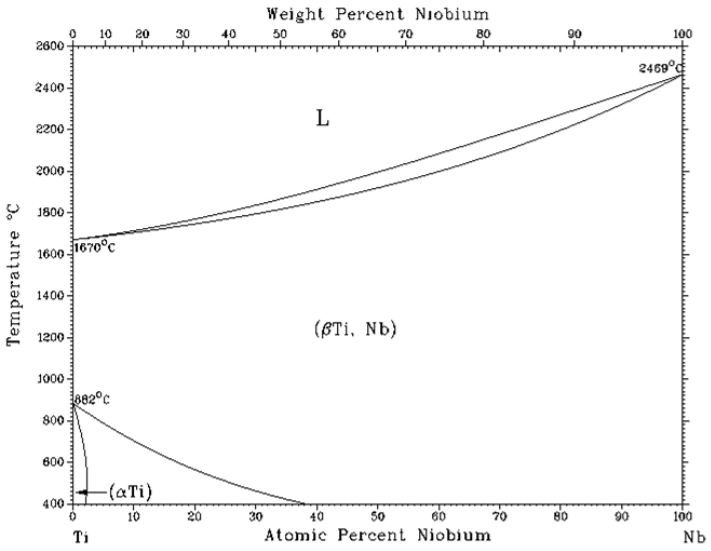


Figure 2.2 The assessed Ti-Nb phase diagram by Murray [32]

2.3.2 The Ti-Si system

The Ti-Si phase diagram is shown in Figure 2.3. Nine stable phases exist in this system, namely the Liquid (L); the body centred cubic terminal solid solution βTi_{ss}; the hexagonal terminal solid solution αTi_{ss}; the tetragonal Ti_3P type Ti_3Si; the hexagonal Mn_5Si_3-type Ti_5Si_3; the tetragonal Zr_5Si_4-type Ti_5Si_4, the orthorhombic TiSi and $TiSi_2$ intermetallics and the diamond cubic terminal solid solution Si_{ss}. According to the phase diagram, the Ti_5Si_3 intermetallic could form via the eutectic reaction $L \rightarrow \beta Ti_{ss} + Ti_5Si_3$ at 1330 °C or congruently at 2130 °C, and the Ti_3Si forms via the pretectoid reaction $Ti_5Si_3 + \beta Ti_{ss} \rightarrow Ti_3Si$.

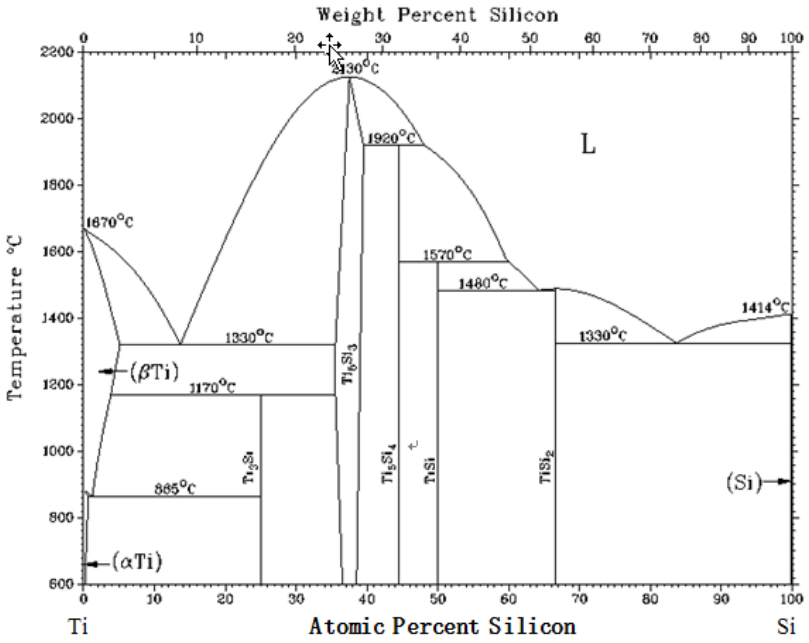


Figure 2.3 The assessed Ti-Si phase diagram by Murray [34]

2.3.3 The Nb-Si-Ti system

A schematic three dimensional metal-rich (up to 37.5 at.% Si) ternary Nb-Ti-Si phase diagram and the corresponding liquidus projection are shown in Figures 2.4 and 2.5 [35, 36].

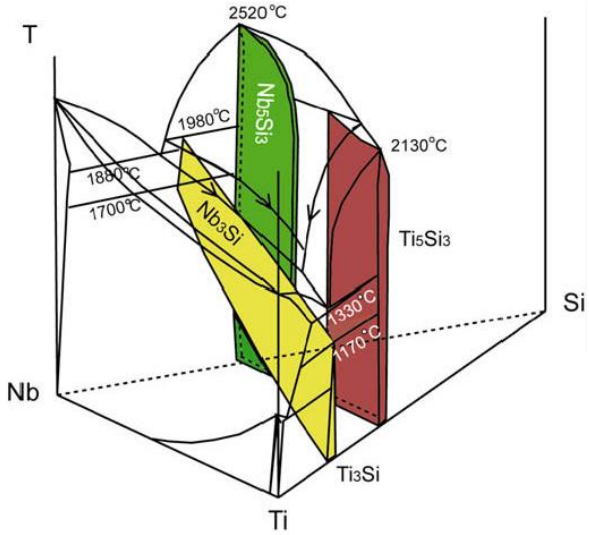


Figure 2.4 A schematic three dimensional metal-rich ternary of the Nb-Ti-Si phase diagram [35, 36]

At the metal rich side of the ternary phase diagram, there is the solid solution and the silicides Nb_3Si, Ti_3Si, Nb_5Si_3 and Ti_5Si_3. As discussed in §2.3.1, the Nb and Ti are miscible in solid solutions, and only have limited solubility for Si atoms. The Nb_5Si_3 and Ti_5Si_3 phases have different crystal structures and Nb and Ti can be in solid solution in the silicides. The Nb_3Si and Ti_3Si intermetallics are isomorphous, whereas Nb_3Si is stable above 1765 °C in the binary, while the latter intermetallic is stable below 1170 °C. Thus, Ti in solution in Nb_3Si stabilises this silicide to lower temperature [28]. A eutectic groove extends between the two binary eutectic reactions in the metal rich part of the Nb-Ti-Si ternary system (see Figure 2.4). As the composition reaches the critical point (U2 in Figure 2.5), the nature of the eutectic groove is changed by the interaction with another peritectic groove from the reaction of $L + Nb_5Si_3 \rightarrow Ti_5Si_3$ which occurs at 1350 °C [35].

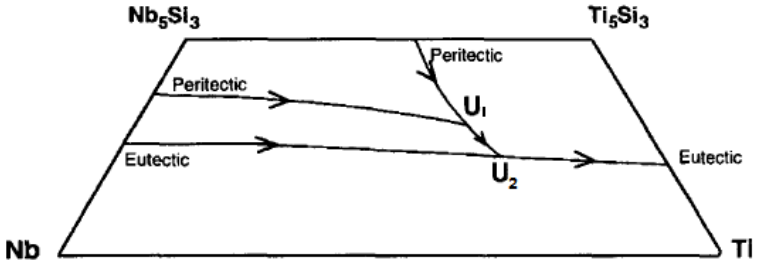


Figure 2.5 Liquidus projection of the ternary Nb-Ti-Si phase diagram [35, 36]

Earlier investigations of the Nb-Ti-Si system were focused on the metal rich corner and high temperatures (above 1350 °C). Zhao *et al* carried out research in the temperature range of 1000-1200 °C with higher Si concentration using the "diffusion multiple" approach [37]. Three isothermal sections at 1000 °C, 1150 °C and 1200 °C were constructed from the experimental data, as shown in Figure 2.6.

The solid triangles indicate well-defined three phase fields. The tie lines are shown with pink lines and open circles show the tie line compositions. The dashed tie triangles were estimated three phase equilibria. The results indicated that the

temperature of the peritectoid reaction Ti + Ti_5Si_3 → Ti_3Si should be below 1150 °C for the binary Ti-Si system, which is lower than 1170 °C of the earlier research.

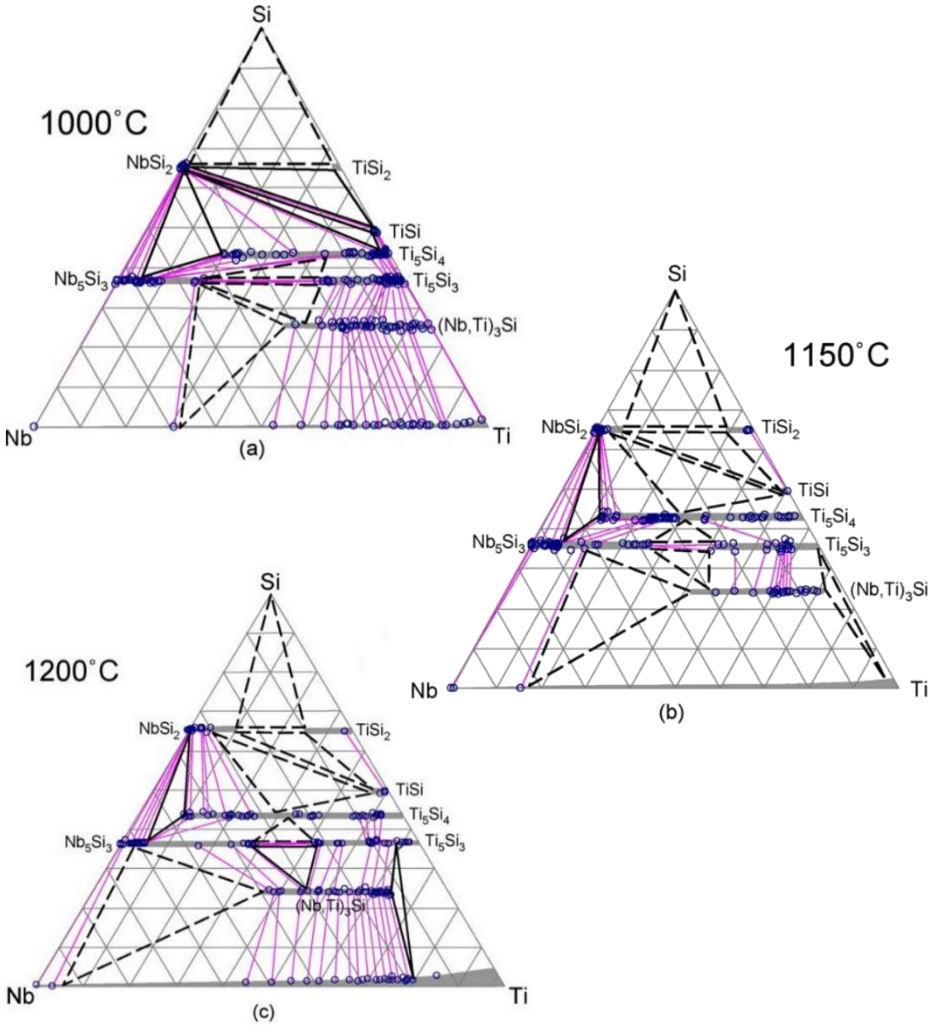


Figure 2.6 Isothermal sections at (a) 1000 °C, (b) 1150 °C and (c) 1200 °C of the Nb-Ti-Si system [37].

It is known that Ti can improve the oxidation behaviour and room temperature fracture toughness of Nb silicide based alloys. However, Nb silicide based alloys should contain less than 25 at.% Ti in order to maintain an eutectic temperature above 1700 °C and also to avoid the formation of the Ti_5Si_3 silicide which is detrimental to the creep resistance of Nb silicide based alloys [28].

2.4 Cr addition to the Nb-Si system

Alloying with Cr can significantly improve the oxidation resistance of the Nb silicide based alloys. This has been attributed to the formation of C14 $NbCr_2$ Laves phase [38]. The Laves phase has excellent strength, creep resistance at elevated temperature, high melting point (1770 °C) and relatively low density (7.7 g/cm^3) [39]. In order to understand the phase equilibria in Cr containing systems, the Nb-Cr and Ti- Cr binaries as well as the Nb-Cr-Si ternary are studied individually.

2.4.1 The Nb-Cr binary system

Figure 2.7 shows the binary Cr-Nb phase diagram assessed by Venkatraman and Neumann [40]. The Cr-Nb system is characterised by one congruently melting intermediate phase Cr_2Nb, also known as Laves phase. The Laves phase can form eutectics with each of the terminal solid solutions: Cr solid solution Cr_{ss} and Nb solid solution Nb_{ss}. The Cr_2Nb Laves phase has a compositional range of existence and is reported to exhibit the hexagonal C14 structure at high temperatures and the cubic C15 $MgCu_2$-type structure at lower temperatures. The crystal structures of the phases of the Cr-Nb binary system are listed in Table 2.3 [40].

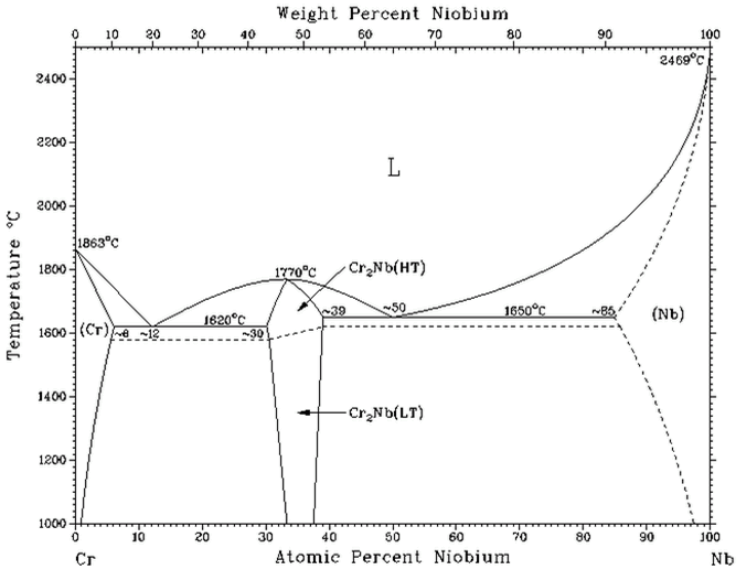


Figure 2.7 The Nb-Cr phase diagram assessed by Venkatraman and Neumann [40].

Table 2.3 The crystal structure of the phases of the Cr-Nb binary system [40].

Phase	Compositions (at.% Nb)	Pearson symbol	Struckturbericht designation
Cr_{ss}	0-6	*cI2*	A2
Cr_2Nb(HT)	30-39	*hP12*	C14
Cr_2Nb(LT)	30-39	*cF24*	C15
Nb_{ss}	85-100	*cI2*	A2

2.4.2 The Cr-Si system

The assessed equilibrium phase diagram of the Cr-Si binary system is shown in Figure 2.7. The following stable phases are presented in the system: (1) The liquid, L; (2) the terminal solutions Cr_{ss}, with a maximum solubility of approximately 9.5 at.% Si at the eutectic temperature of 1705 °C; (3) the terminal solid solution, Si_{ss}, with extremely low solubility of Cr at the eutectic temperature of 1305 °C; (4) the cubic intermetallic phase, Cr_3Si, which melts at 1770 °C; (5) the tetragonal intermetallic phase, Cr_5Si_3, which melts at 1680 °C; (6) the cubic intermetallic phase, CrSi, which decomposes at 1413 °C via peritectic transformation; and (7) the hexagonal intermetallic phase, $CrSi_2$, which melts at 1490 °C. In this system, the Cr_5Si_3 has the same crystal structure as βNb_5Si_3 but the Cr_3Si is an A15 compound like Nb_3Sn and Nb_3Al.

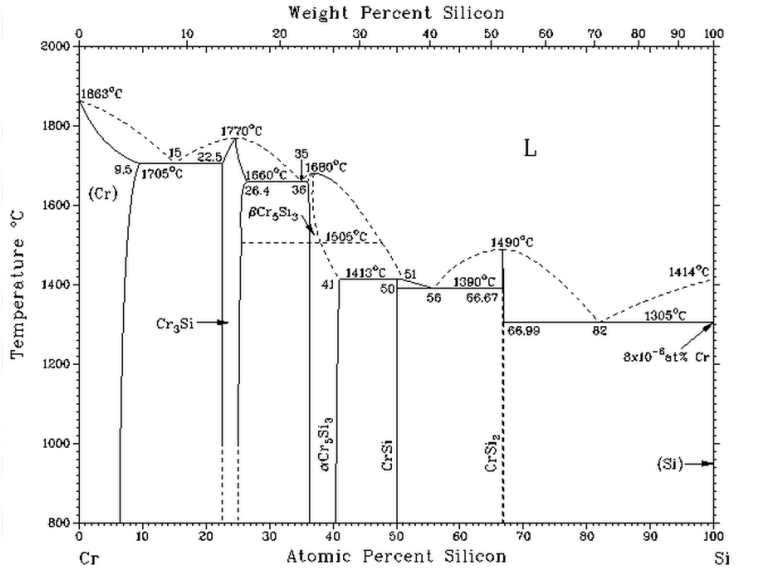


Figure 2.8 The Cr-Si phase diagram assessed by Gokhale and Abbaschian [41].

2.4.3 The Ti-Cr system

The equilibrium phases of the Ti-Cr system are the liquid L, the closed-packed hexagonal (cph) Ti solid solution Ti_{ss} with small Cr solubility, the body centred cubic (bcc) Cr solid solution Cr_{ss} and three Laves phases that are close to the stoichiometry of $TiCr_2$. The high temperature hexagonal $\gamma TiCr_2$ Laves phase has the C36 structure and transforms to hexagonal C14 $\beta TiCr_2$ at ~ 1220 °C. The $\beta TiCr_2$ has the same crystal structure as the high temperature C14 $NbCr_2$ and transforms eutectoidally to $\alpha TiCr_2$ and Cr_{ss} at ~800 °C. The cubic C15 $TiCr_2$ is stable to low temperature like the C15 $NbCr_2$ and forms via the peritectoid reaction $(\beta Ti,Cr) + \gamma TiCr_2 \rightarrow \alpha TiCr_2$.

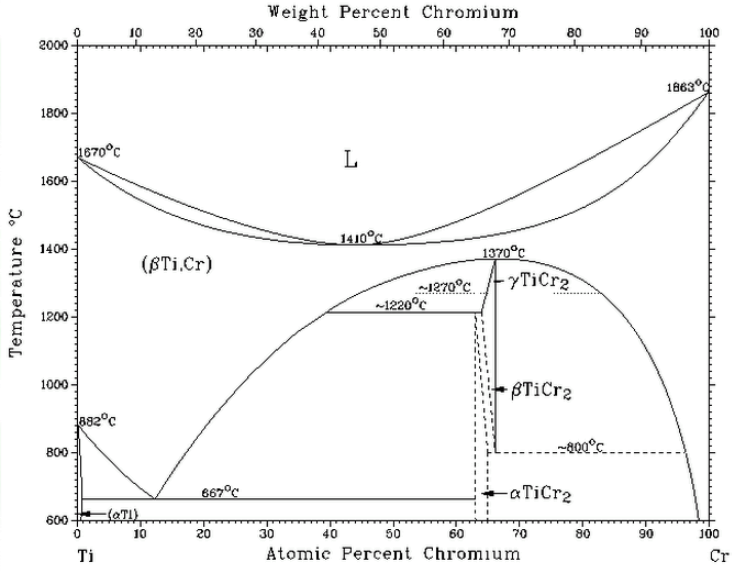


Figure 2.9 The Ti- Cr phase diagram assessed by Murray [42].

2.4.4 The Nb-Si-Cr system

Goldschmidt and Brand determined the isothermal section of Nb-Cr-Si at 1000 °C, as seen in Figure 2.10. At the Nb rich corner of the section, there was a highlighted three phase equilibrium region of the ρ, Nb_5Si_3 and Nb_{ss} phases. The ρ phase was described as a ternary Laves phase similar to the C14 $NbCr_2$ Laves phase, i.e, a hexagonal hP12 $MgZn_2$ type phase with large solubility of Si. This diagram showed that Si stabilised the C14 Laves phase to lower temperature [43].

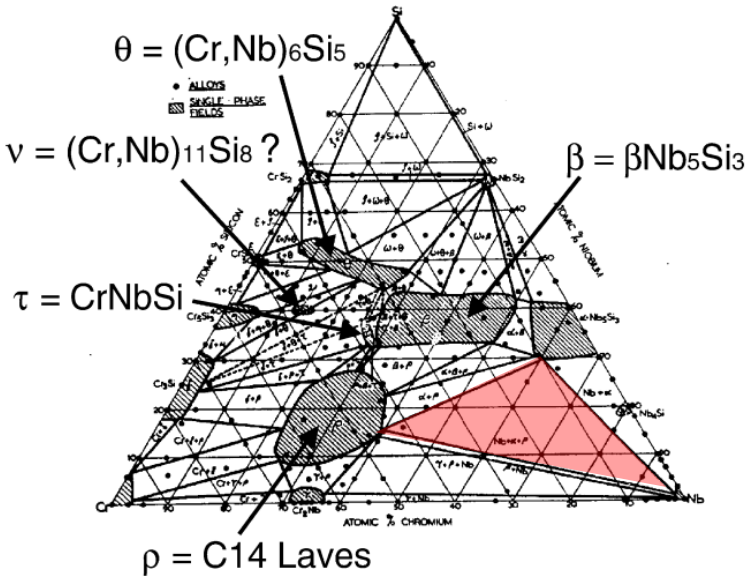


Figure 2.10 The 1000 °C isothermal section of the Nb-Cr-Si ternary system reported by Goldschmidt and Brand [43].

Goldschmidt and Brand used 220 alloys to determine the Nb-Cr-Si ternary system. The alloys were difficult to make and to homogenize. In addition, interstitials such as oxygen, nitrogen and carbon could contaminate the alloys during their preparation and heat treatment. More importantly, the interstitial elements are well known to stabilise intermetallic phases that would otherwise not form in the binary and ternary system.

The Nb-Si-Cr system was studied by Zhao *et al* who used the "diffusion multiple" approach. The 1000 °C isothermal section is shown in Figure 2.11. The equilibrium ternary silicides in the system were described as $(Cr,Nb)_{11}Si_8$, CrNbSi and $(Cr,Nb)_6Si_5$. The main difference with the work of Goldschmidt and Brand is the absence of the three phase equilibrium between Nb_{ss}, Nb_5Si_3 and C14 $NbCr_2$ (ρ phase in Figure 2.10). The latter equilibrium at 1000 °C and 1500 °C was confirmed by experimental work by Geng *et al* [44]. The most recent study of the Nb-Si-Cr system by Bewlay *et al* [45] suggested the presence of the $Nb_9(Cr,Si)_5$ intermetallic in the cast microstructure of Nb-18Si-5Cr together with Nb_{ss}, $NbCr_2$ and Nb_5Si_3.

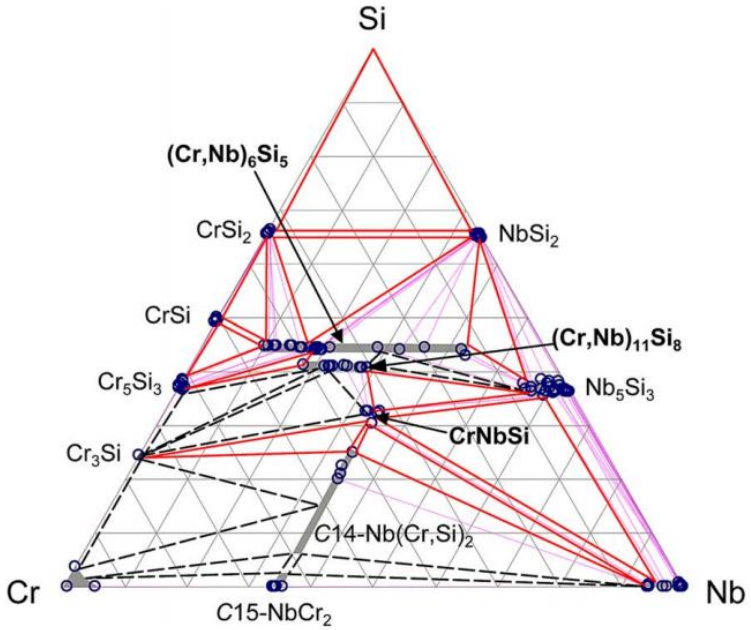


Figure 2.11 The 1000°C isothermal section of the Nb-Si-Cr system produced using the "diffusion multiple" approach [38].

2.4.5 The Nb-Si-Ti-Cr system

In Nb silicide based alloys, Cr additions > 5 at.% can lead to stabilisation of the $NbCr_2$ Laves phase and a substantial improvement in oxidation resistance. As shown in Figure 2.12, Cr concentration larger than 5 at.% stabilises the $NbCr_2$ Laves phase in the composite. The quaternary phase diagram also shows that the Si modified Laves phase can co-exist with hP16 M_5Si_3, tI32 M_5Si_3 and tP32 M_3Si. It should be remembered that the tetragonal Nb_5Si_3 and Nb_3Si have the tI32 and tP32 Pearson symbols respectively and that the hexagonal Nb_5Si_3 or Ti_5Si_3 have prototype the hP16 Mn_5Si_3.

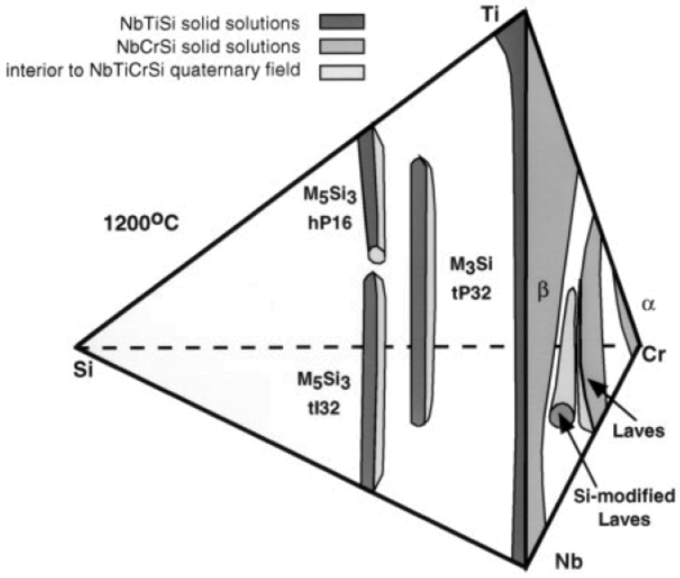


Figure 2.12 Single-phase fields in the Nb-Ti-Cr-Si phase equilibria at 1200 °C for compositions up to 38 at.% Si (the single phase fields originating from the Cr-Si binary are omitted for simplification) [17].

2.5 Al addition in Nb-Si binary alloys

Alloying with Al is often sought to improve the oxidation resistance of alloys. To understand the effect of Al additions in Nb silicide based alloys, knowledge of phase equilibria in the Nb-Si-Al ternary system is required. The binary phase diagrams of Nb-Al, Al-Si and Nb-Si need to be considered before the ternary system of Nb-Si-Al phase diagram. The Nb-Si binary was briefly discussed in § 2.2.

2.5.1 The Nb-Al system

In the Nb-Al system, there are three intermetallic compounds, namely Nb_3Al, Nb_2Al and $NbAl_3$. The Nb_3Al has a maximum homogeneity range from 18.6 at.% Al below 1500 °C to 25 at.% Al at 1940 °C, and the Nb_2Al has a maximum homogeneity range from 30 at.% below 1500 °C to 42 at.% at 1590 °C. The $NbAl_3$ has a narrow homogeneity range with a width of ~1 at.%. The Nb_3Al is an A15 compound, like Nb_3Sn and Cr_3Si. The terminal face centred cubic Al solid solution has extremely low solubility of Nb. The terminal body centred cubic Nb solid solution can dissolve up

to 21.5 at% Al at 2060 °C.

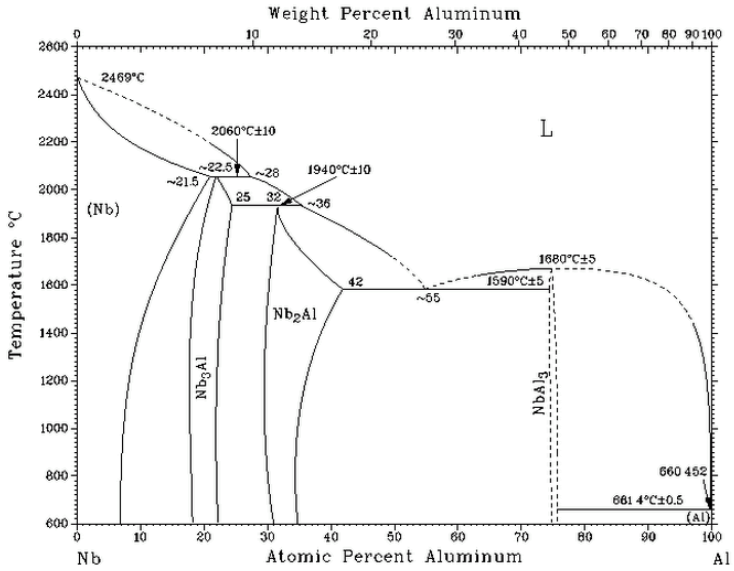


Figure 2.13 The Nb-Al phase diagram assessed by Kattner and Boettinger [46].

2.5.2 The Al-Si system

The Al-Si phase diagram is a simple eutectic system with two solid solution phases, the face centred cubic Al solid solution Al_{ss} and the diamond cubic Si solid solution Si_{ss}. The maximum solubility of Si in Al_{ss} is 1.5 at.% at the eutectic temperature and drops down to 0.05 at.% at around 300 °C. The solubility of Al in Si_{ss} is negligible. No intermetallic compounds were reported in the Al-Si system [47].

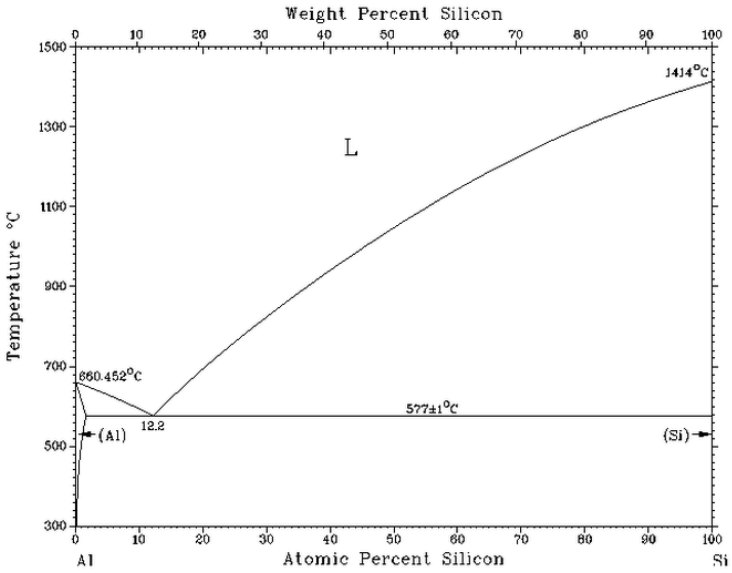


Figure 2.14 The Al- Si phase diagram assessed by Murray and McAlister [47].

2.5.3 The Nb-Si-Al system

An isothermal section of the Nb-Si-Al at 1400 °C was first reported by Brukl *et al* and suggested that the $Nb_3Si_5Al_2$ and $Nb_{10}Si_3Al_3$ phases co-existed in equilibrium [48]. However, later research on the Nb-Si-Al system by Pan *et al* did not confirm this [49]. As seen in Figure 2.15, Pan *et al* found that the Nb_5Si_3 was in equilibrium with $NbAl_3$ at 1500 °C instead of the two ternary compounds. More recently, Zhao *et al* assessed the Nb-Al-Si system using the "diffusion multiple" approach and proposed the isothermal sections at 1000 °C, shown in Figure 2.16 [50].

Zhao *et al* identified the $Nb_{10}Si_3Al_3$ ternary phase and suggested that the ternary compound actually is the binary βNb_5Si_3 phase stabilised by Al to lower temperature at 1400 °C. Al solubility in αNb_5Si_3 phase was measured as ~8 at.% at 1000 °C and Al substitutes for Si atoms in the Nb_5Si_3. When the Nb_5Si_3 is in equilibrium with the Nb solid solution, only 3 at.% Al is needed to form the A15 Nb_3Al compound. It is not known that the solubility of Al in these phases varies with alloying additions such as Ti and Cr. Al can stabilise the C14 Laves phase in the presence of Cr [50]. The crystal structure of phases in the Nb-Al-Si system are given in Table 2.

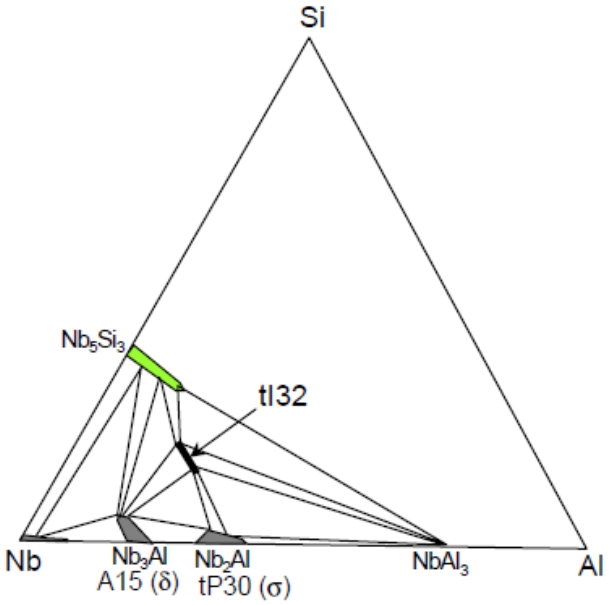


Figure 2.15 A partial isothermal section of the Nb-Si-Al system at 1500 °C [28]

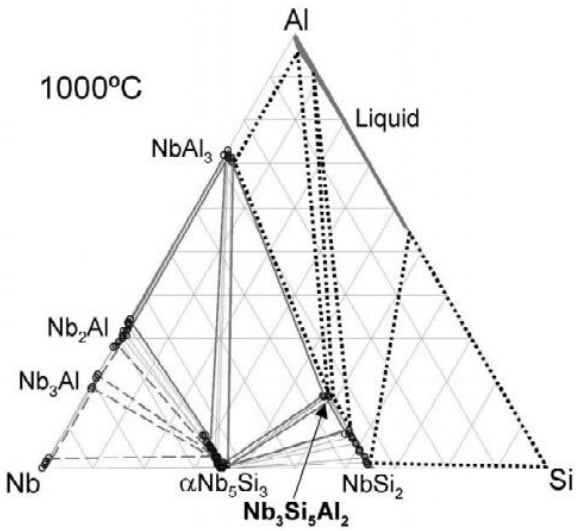


Figure 2.16 The 1000°C isothermal section of the Nb-Al-Si system from the tri-junction area of the "diffusion multiple" approach annealed at 1000°C for 2000 hours [50].

Table 2.4 Crystal structure of phases in the Nb-Al-Si ternary system [50]

Phase	Pearson Symbol	Space group	Lattice parameter (nm)			
			a	b	c	γ
Al	*cF*4	$Fm\bar{3}m$	0.40497			
Nb	*cI*2	$Im\bar{3}m$	0.33067			
Si	*cF8*	$Fd\bar{3}m$	0.54309			
Nb_3Si	*tP*32	*P4₂/n*	1.0224		0.5189	
βNb_5Si_3	*tI*32	*I4/mcm*	1.0040		0.5081	
αNb_5Si_3	*tI*32	*I4/mcm*	0.6571		1.1889	
$NbSi_2$	*hP*9	*P6₂22*	0.481		0.661	120°
Nb_2Al	*tP*30	*P4₂/mnm*	0.9945		0.5171	
Nb_3Al	*cP*8	$Pm\bar{3}n$	0.5186			
$NbAl_3$	*tI*8	*I4/mnm*	0.3844		0.8605	
$Nb_3Si_5Al_2$	*oF*24	*Fddd*	0.8403	0.4901	0.8794	

2.6 Sn additions in the Nb-Si binary alloys

The alloying of Nb silicide based alloys with Sn was found to benefit their intermediate temperature oxidation resistance. Sn additions as low as 1.5 at.% could prevent the Nb silicide based alloys from pesting [51]. Why and/or how Sn has this effect however has not been studied.

2.6.1 The Nb-Sn system

The Nb-Sn system was first assessed by Shunk at 1969 °C. Three intermetallic phases were reported in the binary system, namely the Nb_3Sn, Nb_6Sn_5 and $NbSn_2$ [52]. The Nb_3Sn compound was stable to ~ 800 °C. This was confirmed by Toffolon *et al* in 1998 who reported that the Nb_3Sn was not stable below 796 °C in 2001 [53]. Toffolon *et al* remodelled the binary system by taking into account the experimental enthalpy of formation of Nb_3Sn at 1350 °C and reconsidered the Nb_3Sn compound to be stable to room temperature [53]. The reassessed Nb-Sn phase diagram proposed by Toffolon *et al* is shown in Figure 2.18.

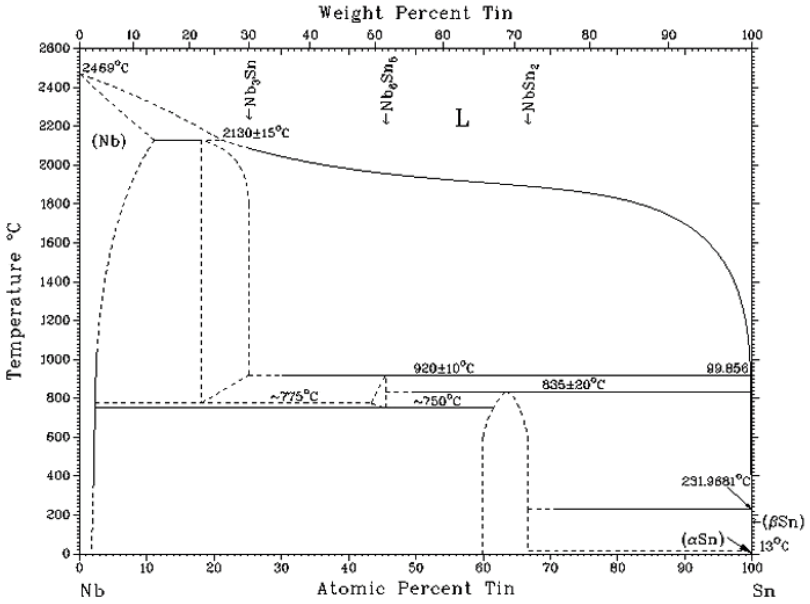


Figure 2.17 The Nb-Sn phase diagram assessed by Shunk in 1969 [52].

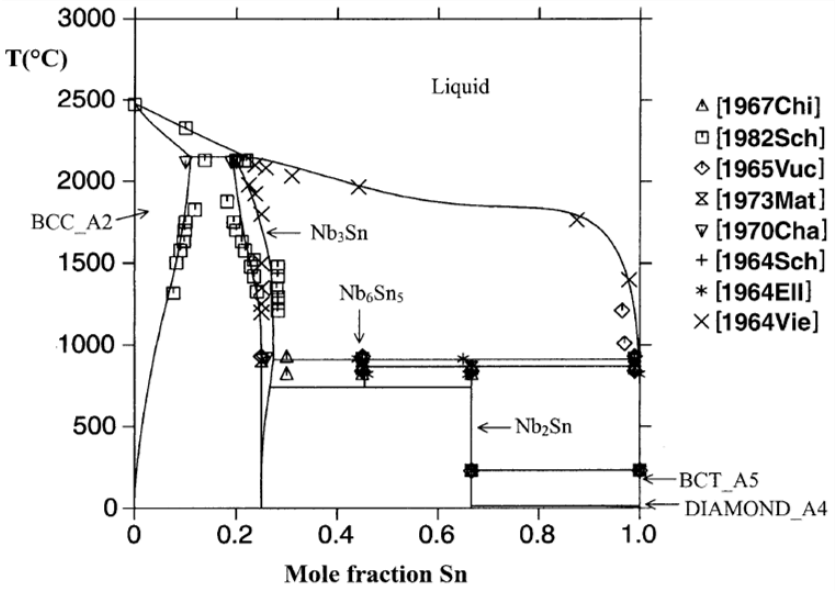


Figure 2.18 Calculated Nb-Sn phase diagram compared with experimental data [53].

2.6.2 The Si-Sn system

The assessed equilibrium phase diagram for the Si-Sn system is shown in Figure 2.19. The stable phases of Si and Sn under normal pressure are (1) the liquid, L; (2) the Si solid solution, (3) and the βSn solid solution. The βSn transforms from tetragonal to diamond-type cubic αSn at 13.05 °C [54, 55]. Si and βSn form a simple eutectic at a

temperature close to the melting point of pure Sn [54].

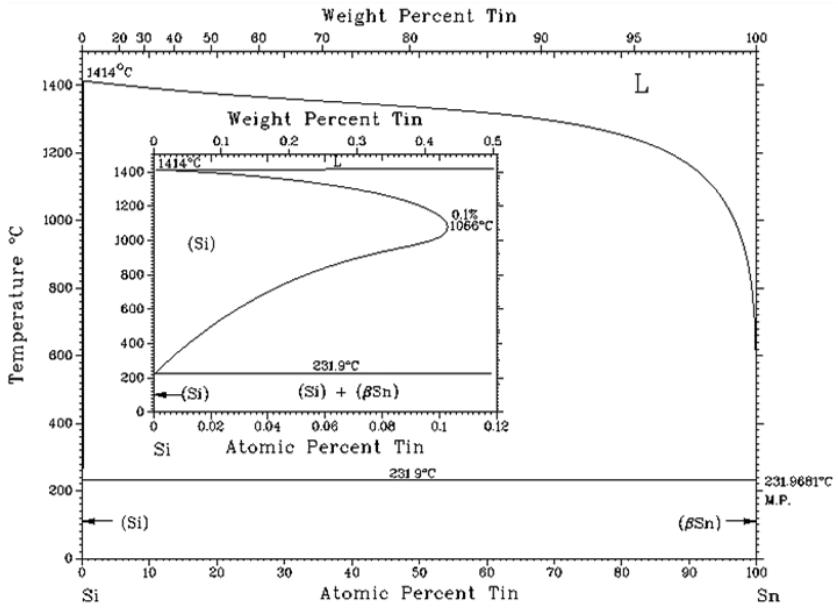


Figure 2.19 The Si-Sn phase diagram assessed by Olesinski and Abbaschian [54].

With the data for the binary Nb-Sn and Si-Sn systems, and the Nb-Si phase diagram which was introduced in § 2.2, Sun *et al* mapped the Nb rich corner of the Nb-Si-Sn ternary system [29]. The data was compared with the partial ternary isothermal section of the Nb-Si-Sn system at 1600 °C by Waterstrat and Müller [55].

2.6.3 The Nb-Si-Sn system

In the work of Waterstrat and Müller the ternary alloy samples were made by sintering pure metals followed by a heat treatment at 1600 °C for 30 hours under 50 atm argon pressure. The A15 Nb_3Sn phase was found to be in equilibrium with the Nb_5Si_3 and the Nb solid solution. The A15 Nb_3Sn is used widely as superconducting material and Si is reported to lower the superconducting transition temperature [51]. Based on the ternary data of Waterstrat and Müller, Sun *et al* calculated the isothermal section of the Nb-Si-Sn ternary system at 1600 °C which is shown in Figure 2.21 [29].

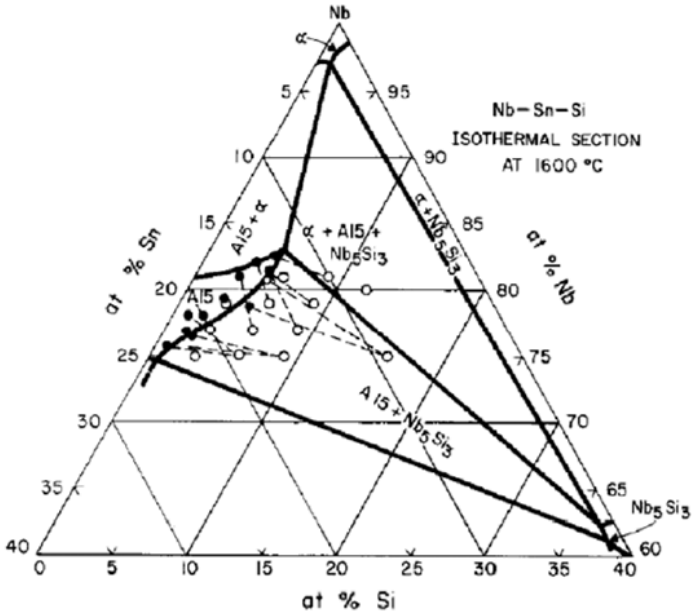


Figure 2.20 Partial ternary isothermal section of the Nb-Sn-Si system at 1600 °C [55].

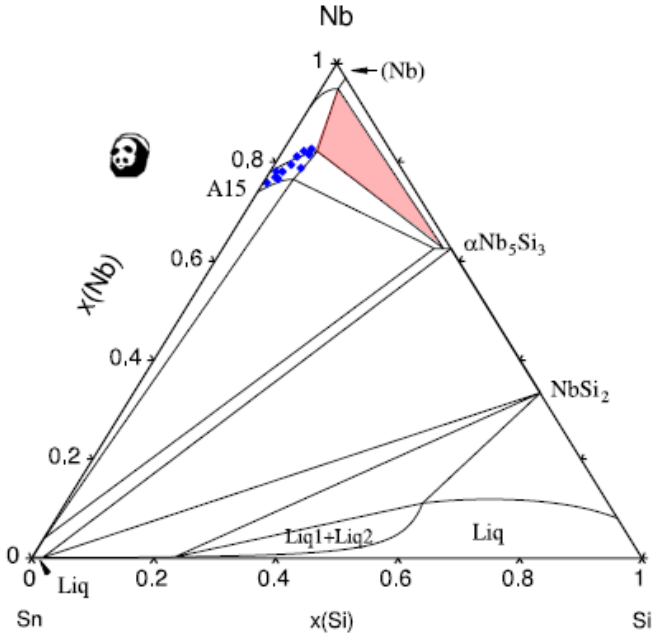


Figure 2.21 Calculated isothermal section at 1600 °C, where the symbols represent the compositions of Nb_3Sn from Waterstrat and Müller (the three phase equilibrium is highlighted in the isothermal section) [29].

The calculated phase relationships were in agreement with Waterstrat *et al*. Three two-phase equilibria were identified in the Nb rich corner: Nb_{ss} + αNb_5Si_3, Nb_{ss} + A15_Nb_3Sn and αNb_5Si_3 + A15_Nb_3Sn. One three-phase equilibrium was described as Nb_{ss} + αNb_5Si_3 + A15_Nb_3Sn. The Nb_{ss} in the tie-triangle region contains 2.7 at.% Si and 2.4 at.% Sn, the αNb_5Si_3 contains 36.2 at.% Si and 1.3 at.% Sn, the A15_Nb_3Sn contains 5.6 at.% Si and 12.2 at.% Sn. The composition of the tie-triangle region was well matched with the experimental work of Waterstrat and Müller and Vellios and Tsakiropoulos [55, 56].

Chapter 3
Oxidation of Nb silicide based alloys

3.1 Introduction

Nb can form a few stable oxides, namely the NbO and NbO_2 oxides and a few polymorphs of Nb_2O_5. Near atmospheric pressure, the Nb_2O_5 forms at 450 ~ 500°C. The aforementioned oxides are easily formed and grow with parabolic kinetics and inward diffusion of oxygen. Due to the dimensional restraint caused by the metal base, compressive stresses develop in the scale leading to periodic cracking which allows further penetration of oxygen [57]. Oxygen diffusion and the nucleation and growth of Nb oxide at the interface of the oxide and metal base give rise to severe oxidation of Nb. The oxidation resistance of Nb may be enhanced using alloying additions to modify the properties of the scale as well as reduce the oxygen diffusion through the scale [57].

As discussed in chapter 1, Nb silicide based alloys are considered for high temperature structural applications. In these alloys the presence of Si was expected to give good oxidation resistance by forming silica (SiO_2), which is one of the most stable oxides at high temperatures [58]. The oxidation of silicides was also expected to contribute to the formation of SiO_2 scale. According to Lyutyi *et.al* [59], the oxidation of Nb_5Si_3 occurs according to the reaction:

$$2Nb_5Si_3 + 17.57O_2 \rightarrow 5Nb_2O_5 + 6SiO_2 \quad (3.1)$$

SiO_2 and Nb_2O_5 have no solubility in the solid state. This give rise to the formation of complex oxide scale on the Nb silicide based alloys [57]. The Nb silicide based alloys can suffer from high metal recession rates and scale spallation, and even pesting [1].

Pesting is the term that is often employed to describe preferential oxidation at microstructural features, such as grain boundaries, which can lead to self-pulverization in samples cycled from room temperature to relatively low temperatures; it is often coupled with oxygen embrittlement, and is a phenomenon observed in many intermetallics and intermetallic alloys [1].

The formation of a protective scale on any alloy depletes the scale forming elements from the underlying alloy, this can lead to destruction of the protective scales, even under isothermal conditions [60]. In most high temperature alloys, the exposure conditions cause this depletion below the scale to occur much quicker than would be anticipated from isothermal oxidation rates. Particularly important among these conditions are temperature cycling, which causes loss of protective scale by spallation and exposure to mixed oxidants or hot corrosive environments, which can result in the protective scale-forming element being localized in a non-protective morphology [61].

3.2 Effects of alloying on the oxidation behaviour of Nb-Si based alloys

3.2.1 The effect of Ti addition

Alloying Nb with Ti leads to the formation of $Nb_2O_5 \cdot TiO_2$, when Ti is up to 25 at.%. According to Menon and Mendiratta, Ti oxides are more thermodynamically stable than SiO_2 in Nb silicide based alloys [62]. And the when Ti addition is higher than 6 at.%, Ti enhances the oxidation behaviour of Nb silicide based alloys at elevated temperatures [57]. The high oxide： metal volume ratio of Nb_2O_5 is due to the large volume occupied by oxygen atoms. As Nb is pentavalent in the oxide, the addition of elements with lower effective valances than that of Nb should reduce the volume ratio and the tendency to form cracks. Ti forms quadrivalent Ti cations in the TiO_2 oxides and thus improves the oxidation resistance of pentavalent niobium oxides [57].

3.2.2 The effect of Cr addition

Cr can form protective oxidation scales on high temperature alloys [6]. This is due to Cr forming corundum Cr_2O_3 at high temperature, which consists of hexagonally close-packed oxygen ions with Cr cations occupying two thirds of the octahedral sites. At temperatures above 850-900 °C, Cr_2O_3 will react with oxygen further to form volatile CrO_3 via the reaction：

$$Cr_2O_3 + 1.5O_2 \rightarrow 2CrO_3 \quad (3.2)$$

The reaction rate increases with increasing partial pressure of oxygen and becomes pronounced at temperatures above 1000 °C. This limits the effectiveness of Cr alloying addition to temperatures below 900 °C [58].

According to Bewlay *et.al*, Cr improves the oxidation resistance of Nb-Si *in situ* composites, when added at concentrations greater than 5 at.%, where the $NbCr_2$ Laves phase is stabilised. This phase is considered to be beneficial for improving the oxidation behaviour of the Nb silicide based alloys [1].

3.2.3 The effect of Al additions

Al containing alloys can form Al_2O_3 scales at temperatures above 900 °C. Alumina scales have long term chemical stability and slow growth rates. However, Al_2O_3 spalls extensively during cooling of the alloys due to the high thermal stress and weak Al_2O_3 that ceramic- metal interface [58]. Bewlay *et al* suggested that Al addition can reduce the pesting susceptibility of Nb silicide based alloys at intermediate temperatures. However, some Nb silicide based alloys can still pest even with Al additions [1].

3.2.4 The effect of Sn addition

Alloying with Sn has been reported to eliminate pest oxidation of Nb silicide based

alloys at intermediate temperatures and to have minimal effect on high temperature oxidation. Bewlay *et al* studied a series of alloys of different compositions and investigated the effect of Sn on the oxidation behaviour of Nb silicide based alloys. After 200 hours exposure in static air at 870 °C, the degree of cracking around the perimeter of alloy samples was measured. It was found that the amount of Sn can be as low as 1.5% for the alloy to be immune from pesting, as shown in Figure 3.1 [1].

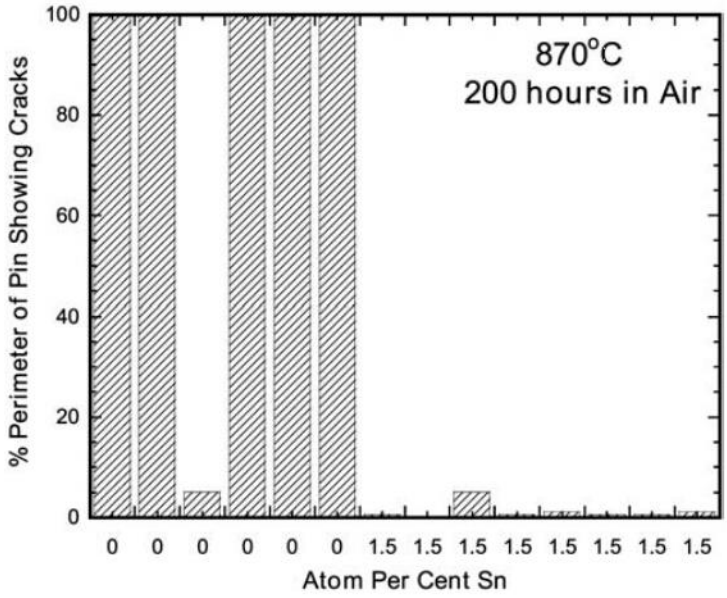


Figure 3.1 Intermediate temperature cyclic oxidation behaviour of Nb silicide based alloys with different Sn contents [1].

As shown in Figure 3.1, the alloy that contained Sn displayed an extremely low level of damage. The typical composition of an alloy that contained Sn was given as Nb-24.5Ti-16Si-1.5Hf-6Cr-3Fe-2Al-2B-6Ge-1.5Sn. The mechanism by which Sn prevents pesting is not known [1]. In the research presented in this thesis, the effect of Sn on the oxidation behaviour at intermediate and high temperature has been studied.

Chapter 4

Mechanical properties of Nb silicide based alloys

4.1 Introduction

Nb silicide based alloys offer a promising balance of properties at both low and high temperatures. This chapter reviews briefly data on their creep behaviour, fracture toughness and yield strength.

4.2 Creep

Nb silicide based alloys have good creep properties at high temperatures. The creep goal for future engine applications is less than 1% creep in 125 hours at a temperature of 1200 °C and stresses higher than 170 MPa [1]. Taking the primary creep of the system into account, a secondary creep rate of 2.2 $\times 10^{-8}$ s^{-1} is required. Figure 4.1 shows the creep behaviour of a 1st generation Nb silicide based alloy, known as MASC alloy, and a later generation Nb silicide based alloy as a function of stress [1].

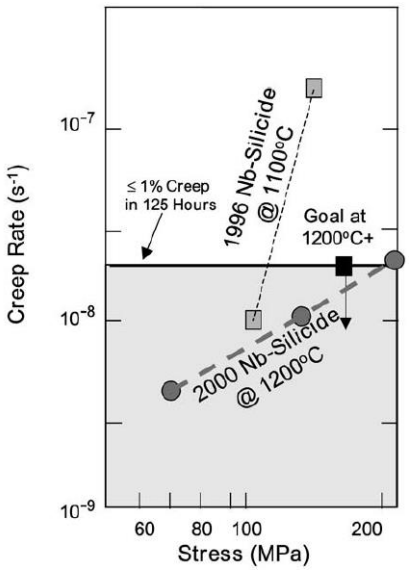


Figure 4.1 Secondary creep behaviour as a function of stress for MASC alloy (1996) and later generation Nb silicide based alloy (2000) [1].

The creep behaviour of the Nb silicide based alloy is a combination of the creep behaviour of the silicide and metallic phases. Most of the creep resistance of the Nb silicide based alloy comes from the silicide phase, which is stronger and bears a higher load than the Nb solid solution phase [16]. Therefore, the volume fraction of the silicide phase in the microstructure of the Nb silicide based alloys determines their creep properties.

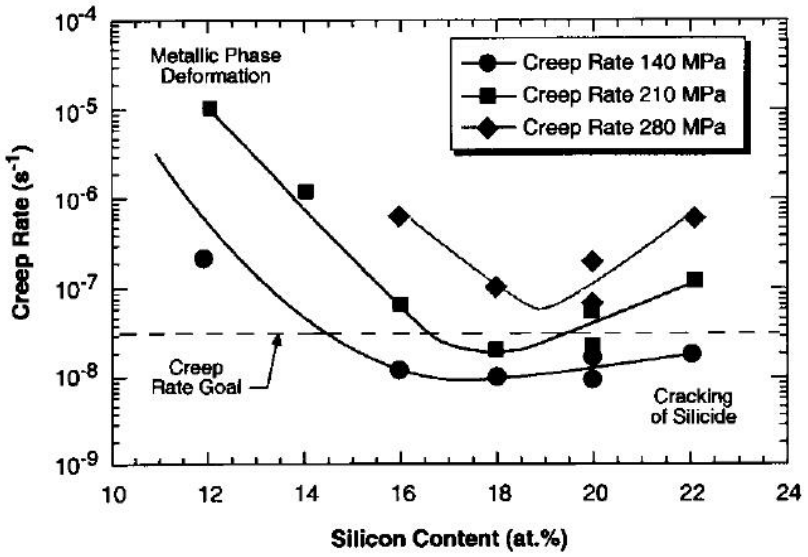


Figure 4.2 The effect of volume fraction of metal and silicide (determined by Si content) on secondary creep rate of Nb silicide based alloys for stresses of 140–280 MPa at 1200 °C [17].

As shown in Figure 4.2, the lowest creep rate was observed for quaternary composites with Si contents from 12 to 22 at.%, where the corresponding volume fraction of the metallic phase varied from ~ 0.70 to 0.30. Figure 4.2 shows that when the Si concentration is around 18 at.% creep rate is at a minimum. The corresponding volume fraction of the silicide phase at minimum creep rate is ~ 0.60 [17].

The data shown in Figure 4.2 also confirms that when the Si concentration was lower than 12 at.%, the creep behaviour of the metallic phase dominated the creep behaviour of the components; when the Si concentration was higher than 20 at.%, the creep behaviour was controlled by the damage of the silicide phase [63]. According to

Subramanian *et al*, the creep behaviour of monolithic Nb_5Si_3 is determined by the Nb diffusion in the Nb_5Si_3 phase [16].

Alloying addition such as Ti, Hf and Mo were also investigated for their effect on the compressive creep behaviour of directionally solidified Nb silicide based alloy at 1200 °C. The experimental results of these studies are summarised in Tables 4.1 and 4.2 for a range of Nb-Hf-Ti-Si alloys and Nb-8Hf-25Ti-16Si modified with Mo, Al and Cr [63].

Table 4.1 Secondary creep rates at 1200 °C for a range of Nb-Hf-Ti-Si alloys [63]

Composition (at.%)	Phases	140MPa Creep rate (s^{-1})	210MPa Creep rate (s^{-1})	280MPa Creep rate (s^{-1})
Nb-7.5Hf-16Si	Nb_{ss}, Nb_3Si	2.3×10^{-8}	4.0×10^{-8}	4.8×10^{-8}
Nb-7.5Hf-21Ti-16Si	Nb_{ss}, Nb_3Si	2.1×10^{-8}	3.2×10^{-8}	1.2×10^{-7}
Nb-7.5Hf-33Ti-16Si	Nb_{ss}, Nb_3Si, $(Ti, Hf)_5Si_3$	1.6×10^{-7}	3.9×10^{-6}	1.1×10^{-5}
Nb-12.5Hf-21Ti-16Si	Nb_{ss}, Nb_3Si, $(Ti, Hf)_5Si_3$	5.5×10^{-8}	4.8×10^{-6}	Failed
Nb-12.5Hf-33Ti-16Si	Nb_{ss}, Nb_3Si, $(Ti, Hf)_5Si_3$	3.8×10^{-5}	Failed	--

Table 4.2 Secondary creep rates at 1200 °C for Nb-8Hf-25Ti-16Si modified with Mo [63].

Composition	70MPa Creep Rate (s^{-1})	140MPa Creep Rate (s^{-1})	210MPa Creep Rate (s^{-1})	280MPa Creep Rate (s^{-1})
Nb-7.5Hf-16Si	--	2.3×10^{-8}	4.0×10^{-8}	4.8×10^{-8}
Nb-8Hf-25Ti-16Si	6.3×10^{-9}	1.2×10^{-8}	8.0×10^{-8}	Failed
Nb-3Mo-8Hf-25Ti-16Si	1.4×10^{-8}	2.5×10^{-8}	6.4×10^{-8}	Failed
Nb-9Mo-8Hf-25Ti-16Si	2.6×10^{-8}	2.2×10^{-7}	4.5×10^{-6}	Failed
Nb-8Hf-25Ti-2Al-2Cr-16Si	9.1×10^{-8}	Failed	--	--
Nb-16Si	1.7×10^{-9}	1.5×10^{-8}	4.9×10^{-8}	Failed

At a fixed stress, addition of 7.5 at.% Hf and 21 at.% Ti to Nb-16Si alloy gave lower creep rates than 12.5 at.% Hf and 33 at.% Ti. The concentration thresholds of Ti, Hf and Mo alloying addition to the Nb-18Si alloy to obtain the best secondary creep rate at the maximum stress were determined [63]. The data in Table 4.2 indicates that the Mo concentration should be below 3 at.%, and that Al and Cr alloying additions did

not benefit the creep behaviour of the Nb silicide based alloys The Ti addition should be controlled to avoid the formation of the hP16 type Ti_5Si_3 silicide which is detrimental to creep behaviour of Nb silicide based alloys. The Ti concentration should be limited to lower than 25 at.%.

The creep goal for engine materials was achieved in alloys of the Nb-Ti-Si-Hf system [63]. The creep behaviour needs to be balanced with other mechanical and environment properties in Nb silicide based alloys.

4.3 Fracture toughness

The fracture toughness goal for ultra high temperature materials in future aero engines is for the materials to have minimum toughness of 20 MPa$\sqrt{m}$. At room temperature, the fracture toughness of Nb_5Si_3 is ~ 3 MPa$\sqrt{m}$. Thus, the fracture toughness of Nb silicide based alloys is dominated by the volume fraction, geometry and fracture toughness of the ductile Nb_{ss} phase [64]. Chan studied the fracture mechanisms of the Nb silicide based alloys. The intermetallic phases in the composites are brittle and easily crack under pressure, while the ductile Nb_{ss} phase can blunt the cracks and bridge the micro cracks. However, high plastic constraint of the ductile phase would lead to failure of bridging [64].

Mendiratta and Dimiduk [19] assumed that ductile phase bridging is the main mode of toughening, and calculated the fracture toughness of the composites using the following equation:

$$K_c=\sqrt{\frac{E_c(1-f)K_m2}{E_m}+\chi f E_c \sigma_0 a_0} \quad (4.1)$$

where E_c is the elastic modulus of the composite, E_m and K_m are the elastic modulus and the fracture toughness of the intermetallic phase respectively, f, σ_0 and α_0 are the

volume fraction, unconstrained yield strength and radius of the Nb ductile phase respectively, and χ is the normalized work of rupture of the ductile phase undergoing deformation and fracture whilst constrained by surrounding intermetallic phase [19].

The fracture toughness of Nb silicide based alloys depends on the volume fraction of the ductile Nb_{ss} phase and their processing. Menditratta and Dimiduk investigated the room temperature fracture toughness of two binary Nb silicide based alloys with 10 at.% and 16 at.% Si using different processing and heat treatments [31]. As shown in Table 4.3, the fracture toughness of Nb-16Si was lower than that of the alloy Nb-10Si which is due to a smaller volume fraction of the Nb_{ss} phase in the former alloy. The extruded Nb-10Si alloy exhibited an increase in fracture toughness compared with the as cast condition. After 100 hours heat treatment at 1500 °C, the K_{IC} of the extruded Nb-10Si increased further.

Table 4.3 Fracture toughness of two alloys subject to different processing conditions [31]

Alloy	Processing/Heat treatment	K_{IC}
Nb-10Si	As-cast	9.5 MPa$\sqrt{m}$
	As-cast + 1500 °C/100h	9.7 MPa$\sqrt{m}$
	Extruded	16.4 MPa$\sqrt{m}$
	Extruded + 1500°C /100h	20.3 MPa$\sqrt{m}$
Nb-16Si	As cast	5.4 MPa$\sqrt{m}$
	As-cast + 1500°C /100h	7.7 MPa$\sqrt{m}$

According to Chan, the fracture toughness of Nb-Si *in situ* composites can be enhanced by alloying addition. Alloying elements increase the toughness of the ductile Nb_{ss} phase and thus improve the toughness of the composite [64].

Ti, Hf, Cr, Al are added to Nb silicide based alloys. These elements go in solution in Nb, and some have very large solid solubility in the Nb_{ss}. Chan reported that alloying additions generally improve the strength of Nb silicide based alloys at the expense of ductility and also increase the Ductile to Brittle Transfer Temperature (DBTT). Adding

5 at.% Al would raise the DBTT from -200 °C to -50 °C, and adding 3 at.% Cr would raise the DBTT to -100 °C [65]. Alloying with Ti and Hf on the other hand would not have a strong effect on the DBTT and would improve the fracture toughness [64, 66]. Bewlay *et al* compared the fracture toughness of binary Nb-Si, ternary Nb-Si-Ti, quaternary Nb-Si-Ti-Al, and higher order Nb-Si-Ti-Hf-Al-Cr alloys, as shown in Figure 4.3 [17].

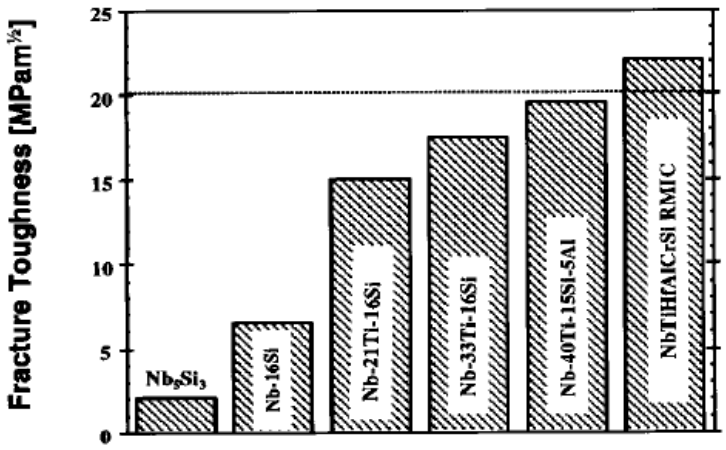


Figure 4.3 Fracture toughness of Nb-silicide based *in situ* composites from binary Nb-Si, ternary Nb-Ti-Si, quaternary Nb-Ti-Si-Al alloys, and the MASC alloy [17].

4.4 Strength

According to Bewlay *et al*, the high temperature (> 1000 °C) strength of Nb silicide based alloys is relatively good. Figure 4.4 compares the tensile strength of different materials as a function of temperature [17].

The Nb silicide based alloys and a Ni based alloy were compared and the results indicated that the high temperature strength of Nb silicide based alloys is better than Ni based superalloys above 1000 °C. However, at intermediate temperatures (400-1000 °C), the strength of Nb silicide based alloys still requires to be increased. It is possible to improve the strength of Nb silicide based alloys through solid solution strengthening and dispersion strengthening [1].

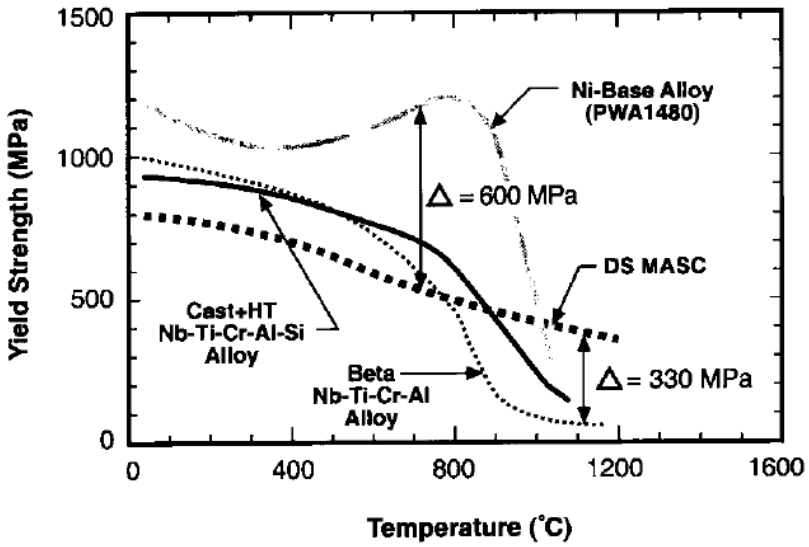


Figure 4.4 Tensile strength of Nb silicide based alloys and a Nb alloy and a Ni superalloy, as a function of temperature [17].

Part II
Present Studies

Chapter 5
Experimental procedures

5.1 Introduction

In this chapter, the experimental work from alloy selection to alloy characterisation is introduced. The studied alloys were prepared using vacuum arc melting equipped with water cooled copper hearth to obtain "button" shaped ingots. The heat treatment was carried out at 1500 °C or 1450 °C or 1200 °C for 100 hours in argon atmosphere and then furnace cooled to room temperature.

The cast and heat treated alloys were studied using XRD to identify the phases that existed in their microstructures and to study phase transformations to equilibrium.

The microstructures of the cast and heat treated alloys were also characterised using SEM microscopy. Back scattered images and EDS analysis were carried out to observe phases and identify their compositions.

The alloys were oxidised for 100 hours at 800 °C and 1200 °C. Oxidation experiments used thermo-gravimetric analysis equipment. The oxidised alloys were studied using SEM and EPMA-WDS.

5.2 Alloy selection

The selected alloys and their nominal compositions are shown in Table 5.1. The alloys ZX1 and ZX2 were firstly studied to help build the ternary Nb-Si-Sn system. The aforementioned two alloys were designed to be in the two phase and three phase regions of the Nb-Si-Sn ternary system in order to modify the iso-thermal section of the ternary phase diagram.

Table 5.1 The nominal compositions of the studied alloys.

Alloy code	Nominal Composition (at.%)					
	Nb	Ti	Si	Cr	Al	Sn
ZX1	Bal.	-	14	-	-	3
ZX2	Bal.	-	12.5	-	-	7.5
ZX3	Bal.	24	18	5	-	2
ZX4	Bal.	24	18	5		5
ZX5	Bal.	24	18	-	5	2
ZX6	Bal.	24	18	-	5	5
ZX7	Bal.	24	18	5	5	2
ZX8	Bal.	24	18	5	5	5

The alloys ZX3, ZX4, ZX5, ZX6, ZX7 and ZX8 were designed based on the reference alloy KZ3 (Nb-24Ti-18Si) [79]. The Ti addition was chosen to be 24 at.% because according to the literature Ti content up to this concentration can help to achieve balanced properties while maintaining high alloy solidus temperature. The Si addition was chosen to be 18 at.% because according to the literature, the best creep behaviour of Nb silicide based alloys is for 16< Si< 20 at.%. The 5 at.% Cr addition is made in Nb silicide alloys to improve their oxidation resistance. The Al addition was made at 5 at.% to offer oxidation resistance while keeping the DBTT below -50 °C. The alloys ZX3 and ZX4 allowed us to compare how the addition of Cr and Sn to the alloy KZ4 (Nb-24Ti-18Si-5Cr) affects microstructure and properties. The same was the case for the alloys ZX5 and ZX6, regarding the addition of Al and Sn to the alloy KZ7 (Nb-24Ti-18Si-5Al). In the alloys ZX7 and ZX8, 5Cr and 5Al were simultaneously present with Sn in order to understand how the synergy of Cr, Al and Sn affect microstructure and properties compared with the alloy KZ5 (Nb-24Ti-18Si-5Cr-5Al).

The Sn addition was set to 2 at.% and 5 at.% because according to the literature the Sn content is crucial for the stability of the Nb_3Sn intermetallic phase in the microstructure of Nb silicide based alloys. This A15 phase is considered to be beneficial to the oxidation resistance. In the alloys that contained 2 at.% Sn, the Nb_{ss} and Nb_5Si_3 were expected to form in the cast microstructure. In the cast alloys that

contained 5 at.% Sn, the Nb_{ss}, Nb_5Si_3 and Nb_3Sn phases were expected to exist in their microstructure. The $NbCr_2$ Laves phase was not expected to form in the cast alloys with 5 at.% Cr. However, owing to macrosegregation during solidification, some parts of the ingots contained more than 5 at.% Cr, which could lead to the formation of the $NbCr_2$ Laves phase.

5.3 Alloy preparation

The alloys were prepared using a vacuum (< 10^{-5} Mbar) arc melting furnace equipped with a water cooled copper hearth. The furnace and a schematic diagram are shown in Figure 5.2. High purity elements Nb (99.99%), Ti (99.99%), Si (99.99%), Al (99.99%), Cr (99.99%) and Sn (99.99%) were placed in the water cooled copper hearth and melted using a non-consumable tungsten electrode. Button ingots were produced using this method. Each charge was melted at least five times. To reduce the oxygen content in the furnace atmosphere, a Ti getter was melted before each melt of the alloy charge.

When preparing the alloys ZX1 and ZX2, it was found that the aforementioned method could not produce the desired ingot. This was because the melting temperature of Nb is 2468 °C and the melting temperature of Sn is 232 °C and thus there was Sn evaporation before Nb had even started to melt. To solve this problem, a new copper mould was designed and a new melting procedure was developed. The latter is described using Figure 5.2. The Sn was placed inside the mould and a Nb sheet was then placed on the top of the mould. The specially designed mould was placed on the copper hearth. After the vacuum of 10^{-5} Mbar was reached, the electrode was used to melt the Nb and then the liquid Nb dropped down the mould to melt the Sn. The Sn was trapped by Nb and formed the master alloy. The master alloy was then removed from the mould and re-melted in the water cooled copper hearth for five times to produce the alloys ZX1 and ZX2. The procedure for the vacuum arc melting is summarised in Figure 5.3.

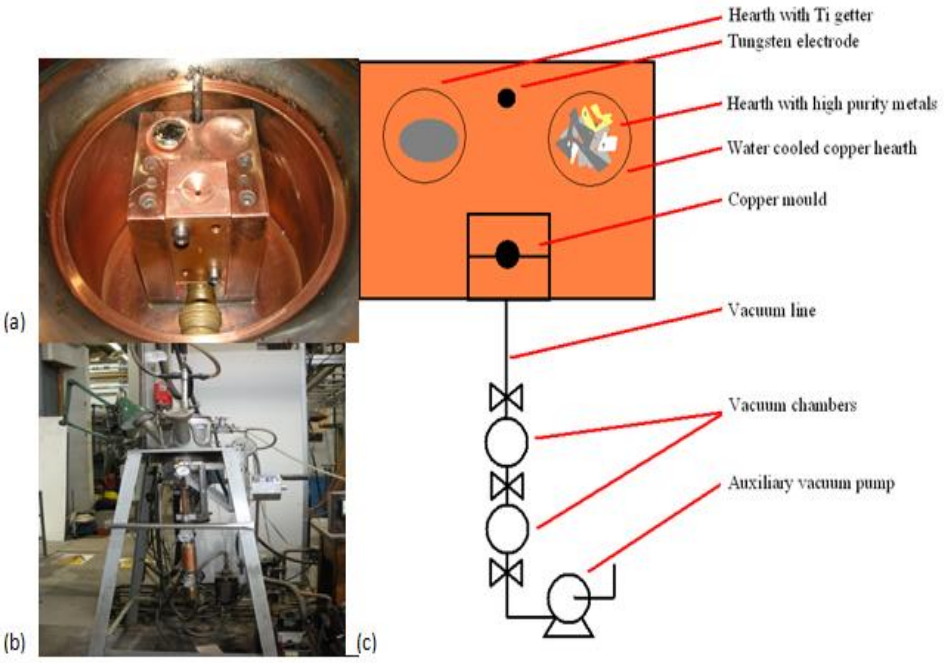


Figure 5.1 The vacuum arc melting furnace used in this research.

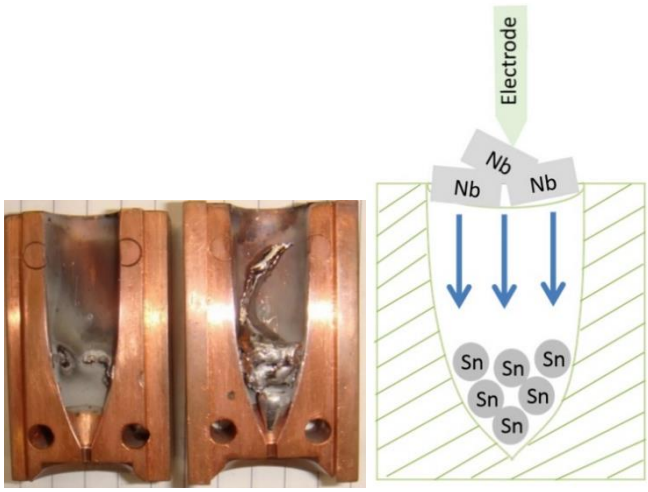


Figure 5.2 The mould used to produce the ingot of this research.

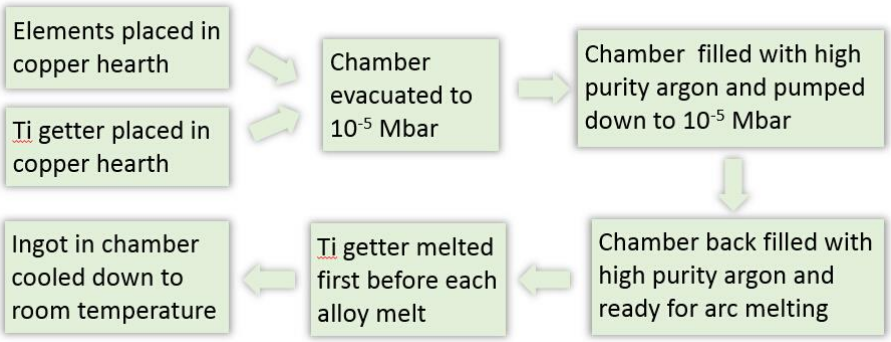


Figure 5.3 Schematic flow diagram of the vacuum arc melting operation procedure diagram.

5.4 Specimen preparation and heat treatments

Each alloy ingot was cut in quarters using a diamond blade. For the study of the alloys ZX1 and ZX2, the centre area of each quarter was sectioned using diamond blades for the study of the as cast and heat treated conditions (1200 °C and 1500 °C), see Figure 5.4 (a). For the alloys ZX3, ZX4, ZX5, ZX6, ZX7 and ZX8, the centre area of the two quarters was cut for the study of the as cast and heat treated alloys. In the other two quarters 3mm cubes were sectioned from the centre of the ingot, as shown in Figure 5.4(b).

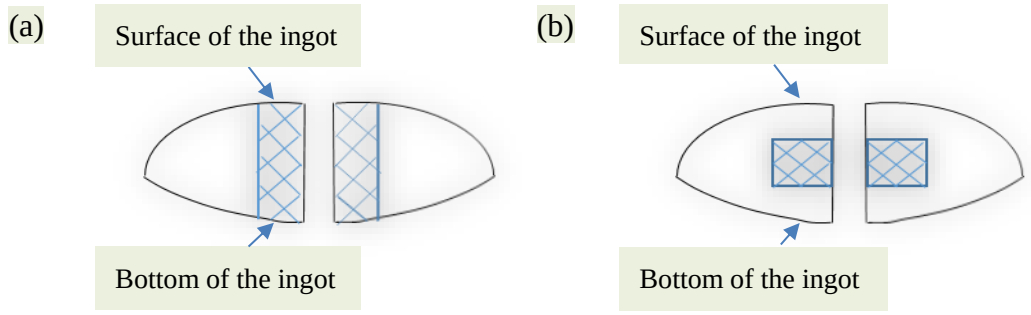


Figure 5.4 Schematic diagrams showing parts of the alloy ingots used to study the alloys (a) the highlighted areas were cut for the study of the as cast and heat treated alloys, (b) the highlighted areas were cut for the TG experiments at 800 °C and 1200 °C

For the heat treatment the specimen was wrapped in high purity Ta foil and then placed in an alumina boat filled with Ti sponge. The specimen was then located in the hot zone of a tube furnace and was heat treated under argon flow for 100 hours. The alloys ZX1 and ZX2 were heat treated at 1200 °C, 1500 °C and 1600 °C and the alloys ZX3, ZX4, ZX5 and ZX6 at 1500 °C. The alloys ZX7 and ZX8 were studied at 1450 °C as these two alloys were partially melted after the 1500 °C heat treatment.

For imaging and phase analysis, the alloy specimens were mounted in conductive bakelite, ground to 2400 grit and polished to 1/4 µm finish. The oxidised alloy specimens were mounted in cold resin, ground to 2400 grit and polished to 1/4µm finish, then carbon coated.

5.5 X-ray Diffraction (XRD)

A Siemens 5000 X-ray diffractometer with monochromatic CuKa (λ=1.540562 nm) radiation was used to identify the phases in the cast and heat treated alloys. The alloy specimen was ground to 1200 grit finish and scanned using 0.02° step. The alloys were scanned with two theta (θ) from 20-100°. The data was compared with the JCPDS (Joint Committee of Powered Diffraction Standard) cards to identify the phases.

5.6 Scanning Electron Microscopy (SEM)

5.6.1 Secondary electron and backscattered electron images

The SE (secondary electron) and the BSE (back scattered electron) images were taken using an Inspect F SEM with FEG (Field Emission Gun). This microscope is also equipped with EDS analysis. The 15KV and 3 µm spot size were applied when taking the SE and BSE images. The voltage was adjusted to 20KV for qualitative EDS analysis.

5.6.2 Quantitative EDS

The quantitative EDS was performed on a Philips 500 SEM and Joel 6400 SEM. In the former SEM, the ZAF correction (Z=atomic number, A=absorption, F=fluorescence) was applied to each analysis. Pure Co standard was used to calibrate the analyser every hour in order to maintain the beam current. At least 10 analyses were taken from each large area and phase. The maximum, minimum and average values and the standard deviation are shown in the results sections. During this research, the Philips 500 SEM was decommissioned. Its replacement, the Joel JSM 6400 SEM was fitted with an Oxford instruments INCA system for quantitative EDS analysis. The analyser was subjected to the XPP matrix correction. The data collected using the Inca software was consistent with the ZAF corrected data from the Philips 500 SEM. At least 10 EDS analyses were taken from each large area and phase. The data taken using the Joel JSM 6400 SEM is also presented with maximum, minimum

and average values and the standard deviation.

5.6.3 Qualitative X-ray elemental maps and line scans

X-ray elemental maps are a straight forward method to show the distribution of elements in a microstructure. For alloys that contain many phases, this method can easily illustrate the distribution of the phases. A Philips XF30 FEG SEM fitted with a Bruker Quantax analyser and ESPRIT software was used to take X-ray maps. This software contains a most comprehensive database including N and O light element lines which assisted the identification for nitrides and oxides in the alloys. For the alloys ZX7 and ZX8, apart from the X-ray elemental maps, X-ray line scans were also used to characterise element distribution in phases.

5.6.4 Electron probe microanalysis (EPMA)

EPMA with Wave Dispersive Spectrometry (WDS) was used to identify the phases in the oxidised specimens. A Cameca SX100 instrument with spatial resolutions of 1μm was used to obtain the data. The instrument calibration was carried out by analysing reference materials with known compositions. The reference materials and their composition used in this work are listed in Table 5.2. The data is presented with maximum, minimum and average value and the standard deviation. The data in chapters 7, 8 and 9 is rounded to the nearest hundredth.

Table 5.2 Standards and their compositions for calibrating the elements of the alloys for EPMA analysis.

Elements	Reference materials	Composition of the reference materials (wt.%)
Nb	Nbmet-Block7	Nb: 100%
Ti	Rutile-BL8	Ti: 59.34%, O: 39.89%, Mg: 0.01%, Fe: 0.59%, Nb: 0.17%
Si	Zircon-BL8	Si: 15.24%, Mn: 0.03%,Zr: 49.14%, Hf: 0.82%, O: 34.77%
Al	Spinel-BL8	Mg: 17.08%, Al: 37.93%, O:44.99 %
Cr	PuCr -BL8	Cr: 100%
Sn	Sn	Sn: 100%
O	Forsterite	O:45.5%, Mg:34.5%, Si:20.0%

5.7 Thermo-gravimetric analysis (TGA)

The thermo-gravimetric analysis (TGA) was carried out using a NETZSCH STA 449 F3 Jupiter thermal analyser supported by the NETZSCH proteus software. The instrument had a weight resolution of 0.1 µg over the entire weighing range (0-35000 mg). A 3 °C/min heating rate from room temperature to 800 °C or 1200 °C was used. 3 mm cubic specimens were cut from the cast alloy ingots (Figure 5.4) and were ground to 1200 grit on each surface. The surface area of the specimen was measured under an optical microscope.

The 100 hours TGA was carried out in static air at 800 °C or 1200 °C. The initial weight and the final weight of each specimen was recorded. The weight change data was analysed using the following equation:

$$ln(\delta w) = lnK + n\ ln\ t \tag{5.1}$$

where δw is the weight change per unit area, t is the reaction (oxidation) time and K and n are constants. The oxidation reaction kinetics could be linear parabolic or cubic depending on the value of the constant K and n.

The calculation of the rate of linear oxidation K_l and parabolic oxidation K_p used the equations:

$$K_l \cdot t = m / A \tag{5.2}$$

$$K_p \cdot t = (m / A)^2 \tag{5.3}$$

Where m is the weight change of the specimen, A is the surface area of the specimen and t is the oxidation time.

Chapter 6
The alloys Nb-14Si-3Sn (ZX1) and Nb-12.5Si-7.5Sn (ZX2)

6.1 Introduction

In this chapter, the effect of Sn on phase stability in two alloys of the Nb-Si-Sn ternary system, namely ZX1 (Nb-14Si-3Sn) and ZX2 (Nb-12.5Si-7.5Sn) was studied. The microstructures of the two alloys are compared with the most recently published Nb-Si-Sn phase diagram and with thermodynamic calculations.

6.2 Results

6.2.1 Alloy Nb-14Si- 3Sn (ZX1)

As cast: The average composition of the alloy, as determined by EDS analysis, was Nb-14.4Si-2.9Sn. The large area EDS data shown in Table 6.1 would suggest macro segregation of Si with its concentration varying between 11.7 at.% and 15.7 at.% in the microstructure. The Sn concentration in the alloy on the other hand did not vary significantly and was close to the nominal composition. The typical cast microstructure of the alloy ZX1 is shown in Figure 6.1 and is composed of the Nb_{ss} and Nb_{ss} + βNb_5Si_3 eutectic. This classification of the lamellar microstructure was based (i) on the XRD data, which showed the presence of βNb_5Si_3 (see below), (ii) on the EDS analysis of the dark contrast phase (see below) and (iii) data in the literature according to which the equilibrium L → Nb_{ss} + Nb_3Si eutectic can be replaced by the metastable L→ Nb_{ss} + βNb_5Si_3 eutectic, depending on solidification conditions [67] and/or alloying. The lamellar eutectic was very fine with nanoscale spacing between the eutectic constituents that could be distinguished only at high magnification (see Figure 6.2). The microstructure in the top and bulk areas was the

same (Figures 6.1 and 6.3) while the microstructure in the bottom area of the cast alloy where the melt was in contact with the crucible was different. As shown in Figure 6.4f, a coarser microstructure consisting of Nb_{ss} and βNb_5Si_3 dominated the area close to the bottom of the ingot. The Nb_5Si_3 phase in this region had formed in larger size (see Figure 6.4f) and could be easily analysed. There was a transition from the coarser two phase Nb_{ss} and Nb_5Si_3 microstructure to the "typical" microstructure seen in the bulk, see Figure 6.4b.

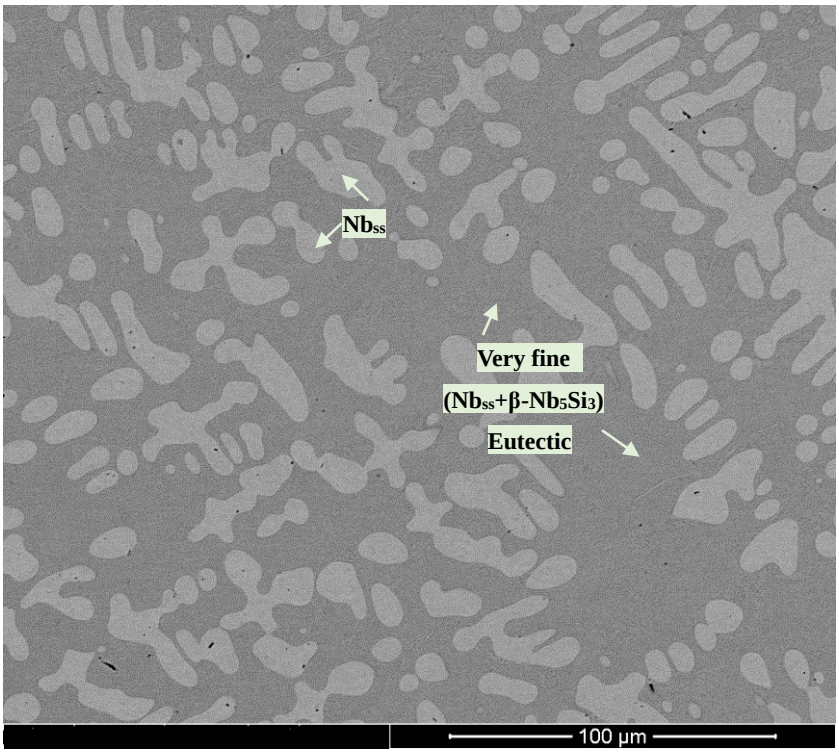


Figure 6.1 BSE image of the microstructure in the top area of the cast alloy ZX1.

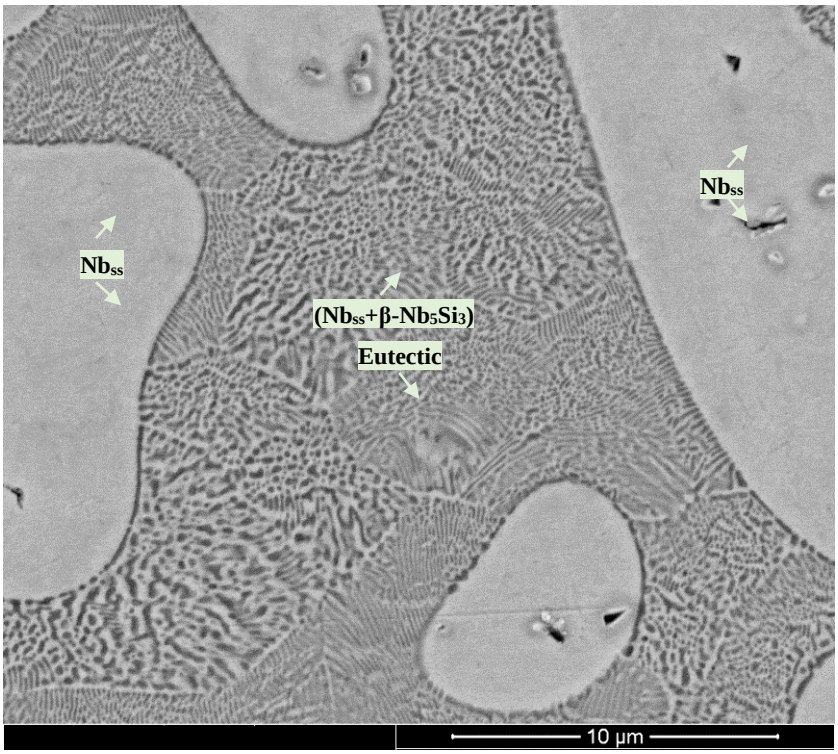


Figure 6.2 BSE image of the microstructure in the top area of the cast alloy ZX1 at high magnification showing the fine eutectic structure.

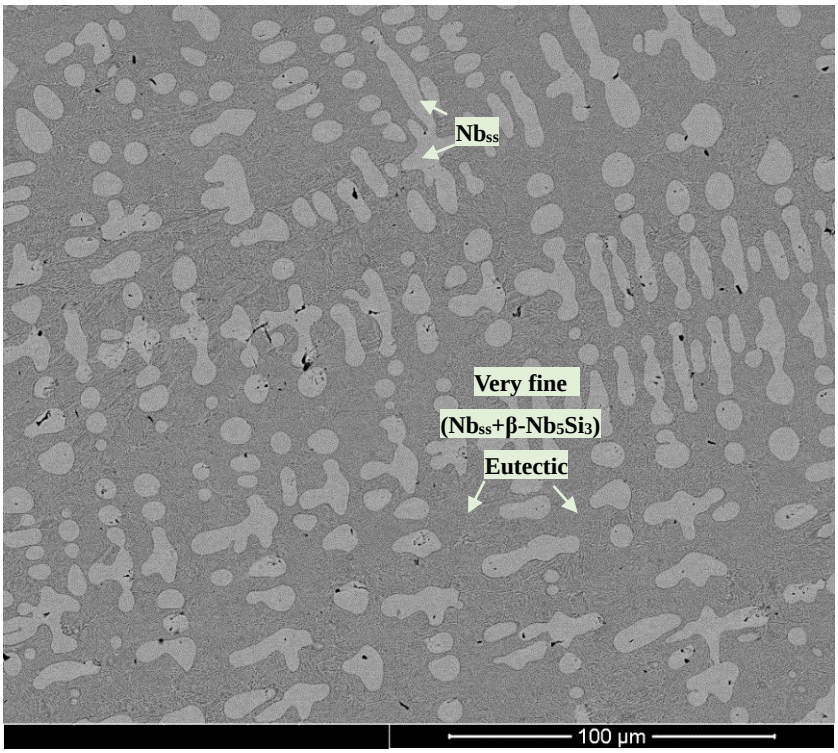
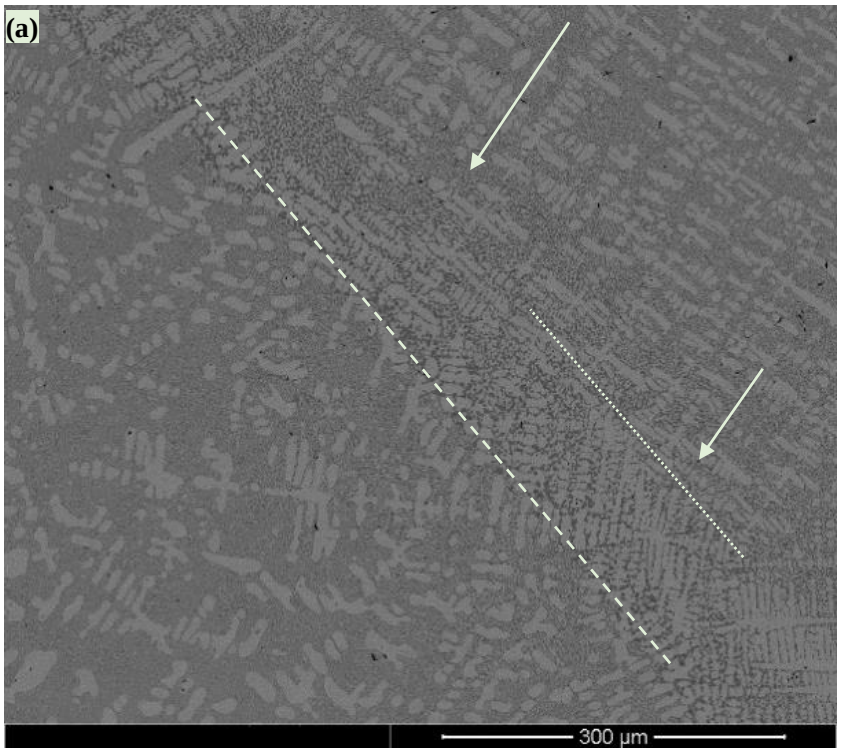
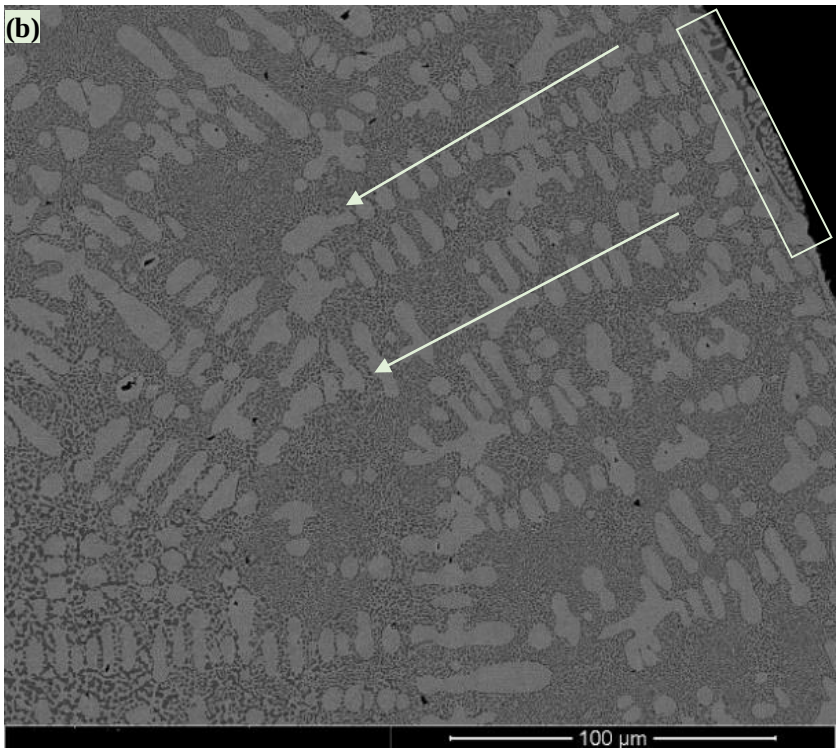
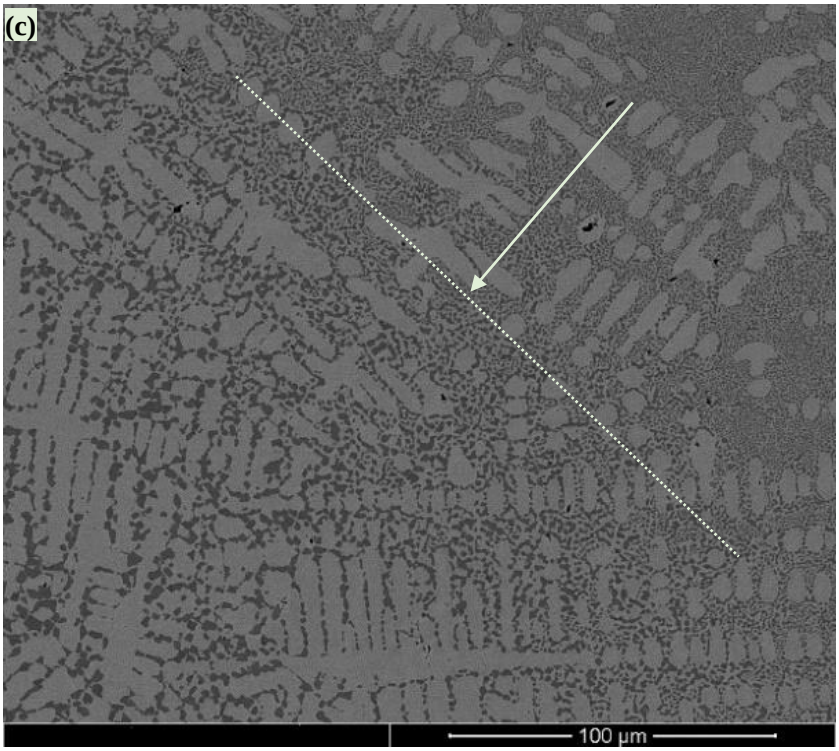
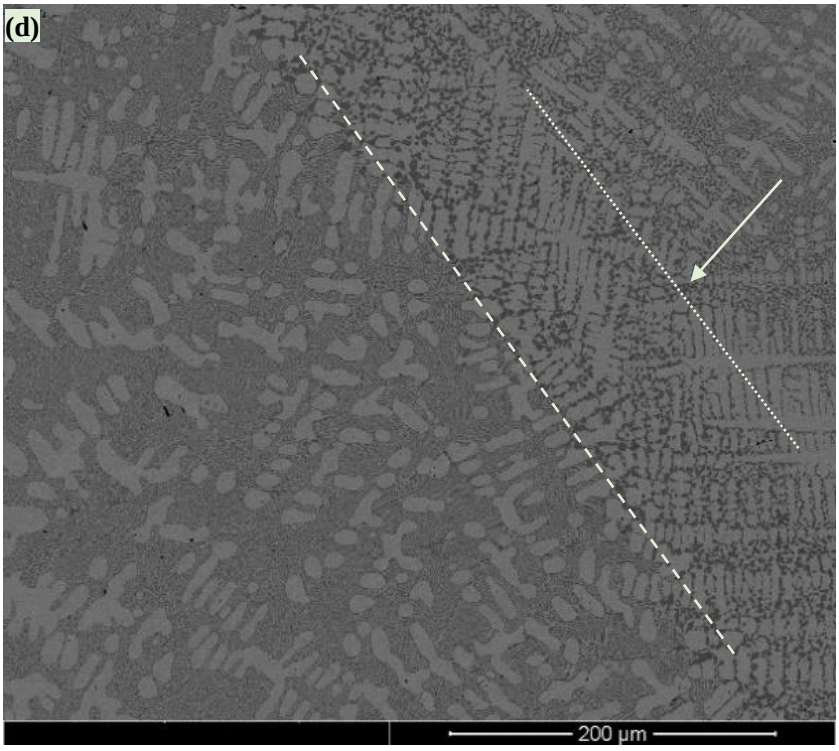


Figure 6.3 BSE image of the microstructure in the bulk of the cast alloy ZX1.


(a)
300 μm


(b)
100 μm


(c)
100 μm


(d)
200 μm

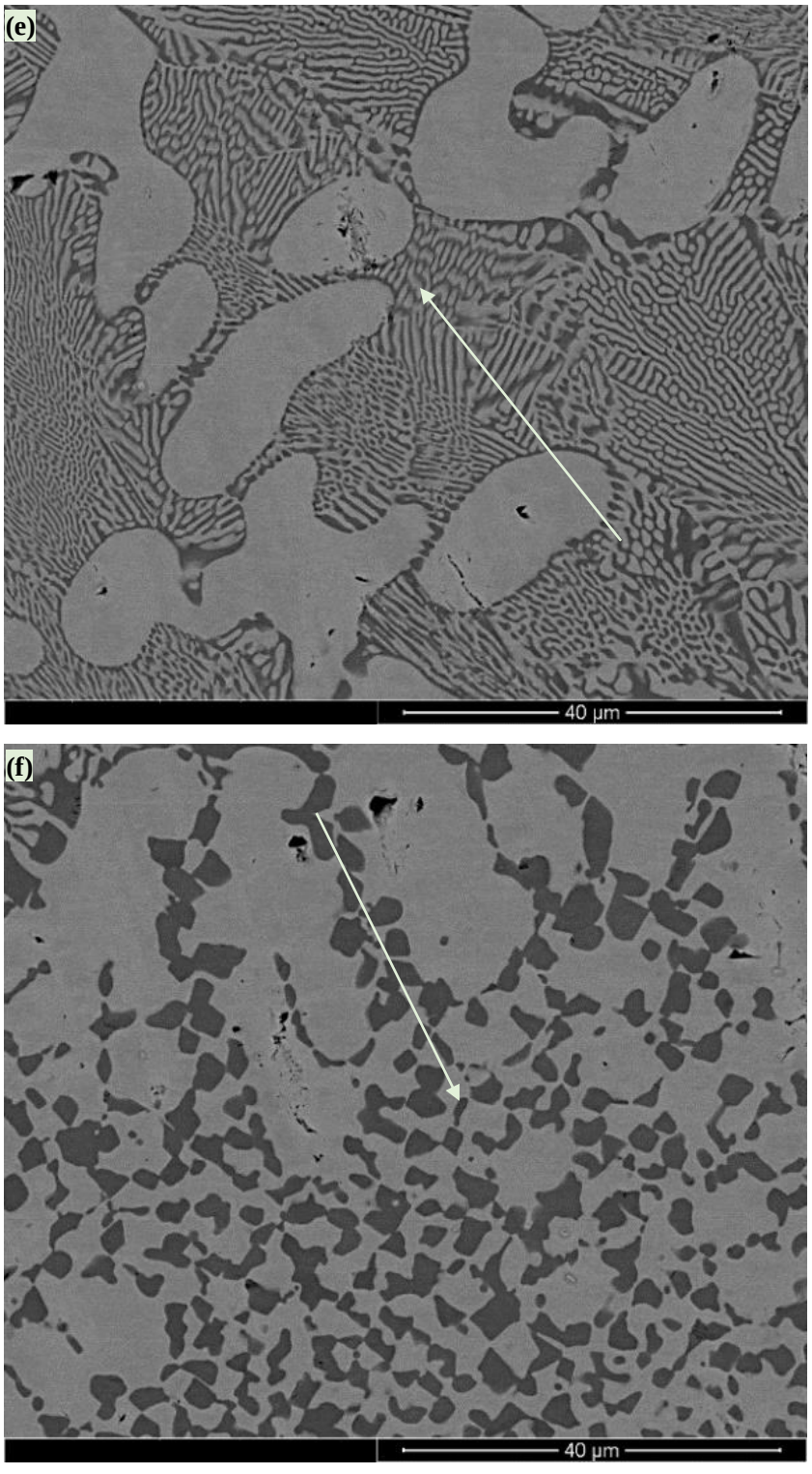


Figure 6.4 BSE images of the cast microstructure in the bottom area of the alloy ZX1. Arrows indicate direction away from (and perpendicular to) the crucible wall. Dashed lines indicate end of transition zone and dotted lines the start (see text). For rectangle see text.

The XRD data shown in Figure 6.5 confirmed that the Nb_5Si_3 in the cast

microstructure was the high temperature silicide βNb_5Si_3. The Nb_{ss} phase was also identified by XRD. In Table 6.1, the analysis data for the Nb_{ss} phase is from the bulk area of the ingot. In the Nb_{ss} the Si and Sn concentrations were 3.5 and 3.8 at.%, respectively, with Si + Sn = 7.3 at.%. The eutectic was also analysed in the bulk area and had Si + Sn = 18.3 at.%. The Nb_5Si_3 was analysed only in the bottom area where the coarser microstructure had formed. In the silicide, the Sn concentration was low (0.9 at.%), and the Si + Sn concentration was 37.4 at.%, which is close to the Si content of unalloyed βNb_5Si_3 (37.5 at.% - 40.5 at.%).

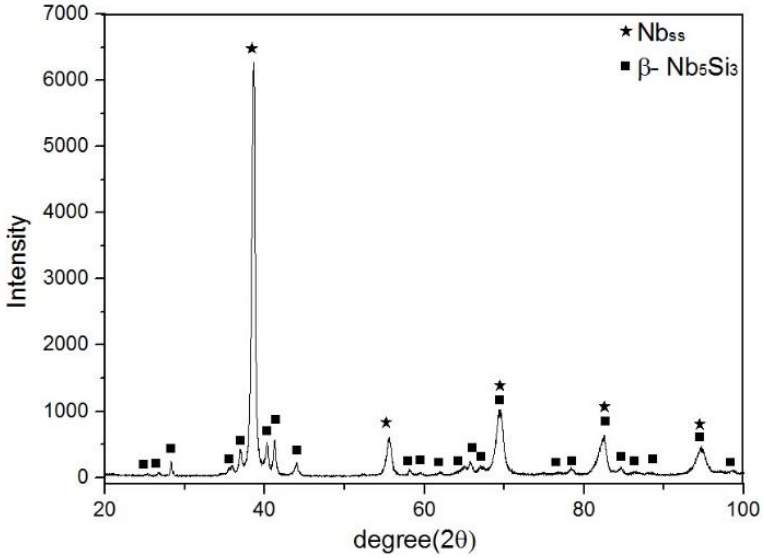


Figure 6.5 The XRD diffractogram of the cast alloy ZX1.

Heat treated at 1200 °C: After the 100 hour heat treatment at 1200 °C, the bulk microstructure of the alloy ZX1 heat treated specimen consisted of Nb_{ss} and the two phase Nb_5Si_3 + Nb_{ss} lamellar microstructure from the prior eutectic in the cast alloy. As shown in Figure 6.6, the lamellar microstructure had become coarser compared with the cast microstructure. This was also the case for the microstructure of that existed in the bottom area of the alloy ZX1 (Figure 6.7). The XRD data (Figure 6.8) suggested that αNb_5Si_3 and βNb_5Si_3 co-existed with the Nb_{ss} in the microstructure. Thus, the βNb_5Si_3 had not transformed to α-Nb_5Si_3 completely at this temperature.

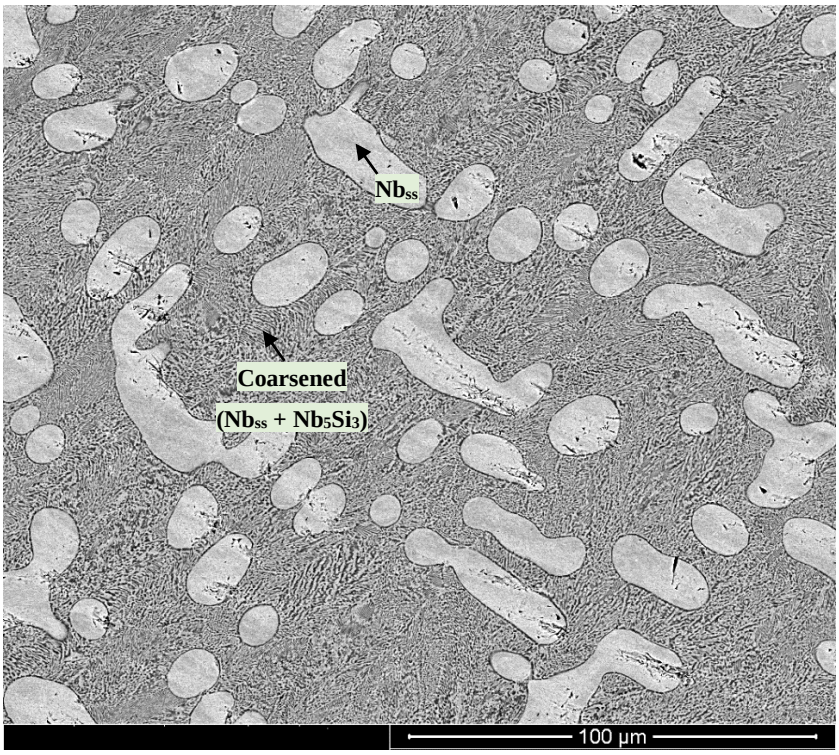


Figure 6.6 BSE image of the microstructure in the bulk area of the 1200 °C heat treated alloy ZX1 specimen.

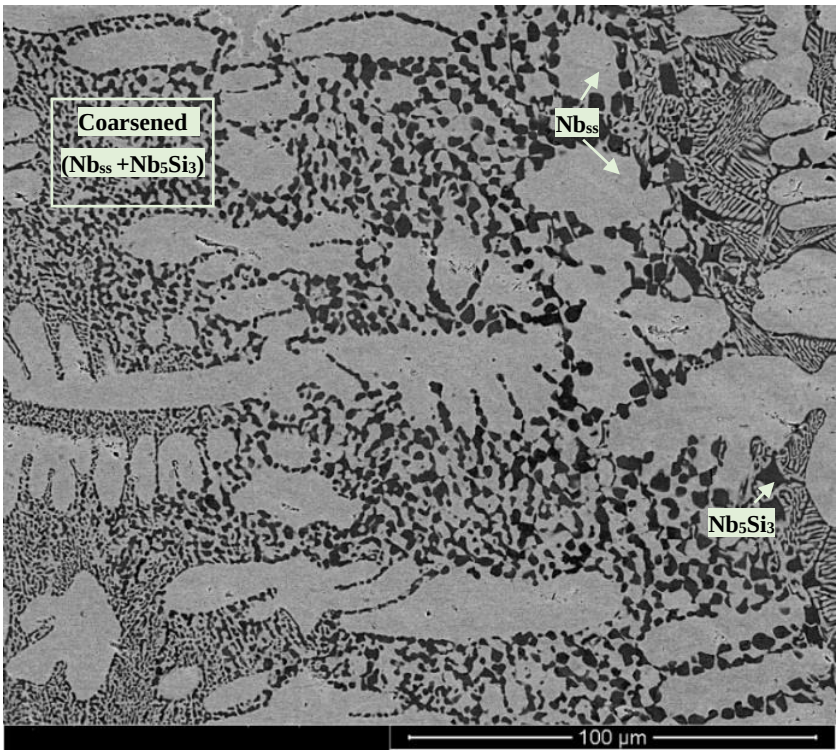


Figure 6.7 BES image of the microstructure in the bottom area of the 1200 °C heat treated alloy ZX1 specimen.

The EDS analysis data (Table 6.1) showed that the average composition of the heat treated specimen was very close to the nominal composition of the alloy and that there was still significant variation in the Si concentration in the microstructure. Within experimental error, the composition of the Nb_{ss} (3.2 at.% Si, 3.4 at.% Sn) had not changed compared with the cast alloy. The Si + Sn content of the lamellar microstructure had increased to 19.4 at.%, about 1 at.% higher than the cast alloy (18.4 at.%). The composition of the Nb_5Si_3 silicide was the same as in the cast alloy.

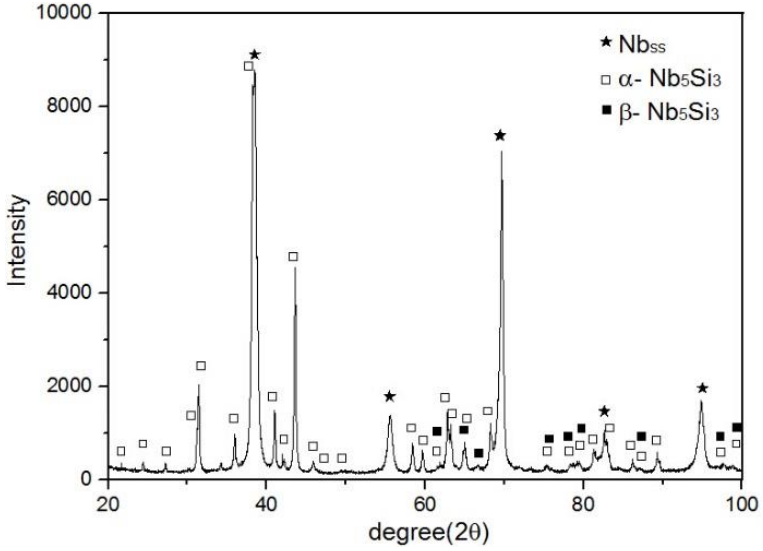


Figure 6.8 XRD diffractogram of the 1200 °C heat treated alloy ZX1 specimen.

Heat-treated at 1500°C: The microstructure of the heat treated alloy ZX1 is shown in Figures 6.9 and 6.10. Both the Nb_{ss} grains and the two phase Nb_{ss} + Nb_5Si_3 microstructure of the prior eutectic in the cast alloy were coarser compared with the heat treated alloy at 1200 °C. The lamellar microstructure that existed in the cast and 1200 °C heat treated alloys was almost not present at 1500 °C. It was also noticed that a bright contrast phase was present in the areas occupied by the eutectic in the cast microstructure. The contrast of this phase was similar to that of the intermetallic Nb_3Sn (see Figure 6.10). The latter was confirmed by the XRD, Figure 6.11. The Nb_3Sn formed with Nb_{ss} and Nb_5Si_3 a three phase region, possibly a Nb_{ss} + Nb_3Sn +

Nb_5Si_3 ternary eutectoid. Apart from identifying Nb_{ss} and Nb_3Sn, it was also confirmed that the βNb_5Si_3 had transformed to αNb_5Si_3 The Nb_3Sn grains were fine and dispersed in the three phase region, this made it hard to analyse their composition.

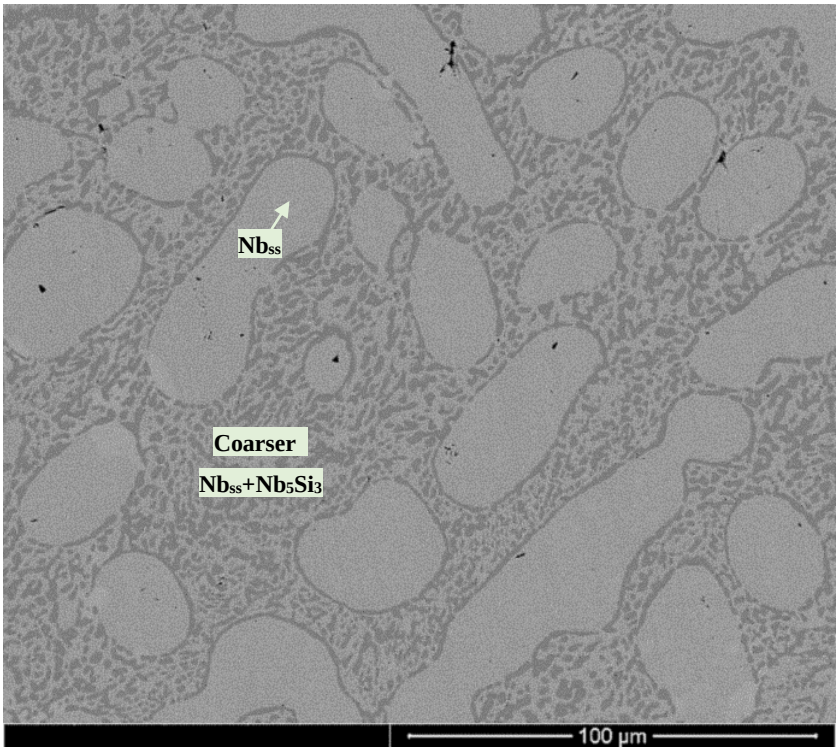


Figure 6.9 BSE image of the microstructure in the bulk area of the 1500 °C heat treated alloy ZX1 specimen.

The large area analysis showed that the average composition of the 1500 °C heat treated specimen was close to the nominal composition and that there was still variation in the Si concentration in the specimen. The Si concentration in the Nb_{ss} was reduced to 1.2 at.% and the Sn concentration was the same as in the 1200 °C heat treated specimen. The Si + Sn concentration in the αNb_5Si_3 was ~ 36.7 at.%, in accordance with Si content in unalloyed Nb_5Si_3. The Si + Sn concentration of the three phase microstructure was 20.3 at.%, higher than in the two phase microstructure in the cast and 1200 °C heat treated alloy.

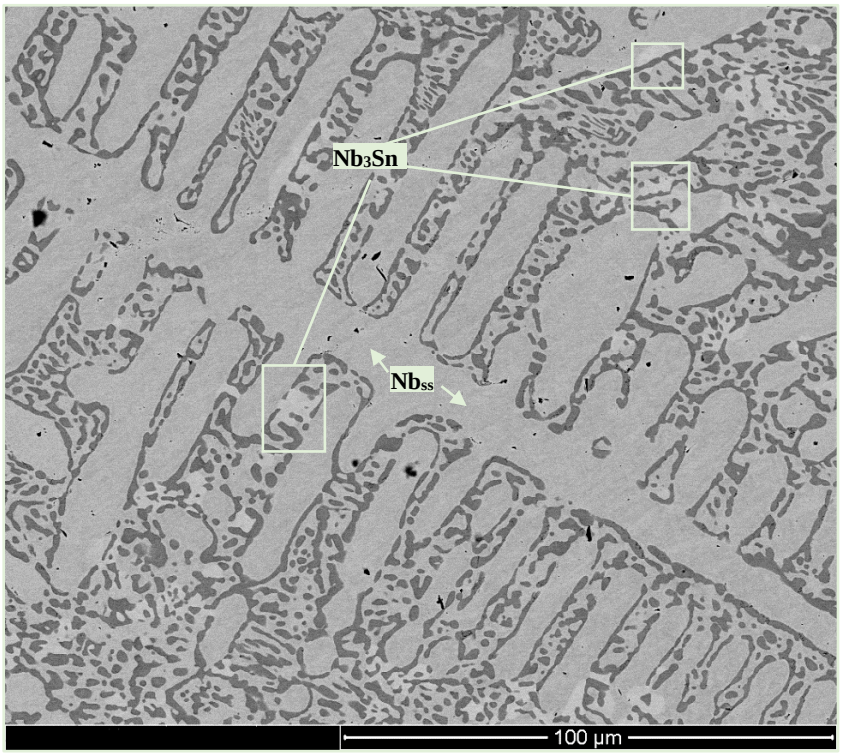


Figure 6.10 BSE image of the microstructure in the bulk area of the 1500°C heat treated alloy ZX1 specimen.

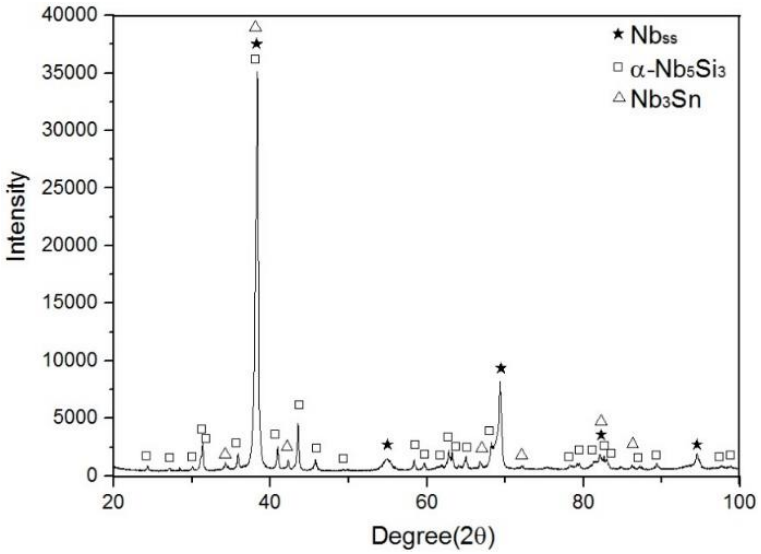


Figure 6.11 XRD diffractogram of the 1500 °C heat treated alloy ZX1 specimen.

Table 6.1 The EDS analysis data (at.%) of the cast and heat treated alloy ZX1.

As cast	Nb	Si	Sn
Top*	**82.6** ± 0.3	**14.5** ± 0.2	**2.9** ± 0.3
	82.2 - 83.1	*14.1 - 14.8*	*2.6 - 3.3*
Bulk*	**83.4** ± 1.2	**13.7** ± 1.2	**2.9** ± 0.1
	81.8 - 85.2	*11.7 - 15.2*	*2.8 - 3.2*
Bottom*	**81.9** ± 0.4	**15.1** ± 0.4	**3.0** ± 0.2
	81.4 - 82.7	*14.3 - 15.7*	*2.6 - 3.3*
Nb_{ss}	**92.7** ± 0.8	**3.5** ± 0.6	**3.8** ± 0.3
	91.4 - 93.4	*2.7 - 4.5*	*3.4 - 4.1*
Eutectic	**81.6** ± 0.8	**16.1** ± 0.9	**2.3** ± 0.2
	80.6 - 82.5	*15.1 - 17.4*	*2.0 - 2.5*
Nb_5Si_3	**62.6** ± 0.5	**36.5** ± 0.6	**0.9** ± 0.5
	62.0 - 63.5	*35.5 - 37.0*	*0.4 - 1.2*
1200°C	Nb	Si	Sn
Bulk*	**83.4** ± 1.5	**13.6** ± 1.6	**3.0** ± 0.3
	81.7 - 86.4	*10.3 - 15.1*	*2.4 - 3.3*
Nb_{ss}	**93.4** ± 0.5	**3.2** ± 0.4	**3.4** ± 0.2
	92.9 - 94.0	*2.7 - 3.6*	*3.0 - 3.7*
Lamellar	**80.6** ± 0.2	**17.0** ± 0.2	**2.4** ± 0.2
microstructure	*80.4 - 80.8*	*16.8 - 17.3*	*2.1 - 2.5*
Nb_5Si_3	**62.2** ± 0.5	**36.9** ± 0.5	**0.9** ± 0.1
	61.7 - 63.0	*36.0 - 37.4*	*0.9 - 1.0*
1500°C	Nb	Si	Sn
Bulk*	**82.6** ± 1.1	**14.3** ± 1.1	**3.1** ± 0.2
	81.4 - 84.5	*12.4 - 15.6*	*2.7 - 3.4*
Nb_{ss}	**95.5** ± 0.7	**1.2** ± 0.5	**3.3** ± 0.2
	94.7 - 96.0	*0.8 - 1.9*	*3.1 - 3.5*
Prior eutectic	**79.7** ± 0.9	**17.9** ± 1.1	**2.4** ± 0.5
areas	*78.9 - 80.9*	*16.6 - 19.1*	*1.9 - 3.1*
Nb_5Si_3	**63.3** ± 1.4	**35.7** ± 1.5	**1.0** ± 0.1
	62.1- 65.6	*33.4 - 37.0*	*0.8 - 1.1*

* Large area analysis

6.2.2 Alloy Nb-12.5Si-7.5Sn (ZX2)

As cast: The actual composition of the cast alloy determined by large area EDS analyses was Nb-12.3Si-7.5Sn. The compositions of different parts of the ingot are given in Table 6.2. There was weak macrosegregation of Si and Sn in the cast microstructure, with the difference between the maximum and minimum

concentration values being about 2 at.% for both elements. The XRD data for the cast alloy is shown in Figure 6.12 and would suggest the presence of Nb_3Sn, βNb_5Si_3 and Nb_{ss}, but with two peaks belonging only to the latter phase.

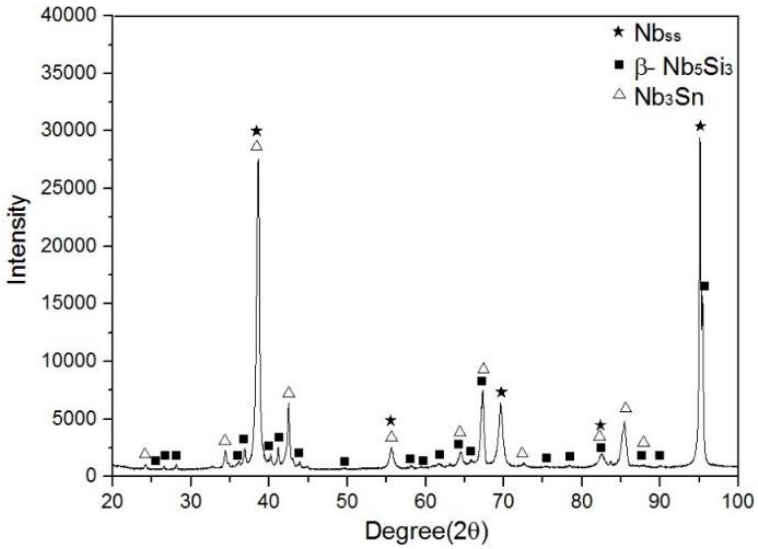


Figure 6.12 XRD diffractogram of the cast alloy ZX2.

The microstructure in the near bottom area of the ingot is shown in Figure 6.13. In Figure 6.13a the part of the ingot that was in contact with the Cu water cooled crucible is on the left hand side. Figure 6.13b shows details of the microstructure to the right of 6.13a. The microstructure consists of dendrites of a grey contrast phase which itself contains areas of brighter contrast, a black contrast phase and a lamellar microstructure in which one of the phases exhibits black contrast. The microstructure in the bulk of the cast ingot is shown in Figure 6.14 and consists of the grey contrast phase and fine lamellar microstructure in which one of the phases exhibits black contrast. The microstructure in areas near the top of the ingot is shown in Figure 6.15. The microstructure in the top was essentially the same as in the bulk (compare Figures 6.15a and 6.14) and the lamellar structure observed in-between the grey contrast phase exhibited similar features to those seen in Figure 6.13b. In the high magnification image in Figure 6.15c the thin lamellar in the black contrast phase exhibits two contrasts, one slightly brighter than the other.

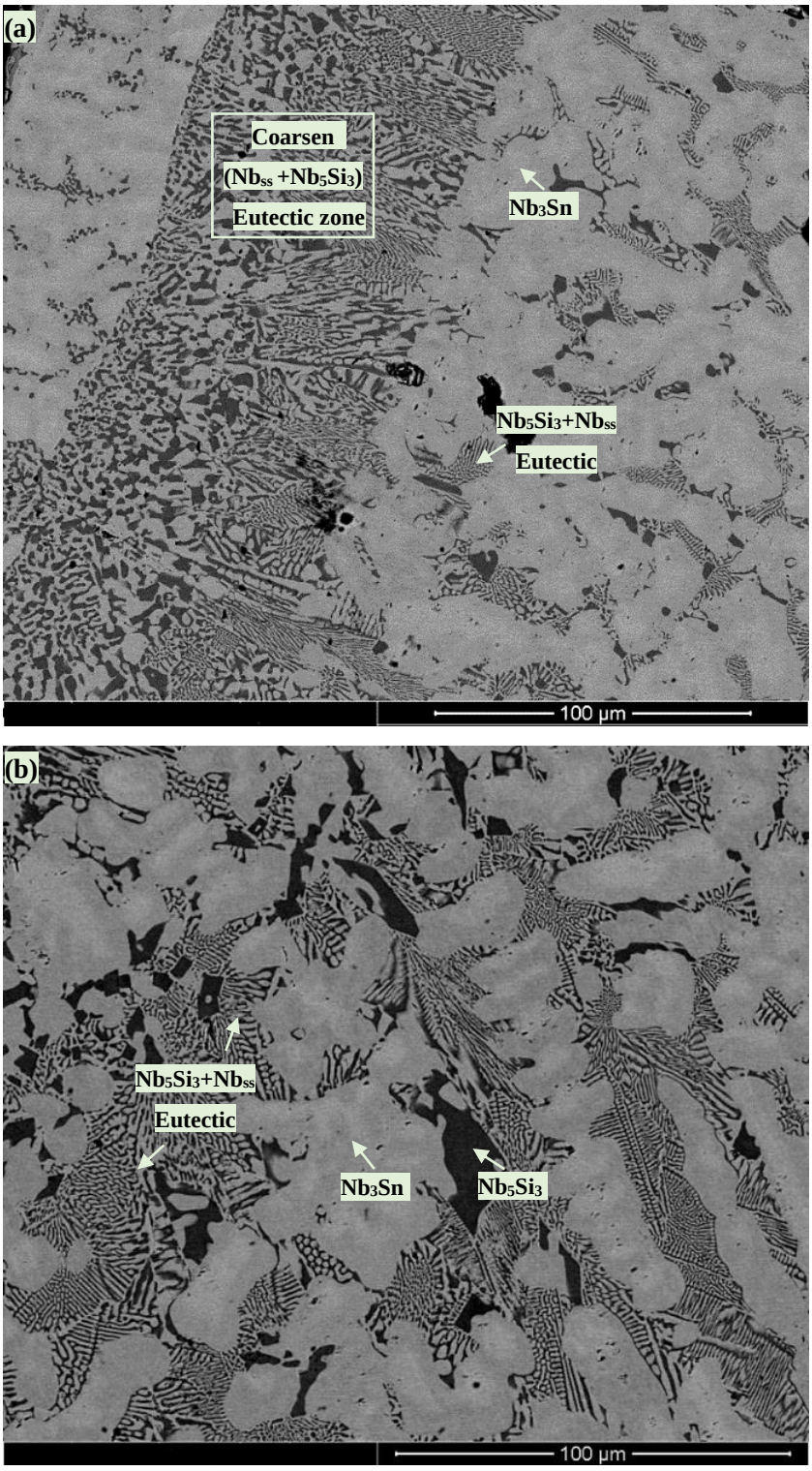


Figure 6.13 BSE images of the microstructure in the bottom area of the cast alloy ZX2.

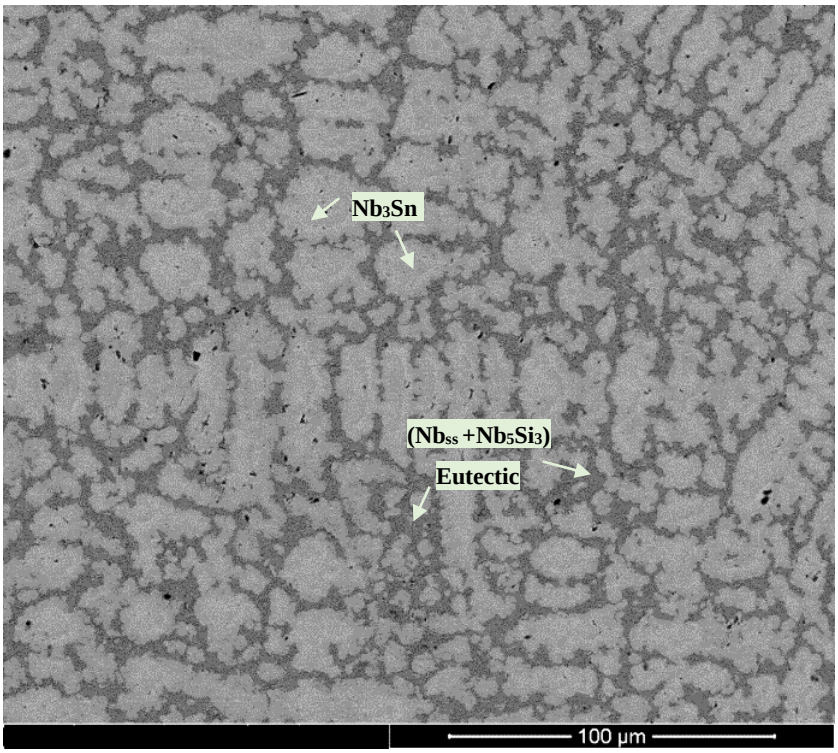
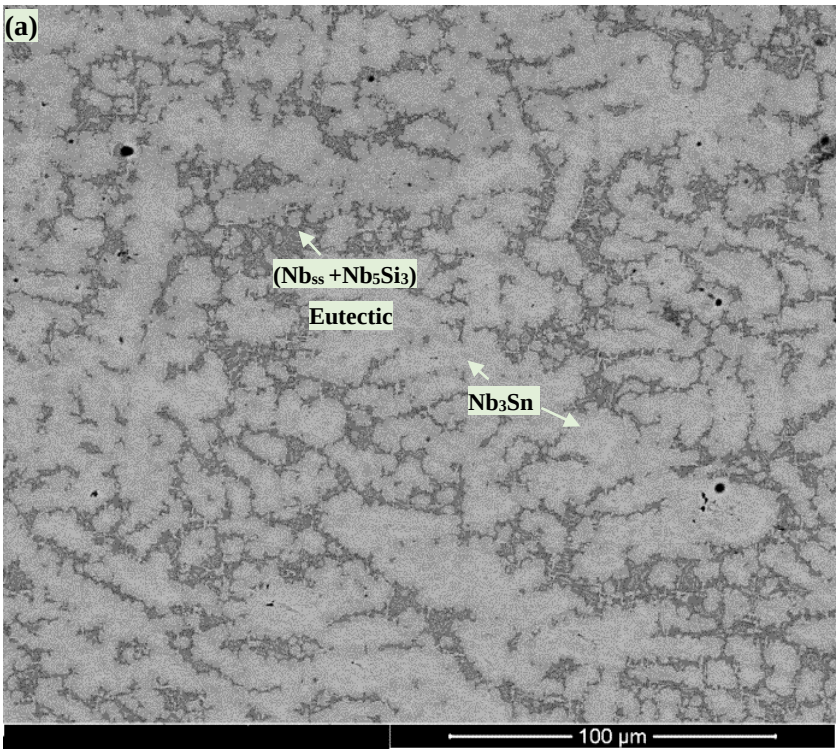
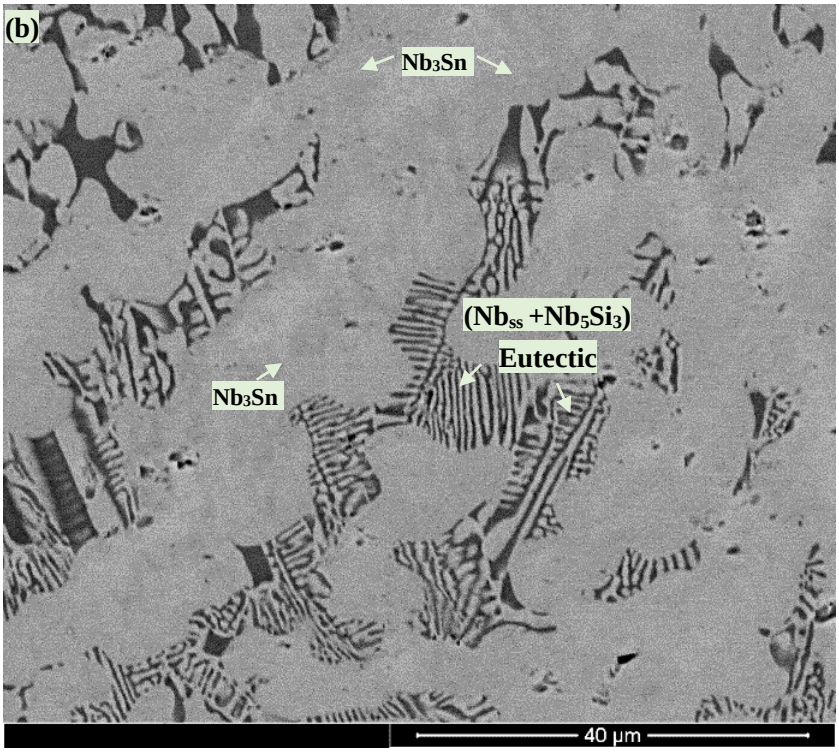


Figure 6.14 BSE image of the microstructure in the bulk area of the cast alloy ZX2.

The compositions of the phases are given in Table 6.2. The grey contrast phase is the Nb_3Sn with average Si + Sn = 19.4 at.%, and in the range 19.0 to 19.7 at.%. This is consistent with the XRD data, and the Sn and Si solubilities in Nb_3Sn [29]. The black contrast phase is the Nb_5Si_3 with Si + Sn = 37.8 at.%, consistent with the Si content of the un-alloyed silicide. The composition of the lamellar structure is also given in Table 6.2, where it is indicated as eutectic and has Si + Sn = 18.3 at.%. The reasons why the term eutectic is used and the phases that make up the eutectic will become clear in the discussion. At this stage it is enough to say that more microstructural data is required to help us with our reasoning about the eutectic because the high concentration of Sn in this alloy makes it extremely difficult to distinguish between the Nb_{ss} and Nb_3Sn phases using atomic number contrast in the SEM and the scale of the eutectic is so fine that EDS analysis of its individual phases is not possible.


(a)
(Nbss +Nb5Si3)
Eutectic
Nb3Sn
100 μm


(b)
Nb3Sn
(Nbss +Nb5Si3)
Eutectic
Nb3Sn
40 μm

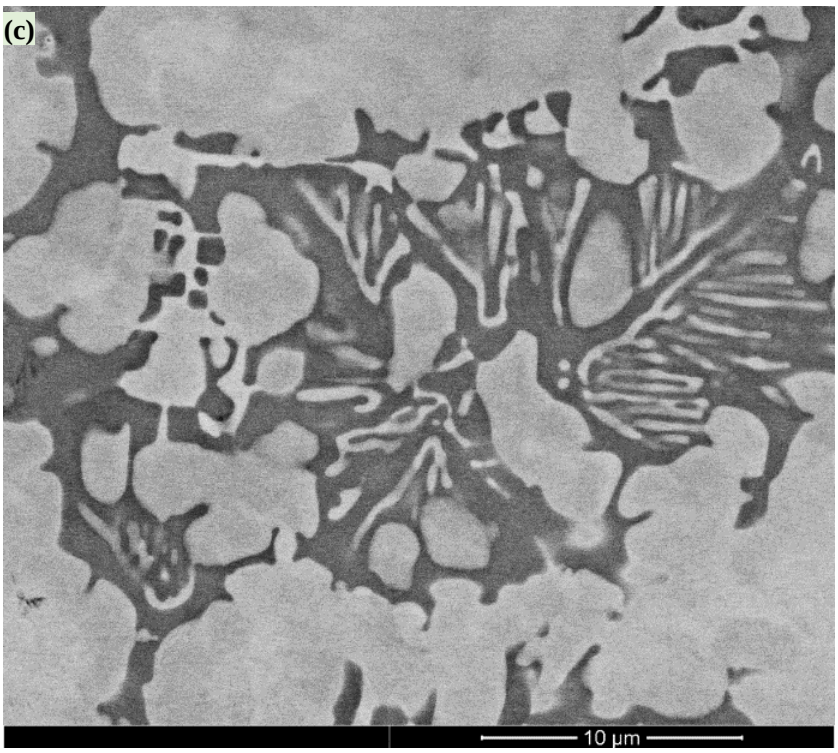


Figure 6.15 BSE images of the microstructure in the top area of the cast alloy ZX2.

Heat treated at 1200°C: The average composition of the heat treated specimen is given in Table 6.2. The concentrations of Si and Sn, within experimental error, are close to the nominal composition and the chemical inhomogeneity of Si and Sn has been reduced compared with the cast alloy. The XRD data is given in Figure 6.16 and would suggest the presence of Nb_{ss}, αNb_5Si_3 and Nb_3Sn in the microstructure. In the diffractogram there are two peaks that correspond only to the Nb_{ss}. The XRD data also indicates that the transformation of βNb_5Si_3 to αNb_5Si_3 was completed during this heat treatment.

The microstructure in the bulk of the heat treated specimen is shown in Figure 6.17. There was some coarsening of the lamellar microstructure (compare Figures 6.17a and 6.14) with different contrasts exhibited by the phases in the lamellar colonies (Figures 6.17b and c). The latter is attributed to the partitioning of Sn. The microstructure in the bottom of the heat treated specimen is shown in Figure 6.18

and also confirms that some coarsening had occurred in the lamellar colonies (compare Figures 6.18 and 6.13a). In the lamellar microstructure the thin lamellae of one phase exhibit brighter contrast than the remnants of the dendrite arms of the grey phase, a feature that was also noted in the cast alloy (see Figure 6.13b).

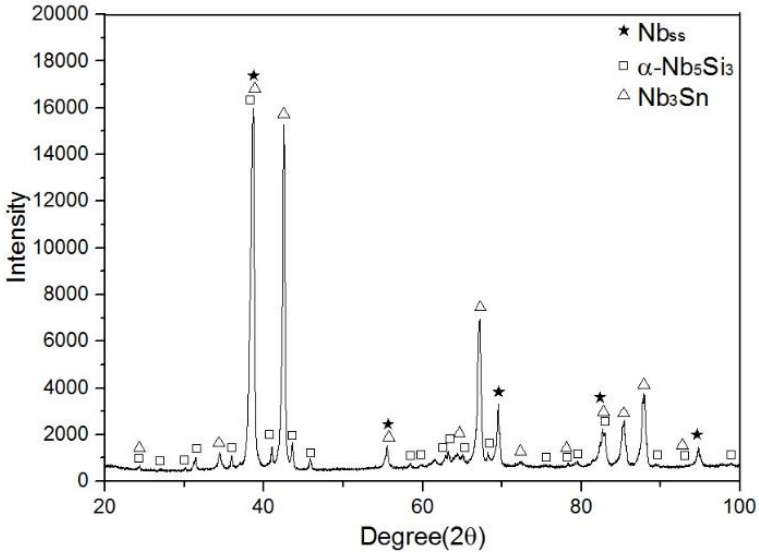
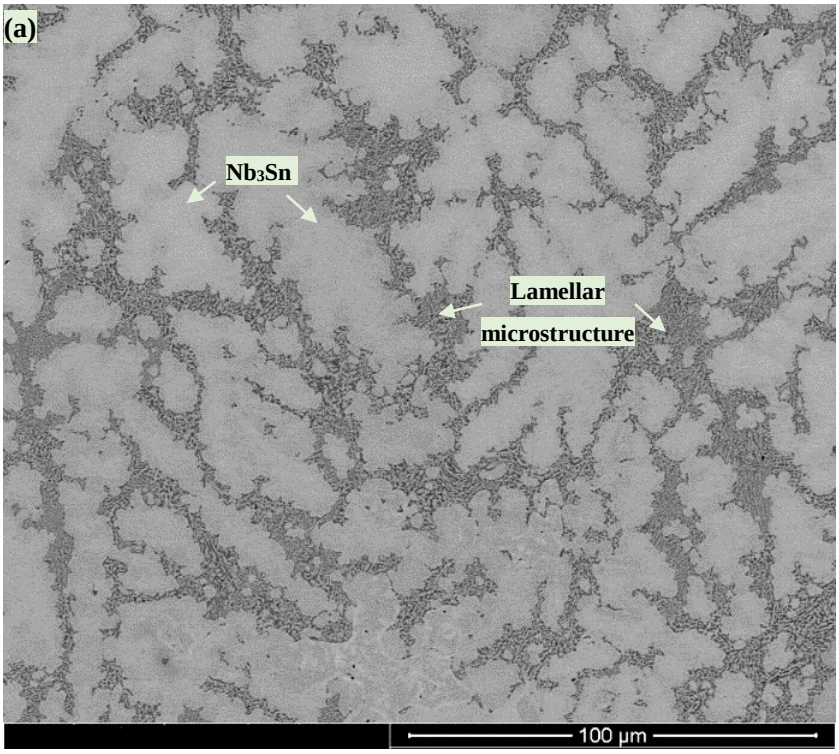


Figure 6.16 XRD diffractogram of the 1200 °C heat treated alloy ZX2.



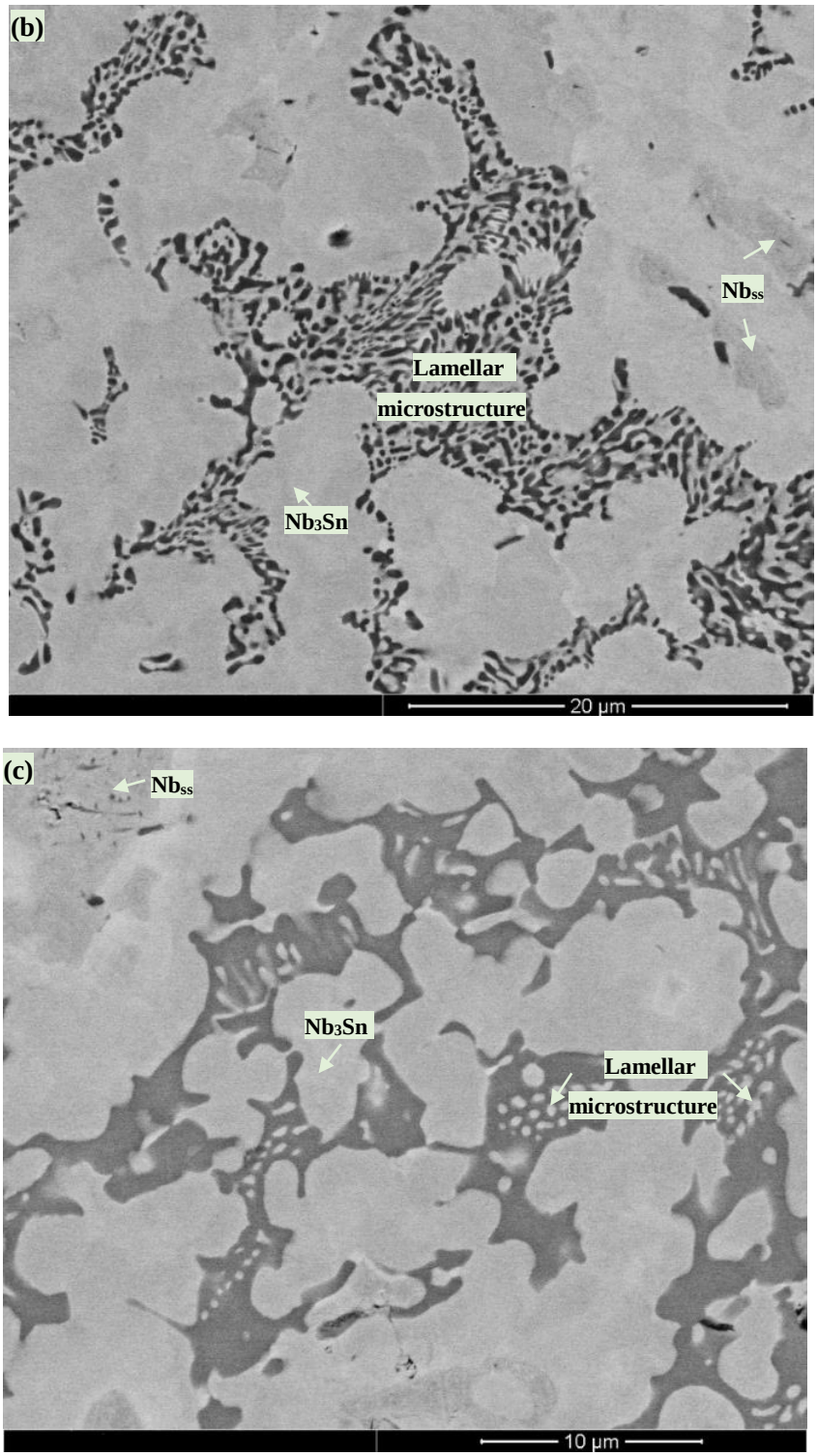


Figure 6.17 BSE images of the microstructure in the bulk area of the 1200°C heat treated alloy ZX2.

The compositions of the phases are given in Table 6.2. The grey contrast phase is the Nb_3Sn with average Si + Sn = 18.4 at.%, and in the range 18.1 to 18.9 at.%. This is

consistent with the XRD data, and the Sn and Si solubilities in Nb_3Sn [29]. The black contrast phase is the Nb_5Si_3 with Si + Sn = 37.4 at.%, essentially the same as in the cast alloy and consistent with the Si content of the un-alloyed silicide. The composition of the lamellar microstructure is also given in the Table 6.2, and has Si + Sn = 20.2 at.%, almost 2 at.% higher than the cast alloy. It should be noted that a shift towards higher Si + Sn was also noted for the Nb_{ss} + Nb_5Si_3 lamellar microstructure in the 1200 °C heat treated specimen of the alloy ZX1 (see Table 6.1). The reason why the phases that make up the lamellar microstructure in alloy ZX2 heat treated at 1200 °C are not specified at this stage of the presentation of the results will become clear in the discussion. It is enough to say that the atomic number contrasts exhibited by the phases in the lamellar microstructure (Figures 6.17b and c) suggest further partitioning of Sn. Unfortunately, as was the case for the cast alloy, the scale of the thin lamellae with different scales of grey contrast was so fine that EDS analysis of its individual phases was not possible.

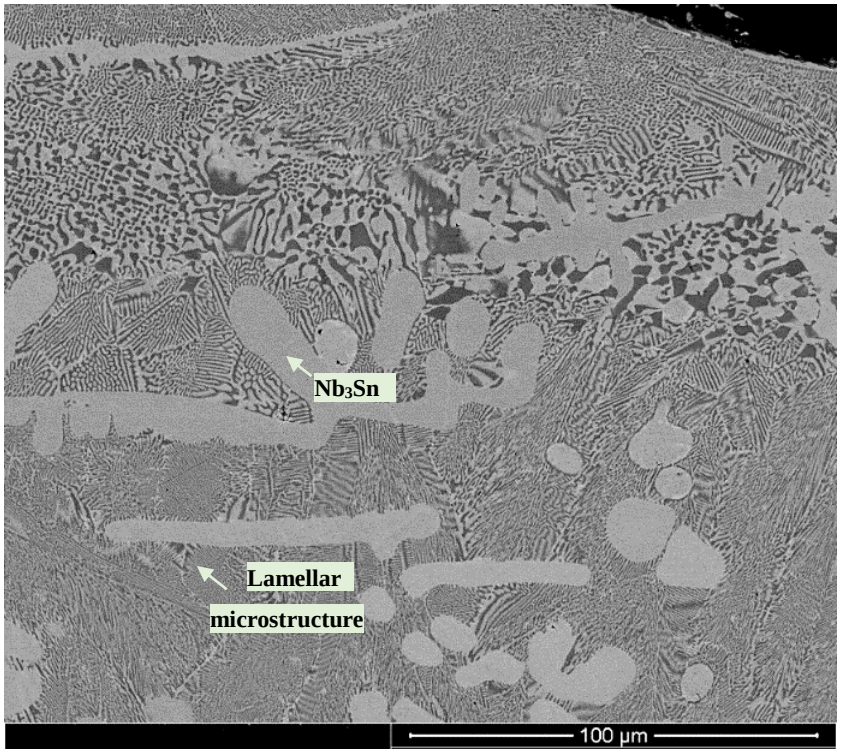


Figure 6.18 BSE image of the microstructure in the bottom area of the 1200 °C heat treated alloy ZX2 specimen.

Heat treated at 1500 °C: The average composition of the heat treated specimen is given in Table 6.2. The concentrations of Si and Sn, within experimental error, are close to the nominal composition and the chemical inhomogeneity of Si and Sn similar to the 1200 °C heat treated alloy specimen. The XRD data is given in Figure 6.19 and would suggest the presence of Nb_{ss}, αNb_5Si_3 and Nb_3Sn in the microstructure. In the diffractogram there are four peaks that correspond only to the Nb_{ss}. The XRD data also confirms the transformation of βNb_5Si_3 to αNb_5Si_3.

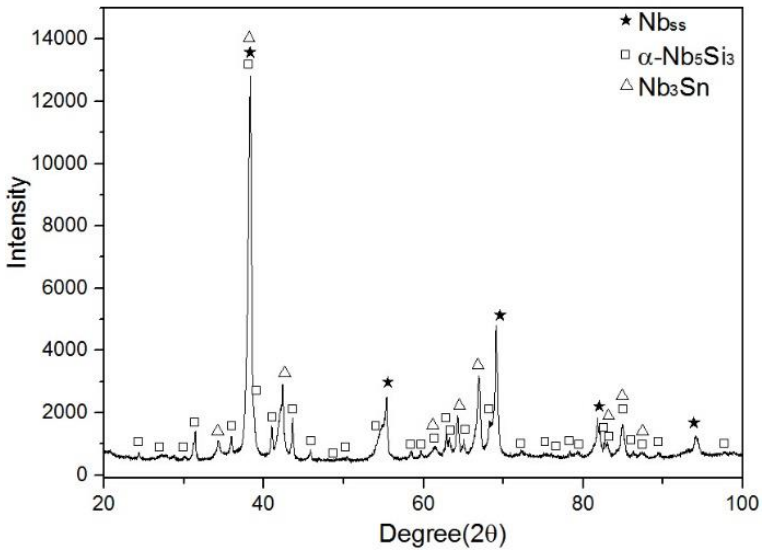


Figure 6.19 XRD diffractogram of the 1500 °C heat treated ZX2.

The microstructure in the bulk of the heat treated specimen is shown in Figure 6.20. There was further coarsening of the areas that were occupied by the lamellar microstructure (compare Figures 6.20a with Figures 6.17a and 6.14) with different contrasts exhibited by the phases in the former lamellar colonies (Figure 6.20a and b). There was also formation of a distinct darker grey contrast phase in the bulk of the Nb_3Sn. All the above are attributed to the partitioning of Sn. Even though Figure 6.20a would suggest two phases, one of dark contrast and one of black contrast in the former lamellar colonies, Figure 6.20b shows that the partitioning of solute (Sn) in these areas was still in progress even after 100h at 1500 °C, as the microstructure

shows thin lamellae of dark grey contrast surrounding a brighter contrast lamellae.

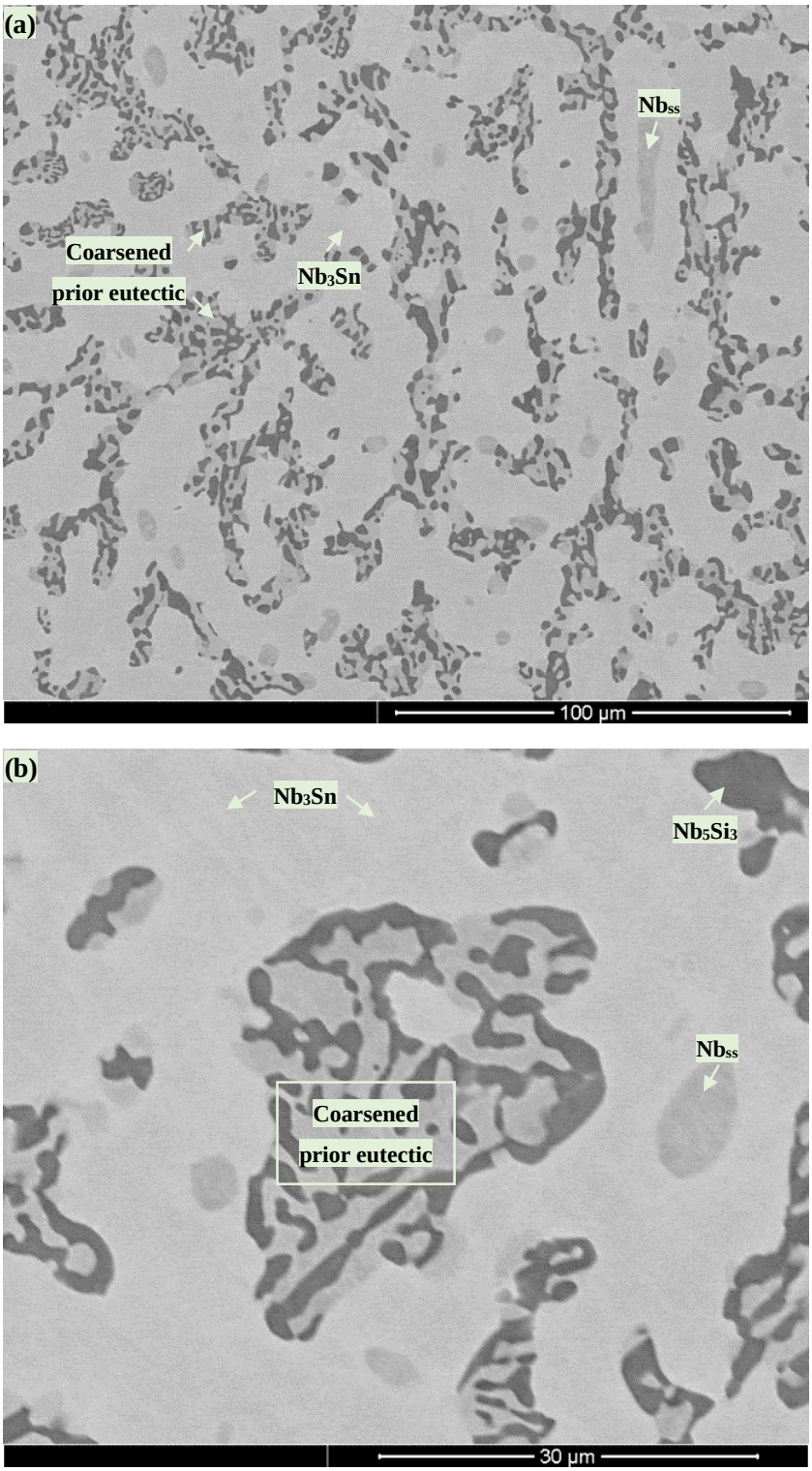


Figure 6.20 BSE images of the microstructure in the bulk area of the 1500 °C heat treated alloy ZX2 specimen.

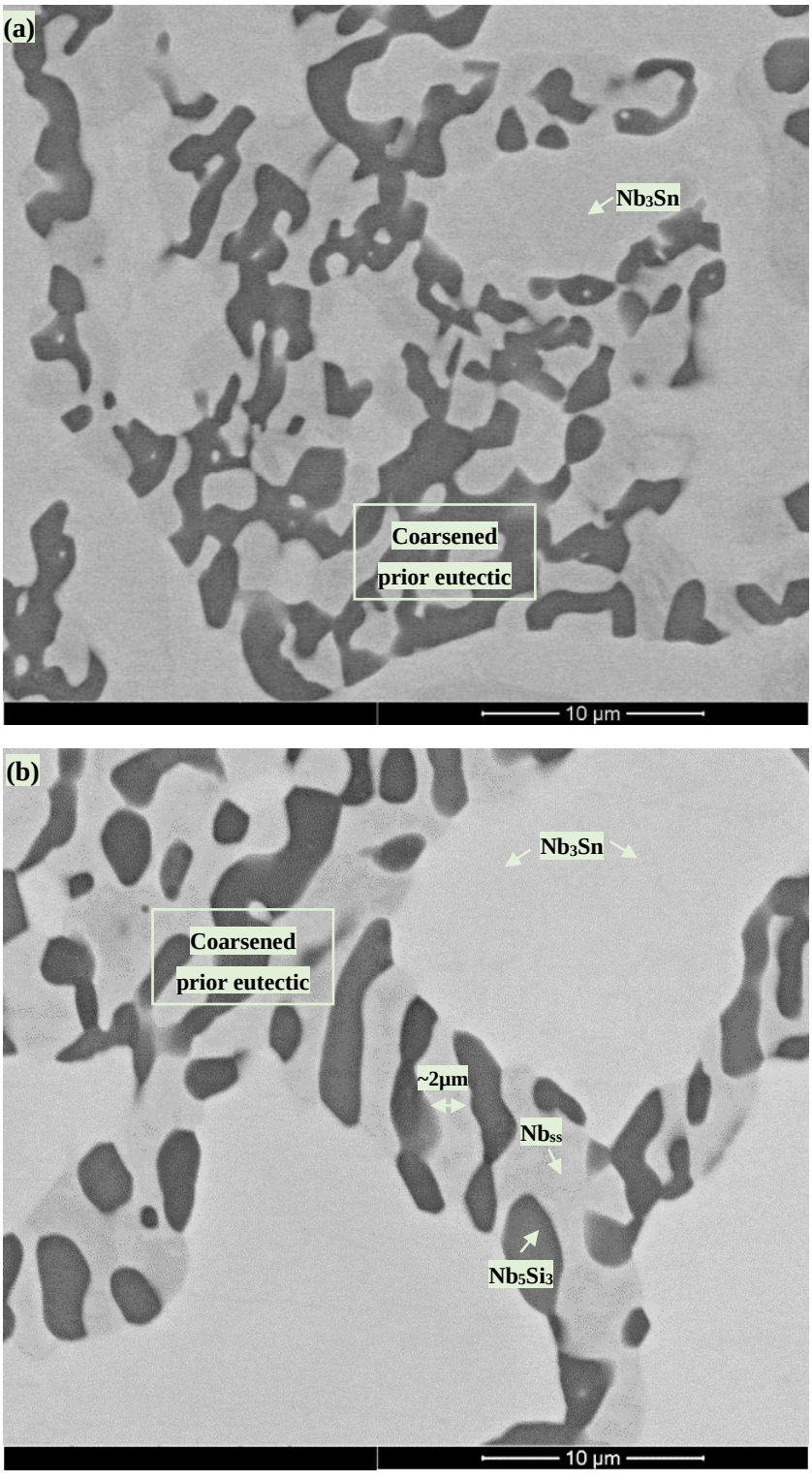


Figure 6.21 BSE images of the microstructure at the bulk area of the 1500 °C heat treated alloy ZX2 specimen.

Further evidence for partitioning of solute (Sn) within the Nb_3Sn and in-between the dark phase lamellae is shown in the higher magnification images in Figure 6.21. In

both Figures 6.20 and 6.21 the darker grey contrast phase between the black contrast lamellae exhibits the same contrast as the phase formed in the bulk of the Nb_3Sn (Figure 6.20). The latter was confirmed by EDS analyses to be the Nb_{ss}, see below. In Figure 6.21b the thickness of the darker grey contrast Nb_{ss} phase is about 2 μm.

The compositions of the phases are given in Table 6.2. The grey contrast phase is the Nb_3Sn with average Si + Sn = 18.8 at.%, and in the range 17.9 to 19.1 at.%. This is consistent with the XRD data, and the Sn and Si solubilities in Nb_3Sn [29]. The black contrast phase is the Nb_5Si_3 with Si + Sn = 37.1 at.%, essentially the same as in the cast and 1200°C heat treated alloy and consistent with the Si content of the un-alloyed silicide. The composition of the Nb_{ss} is consistent regarding its Si content with other data for Nb silicide based alloy [68] and regarding its Si and Sn contents is consistent with the data for the alloy ZX1 (see Table 6.1). Thus, the data shows that the Nb_{ss} participates in the lamellar microstructure in ZX2.

Table 6.2 The EDS analysis data (at.%) of the alloy ZX2.

As cast	Nb	Si	Sn
Surface*	**80.7** ± 0.3	**12.3** ± 0.3	**7.0** ± 0.3
	80.3 - 81.2	*11.8 - 13.1*	*6.6 - 7.7*
Bulk*	**80.4** ± 0.4	**11.8** ± 0.4	**7.8** ± 0.5
	80.0 - 81.0	*11.3 - 12.4*	*7.1 - 8.7*
Bottom*	**79.7** ± 0.3	**12.7** ± 0.7	**7.6** ± 0.7
	79.1-80.2	*11.4-13.5*	*6.6 - 8.4*
Nb_3Sn	**80.6** ± 0.3	**7.4** ± 1.4	**12.0** ± 1.6
	80.3 - 81.0	*6.3 - 9.2*	*9.8 - 13.3*
Eutectic	**81.7** ± 0.7	**16.0** ± 0.8	**2.3** ± 0.2
	80.6 - 82.5	*15.1 - 17.4*	*2.0 - 2.5*
Nb_5Si_3	**62.2** ± 0.3	**36.9** ± 0.3	**0.9** ± 0.1
	62.0 - 62.5	*36.5 - 37.1*	*0.8 - 1.1*
1200°C	Nb	Si	Sn
Bulk*	**80.9** ± 0.3	**11.9** ± 0.2	**7.2** ± 0.2
	80.4 - 81.3	11.5 - 12.2	6.8 - 7.4
Nb_3Sn	**81.6** ± 0.3	**8.3** ± 1.2	**10.1** ± 1.3
	81.1 - 81.9	*7.2 - 8.9*	*9.4 - 11.7*
Lamellar	**79.8** ± 0.8	**17.7** ± 0.9	**2.5** ± 0.7
Microstructure	*79.4 - 80.9*	*16.8 - 18.6*	*1.9 - 3.5*
Nb_5Si_3	**62.6** ± 0.1	**36.3** ± 0.3	**1.1** ± 0.4
	62.6 - 62.7	*36.0 - 36.5*	*0.8 - 1.3*
1500°C	Nb	Si	Sn
Bulk*	**80.2** ± 0.3	**12.2** ± 0.4	**7.6** ± 0.4
	79.8 - 80.7	*11.5 - 12.6*	*7.0 - 8.4*
Nb_{ss}	**96.1** ± 0.2	**0.7** ± 0.2	**3.2** ± 0.3
	95.7 - 96.4	*0.3 - 0.9*	*2.9 - 3.6*
Nb_3Sn	**81.2** ± 0.5	**7.5** ± 0.7	**11.3** ± 0.9
	80.9 - 82.1	*6.3 - 8.1*	*10.3 - 12.7*
Nb_5Si_3	**62.8** ± 0.5	**36.1** ± 0.5	**1.1** ± 0.1
	62.4 - 63.4	*35.5 - 36.6*	*1.0 - 1.1*

* Large area analysis

6.3 Discussion

6.3.1 Alloy Nb-12.5Si-7.5Sn (ZX2)

The microstructural evidence (Figures 6.13 to 6.15) would suggest that the primary phase in the cast microstructure of the alloy ZX2 was the Nb_3Sn, (i) with evidence of coring in the dendrites (Figure 6.13), (ii) with Si + Sn content which is in agreement with the data for the Nb_3Sn intermetallic phase in Nb-Si-Sn based alloys (18 to 19 at.%) [56, 69-71] and (iii) with varying Si and Sn contents (Table 6.2), as was also the case in [56, 69-71]. The black contrast βNb_5Si_3 silicide (Figures 6.13, 6.15b and c) was formed next to the Nb_3Sn. Evidence for the Nb_{ss} in the cast microstructure was weak and only from the XRD data (Figure 6.12).

As the Nb_3Sn was formed, the melt became rich in Si (because of the rejection of Si in the melt by the Nb_3Sn), in the Si rich melt the βNb_5Si_3 silicide formed rejecting Sn to the remaining melt that solidified giving the lamellar structure seen in Figures 6.13 to 6.15. The latter was formed either adjacent to the Nb_5Si_3 or the Nb_3Sn, Figures 6.13b, 6.15b and c. In this microstructure the lamellae of one phase exhibited black contrast, the same as the large Nb_5Si_3 silicides. The contrast of the lamellae of the other phase(s) varied, from being brighter than that of the Nb_3Sn (and sometimes similar to the contrast of the brighter contrast areas in the bulk of the primary Nb_3Sn, see Figure 6.13, 6.15b and c) to being “similar” to the contrast of primary Nb_3Sn, Figures 6.13 to 6.15. Given the atomic numbers of Sn (50) and Nb (41) and Si (14), such contrast variation should be linked with solute partitioning and it is known from this work (alloy ZX1) and the literature [56] that Sn shows preference for the Nb_{ss} rather than the Nb_5Si_3. Vellios and Tsakiropoulos, in their study of the alloy Nb-19Si-4.2Sn (alloy NV9 in [56]) reported that the Nb_{ss} with composition 96.5Nb-0.6Si-2.9Sn had darker grey contrast compared with the majority of Nb_{ss} (grey contrast) and that the Nb_3Sn exhibited brighter than usual contrast when it was richer in Sn.

Tin suppressed the tetragonal Nb_3Si in the alloy Nb-19Si-4.2Sn and also in Nb-24Ti-18Si-5Sn even though Ti is a strong stabiliser of the Nb_3Si [56, 68]. This was also the case in the alloy ZX1. In all these three alloys the Nb_{ss} + Nb_3Si eutectic was replaced by the Nb_{ss} + βNb_5Si_3 metastable eutectic. The latter does not exist in the Nb-Si binary system, but can form in binary Nb-(12 to 25 at.%) Si alloys under rapid solidification conditions [67] and thus it is a metastable eutectic in the binary. The composition of the latter should be slightly higher than that of the equilibrium eutectic. Bendersky et al suggested that its composition should be about 20 at.%Si. This however was not based on actual chemical analysis data but on the binary Nb-Si phase diagram that they used. There is disagreement regarding the composition of the eutectic in the Nb-Si binary with reported values being in the range 15.3 to 18.7 at.% Si [72]. The Si + Sn content and the Si/Sn ratio of the Nb_{ss} + βNb_5Si_3 eutectic in the alloys Nb-19Si-4.2Sn and ZX2 respectively was 20.7 at.% and 6.7 and 18.3 at.% and 7.

In the cast alloy ZX2 the lamellar microstructure had Si + Sn = 18.3 at.% and Si/Sn ≈ 7 and after the 1200 °C heat treatment these values were 20.2 at.% and 7.1 respectively. The only clear evidence of Nb_{ss} being present between the Nb_5Si_3 lamellae of the prior eutectic microstructure was after the 1500 °C heat treatment (Figure 6.21b) where the formation of the Nb_{ss} in the bulk of Nb_3Sn, Figures 6.20, 6.21 (areas that exhibited bright contrast in the cast condition) was promoted by the partitioning of Sn, and the EDS analysis of the Nb_{ss} in these areas gave 96.1Nb-0.7Si-3.2Sn with Si + Sn = 3.9 at.% and Si/Sn = 0.22, similar to the 96.5Nb-0.6Si-2.9Sn solid solution in the 1500 °C heat treated Nb-19Si-4.2Sn [56]. The above discussion would thus suggest that the lamellar structure in the cast ZX2 and the 1200 °C heat treated alloy ZX2 was a eutectic in the former condition and consisted of the βNb_5Si_3 (αNb_5Si_3 in the latter condition) plus the Nb_{ss} and/or Nb_3Sn phases (the evidence we have does not allow us to be definite which one (or both) of

the Nb_{ss} and Nb_3Sn phases was in the lamellar microstructures), and that the remnants of the lamellar structure in the 1500 °C heat treated alloy ZX2 were the αNb_5Si_3 and Nb_{ss}.

The alloy ZX2 is a hypoeutectic alloy considering its Si content and the Nb-Si binary phase diagram, even after allowing for the wide range of eutectic compositions in Nb-Si reported in the literature (see §2.2). In a hypoeutectic alloy the Nb_{ss} would be the primary phase under equilibrium solidification.

In the Nb-Sn binary the Nb_3Sn is formed via the peritectic $L + Nb_{ss} \rightarrow Nb_3Sn$, which, like all peritectic reactions, is controlled by solid state diffusion. Under normal solidification (i.e., non-equilibrium) conditions the previous reaction would result in a microstructure consisting of Nb_{ss} surrounded by Nb_3Sn (like the one shown in Figure 6.20a, which however was observed in the 1500 °C heat treated condition, **not** in the cast alloy) and given time at temperature progression towards equilibrium would mean gradual dissolution of the Nb_{ss} and its eventual disappearance. Exactly the opposite was observed in the case of the alloy ZX2. The Nb_{ss} (if present) was not discernible in the cast microstructure and became distinct after the 1500 °C heat treatment for 100 h.

Directional solidification of binary peritectic alloys at very high temperature gradients can suppress the phase forming above the peritectic temperature (pro-peritectic phase) [73]. Near the crucible wall directional solidification under high temperature gradient is most likely, this would explain the suppression of Nb, especially since Nb-7.5Sn has a narrow freezing range (see below).

Based on the above discussion it is suggested that the solidification path of the alloy ZX2 was $L \rightarrow L + Nb_3Sn \rightarrow L + Nb_3Sn + \beta Nb_5Si_3 \rightarrow Nb_3Sn + \beta Nb_5Si_3 + [(Nb_{ss})$

(Nb_3Sn) + Nb_5Si_3] eutectic, the parentheses are used to indicate that it is not clear which phase(s) are present on the basis of the current experimental data.

The Pandat software was used to calculate the solidification path of the alloy ZX2 with the database in Sun *et al* [29]. The calculations were made for each of the three average compositions in the top, bulk and bottom of the cast alloy, see Table 6.2. In all three cases the calculated solidification paths were essentially the same, namely L → L + bcc (Nb) → L + Nb_3Sn + bcc (Nb) → L + Nb_3Sn → L + Nb_3Sn + αNb_5Si_3 → L + bcc (Nb) + Nb_3Sn + αNb_5Si_3 → bcc (Nb) + Nb_3Sn + αNb_5Si_3, with small differences in the transformation temperatures. Figure 6.22, shows the calculated solidification paths for the three locations. In this figure the coloured lines correspond to Scheil solidification and the black one to equilibrium solidification. It should be noted that Sun *et al* included a parameter to prevent the Nb_3Si from forming [29]. This has been included in these calculations. If this parameter were not to be included then a large mole% of Nb_3Si (40%) is predicted to form.

Compared with the solidification path proposed above, two differences are apparent. First, the calculations give the bcc Nb solid solution as the primary phase and the 5-3 silicide as the low temperature αNb_5Si_3, not the βNb_5Si_3. The formation of αNb_5Si_3 from the liquid in Nb-Si based alloys is a controversy that has not been resolved in the phase equilibria of Nb-Si based systems. Interpretations of solidification microstructures are complicated because of the conditions that prevail in arc melted ingots. The Nb-Si-Sn phase equilibria of Sun *et al* is based on experimental (i.e., EDS) data for Nb-Si-Sn alloys and in the database of Sun *et al* no solubility of Sn in the βNb_5Si_3 is allowed. This might be responsible for the discrepancy between experiment and CALPHAD for the 5-3 silicide in the alloy ZX2.

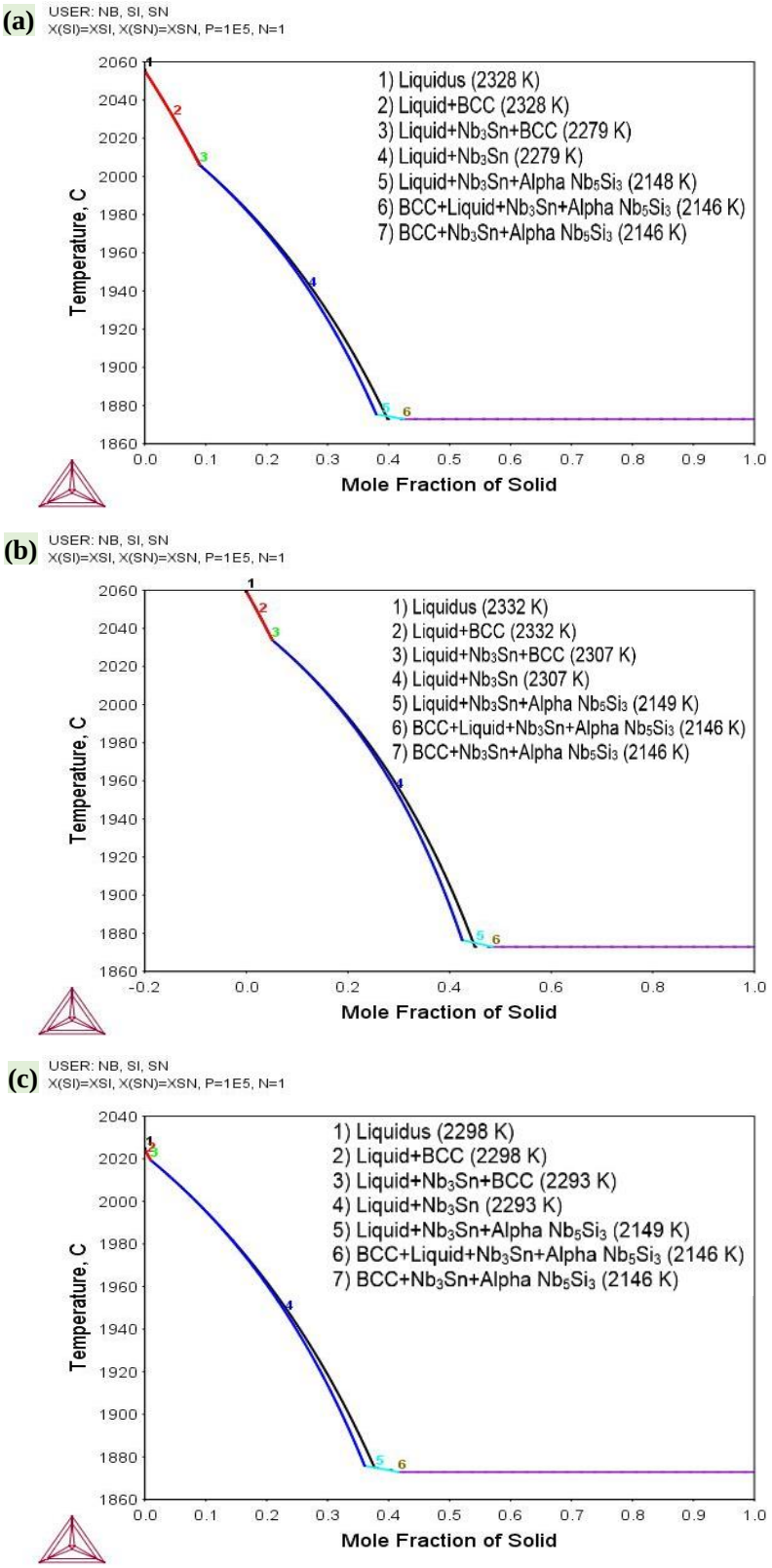


Figure 6.22 The calculated solidification paths, part (a) is for the top area, part (b) is for the bulk area and part (c) is for the bottom area of the alloy ZX2.

The estimated vol.% of phases in the cast ZX2 are given in Table 6.3.These values are estimations based on the molar volume of the unalloyed phase unit cell (i.e., volume changes that occur with substitution were not taken into account). The calculated vol.% of Nb_{ss} is low in all three locations and increases from bottom to top. This could account for the weak evidence for Nb_{ss} in the cast ZX2 (only two peaks in the XRD diffractogram, see Figure 6.12).

Table 6.3. Calculated mole fractions and volume percentages of phases in the cast alloy ZX2.

Position in ingot	Composition*	Mole fraction			volume percent %		
		Nb_3Sn	αNb_5Si_3	Bcc(Nb)	Nb_3Sn	αNb_5Si_3	Bcc(Nb)
top	Nb-12.3Si-7Sn	0.5632	0.1536	0.2808	48.21	45.54	6.25
bulk	Nb-11.8Si-7.8Sn	0.6779	0.1318	0.1872	57.30	38.58	4.11
bottom	Nb-12.7Si-7.6Sn	0.7034	0.1612	0.1333	54.26	43.07	2.67

* see Table 6.2

Let us now return to the solidification of the alloys ZX1 and ZX2 and the formation of primary phase in these two alloys. Solidification started at the walls of the copper water cooled crucible where the temperature gradient in the liquid was positive and high, and the nucleating phase(s) grew at high growth rate. It is assumed that near the crucible wall the solidification was directional, a reasonable assumption.

Consider the schematic diagram of the Nb-Sn peritectic in Figure 6.23. According to the highest interface temperature criterion which says that the primary phase is that which grows at the highest interface temperature, in the alloy ZX1 the leading phase should be the Nb since $T_{S1Nb} > T_{S1Nb3Sn}$ but in the alloy ZX2, where $T_{S2Nb3Sn} > T_{S2Nb}$, the primary phase should be the Nb_3Sn.

Change in phase formation from the primary phase to another phase in solidification near the crucible wall would depend (be controlled) by the nucleation and growth of another phase in the undercooled melt near the S/L interface which overtakes the growing (primary) phase (i.e., occupies the volume of melt ahead of the S/L interface)

and prevents the primary phase from growing. If nucleation of another phase at or ahead of the interface in a constitutionally undercooled melt cannot occur, the growing primary phase is stable.

As the primary Nb_3Sn formed, a solute rich boundary layer forms ahead of the Nb_3Sn/L interface. For a planar interface at steady state, the interface temperature was $T_{S2Nb3Sn}$, see Figure 6.23. The local Nb liquidus and Nb_3Sn liquidus temperatures corresponding to the composition in the boundary layer could have been as shown in Figure 6.24. The melt at some distance ahead of the interface was constitutionally undercooled with respect to the Nb liquidus and thus the Nb could nucleate in the undercooled melt at some distance ahead of the Nb_3Sn plane front. (Depending on the Nb liquidus formation of a Constitutional Supercooled (CS) zone closer to the Nb_3Sn/L interface is of course also possible).

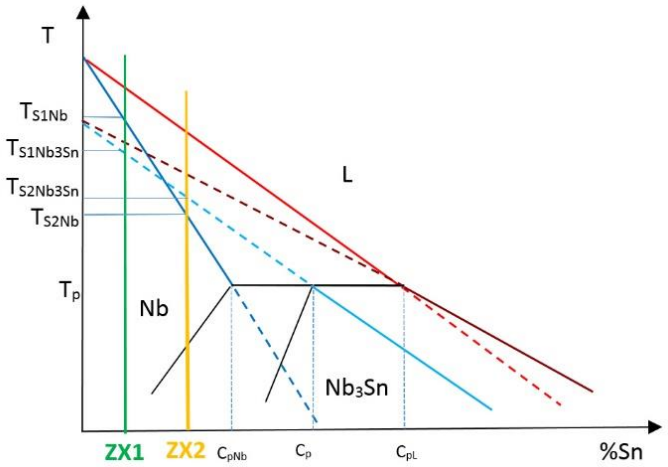


Figure 6.23. Schematic diagram of peritectic in Nb-Sn. Full colour lines are the equilibrium liquidus and solidus of Nb and Nb_3Sn and dashed colour lines are the metastable extensions of the liquidus and solidus of Nb and Nb_3Sn. The alloys ZX1 and ZX2 are shown with the vertical lines. The solidus temperatures of Nb and Nb_3Sn in the alloys ZX1 are T_{S1Nb} and $T_{S1Nb3Sn}$ respectively, and in the alloy ZX2 they are T_{S2Nb} and $T_{S2Nb3Sn}$ respectively.

The microstructure in Figure 6.13 shows Nb_3Sn (with some pockets of eutectic lamellar structure, Figure 6.13a) formed near the Cu water cooled crucible (left side

of image). The composition of Nb_3Sn in this area was 86.9Nb-6.9Si-6.2Sn (Si + Sn = 13.1 at.%). If the melt ahead of the Nb_3Sn became constitutionally undercooled with respect to the Nb liquidus (Figure 6.24) then Nb nucleation is possible and in these areas of the undercooled melt it is likely that the Nb_{ss} was one of the phases in the eutectic (the other being the βNb_5Si_3). As we discussed above, it is extremely difficult to distinguish between Nb_{ss} and Nb_3Sn using atomic number contrast in the SEM.

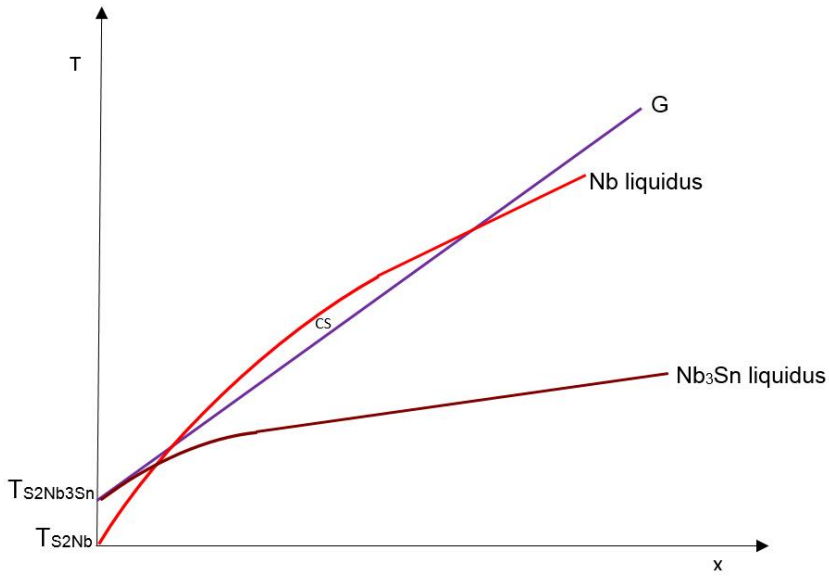


Figure 6.24 Local temperature in the solute rich boundary layer with distance x ahead of the Nb_3Sn/L interface (x=0) with gradient G and the Nb and Nb_3Sn liquidus temperatures. CS is the constitutionally supercooled region defined by G and the Nb liquidus.

Figure 6.13a also shows a change in microstructure after about 50 μm from the start of solidification on the crucible wall with the two microstructures separated by a macroscopic "planar" interface that is more or less parallel to the bottom of the ingot (Figure 6.13a). Sometimes this macroscopic interface was not parallel with the bottom surface of the ingot when the transition had occurred closer to the latter (i.e., at a distance less than 50 μm). On the right hand side of this macroscopic interface, the microstructure consists of anomalous eutectic (composition 80.5Nb-17.3Si-2.2Sn, Si + Sn = 19.5 at.%) and normal (regular) eutectic (composition 81Nb-16.8Si-2.2Sn,

Si + Sn = 19 at.%), with the former being finer closer to the macroscopic interface (which is close to the water cooled crucible wall) and the latter becoming finer further away from the interface (in other words, on the right hand side of the macroscopic interface in Figure 6.13a the microstructure evolution is fine anomalous eutectic – coarser anomalous eutectic – normal lamellar eutectic – finer normal eutectic).

Starting from the macroscopic interface and moving to the right of the image in Figure 6.13a, it is seen that for this cross section of the ingot the grey contrast phase is the continuous phase, in which the black contrast phase (5-3 silicide) is embedded (it is not possible from this image to state categorically whether both phases are continuous and form a network or both phases are discontinuous particulates or one phase is continuous and the other is discontinuous, i.e., based on SEM images it is not feasible to make reliable conclusions regarding the continuity or not of a phase in Figure 6.13a).

As discussed above, in the cast alloy ZX2 there was formation of [(Nb_{ss}) (Nb_3Sn) + Nb_5Si_3] eutectic. If the Nb_{ss} was one of the two phases in the eutectic, then the latter would be between a low entropy of fusion phase (Nb_{ss}, non-facetted) and a high entropy of fusion phase (βNb_5Si_3, facetted), i.e., f-nf eutectic. If however the Nb_3Sn and βNb_5Si_3 were the two eutectic phases then the latter would be f-f eutectic as the intermetallic Nb_3Sn should have a high entropy of fusion. If all three phases were present in the eutectic, the latter would be an f-f-nf ternary eutectic.

Transitions between anomalous and normal eutectics have been reported to occur in the unconstrained (i.e., free) solidification of (bulk) undercooled binary eutectic alloys where f-nf and nf-nf eutectics are formed, e.g., in Ni-18.7Sn (f-nf eutectic) where the anomalous eutectic (Ni_{ss} + Ni_3Sn) changes to anomalous + normal eutectic

to normal eutectic (Ni_{ss} + Ni_3Sn) with decreasing undercooling. Furthermore, a refinement of anomalous eutectic microstructure and increase of its volume fraction have been reported with increasing undercooling for f-nf eutectics [74] and nf-nf eutectics [75]. Numerous (at least 7) mechanisms have been suggested but none of these is generally accepted. Kyribayashi and co-workers have attributed the above transition to differences in the decoupled growth of the two phases owing to their different entropies of fusion [76] where the non-facetted (low entropy of fusion) phase outgrows the faceted phase after eutectic growth starts [77].

To account for the anomalous to eutectic transition observed here on the basis of differences in melt undercooling, the Si rich melt ahead of the aforementioned macroscopic interface must have become "deeply" constitutionally undercooled as solidification had progressed to the location of the macroscopic interface.

In a pure binary eutectic a planar growth front is morphologically stable but in the presence of a third element the front can become morphologically unstable. The latter would also be the case in an undercooled eutectic melt where the front is destabilised by the negative temperature gradient ahead of the front. The macroscopic interface where the transition in microstructure occurred is seen in Figure 6.13a to consist of alternating areas of grey and black contrast, the same contrasts as in the eutectic. Then the anomalous eutectic formed and as the latent heat from the solidifying two phases increased the temperature of the remaining melt the undercooling of the latter became lower and this enabled the normal eutectic to develop.

The microstructure in the cast alloy ZX2 formed under intrinsically non-steady state growth conditions and its evolution was controlled by competition between nucleation and growth of phases, namely Nb_{ss}, Nb_3Sn and Nb_5Si_3. Once a new phase

nucleated the microstructure selection process was controlled by the growth competition between the nuclei of the new phase and the pre-existing phase under non-steady state conditions. It is well known that there is significant fluid flow in arc melting and solidification using water cooled crucibles and the fluid flow is expected to also influence the development of microstructure.

The data for the chemical composition of the Nb_{ss} and the 5-3 silicide in the cast and heat treated alloy ZX2 (Table 6.2) confirmed (i) that Sn partitions to the former and (ii) that Si is substituted by Sn in the latter, both of which are in agreement with [56]. The formation of Nb_3Sn in the cast alloy ZX2 and its absence in the cast alloy ZX1 provides further support that the formation (and stability) of the A15-Nb_3Sn in Nb-Si based alloys depends on the Sn concentration in the alloy and becomes more likely as the latter is increased. The data for the heat treated alloy Nb-19Si-4.2Sn (alloy NV9) in [56] suggested that Sn promotes the $\beta Nb_5Si_3 \rightarrow \alpha Nb_5Si_3$ transformation. This was supported by the data for the alloy ZX1. The data for ZX2 would suggest that the above transformation is enhanced as the Sn concentration in the alloy is increased (both the βNb_5Si_3 and αNb_5Si_3 were present in ZX1-HT1200 but only the αNb_5Si_3 in ZX2-HT1200).

According to the XRD data for the heat treated alloy ZX2 (Figures 6.16 and 6.19) three phases were present in the microstructure, namely the Nb_{ss}, Nb_3Sn and αNb_5Si_3. This was also confirmed by the EDS data for ZX2-HT1500 (Table 6.2). The three phase microstructures in the two heat treated conditions suggested by the XRD are in agreement with the 1200 and 1500 °C isothermal sections in [29] for the average compositions of the heat treated specimens in Table 6.2. The calculated volume fractions of phases for the two conditions are given in Table 6.4. Owing to the difficulties with the identification of the Nb_{ss} in the microstructures of ZX2 it is not possible to compare the data in this table with the experimental microstructures.

Table 6.4. Equilibrium phases and their mole fractions and volume percentages in the heat treated alloy ZX2.

Nb-11.9Si-7.2Sn*, 1200 °C		
equilibrium phases	mole fraction	volume percent %
BCC Nb	0.262	4.94
αNb_5Si_3	0.232	58.24
Nb_3Sn	0.507	36.81
Nb-12.2Si-7.6Sn*, 1500 °C		
equilibrium phases	mole fraction	volume percent %
BCC Nb	0.207	3.79
αNb_5Si_3	0.234	56.96
Nb_3Sn	0.559	39.25

* The alloy compositions are from Table 6.2

6.3.2 Alloy Nb-14Si-3Sn (ZX1)

The microstructure of the cast alloy ZX1 consisted of primary Nb_{ss}, with Si + Sn = 6.8 at % and Si/Sn = 0.8 compared with 5.7 at.% and 0.3 for the alloy Nb-19Si-4.2Sn (alloy NV9) in [56]. The Si + Sn in the Nb_{ss} + Nb_5Si_3 eutectic in the two alloys was 18.4 at.% and 20.7 at.%, respectively. The Si + Sn in the 5-3 silicide was essentially the same in both alloys. The fact that Sn partitions to the solid solution rather than the 5-3 silicide and the macrosegregation of Si in ZX1 ($C^{Si}_{max} - C^{Si}_{min}$ = 4 at.% and ~2 at.% in ZX1 and ZX2, respectively) but not in the alloy NV9 could account for the difference in Si/Sn ratios and the Si + Sn sums in the eutectic.

The formation of Nb_{ss} in ZX1 can be explained using the highest interface temperature criterion, see above and Figure 6.23. The rectangular box in the top right hand corner of Figure 6.4b shows regions of Nb_{ss} and Nb_{ss} + Nb_5Si_3 growing from the crucible wall. This is evidence of differences in Si concentration of the melt in contact with the crucible, the latter being richer in Si and close to the Nb_{ss} + Nb_5Si_3 metastable eutectic composition (see above). In the eutectic region in the rectangle; the Nb_{ss} is seen to outgrow the Nb_5Si_3 and thus after a very short distance the Nb_{ss} "dominates".

In Figure 6.4 the arrows point away from the crucible wall and show that for a distance of about 150 μm from the latter there was some directionality in the microstructure as indicated by the arms of the Nb_{ss} dendrites. In this area of the ingot as the Nb_{ss} formed the liquid became richer in Si and reached the eutectic composition forming the Nb_{ss} + βNb_5Si_3 eutectic. The latter is seen to become slightly coarser with distance away from the crucible wall, which is attributed to the decreasing cooling rate.

Figures 6.4a and c show a change in microstructure, the start and end of this change are indicated by dotted and dashed lines, respectively. In this narrow zone the directions of the dendrites are different (not always parallel to the arrows) and in the cross section of the images whole dendrites are seen. In this zone the inter-dendritic microstructure changes from one like that in Figure 6.4e, which becomes coarser with increasing distance from the dotted line towards the dashed line, to the one shown in Figure 6.4f, which is observed outside the zone after the dashed line.

The microstructures in Figure 6.4e and f are suggestive of the anomalous to normal eutectic transition, which was discussed above, and which is attributed to decreasing melt undercooling. The formation of the aforementioned zone could be attributed to the interrelationships between the various phenomena that are linked with the macrosegregation of Si in Nb silicide based alloys, as discussed in [78] and the different dendrite directions would suggest that fluid flow played an important role.

As the solidification front advanced "directionally" to the dotted line the melt was undercooled ahead of the eutectic front (the eutectic was growing at $T_G < T_E$, where T_G is the growth temperature and T_E is the eutectic temperature) and the undercooling $\Delta T = T_E - T_G$ had some maximum value characteristic for the eutectic spacing at that location. The melt ahead of this interface could become rich or poor

in Si (owing to fluid flow, macrosegregation etc.). Assuming that T_G did not change, as the composition of the Si poor melt moved away from the eutectic composition C_E the undercooling of the Nb_{ss} increased and that of the Nb_5Si_3 decreased, see Figure 6.25. Furthermore, as the composition of the Si rich melt moved away from the eutectic composition the undercooling of the Nb_5Si_3 increased and that of the Nb_{ss} decreased, see Figure 6.25. The differences in undercooling and growth kinetics between the two phases were important for their formation and stability in the Si rich or poor melt. Thus, the chemical inhomogeneity of the melt regarding its Si content, which led to the macrosegregation of Si in the cast alloy, was important for establishing the conditions that drove the anomalous to normal eutectic transition with decreasing undercooling in the zone defined by the dotted and dashed lines in Figure 6.4.

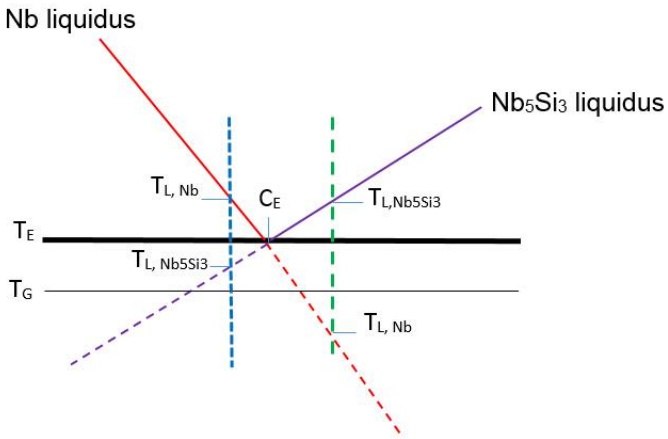


Figure 6.25 Schematic diagram showing the Nb and Nb_5Si_3 stable and metastable liquidus lines, the eutectic and growth temperatures and the eutectic composition. Dashed vertical lines indicate compositions to the left and right of the eutectic.

Based on the above discussion it is suggested that the solidification path of the alloy ZX1 was $L \rightarrow L + Nb_{ss} \rightarrow L + Nb_{ss} + \beta Nb_5Si_3 \rightarrow Nb_{ss} + \beta Nb_5Si_3 + (Nb_{ss} + Nb_5Si_3)$ eutectic. The Pandat software was used to calculate the solidification path of the alloy ZX1 with the database in Sun *et al* [29]. The calculations were made for each

of the three average compositions in the top, bulk and bottom of the cast alloy, see Table 6.1. In all three cases the calculated solidification paths were essentially the same, namely L → L + bcc (Nb) → L+ bcc (Nb) + αNb_5Si_3→ L + bcc (Nb) + αNb_5Si_3 + Nb_3Sn → bcc (Nb) + Nb_3Sn + αNb_5Si_3, with small differences in the transformation temperatures. Figure 6.26 shows the calculated solidification paths for the three locations. In this figure the coloured lines correspond to Scheil solidification and the black one to equilibrium solidification.

Compared with the solidification path proposed above, there is agreement regarding the primary phase, but there are also two important differences. First, the calculations give the 5-3 silicide as the low temperature αNb_5Si_3, not the βNb_5Si_3 and second, the formation of Nb_3Sn in the final microstructure is predicted. The same argument for the αNb_5Si_3 made in the discussion of the solidification path of the alloy ZX2 applies, and will not be repeated. Regarding the presence of Nb_3Sn in the cast microstructure, its absence in the cast alloy could be attributed to the non-equilibrium solidification under high cooling rates in the melting and casting process used in this research. The estimated vol.% of phases in the cast ZX1 are given in Table 6.5. These values are estimations based on the molar volume of the unalloyed phase unit cell (i.e., volume changes that occur with substitution were not taken into account). The calculated vol.% of Nb_3Sn is low in all three locations. This could account for the Nb_3Sn not observed in the cast ZX1.

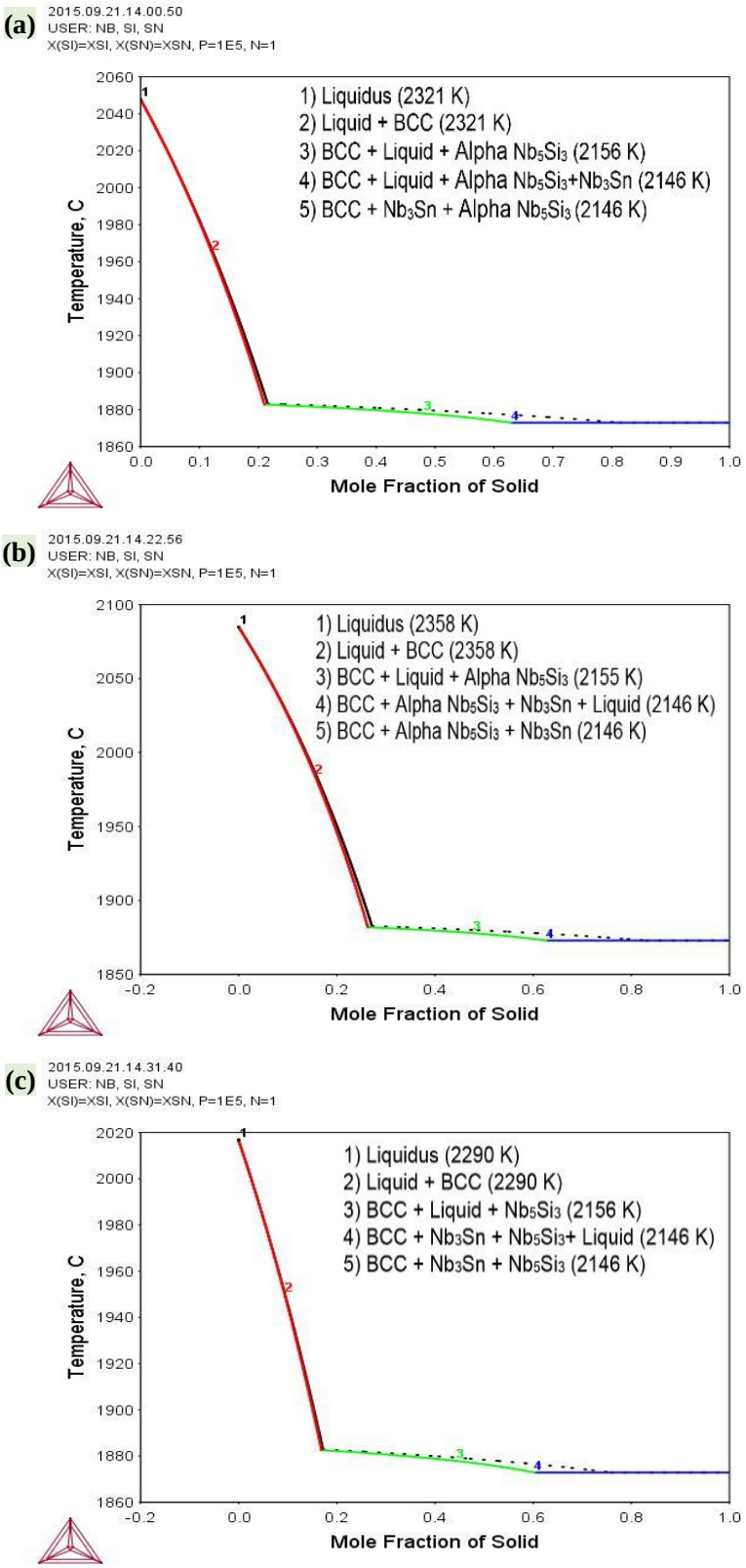


Figure 6.26 The calculated solidification paths, part (a) is for the top area, part (b) is for the bulk area and part (c) is for the bottom area of the alloy ZX1.

There was coarsening of the lamellar microstructures after the two heat treatments, in both ZX1 and ZX2, driven by the high interfacial energy of the thin lamellae. In ZX1, after the 100 h heat treatment at 1200 °C both βNb_5Si_3 and αNb_5Si_3 were present in the microstructure according to the XRD data, see Figure 6.8, which suggests that equilibrium at 1200 °C was not reached. There was also no evidence for the Nb_3Sn, which should be present together with Nb_{ss} and αNb_5Si_3 according to the proposed 1200 °C isothermal section of the Nb-Si-Sn system by Sun *et al* [29]. After the heat treatment at 1500 °C the Nb_{ss}, αNb_5Si_3 and Nb_3Sn were present in the microstructure, Figure 6.11, but not the βNb_5Si_3. This is in agreement with the 1500 °C isothermal for Nb-Si-Sn by Sun *et al* [29] and would suggest that equilibrium at 1500 °C had been reached. The calculated volume fractions of phases for the two conditions are given in Table 6.6. The calculations show minimal changes in vol.% of phases between the two heat treatments. In ZX1-HT1500 the Nb_3Sn was formed in the areas occupied by the prior eutectic and the lamellar microstructure in ZX1-HT1200, and would suggest a ternary Nb_{ss} + Nb_3Sn + αNb_5Si_3 eutectoid, see Figure 6.6.

Table 6.5 Calculated mole fractions and volume percentages of phases in the cast alloy ZX1.

Position in ingot	Composition*	mole fraction			volume percent %		
		Nb_3Sn	αNb_5Si_3	Bcc(Nb)	Nb_3Sn	αNb_5Si_3	Bcc(Nb)
top	Nb-14.5Si-2.9 Sn	0.0322	0.2694	0.6967	2.81	81.39	15.80
bulk	Nb-13.7Si-2.9 Sn	0.0328	0.2326	0.7315	3.19	78.32	18.49
bottom	Nb-15.1Si-3.0 Sn	0.0369	0.2986	0.6609	2.97	83.21	13.83

* see Table 6.1

Table 6.6 Equilibrium phases and their mole fractions and volume percentages in the heat treated alloy ZX1. The alloy compositions are from Table 6.1.

Nb-13.6Si-3Sn, 1200 °C		
Equilibrium phases	mole fraction	volume percent %
BCC Nb	0.559	10.44
αNb_5Si_3	0.327	81.37
Nb_3Sn	0.114	8.19
Nb-14.3Si-3.1Sn, 1500 °C		
Equilibrium phases	mole fraction	volume percent %
BCC Nb	0.553	10.07
αNb_5Si_3	0.339	82.33
Nb_3Sn	0.108	7.59

6.4 Summary

Two ternary alloys with low and high Sn concentrations were studied, namely the alloys Nb-14Si-3Sn (ZX1) and Nb-12.5Si-7.5Sn (ZX2), in the cast and heat treated (1200, 1500 °C) conditions.

In both cast alloys the Nb_3Si was supressed and the Nb_{ss} + Nb_3Si eutectic was replaced by the metastable Nb_{ss} + βNb_5Si_3 eutectic. The lamellar microstructure of the latter coarsened after heat treatments and its Si + Sn concentration shifted to higher values. Only in the high Sn content alloy (ZX2) was the transformation of βNb_5Si_3 to αNb_5Si_3 completed at 1200 °C, and in both alloys the latter silicide was present after the heat treatment at 1500 °C, thus supporting the conclusion of previous research that Sn promotes the above transformation.

The Nb_3Sn was formed during the solidification only of the high Sn content alloy (ZX2) and was stable in both alloys. In the low content alloy (ZX1) the Nb_3Sn formed only after the heat treatment at 1500 °C.

Chapter 7

The alloys Nb-24Ti-18Si-5Cr-2Sn (ZX3) and Nb-24Ti-18Si-5Cr-5Sn (ZX4)

7.1 Introduction

The alloys Nb-24Ti-18Si-5Cr-2Sn (ZX3) and Nb-24Ti-18Si-5Cr-5Sn (ZX4) are studied in this chapter to understand how the synergy of Cr and Sn affects phase stability and oxidation behaviour. The as cast and heat treated microstructure of the alloys are studied using SEM, XRD and EDS and the data is used to understand phase equilibria in the alloys. The isothermal oxidation behaviour of the two alloys is studied at 800 °C and 1200 °C. Oxidation kinetics are discussed and the microstructure of oxidised specimens are studied using SEM-EDS and EPMA-WDS.

7.2 Results

7.2.1 Alloy Nb-24Ti-18Si-5Cr-2Sn (ZX3)

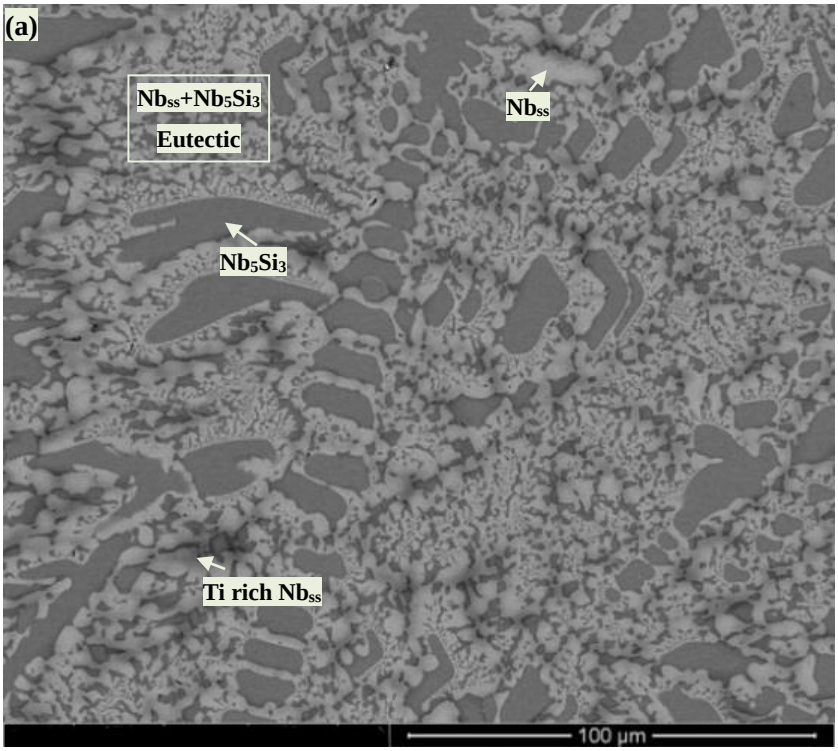
As-Cast: The actual composition of the alloy was Nb-24.9Ti-20.8Si-4.5Cr-2.0Sn. The large area analysis of the alloy and the compositions of the phases are given in Table 7.1. The Si content of the alloy varied from 18.7 at.% to 22.3 at.%, which is higher than the nominal composition and there was macrosegregation of Si. The Ti and Cr concentrations were in the ranges 23.0 at.% to 26.8 at.%, 3.7 at.% to 5.4 at.%, respectively, and there was macrosegregation of Ti. The concentrations of Ti and Cr were lower in the near surface areas of the alloy ingot than in the bottom area. The Si concentration in the alloy behaved in the opposite way.

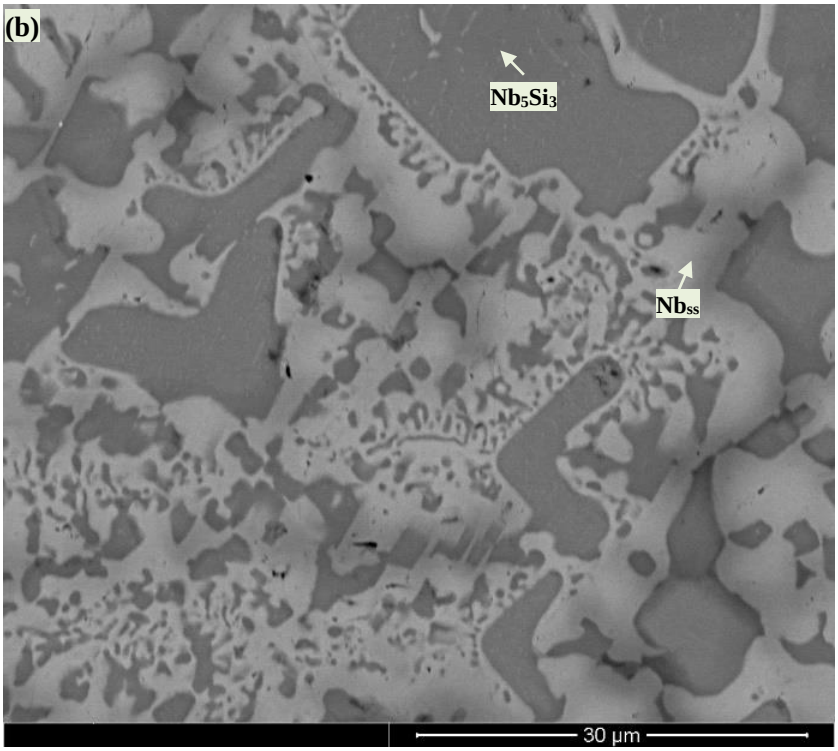
Table 7.1 EDS analysis (at.%) of the as cast and heat treated alloy ZX3.

	Nb	Ti	Si	Cr	Sn
As cast					
Surface*	**49.0** ± 0.3	**23.5** ± 0.5	**21.6** ± 0.8	**4.0** ± 0.2	**1.9** ± 0.1
	48.5 - 49.4	*23.0 - 24.4*	*20.3 - 22.3*	*3.7 - 4.3*	*1.7 - 2.1*
Bulk*	**47.9** ± 1.6	**25.1** ± 1.0	**20.3** ± 1.1	**4.7** ± 0.3	**2.0** ± 0.4
	45.2 - 49.5	*23.4 - 26.8*	*18.7 - 21.8*	*4.2 - 5.4*	*1.9 - 2.3*
Bottom*	**46.5** ± 0.2	**26.0** ± 0.3	**20.4** ± 0.4	**4.9** ± 0.2	**2.2** ± 0.2
	46.4 - 47.0	*25.5 - 26.5*	*19.7 - 21.1*	*4.6 - 5.0*	*1.9 - 2.3*
Nb_{ss}	**63.7** ± 2.1	**24.7** ± 1.7	**3.1** ± 0.7	**5.1** ± 0.5	**3.4** ± 0.5
	61.1 - 66.9	*21.5 - 26.9*	*2.3 - 4.3*	*4.0 - 5.5*	*2.7 - 4.3*
Nb_5Si_3	**44.8** ± 1.7	**17.8** ± 1.5	**35.9** ± 0.4	**0.7** ± 0.4	**0.8** ± 0.2
	41.2 - 46.2	*16.8 - 20.9*	*35.3 - 36.7*	*0.2 - 1.2*	*0.5 - 1.0*
Ti-rich Nb_{ss}	**43.9** ± 5.5	**37.0** ± 3.5	**3.2** ± 1.0	**13.0** ± 1.7	**2.9** ± 0.3
	36.1 - 48.8	*34.3 - 41.9*	*1.9 - 4.1*	*11.0 - 14.8*	*2.6 - 3.3*
Eutectic	**53.0** ± 2.1	**24.9** ± 1.4	**15.1** ± 1.9	**4.6** ± 0.7	**2.4** ± 0.3
	50.5 - 55.5	*23.3 - 27.0*	*12.8 - 17.9*	*4.0 - 5.7*	*1.9 - 2.8*
Heat treated					
Bulk*	**47.9** ± 0.4	**25.7** ± 0.2	**19.7** ± 0.6	**4.6** ± 0.2	**2.1** ± 0.1
	47.5 - 48.8	*25.4 - 26.2*	*18.7 - 20.5*	*4.2 - 5.1*	*1.9 - 2.3*
Nb_{ss}	**55.0** ± 0.2	**31.8** ± 0.2	**0.7** ± 0.1	**9.1** ± 0.2	**3.4** ± 0.1
	54.7 - 55.4	*31.4 - 32.1*	*0.5 - 0.9*	*8.9 - 9.4*	*3.3 - 3.5*
Ti-rich Nb_5Si_3	**40.8** ± 0.4	**21.8** ± 0.4	**36.4** ± 0.2	**0.4** ± 0.1	**0.6** ± 0.1
	40.0 - 41.6	*21.2 - 22.5*	*36.2 - 36.7*	*0.3 - 0.6*	*0.5 - 0.8*
Nb_5Si_3	**44.6** ± 0.3	**18.3** ± 0.5	**35.8** ± 0.3	**0.6** ± 0.2	**0.7** ± 0.1
	43.9 - 44.8	*17.8 - 19.0*	*35.3 - 36.4*	*0.4 - 0.8*	*0.6 - 0.9*

* Large area analysis

The microstructure was similar in the near surface and bulk of the ingot and was composed of primary Nb_5Si_3 dendrites and a Nb_{ss} + Nb_5Si_3 eutectic consisting of small Nb_5Si_3 islands dispersed in the Nb_{ss} matrix. Some of the Nb_{ss} was enriched in Ti and thus exhibited a darker contrast in the back scattered image, as seen in Figure 7.1. The $NbCr_2$ Laves phase was not observed in the bulk and top of the cast ZX3. The microstructure of the bottom area was different compared with the near surface and bulk areas. Instead of the Nb_{ss} + Nb_5Si_3 eutectic structure, a co-continuous formation of Nb_{ss} and Nb_5Si_3 was found in this area, as shown in Figure 7.2.


(a)
$Nb_{ss}+Nb_5Si_3$
Eutectic
Nb_{ss}
Nb_5Si_3
Ti rich Nb_{ss}
100 μm


(b)
Nb_5Si_3
Nb_{ss}
30 μm

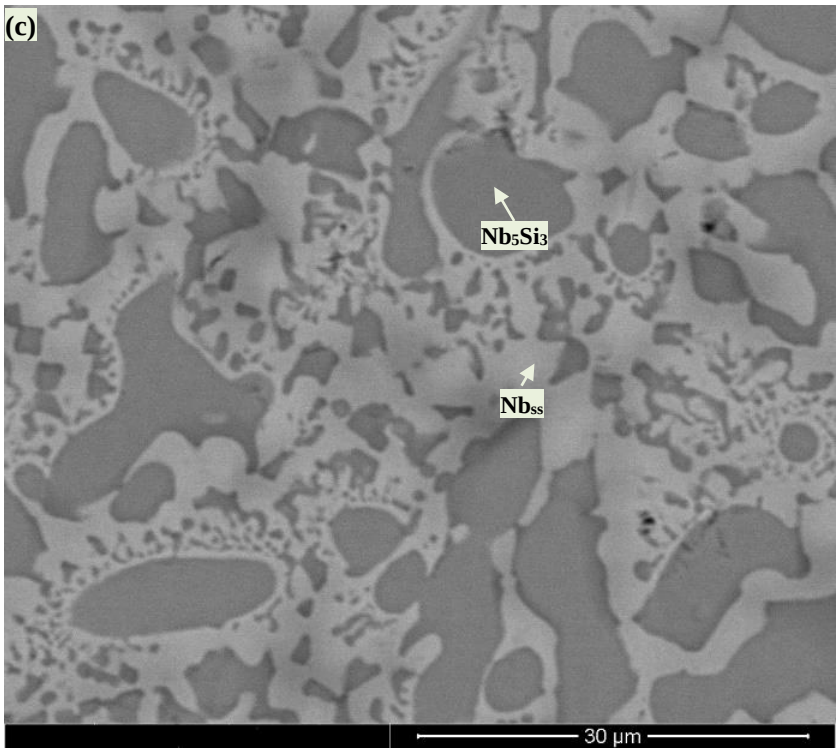


Figure 7.1 BSE images of the microstructure in the bulk (a),(b) and top (c) of the ingot of the cast alloy ZX3.

Some Cr-rich C14 Laves phase was observed near the Ti rich Nb_{ss} phase in the bottom area of the ingot. The phase was too small to be analysed by EDS. X-ray elemental maps confirmed that it was a Cr rich phase, see Figure 7.4. The XRD data confirmed the existence of Nb_{ss} and βNb_5Si_3 but not the Laves phase owing to its low volume fraction (Figure 7.4). The same number of peaks corresponded either to αNb_5Si_3 or βNb_5Si_3 and only one to γNb_5Si_3. Thus, in the cast alloy ZX3, both α and βNb_5Si_3 were present. Some very fine eutectic structure was observed in the bottom area of the ingot (Figure 7.5), which is believed to be a ternary eutectic composed of Ti rich Nb_{ss} + Nb_5Si_3 + C14 Laves phase. A ternary eutectic of Nb_{ss} + C14 Laves + $Nb_5(Cr,Si)_3$ has been proposed by Bewlay *et al* [45].

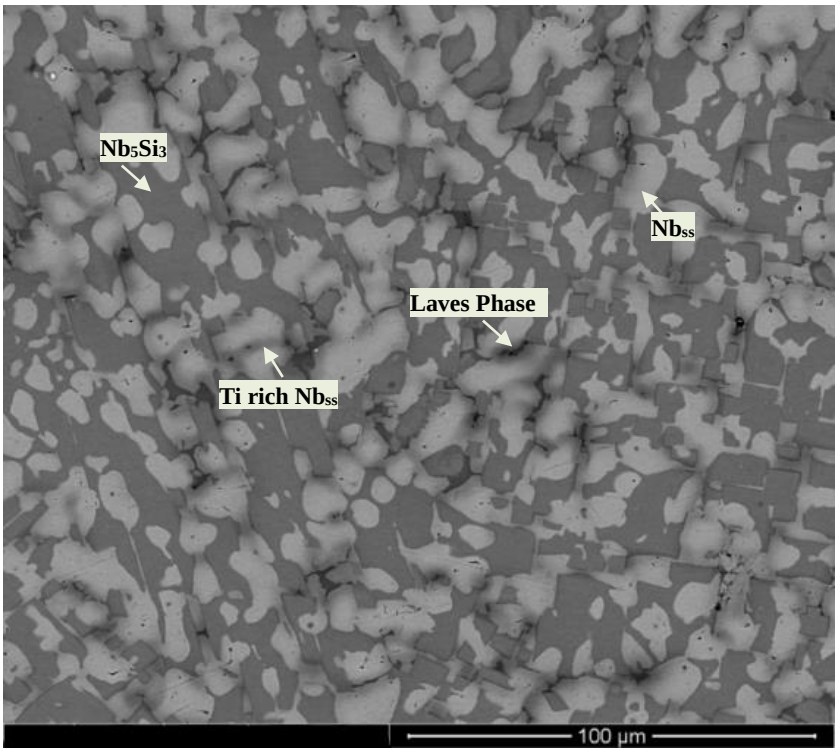


Figure 7.2 BSE image of the microstructure in the bottom area of the ingot of the cast alloy ZX3.

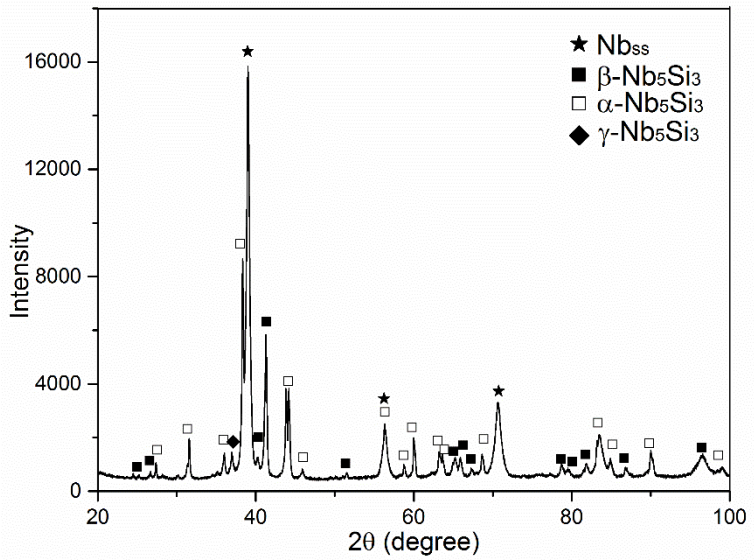


Figure 7.3 X-ray diffractogram of the cast alloy ZX3.

This (ternary) eutectic was examined by X-ray elemental maps, see Figure 7.6. The Ti partitioned in both the Nb_{ss} and Nb_5Si_3 where it substituted the Nb atoms. Ti rich Laves phase was observed at grain boundaries of the Nb_{ss} and Nb_5Si_3.The Cr and Sn on the other hand partitioned to the Nb_{ss} rather than the Nb_5Si_3. The Cr content of the Nb_{ss}

increased in the Ti rich areas of the Nb_{ss} where the Sn concentration was slightly reduced. The partitioning behaviour of Ti between the Nb_{ss} and Nb_5Si_3 and of Cr in the Nb_{ss} is in agreement with the previous work of Zelenistas and Tsakiropoulos [68]. The data for Sn would suggest opposite partitioning behaviour for Ti and Sn or, to put it another way, Ti and Sn do not like each other in the Nb_{ss}.

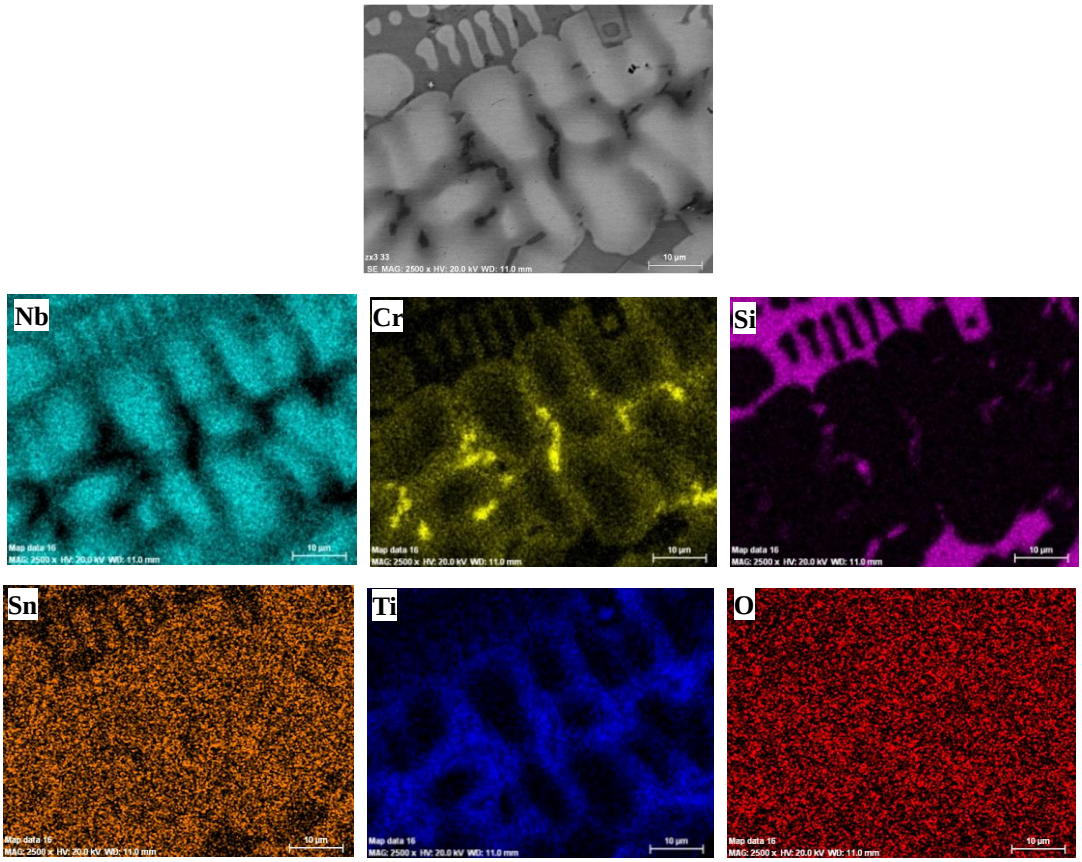


Figure 7.4 The X-ray maps of the C14 Laves phase in the bottom area of the ingot of the cast alloy ZX3.

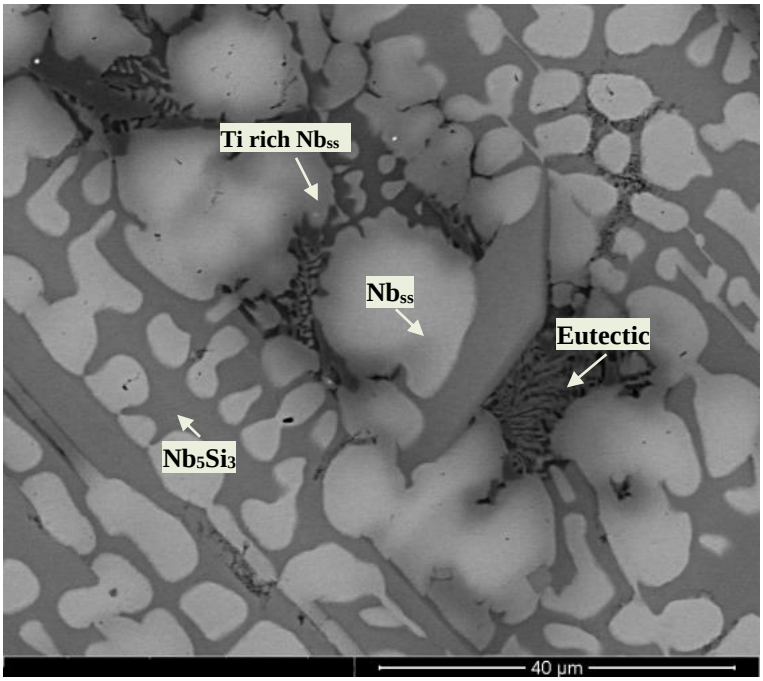


Figure 7.5 BSE image of the microstructure in the bottom area of the ingot of the cast ZX3.

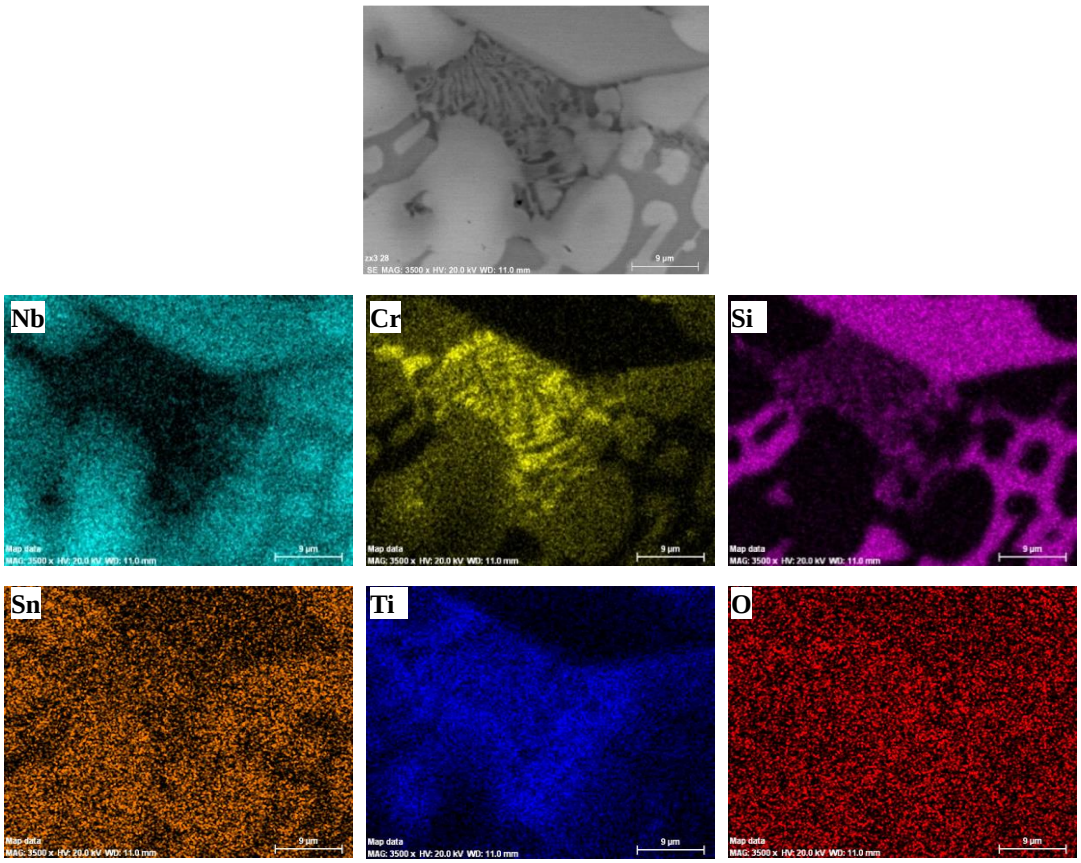
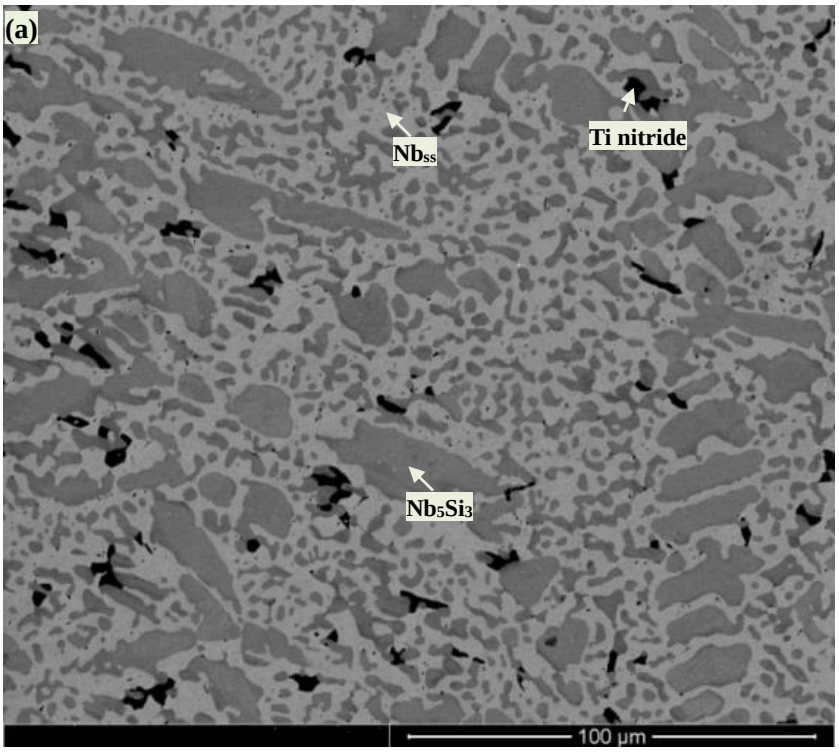


Figure 7.6 The X-ray elemental maps of eutectic observed in the bottom area of the ingot of the alloy cast ZX3.

Heat treated: The alloy was heat-treated at 1500 °C for 100 hours in argon atmosphere in a tube furnace and was furnace cooled. The composition of the heat treated specimen is given in Table 7.1. As seen in Figure 7.7, the microstructure of the heat treated alloy composed of the Nb_5Si_3 silicide and a coarsened prior eutectic Nb_5Si_3 and Nb_{ss} structure. There were no more Ti rich areas in the Nb_{ss} phase but there were grains that were noticeably poorer in Ti. The XRD data of the heat treated alloy confirmed the complete transformation of βNb_5Si_3 to αNb_5Si_3, see Figure 7.8.



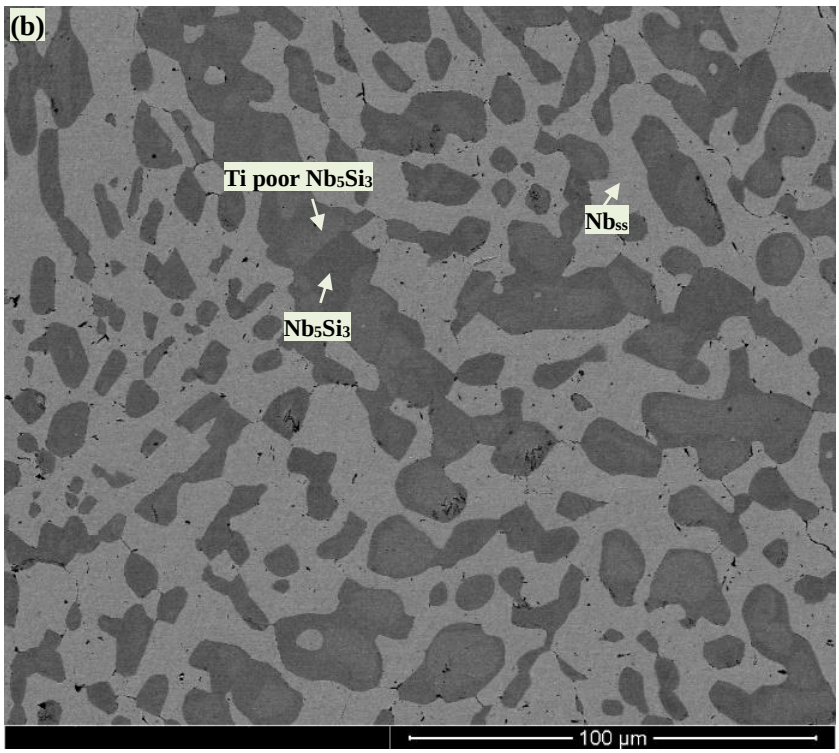


Figure 7.7 BSE images of the microstructure of the heat treated ZX3, (a) area with Ti nitride grains, (b) area with different contrasts in Nb_5Si_3 grains.

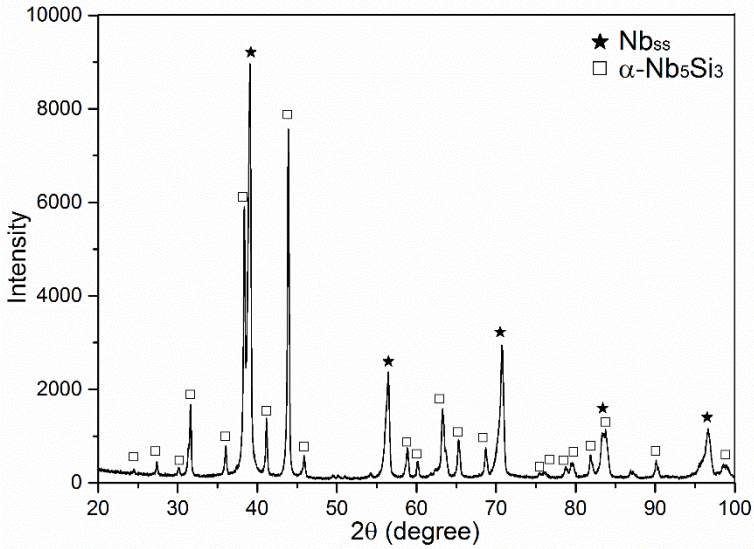


Figure 7.8 X-ray diffractogram of the heat treated alloy ZX3.

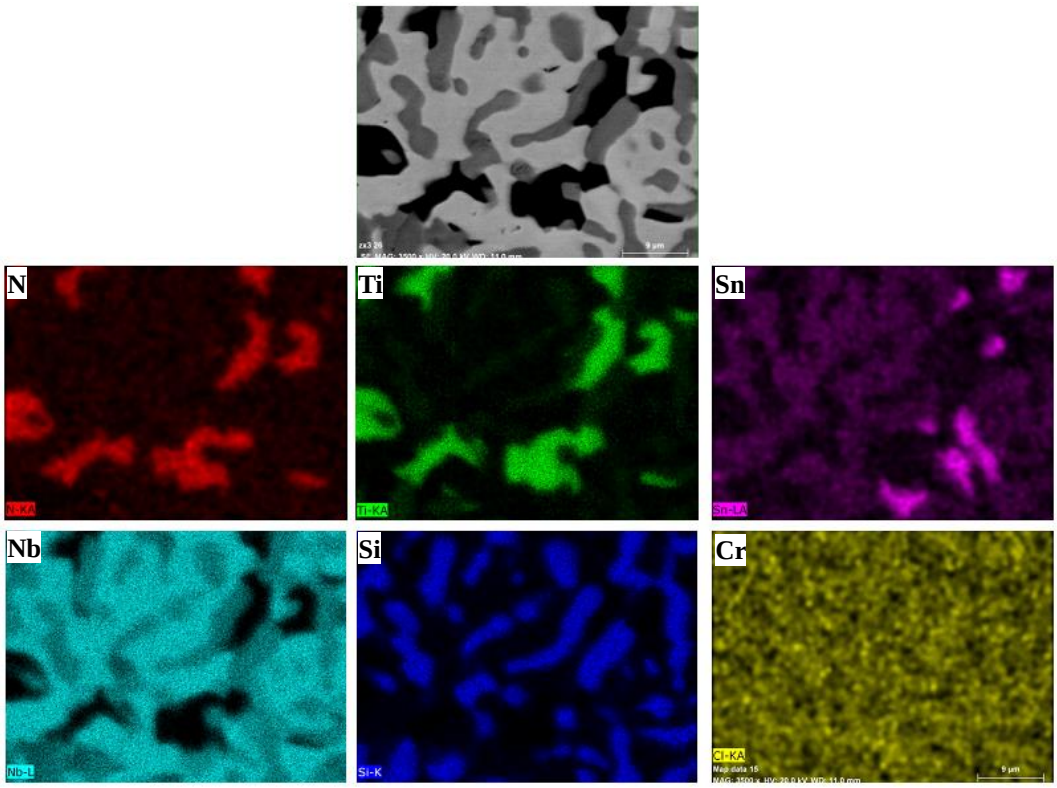


Figure 7.9 The X-ray maps of the bulk area showing Ti nitrides in the heat treated alloy ZX3.

In the Nb_{ss} phase the Si content had decreased to 0.7 at.% while the Cr and Ti concentration were increased to 9.1 at.% and 31.8 at.%, respectively. The concentrations of Cr, Si and Sn in the Nb_5Si_3 on the other hand were very stable after the heat treatment but there were grains that were noticeably poorer in Ti. Some black contrast features were found in the heat treated microstructure and were generally located at interfaces between Nb_{ss} and Nb_5Si_3, which, as we discussed previously, were Ti rich in the as cast microstructure. These features were Ti nitride grains, as confirmed by X-ray elemental maps, see Figure 7.9.

7.2.2 Alloy Nb-24Ti-18Si-5Cr-5Sn (ZX4)

As cast: The actual composition of the cast alloy was Nb-25.4Ti-18.8Si-4.9Cr-5Sn. The EDS data in Table 7.2 shows that there was macrosegregation of Si, Ti and Cr, as the concentrations of these elements varied between 14.7 to 22.0 at.%, 22.2 to 28.8 at.% and 3.5 at.% to 7.1 at.%, respectively. The above ranges of the concentrations of

Ti, Si and Cr were observed between the bottom and bulk of the ingot, i.e, between the parts that had experienced the highest and lowest cooling rates during solidification.

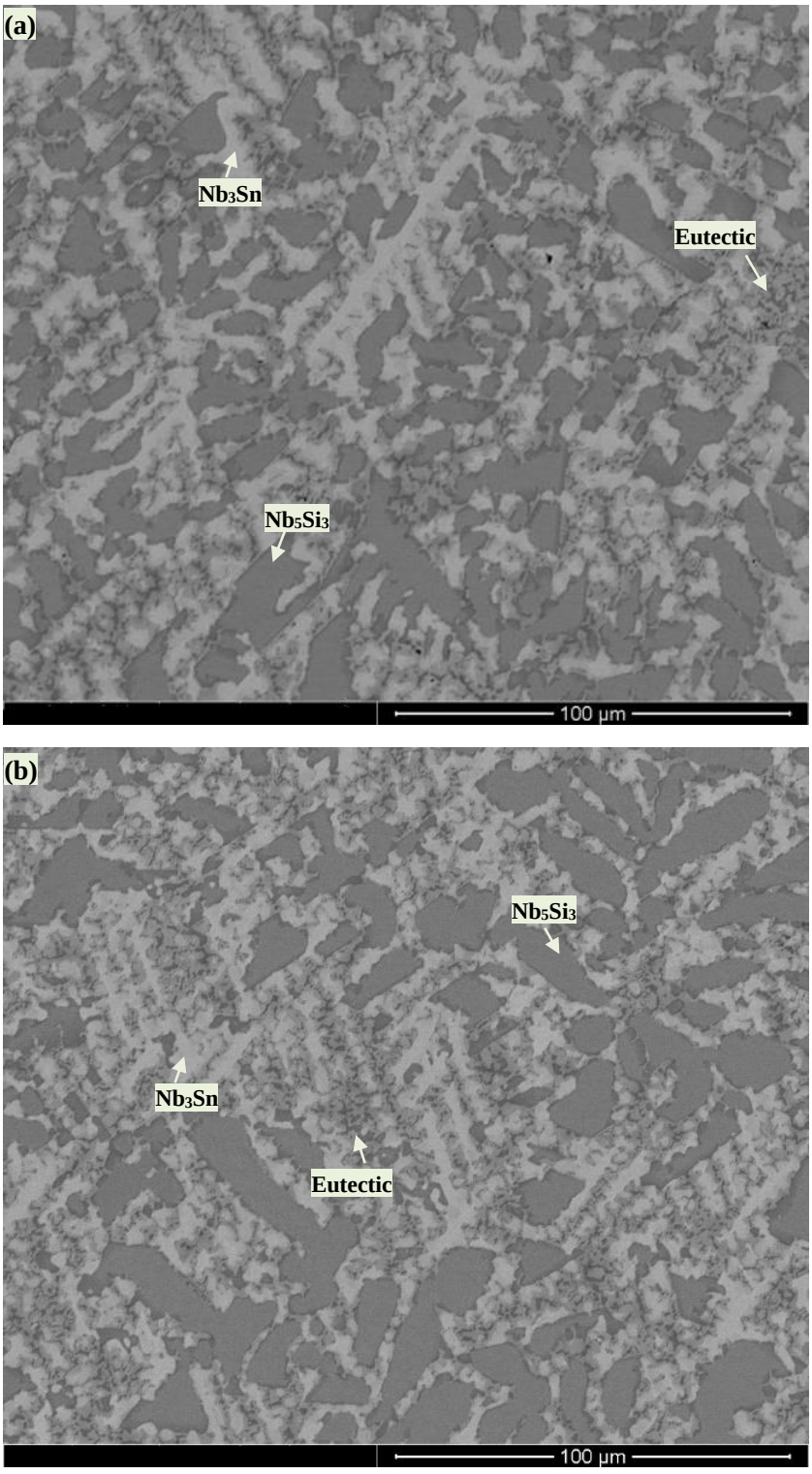


Figure 7.10 BSE images of the microstructure in the (a) top and (b) bulk areas of the as cast alloy ZX4.

The phases observed in the microstructure of the cast alloy were the Nb_5Si_3, Nb_3Sn and some Nb_{ss} + Nb_5Si_3 eutectic and a low volume fraction of the Cr rich C14 $NbCr_2$ Laves phase. The top and bulk of the ingot had similar microstructures that were different compared with the microstructure in the bottom area of the ingot. In the former areas, a large volume fraction of Nb_5Si_3 and Nb_3Sn dendrites were formed, with Nb_{ss} + Nb_5Si_3 eutectic in the interdendritic areas, see Figure 7.10. Ti rich areas were observed near the edges of Nb_5Si_3 dendrites. However, no evidence was found of the Laves phase in the top and bulk area of the ingot.

In the bottom area, the Nb_{ss} + Nb_5Si_3 eutectic was less evident, and the Nb_{ss}, Nb_5Si_3 and Nb_3Sn phases were present as a co-continuous structure. Some Laves phase was formed in the interdendritic area of the Nb_{ss} grains either as individual grains or as part of a eutectic structure (see Figures 7.11 and 7.12).The Cr-rich C14 Laves phase was also found in the bottom area of the ingot of the alloy ZX3 (see Figures 7.2).

The Nb_{ss} was rich in Sn and its Ti, Si and Cr concentrations were close to those in the Ti rich Nb_{ss} in the cast alloy ZX3, see Tables 7.2 and 7.1. The Nb_5Si_3 was also richer in Sn in the alloy ZX4. In the Nb_3Sn phase, the (Si + Sn) concentration was 19.4 at.% with Si/Sn ~ 0.6. The XRD data confirmed the aforementioned phases. Both the αNb_5Si_3 and βNb_5Si_3 phases were present in the as cast alloy ZX4, see Figure 7.13. Only one peak corresponded to γNb_5Si_3 as was the case in the cast alloy ZX3, and thus it is considered unlikely that this phase, which is stabilised by interstitials, was present.

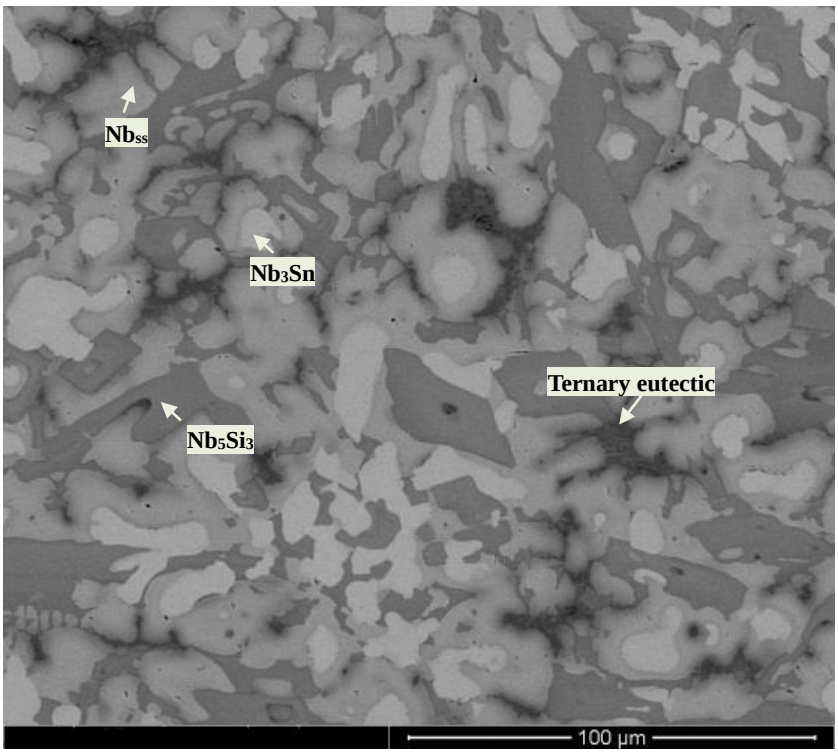


Figure 7.11 BSE image of the microstructure in the bottom area of the as cast alloy ZX4.

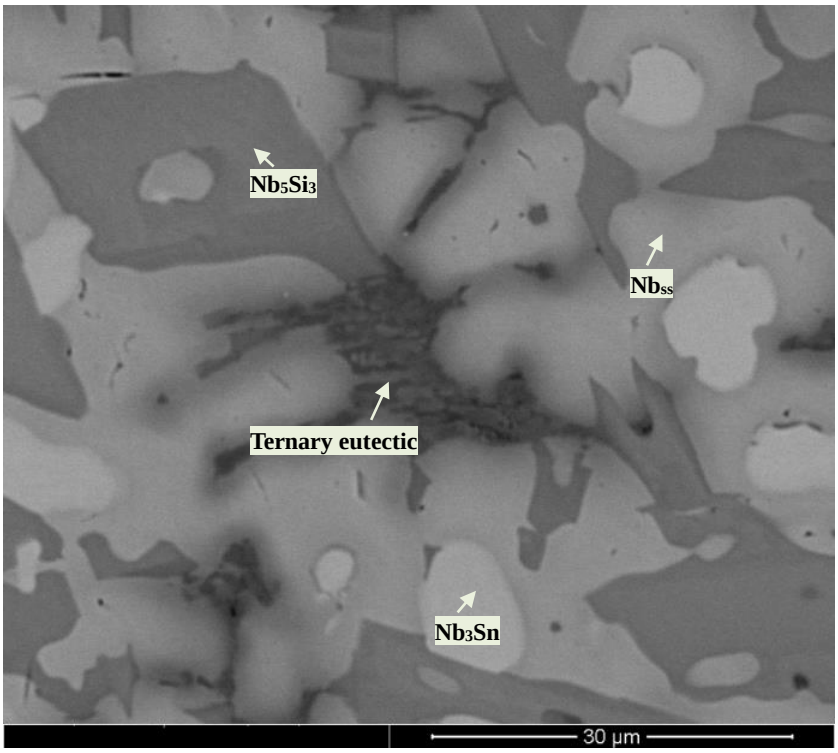


Figure 7.12 BSE image of the microstructure in the bottom area of the cast alloy ZX4.

Table 7.2 EDS analysis (at.%) of the as cast and heat treated alloy ZX4.

	Nb	Ti	Si	Cr	Sn
As cast					
Surface*	**46.1** ± 0.3	**24.8** ± 0.3	**19.5** ± 0.5	**4.7** ± 0.1	**4.9** ± 0.2
	45.6 - 46.5	*24.3 - 25.3*	*18.8 - 20.4*	*4.4 - 4.9*	*4.8 - 5.3*
Bulk*	**46.5** ± 0.3	**24.2** ± 0.9	**20.3** ± 1.8	**4.0** ± 1.1	**5.0** ± 0.4
	45.8 - 46.7	*22.2 - 25.3*	*17.8 - 22.0*	*3.5 - 4.9*	*4.2 - 5.6*
Bottom*	**44.7** ± 0.6	**27.3** ± 1.0	**16.7** ± 1.4	**6.1** ± 0.7	**5.2** ± 0.2
	44.1 - 45.7	*25.7 - 28.8*	*14.7 - 19.1*	*5.2 - 7.1*	*4.9 - 5.6*
Nb_{ss}	**44.5** ± 2.6	**35.0** ± 1.6	**3.6** ± 0.8	**11.3** ± 0.9	**5.6** ± 0.5
	40.3 - 46.8	*33.3 - 37.7*	*2.2 - 4.5*	*10.2 - 12.1*	*4.7 - 6.1*
Nb_3Sn	**55.8** ± 0.4	**22.3** ± 0.5	**7.5** ± 0.5	**2.5** ± 0.3	**11.9** ± 0.7
	55.5 - 56.4	*21.6 - 23.0*	*6.8 - 8.4*	*2.2 - 3.0*	*10.7 - 12.5*
Ti-rich	**41.1** ± 0.4	**22.1** ± 0.9	**33.1** ± 1.4	**1.9** ± 0.5	**1.8** ± 0.2
Nb_5Si_3	*40.7 - 41.7*	*20.9 - 23.4*	*31.1 - 34.3*	*1.1 - 2.7*	*1.4 - 2.1*
Nb_5Si_3	**45.2** ± 0.5	**17.2** ± 0.4	**34.8** ± 0.2	**0.9** ± 0.1	**1.9** ± 0.2
	44.5 - 45.8	*16.7 - 17.9*	*34.5 - 35.2*	*0.8 - 1.1*	*1.7 - 2.2*
Laves phase	**20.8** ± 2.3	**28.3** ± 4.2	**10.7** ± 2.2	**38.4** ± 3.9	**1.8** ± 0.7
	18.7 - 24.4	*21.0 - 34.7*	*8.5 - 12.0*	*34.0 - 44.8*	*0.7 - 3.0*
Heat treated					
Bulk*	**44.6** ± 0.5	**26.0** ± 0.5	**20.0** ± 0.5	**4.3** ± 0.2	**5.1** ± 0.4
	43.9 - 45.6	*25.0 - 26.4*	*19.1 - 20.7*	*4.1 - 4.6*	*4.6 - 5.5*
Nb_{ss}	**52.1** ± 0.8	**33.3** ± 0.8	**0.7** ± 0.1	**9.0** ± 0.4	**4.9** ± 0.2
	50.9 - 53.4	*32.3 - 34.2*	*0.5 - 1.0*	*8.7 - 9.7*	*4.7 - 5.2*
Nb_3Sn	**49.8** ± 0.3	**26.3** ± 0.3	**5.2** ± 0.5	**5.0** ± 0.2	**13.7** ± 0.2
	49.3 - 50.4	*25.8 - 26.8*	*4.7 - 6.5*	*4.6 - 5.2*	*13.3 - 13.9*
Nb_5Si_3	**42.9** ± 0.9	**19.5** ± 0.8	**35.6** ± 0.6	**0.5** ± 0.1	**1.5** ± 0.4
	41.7 - 44.4	*18.4 - 21.0*	*34.8 - 36.2*	*0.4 - 0.8*	*1.1 - 2.2*

* Large area analysis

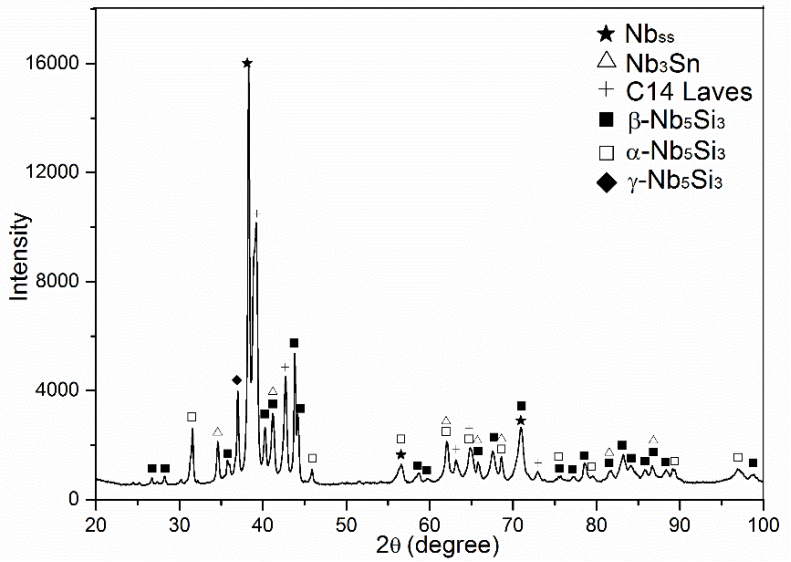


Figure 7.13 X-ray diffractogram of the cast alloy ZX4.

Heat-treated: The alloy was heat-treated at 1500 °C for 100 hours in argon atmosphere in a tube furnace and furnace cooled. The average composition of the heat treated sample is given in Table 7.2 and would suggest that the alloy was homogenised after this heat treatment. As can be seen in Figure 7.14, the prior eutectic structure was not present after the heat treatment. In the heat treated microstructure, the Nb_{ss}, Nb_5Si_3 and the Nb_3Sn were stable. The XRD data of the heat treated ZX4 confirmed that the transformation of βNb_5Si_3 to αNb_5Si_3 was complete, see Figure 7.15.

Some precipitates were observed within the Nb_5Si_3 phase with size less than 3 µm in diameter. The Nb_{ss} grains boundaries were "surrounded" by dark contrast "fine lines" that could be clearly seen in the microstructure. Some black features were also found inside the Nb_{ss} phase. X-ray maps were used to "identify" the chemistry of the aforementioned features and the data indicated that the fine lines were Cr rich and the dark features were Ti and nitrogen rich, as seen in Figures 7.16 and 7.17. The former were observed in the same area as the Laves phases in the heat treated alloy Nb-24Ti-18Si-5Al-5Cr (alloy KZ5 in [68]) and are therefore taken to be evidence for Laves phase. The Sn and Si maps in Figures 7.16 and 7.17 would suggest that the fine precipitates in αNb_5Si_3 were Nb_3Sn, as the latter is ≈ 3 times richer in Sn than Nb_{ss}.

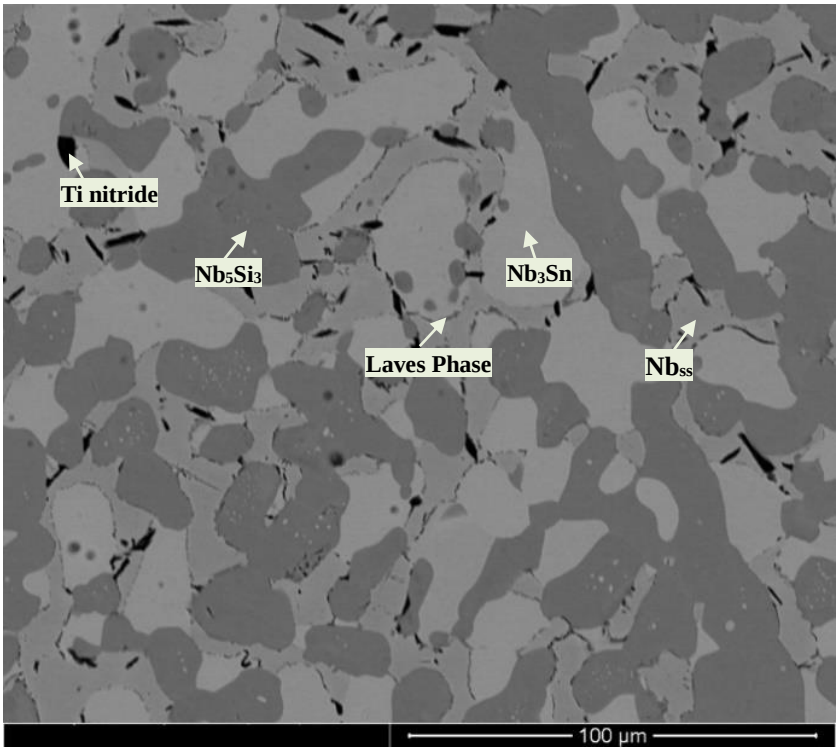


Figure 7.14 The BSE image of the microstructure of the heat treated alloy ZX4.

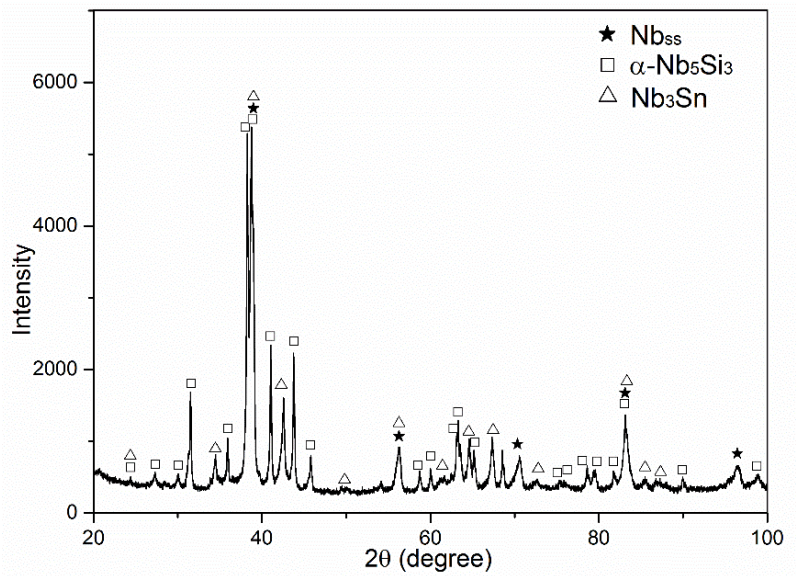


Figure 7.15 X-ray diffractogram of the heat treated alloy ZX4.

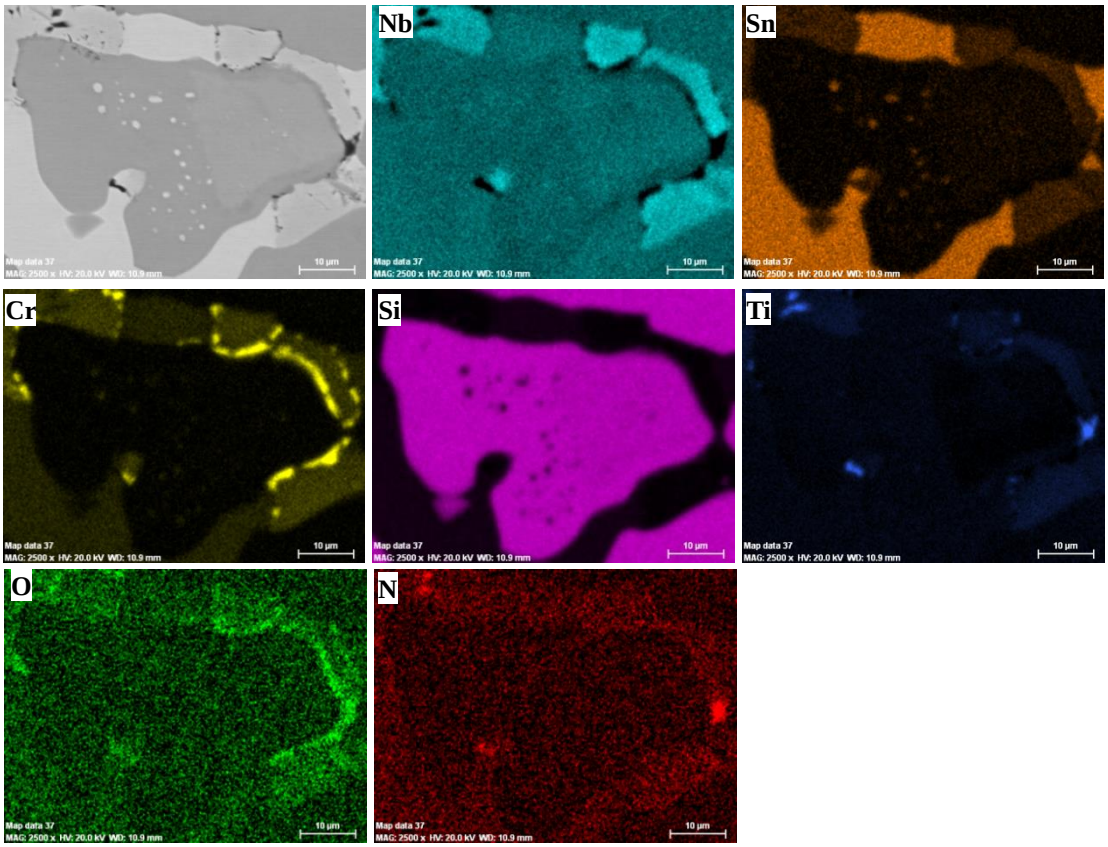


Figure 7.16 The X-ray maps of the heat treated alloy ZX4 showing the "fine line" Cr rich Laves phase.

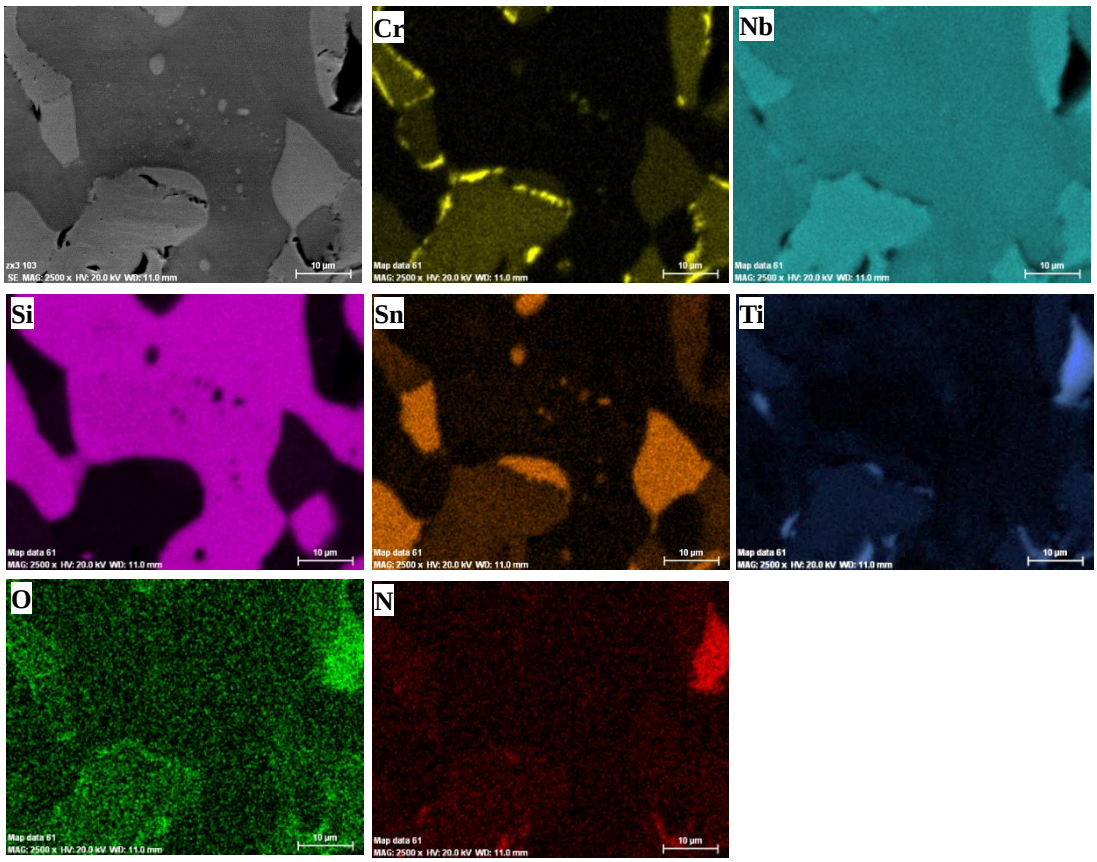


Figure 7.17 The X-ray maps of the heat treated alloy ZX4 showing the Cr rich "line".

7.3 Thermo-gravimetric analysis of the alloys ZX3 and ZX4

The oxidation behaviour of the cast alloys Nb-24Ti-18Si-5Cr-2Sn (ZX3) and Nb-24Ti-18Si-5Cr-5Sn (ZX4) was studied at 800 °C and 1200 °C using TGA. The 800 °C oxidation experiment was chosen to understand the oxidation behaviour of the alloys in the pest oxidation regime. The 1200 °C oxidation experiment was chosen to find out if alloying with Sn benefits the higher temperature oxidation. Both temperatures allowed data from this research to be compared with data in the literature. The data for both alloys is shown in Figures 7.18 to 7.20. After 100 hours oxidation in static air at 800 °C, the specimens of both alloys did not pest. The oxidised specimens had adherent oxides on their surfaces, as seen in Figure 7.18.

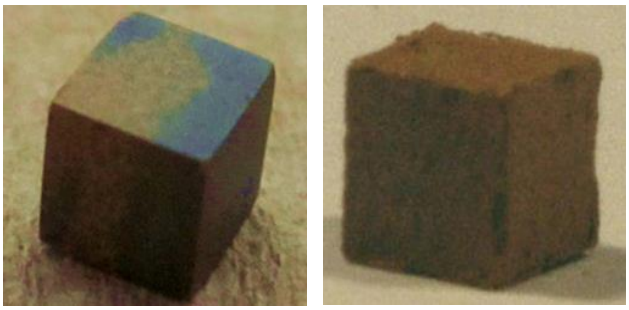


Figure 7.18 The oxidised specimens of alloy ZX3 (left) and alloy ZX4 (right) at 800 °C.

During oxidation at 1200 °C, the weight change of the alloys was more severe compared with the oxidation at 800 °C (Figure 7.20), and there was spallation of the scale (Figure 7.19). Those scales were ~ 300 μm thick. Some WDS analysis was carried out to identify the composition of the oxides.



Figure 7.19 The oxidised specimens of the alloys ZX3 (left) and alloy ZX4 (right) at 1200 °C.

Oxidation kinetics and the microstructures of the oxidised alloys at 800 °C and 1200 °C are introduced in the following sections. The oxidation behaviour of the alloys ZX3 and ZX4 is then compared to show the effect of Sn on the oxidation resistance of the Nb-24Ti-18Si-5Cr base alloy.

7.3.1 Oxidation kinetics of the alloys ZX3 and ZX4 at 800 °C and 1200 °C

The thermo-gravimetric data of the alloys ZX3 and ZX4 after oxidation at 800 °C and 1200 °C in static air for 100 hours is shown in Figure 7.20, where the alloy weight change in g/cm^2 is plotted as a function of oxidation time (min). At 800 °C the alloy ZX3 followed linear oxidation kinetics and the alloy ZX4 parabolic oxidation kinetics, see Table 7.3. After oxidation in static air at 1200 °C for 100 hours, both alloys

exhibited linear oxidation kinetics. The oxidation kinetic rates of the alloys ZX3 and ZX4 are listed in Table 7.3.

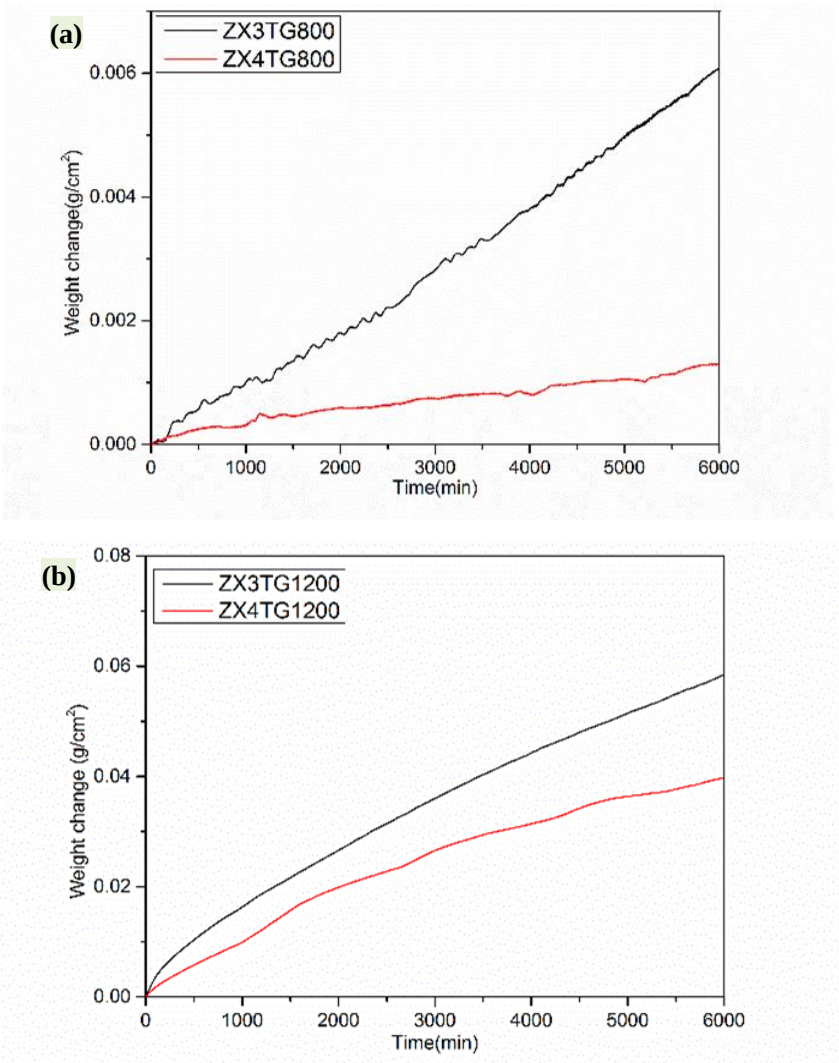


Figure 7.20 Thermo-gravimetric curves of the alloys ZX3 and ZX4 at (a) 800 °C, and (b) 1200 °C.

Table 7.3 The oxidation kinetic rates K_l ($g \bullet cm^{-2} \bullet s^{-1}$) and K_p ($g^2 \bullet cm^{-4} \bullet s^{-1}$) of the alloys ZX3 and ZX4.

	ZX3	ZX4
800 °C	$K_l = 1.69 \times 10^{-8}$	$K_p = 4.69 \times 10^{-12}$
1200 °C	$K_p = 4.54 \times 10^{-9}$ (t ≤1000mim) $K_l = 1.42 \times 10^{-7}$ (t >1000mim)	$K_p = 1.65 \times 10^{-9}$ (t ≤1000mim) $K_l = 1.00 \times 10^{-7}$ (t >1000mim)

The weight gains of the alloys ZX3 and ZX4 at 800 °C were ~ 6 and 1 mg/cm^2, respectively, compared with 95 mg/cm^2 for the base alloy without Sn addition [45]. At

1200 °C the weight gains for the alloys ZX3 and ZX4 were ~ 60 and 40 mg/cm^2, respectively, compared with ~ 135 mg/cm^2 for the base alloy without Sn [79].

7.3.2 Microstructures of the oxidised alloys ZX3 and ZX4 at 800 °C

The oxidised specimens of the alloys ZX3 and ZX4 were shown in Figure 7.18. Pest oxidation is often observed in Nb silicide based alloys. Both alloys did not pest. Adherent oxide scales were formed on the surfaces of the cubic specimens of both alloys. The oxides were studied by SEM-EDS, and cross sections of the oxidised specimens were studied using SEM-EDS and WDS-EPMA.

The microstructure of the oxidised alloy ZX3 at 800 °C is shown in Figure 7.21. The oxide scale was ~ 15 μm thick, with the different oxides showing different contrasts in the back scattered image. The scale had cracks parallel to its surface (see Figure 7.21).

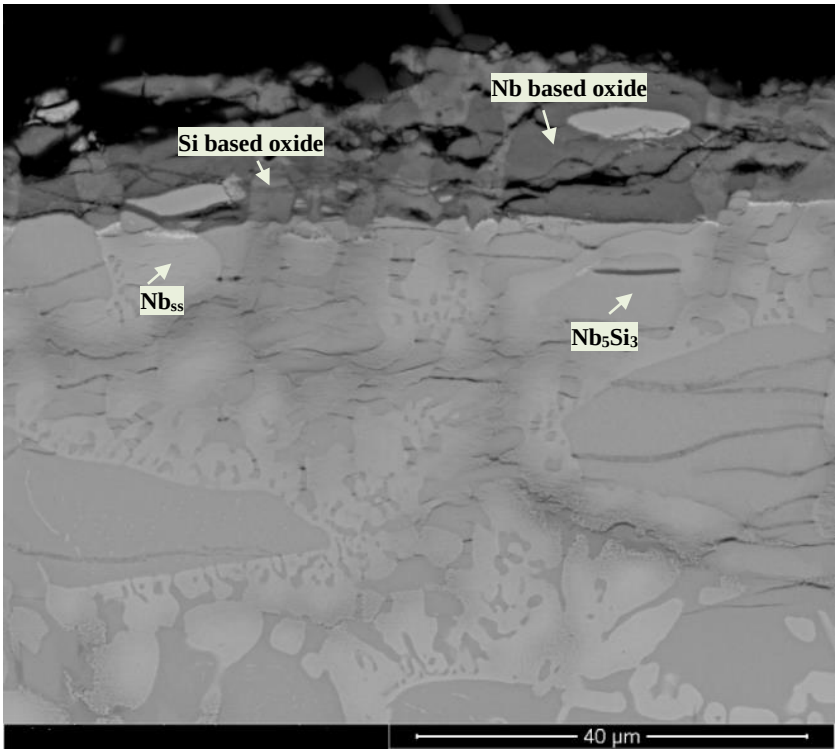


Figure 7.21 BSE image of the microstructure of the oxidised alloy ZX3 at 800 °C.

Beneath the oxide scale, an internal oxygen diffusion zone was present where the Nb_{ss} phase was attacked by oxygen while the Nb_5Si_3 silicide was intact. This oxygen diffusion zone was about 40 µm deep below the surface. In the oxidised Nb_{ss} in this region, oxide precipitates exhibiting dark contrast were formed inside the solid solution by the Nb_{ss} / Nb_5Si_3 interfaces. The Nb_5Si_3 in the oxygen diffusion zone showed cracks that were mostly parallel to the surface of the specimen, as seen in Figure 7.22. The WDS analysis was applied on the oxides and the bulk phases and the data is summarised in Table 7.4.

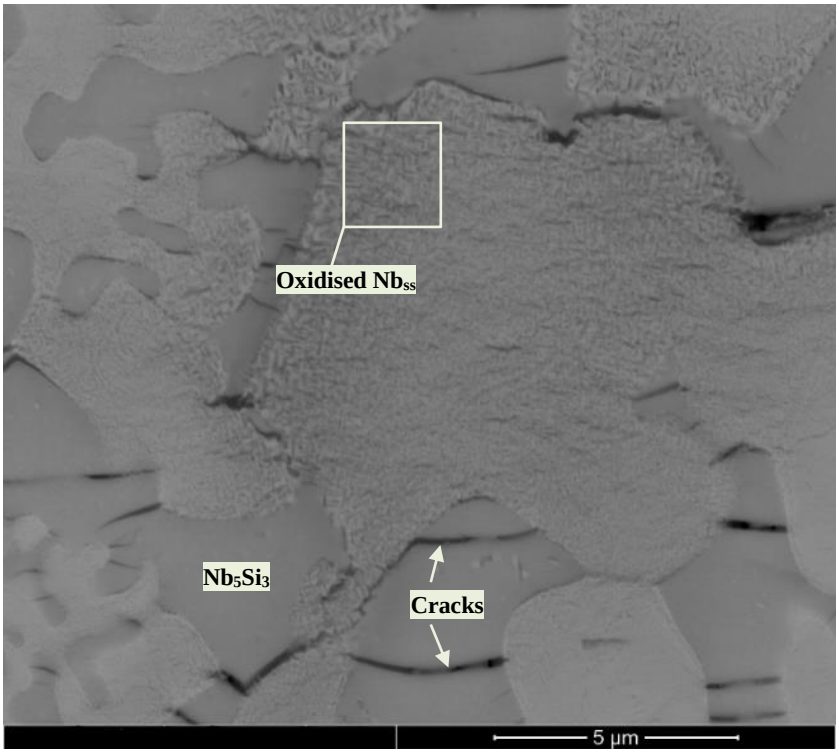


Figure 7.22 BSE image of the microstructure of the oxidised alloy ZX3 at 800 °C showing the parallel cracks in the Nb_5Si_3 phase.

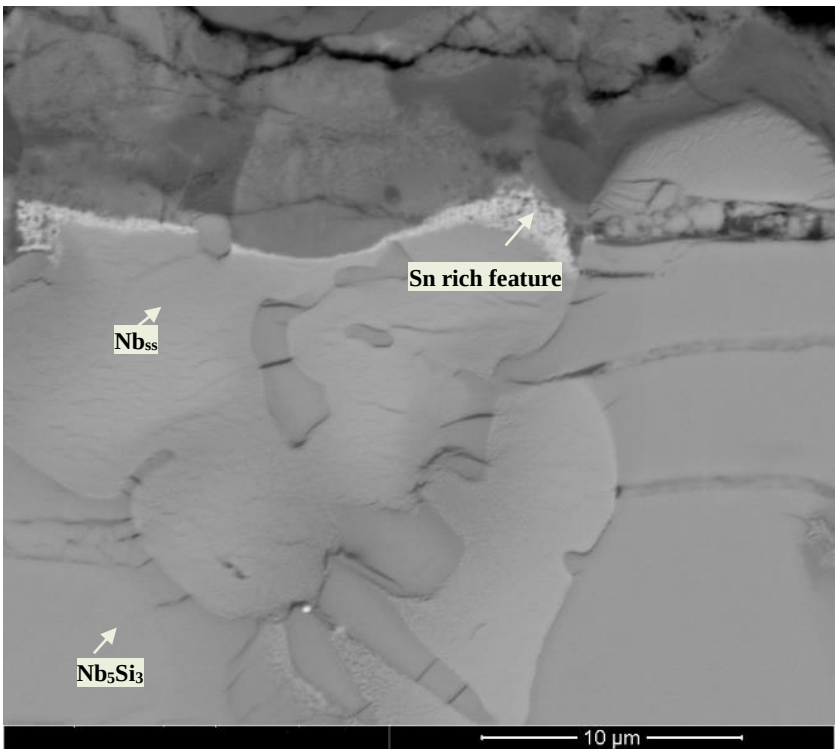


Figure 7.23 BSE image of the microstructure of the oxidised alloy ZX3 at 800 °C showing the Sn rich feature below the oxide scales.

In the oxidised alloy ZX3, a bright contrast thin layer was observed between the scale and the oxygen diffusion zone (see Figure 7.23). This layer only formed continuously in those areas between the oxide scale and Nb_{ss}, in other words it was not observed in the areas between the Nb_5Si_3 and oxide scale. Owing to its thickness, it was not possible to quantify the composition of the bright contrast thin layer.

Table 7.4 The WDS analysis (at.%) of the phase and the oxides in the alloy ZX3 at 800 °C.

Phase	Nb	Ti	Si	Cr	Sn	O
Bulk	**42.30** ± 0.34	**16.10** ± 0.27	**35.83** ± 0.31	**0.95** ± 0.03	**0.66** ± 0.03	**4.16** ± 0.39
Nb_5Si_3	*41.76 - 42.59*	*15.78 - 16.40*	*35.37 - 36.12*	*0.90 - 0.97*	*0.62 - 0.70*	*3.76 - 4.57*
Bulk	**56.67** ± 4.18	**25.91** ± 2.33	**1.68** ± 0.65	**7.17** ± 1.42	**2.73** ± 0.09	**5.84** ± 0.63
Nb_{ss}	*50.98 - 62.20*	*22.6 - 28.67*	*1.29 - 2.99*	*5.53 - 9.21*	*2.66 - 2.91*	*5.41 - 7.09*
Si rich	**13.85** ± 0.33	**4.33** ± 0.48	**11.84** ± 0.93	**0.28** ± 0.07	**0.28** ± 0.10	**69.42** ± 0.26
Oxide	*13.48 - 14.17*	*3.87 - 4.79*	*11.00 - 12.82*	*0.21 - 0.35*	*0.21 - 0.44*	*69.11 - 69.72*
Nb rich	**15.97** ± 1.69	**9.02** ± 1.29	**0.34** ± 0.03	**3.66** ± 1.47	**0.29** ± 0.15	**70.72** ± 0.66
Oxide	*14.19 - 18.24*	*7.27 - 10.33*	*0.30 - 0.38*	*2.06 - 5.62*	*0.08 - 0.45*	*70.04 - 71.61*

Figure 7.24 shows a cross section of the microstructure of the alloy ZX4 oxidised at 800 °C. The oxide scale adhered better to the bulk of the specimen, compared with the oxidised alloy ZX3. The scale was compact, which is beneficial for oxidation resistance. In the oxygen diffusion zone below the scale, it was evident that oxygen had penetrated through the Nb_{ss} phase and dark contrast oxide precipitates were formed within the Nb_{ss} and at its grain boundaries, see Figure 7.26. The Nb_5Si_3 and Nb_3Sn intermetallic on the other hand did not show signs of oxidation. A bright contrast layer, formed between the scale and oxygen diffusion zone, was also observed in the oxidised alloy ZX4.

The backscatter electron image in Figure 7.25 shows a variety of contrasts (phases) inside this bright contrast layer. Different from the oxidised alloy ZX3, this layer not only formed continuously between the scale/Nb_{ss} interface, but also formed at the oxides/ Nb_3Sn interface.

It was noticed that in the microstructure of the oxidised alloy ZX4, the Nb_{ss} had acicular precipitates formed inside its grains, as seen in Figure 7.26. Those sub-micron precipitates are believed to be oxides [80] which would suggest that the oxygen had penetrated in the specimen. The phases of the oxidised alloy were studied using WDS and the analysis data is given in Table 7.5.

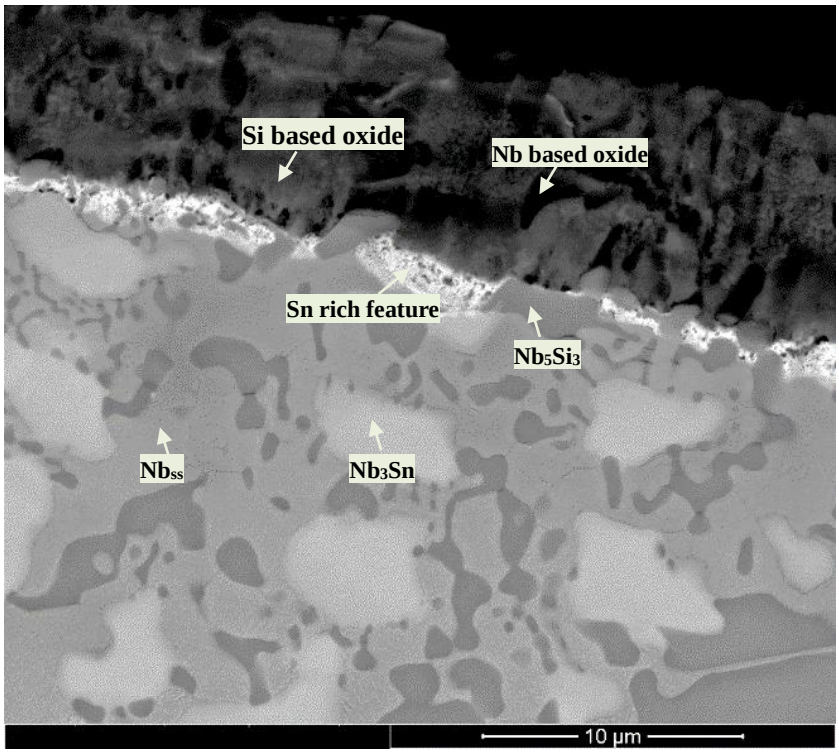


Figure7.24 The cross session of the oxidised microstructure of alloy ZX4 at 800 °C.

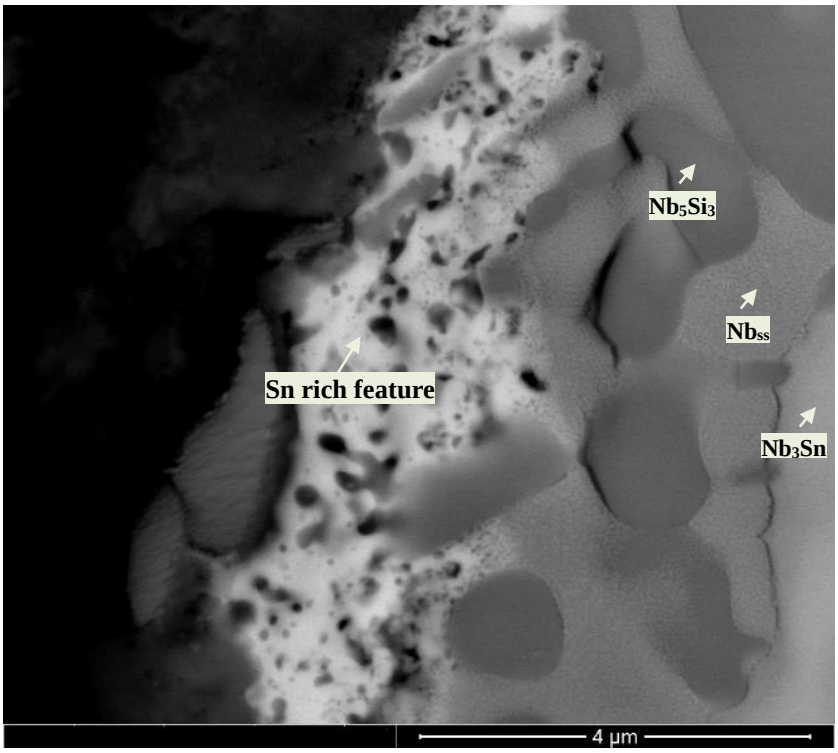


Figure7. 25 BSE image of the microstructure of oxidised alloy ZX4 at 800 °C showing the various phase inside the Sn rich layer.

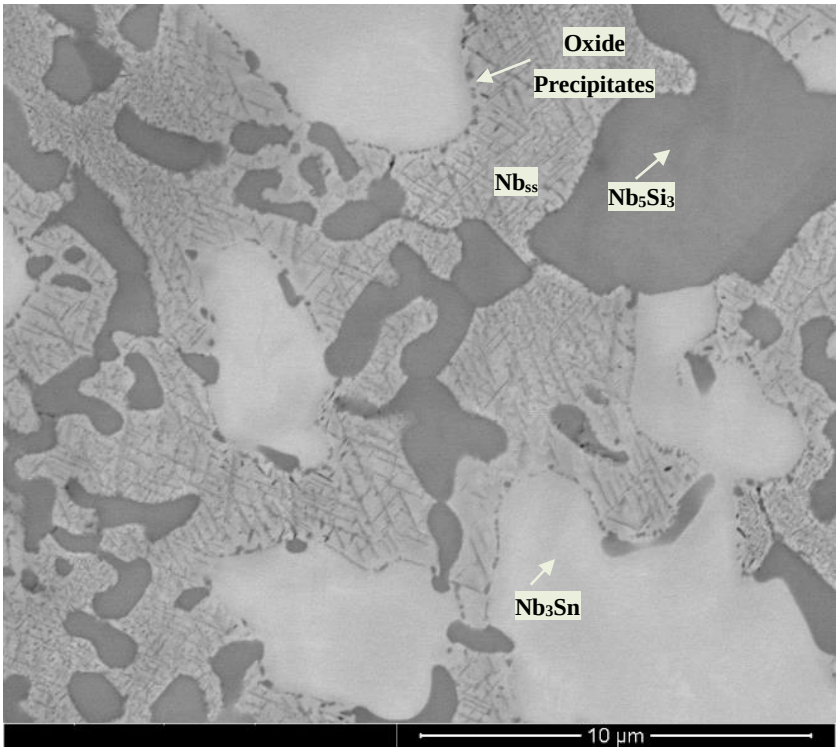


Figure 7.26 The oxidised microstructure of the alloy ZX4 at 800 °C showing acicular precipitates inside the Nb_{ss} phase.

Table 7.5 The WDS analysis of the phases in the bulk of the oxidised alloy ZX4 at 800 °C.

Phase	Nb	Ti	Si	Cr	Sn	O
Bulk	**43.63** ± 0.14	**15.63** ± 0.39	**34.03** ± 0.67	**1.04** ± 0.08	**1.52** ± 0.46	**4.15** ± 0.62
Nb_5Si_3	*43.38 - 43.83*	*15.06 - 16.27*	*33.03 - 34.83*	*0.96 - 1.15*	*0.64 - 1.85*	*3.30 - 4.69*
Bulk	**55.04** ± 0.84	**20.51** ± 0.92	**5.93** ± 0.20	**2.90** ± 0.55	**9.36** ± 0.64	**6.26** ± 0.55
Nb_3Sn	*53.87 - 56.19*	*19.46 - 21.85*	*5.74 - 6.25*	*2.41 - 3.77*	*8.34 - 10.06*	*5.79 - 7.09*
Bulk	**46.69** ± 1.23	**29.41** ± 1.07	**2.67** ± 0.76	**9.16** ± 0.67	**4.84** ± 0.38	**7.23** ± 0.81
Nb_{ss}	*45.83 - 48.81*	*28.02 - 31.02*	*1.66 - 3.65*	*8.62 - 10.30*	*4.53 - 5.49*	*5.49 - 7.99*

The topology of the scale formed on ZX4 at 800 °C is shown in Figure 7.27. Generally, oxides of three contrasts were observed. The EDS data is given in Figure 7.27. It is shown that the smoothest appearance oxides were Si rich, the slightly brighter contrast oxide was Nb rich, while in some areas in between the aforementioned two oxides some Ti rich oxide was found. The WDS results for the compositions of the Nb rich and Nb-Si rich oxides are shown in Table 7.6.

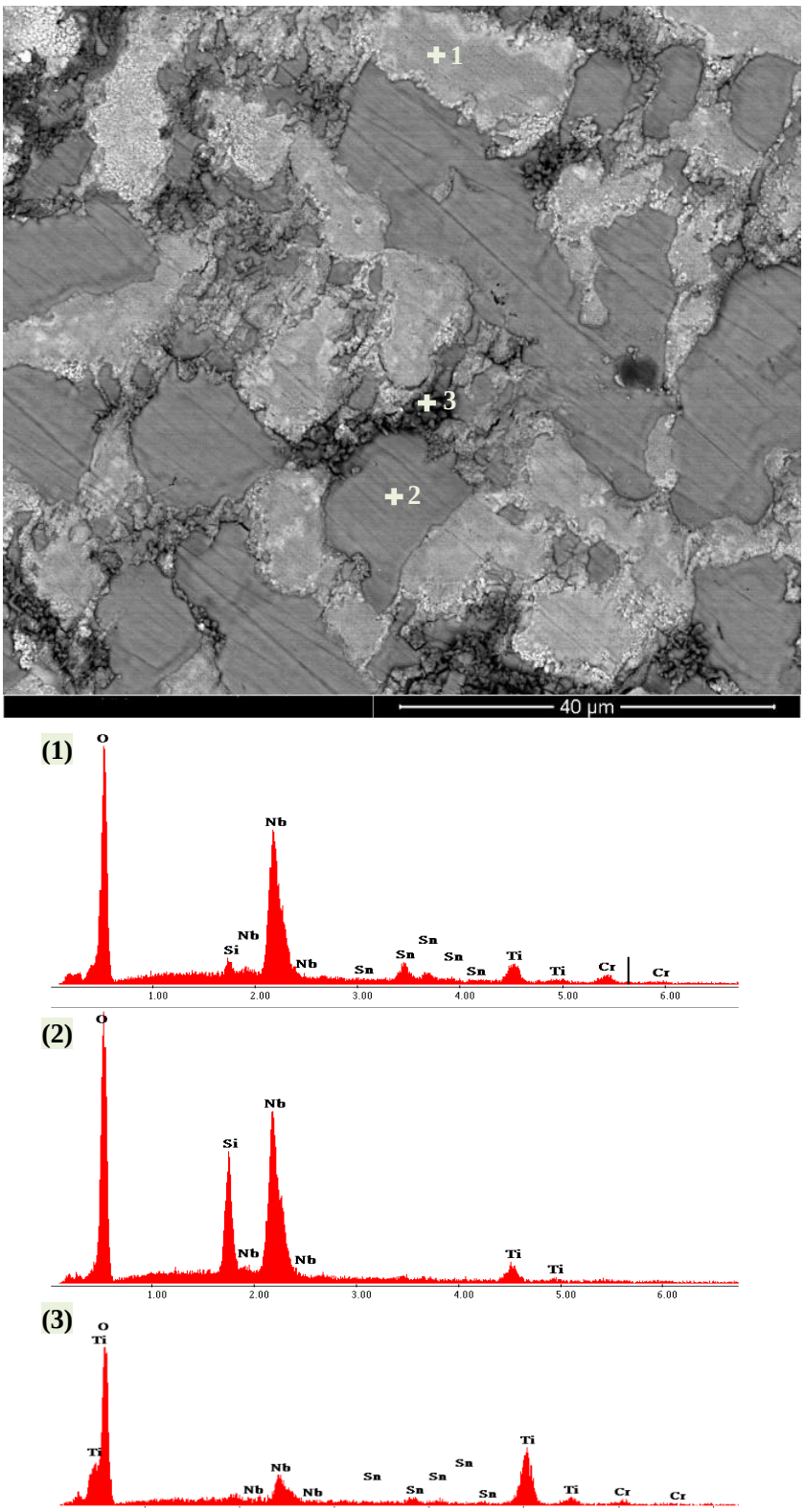


Figure 7.27 BSE image of the oxide scale formed on the alloy ZX4 at 800 °C and the corresponding EDS data.

Table 7.6 The WDS analysis (at.%) of the two types of oxides formed on the alloy ZX4 at 800 °C.

Phase	Nb	Ti	Si	Cr	Sn	O
Nb rich oxide	18.39	10.99	1.64	2.99	0.08	65.91
Nb-Si rich oxide	14.21	5.83	13.30	0.54	0.15	65.97

7.3.3 Microstructure of the oxidised alloys ZX3 and ZX4 at 1200 °C

The oxidised specimens of the alloys ZX3 and ZX4 at 1200 °C were shown in Figure 7.19. Both oxidised samples survived after 100 hours isothermal oxidation, but their scales had spalled off. Figure 7.28 shows images of cross sections of the scale formed on the alloy ZX3 at 1200 °C. Different oxides formed in the scale. WDS spot analysis confirmed the formation of Ti rich, Nb rich and Nb-Si rich oxides, see Table 7.7. The cross section microstructures of the oxidised specimens were also studied using SEM. In the oxidised alloy ZX3, the dark contrast features, which are believed to be Ti nitride, were formed throughout the whole specimen and would suggest contamination throughout all the specimen, as seen in Figure 7.29. Those Ti nitrides were found both inside and on the grain boundaries of the Nb_{ss} phase. The WDS analysis of the phases is given in Table 7.9. In the substrate below the scale of the oxidised specimen of the alloy ZX3, the Sn rich layer was present. Compared with the similar feature observed in the oxidised alloy ZX3 at 800 °C, the continuous Sn rich layer was thicker and showed no dark features. However, at higher magnifications, it was found that different contrast Sn rich phases were formed (see Figure 7.30). This seemed to be related to the presence of Nb_5Si_3 inside the Sn rich layer. The WDS data for the Sn rich phases is given in Table 7.9.

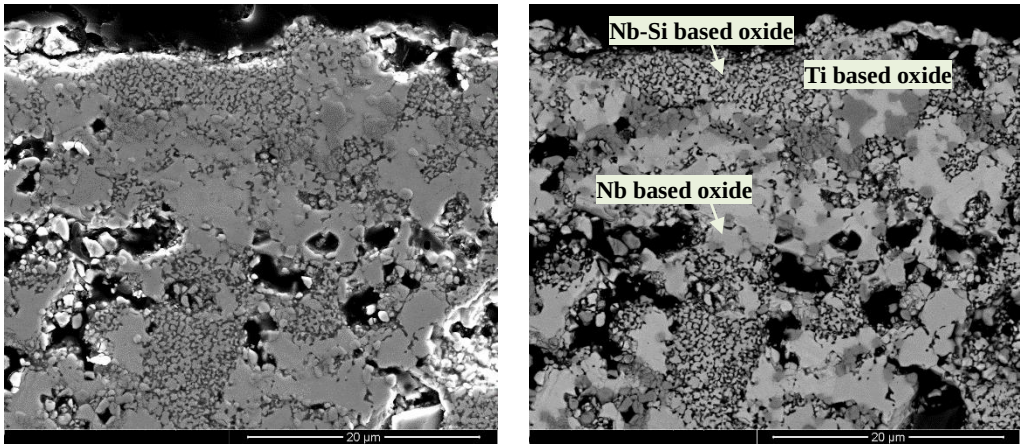


Figure 7.28 Cross section microstructures of the scale formed on ZX3 at 1200 °C on (left) SE mode and (right) BSE mode.

Table 7.7 The WDS analysis (at.%) of the oxides in the scale of the alloy ZX3 at 1200 °C.

Phase	Nb	Ti	Si	Cr	Sn	O
Nb rich oxide	18.34	5.87	4.46	0.41	0.04	70.88
Ti rich oxide	6.10	17.49	0.16	6.01	0.24	70.00
Nb-Si rich oxide	13.08	5.53	9.31	0.26	0.03	71.79

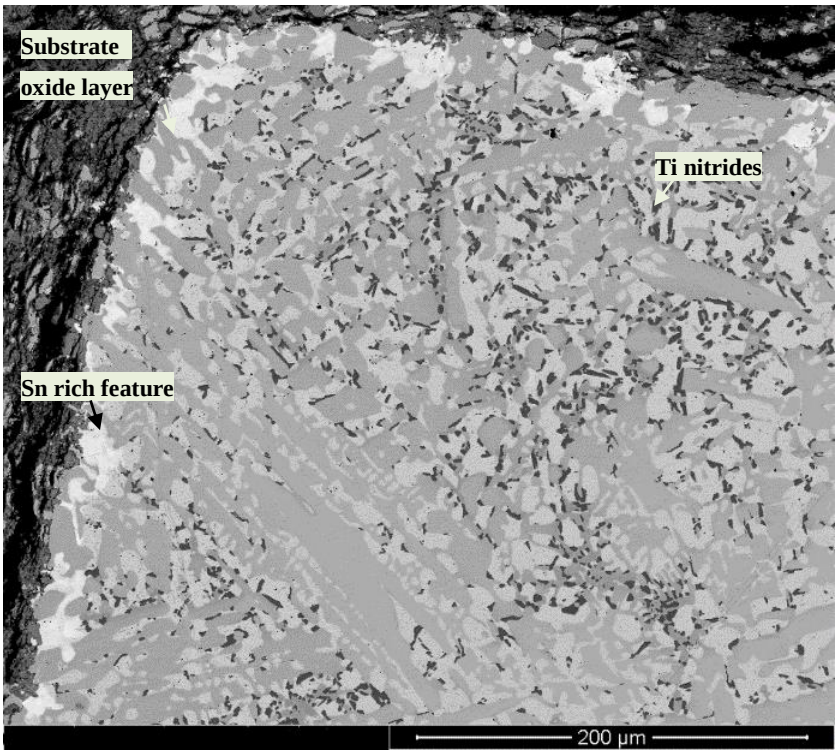


Figure 7.29 Cross section microstructure of the oxidised alloy ZX3 at 1200 °C.

Table 7.8 The WDS analysis (at.%) of the phases of the alloy ZX3 at 1200 °C.

Phase	Nb	Ti	Si	Cr	Sn	O
Bulk	**43.92** ± 0.19	**16.59** ± 0.11	**34.29** ± 0.69	**0.86** ± 0.22	**0.67** ± 0.06	**3.67** ± 0.29
Nb_5Si_3	*43.61 - 44.11*	*16.46 - 16.79*	*32.95 - 34.78*	*0.48 - 1.16*	*0.62 - 0.79*	*3.40 - 4.21*
Bulk	**56.96** ± 0.52	**23.47** ± 0.27	**0.18** ± 0.03	**7.48** ± 0.13	**3.26** ± 0.11	**8.65** ± 0.68
Nb_{ss}	*56.24 - 57.61*	*23.26 - 23.89*	*0.13 - 0.21*	*7.27 - 7.58*	*3.11 - 3.35*	*7.72 - 9.58*

Table 7.9 The WDS analysis (at.%) of the Sn rich layer formed in the alloy ZX3 at 1200 °C.

Phase	Nb	Ti	Si	Cr	Sn	O
$NbSn_2$	31.38	0.98	0.65	0.29	**59.45**	7.25
Nb_3Sn	51.98	15.84	0.34	3.04	**22.84**	5.96
Nb_5Sn_2Si	46.10	13.88	9.30	2.72	**24.07**	3.93

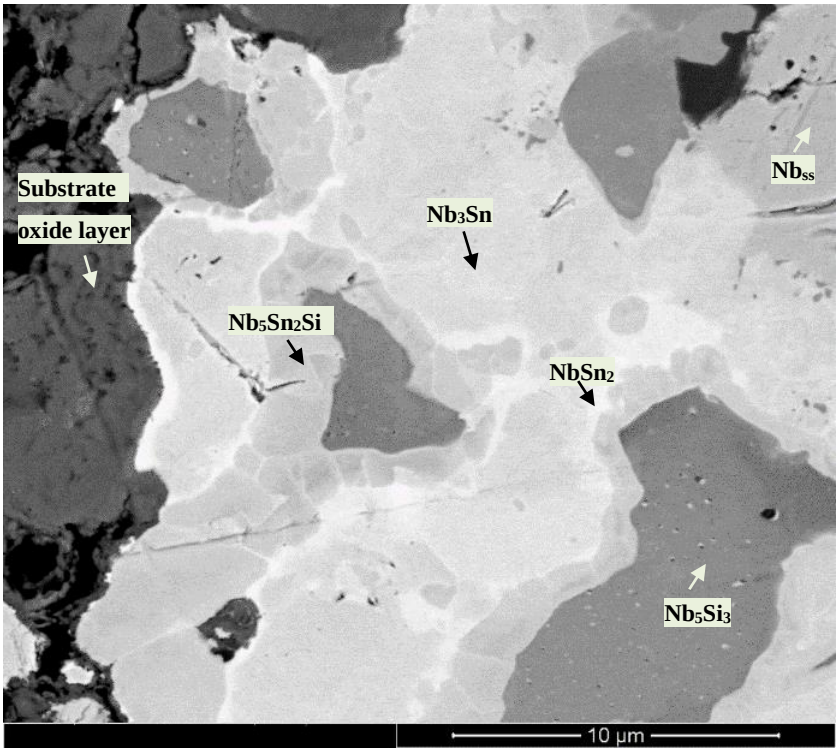


Figure 7.30 Cross section microstructure of the Sn rich layer of the oxidised alloy ZX3 at 1200 °C.

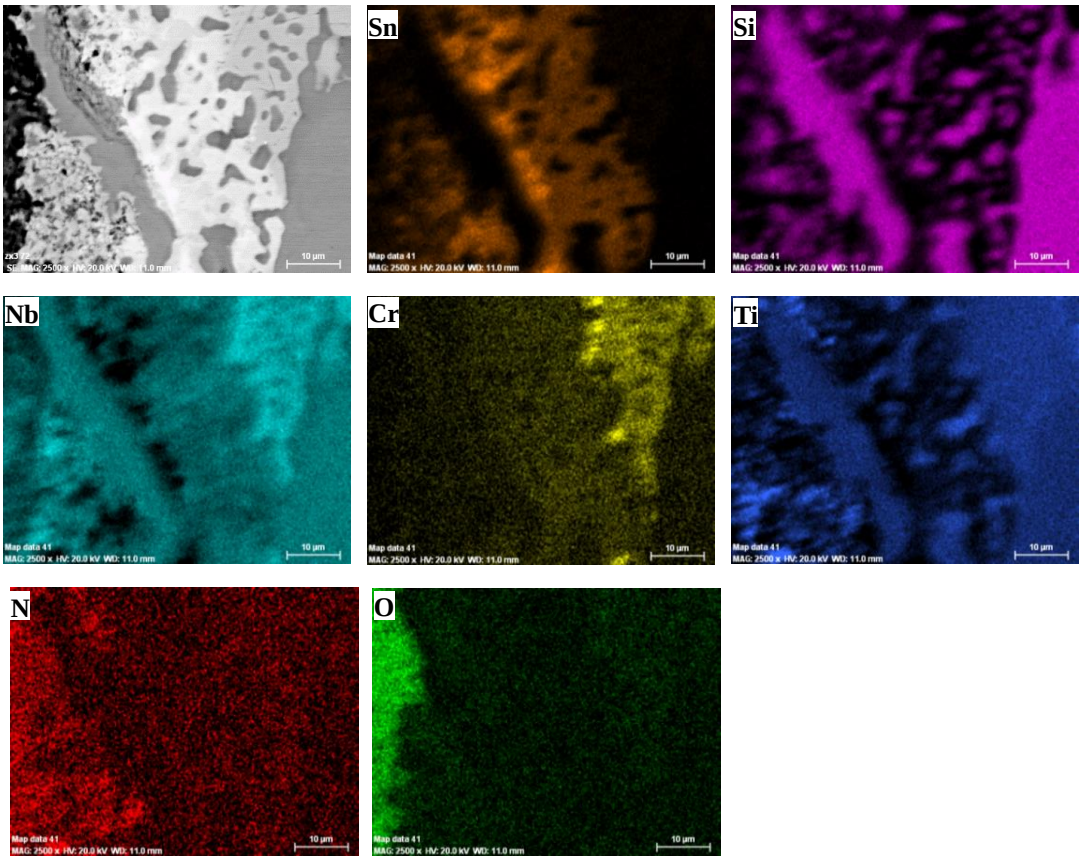


Figure 7.31 X-ray elemental maps of the Sn rich layer of the oxidised alloy ZX3 at 1200 °C.

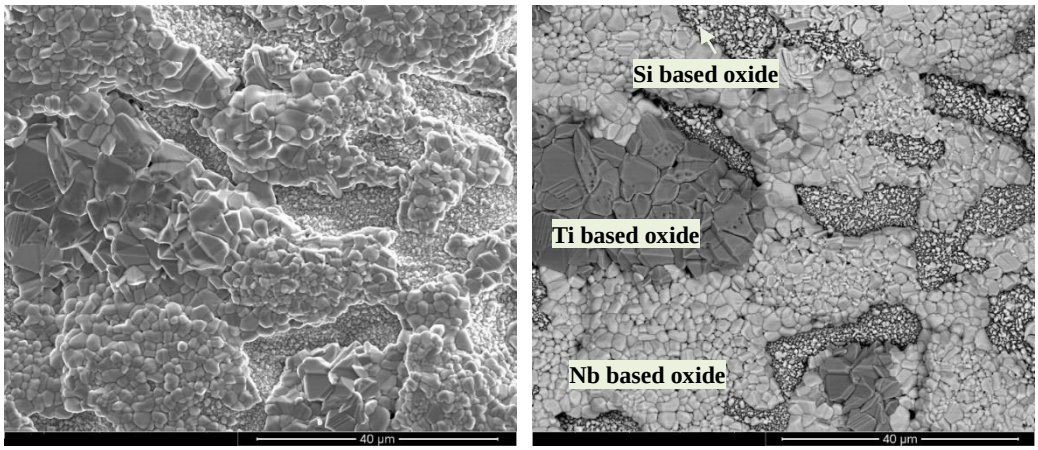
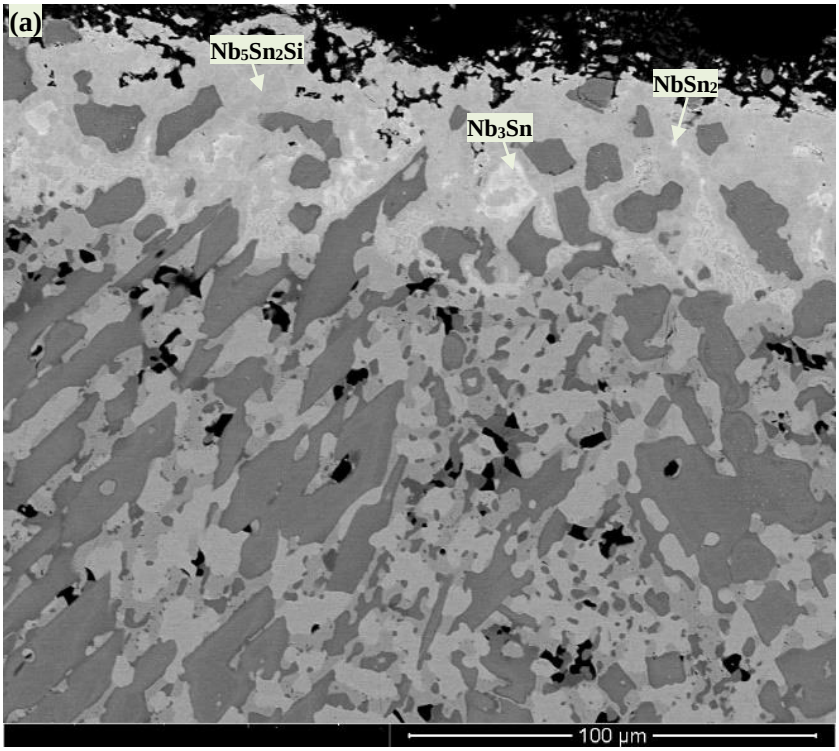


Figure 7.32 Scale formed on alloy ZX4 at 1200 °C observed under SE mode (left) and BES mode (right), images of the same area.

The topology of the scale of ZX4 at 1200 °C is shown in Figure 7.32. Different oxides formed during the high temperature oxidation. The Ti nitride phase was also found in the oxidised alloy ZX4 at 1200 °C, however the amount of the phase was much less

compared with the oxidised alloy ZX3 at the same temperature (see Figure 7.33). On the substrate, the Sn rich layer was still present. The X-ray map in Figure 7.34 shows a continuous Sn rich layer surrounding the specimens. Like the alloy ZX3, it was noticed that fewer Nb_5Si_3 grains were located in the Sn layer compared with the bulk. The compositions of the Sn rich phases were analysed by WDS and the results are shown in Table 7.10.

In the bulk, Ti nitrides and some oxides were found in the grain boundaries of the Nb_{ss} phase. The Ti nitrides, which exhibited black contrast, were formed at a lower volume fraction compared with the oxidised alloy ZX3 at the same oxidation temperature. The oxides were high in Cr and O, see X-ray maps in Figure 7.35, similar to the alloy ZX3. The Nb_5Si_3 phase had a Ti rich area. Both the Nb_5Si_3 and Nb_3Sn were contaminated by oxygen. The WDS analysis data of the bulk area is shown in Table 7.11.



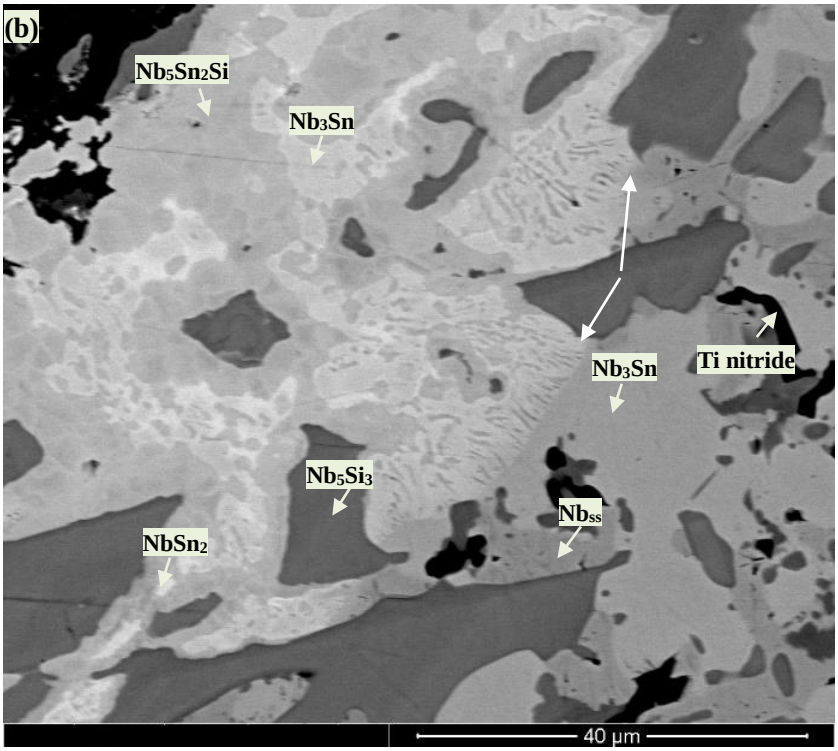


Figure 7.33 Cross section of the oxidised specimen of the alloy ZX4 showing the (a) the dark contrast Ti nitrides below a zone of bright contrast below the scale and (b) details of microstructure in this zone.

Table 7.10 The WDS analysis on the Sn rich layer of the alloy ZX4 at 1200 °C.

Phase	Nb	Ti	Si	Cr	Sn	O
$NbSn_2$	31.01	1.34	0.23	0.35	**62.68**	4.39
Nb_3Sn	57.39	4.75	2.44	2.53	**27.52**	5.37
Nb_5Sn_2Si	46.96	10.20	**11.94**	2.14	**23.78**	4.98

Table 7.11. The WDS analysis (at.%) of the phases in ZX4 at 1200 °C.

Phase	Nb	Ti	Si	Cr	Sn	O
Bulk	**43.58** ± 0.36	**15.35** ± 0.28	**34.93** ± 0.48	**0.91** ± 0.11	**1.63** ± 0.09	**3.60** ± 0.45
Nb_5Si_3	*43.29 - 44.17*	*15.15 - 15.80*	*34.08 - 35.23*	*0.73 - 1.02*	*1.51 - 1.73*	*3.09 - 4.04*
Bulk	**48.83** ± 0.31	**26.41** ± 0.37	**2.94** ± 0.28	**3.75** ± 0.22	**12.42** ± 0.49	**5.65** ± 0.40
Nb_3Sn	*48.57 - 49.35*	*25.84 - 26.77*	*2.73 - 3.41*	*3.50 - 4.06*	*11.58 - 12.74*	*5.18 - 6.21*
Bulk	**54.70** ± 0.46	**26.38** ± 0.70	**2.91** ± 1.65	**6.44** ± 0.24	**3.14** ± 0.17	**6.43** ± 0.08
Nb_{ss}	*54.23 - 55.16*	*25.68 - 27.08*	*1.26 - 4.56*	*6.20 - 6.68*	*2.98 - 3.31*	*6.34 -6.51*

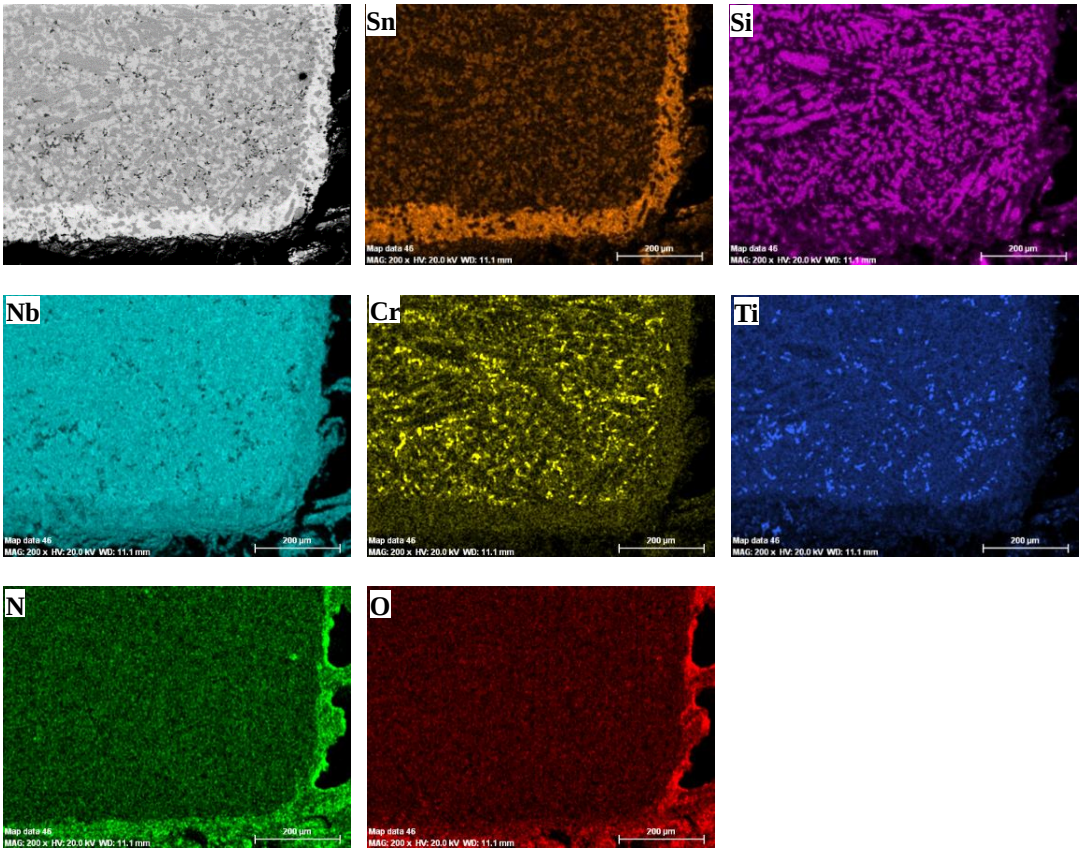


Figure 7.34 X-ray maps of the bulk area microstructure of the oxidised alloy ZX4 at 1200 °C showing the Sn rich layer.

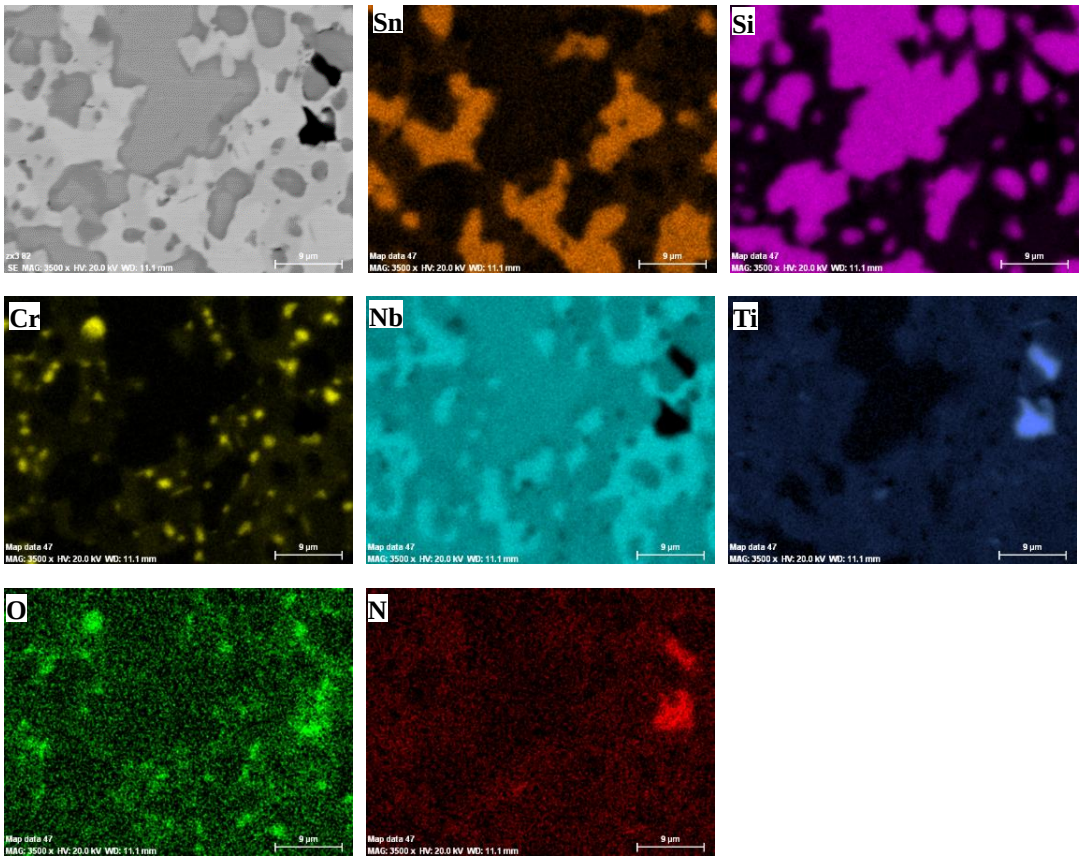


Figure 7.35 X-ray maps of the bulk area microstructure of the oxidised alloy ZX4 at 1200 °C.

7.4 Discussion

7.4.1 Macrosegregation of Si

In the cast ingot buttons of the alloys ZX3 and ZX4 there was macrosegregation of Si and Ti, and also of Cr in the alloy ZX4. For Nb silicide based alloys the macrosegregation of an element i has been defined as C_{max}^{i} - C_{min}^{i}, i.e., as the difference between the maximum and minimum concentrations of the element in the alloy [69]. Macrosegregation of an element is considered to occur when MACS = C_{max}^{i} - C_{min}^{i} > 2 at.%. Phenomena linked with the macrosegregation of elements in cast alloys including Nb silicide based alloys were discussed in [78] where the macrosegregation of Si was linked with the partitioning of other solutes between the key phases in the microstructure of Nb silicide based alloys, namely the Nb_{ss}, Nb_5Si_3, $NbCr_2$ Laves (and the Nb_{ss} + Nb_5Si_3 eutectic). Tin is one of the alloying additions that have a strong effect on macrosegregation [78].

There was strong partitioning of Ti in the microstructure of both alloys, with the highest C_{max}^{i} - C_{min}^{i} between the bulk and bottom of the ingots, i.e., areas where the melt had experienced the highest and lowest cooling rates, respectively. The same was the case for the macrosegregation of Cr in ZX4.

In [78] the macrosegregation of Si in sixty nine Nb silicide based alloys with different microstructure (meaning not all alloys had the same phases and the same volume fractions of phase) was studied using a number of material parameters. The ranking of alloys in terms of increasing Si macrosegregation indicated that the latter tended to increase in Nb silicide based alloys when the parameters $\Delta H_m/T_m$ (“alloys entropy of fusion”), T_m^{sp} (melting temperature of sp electronic configuration elements) and $[\Delta H_m/T_m][\Delta H_m^{sd}/\Delta H_m^{sp}]^{-1}$ increased and the ratios $\Delta H_m^{sd}/\Delta H_m^{sp}$ and T_m^{sd}/T_m^{sp} and the parameters ΔH_m (“alloy enthalpy of melting”), T_m (alloy melting temperature) and T_m^{sd} (melting temperature of the sd electronic configuration elements) decreased.

In Table 7.12 the aforementioned parameters of the alloys ZX3 and ZX4 are given. The increase in the macrosegregation of Si in ZX4 (C_{max}^{i} - C_{min}^{i} = 7.3 at.% compared with 3.6 at.% in ZX3) is associated with the decrease in the values of ΔH_m, T_m and T_m^{sd} in the alloy ZX4 compared with ZX3, that are highlighted with bold numbers in Table 7.12. This is consistent with [78] where of the sixty nine Nb silicide based alloys studied only a few contained Sn and Si as the only sp electronic configuration elements [81].The reason why the trends in all the parameters of ZX3 and ZX4 in Table 7.12 is not as expected from [78] could be the fact that different phases were present in the cast alloys ZX3 and ZX4 (no Nb_3Sn was present in ZX3). Support for the latter suggestion is provided when the data for the alloy KZ4 (see Table 7.12) is considered, as this was the "base" alloy without Sn additions and its cast microstructure consisted of Nb_{ss}, Nb_3Si, $NbCr_2$ and αNb_5Si_3 [68]. The same trends are exhibited by T_m and T_m^{sd} but not by ΔH_m compared with ZX3 and ZX4.

Table 7.12 Alloy parameters of the macrosegregation of Si in the cast alloys ZX3 and ZX4.

Alloy	ΔH_m kJ/mol	T_m (K)	$\Delta H_m/T_m$ J/molK	$\Delta H_m^{sd}/\Delta H_m^{sp}$	T_m^{sd} (K)	T_m^{sp} (K)	T_m^{sd}/T_m^{sd}	$[\Delta H_m/T_m]\times[\Delta H_m^{sd}/\Delta H_m^{sp}]^{-1}$	MACS
ZX4	**27.84**	**2205**	12.63	1.845	**1862**	342	5.44	6.85	7.3
ZX3	**28.97**	**2257**	12.84	1.738	**1896**	361	5.25	7.39	3.6
KZ4	28.20	**2335**	12.1	2.44	**2060**	275	7.5	4.96	1.9

According to [78] the parameters ΔH_m, T_m and T_m^{sd} have respectively strong and weak potency for Sn in synergy with other alloying elements affecting the macrosegregation of Si in Nb silicide based alloys.

7.4.2 Phase stability in Nb-24Ti-18Si-5Cr-2Sn (alloy ZX3)

As-cast: In the cast alloy ZX3 the Si + Sn concentration was ~ 22 at.%. Taking Si and Sn as equivalent elements the alloy was hyper-eutectic according to the Nb-Si binary phase diagram, and thus the βNb_5Si_3 would be the primary phase. Following the binary phase diagram, the Nb_3Si silicide would then form through the peritectic

transformation L + βNb_5Si_3 → Nb_3Si, and as the temperature decreased, the Nb_3Si would transform to Nb_{ss} + αNb_5Si_3 via the eutectoid reaction at 1765 °C. In practice when the Nb_3Si is present in the cast microstructures of Nb silicide based alloys its eutectoid transformation during cooling is unlikely owing to the sluggish transformation kinetics [82].

The Ti addition to Nb-18Si based alloys stabilises the Nb_3Si [68]. In the alloys Nb-19Si-4.2Sn (NV9), ZX1 and ZX2 the formation of Nb_3Si was suppressed owing to the addition of Sn. In the alloy Nb-25.5Ti-18.1Si-4.9Sn (NV6) which had higher Sn content than ZX3, the addition of Ti did not destabilise the effect of Sn on the stability of Nb_3Si. However, in the alloy Nb-24.7Ti-16.3Si-7.3Cr (KZ4) [68], the Nb_3Si silicide was present in the cast microstructure, and in parts of it the eutectoid transformation Nb_3Si → Nb_{ss} + αNb_5Si_3 had occurred during solid state cooling owing to Ti stabilising the Nb_3Si to lower temperature and thus the eutectoid transformation occurred at a higher homologous temperature compared with the Nb-Si binary. The Nb_3Si silicide was not observed in the cast alloy ZX3. Thus, comparison of the data for the alloys ZX1, ZX2, NV9 (Nb-19Si-4.2Sn) and KZ4 (Nb-24.7Ti-16.3Si-7.3Cr) with the data for the alloy ZX3 would suggest that Sn destroyed the effect of the synergy of Ti and Cr on the formation of Nb_3Si during solidification.

Ge, which in the same group as Sn in the periodic table, has the same effect as Sn on the stability of Nb_3Si in Nb-Si-Ge alloys [83]. The XRD data confirmed the presence of αNb_5Si_3 in the cast microstructure which would suggest that some βNb_5Si_3 had transformed to αNb_5Si_3 during solidification in agreement with NV9 and NV6 in [69]. As the βNb_5Si_3 formed in the melt (primary phase) the latter became rich in Cr, Sn and Ti and from the latter formed either the Nb_{ss} on the βNb_5Si_3 dendrites making the melt rich in Si and then the Nb_{ss} + βNb_5Si_3 eutectic formed or the eutectic formed in between the βNb_5Si_3 dendrites, see Figure 7.1. It is suggested that the solidification

path in the bulk of ZX3 was: L→ L + βNb_5Si_3 → βNb_5Si_3 + (Nb_{ss}+ βNb_5Si_3)$_{eutectic}$ → βNb_5Si_3 + αNb_5Si_3 + (Nb_{ss}+ βNb_5Si_3)$_{eutectic}$. The Si + Sn concentration of the eutectic microstructure was 17.5 at.%, slightly lower than the composition of the eutectic in the alloys ZX1 and ZX2.

Similar microstructures were observed in the top and bulk areas of the cast alloy ZX3, namely primary βNb_5Si_3 dendrites and eutectic Nb_{ss} + βNb_5Si_3. Microsegregation of Ti and Cr was evident in the Nb_{ss} owing to solute redistribution during solidification. The concentration of Cr in the Nb_{ss} increased with Ti concentration, in agreement with [68].

The microstructure in the bottom of the ingot of the alloy ZX3 was different compared with the bulk and top of the ingot. The Nb_{ss} + Nb_5Si_3 eutectic was not observed (compare Figures 7.1 and 7.2), instead, there was formation of the $NbCr_2$ Laves phase in some Nb_{ss} interdendritic areas (see Figure 7.4) in a microstructure of co-continuous Nb_{ss} and Nb_5Si_3, and there was also evidence of formation of ternary eutectic in some of the Nb_{ss} interdendritic areas (see Figure 7.5). Compared with the alloy Nb-24.7Ti-16.3Si-7.3Cr (alloy KZ4) in [68], there is agreement regarding the location of the formation of the Laves phase in the constituents of the microstructure (in the last to solidify Cr rich melt in-between Nb_{ss} dendrites) but disagreement regarding the location of the formation of the $NbCr_2$ Laves phase in the ingot. Indeed, in the alloy KZ4 the Laves phase was observed in all parts of the ingot but in the alloy ZX3 only in the bottom. The former alloy was richer in Cr than the latter in all parts of the ingot (7 to 7.5 at.% vs 4 to 4.5 at.%), and in the alloy ZX3 the melt near the bottom was richer in Cr than the top but still poorer in Cr compared with the alloy KZ4. This would suggest that in the alloy ZX3 the formation of the $NbCr_2$ Laves phase depended on the synergy of Sn with Cr and Ti and on cooling rate, i.e., on solidification conditions.

Without the Laves phase and the ternary eutectic the microstructure in the bottom of the alloy ZX3 resembles that in Figure 6.4e, which is from the bottom of the cast alloy ZX1. It also resembles that formed in the bottom of the alloy Nb-18Si-5Ge (ZF1) [83].

The composition of ZX3 in the bottom of the ingot is given in Table 7.1 and in this area the Si + Sn was 22.6 at.%, higher than the eutectic composition in the Nb-Si binary (reported to be in the range 15 to 19 at.%, [72]) and on the right side of the expected composition of the metastable Nb_{ss} + Nb_5Si_3 eutectic [67]. Thus, it is suggested that next to the water cooled copper crucible the melt solidified as explained for the alloy ZX1 in the previous chapter, with the growth of Nb_{ss} being easier than that of the βNb_5Si_3 owing to the higher entropy of fusion of the latter ($\Delta S_f^{Nb5Si3} \approx 14.55$ J/molK) [84] compared with the former ($\Delta S_f^{Nb} \approx 9.45$ J/molK). However, as the growth of both Nb_{ss} and βNb_5Si_3 progressed under decreasing melt undercooling (i.e., as solidification progressed away from the crucible wall towards the bulk of ZX3) there was rejection of Cr, Sn and Ti and of Si to the melt respectively from the 5-3 silicide and the Nb_{ss}, and in the Cr rich parts of the melt the Laves phase formed, while in the areas of the melt where the composition reached that of the ternary Nb_{ss} + $NbCr_2$ + βNb_5Si_3 eutectic, the latter formed. A ternary eutectic in Nb-Si-Cr alloys involving the Nb_{ss} and Laves phases has been suggested by Bewlay *et al* [45]. This eutectic has not been confirmed by other researchers in Nb-Si-Cr alloys and its formation is believed to depend on cooling conditions. Ternary eutectics were observed in the inter-dendritic areas that were possibly composed of the Nb_{ss} + Nb_5Si_3 + Laves phases, as suggested by Ying *et al*. for the solidification path of the Nb-23Ti-15Si-10Cr alloy [85]. Thus it is suggested that in the bottom of ZX3 the solidification path was L→ L + Nb_{ss} + βNb_5Si_3 → L + Nb_{ss} + βNb_5Si_3 + $NbCr_2$ (interdendritic) → Nb_{ss} + βNb_5Si_3 +$NbCr_2$ + (Nb_{ss} + βNb_5Si_3 + $NbCr_2$) ternary eutectic.

In the cast ZX3 the Nb_{ss} had Si + Sn = 6.5 at.% and Si/Sn = 0.9 compared with 6.8

at.% and 0.8 for the cast alloy ZX1 (low Sn content ternary alloy with no Nb_3Sn in the cast microstructure). The Cr content in the Ti rich Nb_{ss} was significantly higher than that in the "normal" Nb_{ss}, in agreement with [68].

Heat-treated: The microstructure of the heat treated alloy ZX3 consisted of the Nb_5Si_3 and Nb_{ss} phases, and there was no evidence of the eutectic areas. The XRD confirmed that the transformation of βNb_5Si_3 to αNb_5Si_3 had been completed at 1500 °C and the back electron scattered image showed partitioning of Ti in the Nb_5Si_3 (Figure 7.7b).

In the Nb-24Ti-18Si-5Cr alloy (alloy KZ4 in [68]) the formation of αNb_5Si_3 was observed in the cast microstructure and was linked with the formation of Nb_3Si in it and the eutectoid transformation of the latter, in other words the synergy of Ti and Cr stabilised the αNb_5Si_3 in the cast microstructure. With the addition of Sn however, the formation of Nb_3Si was suppressed and Sn in synergy with Si promoted the transformation of βNb_5Si_3 to αNb_5Si_3 during solidification (alloy ZX1, ZX2) which was completed in ZX3 after the heat treatment at 1500 °C for 100 h, as was the case in the alloys ZX1 and ZX2 with higher Sn contents than ZX3. This therefore would suggest that Sn does tend to destabilise the βNb_5Si_3, and the evidence of ZX3 provides further support for the above, which was also suggested in [69].

According to the EDS analysis the Si content in the Nb_{ss} phase had dropped from 3.1 at.% to 0.7 at.% after the heat treatment which is in agreement with data for Nb silicide based alloys [68]. Indeed, the Si concentration in the Nb_{ss} of the as cast alloy KZ4 was ~ 1.6 at.%, lower than in the cast ZX3 and after the heat treatment decreased to ~ 0.7 at.% (KZ4HT1500) [68]. The concentration of Si in the Nb_5Si_3 before and after the heat treatment was essentially the same and in agreement with the heat treated alloys KZ4 and NV6 [56, 68].

Ti nitride was found in the whole heat treated specimen. The formation of Ti nitrides was attributed to the high reactivity of Ti and N at high temperatures and the phase was most like to locate at the edge of Nb_5Si_3 and Nb_{ss}, i.e., in the Ti-rich area in the cast microstructure. Thus, the synergy of Sn with Ti and Cr would not prevent the contamination of the alloy by nitrogen, which was also observed in the alloy Nb-24Ti-18Si-5Cr (alloy KZ4) [68].

7.4.3 Macrosegregation of Si and Phase stability in Nb-24Ti-18Si-5Cr-5Sn (alloy ZX4)

The alloy ZX4 can be compared with the alloy Nb-25.5Ti-18.1Si-4.9Sn (alloy NV6 in [69]) and Nb-24.7Ti-16.3Si-7.3Cr (alloy KZ4 in [68]) (actual compositions in at.% of both alloys). Comparison of NV6 and ZX4 would allow us to deduce how the Cr addition affects the microstructure and comparison of KZ4 with ZX4 to infer the effect of Sn addition.

In the cast alloy NV6 the microstructure consisted of the Nb_5Si_3 (primary phase), Nb_{ss}, Nb_3Sn and Nb_{ss} + Nb_5Si_3 eutectic with strong partitioning of Ti in the Nb_5Si_3 and strong macrosegregation of Si and Ti (MACS of 5.5 and 8.4 at.%, respectively). In the cast ZX4 the microstructure consisted of Nb_5Si_3 (primary phase), Nb_{ss}, Nb_3Sn, a very low volume fraction of Nb_{ss} + Nb_5Si_3 eutectic, not a strong partitioning of Ti in Nb_5Si_3 and very low volume fraction of $NbCr_2$ Laves, some of which participated in a ternary eutectic in the bottom of the ingot, and strong macrosegregation of Si and Ti (MACS of 7.3 and 6.6 at.%, respectively). In both alloys the Nb_5Si_3 was present in its β and α types. In the Nb_{ss} the Si + Sn was 7.7 and 9.2 at.% and the ratio Si/Sn was 0.3 and 0.64, respectively in the two alloys. Thus, the addition of Cr did not eliminate the macrosegregation of Si and Ti (but reversed their severity), reduced the partitioning of Ti in Nb_5Si_3 (allowing more Ti in the last to solidify melt), reduced significantly the fraction of the Nb_{ss} + Nb_5Si_3 eutectic, and encouraged the formation of the $NbCr_2$

Laves phase in the last to solidify melt and the ternary eutectic in the bottom of the ingot of ZX4, which was also richer in Cr compared with the top and bulk.

The alloy ZX4 is compared with the Nb_3Sn containing alloys NV6 and Nb-19Si-4.2Sn (alloy NV9 in [69]) in Table 7.13. According to [78], the macrosegregation of Si should increase (i) as the material parameters T_m^{sp}, $\Delta H/T_m$, and $(\Delta H/T_m)/(\Delta H_m^{sd}/T_m^{sd})$ increase and (ii) as the material parameters T_m, ΔH_m, T_m^{sd}, $\Delta H_m^{sd}/\Delta H_m^{sp}$ and T_m^{sd}/T_m^{sp} decrease. Only the data for T_m^{sp} does not "obey" (i) and (ii). It should be noted that according to [78] the potency of the parameters T_m, ΔH_m, T_m^{sd}, $\Delta H_m^{sd}/\Delta H_m^{sp}$ and T_m^{sp} is strong and weak for the other parameters.

Table 7.13 Alloy parameters linked with macrosegregation of Si in cast alloys with Nb_3Sn (alloys ZX4, NV6 and NV9).

Alloy	ΔH_m kJ/mol	T_m (K)	$\Delta H_m/T_m$ J/molK	$\Delta H_m^{sd}/\Delta H_m^{sp}$	T_m^{sd} (K)	T_m^{sp} (K)	T_m^{sd}/T_m^{sd}	$[\Delta H_m/T_m]\times[\Delta H_m^{sd}/\Delta H_m^{sp}]^{-1}$	MACS
ZX4	**27.84**	**2205**	**12.63**	**1.845**	**1862**	342	**5.44**	**6.85**	7.3
NV6	**28**	**2241**	**12.49**	**1.98**	**1911**	330	**5.79**	**6.31**	5.5
NV9	**30.4**	**2454**	**12.39**	**2.1**	**2112**	342	**6.18**	**5.9**	2.5
KZ4	28.20	2335	**12.1**	**2.44**	2060	275	**7.5**	**4.96**	1.9

In the cast alloy KZ4 [68] the microstructure consisted of Nb_{ss}, Nb_3Si, $NbCr_2$ Laves phase and αNb_5Si_3 with partitioning to the Nb_{ss} but not to the 5-3 silicide. The macrosegregation of Si was weak (MACS ~ 1.9 at.%). Thus, the addition of Sn destabilised the Nb_3Si but not the Laves phase and led to the formation of αNb_5Si_3 from the transformation of βNb_5Si_3, not the eutectoid transformation of Nb_3Si. The data for the alloys KZ4 and ZX3 are included in Tables 7.13 and 7.14 and show no agreement with the trends of the parameters ΔH_m, T_m, T_m^{sd} and T_m^{sp} in the former case, and ΔH_m and T_m in the latter, and thus provide further support for the conclusion in [78] that the macrosegregation of Si depends on the phases present in the microstructure and the partitioning of solute(s) between them.

Table 7.14 Alloy parameters linked with macrosegregation of Si in the cast alloys ZX3, ZX4, NV6 and NV9.

Alloy	ΔH_m kJ/mol	T_m (K)	$\Delta H_m/T_m$ J/molK	$\Delta H_m^{sd}/\Delta H_m^{sp}$	T_m^{sd} (K)	T_m^{sp} (K)	T_m^{sd}/T_m^{sd}	$[\Delta H_m/T_m]\times[\Delta H_m^{sd}/\Delta H_m^{sp}]^{-1}$	MACS at.%
ZX4	**27.84**	**2205**	12.63	1.845	1862	342	5.44	6.85	7.3
NV6	**28**	**2241**	12.49	1.98	1911	330	5.79	6.31	5.5
ZX3	**28.97**	**2257**	12.84	1.74	1898	361	5.25	7.39	3.6
NV9	**30.4**	**2454**	12.39	2.1	2112	342	6.18	5.9	2.5

The microstructure in the top and bulk of the cast alloy ZX4 consisted of Nb_5Si_3, Nb_{ss} and Nb_3Sn and Nb_{ss} + Nb_5Si_3 eutectic. As the dendrites of the primary βNb_5Si_3 formed, the surrounding melt became rich in Cr, Sn and Ti and poor in Si. Because Sn has a strong effect on the partitioning of Ti in Nb_5Si_3 (data from the alloy NV6 in [69]), the concentration of Ti in the melt near the Nb_5Si_3 dendrites differed. Next to Ti rich Nb_5Si_3 formed the A15 Nb_3Sn (making the surrounding melt richer in Cr and Si and poorer in Sn) and next to the less Ti rich Nb_5Si_3 formed the Nb_{ss} (making the surrounding melt richer in Si and poorer in Cr and Sn). The Nb_{ss} + Nb_5Si_3 eutectic formed in the last to solidify melt. Thus, it is suggested that the solidification path in the bulk and top of ZX4 was $L \rightarrow L + \beta Nb_5Si_3 \rightarrow L + \beta Nb_5Si_3 + Nb_3Sn$ and/or $L + \beta Nb_5Si_3 + Nb_{ss} \rightarrow L + \beta Nb_5Si_3 + Nb_3Sn + Nb_{ss} + (Nb_{ss} + \beta Nb_5Si_3)_{eutectic}$.

In the bottom of ZX4 the microstructure consisted of primary βNb_5Si_3, A15 Nb_3Sn, Nb_{ss} and $NbCr_2$ and in some areas the last to solidify melt gave a ternary eutectic. The Nb_{ss} + βNb_5Si_3 eutectic formed some distance away from the water cooled crucible and as the $NbCr_2$ Laves was not observed in the areas with the Nb_{ss} + βNb_5Si_3 eutectic, the transition (indicated by the dashed line in Figure 7.36) must have occurred when the interdendritic melt became lean in Cr. The partitioning of Cr (and other elements) between Nb_{ss}, Nb_3Sn and Nb_5Si_3 must have played a role in the transition from the bottom to the bulk microstructure.

The microstructures in Figures 7.11 and 7.12 show Nb_3Sn surrounded by Nb_{ss}. This

was not observed in the bulk and top of the ingot of ZX4. Such a microstructure could be the product of the peritectic reaction L + $Nb_3Sn \rightarrow Nb_{ss}$. The latter, however, does not exist in the Nb-Sn binary, where in the Nb rich side of the binary the peritectic reaction is L + $Nb_{ss} \rightarrow Nb_3Sn$. Thus, if the former reaction was indeed the case in ZX4, then this reaction must have been promoted by the synergy of Sn with Cr and Ti in the solidification of the Cr richer melt under higher cooling rates (compared with the bulk) in the bottom of ZX4.

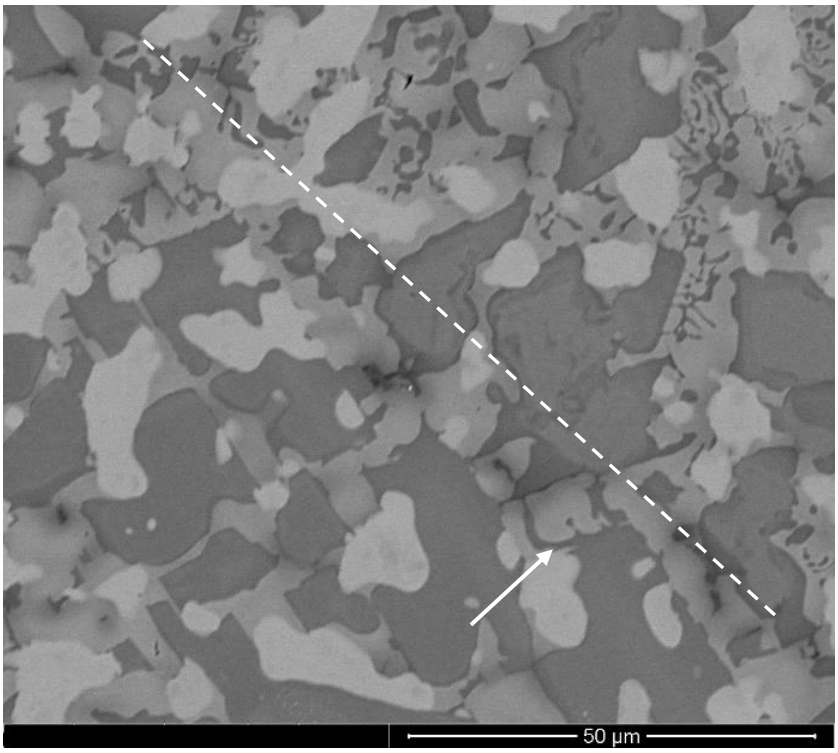


Figure 7.36 BSE image of the microstructure of the cast alloy ZX4 showing (dashed line) the change in microstructure from the bottom to the bulk. The arrow points away from the water cooled crucible.

As the dendrites of the primary βNb_5Si_3 formed the surrounding melt became rich in Cr, Sn and Ti and poor in Si. Because of the higher cooling rate in the bottom of ZX4, in the solidifying melt the partitioning of Ti in Nb_5Si_3 was not as strong as in the bulk and top and therefore the concentration of Ti in the melt near the Nb_5Si_3 dendrites was high. In Ti and Sn rich interdendritic constitutionally undercooled melt formed the

A15 Nb_3Sn (Ti_3Sn is in equilibrium with the melt at a lower temperature than Nb_3Sn, thus Ti (substituting Nb) in Nb_3Sn is expected to depress this temperature meaning less undercooling is required for the formation of the A15) and the surrounding melt became rich in Cr and Si and from this melt the Nb_{ss} formed via the aforementioned peritectic reaction. In Cr rich melt the $NbCr_2$ Laves subsequently formed and in interdendritic areas where the melt reached the ternary eutectic composition the ternary eutectic formed. Thus, it is suggested that the solidification path in the bottom of ZX4 was $L \rightarrow L + \beta Nb_5Si_3$ then $L + \beta Nb_5Si_3 + Nb_3Sn$ and $L + \beta Nb_5Si_3 + Nb_{ss} + Nb_3Sn$ (in parts with $L + Nb_3Sn \rightarrow Nb_{ss}$), then $L + \beta Nb_5Si_3 + Nb_3Sn + Nb_{ss} + NbCr_2$ and finally $L \rightarrow \beta Nb_5Si_3 + Nb_3Sn + Nb_{ss} + NbCr_2 + (\beta Nb_5Si_3 + Nb_{ss} + NbCr_2)$ eutectic.

The microstructure of the heat treated alloy NV6 (1200 °C/100 h) consisted of Nb_{ss}, Nb_3Sn, αNb_5Si_3 with Ti rich areas and coarsened prior eutectic microstructure. The same phases plus Ti nitrides but with no Ti rich αNb_5Si_3 and no $NbCr_2$ Laves were observed in the heat treated ZX4 (1500 °C/100 h). There were brighter contrast second phase precipitates in the bulk αNb_5Si_3 grains (not seen in NV6-HT). The absence of $NbCr_2$ Laves and presence of Ti nitrides were also confirmed in the heat treated alloy KZ4 (1500 °C/ 100 h). In all three alloys (i.e., NV6, KZ4 and ZX4), the Si solubility in the Nb_{ss} was in the same range. In the Nb_3Sn the Si + Sn was 16.3 and 18.9 at.% and the ratio Si/Sn was 0.5 and 0.4 respectively in the alloys NV6 and ZX4. In the Nb_{ss} the Si + Sn was 4.3 and 5.6 at.% and the ratio Si/Sn was 0.1 and 0.14, respectively in the alloys NV6 and ZX4. In other words, the synergy of Cr with Sn had minor effects on the chemical composition of the Nb_3Sn and Nb_{ss}. Furthermore, as was the case in ZX3, the synergy of Cr and Sn was not able to eliminate the contamination of the alloy ZX4 by nitrogen.

7.4.4 Oxidation of alloys ZX3 and ZX4 at 800 °C

The oxide scales formed on the alloys ZX3 and ZX4 adhered to the substrate. This

was not the case in the alloy KZ4 which contained no Sn. In the alloy NV6, the scale did not spall off compared with the alloy NV9 which suffered from pest oxidation [69]. Thus, the 2 and 5 at.% Sn additions to the alloys ZX3 and ZX4 increased the oxidation resistance of the alloys at 800 °C compared with KZ4 and this must be attributed to the addition of Cr strengthening the synergy of Ti and Sn in improving oxidation at 800 °C, i.e., in the pest regime. The kinetics of oxidation can be studied using the equation 5.1. In the equation, the constant n defines the oxidation reaction type, i.e, the oxidation is said to be parabolic when the constant n = 0.5, and is linear when n = 1. In Figure 7.37, the weight change data from TG for the alloys ZX3 and ZX4 is plotted. The figure shows that the alloy ZX3 followed linear oxidation kinetics in the 100 h oxidation period while the alloy ZX4 exhibited parabolic oxidation kinetics.

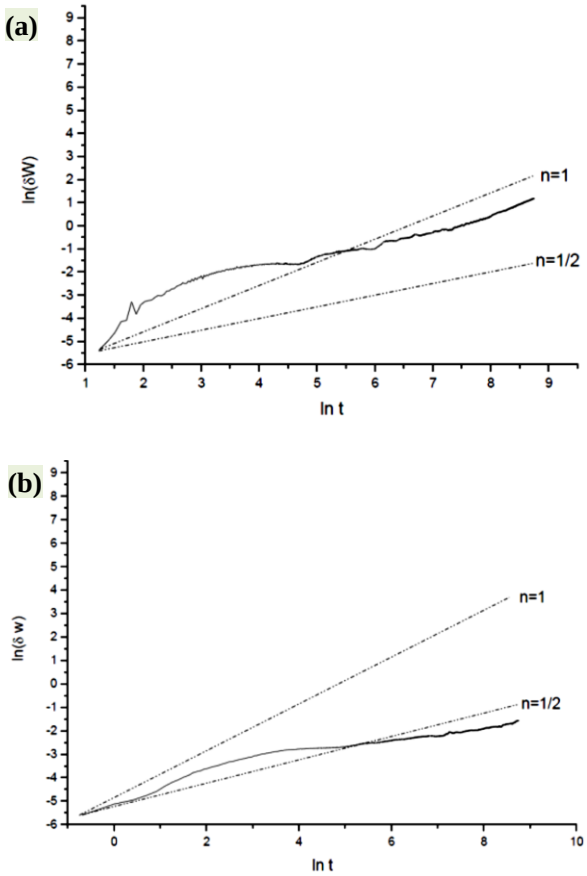


Figure 7.37 Oxidation kinetics of the alloys ZX3 (a) and ZX4 (b) at 800 °C.

The good oxidation of the alloy ZX4 was attributed to the 5 at.% Sn addition which

gave rise to the formation of the A15 Nb_3Sn intermetallic phase. As shown in Figure 7.21, the oxide scale formed on the alloy ZX3 was not compact. On the contrary, the oxide scale formed on the alloy ZX4 was very compact, as shown in Figure 7.24. The Nb rich and Nb-Si rich oxides were confirmed by the WDS data in Tables 7.4 and 7.6. Based on the thermodynamic stability of oxides, Nb oxide is less stable than TiO_2 and SiO_2.

Both phases (i.e., the Nb_{ss} and Nb_5Si_3) were contaminated by oxygen in the alloy ZX3 (Table 7.4) with the solubility of oxygen in the Nb_{ss} being higher. The same was the case in the alloy ZX4 (Table 7.5) where the Nb_3Sn was also contaminated by oxygen but to a lower extent than the Nb_{ss}. In the diffusion zone the effect was particularly evident for the Nb_{ss} phase (see Figures 7.22 and 7.25). The volume expansion of the oxidised Nb_{ss} led to the cracking of the Nb_5Si_3 (see Figures 7.21 to 7.23 and 7.25). Inside the Nb_{ss}, the Ti and Cr were consumed to form oxides most likely of TiO_2 and Cr_2O_3, see Figure 7.26.

A discontinuous Sn rich area formed between the oxide scale and the substrate alloy. The extent and thickness of this layer increased in ZX4. This layer is thought to have acted as a "glue", preventing the scale from spalling off the substrate. Geng *et al* [86] in their study of the effect of Sn on the oxidation of Nb silicide based alloys suggested that the Sn addition encouraged the oxidation resistance of the Nb_{ss} and thus improved the oxidation behaviour of the alloys compared with the non Sn containing alloys. No evidence was provided for the Sn rich layer forming at 800 °C in the interfacial area between the oxide scale and substrates even when 5 at.% of Sn was added to one of their alloys. Their comment was based on evidence for Sn rich phase forming below the scale during oxidation at 1200 °C.

Knittel *et al* [87] carried out a study of the oxidation of the MASC alloy with various Sn additions. In their work, a Sn rich layer was reported, and it was suggested that this

Sn rich layer performed as a diffusion barrier against oxygen and contributed to eliminate pest oxidation. The result of this work confirmed that the Sn rich area does not stop the diffusion of oxygen to the bulk. Vellios [88] showed that the synergy of Ti with Sn (and Cr) eliminates pest oxidation. Vellios [88] also provided evidence for the formation of a Sn rich layer at the scale substrate interface during oxidation at 800 °C.

The Sn rich layer formed during the 800 °C oxidation of the alloys ZX3 and ZX4 was very thin and thus it was difficult to identify its composition using WDS. The high magnification back electron scatter images clearly showed that it was not a single phase as dark contrast phase(s) were embedded inside the Sn rich layer. A thicker Sn rich layer was found at 1200 °C and it was possible to study it using WDS analysis.

7.4.5 Oxidation of the alloys ZX3 and ZX4 at 1200 °C

At 1200 °C, the oxide scale formed on the alloys ZX3 and ZX4 spalled off from the substrate, as reported for most of the studied Nb silicide based alloys with/without Sn. TG data for the alloys ZX3 and ZX4 is plotted in Figure 7.38 using equation 5.1. Both alloys followed parabolic and linear oxidation kinetics at 1200 °C. However, the addition of Sn in the alloys ZX3 and ZX4 had an effect on the microstructure of the alloys below the scale and on the oxides forming the scale. The latter were mixed Nb rich and Ti rich oxides (niobates) and an oxide rich in Nb and Si. (see Table 7.7).

A Sn rich area was formed in the substrate below the scale in both alloys instead of the Sn rich layer formed at 800 °C (compare Figures 7.23, 7.24 with 7.29, 7.30 and 7.33). Knittel *et al* [87] also reported that a Sn rich area formed at 1100 °C oxidation and that its thickness increased with the Sn addition.

Geng *et al* [86] were the first researchers to report enrichment with Sn of the diffusion zone below the scale in their Sn containing alloy JG6 (nominal composition Nb-24Ti-

18Si-5Al-5Cr-5Hf-5Sn-2Mo) oxidised at 1200 °C for 100 h, and based on their WDS data, suggested that Sn rich intermetallics like Nb_3Sn and Nb_5Sn_2Si were most likely present in the Sn rich regions. In the alloy ZX3, the WDS data in Table 7.9 would suggest the presence of Nb_3Sn, Nb_5Sn_2Si and $NbSn_2$, all of which were contaminated by oxygen. According to Figure 7.30, Sn rich areas surrounded the Nb_5Si_3 (which was itself contaminated by oxygen, see Table 7.8) and were formed in the areas that were occupied by the Nb_{ss} in the cast and heat treated alloy, see Figure 7.7. The Nb_{ss} was also contaminated by oxygen, and this was more severe compared with Nb_5Si_3 (Table 7.8). In the alloy ZX4 the width of the Sn rich area in the diffusion zone below the scale was wider compared with the alloy ZX3 (Figures 7.29 and 7.33a), in agreement with Knittel *et al* [87], and in this region the Sn rich intermetallics were "better formed", meaning their compositions (see Table 7.10) were closer to $NbSn_2$, Nb_3Sn and Nb_5Sn_2Si. The aforementioned three intermetallics were contaminated by oxygen (Table 7.10).

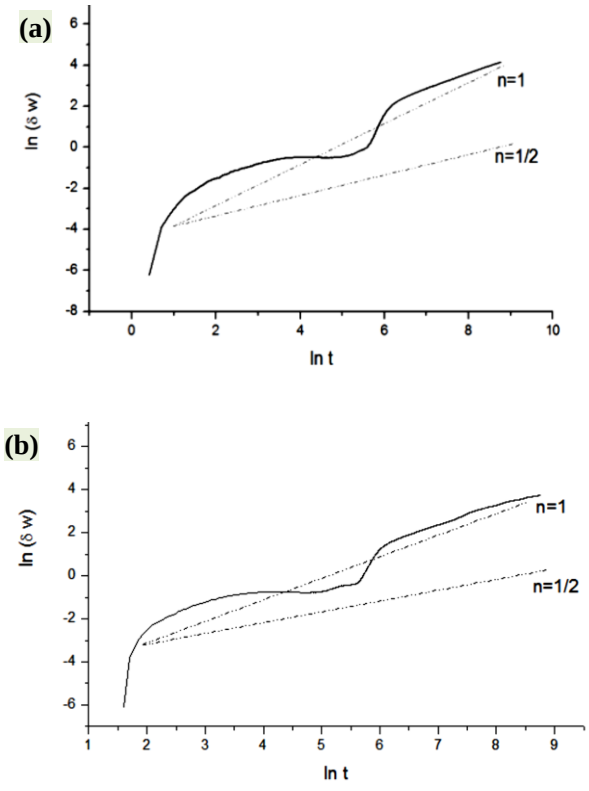


Figure 7.38. Oxidation kinetics of the alloys ZX3 (a) and alloy ZX4 (b) at 1200 °C.

Figure 7.33b shows that the enrichment of the diffusion zone below the scale with Sn was associated with the existing Nb_3Sn in the microstructure of ZX4 and the evidence in this figure would suggest a transformation of the Nb_3Sn occurring at a planar interface (indicated by arrows in Figure 7.33b) with lamellar features. In the Nb-Sn binary the Nb_3Sn transforms eutectoidally to Nb_{ss} + Nb_6Sn_5 and the latter transforms eutectoidally to Nb_{ss} + $NbSn_2$. Thus, it is suggested that as the surface regions became enriched with Sn (the reasons why this happens will be discussed in a later chapter, after we have considered all the evidence for the alloys studied in this thesis) the Nb_3Sn formed in the case of the alloy ZX3 and in both alloys the composition of the Nb_3Sn (newly formed and existing) moved close to the composition for the first of the two eutectoid reactions mentioned above and thus the transformations leading to the microstructure seen in Figure 7.33 started.

7.5 Summary

Two Nb-24Ti-18Si-5Cr based alloys with low and high Sn concentrations were studied, namely the alloys Nb-24Ti-18Si-5Cr-2Sn (ZX3) and Nb-24Ti-18Si-5Cr-5Sn (ZX4), in the cast and heat treated (1500 °C) conditions and after isothermal oxidation at 800 °C and 1200 °C.

Both alloys were hyper-eutectic with βNb_5Si_3 the primary phase. In both cast alloys there was macrosegregation of Si and Ti, the magnitudes of which increased with Sn concentration in the alloy ZX4, which also led to macrosegregation of Cr in the alloy. In both alloys the Nb_3Si was supressed and the Nb_{ss} + Nb_3Si eutectic was replaced by the metastable Nb_{ss} + βNb_5Si_3 eutectic, the $NbCr_2$ Laves phase formed in the bottom of the ingots, where it is likely that it was part of a ternary eutectic and the Nb_3Sn formed only in the cast alloy with the high Sn content (ZX4).

In both alloys the transformation of βNb_5Si_3 to αNb_5Si_3 had started during

solidification and was completed at 1500 °C.

The prior eutectic microstructure had coarsened in the alloy with low Sn (ZX3) and was not present at all in the alloy with high Sn content (ZX4). The Laves was stable only in the high Sn content alloy (ZX4) after the heat treatment and the Nb_3Sn was not observed in the heat treated alloy with low Sn concentration (ZX3) but was stable in the alloy ZX4 after the heat treatment.

Both alloys did not pest during isothermal oxidation at 800 °C and their scales spalled off at 1200 °C. Parabolic oxidation kinetics was followed only by the alloy with high Sn concentration (ZX4) at 800 °C.
At 800 °C the scale formed on the alloy ZX4 was more compact than that formed on the alloy ZX3, and the scales of both alloys consisted of Nb rich and Nb and Si rich oxide, for the alloy ZX4 there was evidence for Ti oxide also forming in the scale, however WDS data was available only for the former two oxides for both alloys. At 1200 °C the same oxide types formed the scales in both alloys and there was WDS data for all three types.

In both alloys there was enrichment in Sn of the microstructure below the scale and formation of Sn rich phases in this area and at the scale/substrate interface. In both alloys at 1200 °C the phases were the Sn rich intermetallics Nb_3Sn, Nb_5Sn_2Si and $NbSn_2$.

In both alloys the bulk microstructures were contaminated by oxygen.

Chapter 8
The alloys Nb-24Ti-18Si-5Al-2Sn (ZX5) and Nb-24Ti-18Si-5Al-5Sn (ZX6)

8.1 Introduction

The alloys Nb-24Ti-18Si-5Al-2Sn (ZX5) and Nb-24Ti-18Si-5Al-2Sn (ZX6) are studied in this chapter to understand how the synergy of Al and Sn affects phase stability and oxidation behaviour. The as cast and heat treated microstructures of the alloys are studied using SEM, XRD and EDS. The data is used to understand phase equilibria in the alloys. The isothermal oxidation behaviour of the two alloys is studied at 800 °C and 1200 °C. Oxidation kinetics and the microstructures of oxidised specimens are investigated using SEM, EDS and EPMA-WDS.

8.2 Results

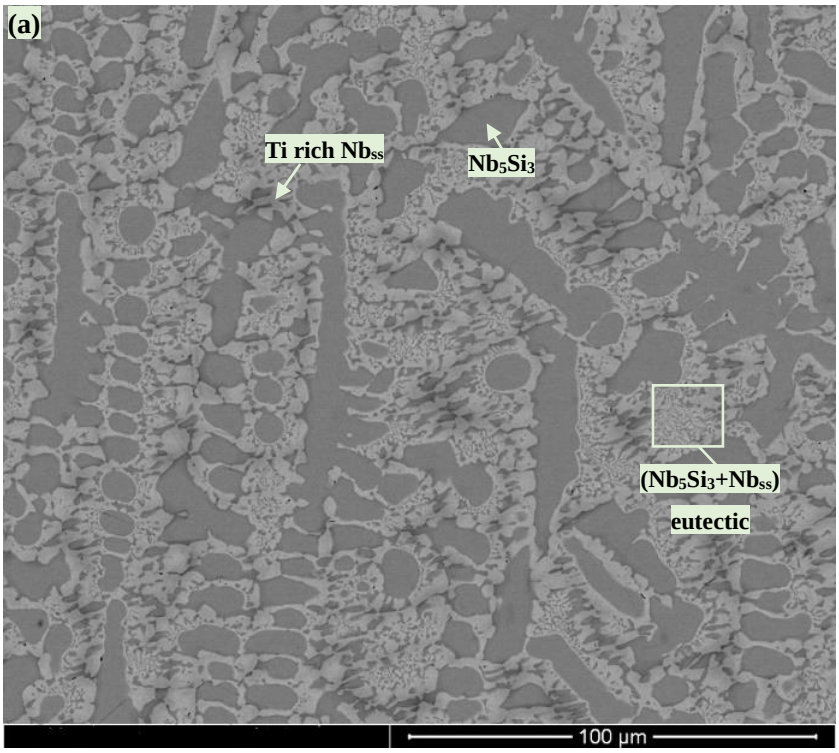
8.2.1 Alloy Nb-24Ti-18Si-5Al-2Sn (ZX5)

As cast: The large area EDS analyses of the ingot of the alloy ZX5 are shown in Table 8.1. The actual composition of the cast alloys ZX5 was Nb-25.1Ti-19.1Si-4.9Al-1.8Sn. There was macrosegregation of Si and Ti. The Si content varied from 15.7 at.% to 21.3 at.% with the bottom area of the ingot being leaner than the nominal Si composition while its concentration was higher than the nominal in the top and bulk area of the ingot. The Ti composition of the cast alloy ZX5, which varied between 23.5 at.% and 27.6 at.%, on the other hand behaved in the opposite way.

As shown in Figures 8.1a and 8.2a, the microstructure in the top area of the cast alloy ZX5 consisted of Nb_5Si_3 dendrites and a eutectic of Nb_5Si_3 + Nb_{ss}. Ti rich areas were observed in the Nb_{ss} and Nb_5Si_3 under back scatter electron imaging. The same but slightly coarser microstructure was observed in the bulk area of the alloy (Figures 8.1b

and 8.2b). In the bottom of the ingot the overall impression was that there was more lamellar Nb_5Si_3 + Nb_{ss} eutectic (Figure 8.1c), the facetting of the Nb_5Si_3 was more pronounced, Figure 8.2c, and Ti rich areas were mainly observed in the Nb_5Si_3. The XRD confirmed the presence of the βNb_5Si_3 and Nb_{ss}, as shown in Figure 8.3.

The EDS analysis of the phases in the cast alloy ZX5 is given in Table 8.1. The Si + Al + Sn content of the Nb_5Si_3 and Ti rich Nb_5Si_3 was 36.7 at.% and 35.5 at.% respectively, close to the Si concentration of unalloyed Nb_5Si_3. The Si + Sn + Al in the Nb_5Si_3 + Nb_{ss} eutectic was 19.8 at.%, higher than the eutectic composition in the Nb-Si binary. In the Nb_{ss} and Ti rich Nb_{ss} the Si + Sn was ~ 5.2 at.% and the Si + Al + Sn was ~11.1 at.%, and did not vary with increased Ti solubility.



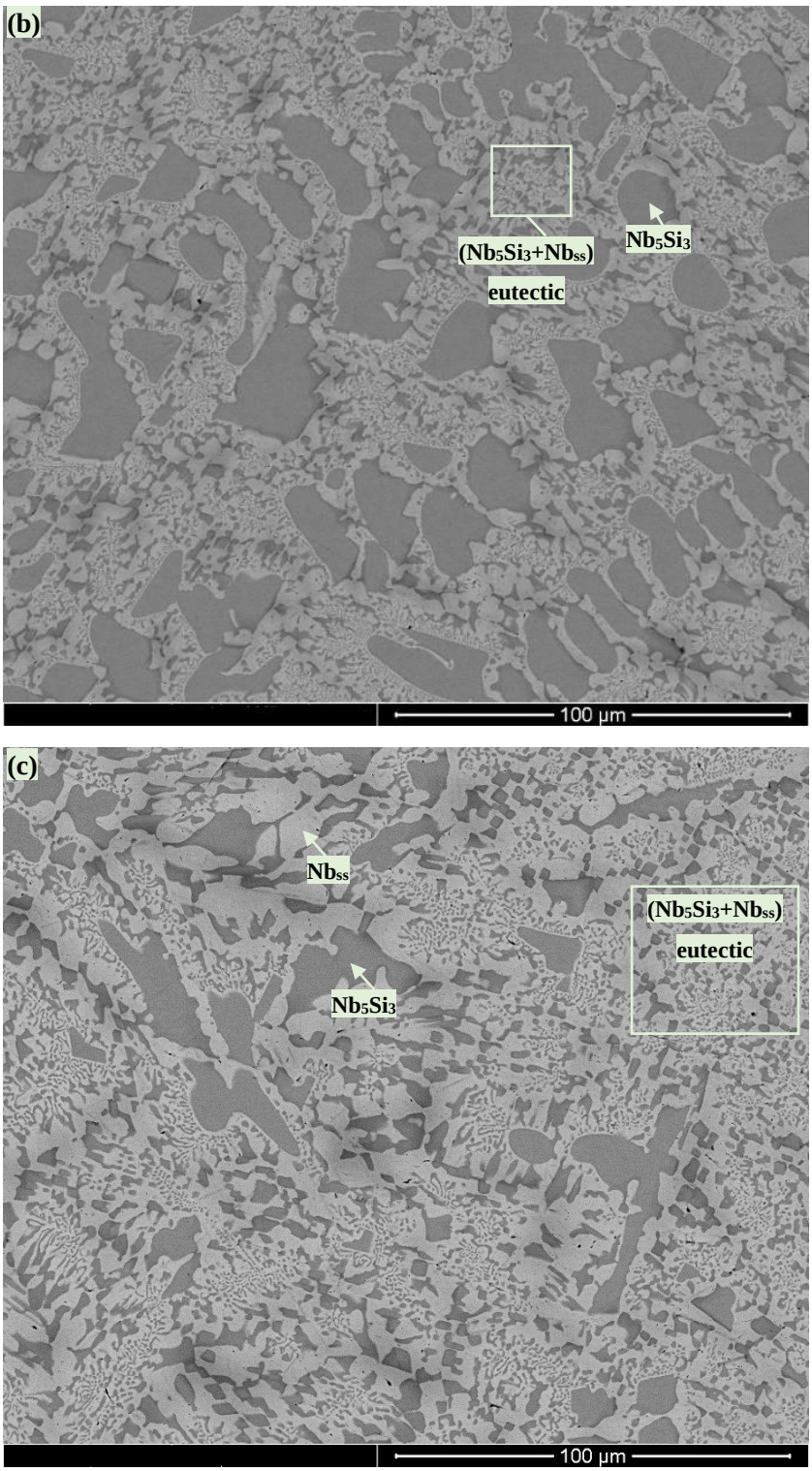
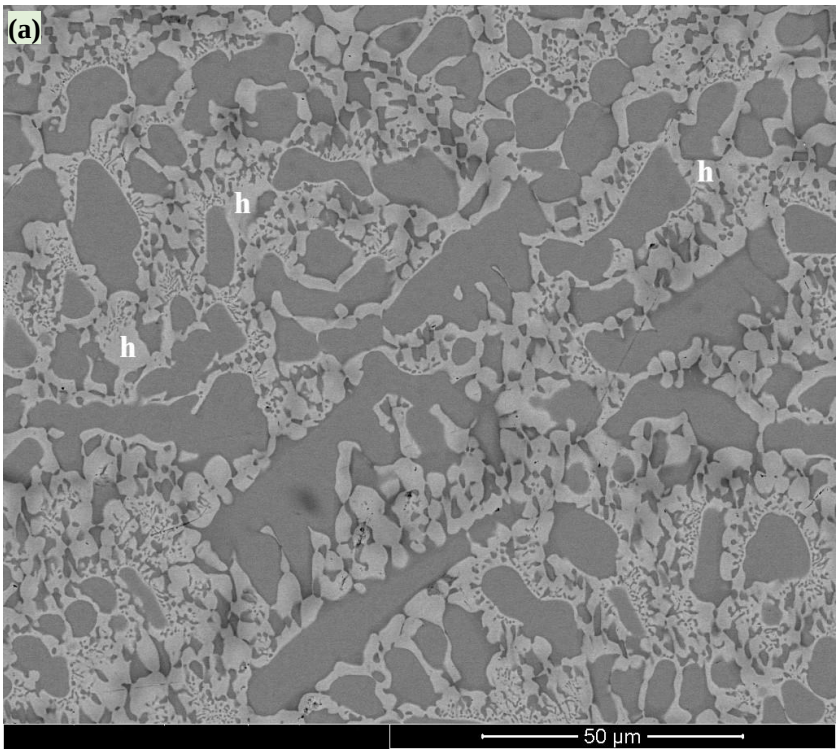
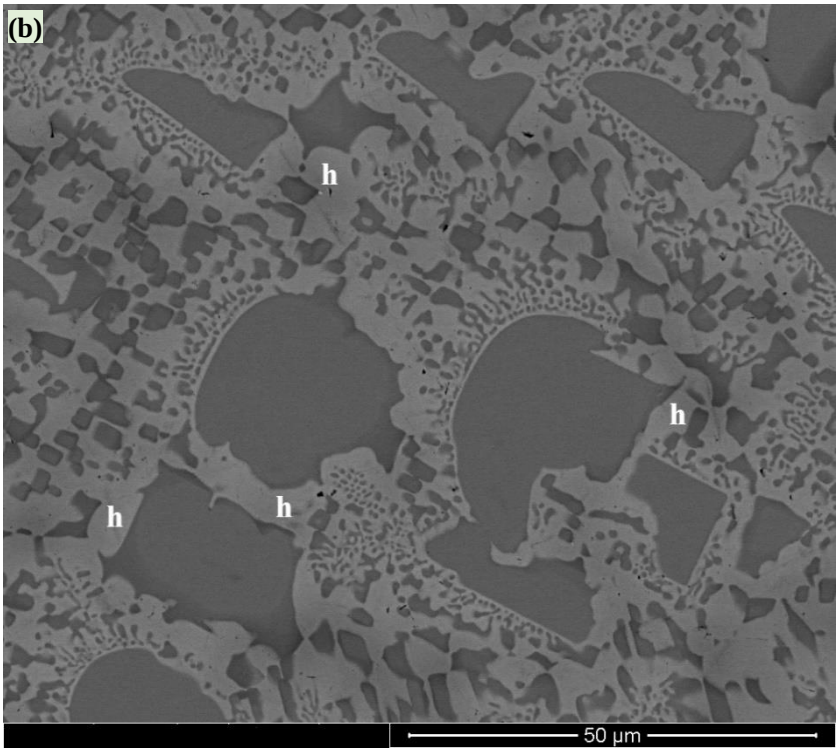


Figure 8.1 BSE images of the microstructure of the cast alloy ZX5 (a) top, (b) bulk, (c) bottom area of ingot.


(a)
h
h
h
h
50 μm


(b)
h
h
h
h
50 μm

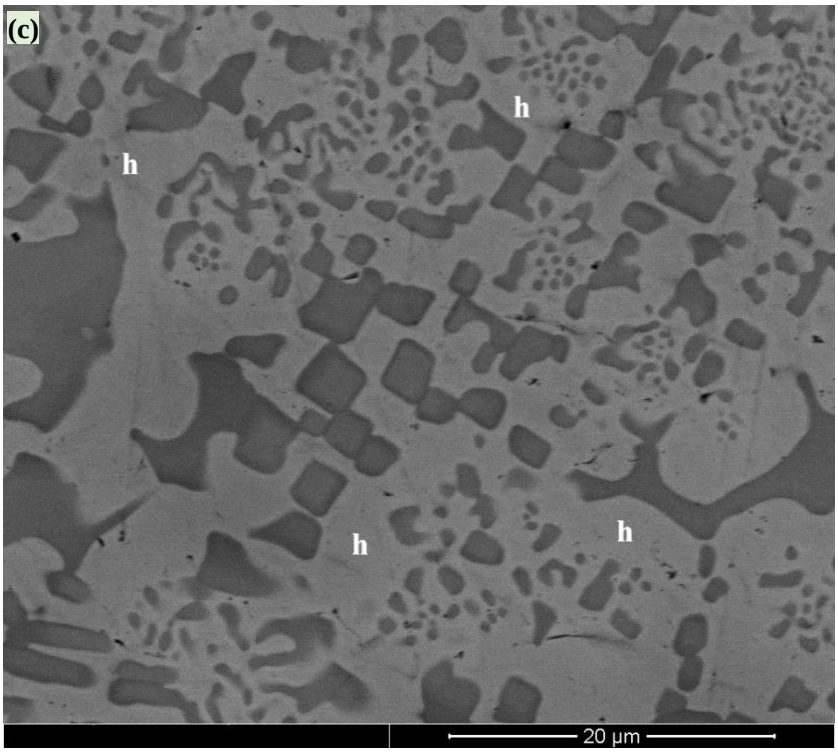


Figure 8.2 BSE images of the cast microstructure of the alloy ZX5 (a) top, (b) bulk, and (c) bottom. The letter h indicates Nb_{ss} halo.

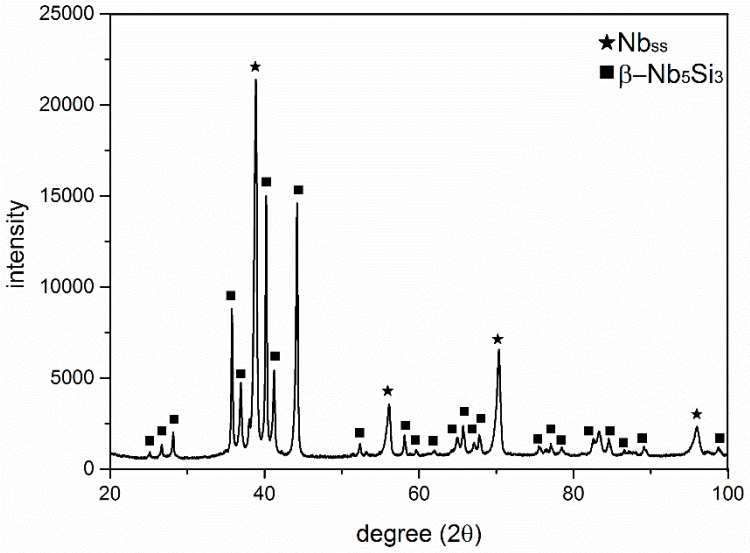


Figure 8.3 The XRD diffractogram of the as cast alloy ZX5.

Table 8.1 EDS analysis (at.%) of the as cast and heat treated alloy ZX5.

	Nb	Ti	Si	Al	Sn
As cast					
Surface*	**49.0** ± 0.2	**24.3** ± 0.5	**20.1** ± 0.4	**4.9** ± 0.3	**1.7** ± 0.1
	48.5 - 49.4	*23.5 - 25.0*	*19.4 - 20.7*	*4.5 - 5.3*	*1.6 - 1.9*
Bulk*	**48.9** ± 0.3	**24.7** ± 0.4	**19.9** ± 0.7	**4.7** ± 0.2	**1.8** ± 0.1
	48.5 - 49.5	*24.1 - 25.4*	*18.9 - 21.3*	*4.5 - 5.0*	*1.6 - 1.9*
Bottom*	**49.5** ± 0.4	**26.4** ± 0.6	**17.2** ± 1.0	**5.0** ± 0.3	**1.9** ± 0.2
	48.9 - 50.1	*25.9 - 27.6*	*15.7 - 18.4*	*4.6 - 5.5*	*1.6 - 2.4*
Nb_{ss}	**59.9** ± 0.8	**29.1** ± 0.9	**2.6** ± 0.2	**5.8** ± 0.1	**2.6** ± 0.1
	59.0 - 61.0	*28.1 - 30.0*	*2.4 - 2.9*	*5.7 - 6.0*	*2.5 - 2.8*
Ti-rich Nb_{ss}	**54.9** ± 2.6	**33.9** ± 2.3	**2.5** ± 0.2	**6.0** ± 0.2	**2.7** ± 0.2
	50.3 - 57.2	*31.8 - 38.1*	*2.2 - 2.7*	*5.7 - 6.2*	*2.5 - 3.0*
Nb_5Si_3	**47.7** ± 0.1	**15.6** ± 0.2	**33.0** ± 0.3	**3.0** ± 0.2	**0.7** ± 0.1
	47.6 - 48.0	*15.3 - 15.9*	*32.4 - 33.4*	*2.6 - 3.5*	*0.6 - 0.8*
Ti-rich Nb_5Si_3	**42.0** ± 1.5	**22.5** ± 1.6	**30.8** ± 1.0	**3.7** ± 0.1	**1.0** ± 0.1
	39.6 - 44.0	*20.2 - 25.1*	*28.6 - 31.6*	*3.6 - 4.0*	*0.8 - 1.1*
Eutectic	**57.0** ± 0.9	**23.2** ± 0.6	**12.6** ± 0.6	**5.1** ± 0.3	**2.1** ± 0.3
	55.7 - 58.3	*22.3 - 24.2*	*11.5 - 13.5*	*4.8 - 5.8*	*1.9 - 2.9*
Heat treated					
Bulk*	**51.3** ± 0.6	**22.7** ± 0.7	**20.1** ± 1.6	**4.3** ± 0.4	**1.6** ± 0.1
	50.4 - 52.3	*21.9 - 23.9*	*17.5 - 22.4*	*3.9 - 4.9*	*1.4 - 1.9*
Nb_{ss}	**60.2** ± 0.2	**30.7** ± 0.3	**0.5** ± 0.1	**6.5** ± 0.3	**2.1** ± 0.2
	59.8 - 60.4	*30.4 - 31.0*	*0.4 - 0.8*	*6.3 - 7.1*	*1.8 - 2.3*
Nb_5Si_3	**46.1** ± 1.5	**17.2** ± 1.5	**33.8** ± 0.5	**2.3** ± 0.4	**0.6** ± 0.1
	43.9 - 47.9	*15.2 - 19.3*	*33.0 - 34.6*	*1.5 - 3.0*	*0.5 - 0.8*
Nb_3X-A15	**58.9** ± 0.4	**22.4** ± 0.7	**4.9** ± 0.7	**8.4** ± 0.5	**5.4** ± 0.2
	58.4 - 59.4	*21.8 - 23.4*	*3.9 - 5.6*	*7.6 - 9.0*	*5.2 - 5.6*

* Large area analysis

Heat treated: The microstructure of the heat treated alloy ZX5 is shown in Figure 8.4. The lower magnification image (Figure 8.4a) shows individual Nb_5Si_3 grains and darker contrast Ti rich Nb_5Si_3 areas and grains. There was no evidence of the prior eutectic microstructure. The XRD (Figure 8.5) confirmed that the βNb_5Si_3 had completely transformed to αNb_5Si_3. The existence of A-15 intermetallic was confirmed in the heat treated alloy ZX5 even though its Sn concentration was lower than 2 at.%.

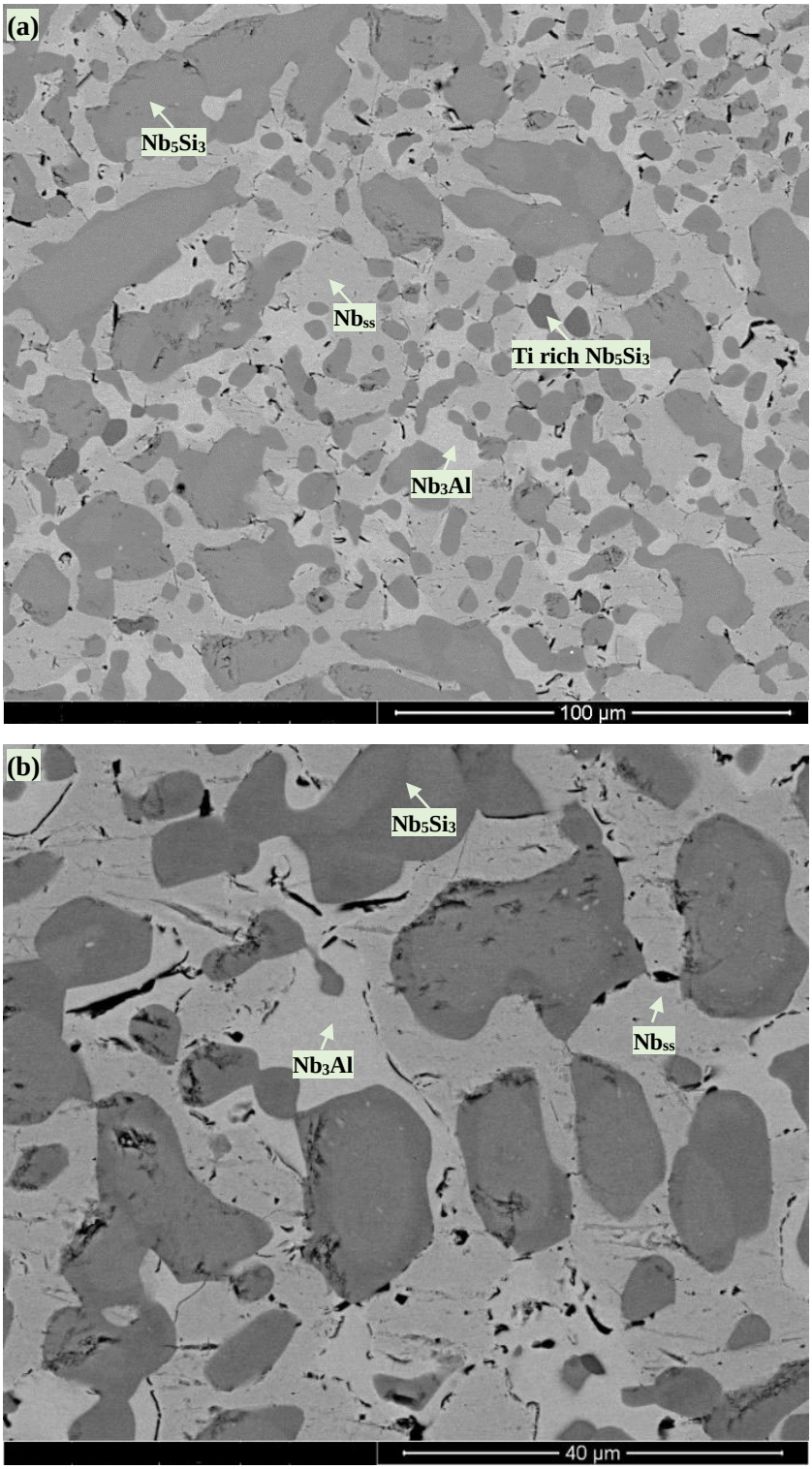


Figure 8.4 BSE images of the microstructure of the heat treated alloy ZX5 (a) low, and (b) high magnification.

The Nb_{ss} and the A-15 intermetallic phase can be distinguished in the higher magnification image in Figure 8.4b. The Nb_{ss} phase was contaminated during the heat

treatment and dark contrast Ti nitrides were formed inside and around Nb_{ss} grains. The A-15 intermetallic phase on the other hand showed a clean uncontaminated microstructure. After the heat treatment there were fine precipitates inside some Nb_5Si_3 grains. These precipitates were very small in size and exhibited similar contrast to Nb_{ss} and the A-15 intermetallic phase.

EDS data of the phases in the heat treated alloy ZX5 is shown in Table 8.1. The Si content in the Nb_{ss} was 0.5 at.%, which is similar to that reported in the Nb_{ss} in heat treated Nb silicide based alloys, and the Si + Al + Sn content was reduced to 9.1 at.%. In the Nb_5Si_3 the Si + Al + Sn content was essentially the same as in the cast alloy. In the newly formed A-15 intermetallic phase, the Si + Sn + Al concentration was 18.7 at.% and in agreement with that of the Nb_3Sn phase in Sn containing Nb silicide based alloys.

X-ray elemental maps of the microstructure of the heat treated alloy ZX5 are shown in Figure 8.6. The A-15 intermetallic phase and Nb_{ss} can be distinguished using the Sn and Si maps. The dark contrast Ti nitrides in the microstructure were confirmed from the Ti and N maps.

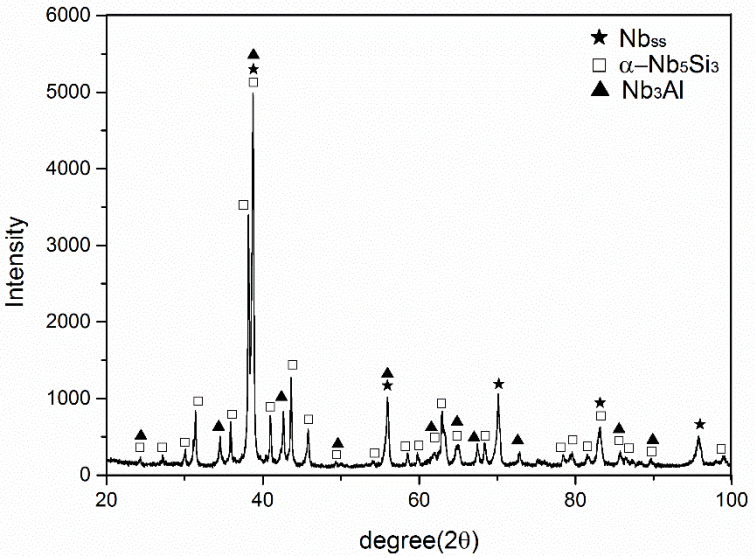


Figure 8.5 The XRD difrractogram of the heat treated alloy ZX5.

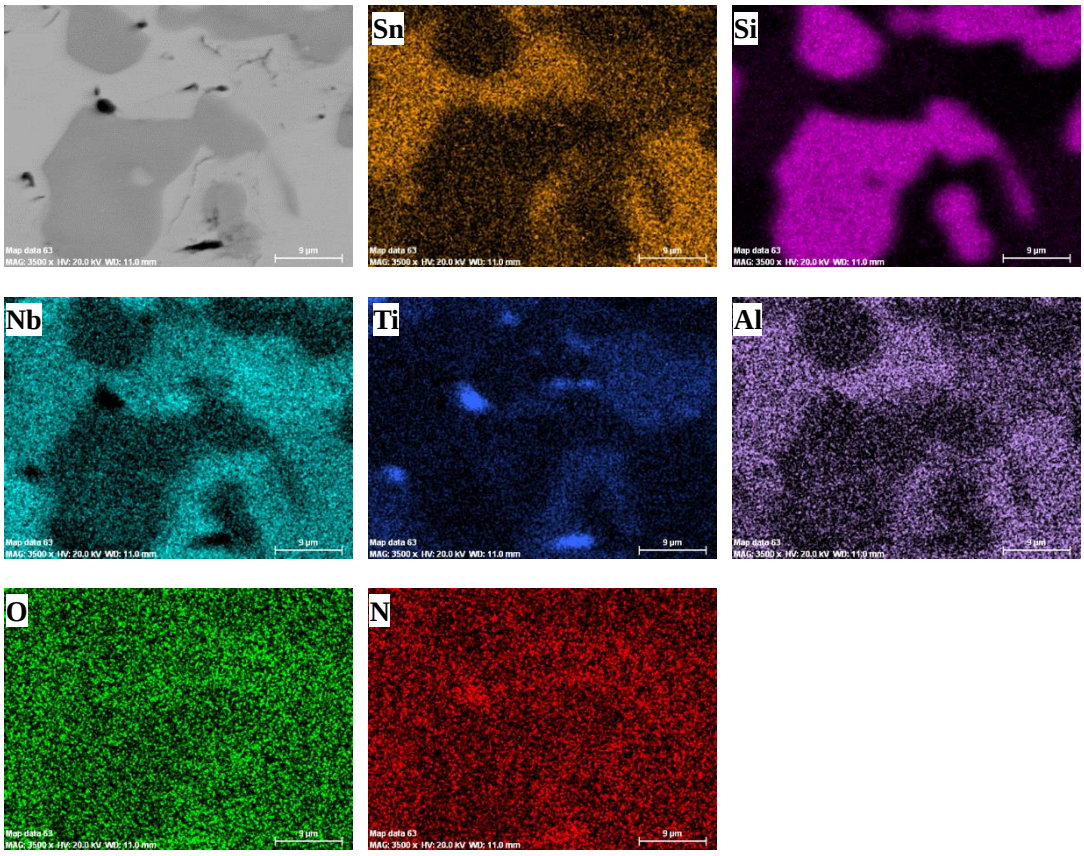


Figure 8.6 X-ray elemental maps of microstructure of the heat treated alloy ZX5.

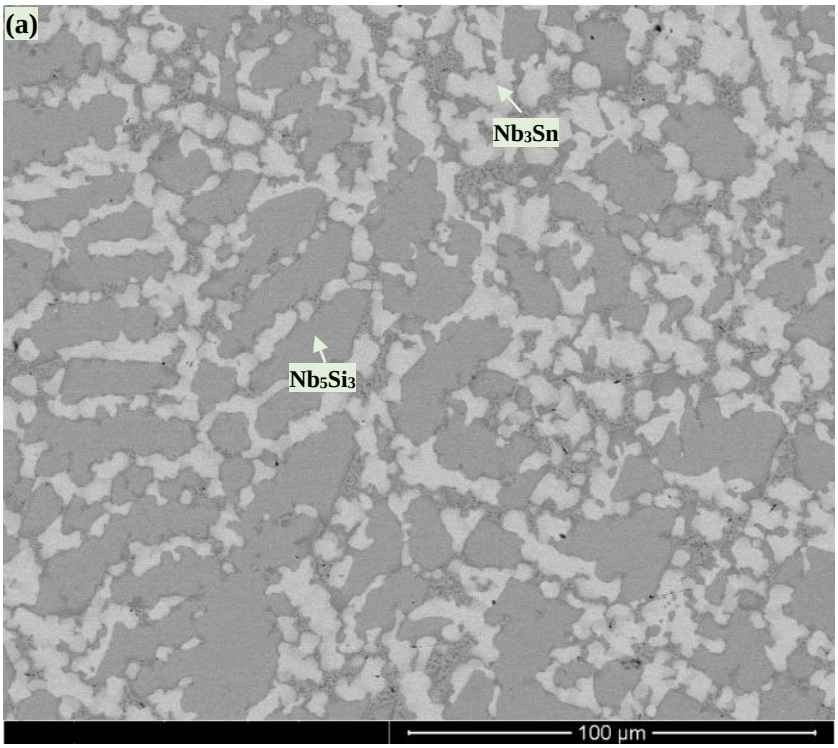
8.2.2 Alloy Nb-14Ti-18Si-5Al-5Sn (ZX6)

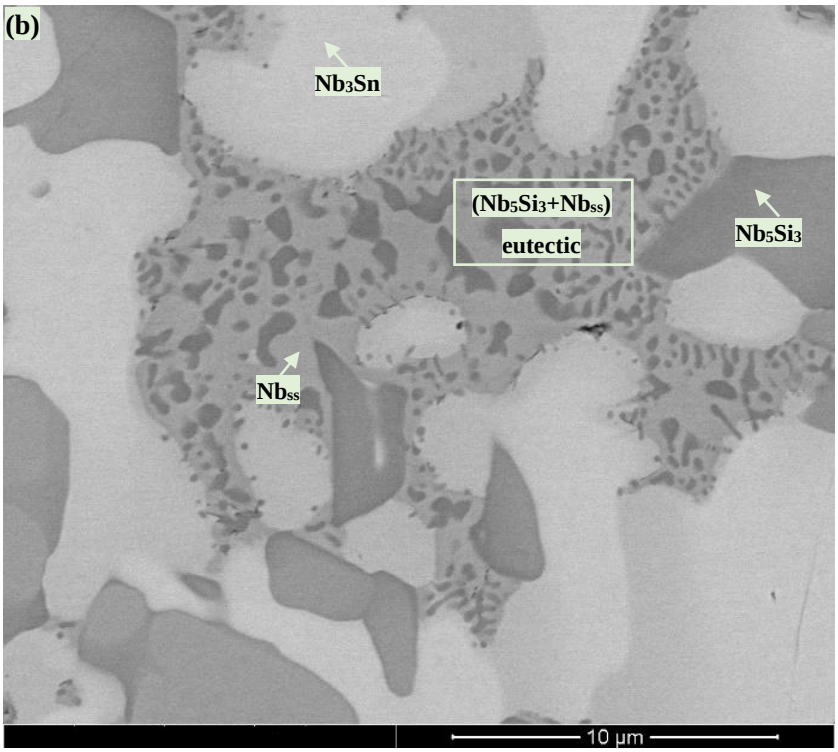
As cast: The large area EDS analyses of the cast alloy ZX6 are shown in Table 8.2. The actual composition of the cast alloy ZX6 was Nb-25.2Ti-18.5Si-4.9Al-5.0Sn.There was macrosegregation of Si and Ti in the alloy. The Si concentration ,varied between 16.0 and 21.5 at.% with the bottom being leaner in Si than the nominal composition. The Ti concentration varied between 22.1 and 29.4 at.%, and therefore the Ti macrosegregation was more severe. The Ti concentration in the bottom area was at least 3 at.% lower than in the top and bulk of the ingot. The concentrations of Al and Sn were close to the nominal composition.

The microstructure in various areas of the ingot of the cast alloy ZX6 is shown in Figures 8.7 and 8.8. According to the XRD data, Figure 8.9, the phases in the microstructure of the cast alloy ZX6 were the βNb_5Si_3, Nb_3Sn and Nb_{ss}. The SEM

images in Figure 8.7 show that the Nb_{ss} + Nb_5Si_3 eutectic was formed in-between the former two phases (Figure 8.7b). A small volume fraction of the Nb_{ss} phase formed in the bottom area of the ingot. The Nb_{ss} exhibited similar contrast to the A-15 intermetallic phase.

The microstructure in the top and bulk area of the cast alloy ZX6 consisted of βNb_5Si_3 and A-15 intermetallic phase and the Nb_{ss} + Nb_5Si_3 eutectic formed between the two intermetallic phases. Higher volume fractions of the A-15 intermetallic and the eutectic were observed in the bulk area of the alloy. The microstructure in the bottom area was different compared with the top and bulk. The volume fractions of the eutectic and the Nb_{ss} were low in this area. Figure 8.8 shows the microstructure near the water cooled Cu crucible. A zone ~ 50 µm thick consisting of Nb_{ss} and βNb_5Si_3 with some Ti rich Nb_5Si_3 was formed next to the crucible wall (Figure 8.8a). Then there was a change in microstructure to one consisting mainly of A-15 and βNb_5Si_3 with strong segregations of Ti in the latter (Figure 8.8b) and a very low volume fraction of Nb_{ss} and no Nb_{ss} + Nb_5Si_3 eutectic. The transition appears to start from a thin layer of uniform thicker Nb_{ss} formed parallel to the crucible wall (Figure 8.8). Overall, the A-15 intermetallic phase was present at a higher volume fraction in the bottom area of ZX6 and Ti rich Nb_5Si_3 was observed which showed a dark contrast around the Nb_5Si_3, as seen in Figure 8.8b. In the Nb_5Si_3, the Si + Al + Sn concentration was ~ 37 at.% and this value did not change in the Ti rich Nb_5Si_3 areas. The Ti concentration in the Nb_{ss} was high (~ 34 at. %), see Table 8.2.


(a)
Nb3Sn
Nb5Si3
100 μm


(b)
Nb3Sn
(Nb5Si3+Nbss)
eutectic
Nb5Si3
Nbss
10 μm

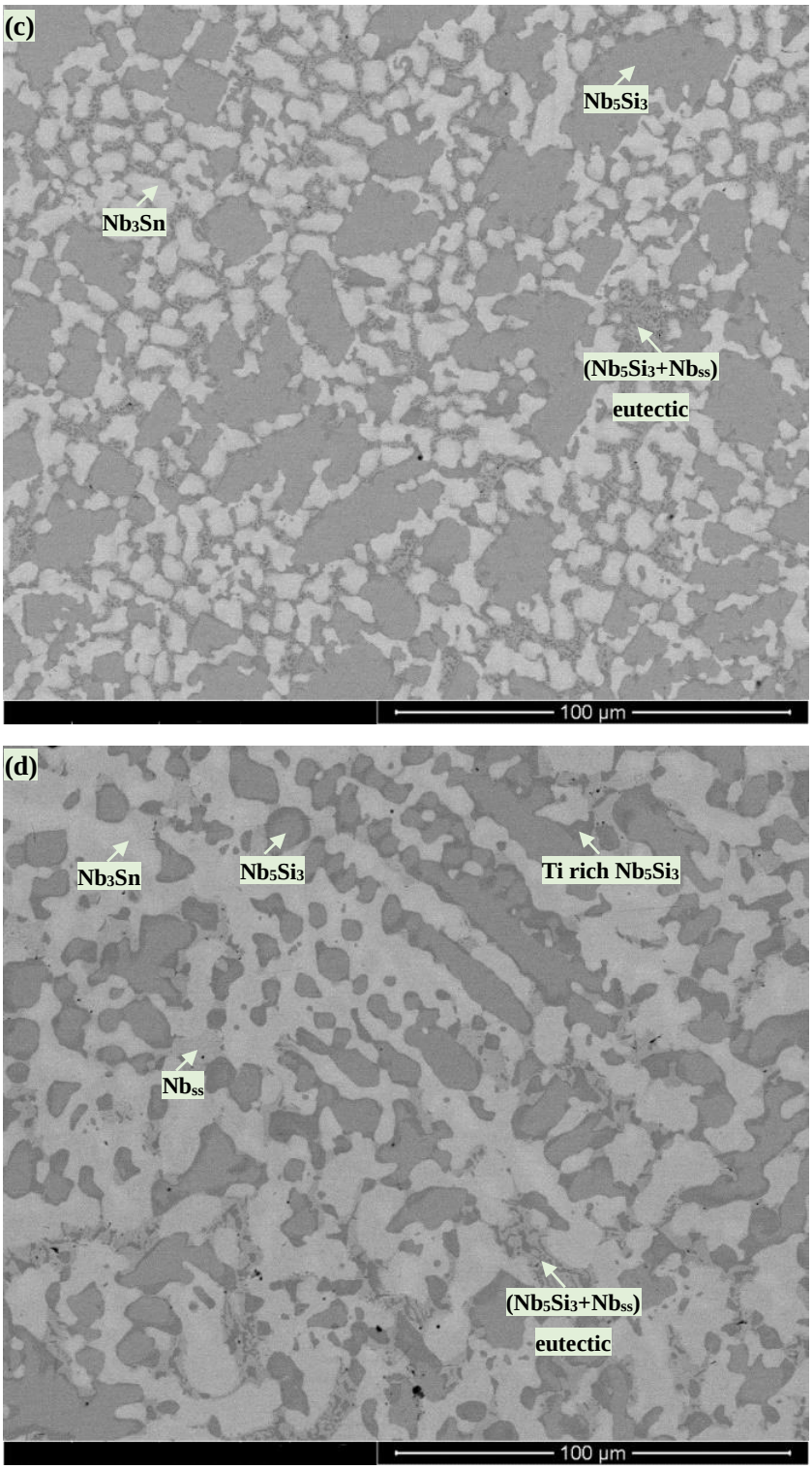


Figure 8.7 BSE images of the microstructure in the (a,b) top, (c)bulk, and (d).bottom of the cast alloy ZX6.

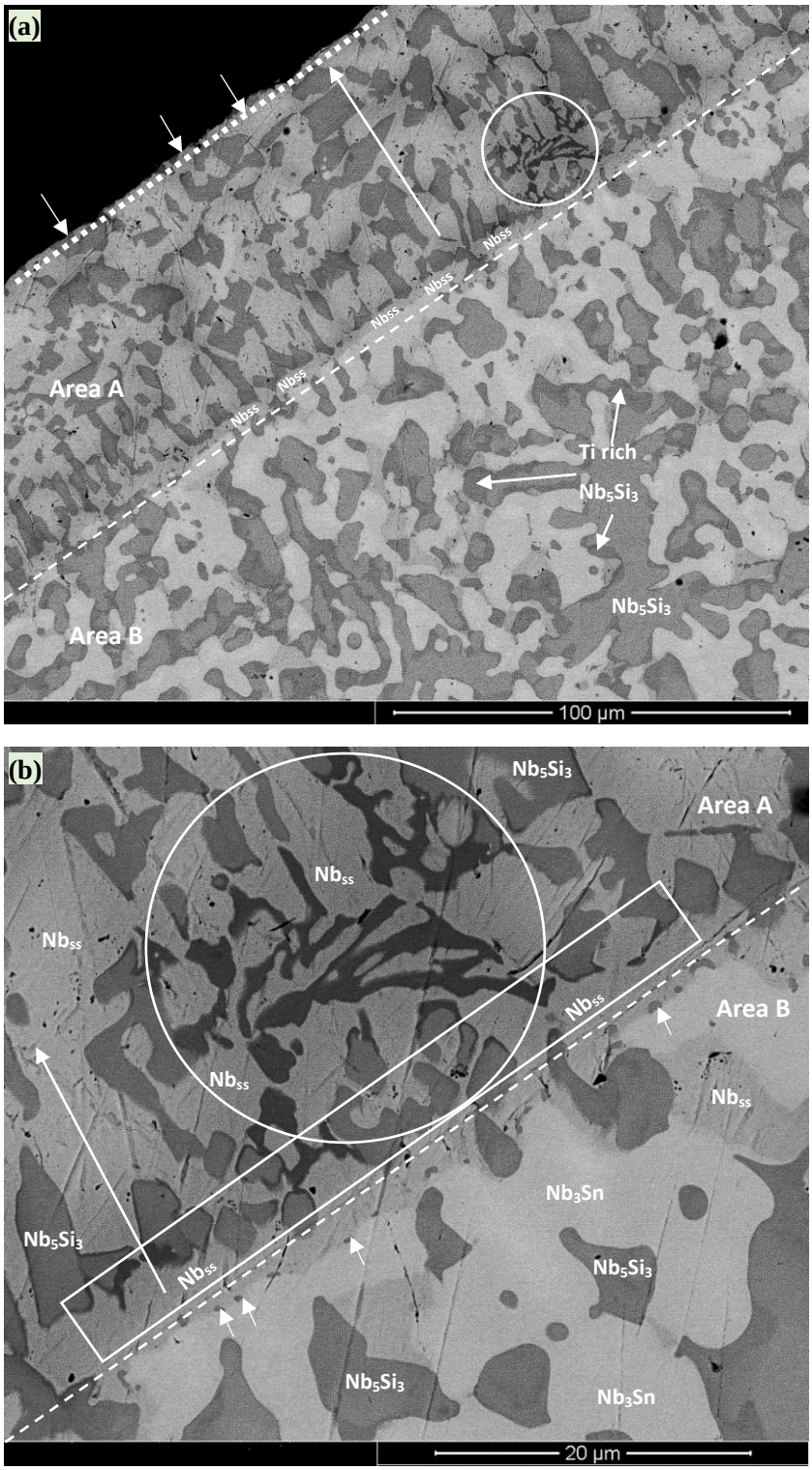


Figure 8.8 BSE images of the microstructure of the cast alloy ZX6 in the bottom of the ingot button next to the water cooled crucible at low (a) and high (b) magnifications. For areas A and B see text. Dashed line shows Nb_{ss} interface between areas A and B. Dotted line in (a) indicates part of ingot in contact with crucible wall. The arrow in area A shows direction of heat dissipation. The circle shows area where Ti rich Nb_5Si_3 formed in area A. For short arrows in (a) and (b) see text.

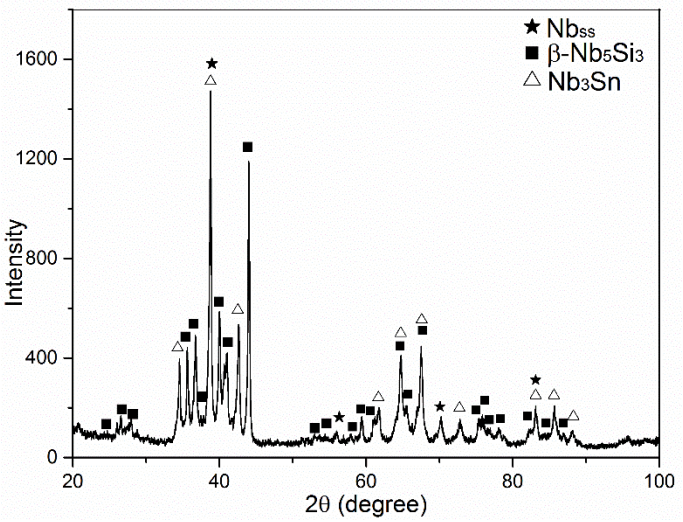


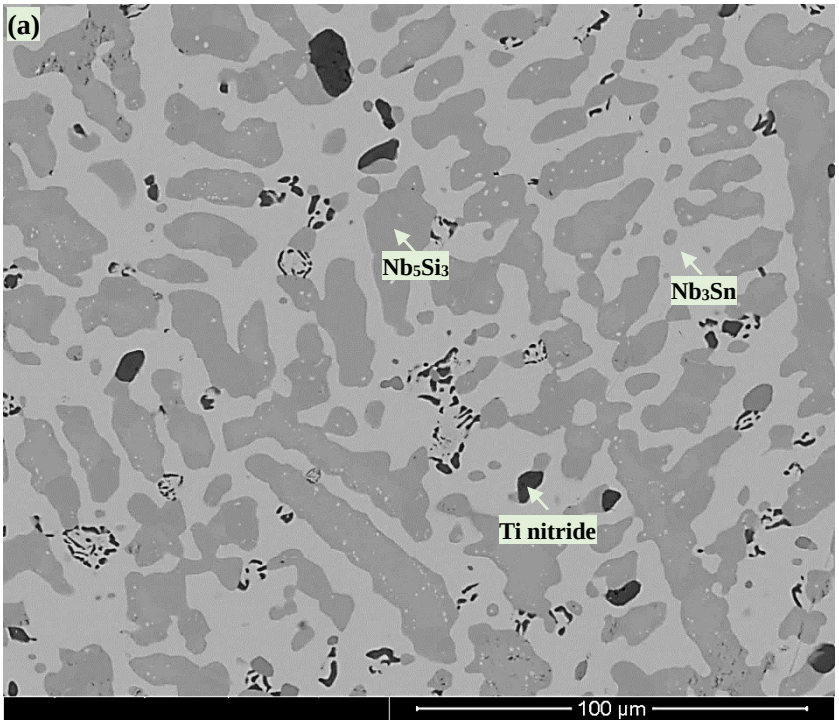
Figure 8.9 The XRD diffractogram of the as cast alloy ZX6.

Table 8.2 EDS analysis (at.%) of the as cast and heat treated alloy ZX6

	Nb	Ti	Si	Al	Sn
As cast					
Top*	**44.8** ± 0.1	**26.3** ± 0.3	**19.2** ± 0.3	**4.8** ± 0.2	**4.9** ± 0.2
	44.6 - 45.1	*25.8 - 26.9*	*18.8 - 19.7*	*4.4 - 5.1*	*4.7 - 5.2*
Bulk*	**45.1** ± 2.7	**26.0** ± 1.7	**18.9** ± 1.5	**5.1** ± 0.3	**4.9** ± 0.4
	40.6 - 49.6	*23.3 - 29.4*	*16.1 - 21.5*	*4.7 - 5.6*	*3.7 - 5.4*
Bottom*	**49.9** ± 0.3	**23.2** ± 0.6	**16.9** ± 0.5	**4.9** ± 0.2	**5.1** ± 0.1
	49.4 - 50.3	*22.1 - 24.4*	*16.0 - 18.0*	*4.5 - 5.1*	*5.0 - 5.4*
Nb_{ss}	**52.4** ± 3.6	**34.1** ± 3.2	**2.8** ± 0.7	**5.9** ± 0.2	**4.8** ± 0.3
	45.9 - 56.9	*30.2 - 38.9*	*1.8 - 4.3*	*5.5 - 6.1*	*4.5 - 5.4*
Nb_5Si_3	**45.7** ± 1.3	**17.1** ± 1.4	**32.5** ± 0.8	**2.9** ± 0.5	**1.8** ± 0.4
	44.5 - 47.4	*15.3 - 18.3*	*31.5 - 33.3*	*2.2 - 3.5*	*1.3 - 2.4*
Ti rich	**42.2** ± 1.2	**20.9** ± 1.3	**31.3** ± 0.3	**4.0** ± 0.2	**1.6** ± 0.2
Nb_5Si_3	*40.1 - 43.5*	*19.4 - 23.4*	*30.6 - 31.7*	*3.6 - 4.2*	*1.2 - 1.8*
Nb_3Sn	**54.8** ± 1.4	**24.0** ± 1.2	**6.6** ± 0.4	**5.9** ± 0.5	**8.7** ± 1.0
	52.7 - 57.2	*21.6 - 25.8*	*6.1 - 7.3*	*5.2 - 6.8*	*7.3 - 9.9*
Heat treated					
Bulk*	**47.9** ± 0.2	**23.9** ± 0.6	**19.3** ± 0.9	**4.5** ± 0.2	**4.4** ± 0.2
	47.6 - 48.2	*23.1 - 25.0*	*17.7 - 21.2*	*4.1 - 4.9*	*4.0 - 4.7*
Nb_5Si_3	**46.5** ± 0.8	**16.8** ± 0.7	**33.2** ± 0.1	**2.1** ± 0.1	**1.4** ± 0.1
	45.6 - 47.5	*15.8 - 17.6*	*33.0 - 33.4*	*2.0 - 2.4*	*1.3 - 1.6*
Ti-rich	**44.0** ± 0.8	**19.2** ± 0.6	**34.2** ± 0.4	**1.7** ± 0.2	**0.9** ± 0.2
Nb_5Si_3	*43.2 - 45.6*	*18.1 - 19.8*	*33.5 - 34.6*	*1.4 - 2.0*	*0.7 - 1.2*
Nb_3Sn	**55.0** ± 0.5	**25.1** ± 0.6	**4.7** ± 0.3	**7.0** ± 0.2	**8.2** ± 0.1
	53.9 - 55.5	*24.3 - 26.3*	*4.2 - 5.0*	*6.7 - 7.3*	*8.0 - 8.4*

* Large area analysis

Heat treated: The heat treated specimen was homogenised compared with the cast alloy, see Table 8.2. The microstructure of the heat treated alloy ZX6 is shown in Figure 8.10. The XRD data is shown in Figure 8.11. It confirmed the presence of the αNb_5Si_3 and A-15 intermetallic phases and Ti nitride in the heat treated ZX6. After the 100 hours heat treatment at 1500 °C the eutectic structure that was present in the cast alloy had disappeared in the heat treated microstructure, which was also free of the Nb_{ss} phase. Small precipitates were formed in the Nb_5Si_3 during the heat treatment. This was also observed in the heat treated alloy ZX5. The X-ray maps in Figure 8.10b would suggest that these precipitates were Sn rich and thus were the Nb_3Sn phase. The EDS analyses of the phases in the heat treated alloy ZX6 are given in Table 8.2. The Al and Sn concentrations in the Nb_5Si_3 had decreased slightly. The Si + Al + Sn concentration in the A-15 intermetallic phase had also decreased.



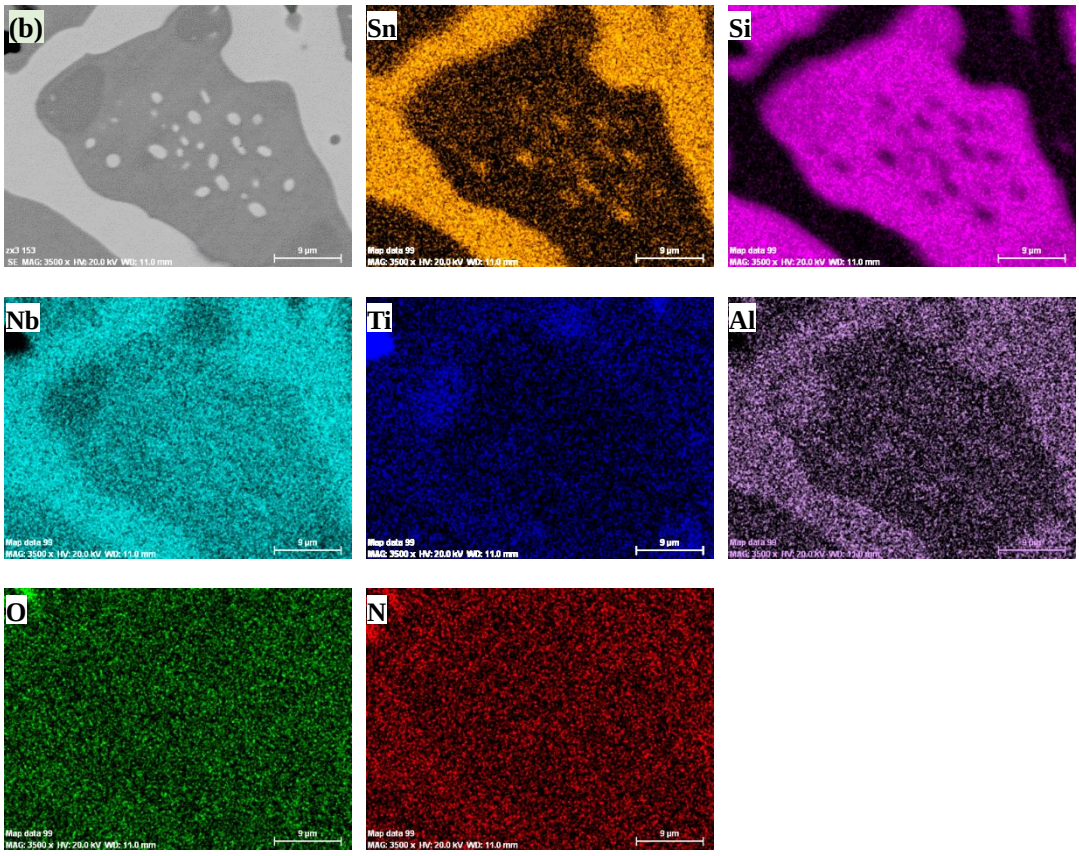


Figure 8.10 (a) BSE image of the microstructure in the bulk area of the heat treated alloy ZX6, (b) X-ray maps of Nb_5Si_3 with fine precipitates.

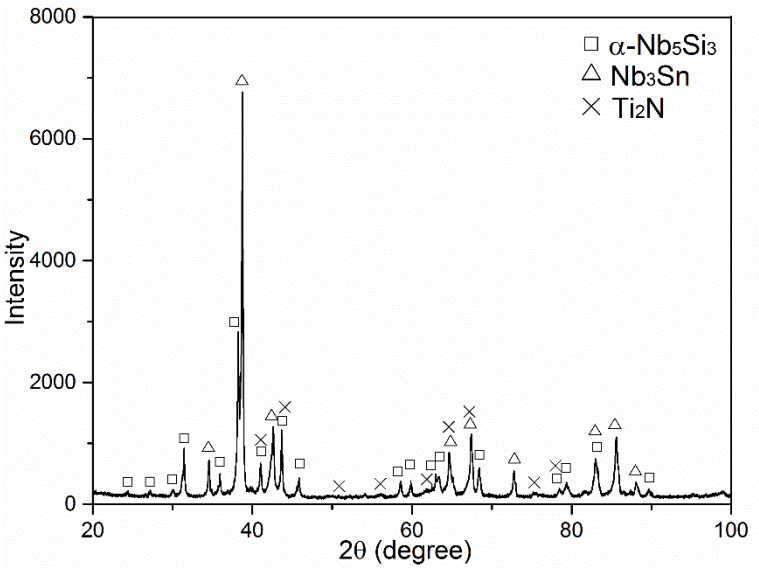


Figure 8.11 The XRD diffractogram of the heat treated alloy ZX6.

8.3 Thermo-gravimetric study of the alloys ZX5 and ZX6

The oxidation of the cast alloys ZX5 and ZX6 was investigated at 800 °C and 1200 °C. The oxidised specimens of the alloys ZX5 and ZX6 at 800 °C are shown in Figure 8.12. Grey rough scale was formed on the cubic specimen of the oxidised alloy ZX5. The oxidised alloy ZX6 specimen on the other hand showed a compact and smooth surface after 100 hours at 800 °C in static air. Both specimens had gained weight. At 1200 °C, the oxidation of the alloys ZX5 and ZX6 was much more severe than that at 800 °C; the oxide scales formed on both specimens had spalled off from the substrate. As shown in Figure 8.13, the oxide scales on both ZX5 and ZX6 were light yellow in colour.

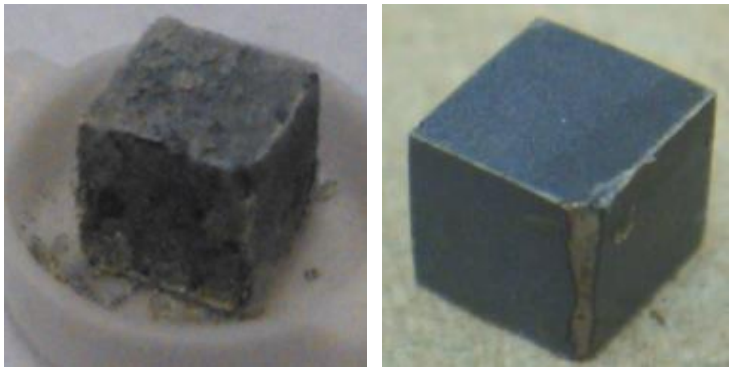


Figure 8.12 The oxidised specimens of the alloys ZX5 (left) and ZX6 (right) after 100 hours in static air at 800 °C.



Figure 8.13 The oxidised specimens of the alloys ZX5 (left) and ZX6 (right) after 100 hours in static air at 1200 °C.

8.3.1 Oxidation kinetics of the alloys at 800 °C and 1200 °C

The thermo-gravimetric (TG) data at 800 °C and 1200 °C is plotted as weight gain versus oxidation time, in Figure 8.14. The oxidation kinetic rates of ZX5 and ZX6 at 800 °C and 1200 °C are calculated as described in chapter 5 and were shown in Table 8.3.

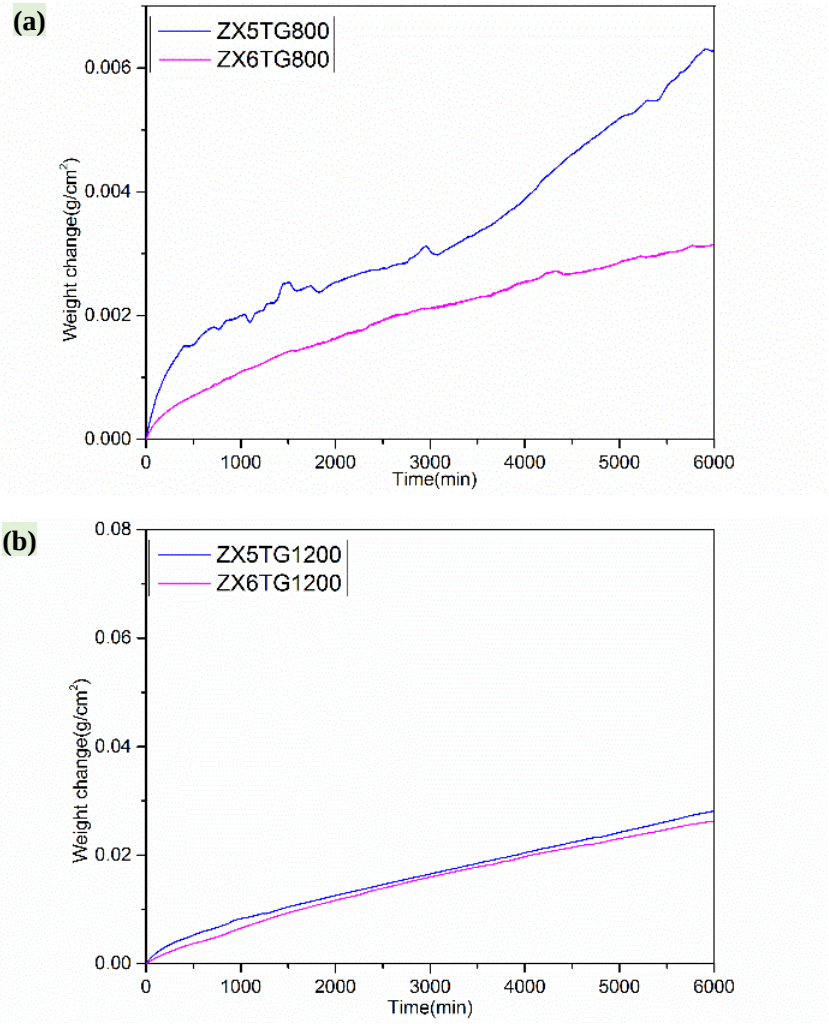


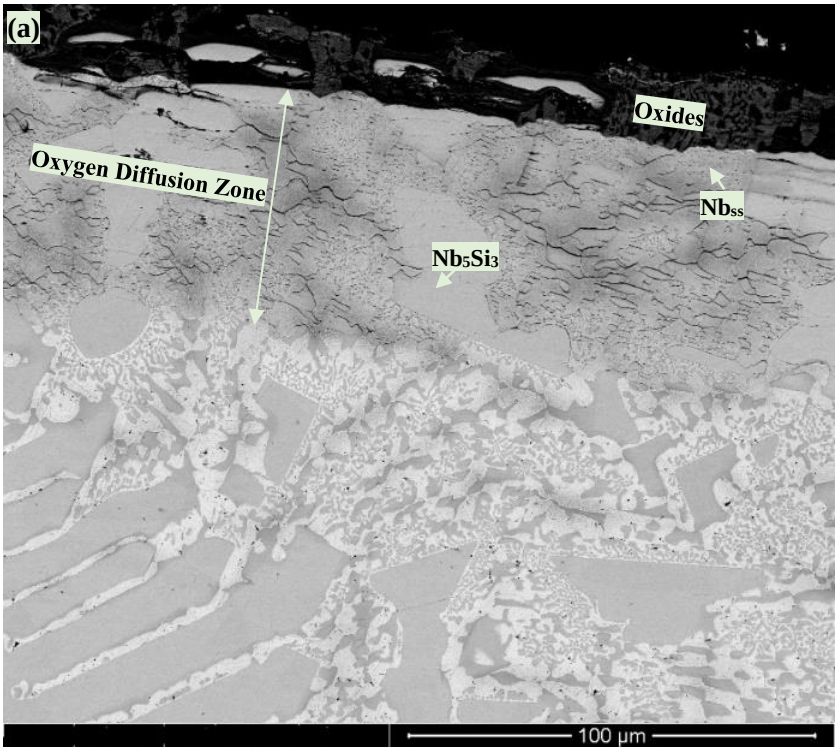
Figure 8.14 The TGA data of the alloys ZX5 and ZX6 at (a) 800 °C, (b) 1200 °C for 100 hours.

Table 8.3 The oxidation kinetic constants of the alloys ZX5 and ZX6, linear rate K_l ($g \bullet cm^{-2} \bullet s^{-1}$) and parabolic rate K_p ($g^2 \bullet cm^{-4} \bullet s^{-1}$)

	ZX5	ZX6
800 °C	$K_p = 5.16 \times 10^{-11}$ ($t \leq 3000$ mins) $K_l = 1.80 \times 10^{-8}$ ($t > 3000$ mins)	$K_p = 2.22 \times 10^{-11}$ ($t \leq 1500$ mins) $K_l = 6.40 \times 10^{-9}$ ($t > 1500$ mins)
1200 °C	$K_p = 1.15 \times 10^{-9}$ ($t \leq 1300$ mins) $K_l = 6.70 \times 10^{-8}$ ($t > 1300$ mins)	$K_l = 7.31 \times 10^{-8}$

8.3.2 Microstructures of the oxidised alloys ZX5 and ZX6 at 800 °C

The thickness of the oxide scale formed on the alloy ZX5 was around 10-15 μm. The scale was cracked and voids were formed. The oxygen diffusion zone below the oxide scale was around 50 μm thick. In the oxygen diffusion zone the Nb_5Si_3 and Nb_5Si_3 + Nb_{ss} eutectic were present and the Nb_{ss} phase exhibited a similar contrast to the Nb_5Si_3 (see Figure 8.15a). Below the oxygen diffusion zone, the bulk microstructure was similar to the as cast microstructure of ZX5, see Figure 8.15b.



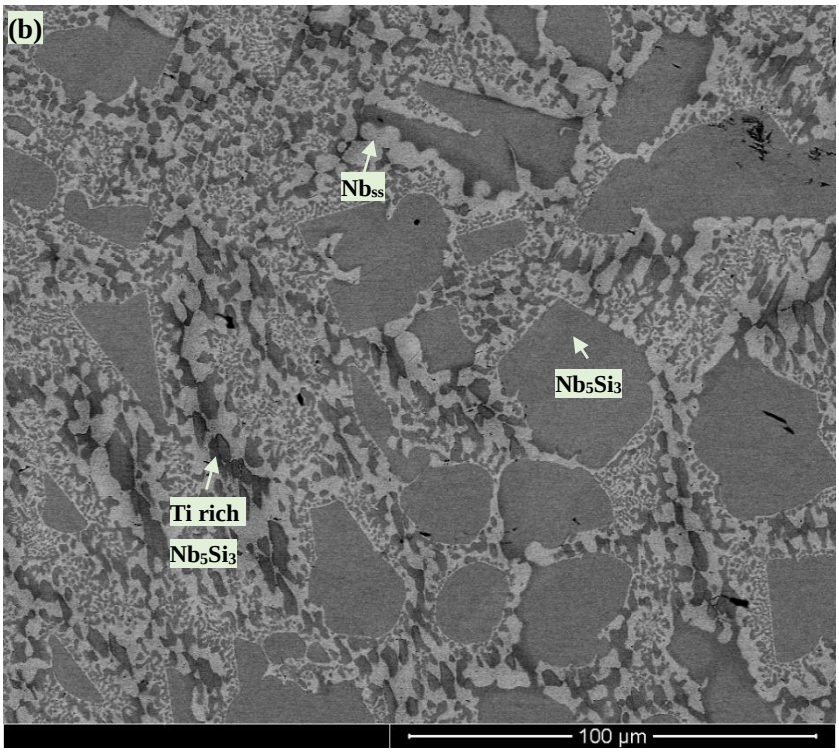
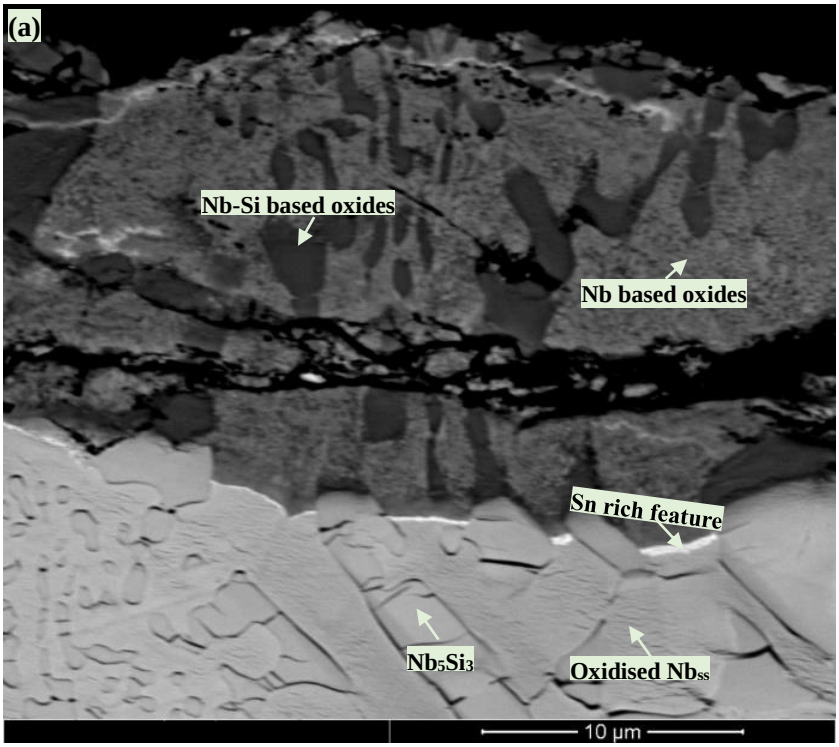


Figure 8.15 Cross section microstructures of the oxidised alloy ZX5 at 800 °C showing (a) the oxide scale and part of the oxygen diffusion zone, (b) details of the substrate microstructure below the scale.



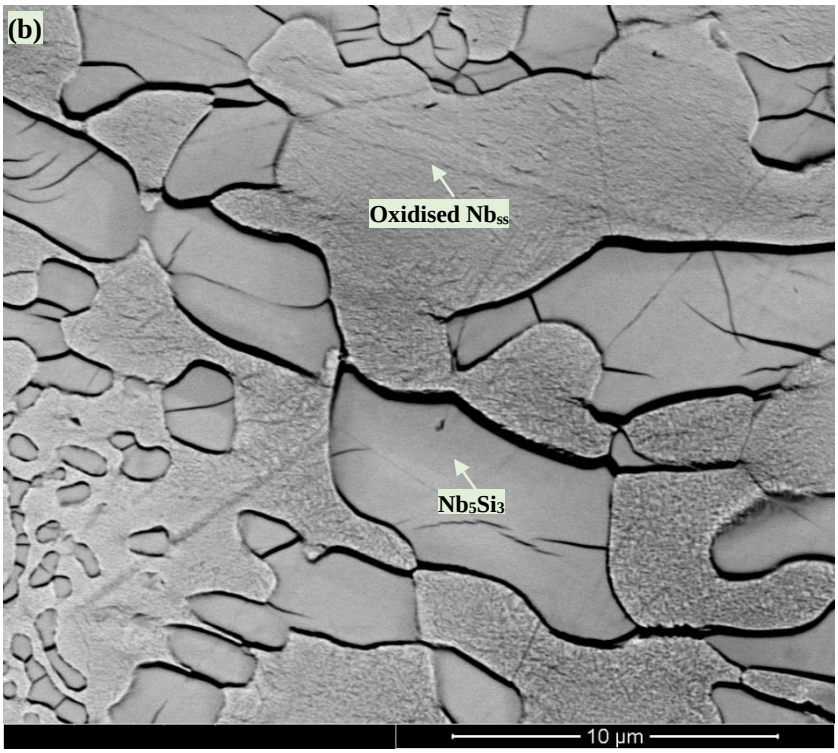


Figure 8.16 Cross section microstructures of the oxidised alloy ZX5 at 800 °C showing (a) the oxide scale and part of the oxygen diffusion zone, (b) details of the substrate microstructure below the scale.

The high magnification BSE image in Figure 8.16a shows two features of different contrast in the oxide scale. The EPMA- WDS results in Table 8.4 would suggest that the light grey oxide was Nb rich oxide, and the dark grey oxide was Nb-Si rich oxide. Details of the microstructure of the substrate below the scale are shown in Figure 8.16b. It can be seen that the Nb_{ss} was mostly contaminated compared with the Nb_5Si_3 and that the latter was cracked.

Table 8.4 The WDS analysis (at.%) of the two oxides of different contrast in the alloy ZX5 scale formed at 800 °C.

Phase	Nb	Ti	Si	Al	Sn	O
Nb rich oxide	20.15	8.44	1.48	1.78	1.26	**66.89**
Nb-Si rich oxide	15.50	4.93	12.75	0.54	0.19	**66.09**

The oxygen diffusion zone was also studied using WDS to find out the extent of contamination of each phase in this area. The results are summarised in Table 8.5. The

oxygen content of the Nb_{ss} phase was ~ 34.8 at.%, which is almost 12 times that of the Nb_5Si_3 phase. Comparison with the chemical compositions of the Nb_{ss} and Nb_5Si_3 in the cast alloy (Table 8.1) shows that in the Nb_{ss} all elements were oxidised (concentrations in Table 8.5 lower than that in Table 8.1) and Ti in the Nb_5Si_3.

Table 8.5 The WDS analysis (at.%) of the phases in the oxygen diffusion zone of the alloy ZX5 at 800 °C.

Phase	**Nb**	**Ti**	**Si**	**Al**	**Sn**	**O**
$Nb_{ss(eut)}$	**38.66** *35.78-40.21*	**20.24** *18.79-21.74*	**1.11** *1.00-1.18*	**3.31** *3.13-3.52*	**1.88** *1.81-1.97*	**34.80** *33.08-36.10*
Nb_5Si_3 (dendrites)	**44.86** *44.53-45.11*	**14.90** *14.59-15.06*	**34.94** *34.30-35.44*	**1.80** *1.61-2.16*	**0.56** *0.46-0.67*	**2.94** *2.02-3.37*
$Nb_5Si_{3(eut)}$*	**39.56**	**20.35**	**33.41**	**2.46**	**0.74**	**3.48**

*One WDS result of the eutectic Nb_5Si_3 phase due to its small size.

In the bulk area of the oxidised alloy specimen, less contaminated microstructure was present and the Nb_{ss} and Nb_5Si_3 phases in the eutectic structure were easily distinguished (Figure 8.15b). WDS analyses was applied on the Nb_{ss} and Nb_5Si_3 phases. The data showed that the oxygen content of Nb_5Si_3 was the same as in the oxygen diffusion zone while the oxygen content of the Nb_{ss} in the bulk area had decreased to ~ 5.5 at.%, as seen in Table 8.6.

Table 8.6 The WDS analyses (at.%) of the two phases in the bulk of the alloy ZX5 after oxidation at 800 °C (at.%).

Phase	Nb	Ti	Si	Al	Sn	O
Nb_{ss}	54.22	31.78	1.50	4.18	2.58	5.54
Nb_5Si_3	44.67	14.99	35.00	1.77	0.60	2.97

The oxidised microstructure of ZX6 at 800 °C is shown in Figure 8.17. The oxide scale of the alloy ZX6 was less porous than that of the alloy ZX5. The thickness of the oxide layer was around 10μm which is similar to the oxidised alloys ZX3 and ZX4 at 800 °C. The Nb_5Si_3 showed cracks parallel to the surface in the oxygen diffusion zone of the alloy ZX6, Figure 8.17.

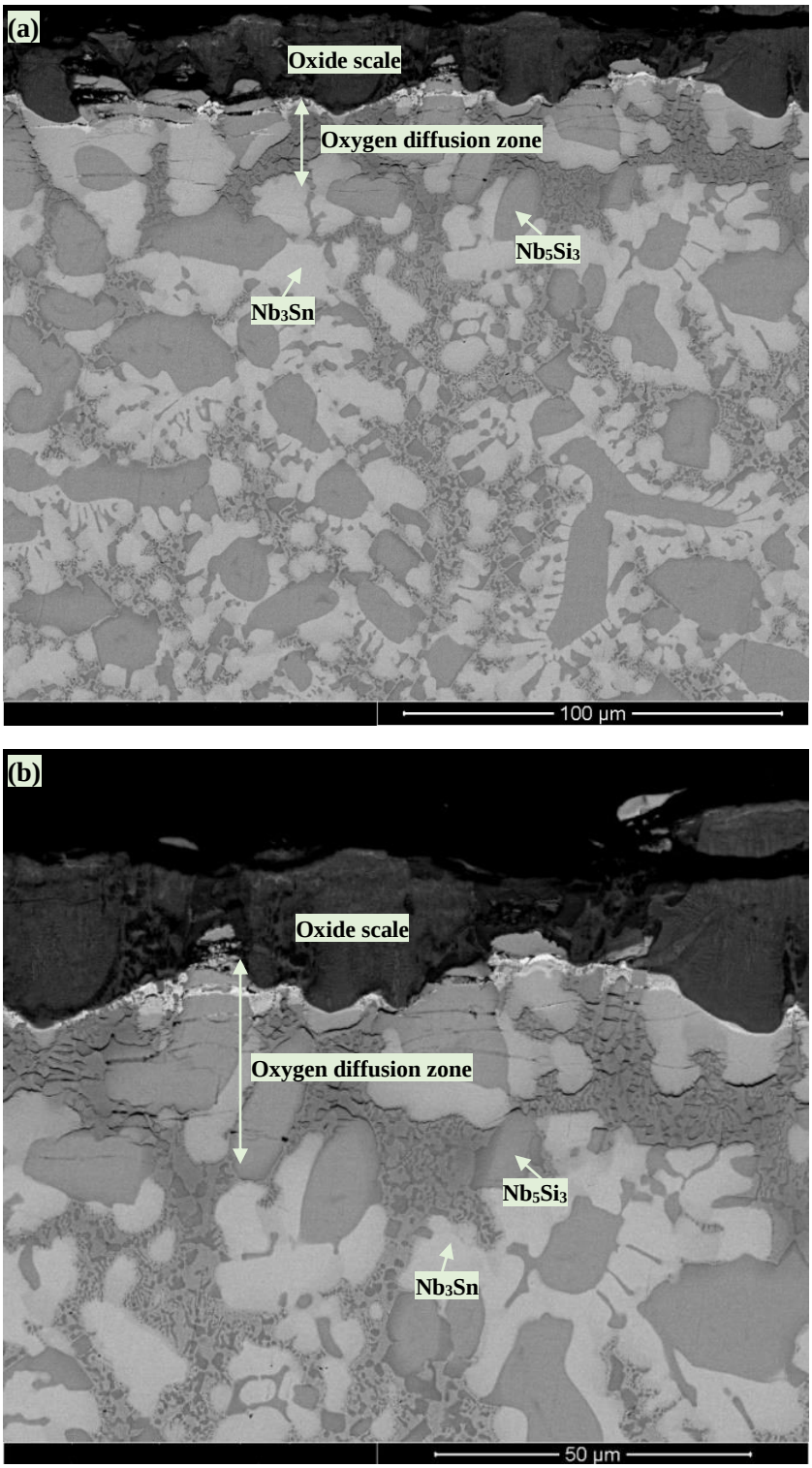


Figure 8.17 BSE images of cross section microstructure of oxidised alloy ZX6 at 800 °C details of the top night hand corner in (a) are shown in (b).

The depth of the oxygen diffusion zone in the alloy ZX6 was around 30 μm, which is smaller than that of the alloy ZX5. Micro-cracking occurred during oxidation in the

Nb_5Si_3 and Nb_3Sn phases. Those cracks were mostly parallel to the surface of the specimen and appeared more severe in the Nb_5Si_3 than in the Nb_3Sn. Comparing the contrast of phases in the oxygen diffusion zone and bulk area in Figure 8.17, the eutectic structure and the Nb_3Sn are both presenting darker contrast in the oxygen diffusion zone while the Nb_5Si_3 grains in these two areas show similar contrast. Figure 8.17a would suggest that contamination of the microstructure had progressed along the areas where the Nb_{ss} was formed in the cast alloy.

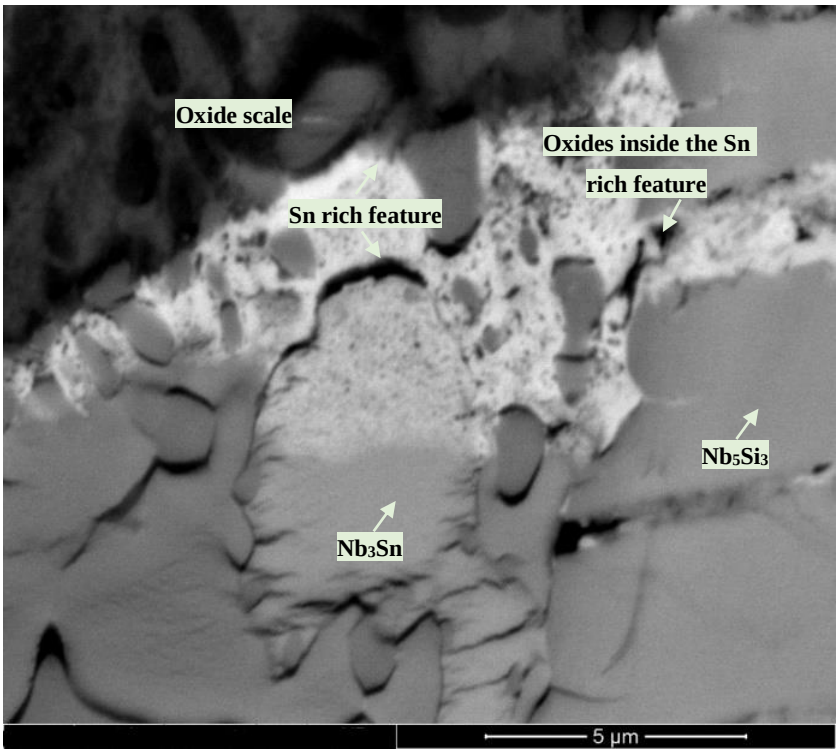


Figure 8.18 BSE image of the cross section microstructure showing the Sn rich feature in the oxidised ZX6 at 800 °C.

An Sn rich area in the oxidised alloy ZX6 was noticeable in between the oxide scale and the oxygen diffusion zone. As seen in Figure 8.18, the Sn rich feature was formed where the Nb_{ss} was in the eutectic structure and also in parts of the Nb_3Sn grains. Some dark particles were observed inside the Sn rich feature at higher magnification. WDS analysis was applied on the features and other phases seen in Figures 8.18 and 8.19. The results of this WDS study are summarised in Table 8.7.

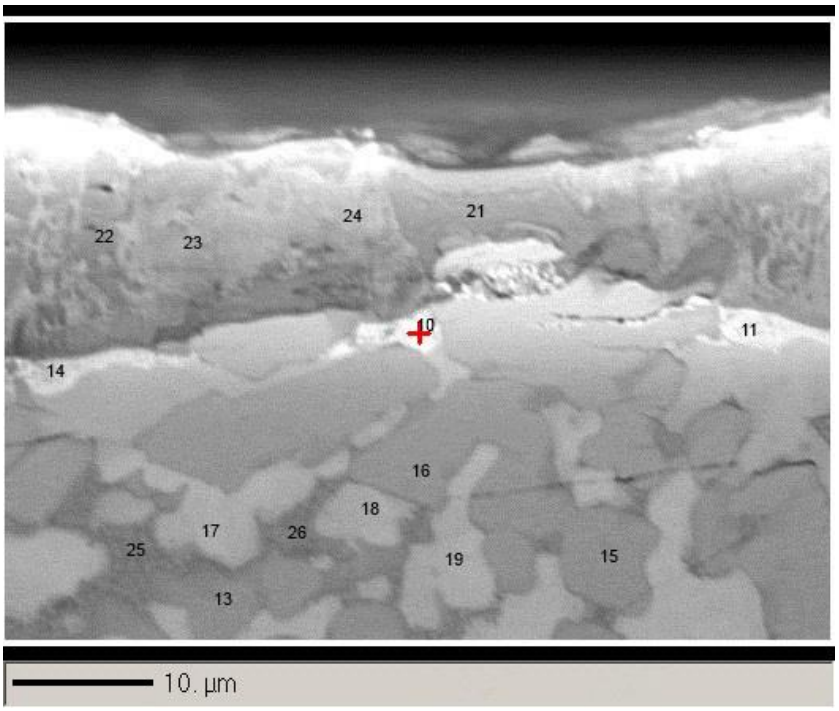


Figure 8.19 The WDS spot analysis of the oxidised microstructure of ZX6 at 800 °C with spot identification.

Table 8.7 WDS analysis (at.%) of phases in the oxidised ZX6 at 800 °C. For spot number see Figure 8.19.

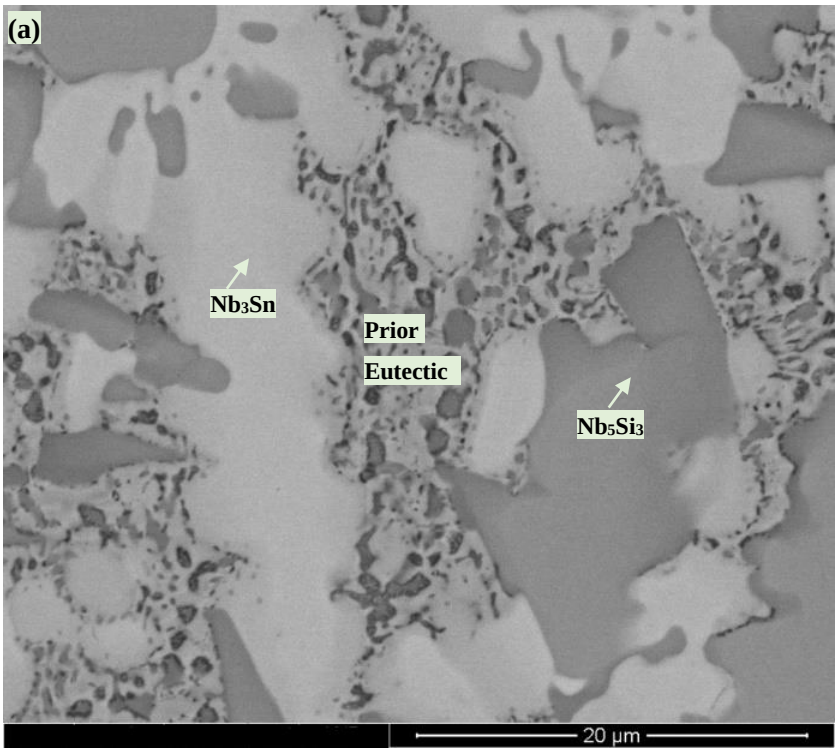
Sn rich feature	Nb	Ti	Si	Al	Sn	O
Spot 10	33.24	13.18	5.58	3.97	16.68	27.35
Spot 11	30.59	14.20	3.91	3.67	16.40	31.23
Spot 14	40.32	8.75	4.10	4.33	21.85	20.67
Oxides	Nb	Ti	Si	Al	Sn	O
Spot 21	16.08	5.75	11.53	0.68	0.25	65.71
Spot 22	14.15	9.42	7.29	1.57	0.71	66.86
Spot 23	18.44	9.71	1.47	2.47	0.83	67.08
Spot 24	16.60	11.85	1.22	2.05	0.26	68.02
Nb_3Sn	Nb	Ti	Si	Al	Sn	O
Spot 17	55.03	20.70	5.05	4.30	9.06	5.86
Spot 18	51.09	23.28	5.05	4.94	7.77	7.87
Spot 19	54.33	21.92	5.18	4.45	8.86	5.26
Nb_5Si_3	Nb	Ti	Si	Al	Sn	O
Spot 13	42.06	17.96	32.44	3.11	2.28	2.15
Spot 15	43.75	15.84	33.97	2.31	1.90	2.23
Spot 16	43.35	15.69	34.53	1.91	1.74	2.78
Prior eutectic	Nb	Ti	Si	Al	Sn	O
Spot 25	35.54	31.84	10.87	4.05	3.11	14.59
Spot 26	34.42	31.16	9.16	4.05	3.42	17.79

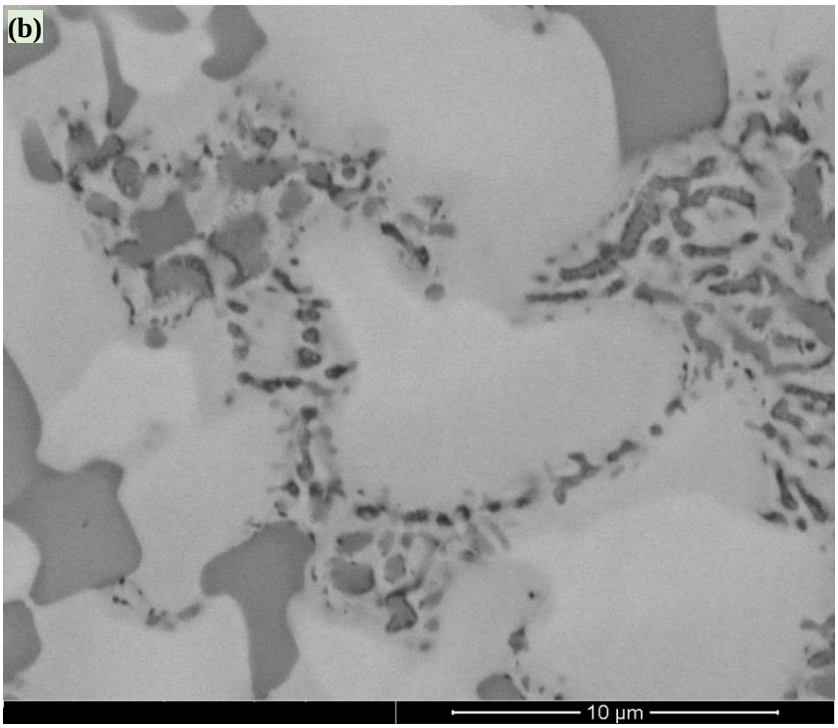
The data in Table 8.7 show (i) that the Sn rich feature was contaminated with oxygen and had Si + Al + Sn content in the range 24 to 30 at.%, i.e., within the solubility range of Nb_3Sn in the Nb-Sn binary, (ii) that niobates rich in Ti or Si were formed in the scale, (iii) that the oxygen contamination was reduced significantly at a depth of about 20 μm below the scale, (iv) that the Nb_5Si_3 was less severely contaminated by oxygen compared with the Nb_3Sn, and (v) that the prior eutectic microstructure was more severely contaminated than the Nb_3Sn and Nb_5Si_3, owing to the presence of the Nb_{ss} in the prior eutectic.

In the bulk, the eutectic constituent Nb_5Si_3 had been affected by oxygen contamination, probably owing to its neighbouring Nb_{ss} (Figure 8.20). The Ti concentration in the Nb_5Si_3 was lower than that in the cast microstructure, where also Ti rich Nb_5Si_3 was formed (Table 8.2). Ti was also found in the oxide formed in the scale (Table 8.7). As shown in Figure 8.20, the Nb_5Si_3 was depleted in Ti near the centre of the grains and presented a "darker ring" around the Nb_5Si_3 (Figure 8.20a, b). WDS spot analyses were applied on the Nb_5Si_3 dendrites, Nb_3Sn and the prior eutectic (see Table 8.8). The average chemical composition of the Nb_3Sn and Nb_5Si_3 below the scale (Table 8.7) was essentially the same as that of the same phases in the contaminated eutectic areas in the bulk (Table 8.8). It should be noted that at low magnification, the microstructure of the eutectic areas in Figure 8.20a "looks the same" as that in Figure 8.7b. It was only at higher magnification that we were able to distinguish the difference between the two arising from contamination by oxygen of the bulk. This shows that it is easy to miss out contamination of the bulk if studies do not use high magnification.

Table 8.8 WDS spot analysis (at.%) of the bulk area of the oxidised alloy ZX6 at 800 °C.

Phase	*Nb*	*Ti*	*Si*	*Al*	*Sn*	*O*
Nb_3Sn	52.83	22.67	4.94	4.51	8.20	6.85
Nb_5Si_3	43.28	16.42	33.55	2.35	1.88	2.52
Prior eutectic	40.82	35.84	10.10	4.59	3.63	5.02


(a)
Nb3Sn
Prior
Eutectic
Nb5Si3
20 μm


(b)
10 μm

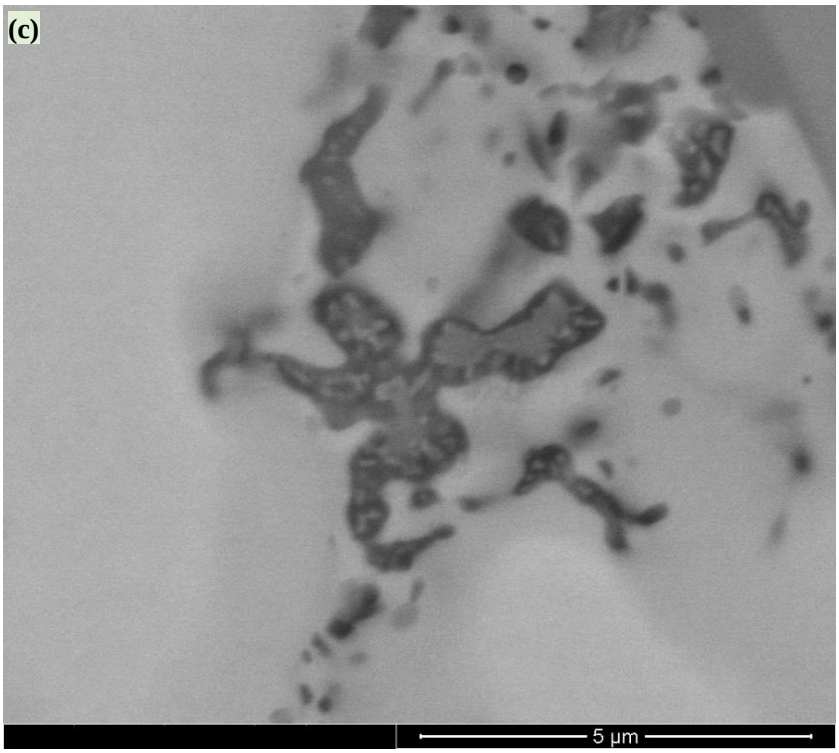


Figure 8.20 Cross section microstructure of the bulk area of the oxidised alloy ZX6 at 800 °C showing contamination of prior eutectic structure in (a) and at high magnifications in (b) and (c).

8.3.3 Microstructure of the oxidised alloys ZX5 and ZX6 at 1200 °C

The oxidised specimen of the alloy ZX5 at 1200 °C shown in Figure 8.13 indicated that the oxide scales spalled off from the substrate. It is not clear whether the spallation occurred at 1200 °C or during the cooling of the specimen to room temperature. Figure 8.21 shows the cross section microstructure of the alloy ZX5 at 1200 °C below the scale which is seen at the top of the substrate.

Sn rich feature (s) were observed in the BSE image (Figure 8.22) and the black contrast phase (s) that was found throughout the cross section of the specimen (Figures 8.21, 8.22) is believed to be Ti nitrides. The Nb_{ss} and A-15 intermetallic phases existed in the microstructure, but owing to their similar contrast they are difficult to distinguish in the images.

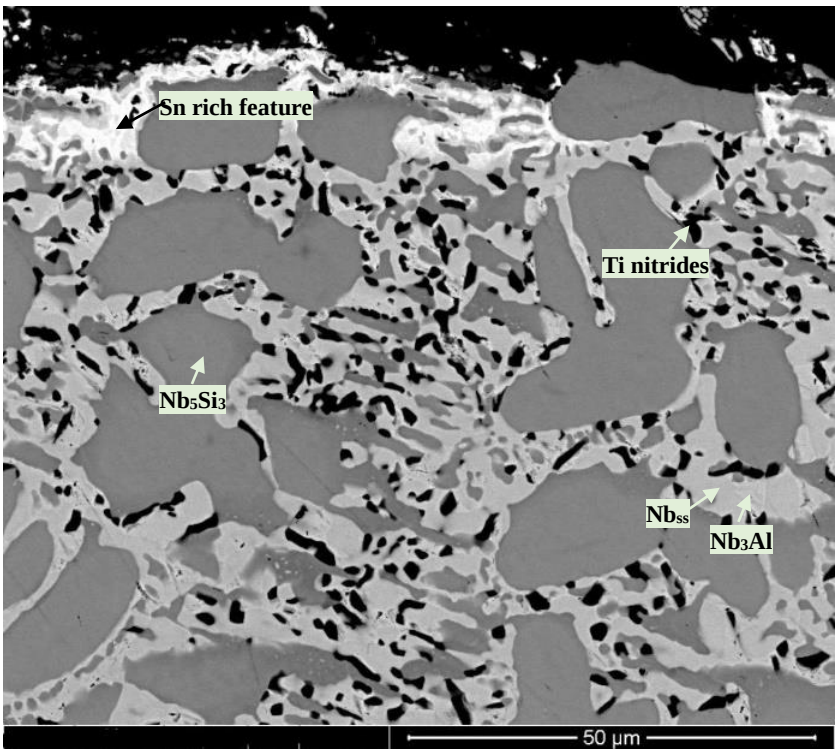


Figure 8.21 BSE image of the cross section microstructure of the oxidised alloy ZX5 at 1200°C.

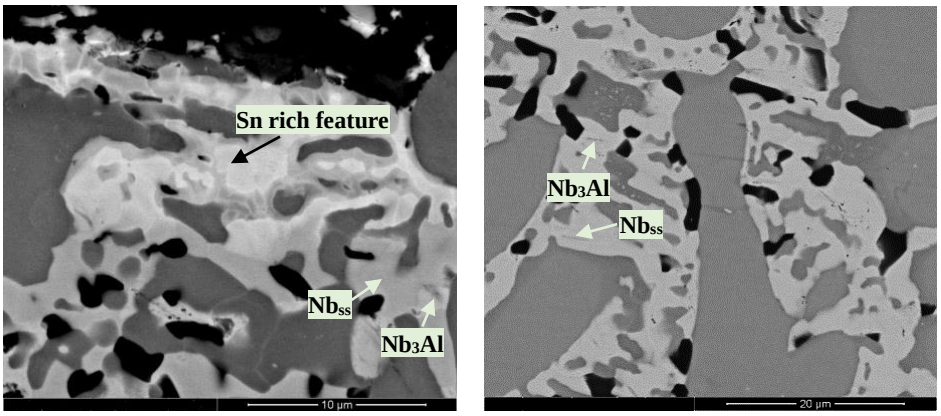


Figure 8.22 BSE image of cross section microstructure of the oxidised alloy ZX5 at 1200 °C of the Sn rich area (left), and the bulk area (right).

The bulk microstructure was studied using X-ray elemental maps to demonstrate the elemental distribution in the selected microstructure and the existence of both the Nb_3Sn and Nb_{ss} phases, see Figure 8.23. The X-ray maps for Ti and N confirmed that the dark contrast phase was rich in Ti and N. WDS analysis of the phases in the bulk of the alloy ZX5 confirmed their contamination by oxygen (see Table 8.9). The oxygen content in the Nb_{ss} phase was around 8 at. % at 1200 °C compared with 5 at. % at

800 °C. The oxygen concentrations in the Nb_5Si_3 intermetallic phase were much closer to each other in the two temperatures， i.e, ~ 4 at % at 1200 °C and ~ 3 at.% at 800 °C.

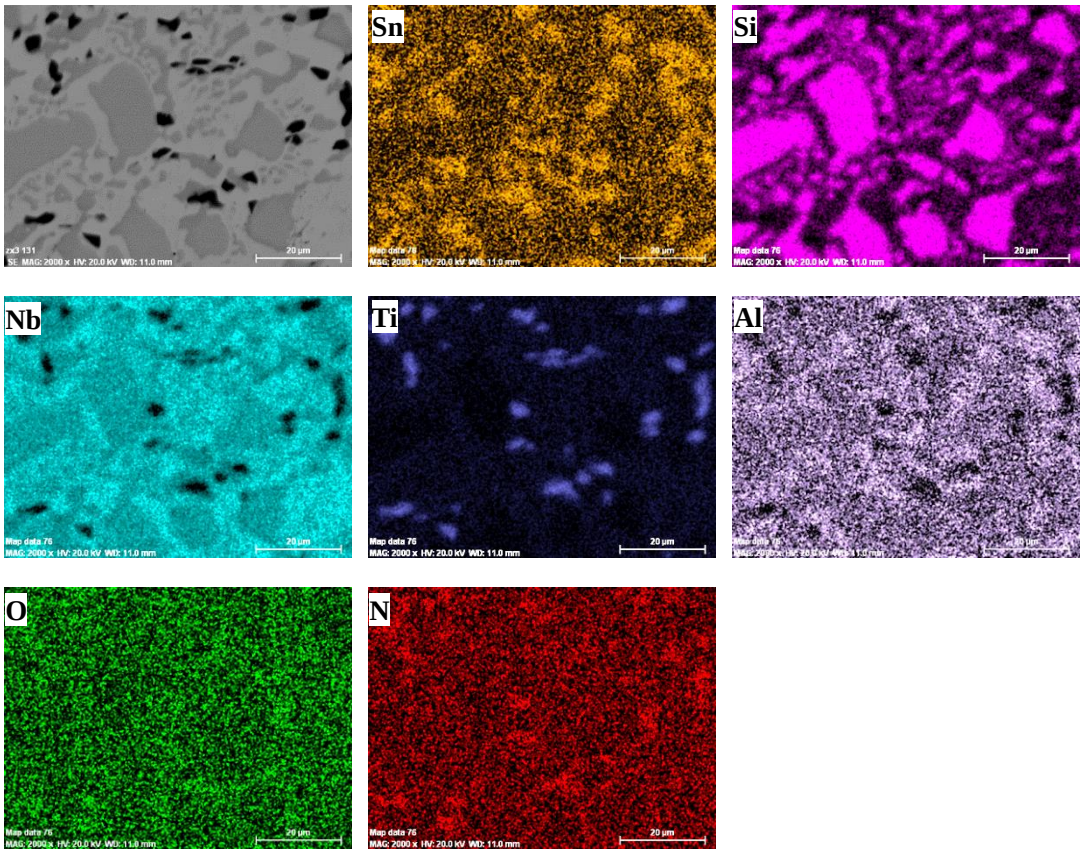


Figure 8.23 EDS X-ray elemental maps of the microstructure in the bulk area of the oxidised alloy ZX5 at 1200 °C.

Similar to the oxidised alloys ZX3 and ZX4, an Sn rich area was found in the substrate just below the scale formed on the oxidised specimen. WDS spot analyses have been applied on the features shown in Figure 8.24 and the results are summarised in Table 8.10. Apart from the Nb_5Si_3 which was not heavily contaminated by oxygen (spots 21, 22) the Sn rich intermetallics Nb_3Sn (spots 15, 16) and probably Nb_5Sn_2Si (spot 19) were present in the Sn rich area below the scale. The oxide scale of the alloy ZX5 at 1200 °C is shown in Figure 8.25. The thickness of the scale was around 300 μm. Porosity was observed close to the top surface of the scale but the microstructure was compact in the bulk of the scale. The scale was composed of oxides of different

contrast (see Figure 8.25). WDS analysis was applied on each oxide and the results in general agreed with the oxides in the scales of the alloys ZX5 and alloy ZX6 formed at 800 °C, see Table 8.11 and compare with Table 8.4.

Table 8.9 WDS analysis (at.%) of phases in the bulk of the oxidised alloy ZX5 at 1200 °C.

Phase	**Nb**	**Ti**	**Si**	**Al**	**Sn**	**O**
Nb_5Si_3	**44.23**	**14.90**	**34.63**	**1.68**	**0.56**	**4.00**
	43.76-44.59	*14.79-15.06*	*34.56-34.72*	*1.67-1.69*	*0.54-0.58*	*3.40-4.59*
Nb_3Al	**56.81**	**21.95**	**3.12**	**7.23**	**5.06**	**5.83**
	54.17-59.08	*21.13-23.70*	*2.87-3.49*	*7.06-7.53*	*4.84-5.25*	*4.48-6.96*
Nb_{ss}	**58.78**	**28.00**	**0.31**	**3.39**	**1.39**	**8.13**
	57.40-62.09	*24.96-30.19*	*0.27- 0.44*	*3.32-3.44*	*1.26-1.53*	*6.06-10.74*

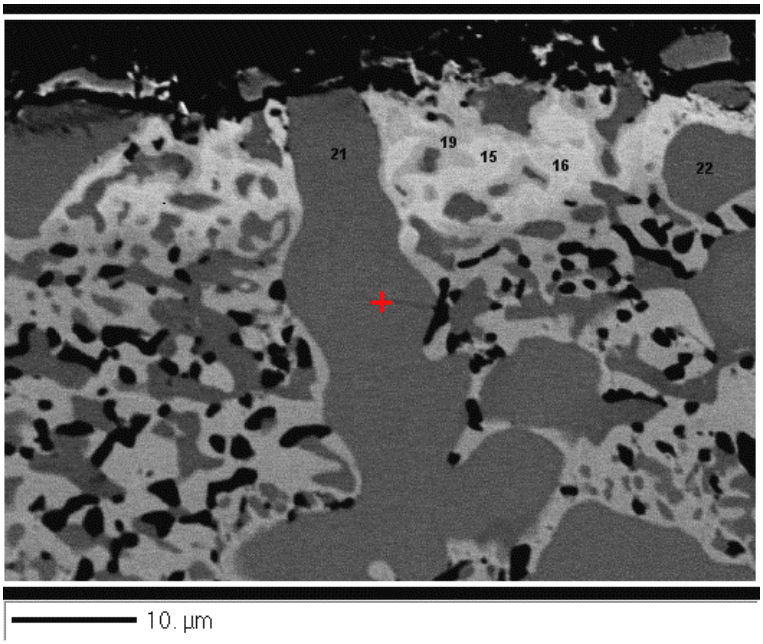


Figure 8.24 BSE image of cross section of the oxidised microstructure of the alloy ZX5. Numbers indicate WDS analysis spots.

Table 8.10 The WDS spot analysis data (at.%) of the phases labelled in Figure 8.24.

	Nb	**Ti**	**Si**	**Al**	**Sn**	**O**
Spot 15	56.59	10.71	1.38	0.68	23.21	7.43
Spot 16	58.67	9.35	1.42	0.59	23.56	6.41
Spot 19	48.97	10.73	9.73	1.74	22.36	6.47
Spot 21	39.13	19.46	33.85	2.23	2.11	3.22
Spot 22	40.08	18.51	34.37	2.36	1.63	3.06

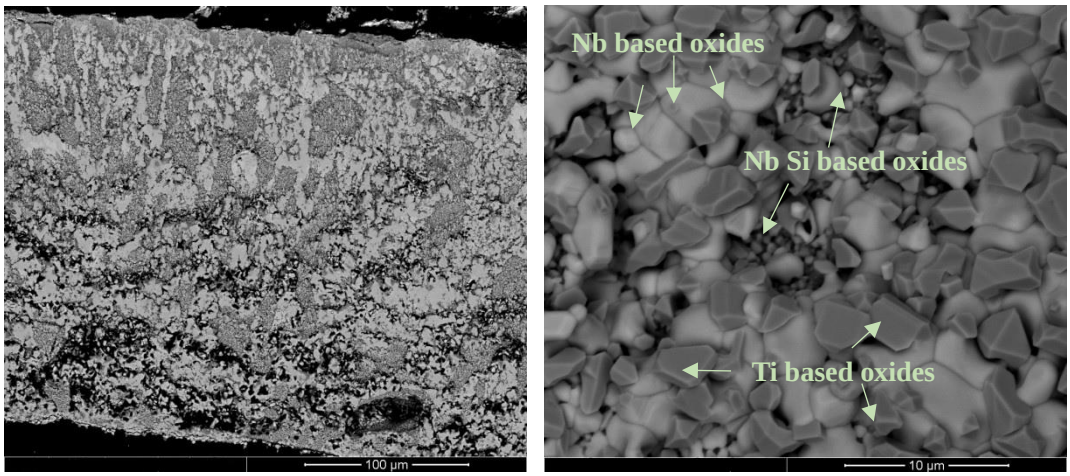


Figure 8.25 BSE image of cross section (left) and microstructure (right) of the oxide scale of the alloy ZX5 at 1200 °C.

Table 8.11 WDS analysis of the oxides in alloy ZX5 at 1200°C

	Nb	Ti	Si	Al	Sn	**O**
Nb rich oxides	20.70	9.78	0.47	1.83	0.16	**67.06**
Nb-Si rich oxides	16.26	4.87	10.83	0.52	0.15	**67.37**

The cross section microstructure of the alloy ZX6 at 1200 °C is shown in Figure 8.26. Similar to the alloy ZX5, the oxide scale spalled off. Cracks parallel to the surface were formed in the substrate just below the scale in the Nb_5Si_3 and the Sn rich area (see Figure 8.26). The Nb_5Si_3 and Nb_3Sn phases were found in the oxidised microstructure but not the Nb_{ss}. The Sn rich area was about 50 µm thick. Dark contrast Ti nitrides were present throughout the cross section microstructure apart from in the Sn rich area formed below the scale.

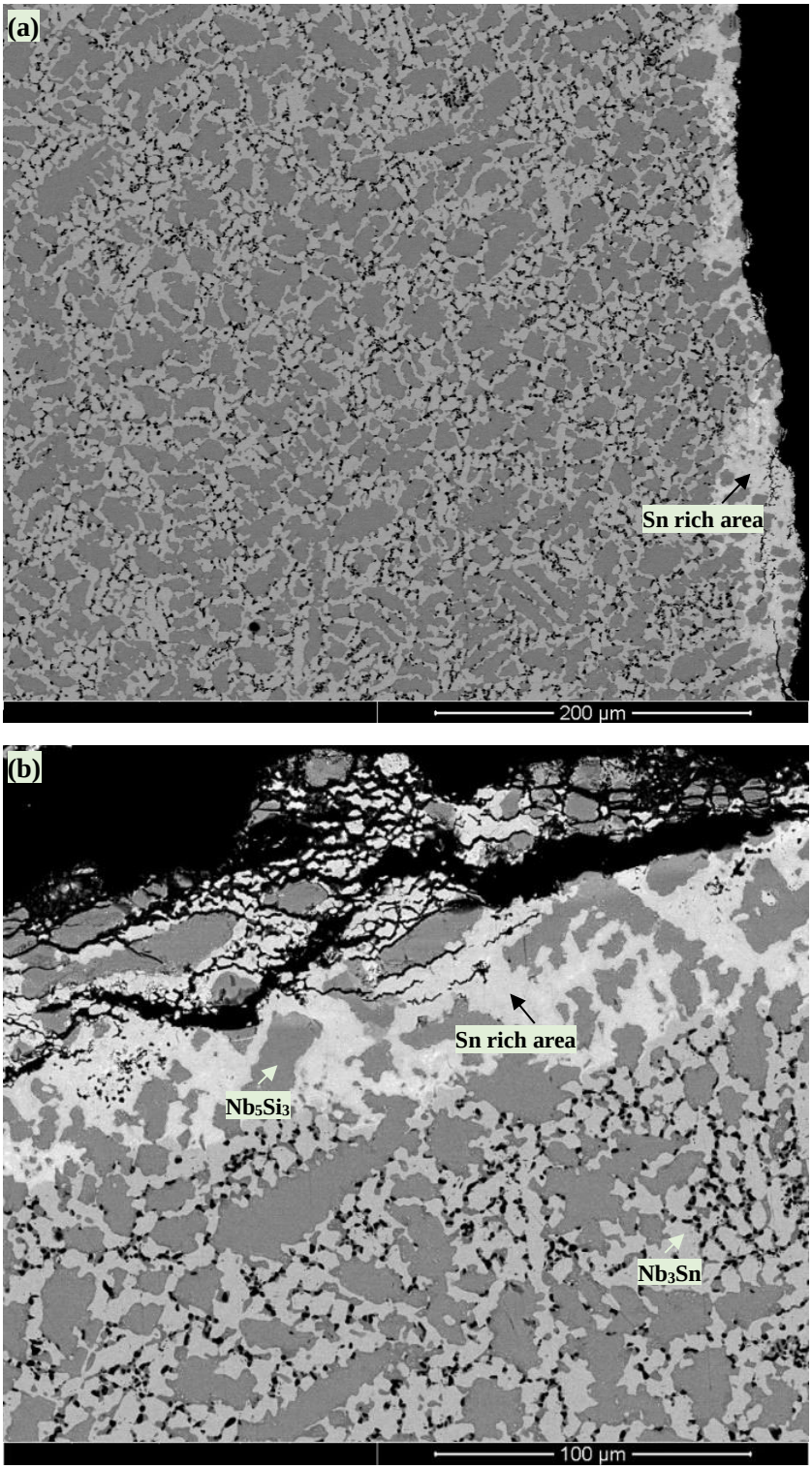


Figure 8.26 BSE images of cross section microstructures of the alloy ZX6 at 1200 °C, (a) low magnification and (b) higher magnification.

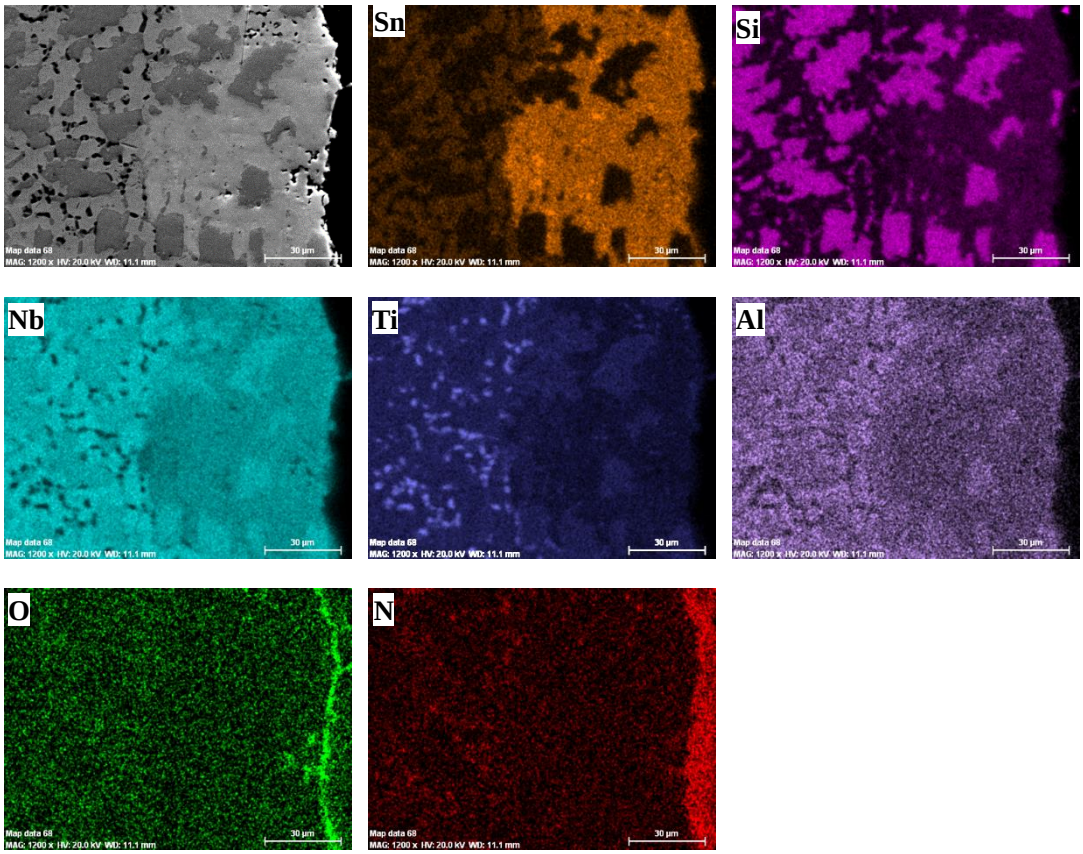


Figure 8.27 X-ray elemental maps of cross section of the oxidised alloy ZX6 at 1200 °C.

The Sn rich area was studied using EDS, X-ray elemental maps and WDS analysis. The X-ray elemental maps in Figure 8.27 show (i) Ti nitride particles below the Sn rich area but not in it, (ii) that Sn rich phase (s) were formed around Nb_5Si_3 grains, (iii) that the Al concentration in the Sn rich area is lower than below it and in the Nb_5Si_3 grains. The results of WDS analysis of the Sn rich area are summarised in Table 8.12 and the points of each analysis are shown in Figure 8.28.

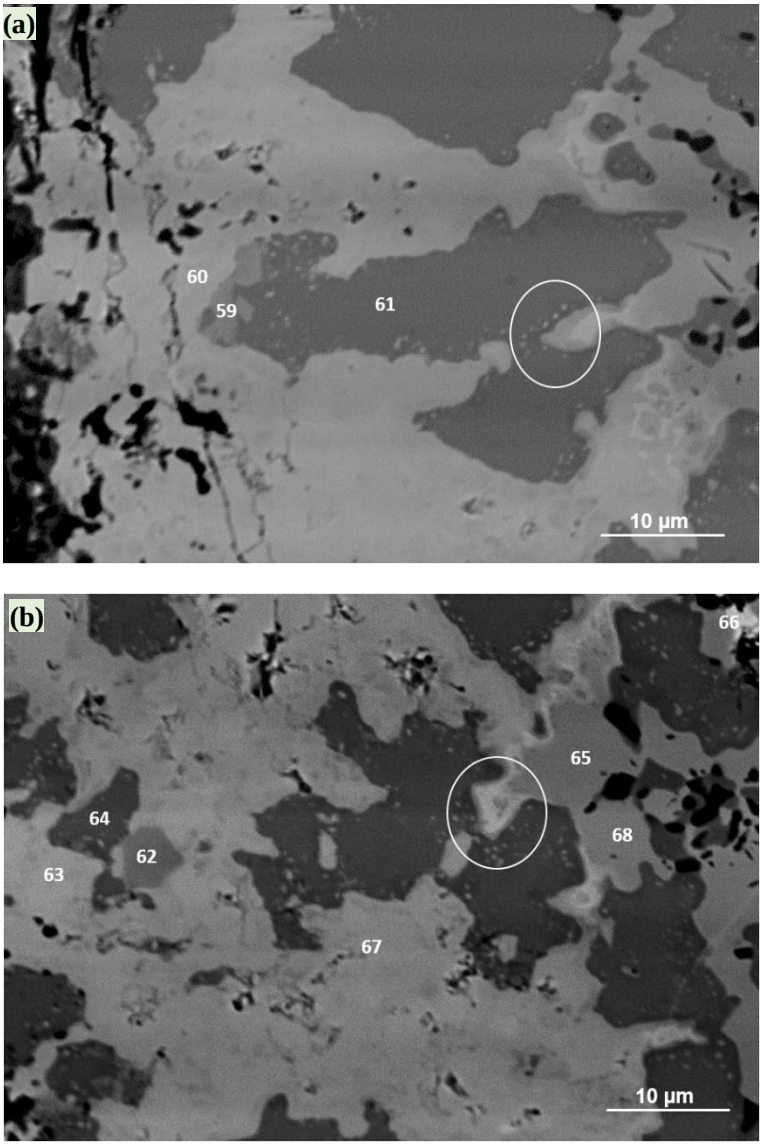


Figure 8.28 The microstructure of the Sn rich area (a) and (b) where the WDS spot analysis area labelled (the images were taken in EPMA, thus the poor resolution).

In the Sn rich area, three phases were observed using BSE imaging in EPMA, see Figure 8.28. The WDS data confirmed that all phases had been contaminated by oxygen. Spots 60, 63 and 67 were from the major phase in the Sn rich area. In the aforementioned phase, the Si + Al + Sn composition was around 35 at.%, with Sn concentrations between 21 and 24 at. %, Si from 8 to 14 at.% and Al in the range 0.6 to 1.8 at.%. The Nb_5Si_3 phase in the Sn rich area (spots 59, 61, 62, 64) had Si + Al + Sn around 37 at.%, with Si in the range 30.5 to 33 at.%, Sn in the range 1.8 to 6.7 at.%

and Al in the range 0.3 to 2 at.%. The Nb_3Sn (see spots 65, 66) was more heavily contaminated than the Nb_5Si_3. The composition of the Nb_3Sn phases adjacent to the Sn rich area (spots 65, 68) agreed with their composition in the bulk, see Table 8.13. The Nb_5Si_3 phase in the bulk contained less Sn (~ 0.6 at.%) compared with that of the silicide in the Sn rich area.

Table 8.12 The WDS analysis data (at.%) of the phases in the Sn rich area of the alloy ZX6 at 1200 ℃.

Nb_5Si_3	Nb	Ti	Si	Al	Sn	O
Spot 59	48.41	9.50	30.48	0.30	6.73	4.58
Spot 61	42.74	15.96	32.91	1.87	3.13	3.39
Spot 62	50.28	8.21	30.93	0.16	6.18	4.24
Spot 64	43.03	15.84	33.24	1.88	1.80	4.21
Nb_5Sn_2Si	Nb	Ti	Si	Al	Sn	O
Spot 60	46.87	10.85	13.58	0.61	21.17	6.92
Spot 63	50.40	8.86	10.94	1.22	22.84	5.74
Spot 67	45.08	13.47	8.44	1.81	24.43	6.77
A-15 Nb_3Sn	Nb	Ti	Si	Al	Sn	O
Spot 65	54.14	21.50	3.33	5.42	8.58	7.03
Spot 66	56.40	11.91	0.95	1.68	21.86	7.20
Spot 68	55.70	21.48	3.03	6.12	8.68	4.99

Table 8.13 The WDS analysis data (at.%) of phases in the bulk area of the alloy ZX6 at 1200 ℃.

Phase	Nb	Ti	Si	Al	Sn	O
Nb_5Si_3	**43.14**	**15.57**	**33.90**	**1.52**	**1.40**	**4.47**
	42.72-43.52	*15.42-15.74*	*33.66-34.19*	*1.45-1.59*	*1.37-1.41*	*3.73-5.18*
Nb_3Sn	**54.34**	**23.49**	**3.05**	**5.00**	**8.55**	**5.57**
	53.33-55.29	*22.84-24.21*	*2.73-3.22*	*4.46-5.38*	*8.19-8.91*	*4.87-7.01*

The oxides in the scale formed on the alloy ZX6 after oxidation at 1200 °C were analysed using WDS, see Table 8.14. BSE imaging of the microstructure showed that three oxides were formed during oxidation (Figure 8.29). The coarse oxide grains were identified as Nb rich and Ti rich oxides. The cross section microstructure also showed voids and porosity in the oxides. The other oxide was more compact and was Nb-Si rich. The compositions of the Nb and Nb-Si rich oxides were similar to those formed

on the alloy ZX5 at 1200 °C, see Table 8.11.

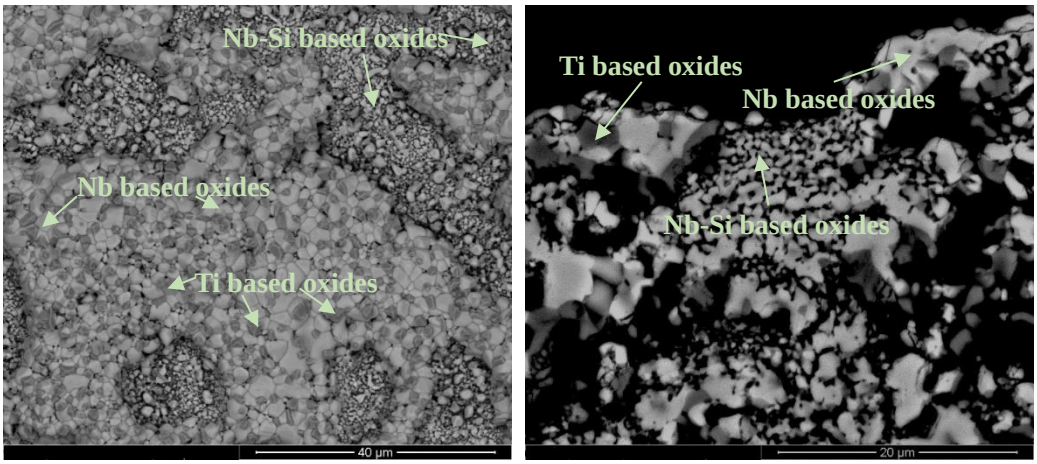


Figure 8.29 BSE images of the scale formed on the alloy ZX6 at 1200 °C, showing topology (left) and cross section microstructure (right).

Table 8.14 The WDS analysis of the oxides of the alloy ZX6 at 1200°C.

	Nb	Ti	Si	Al	Sn	O
Nb rich oxides	24.26	7.99	0.04	1.20	0.00	66.51
Nb rich oxides	24.34	7.64	0.04	1.33	0.00	66.65
Ti rich oxides	6.28	20.29	0.26	5.48	0.10	67.59
Ti rich oxides	6.86	21.93	0.02	5.52	0.02	65.65
Nb-Si rich oxides	13.85	5.85	14.83	0.49	0.00	64.98
Nb-Si rich oxides	15.56	5.43	12.27	0.47	0.01	66.26

8.4 Discussion

8.4.1 Macrosegregation of Si

In the previous chapter the definition of macrosegregation was given as $C_{max}^{i} - C_{min}^{i}$ i.e., as the difference between the maximum and minimum concentrations of the element in the alloy. Macrosegregation of an element is considered to occur when MACS = $C_{max}^{i} - C_{min}^{i} > 2$ at.%. In the cast ingot buttons of the alloys ZX5 and ZX6 there was macrosegregation of Si and Ti. In the alloy ZX6 the macrosegregation of Ti was more severe compared with that of Si. How macrosegregation occurs in cast Nb silicide based alloys has been discussed in [78] where the macrosegregation of Si was linked with the partitioning of other solutes between the key phases in the microstructures of Nb silicide based alloys. Sn is one of the alloying additions that have a strong effect on the macrosegregation of Si [78].

There was also strong partitioning of Ti between phases in the microstructure of both alloys. For Ti the highest $C_{max}^{i} - C_{min}^{i}$ difference was between the top or bulk and bottom of the ingots, i.e., areas where the melt had experienced the highest and lowest cooling rates, respectively.

In [78] the ranking of alloys in terms of increasing Si macrosegregation indicated that the latter tended to increase in Nb silicide based alloys when the parameters $\Delta H_m/T_m$ ("alloy entropy of fusion"), T_m^{sp} (melting temperature of sp electronic configuration elements) and $[\Delta H_m/T_m][\Delta H_m^{sd}/\Delta H_m^{sp}]^{-1}$ increased and the ratios $\Delta H_m^{sd}/\Delta H_m^{sp}$ and T_m^{sd}/ T_m^{sp} and the parameters ΔH_m ("alloy enthalpy of melting"), T_m (alloy melting temperature) and T_m^{sd} (melting temperature of the sd electronic configuration elements) decreased.

In the case of the alloys ZX5 and ZX6 the macrosegregation of Si was essentially the same considering the error for Si analysis in EDS. This makes it difficult to "rank" the

two alloys using the aforementioned parameters. It was decided to assume that the trends reported in [78] and established in the previous chapter for the macrosegretation of Si in the alloys ZX3 and ZX4 (see Table 7.12) apply also in the case of the alloys ZX5 and ZX6 and to compare these two alloys with the alloy Nb-26Ti-16.3Si-5.2Al (alloy KZ7 in [68]). Thus, the Table 8.15 was produced where the aforementioned parameters of the alloys ZX5 and ZX6 are given and the alloy KZ7 is included for comparison purposes. The ranking of the alloys in Table 8.15 shows that the trends shown by the alloys ZX3 and ZX4 are followed by the alloys ZX5 and ZX6, and that when the latter are compared with the alloy KZ7 there are trends for all the paremeters excluding the parameter ΔH_m. The reason why the trend in the latter parameter is not as expected from [78] could be the fact that different phases were present in the three cast alloys (no Nb_3Sn was present in ZX5 and KZ7).

Table 8.15 Alloy parameters for the macrosegregation of Si in the cast alloys ZX5 and ZX6.

alloy	ΔH_m kJ/mol	T_m (K)	$\Delta H_m/T_m$ J/molK	$\Delta H_m^{sd}/\Delta H_m^{sp}$	T_m^{sd} (K)	T_m^{sp} (K)	T_m^{sd}/T_m^{sp}	$[\Delta H_m/T_m]\times[\Delta H_m^{sd}/\Delta H_m^{sp}]^{-1}$	MACS at.%
ZX6	**27.31**	**2148**	**12.71**	**1.69**	**1765**	**383**	**4.61**	**7.52**	5.5
ZX5	**28.1**	**2215**	**12.68**	**1.74**	**1837**	**377**	**4.87**	**7.29**	5.5
KZ7	27.7	**2272**	**12.19**	**2.15**	**1948**	**324**	**6**	**5.67**	2.3

The macrosegregation in the alloy ZX6 was compared with the alloys NV9 (Nb-19Si-4.2Sn) and NV6 (Nb-25.5Ti-18.1Si-4.9Sn) [56] that have the same phases, namely Nb_{ss}, Nb_5Si_3 and Nb_3Sn. Given that the Si macrosegregation in the alloys NV6 and ZX6 is essentially the same (considering the error in Si analysis in EDS), the same criterion for the "ranking" of the alloys NV6 and NV9 as above was adopted. The data in Table 8.16 shows that the trends in the studied parameters reported in [78] are obeyed with the exception of the parameter T_m^{sp}. It should be noted that the same was the case for the alloys ZX4, NV6 and NV9, see Table 7.13.

Table 8.16 Alloy parameters linked with macrosegregation of Si in the cast alloys ZX6, NV6 and NV9.

alloy	ΔH_m kJ/mol	T_m (K)	$\Delta H_m/T_m$ J/molK	$\Delta H_m^{sd}/\Delta H_m^{sp}$	T_m^{sd} (K)	T_m^{sp} (K)	T_m^{sd}/T_m^{sp}	$[\Delta H_m/T_m]\times[\Delta H_m^{sd}/\Delta H_m^{sp}]^{-1}$	MACS at.%
ZX6	**27.31**	**2148**	**12.71**	**1.69**	**1765**	383	**4.61**	**7.52**	5.5
NV6	**28**	**2241**	**12.49**	**1.98**	**1911**	330	**5.79**	**6.31**	5.5
NV9	**30.4**	**2454**	**12.39**	**2.1**	**2112**	342	**6.18**	**5.9**	2.5

8.4.2 Phase stability in the alloy Nb-24Ti-18Si-5Al-2Sn (ZX5)

The actual composition of the alloy makes it a hyper-eutectic alloy considering its Si or Si + Al + Sn contents (respectively 19.1 and 25.8 at.%) and the Nb-Si binary. As the βNb_5Si_3 formed from the melt (primary phase) the surrounding melt became richer in Ti, Al and Sn and poorer in Si. There were some differences in the Ti content of the melt owing to the partitioning of Ti in Nb_5Si_3. In the melt surrounding the βNb_5Si_3 the Nb_{ss} formed making the surrounding melt richer in Si and poorer in Al, Sn and Ti. There were some differences in the Ti content of the melt owing to the partitioning of Ti in Nb_{ss}. Nb_{ss} haloes formed on the βNb_5Si_3, see h in Figure 8.2. In the areas of the melt surrounding the primary βNb_5Si_3 and the Nb_{ss} the melt reached the composition where the Nb_{ss} + βNb_5Si_3 eutectic could form with Si + Sn + Al = 19.8 at.%. The latter is as expected for the composition of the aforementioned metastable eutectic in the Nb-Si binary.

The formation of βNb_5Si_3 in the cast alloy ZX5 (according to the XRD data there were no peaks of the αNb_5Si_3, Figure 8.3), the XRD data for the alloy KZ7, which showed only βNb_5Si_3 in the cast microstructure, and the data for the alloy NV9 and the ternary alloys of this thesis provides further support to the conclusion of Zelenitsas and Tsakiropoulos [68] that Al stabilises the βNb_5Si_3 during solidification and would suggest that Al in synergy with Sn in Nb silicide based alloys increases the sluggishness of the $\beta Nb_5Si_3 \rightarrow \alpha Nb_5Si_3$ transformation during solidification.

It is suggested that the solidification path in all parts of the cast alloy ZX5 was L → L + βNb_5Si_3 → L + βNb_5Si_3 + Nb_{ss} → βNb_5Si_3 + Nb_{ss} + (Nb_{ss} + βNb_5Si_3) $_{eutectic}$. Nb_{ss} haloes formed owing to competitive growth of the Nb_{ss} and βNb_5Si_3 phases from melt of eutectic composition. The slight differences in the microstructures observed in the top, bulk and bottom of the ingot button are attributed to the different Si + Al + Sn contents of these areas (respectively 26.7, 26.4 and 24.1 at.%).

The Si + Sn content in the Nb_{ss} (5.2 at.%) is in agreement with data for other Sn containing Nb silicide based alloys. The solid solubility of Al in Nb_{ss} is reported to increase with that of Ti (as does that of Cr [68, 89] but this effect was not noticed in the cast alloy ZX5, which could be taken to suggest that the presence of Sn in the alloy does have an effect on the solid solubility of Al in the Nb_{ss}). This however is suggested to be a "dangerous" conclusion as the data for the Nb_{ss} in the heat treated alloy confirmed the increase of the solid solubility of Al with Ti content.

After the heat treatment the actual composition of the heat treated specimen was still not close to the nominal alloy composition but was closer to the average composition of the top and bulk areas of the cast alloy. The βNb_5Si_3 → αNb_5Si_3 transformation had been completed. This together with the data for the alloy KZ7 and the data for the alloy NV9 and the ternary alloys of this thesis would suggest that the synergy of Al and Sn in Nb silicide based alloys enhances the above transformation during heat treatment. The A-15 intermetallic was stable in the microstructure. Al like Sn can form the A-15 Nb_3Al phase, thus it is expected that Al will enhance the stability of the A-15 structure intermetallic phase.

The heat treated alloy can be considered in the 1500 °C isothermal section proposed by Pan *et al* [49] either by considering Sn and Al as equivalent or Si and Sn as equivalent. In the former case the alloy lies in the three phase field Nb_{ss} – αNb_5Si_3 –

A-15 Nb_3Al and in the latter case it still lies in the aforementioned three phase field but close to the phase boundary separating this field from the two phase Nb_{ss} - αNb_5Si_3 phase field, see Figure 8.30.

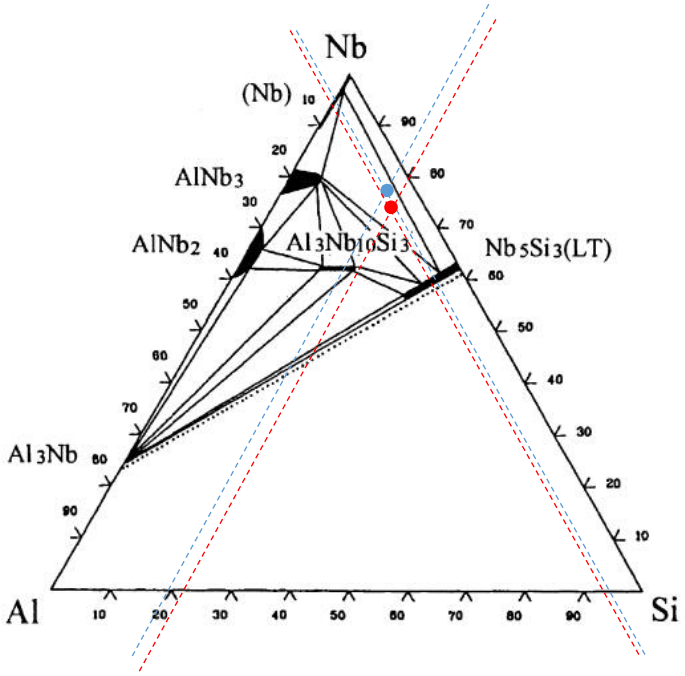


Figure 8.30 The partial iso-thermal sessions of the Nb- Si- Al ternary phases at 1500°C (blue dot indicate the composition alloy Nb-18Si-5Al, red dot indicate the composition of heat treated ZX6) [49]

The Si content of the Nb_{ss} was in agreement with the data for other heat treated Nb silicide based alloys and with alloy KZ7 and had Si + Sn = 2.6 at.%, lower than the cast alloy. In the A-15 phase the Si + Sn + Al content was 18.7 at.%, in agreement with [71]. The microstructure of the heat treated alloy showed evidence of contamination of the Nb_{ss} but not of the A-15 phase, see Figure 8.4. This suggested that the synergy of Al, Sn and Ti was not good enough to stop contamination of the bulk during heat treatment in argon atmosphere.

8.4.3 Phase stability in the alloy Nb-24Ti-18Si-5Al-5Sn (ZX6)

The actual composition of the alloy makes it a hyper-eutectic alloy considering its Si

+ Al + Sn content (28.4 at.%) and the Nb-Si binary. The average Si concentration in the bottom of the ingot button was lower than the "accepted" eutectic composition in the Nb-Si binary [27]. Furthermore, the lower values of Si concentration in the Si content ranges observed in the bottom and bulk of the alloy were also lower than the "accepted" eutectic composition in the Nb-Si binary.

In the top and bulk of the alloy ZX6, as the βNb_5Si_3 formed from the melt (primary phase) the surrounding melt became richer in Ti, Al and Sn and poorer in Si. There were some differences in the Ti content of the melt owing to the partitioning of Ti in Nb_5Si_3. In the melt surrounding the βNb_5Si_3 the Nb_3Sn formed making the surrounding melt richer in Si and poorer in Al, Sn and Ti. There were some differences in the Ti content of the melt owing to the partitioning of Ti in Nb_{ss}. In the areas of the melt surrounding the primary βNb_5Si_3 and the Nb_3Sn, the melt reached the composition where the Nb_{ss} + βNb_5Si_3 eutectic could form.

As was the case in the alloy ZX5, the formation of βNb_5Si_3 in the cast alloy ZX6 (Figure 8.9), the XRD data for the alloy KZ7 [68], which showed only βNb_5Si_3 in the cast microstructure, and the data for the alloy NV9 [56] and the ternary alloys of this thesis, all provide further support to the conclusion of Zelenitsas and Tsakiropoulos [68] that Al stabilises the βNb_5Si_3 during solidification and would suggest that Al in synergy even with higher Sn content in Nb silicide based alloys increases the sluggishness of the $\beta Nb_5Si_3 \rightarrow \alpha Nb_5Si_3$ transformation during solidification.

It is suggested that the solidification path in the bulk and top of the cast alloy ZX6 was $L \rightarrow L + \beta Nb_5Si_3 \rightarrow L + \beta Nb_5Si_3 + Nb_3Sn \rightarrow \beta Nb_5Si_3 + Nb_3Sn + (Nb_{ss} + \beta Nb_5Si_3)_{eutectic}$.

The microstructure formed from the melt that solidified next to the water cooled crucible (microstructure formed from highly undercooled melt) was different, see

Figure 8.8. An area about 50 µm thick (we shall call this area A) was formed first and consisted of Nb_{ss} and Nb_5Si_3 with some Ti rich Nb_5Si_3 (circle in Figure 8.8) forming away from the side that was in contact with the water cooled crucible (shown with dotted line in Figure 8.8a) and before the transition to an area consisting mainly of Nb_3Sn and Nb_5Si_3, which is indicated by the dashed line in Figure 8.8 (we shall call the latter area B). It is suggested that the formation of these two areas can be linked with the strong macrosegregation of Si and Ti in the alloy ZX6.

From the area B evolved the bulk microstructure shown in Figure 8.7. There was no normal eutectic (i.e., like the eutectic observed in the bulk and top of the cast ZX6) in the area A and also in the area B close to the Nb_{ss} layer forming the interface separating the two areas (Figure 8.8). Consider the different entropies of fusion of the Nb_{ss}, Nb_3Sn and Nb_5Si_3. The entropies of fusion of the Nb, Nb_3Sn and Nb_5Si_3 respectively are 9.45, 11.6 and 14.55 J/molK, meaning that the 5-3 silicide has the "greater difficulty for growth" (or needs more kinetic undercooling) than the Nb_3Sn and the Nb_{ss}. In the alloy ZX6 three phases can form, namely the Nb_{ss}, Nb_5Si_3 and Nb_3Sn. In area A the latter was not observed. Considering the highest interface temperature criterion (see Figure 6.23), the formation of Nb_{ss} instead of Nb_3Sn would require the melt that solidified in area A to be poorer in Si + Al + Sn compared with that in area B. We suggest that this was the case owing to the strong macrosegregation in the alloy ZX6 (see above).

After nucleation of the Nb_{ss} and Nb_5Si_3 on the crucible wall from the highly undercooled melt (notice the larger patches of Nb_{ss} (small arrows in Figure 8.8a) and the comparatively smaller patches of Nb_5Si_3 formed next to the crucible wall) the Nb_{ss} grew faster than (i.e., outgrew) the Nb_5Si_3 in area A. As the Nb_{ss} grew, the surrounding melt became rich in Si and poor in Ti, Al and Sn. As the Nb_5Si_3 grew the surrounding melt became poor in Si and rich in Al, Sn and Ti. In some parts of area A the melt became very rich in Ti and Si and some Ti rich Nb_5Si_3 formed in these parts of area A

from the very Ti rich melt (circle in Figure 8.8).

As the macroscopic S/L interface advanced towards the interface with area B (and the melt undercooling ΔT decreased) and solutes partitioned between the Nb_{ss}, Nb_5Si_3 and the melt, the latter became rich in Ti and poor in Si ahead of Nb_5Si_3 (rectangle in Figure 8.8b) and a continuous Nb_{ss} layer formed from this melt (Figure 8.8). After some growth of the Nb_{ss} in the aforementioned continuous layer the Nb_5Si_3 started to form (small patches of Nb_5Si_3 are indicated by arrows in Figure 8.8b). Ahead of this macroscopic interface (forming the boundary between areas A and B) that consisted mainly of Nb_{ss} with some Nb_5Si_3, the melt became richer in Si + Al + Sn (it is suggested that this was possible because (i) of solidification conditions in area A and (ii) the strong macrosegregation in ZX6) and in this melt growth of Nb_3Sn instead of Nb_{ss} became possible (highest interface temperature criterion). The Nb_3Sn grew faster than the Nb_5Si_3 owing to its lower entropy of fusion (see above). As the Nb_3Sn grew the surrounding melt became richer in Si and poorer in Sn, as the Nb_5Si_3 grew the surrounding melt became richer in Ti, Al and Sn, there was also partitioning of Ti in the Nb_5Si_3 (see Figure 8.8a), (meaning the melt near the Ti rich Nb_5Si_3 became poorer in Ti compared with the melt near the "normal" Nb_5Si_3) and after some distance from the macroscopic interface, formation of some Nb_{ss} was possible, see Figure 8.8. The above could explain why the volume fraction of Nb_{ss} in the bottom of ZX6 was lower compared with the bulk and top.

After the heat treatment the composition of the heat treated specimen was closer to the nominal composition compared with the cast alloy. Two phases were observed, namely the αNb_5Si_3 and the A-15Nb_3Sn and there were still Ti rich areas in the 5-3 silicide. In other words, in the heat treated microstructure the Nb_{ss} was not stable, which would suggest that the synergy of Sn with Al and Ti in the alloy ZX6 had destabilised the Nb_{ss}. The two phase microstructure is in agreement with the 1400 °C and 1500 °C

isothermal sections of the Nb-Si-Al system proposed by Brukl *et al* [48] and Pan *et al* [49] if in the composition of the heat treated alloy in Table 8.2 the Al and Sn are considered as equivalent, but not if the Si and Sn are considered as equivalent, see Figure 8.30. Given the important role that Nb_{ss} plays in oxidation (The Nb_{ss} is the Achilles heel if present at high volume fraction and forms a continuous network), toughness (desirable for ductile phase toughening) and high temperature strength, the results for the alloy ZX6 show a possible way for controlling the Nb_{ss} in the microstructure of Nb silicide based alloys.

8.4.4 Oxidation of the alloys ZX5 and ZX6 at 800 °C

At 800 °C the oxidation of the alloy ZX5 followed parabolic and linear oxidation kinetics (Table 8.3). The former alloy formed dark grey scale that was rough and porous compared with the smoother more compact lighter colour (bluish) scale on ZX6 (Figure 8.12). In both alloys (i) diffusion zones (DZ) formed below the scales, in agreement with other Nb silicide based alloys [90], and the DZ and scale thicknesses were 50 and 30 μm and 10-15 and 10 μm, respectively in the alloys ZX5 and ZX6, (ii) the Nb_{ss} was contaminated with oxygen more severely than the Nb_5Si_3 in the DZ, see Figure 8.17b and Table 8.5, and there was contamination of both phases with oxygen in the bulk, see Tables 8.6 to 8.8 and Figures 8.18a and 8.20b and c, (iii) there were cracks in the Nb_5Si_3 that were parallel to the substrate/scale interface, see Figures 8.17b and 8.18a and (iv) Sn rich areas were formed at the substrate/scale interface, the extent of the former being greater in the alloy ZX6, see Figures 8.17 and 8.18.

In the alloy ZX5 the Si + Al + Sn and Ti contents and the (Si + Al + Sn)/O_2 ratio of the Nb_5Si_3 were the same as in the bulk (respectively, 37.3 at.%, and 15 at.% and 12.6) with slightly higher Ti concentration in the Nb_5Si_3 in the prior eutectic microstructure, probably owing to overlap of analysis area with the Nb_{ss} in the two phase microstructure, see Tables 8.5 and 8.6.

The same oxides were observed in the scales formed on the alloys ZX5 and ZX6, see Tables 8.4 and 8.7. One oxide type was rich in Nb + Ti and lean in Si and Si + Al + Sn and the other was leaner in Nb + Ti and richer in Si and Si + Al + Sn. In the alloy ZX5 the former oxide had [Nb + Ti]/[Si + Al + Sn] = 28.6/4.5 = 6.3 and Nb/Ti = 2.4 and in the latter these ratios were 20.44/13.5 = 1.5 and 3.14. In the alloy ZX6 the former oxide had [Nb + Ti]/[Si + Al + Sn] = 28.3/4.15 = 6.8 and Nb/Ti = 1.6 and in the latter these ratios were 22.7/11.02 = 2.06 and 2.

In the DZ formed in the alloy ZX6 the Nb_5Si_3 had essentially the same average Si + Al + Sn content (38.1 at.%) as in the ZX5 (37.3 at.%) and slightly higher (Si + Al + Sn)/O_2 ratio (15.9 vs 12.6) owing to its higher Ti content (16.5 vs 15 at.%), see Table 8.7. Furthermore, in the alloy ZX6 the composition of the Nb_5Si_3 in the DZ was the same as in the bulk (Tables 8.7 and 8.8) with Si + Al + Sn = 37.9 at.% and (Si + Al + Sn)/O_2 = 15 in the latter.

The Sn rich area formed at the substrate/scale interface in the alloy ZX6 could be studied using WDS owing to its extent and was found to consist of Nb_3Sn with 0.19 < Si/Sn < 0.33, 26.2 at.% < (Si + Al + Sn) < 30.3 at.% and average oxygen content 26.4 at.%, compared with Si/Sn = 0.6, Si + Al + Sn = 18.2 at.% (owing to lower Sn content compared with the Nb_3Sn formed at the interface) and oxygen concentration 6.3 at.% in the DZ, Table 8.7. In the bulk, the Nb_3Sn was also contaminated with oxygen and had Si/Sn = 0.6, Si + Al + Sn = 17.6 at.% (similar Sn content as in DZ) and oxygen concentration 6.9 at.%, Table 8.8. The data would suggest that the formation of Sn rich area was accompanied by consumption of Ti and Nb in the scale formation (see above about composition of oxides in scale) and this was the reason that the Nb_3Sn at the interface had lower Si/Sn and higher Si + Al + Sn compared with DZ and bulk. Figure 8.18 shows formation of Sn rich areas linked with the Nb_3Sn, the difference in contrast indicative of the higher Sn content of the Nb_3Sn in the Sn rich area.

The eutectic areas in the DZ in ZX6 were more heavily contaminated compared with the bulk (Tables 8.7 and 8.8) owing to the more severe contamination of the Nb_{ss} by oxygen compared with the Nb_5Si_3 (we do not have any actual analysis data for the Nb_{ss} in the ZX6 oxidised at 800 °C owing to the size of the solid solution phase, thus this statement is (we believe) justified form our knowledge about the Nb_{ss} in the alloys ZX3 and ZX4 and data in the literature). In both areas (i.e., DZ and bulk) the Si + Al + Sn content of the eutectic was essentially the same but in the DZ the Nb and Ti content were lower compared with those in the bulk but the Nb/Ti ratio was essentially the same (1.11 vs 1.14), which would suggest that the consumption of Nb and Ti from the eutectic areas for the formation of the scale was comparable.

8.4.5 Oxidation of the alloys ZX5 and ZX6 at 1200°C

The alloy ZX5 followed parabolic and linear oxidation kinetics while the alloy ZX6 followed linear oxidation kinetic (Table 8.3) and their scales spalled off, Figure 8.13. The scales on both alloys were compact and yellow in colour, the scale formed on ZX5 spalled off easier than that on ZX6. The scale formed on the alloy ZX5, which was at least 300 µm thick, had porosity towards the top surface and was more compact closer to the substrate.

Sn rich areas formed in both alloys at the scale/substrate interface, with thickness 10 µm and 50 µm respectively in ZX5 and ZX6, see Figures 8.21, 8.22, 8.24, and 8.26 to 8.28. Furthermore, both alloys were contaminated with nitrogen that formed Ti nitride particles, see Figures 8.21 to 8.24 and 8.26, 8.27. There was contamination of the Nb_{ss} and Nb_5Si_3 in the bulk of both alloys. In the alloy ZX5 the oxygen content of the Nb_{ss} in the bulk was 60 at.% higher than that at 800 °C and in the case of Nb_5Si_3 it was 33 at.% higher, see Tables 8.6 and 8.9.

In the Sn rich area formed in the alloy ZX5 the Nb_3Sn was observed with Si + Al + Sn = 25.45 at.%, Si/Sn = 0.06 and (Si + Al + Sn)/O_2 = 25.45/6.9 = 3.7 (Table 8.10), compared with same average Si + Al + Sn and average (Si + Al + Sn)/O_2 = 24.83/26.42 = 0.94 and Si/Sn = 0.22 for ZX6 at 800 °C (Table 8.7). In other words, the Nb_3Sn in the Sn rich layer in ZX5 at 1200 °C was less contaminated than the Nb_3Sn in ZX6 at 800 °C. This could be attributed to its lower Si/Sn ratio.

The Nb_3Sn observed in the Sn rich area of the alloy ZX5 was poorer in Al, Si and Ti and richer in Sn compared with the bulk of the oxidised specimen where the Nb_3Sn had Si + Al + Sn = 15.4 at.%, Si/Sn = 0.6 and (Si + Al + Sn)/O_2 = 2.6 (Table 8.9). These values are comparable with those in the Nb_3Sn in the bulk of ZX6 oxidised at 800 °C (17.6 at.%, 0.55 and 2.6, respectively) where the Nb_3Sn had the same Ti content. Thus, the alloy ZX5, with less Sn content than ZX6, at 1200 °C formed the Nb_3Sn in its bulk with composition similar to that in the alloy ZX6 at 800 °C but with significantly lower oxygen content in the Nb_3Sn in the Sn rich area compared with the same phase in the ZX6 at 800 °C. It should be noted that in the bulk of the alloy ZX5 that was heat treated at 1500 °C the Nb_3Sn had (Si + Al + Sn)/O_2 = 2.6 with Si + Al + Sn = 18.75 at.% and Si/Sn = 0.9 (Table 8.1). Furthermore, in the Sn rich area of ZX5 the Nb_5Si_3 was slightly richer in Al, Sn and Ti compared with the bulk (Tables 8.9, 8.10) and with similar oxygen concentration.

The above data would suggest (i) that the nature of the scale in the alloy ZX5 and (ii) other phase(s) in the Sn rich area in the alloy ZX5 had contributed in the significantly lower oxygen contamination of Nb_3Sn in the Sn rich area at 1200 °C. As we shall discuss below, the oxides formed in the scale of the alloy ZX5 at 1200 °C were the same as those formed on the alloys ZX5 and ZX6 at 800 °C (which makes (i) unlikely) but there was formation of Nb_5Sn_2Si in the Sn rich area in ZX5, which would suggest that this intermetallic plays an important role.

In the Sn rich area of the alloy ZX5 the Nb_5Sn_2Si was formed (Table 8.10, spot analysis 19) with (Si + Al + Sn)/O_2 = 5.23. This intermetallic was not observed in the oxidised specimens at 800 °C (but as we shall see below, it was observed in the alloy ZX6 oxidised at 1200 °C with the same ratio as above).

The same oxides as in the alloys ZX5 and ZX6 oxidised at 800 °C were formed in the scale of ZX5 at 1200 °C, namely one oxide rich in Nb + Ti and lean in Si and Si + Al+ Sn and the other leaner in Nb + Ti and richer in Si and Si + Al + Sn. In the alloy ZX5 the former oxide had [Nb + Ti]/[Si + Al + Sn] = 30.5/2.46 = 12.4 and Nb/Ti = 2.1 and in the latter these ratios were 21.13/11.5 = 1.84 and 3.4, Table 8.11.

In the Sn rich area in the alloy ZX6 the Nb_5Si_3 was observed with Si + Al + Sn = 37.4 at%, (Si + Al + Sn)/O_2 = 9.1 and 8 < Ti < 16 at.%, compared with 36 at.%, 8.1 for the former two parameters and Ti = 15.6 at.% in the bulk, which would suggest that the Ti of some Nb_5Si_3 grains near the scale had been consumed to form the oxides. Indeed, in the scale formed on the alloy ZX6 at 1200 °C the oxide types observed in the alloys ZX5 and ZX6 at 800 °C and ZX5 at 1200 °C were present together with a Ti rich oxide. One oxide type was rich in Nb + Ti and lean in Si and Si + Al + Sn, another was lean in Nb + Ti and richer in Si and Si + Al + Sn and an third oxide had Nb + Ti between the other two and was also richer in Al that the other two. In the alloy ZX6 the former oxide had [Nb + Ti]/[Si + Al + Sn] = 32.1/1.31 = 24.5 and Nb/Ti = 3.1 in the second oxide type these ratios were 20.34/14 = 1.45 and 2.6, and in the third oxide type (Ti rich oxide) they were 27.7/5.7 = 4.86 and 0.3, Table 8.14.

In the Sn rich layer the Nb_3Sn had Si + Al + Sn = 24.49 at.%, Si/Sn = 0.04 and (Si + Al + Sn)/O_2 = 3.4 (Table 8.12), similar to the values of these parameters for the same phase in the alloy ZX5 at 1200 °C. However, in the Sn rich area of the alloy ZX6 there

was Nb_3Sn with composition similar to the Nb_3Sn in the bulk. This Nb_3Sn (i.e., the one in the Sn rich area) had Si + Al + Sn = 17.6 at.%, Si/Sn = 0.37 and (Si + Al + Sn)/O_2 = 2.9 (Table 8.12) compared with 16.6 at.%, 0.36 and 2.98 of the same parameters in the bulk (Table 8.13). In other words, in the Sn rich area in ZX6 there were "existing" Nb_3Sn grains and "newly formed" Nb_3Sn from the enrichment in Sn (which was also responsible for the formation of Nb_5Sn_2Si, see also above). The Nb_5Sn_2Si was observed in the Sn rich area in ZX6 with (Si + Al + Sn)/O_2 = 5.4, the same as in ZX5 at 1200 °C. The enrichment of the substrate at its interface with the oxide scale with Sn will be discussed in a later chapter.

In the Figure 8.28 spots 65, 68 show Sn rich areas to form from A15 Nb_3Sn (Table 8.12), in agreement with ZX6 at 800 °C (Figure 8.18) and with the discussion in chapter 7 (see also Figure 7.33). Details of the microstructures indicated by circles in the Figure 8.28 are shown in Figure 8.31. Similar features were observed in the Sn rich area formed in the alloy ZX3 at 1200 °C, as shown in Figure 8.32. The microstructures in the latter two figures would suggest recrystallization in the Sn rich area. If the latter was indeed the case, then it is worth considering possible source(s) for the strain energy that drove recrystallization.

As we discussed above, formation of Sn rich areas was observed in oxidised alloys. During oxidation of a specimen the oxidation of the different phases present in the microstructure of the substrate where the Sn rich area formed depended on the chemistry and crystal structure of phases. Diffusion of oxygen is expected to be easier via the Nb_{ss} owing to the inherent high solid solubility of oxygen in the latter and its content of reactive solute elements like Ti and Al. Inward diffusion of oxygen was accompanied by enrichment of the surface areas (i.e., of the substrate) by Sn and the formation of Sn rich intermetallics.

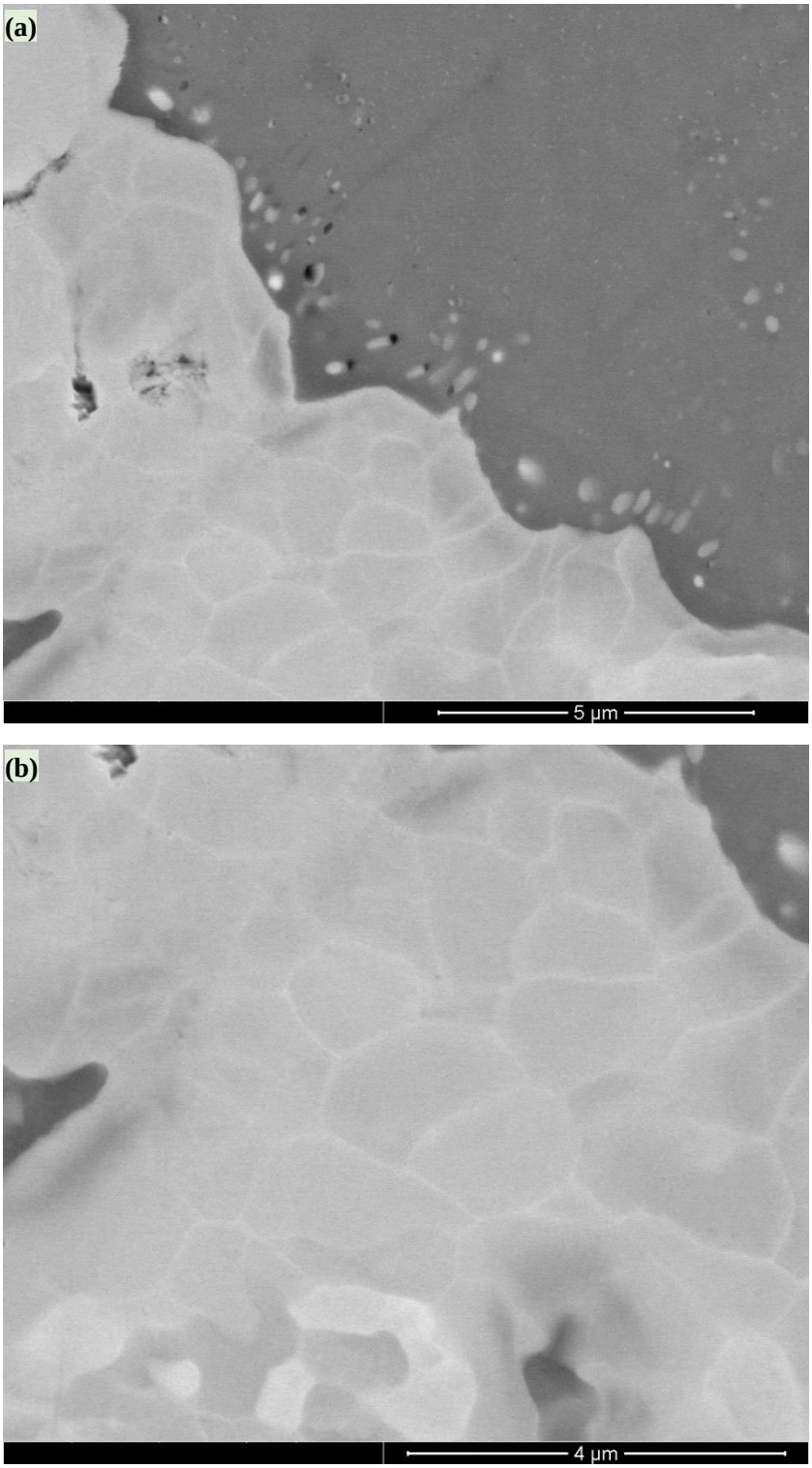


Figure 8.31 Details of the microstructure of ZX6 at 1200 °C circled in Figure 8.28.

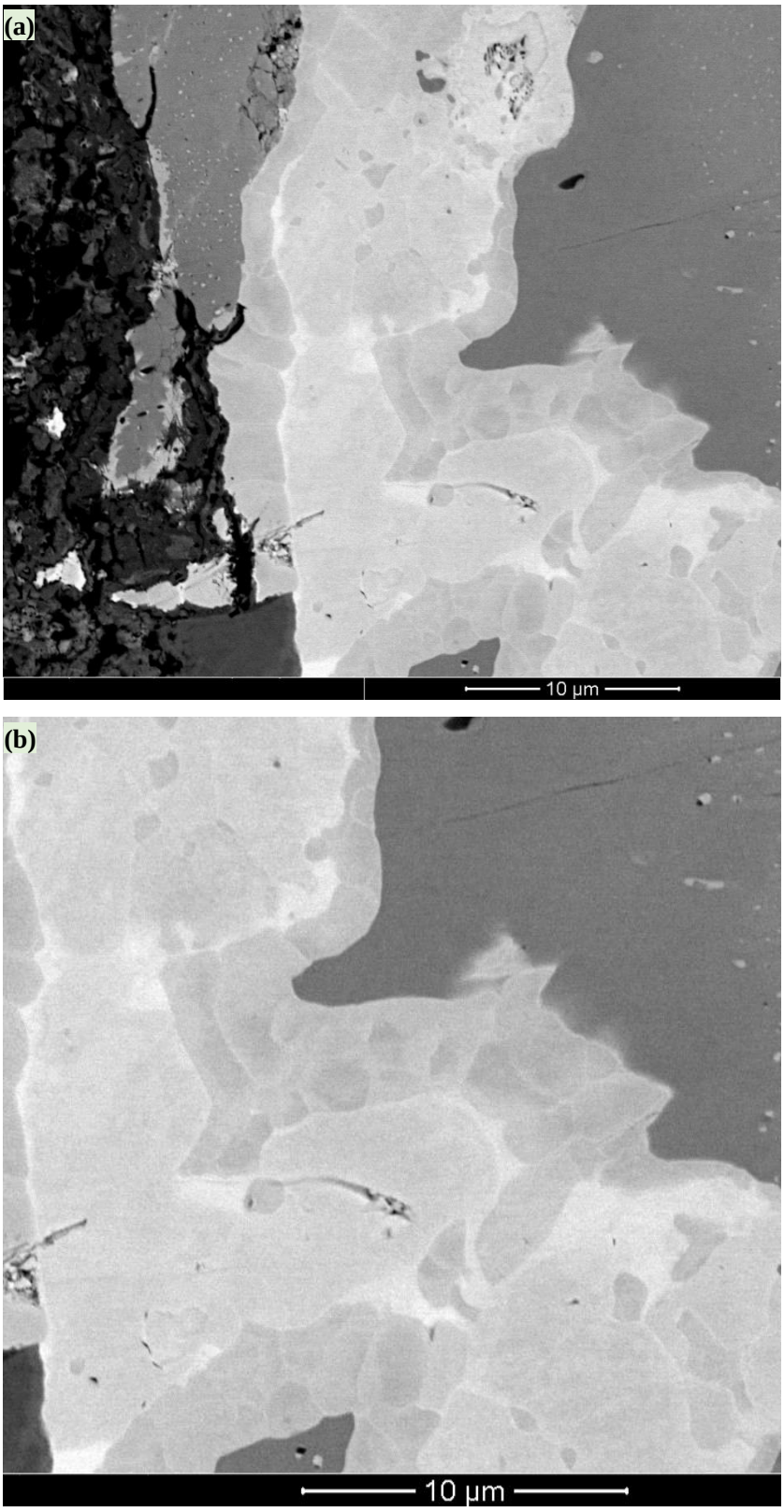


Figure 8.32 Details of microstructure in the Sn rich area of alloy ZX3 at 1200 ℃ showing the similar features to that in the Sn rich area of ZX6 at 1200 ℃.

The formation of oxides, the enrichment of the surface areas with Sn prior to the formation of Sn rich intermetallics, the contamination of existing phases like Nb_{ss}, Nb_5Si_3 and Nb_3Sn and the formation of Sn rich intermetallics must have been accompanied with increased defect density and internal stress level arising from differences of the density of phases, their coefficients of thermal expansion and moduli of elasticity. For example the moduli of elasticity of Nb, βNb_5Si_3, αNb_5Si_3 and Nb_3Sn respectively are 105, 269, 291 [91] and 173 GPa [92] but for the latter the values of 127 GPa [93], 195 GPa [94] and 135 GPa [95] have been reported, the latter for 1000 K. Furthermore, the modulus of elasticity of Nb_6Sn_5 is 144 GPa [92] and of Nb_3Al (which has the A-15 structure and as we have seen in this work the A-15 intermetallic in ZX5 was Al rich) is 164 GPa [96] or 193 GPa [94]. The CTE (coefficients of thermal expansion) of Nb is 7.6 10^{-6} K^{-1} and of Nb_3Sn is 10.3 10^{-6} K^{-1} [97]. The βNb_5Si_3 and αNb_5Si_3 exhibit anisotropy in CTE and the ratio of CTE values along the a and c axes of their lattices (i.e., the CTE anisotropy ratio) is different for each phase. All the aforementioned values are for the unalloyed phases and are expected to change as they become alloyed.

To demonstrate the dependence of stresses arising in the Sn rich area from differences in the values of E and CTE of phases, the stress is estimated as $\sigma = E_{SRA}E_{sub}\,\Delta T\,(\alpha_{sub} - \alpha_{SRA})\,[E_{sub} + 2E_{SRA}\,(d_{SRA}/d_{sub})]^{-1}$ [98] where E_i and α_i respectively are moduli of elasticity and coefficient of thermal expansion, ΔT is temperature difference and d_i is thickness [i = SRA (Sn rich area) or Sub (substrate)].

If we consider the data given above for Nb and Nb_3Sn, with the former as the substrate and the latter the phase formed in the SRA and take d_{SRA} = 10 μm and d_{sub} =100 μm then the calculated stress for ΔT = 1000 K is $|\sigma|$ = 276 MPa for the lowest reported modulus of elasticity of Nb_3Sn (127 GPa) and $|\sigma|$ = 384 MPa for the highest reported value (195 GPa). For d_{SRA} = 50 μm and d_{sub} =100 μm the corresponding stresses for

ΔT = 1000 K are $|\sigma|$ = 155 MPa and 184 MPa. For d_{SRA} = 1 μm and d_{sub} = 100 μm the corresponding stresses for ΔT = 1000 K are $|\sigma|$ = 343 MPa and 508 MPa.

The estimated values of σ show that the stress is very high at the early stages of SRA formation and decreases as d_{SRA} increases and for the same d_{SRA} increases with the modulus of elasticity of the substrate. Given the high homologous temperatures of the oxidation experiments recovery processes and therefore gradual reduction in defect density and stresses should have occurred before recrystallization set-in in parts of the Sn rich area in an oxidised alloy driven by reduction in strain energy that depended on the substrate phase(s), the thickness of and the type(s) of SRA phase(s) formed.

8.5 Summary

Two Nb-24Ti-18Si-5Al based alloys with low and high Sn concentrations were studied, namely the alloys Nb-24Ti-18Si-5Al-2Sn (ZX5) and Nb-24Ti-18Si-5Al-5Sn (ZX6), in the cast and heat treated (1500 °C) conditions and after isothermal oxidation at 800 °C and 1200 °C.

Both alloys were hyper-eutectic with βNb_5Si_3 the primary phase. In both cast alloys there was macrosegregation of Si and Ti, the magnitudes of which respectively decreased and increased slightly with Sn concentration in the alloy ZX6. In both alloys the Nb_3Si was supressed and the Nb_{ss} + Nb_3Si eutectic was replaced by the metastable Nb_{ss} + βNb_5Si_3 eutectic, and the Nb_3Sn formed only in the cast alloy with the high Sn content (ZX6) but was stable in both alloys after the heat treatment at 1500 °C. The prior eutectic microstructure was not present it both alloys after the heat treatment.

In both alloys the transformation of βNb_5Si_3 to αNb_5Si_3 did not start during solidification and was completed at 1500 °C. In the latter condition there was precipitation of second phase(s?) in some αNb_5Si_3 grains. The Nb_{ss} was destabilised

by the higher Sn concentration in the alloy ZX6 (not present in the heat treated (1500 °C) microstructure and the oxidised (1200 °C) microstructure).

Both alloys did not pest during isothermal oxidation at 800 °C and their scales spalled off at 1200 °C, the spallation of the scale formed on ZX5 being easier than that on ZX6.

At 800 °C the scale formed on the alloy ZX5 was rough while that formed on the alloy ZX6 was smoother and compact, and the scales of both alloys consisted of Nb rich and Nb and Si rich oxide. At 1200 °C the scales on both alloys were compact and the same oxide types plus Ti rich oxide were formed the scales in both alloys and there was WDS data for all three types.

In both alloys there was enrichment in Sn of the microstructure below the scale and formation of Sn rich phases in this area and at the scale/substrate interface. In both alloys at 1200 °C the phases were the Sn rich intermetallics Nb_3Sn and Nb_5Sn_2Si, i.e., the $NbSn_2$ was not formed.

In both alloys the bulk microstructures were contaminated by oxygen. Contamination followed the Nb_{ss} that was formed in the cast microstructure.

Chapter 9

The alloys Nb-24Ti-18Si-5Cr-5Al-2Sn (ZX7) and Nb-24Ti-18Si-5Cr-5Al-5Sn (ZX8)

9.1 Introduction

The alloys Nb-24Ti-18Si-5Cr-5Al-2Sn (ZX7) and Nb-24Ti-18Si-5Cr-5Al-5Sn (ZX8) are studied in this chapter to understand how the simultaneous presence of Cr, Al and Sn in Nb silicide based alloys affects the phase stability and oxidation behaviour. The cast and heat treated microstructures of the alloys are studied using SEM, XRD and EDS. The isothermal oxidation behaviour of the two alloys is studied at 800 °C and 1200 °C, respectively. Oxidation kinetics and the microstructure of oxidised specimens are investigated using SEM-EDS and EPMA-WDS.

9.2 Results

9.2.1 Alloy Nb-24Ti-18Si-5Cr-5Al-2Sn (ZX7)

As cast: The actual composition of the alloy was Nb-24.7Ti-15.8Si-5.0Cr-5.1Al-2.1Sn. Its Si content was significantly lower than the nominal composition. The EDS large area analysis of the cast alloy is shown in Table 9.1 and indicated macrosegregation of Si whose concentration varied from 14.7 at.% to 17.7 at.% with the largest difference in Si content observed between the bulk and bottom of the ingot.

The microstructure of the cast alloy ZX7 as shown in Figures 9.1 to 9.3. As shown in Figures 9.1 and 9.2, the top and bulk of the alloy consisted of Nb_5Si_3, Nb_{ss} and Nb_{ss}+Nb_5Si_3 eutectic. Some area of the Nb_{ss} exhibited darker contrast owing to being rich in Ti.

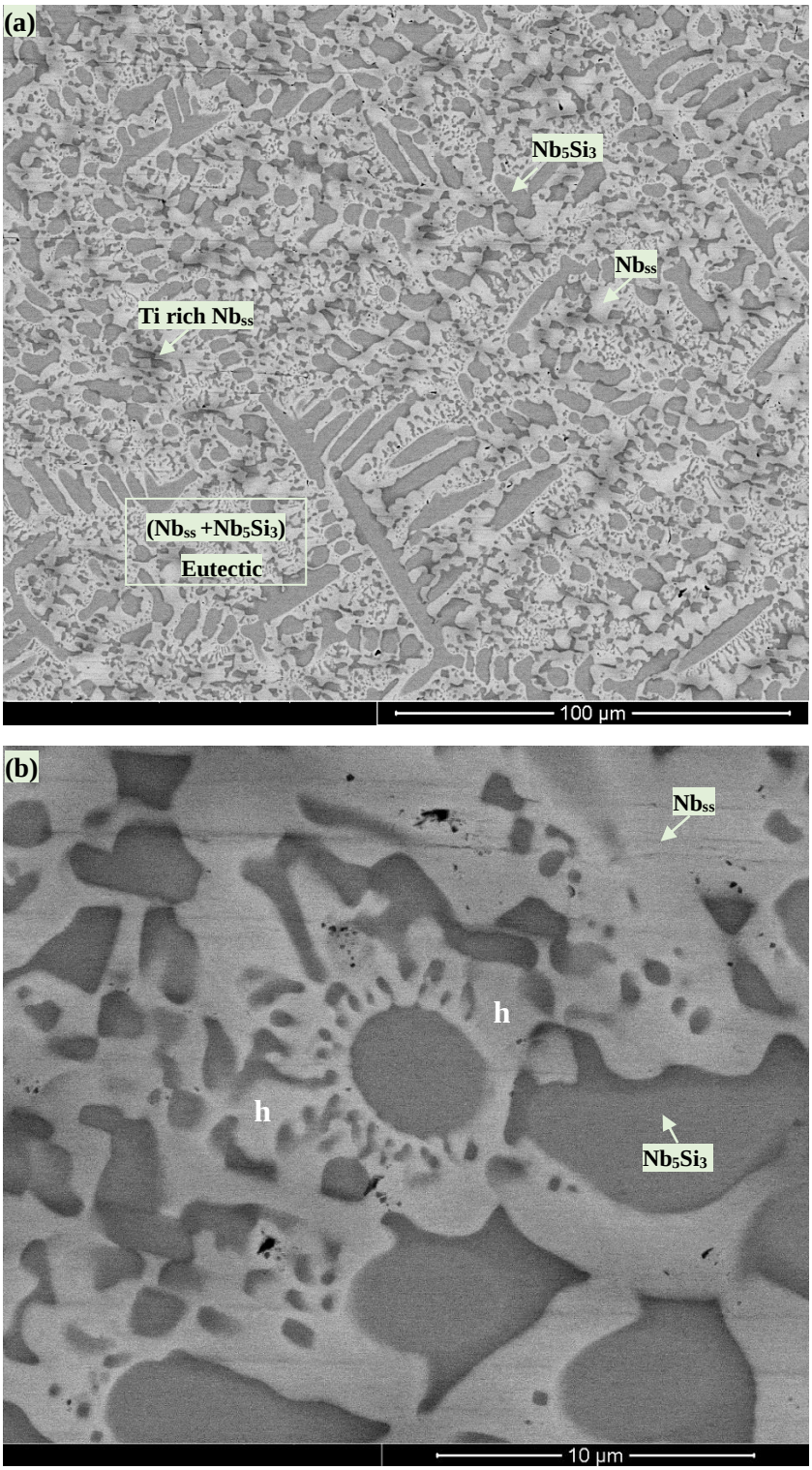


Figure 9.1 BSE images of the microstructure in the top area of the cast alloy ZX7, (a) low and (b) high magnification. In (b) haloes of Nb_{ss} are indicated by h.

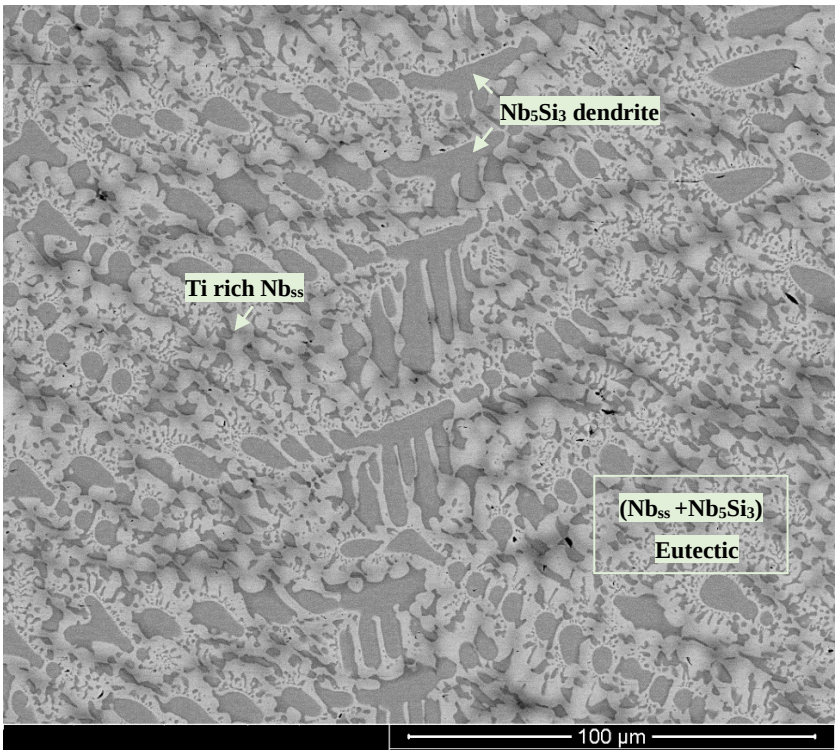
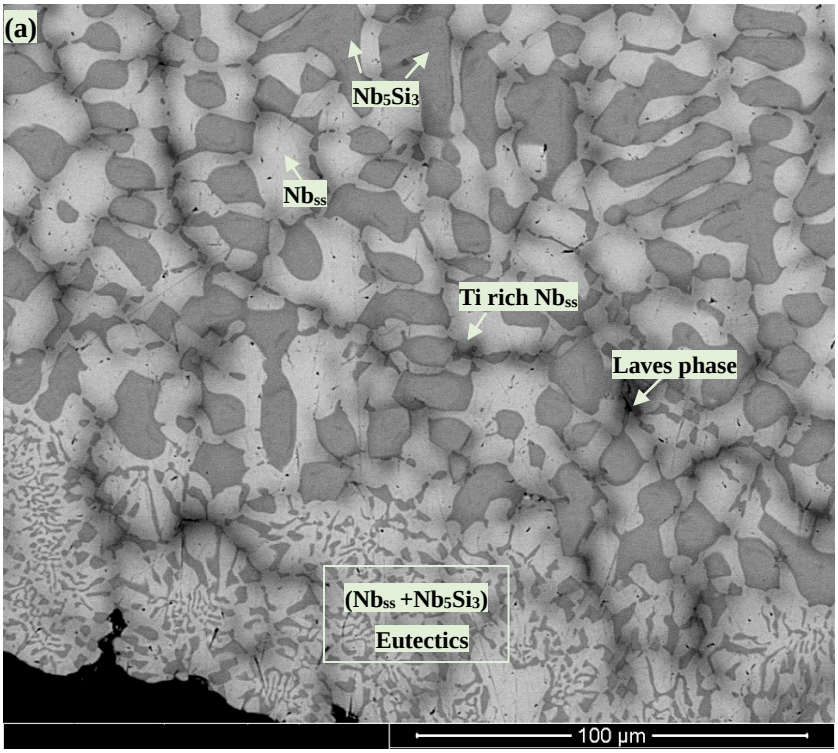


Figure 9.2 BSE image of the microstructure in the bulk area of the cast alloy ZX7.



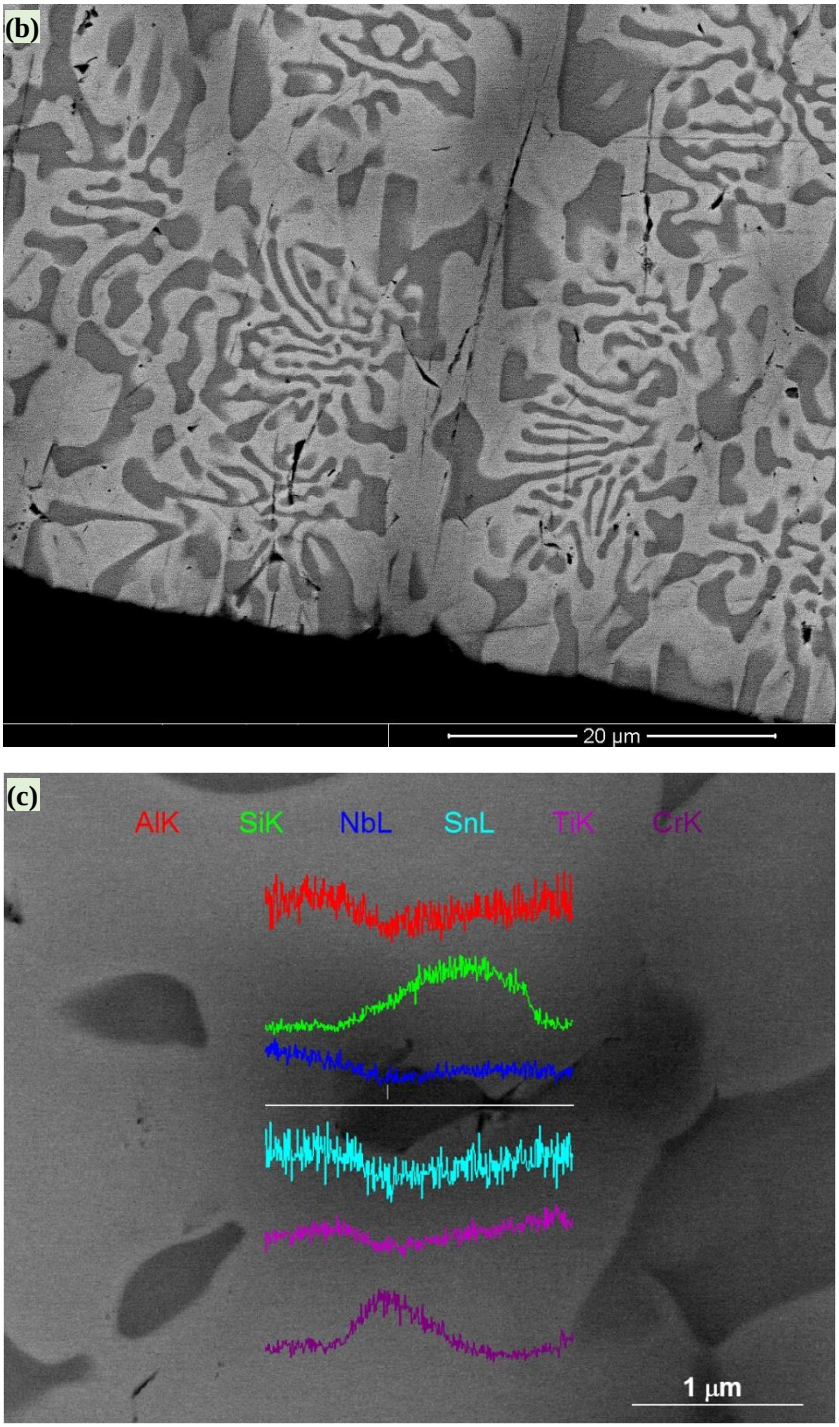


Figure 9.3 BSE images of the microstructure in the bottom area of the cast alloy ZX7, (a) low, (b) high magnification, (c) Laves phase.

In the bottom area of the cast alloy, the microstructure was different compared with the top and bulk area. A zone about 50 μm thick containing Nb_{ss} + Nb_5Si_3 eutectic was observed in the bottom where the melt had been in contact with the water cooled

crucible. Beyond this zone, the co-continuous structure of Nb_{ss} and Nb_5Si_3 that was observed before in the alloy ZX3 (see Chapter 7) was formed. Some very fine Laves phase was also observed, as indicated in Figure 9.3.

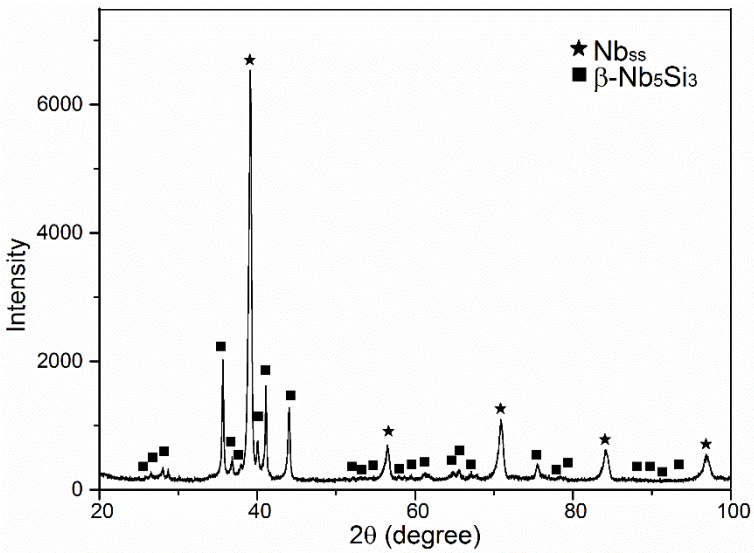


Figure 9.4 The XRD diffractogram of the cast alloy ZX7.

The XRD data of the cast alloy is shown in Figure 9.4. The Nb_{ss} and Nb_5Si_3 were identified, and the latter phase was the high temperature βNb_5Si_3. The Laves phase was not identified by the XRD because of its low volume fraction in the microstructure (see Figure 9.3a), but its presence was confirmed using line scans (see Figure 9.3c) and X-ray maps, as seen in Figure 9.5.

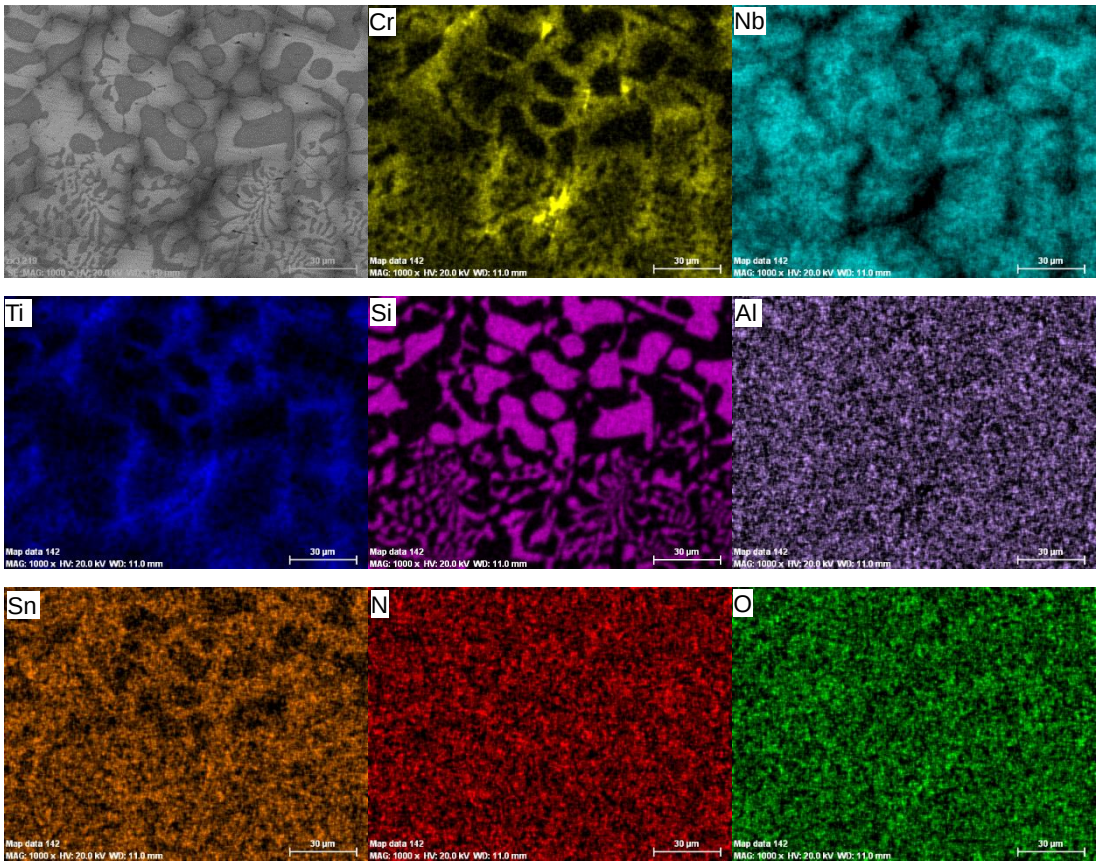


Figure 9.5 X-ray elemental maps of the bottom area of the cast alloy ZX7.

The EDS analysis of the phases is shown in Table 9.1. The data confirmed that the Ti rich Nb_{ss} was also richer in Cr (8.4 at.%). The Nb_{ss} had Si + Sn = 5.1 at.% with Si/Sn = 0.8. The Si content of the 5-3 silicide was 29.9 at.% and the Al content was (4.3 at.%) with Si + Al + Sn = 35.4 at.%, which is very close to the nominal Si content of the un-alloyed Nb_5Si_3 (37.5 at.%). The Si + Al + Sn of the eutectic was around 19.8 at.%, in agreement to the cast alloy ZX5 (see chapter 8).

Table 9.1 EDS analysis (at.%) of the as cast and heat treated alloy ZX7

As cast	Nb	Ti	Si	Cr	Al	Sn
Surface*	**47.7** ± 0.2	**24.5** ± 0.2	**15.8** ± 0.3	**4.8** ± 0.1	**5.2** ± 0.1	**2.0** ± 0.1
	47.5 - 47.9	*24.0 - 24.7*	*15.4 - 16.4*	*4.6 - 5.1*	*5.0 - 5.3*	*1.9 - 2.2*
Bulk*	**47.4** ± 0.3	**25.1** ± 0.2	**15.0** ± 0.2	**5.1** ± 0.2	**5.3** ± 0.2	**2.1** ± 0.1
	47.1 - 48.1	*24.6 - 25.4*	*14.7 - 14.7*	*4.9 - 5.4*	*5.1 - 5.6*	*2.0 - 2.3*
Bottom*	**47.1** ± 0.4	**24.5** ± 0.5	**16.7** ± 0.5	**4.9** ± 0.2	**4.8** ± 0.2	**2.0** ± 0.1
	46.5 - 47.6	*23.8 - 25.5*	*16.1 - 17.7*	*4.7 - 5.2*	*4.6 - 5.0*	*1.8 - 2.1*
Nb_{ss}	**61.7** ± 0.8	**22.9** ± 0.5	**2.3** ± 0.1	**4.4** ± 0.3	**5.9** ± 0.2	**2.8** ± 0.2
	60.9 - 62.7	22.3 - 23.3	2.2 - 2.4	4.1 - 4.7	5.7 - 6.1	2.7 - 3.1
Ti-rich Nb_{ss}	**49.4** ± 2.4	**29.9** ± 1.3	**3.5** ± 0.8	**8.4** ± 0.4	**6.1** ± 0.1	**2.7** ± 0.1
	47.6 - 52.1	*28.5-31.1*	*2.7 - 4.2*	*8.0 - 8.6*	*6.0 - 6.2*	*2.6 - 2.8*
Nb_5Si_3	**45.7** ± 0.4	**17.7** ± 0.5	**29.9** ± 0.4	**1.2** ± 0.2	**4.3** ± 0.1	**1.2** ± 0.1
	44.7 - 46.2	*17.3 - 18.7*	*28.9 - 30.2*	*1.0 - 1.6*	*4.2 - 4.5*	*1.1 - 1.3*
Eutectic	**48.7** ± 1.5	**25.9** ± 0.8	**12.4** ± 1.0	**5.6** ± 0.4	**5.2** ± 0.1	**2.2** ± 0.1
	46.5 - 50.9	*24.6 - 27.5*	*10.7 - 13.7*	*4.8 - 6.3*	*5.0 - 5.4*	*2.1 - 2.3*
Heat treated	Nb	Ti	Si	Cr	Al	Sn
Bulk*	**47.0** ± 0.9	**26.4** ± 1.2	**14.6** ± 0.4	**5.4** ± 0.2	**4.6** ± 0.2	**2.0** ± 0.1
	45.5 - 48.0	*24.5 - 28.1*	*13.8 - 15.2*	*5.1 - 5.8*	*4.3 - 4.9*	*1.9 - 2.2*
Nb_{ss}	**56.7** ± 1.4	**23.4** ± 0.6	**0.6** ± 0.2	**10.7** ± 0.7	**6.8** ± 0.3	**1.8** ± 0.3
	55.6 - 59.3	*22.6 - 24.4*	*0.4 - 0.8*	*9.3 - 11.3*	*6.4 - 7.2*	*1.4 - 2.2*
Nb_5Si_3	**44.8** ± 0.4	**17.9** ± 0.3	**34.5** ± 0.4	**0.4** ± 0.1	**1.7** ± 0.2	**0.7** ± 0.1
	44.3 - 45.4	*17.3 - 18.2*	*34.0 - 34.9*	*0.3 - 0.6*	*1.5 - 1.9*	*0.6 - 0.9*
A15	**57.5** ± 0.9	**18.4** ± 0.8	**4.5** ± 1.0	**5.5** ± 0.3	**8.9** ± 0.9	**5.2** ± 0.3
Nb_3X	*56.1 - 58.6*	*17.3 - 19.7*	*3.4 - 6.3*	*4.7 - 5.8*	*7.6 - 9.8*	*4.9 - 5.6*

* Large area analysis

Heat treated: The alloy was heat treated at 1450°C for 100 hours. The composition of the heat treated specimen was also leaner in Si compared with the nominal composition. The microstructure had been homogenised though out the specimen. The microstructure of the bulk area is shown in Figure 9.6. The microstructure consisted of Nb_5Si_3, Nb_{ss} and the newly formed A-15 Nb_3Al intermetallic (according to the XRD data, see Figure 9.7). The A-15 intermetallic phase was also observed in the heat treated alloy ZX5 (see Chapter 8). Furthermore, dark contrast Ti nitrides were formed in the Ti rich areas of the cast microstructure, as was observed in the alloys ZX3 and ZX5. Inside the Nb_5Si_3 there was precipitation of a phase with contrast similar to that of Nb_{ss} or the A-15 intermetallic, see circle in Figure 9.6b.

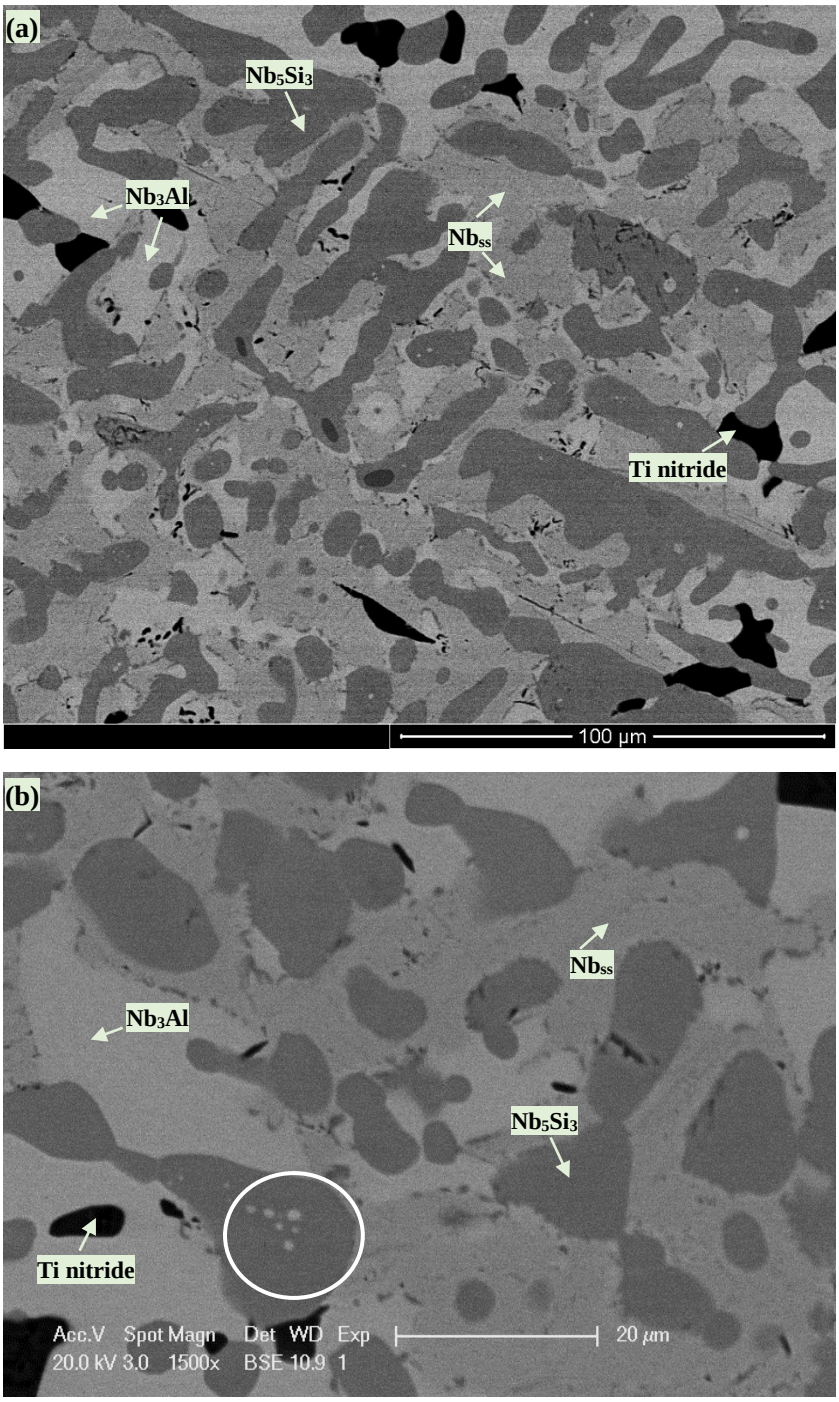


Figure 9.6 BSE images of the microstructure in the bulk area of the heat treated alloy ZX7, (a) low and (b) high magnification.

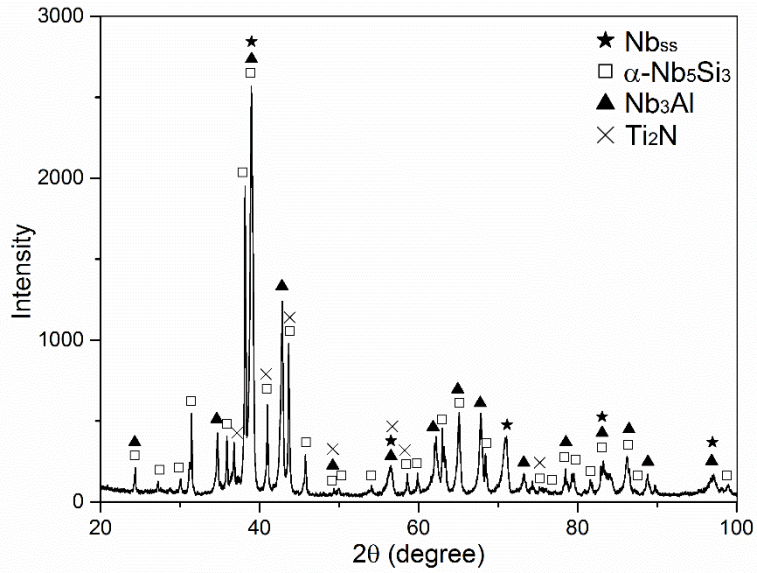


Figure 9.7 The XRD differactogram of the heat treated alloy ZX7.

The XRD data is shown in Figure 9.7. The high temperature βNb_5Si_3 had transformed to the low temperature αNb_5Si_3 completely. The EDS analysis data of the phases is summarised in Table 9.1. The Al concentration in Nb_5Si_3 was decreased to 1.7 at.% while its Si content increased to 34.5 at.% after the heat treatment. The Si + Al + Sn concentration was 36.9 at.%, close to the stoichiometric composition. The Cr concentration in the Nb_{ss} had increased to 10.7 at.%, which is consistent with that for the Nb_{ss} in the heat treated alloy ZX3 (9.0 at.%), see Table 7.1. The Al solubility in the Nb_{ss} in the heat treated ZX7 was 6.8 at.%, essentially the same as in the alloy ZX5 (6.5 at.%), see Table 8.1. The Si concentration in the Nb_{ss} was 0.6 at.%, in agreement with data for heat treated Nb silicide based alloys and the Si/Sn was decreased to 0.33. The A-15 intermetallic formed in the heat treated alloy ZX7 was Al rich and had Si + Al + Sn = 18.6 at.%. The alloying elements in the Nb_3Al had very similar concentration as in the heat treated ZX5, see Table 8.1. The X-ray elemental maps, shown in Figure 9.8, suggested that the Laves phase existed in the heat treated microstructure surrounding the Nb_{ss}, which was also rich in Cr.

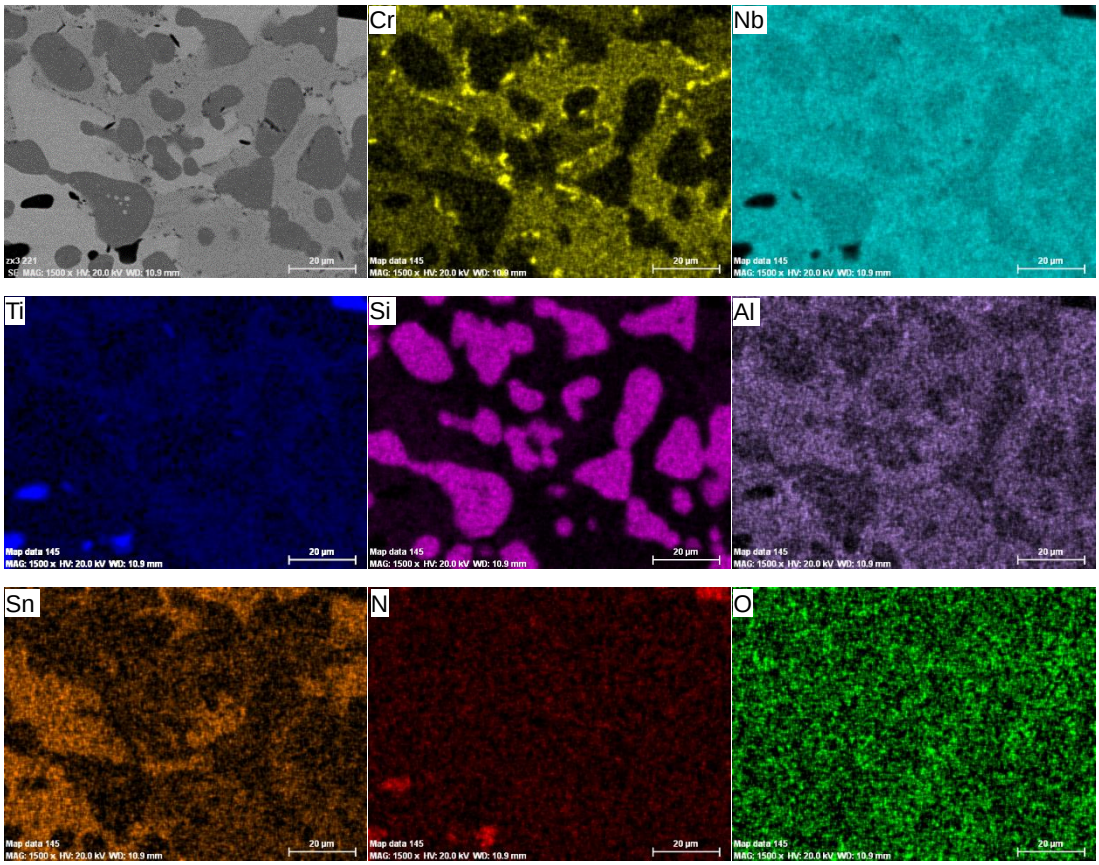
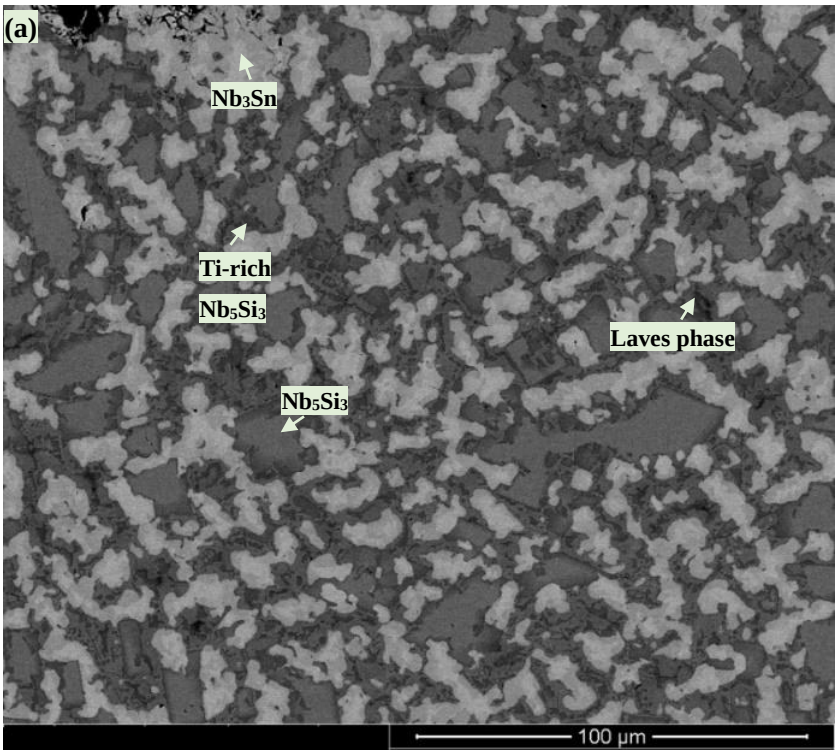


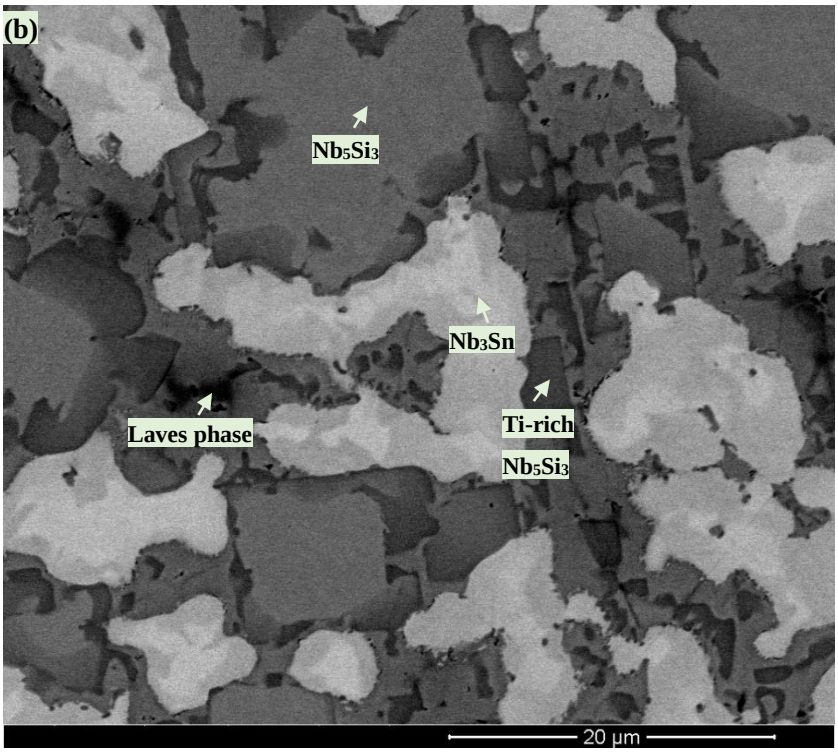
Figure 9.8 X-ray elemental maps of the bottom area of the heat treated specimen of the alloy ZX7.

9.2.2 Alloy Nb-24Ti-18Si-5Cr-5Al-5Sn (ZX8)

The actual composition of the cast alloy ZX8 was Nb-23.9Ti-17.2Si-5.4Cr-4.8Al-4.6Sn. The large area EDS analysis is shown in Table 9.2. There was macrosegregation of all elements with the exception of Sn. The Si concentration varied between 10.9 and 20.9 at.%, that of Ti between 20.3 and 30 at.%, that of Cr between 3.3 and 8 at.%, and that of Al between 3.7 and 5.6 at.%. For all the aforementioned elements the largest concentration difference was observed between the bulk and top of the ingot. Only in the case of Si, the highest concentration was observed in the bulk. These composition differences resulted in significant inhomogeneous microstructure in the bulk, top and bottom of the alloy.

.


(a)
Nb3Sn
Ti-rich
Nb5Si3
Laves phase
Nb5Si3
100 μm


(b)
Nb5Si3
Nb3Sn
Laves phase
Ti-rich
Nb5Si3
20 μm

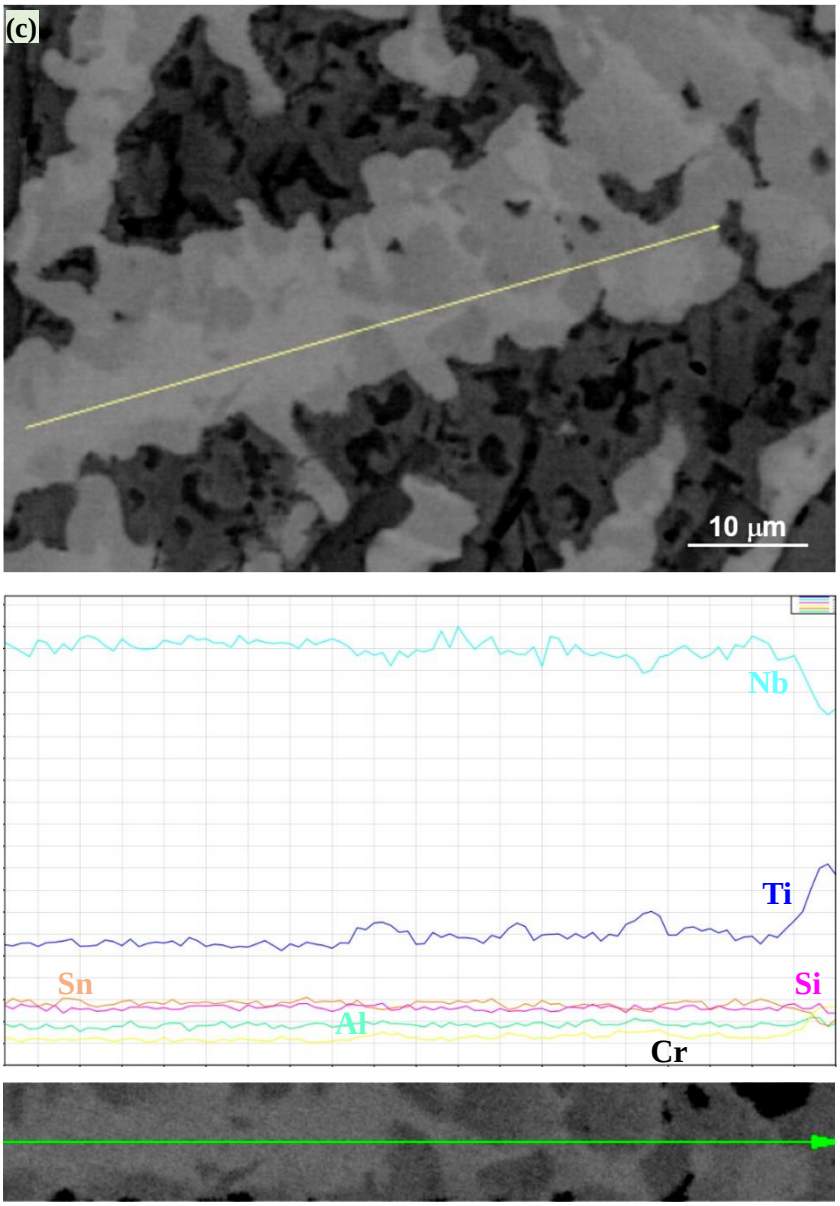
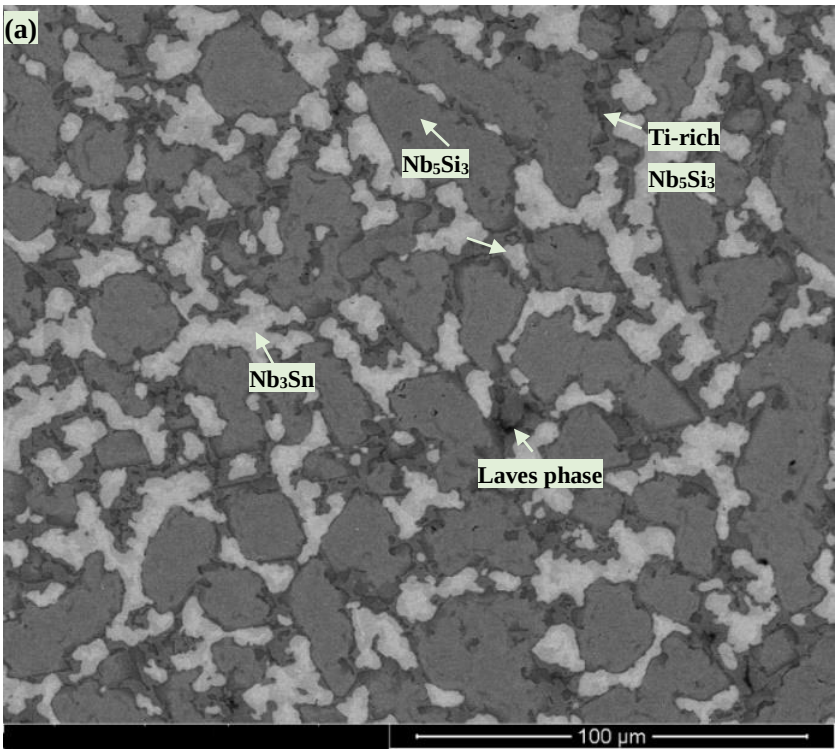
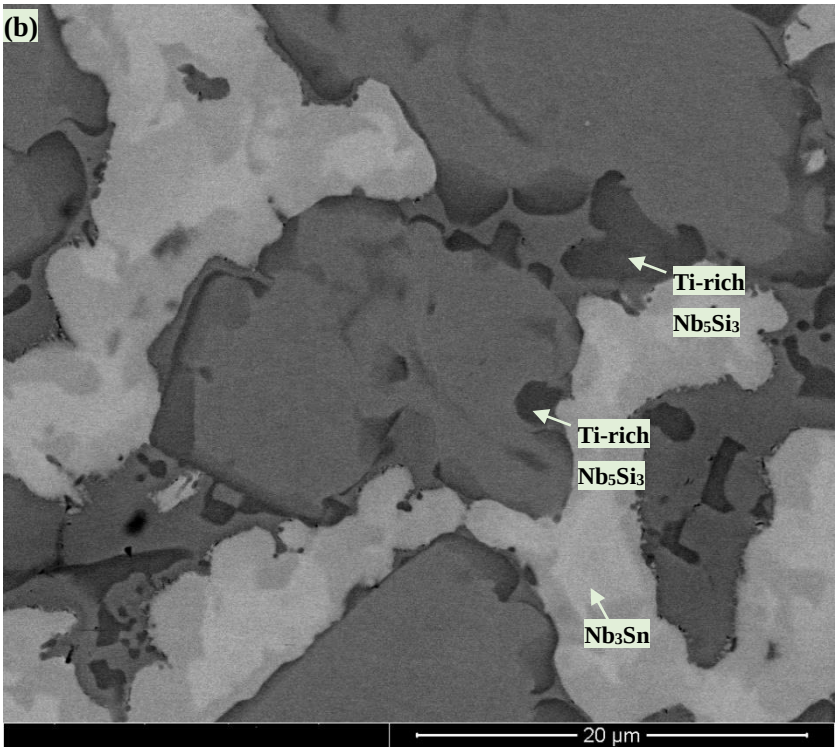


Figure 9.9 BSE images of the microstructure at the top area of the cast alloy ZX8, (a) low and (b) high magnification, (c) line scan along Nb_3Sn grain.

The microstructure of the cast alloy in different parts of the ingot is shown in Figures 9.9 to 9.11. In contrast to the cast microstructures of the alloys ZX4 and ZX6, no Nb_{ss} and no eutectic were observed. The cast alloy consisted of Nb_5Si_3, Nb_3Sn and small volume fraction of Laves phase that were confirmed by XRD (Figure 9.12) and EDS analysis (Table 9.2). The Nb_5Si_3 dendrites were larger in the bulk compared with the top and bottom areas of the alloy. The Laves phase was found through out the alloy and formed very fine grains, see Figures 9.10c and 9.13.


(a)
Nb5Si3
Ti-rich
Nb5Si3
Nb3Sn
Laves phase
100 μm


(b)
Ti-rich
Nb5Si3
Ti-rich
Nb5Si3
Nb3Sn
20 μm

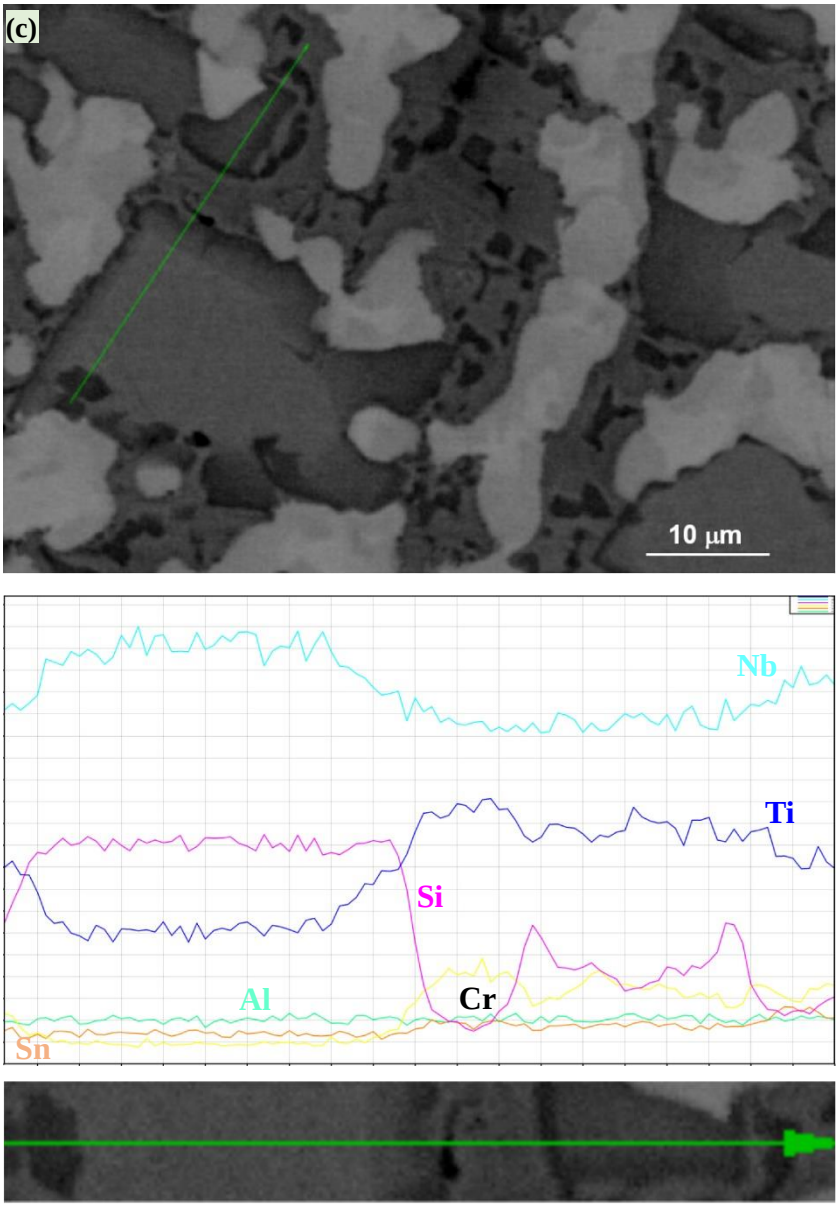


Figure 9.10 BSE images of the microstructure at the bulk area of the cast alloy ZX8, (a) low, (b) high magnification and (c) line scan across different phase.

The Nb_5Si_3 and Ti rich Nb_5Si_3 had Si + Al + Sn close but slightly lower than the stoichiometric Si composition, particularly the former. The A15 intermetallic was rich in Sn (Nb_3Sn) with Si + Al + Sn = 20.1 at.%, which is close to that of ZX6. The composition of the Laves phase could be analysed only in the top area of the ingot, where its Si + Cr + Al + Sn content was 52.2 at.%.

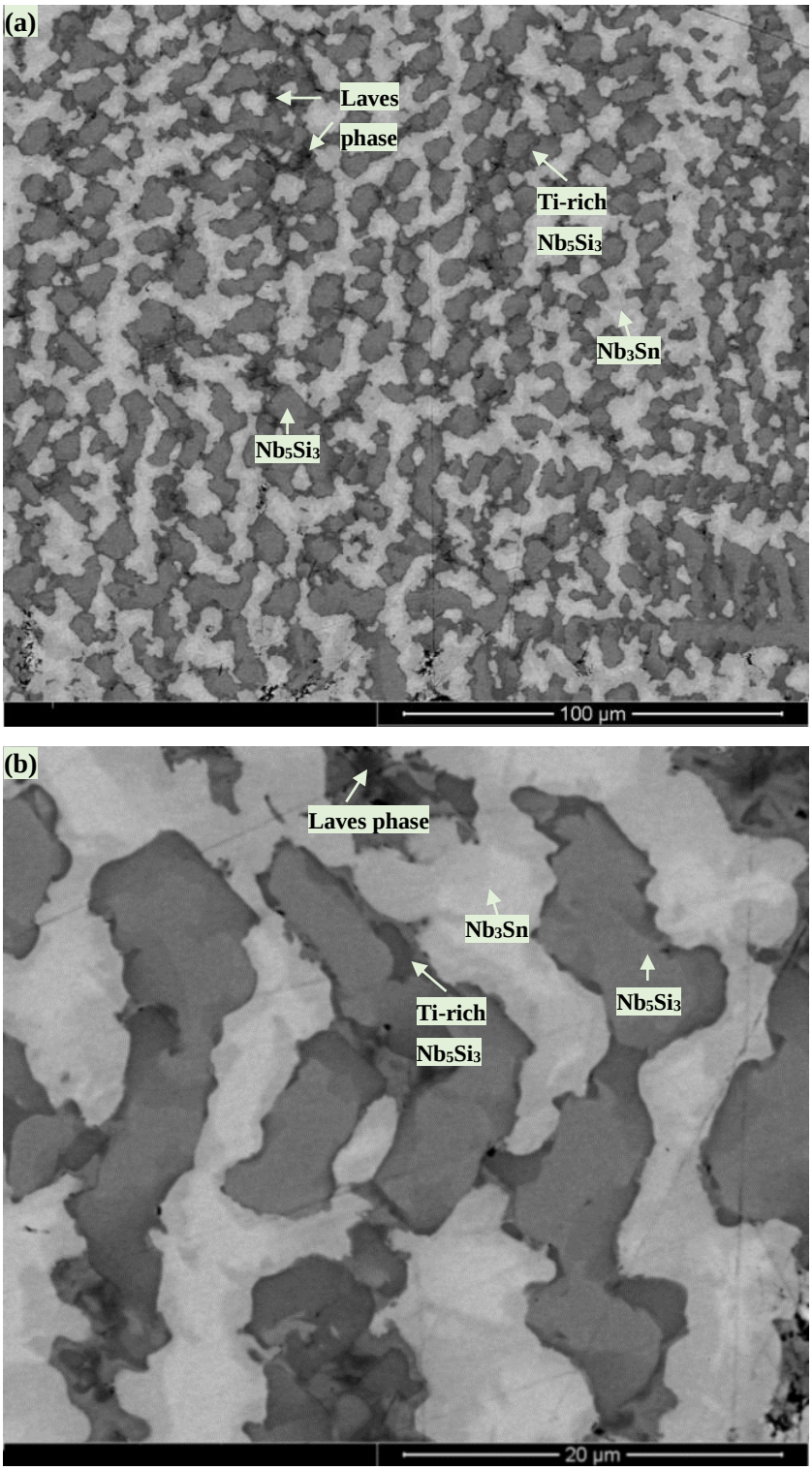


Figure 9.11 BSE images of the microstructure at the bottom area of the cast alloy ZX8, (a) low and (b) high magnification.

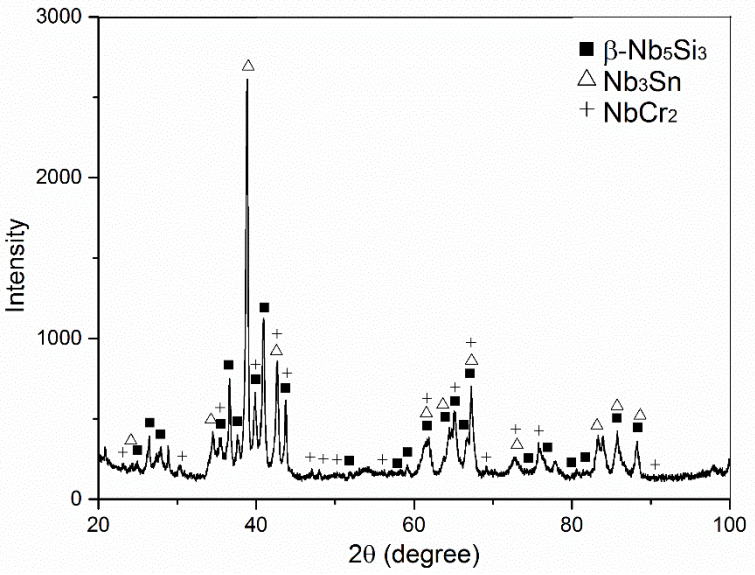


Figure 9.12 The XRD differactogram of the cast alloy ZX8.

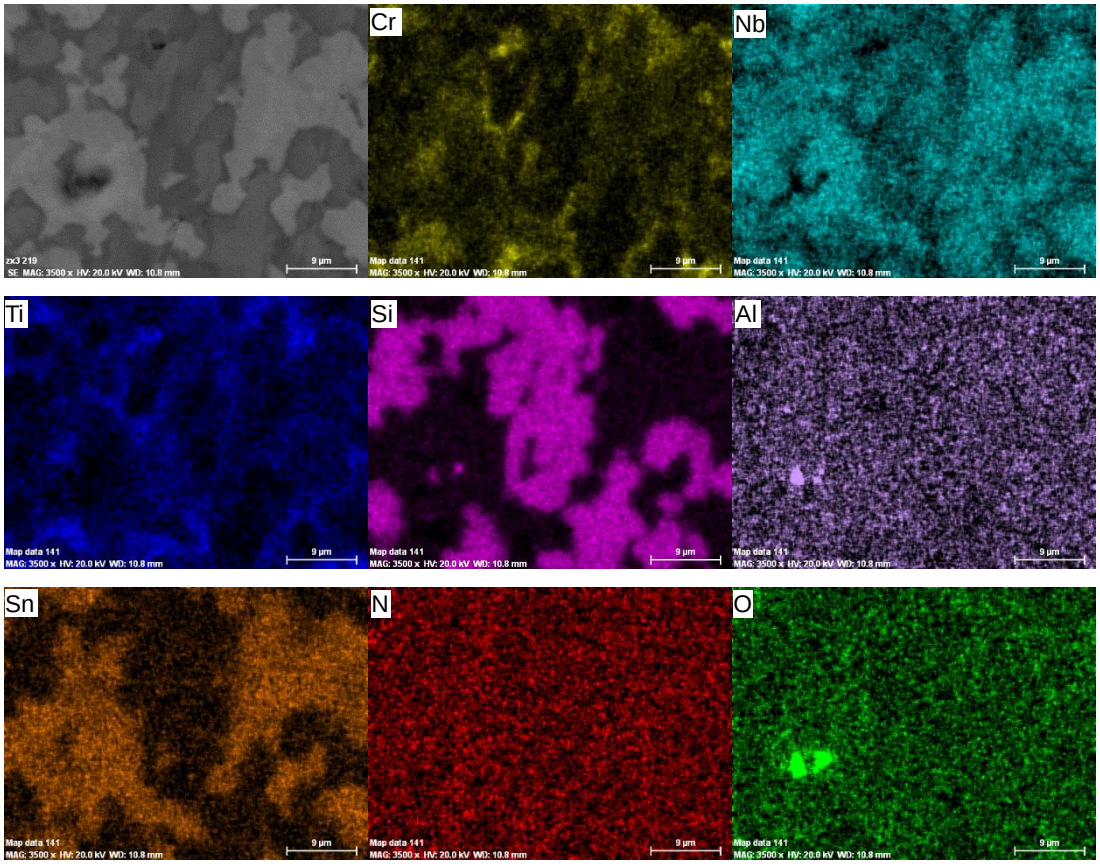


Figure 9.13 X-ray elemental maps of the cast alloy ZX8.

Table 9.2 EDS analysis (at.%) of the as cast and heat treatment alloy ZX8.

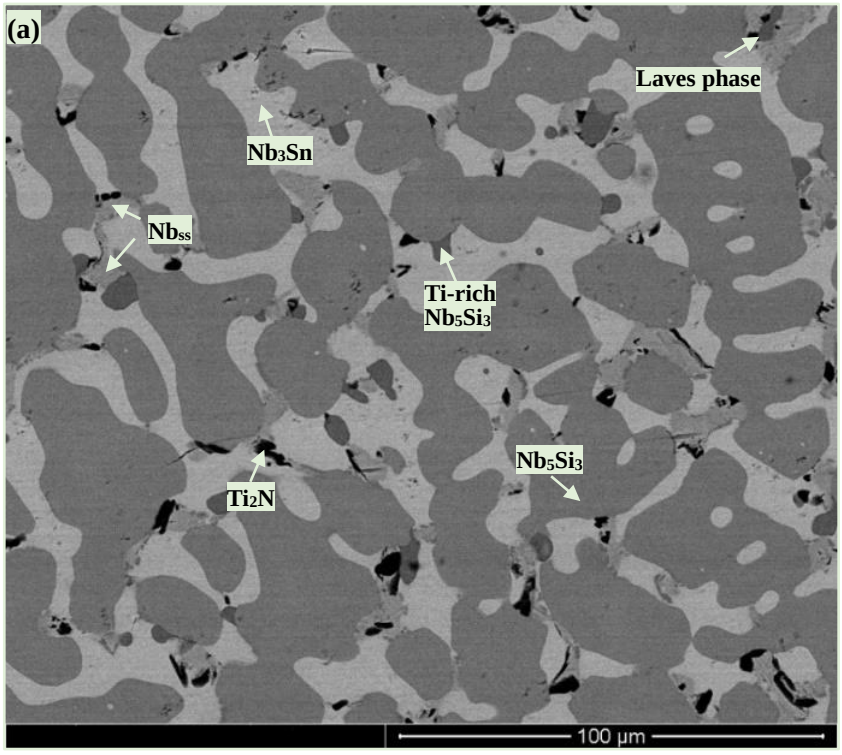
As cast	Nb	Ti	Si	Cr	Al	Sn
Surface*	**41.3** ± 0.7	**28.1** ± 1.1	**14.1** ± 1.9	**6.4** ± 0.7	**5.2** ± 0.2	**4.9** ± 0.3
	40.4 - 43.0	*25.8 - 30.0*	*10.9 - 18.8*	*4.8 - 8.0*	*4.9 - 5.6*	*4.3 - 5.3*
Bulk*	**45.8** ± 0.9	**21.4** ± 0.9	**19.7** ± 1.0	**4.5** ± 0.8	**4.3** ± 0.5	**4.3** ± 0.2
	43.3 - 46.6	*20.3 - 23.9*	*18.0 - 20.9*	*3.3 - 5.3*	*3.7 - 5.2*	*4.0 - 4.8*
Bottom*	**45.4** ± 0.4	**22.1** ± 0.3	**17.7** ± 0.5	**5.5** ±0.3	**4.8** ± 0.2	**4.5** ± 0.1
	44.9 - 46.3	*21.6 - 22.6*	*16.9 - 18.6*	*5.0 - 6.2*	*4.6 - 5.1*	*4.3 - 4.8*
Nb_5Si_3	**42.0** ± 0.6	**20.6** ± 0.5	**31.9** ± 0.9	**1.1** ± 0.2	**2.6** ± 0.5	**1.8** ± 0.4
	41.2 - 43.2	*19.9 - 21.4*	*30.7 - 33.3*	*0.8 - 1.4*	*1.7 - 3.2*	*1.2 - 2.2*
Ti-rich	**35.2** ± 1.1	**27.5** ± 1.2	**29.2** ± 0.9	**2.6** ± 0.6	**3.7** ± 0.2	**1.8** ± 0.2
Nb_5Si_3	*33.2 - 36.6*	*26.2 - 29.9*	*27.5 - 30.0*	*1.9 - 3.6*	*3.3 - 4.0*	*1.6 - 2.3*
Nb_3Sn	**50.3** ± 1.3	**26.2** ± 1.1	**5.3** ± 0.2	**3.4** ± 0.3	**5.2** ± 0.4	**9.6** ± 0.6
	48.0 - 52.0	*24.8 - 28.3*	*5.0 - 5.6*	*2.9 - 4.1*	*4.6 - 6.2*	*8.2 - 10.1*
Laves**	**27.0** ± 1.6	**20.8** ± 0.6	**9.6** ± 1.8	**38.8** ± 2.5	**2.7** ± 0.4	**1.1** ± 0.4
	25.9 - 28.8	*20.1 - 21.3*	*8.4 - 11.7*	*36.7 - 41.6*	*2.3 - 3.1*	*0.7 - 1.6*
Heat treated	Nb	Ti	Si	Cr	Al	Sn
Bulk*	**46.6** ± 0.7	**21.1** ± 0.8	**18.6** ± 1.1	**5.1** ± 0.4	**4.0** ± 0.2	**4.6** ± 0.3
	45.9 - 47.5	*20.3 - 22.2*	*17.4 - 20.4*	*4.6 - 5.7*	*3.8 - 4.5*	*4.0 - 5.0*
Nb_5Si_3	**45.3** ± 0.6	**17.1** ± 0.7	**34.3** ± 0.2	**0.7** ± 0.1	**1.5** ± 0.2	**1.1** ± 0.2
	44.7 - 46.1	*16.1 - 17.7*	*34.1 - 34.5*	*0.6 - 0.9*	*1.3 - 1.7*	*0.9 - 1.2*
Ti rich	**34.7** ± 0.6	**27.0** ± 0.9	**32.5** ± 0.6	**2.3** ± 0.2	**3.2** ± 0.1	**0.3** ± 0.1
Nb_5Si_3	*33.9 - 35.4*	*26.2 - 28.4*	*31.8 - 33.3*	*2.0 - 2.6*	*3.0 - 3.3*	*0.3 - 0.4*
Nb_3Sn	**51.9** ± 0.4	**22.5** ± 0.6	**4.8** ± 0.2	**6.3** ± 0.6	**5.8** ± 0.2	**8.7** ± 0.1
	51.4 - 52.5	*21.6 - 23.4*	*4.2 - 5.0*	*5.8 - 7.6*	*5.4 - 6.1*	*8.5 - 8.9*
Nb_{ss}	**50.4** ± 2.7	**32.0** ± 2.4	**0.6** ± 0.3	**9.2** ± 0.5	**6.0** ± 0.5	**1.8** ± 0.2
	48.1 - 54.6	*28.5 - 34.4*	*0.4 - 1.1*	*8.4 - 9.6*	*5.1 - 6.5*	*1.5 - 2.0*
Laves	**27.3** ± 0.4	**13.7** ± 3.6	**8.3** ± 1.89	**48.5** ± 2.2	**1.9** ± 0.2	**0.3** ± 0.2
	26.6 - 27.8	*11.2 - 20.0*	*6.1 - 10.4*	*45.1 - 50.6*	*1.6 - 2.1*	*0.1 - 0.6*

* Large area analysis.

** Laves phase data from the top of the ingot.

Heat treated: The heat treated specimen was from the bulk of the ingot. Its actual composition was close to the nominal alloy composition and the bulk composition (Table 9.2). After the heat treatment at 1450 °C for 100 hours, the microstructure was homogenised, compare Figures 9.10 and Figure 9.14. Apart from the coarsened Nb_5Si_3 and Nb_3Sn phases, the Nb_{ss} phase was also found in the heat treated microstructure. The latter phase was formed in low volume fraction and near the Nb_5Si_3. Some Ti rich Nb_5Si_3 was also found in the microstructure with contrast similar to that of the Laves

phase, as seen in Figure 9.14. The presence of Cr rich Laves phase was confirmed using X-ray elemental maps (Figure 9.16). There was some evidence for fine precipitates inside few of the Nb_5Si_3 grains. Those precipitates exhibited contrast similar to that of the Nb_{ss} and Nb_3Sn. The XRD confirmed the presence of the Nb_{ss} phase and the Nb_3Sn and Nb_5Si_3 and also confirmed that the latter phase had transformed to the low temperature αNb_5Si_3. As shown in Table 9.2, the Nb_{ss} phase was rich in Cr (9.2 at.%) and Al (6.0 at.%), as was the case for the Nb_{ss} in the heat treated alloy ZX7. The Si concentration in the Nb_{ss} was 0.6 at.% and the Si/Sn ratio was 0.33, the same as for the alloy ZX7. The Ti concentration in Nb_5Si_3 had dropped to 17.1 at.% after the heat treatement, but the Si + Al + Sn content was essentially the same. The Ti rich areas of the Nb_5Si_3 had become richer in Si and leaner in Sn compared with the cast alloy and the Si + Al + Sn had increased and moved closer to the stoichiometric composition of unalloyed Nb_5Si_3. The Nb_3Sn was also leaner in Ti after the heat treatment.



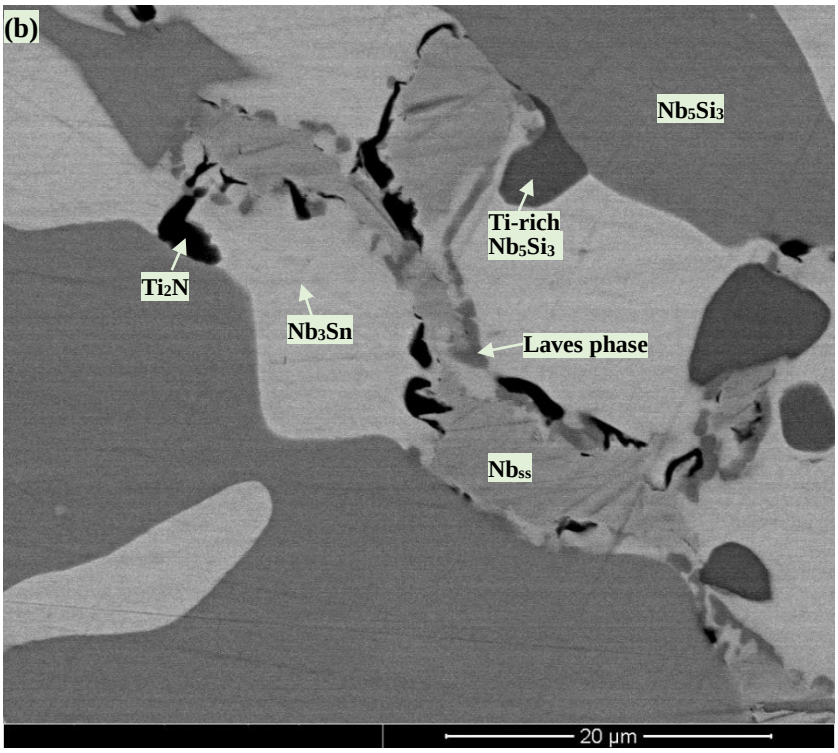


Figure 9.14 BSE images of the bulk area microstructure of the heat treated alloy ZX8, (a) low magnification and (b) high magnification showing details of microstructure.

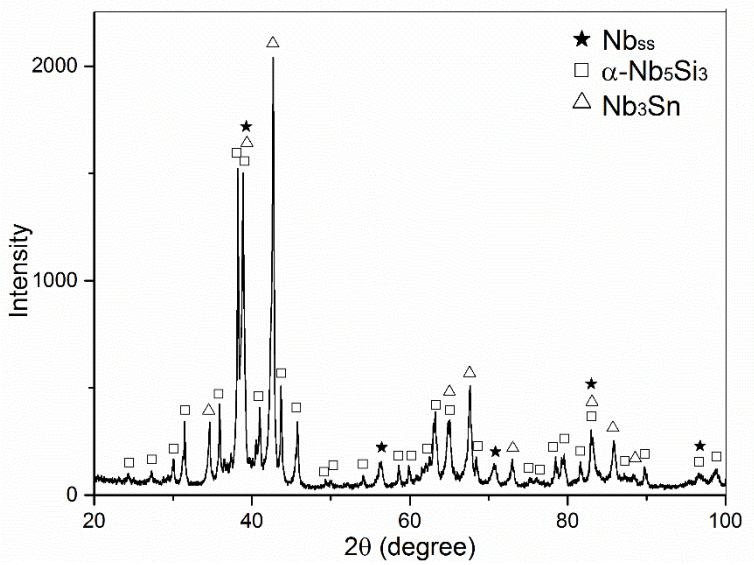


Figure 9.15 The XRD differactogram of the heat treated alloy ZX8.

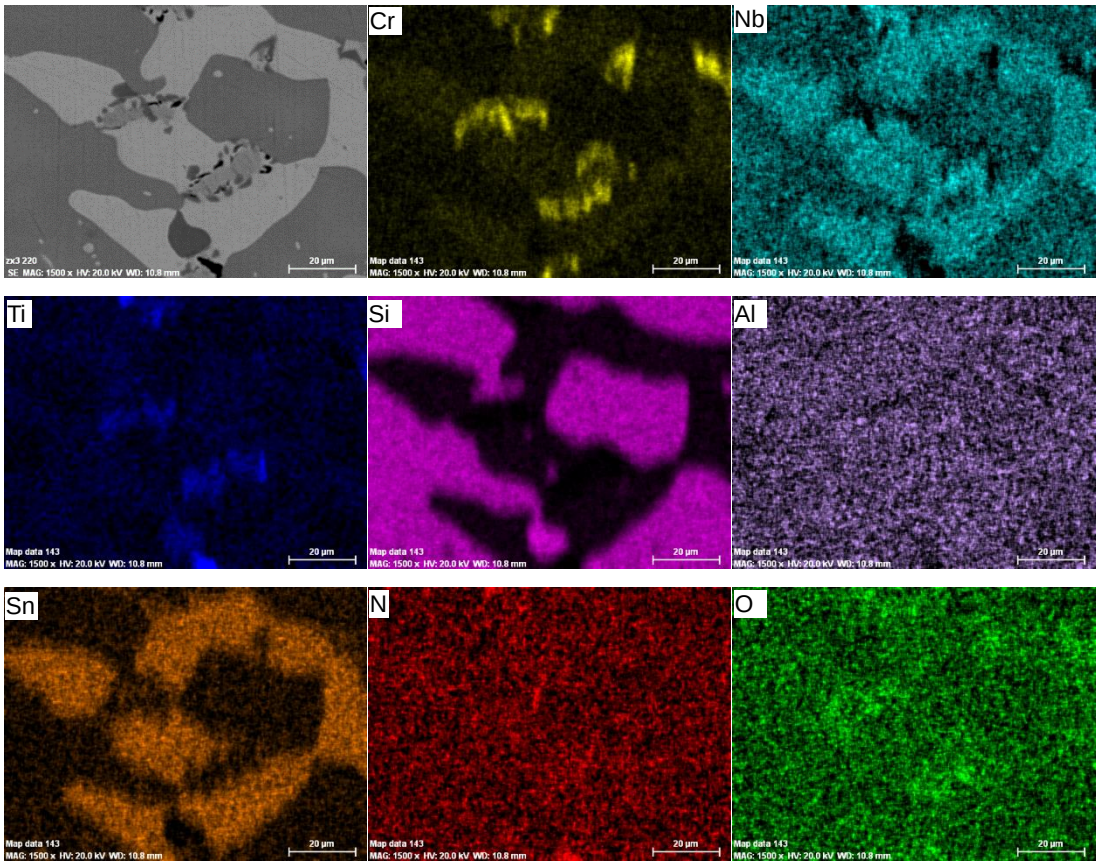


Figure 9.16 X-ray elemental maps of the heat treated alloy ZX8.

9.3 Thermo-gravimetric study of the alloys ZX7 and ZX8

The isothermal oxidation behaviour of the cast alloys ZX7 and ZX8 was investigated at 800 °C and 1200 °C in order to understand the effect of the simultaneous presence of Sn, Al and Cr on the oxidation of the Nb-24Ti-18Si based alloys.

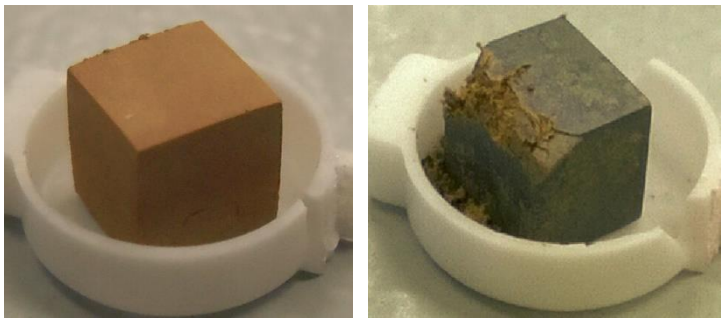


Figure 9.17 The oxidised specimens of the alloys ZX7 (left) and ZX8 (right) after 100 hours in static air at 800°C.

The oxidised specimens of the alloys ZX7 and ZX8 at 800 °C are shown in Figure 9.17. The oxidised alloy ZX7 formed a compact oxide scale on its surface which was very similar to the oxidised alloy ZX3 at 800 °C. The oxidised alloy ZX8 showed severe attack spallation on one corner of the cubic specimen but the other surfaces of the oxidised alloy ZX8 were less severely oxidised than the alloy ZX7. It is believed that the specimen shown in Figure 9.17 does not represent the inherent oxidation resistance of the alloy ZX8 at 800 °C owing to pre-existing cracks in the specimen. Their cracks were probably the result of specimen preparation owing to the absence of Nb_{ss} in the microstructure. It was not possible to repeat the experiment because of the limited available alloy. The melting/cutting of the alloys ZX7 and ZX8 was extremely challenging and many attempts was made before finally making small amount of alloy ZX8 of the desired composition.

Similar to the studied alloys introduced in the previous chapters, the oxide scales of the alloys ZX7 and ZX8 were separated from the substrate at 1200 °C. The oxide scales were similar to those formed on the alloys ZX3 and ZX4 at 1200°C (Figure 9.18).



Figure 9.18 The oxidised specimens of the alloys ZX7 (left) and ZX8 (right) after 100 hours in static air at 1200 °C.

9.3.1 Oxidation kinetics of the alloys ZX7 and ZX8 at 800 °C and 1200 °C

The thermo-gravimetric analysis (TGA) data was plotted using weight change as a function of time. The 800 °C and 1200 °C TGA curves are shown in the Figure 9.19.

The oxidation kinetic rate constant of the two alloys are listed in Table 9.3. The oxidation rate constant of the alloy ZX8 at 800 °C should be considered with calculation for the reasons given in the previous section.

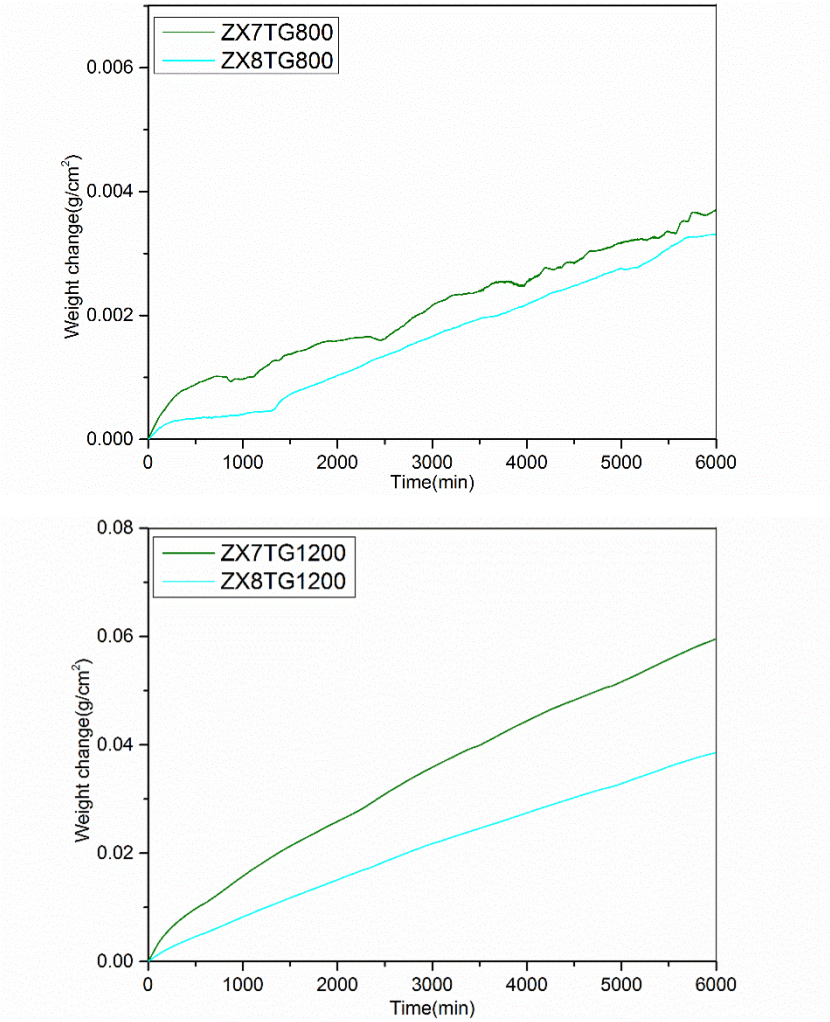


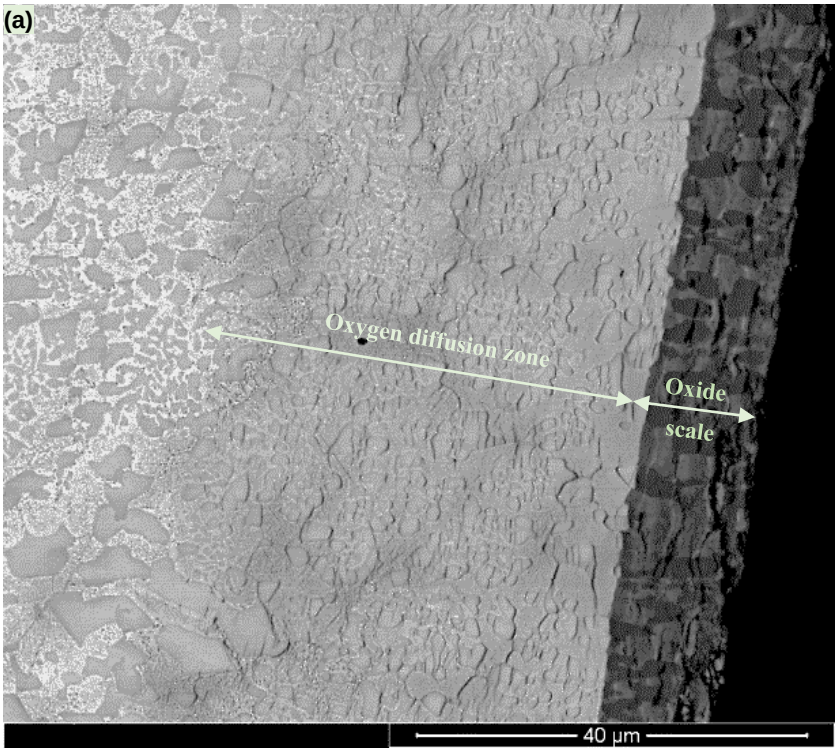
Figure 9.19 TGA data of the alloys ZX7 and ZX8 at (a) 800 °C and (b) 1200 °C for 100 hours.

Table 9.3 The oxidation kinetic rate constant K of the alloys ZX7 and ZX8 ($g \bullet cm^{-2} \bullet s^{-1}$)

	ZX7	**ZX8**
800°C	$K_p = 1.76 \times 10^{-11}$ ($t \leq 2500$ mins) $K_l = 9.94 \times 10^{-9}$ ($t > 2500$ mins)	$K_p = 2.81 \times 10^{-12}$ ($t \leq 1320$ mins) $K_l = 1.01 \times 10^{-8}$ ($t > 1320$ mins)
1200°C	$K_l = 5.91 \times 10^{-9}$ ($t \leq 2200$ mins) $K_l = 1.42 \times 10^{-7}$ ($t > 2200$ mins)	$K_l = 1.07 \times 10^{-7}$

9.3.2 Microstructure of Oxidised alloys ZX7 and ZX8 at 800 °C

A cross section of the oxide scale, oxygen diffusion zone and the bulk microstructure of the oxidised alloy ZX7 is shown in Figure 9.20a. A higher magnification image of the oxide scale and oxygen diffusion zone of the ZX7 is shown in Figure 9.20b and X-ray elemental maps in Figure 9.20c. The oxide scale had uniform thickness of around 10 µm and was composed of two oxides of different contrast. Voids and cracks were observed in the scale suggesting that it was not compact. The oxygen diffusion zone in the alloy ZX7 was around 40 µm thick where the Nb_{ss} are oxidised and the Nb_5Si_3 was cracked, Figure 9.20b.



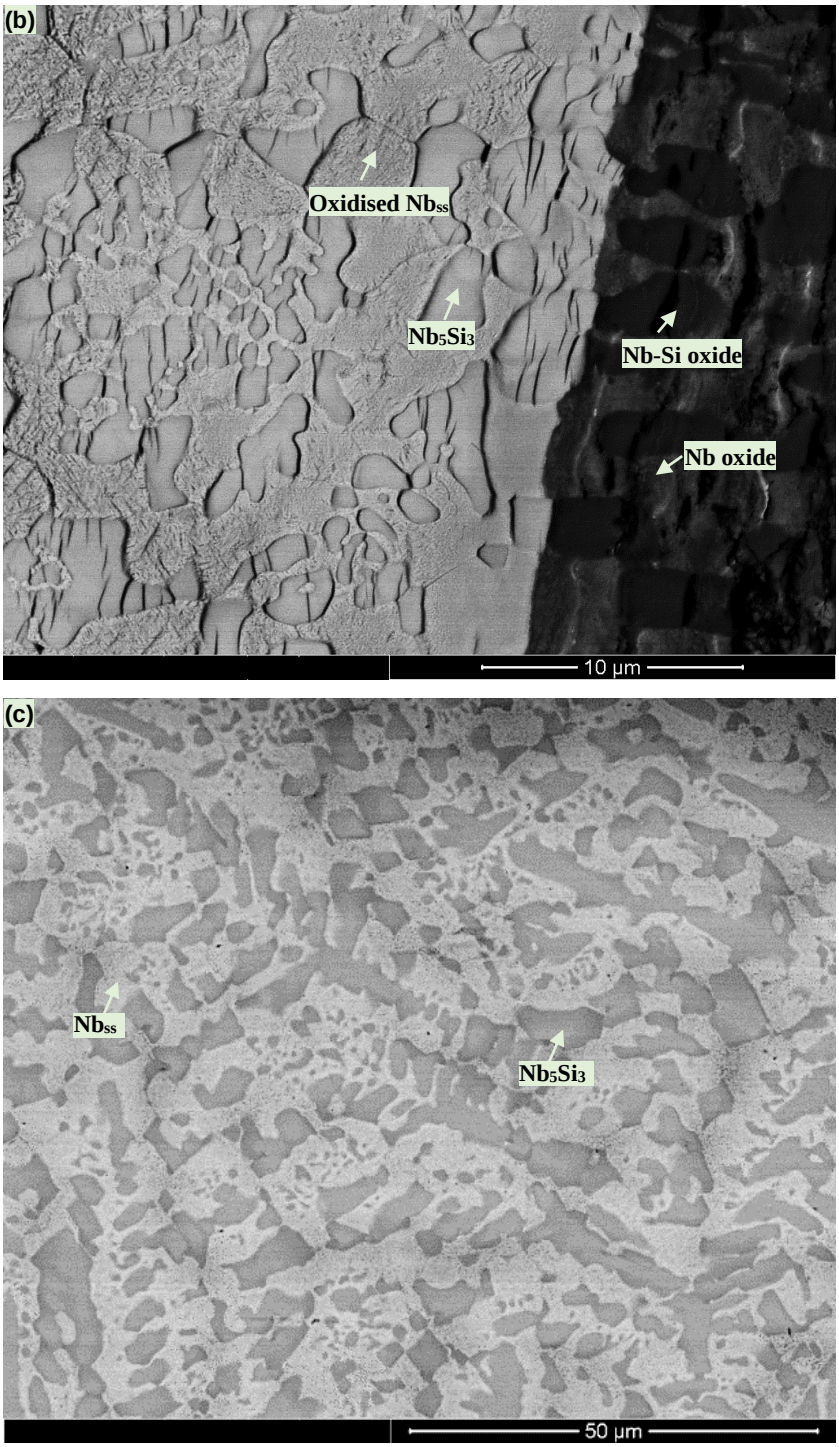


Figure 9.20 BSE images of the microstructure of the oxidised alloy ZX7, (a) cross section of the oxide and oxygen diffusion zone (b) high magnification of the sale/substrate interface and (c). cross section of the bulk area.

The bulk microstructure of the oxidised alloy ZX7 was similar to the cast microstructure. The phases in different area of the oxidised alloy ZX7 were analysed

using WDS. Figure 9.21 shows a "band" of "continuous" Nb_{ss} near the substrate/scale interface (spots 28, 34) and a "band" of "continuous" dendritic Nb_5Si_3 about 15 to 20 μm below this interface (spot 33), with "islands" of Nb_5Si_3 in between (spots 30, 31). The quality of the image is poorer compared with those in Figure 9.20 because Figure 9.21 was taken in EPMA. As shown in Figure 9.21 and Table 9.4, spot analyses 28, 32 and 34 are from the oxidised Nb_{ss} phase in the oxygen diffusion zone of the alloy ZX7. The oxygen content of the solid solution was around 32 at.% which agrees with that of the oxidised alloy ZX5 (~ 34 at.%). The concentrations of Si, Al and Sn are in agreement with those of the Nb_{ss} in the heat treated ZX7. The Si + Al + Sn content of the oxidised Nb_{ss} was ~6.8 at.%. The lower Nb, Ti and Cr contents would suggest that these elements were consummed to form the oxide in the scale. The lower Si content compared with the bulk (see below) would suggest that Si of the Nb_{ss} area also consummed for the formation of the scale. Spot analyses 30, 31 and 33 correspond to the Nb_5Si_3 in the oxygen diffusion zone. The O concentration in the Nb_5Si_3 was around 5 at.%, significantly lower than the Nb_{ss} in the same area. The concentrations of Si, Ti, Al, Cr and Sn were similar to those in the Nb_5Si_3 in the cast alloy ZX7, as seen in Tables 9.1 and 9.4 and the Si + Al + Sn was about 33.6 at.%.

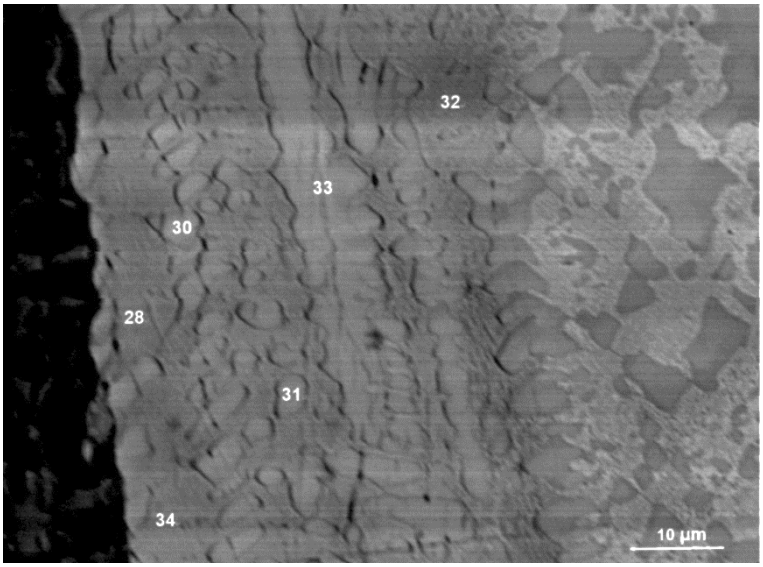


Figure 9.21 BSE image of the microstructure of the diffusion zone showing the numbers of spot WDS analyses of phases.

Table 9.4 WDS analysis (at.%) of phases in the oxygen diffusion zone of the oxidised alloy ZX7 at 800 °C.

	Nb	Ti	Si	Cr	Al	Sn	O
Spot 28	36.05	18.85	0.84	5.72	4.07	1.95	32.52
Spot 32	34.21	19.65	0.85	6.72	4.05	1.94	32.58
Spot 34	36.08	18.47	0.80	5.14	4.05	1.87	33.59
Spot 30	40.33	19.46	29.57	1.28	3.25	1.00	5.11
Spot 31	42.50	18.63	29.15	1.18	3.45	1.07	4.02
Spot 33	42.62	17.42	28.60	1.08	3.60	1.14	5.54

The Nb_{ss} and Nb_5Si_3 in the bulk microstructure were also analysed by WDS. As seen in Figure 9.22 and Table 9.5, spot analyses 35, 36 and 37 are from the Nb_5Si_3 in which in some grains the O concenteration is decreased slightly (2.7 at.% ~ 4.6 at.%). The concertrations of the other alloying elements were the same as for the Nb_5Si_3 in the oxygen diffusion zone and the average Si + Al + Sn was about 34 at.%, slightly lower than in th cast microstructure. Spot analyses 38, 39 and 40 were from the Nb_{ss} which contained only ~ 6 at.% O, which is much lower than that of the Nb_{ss} in the oxygen diffusion zone (~ 32 at.%). The concentrations of the other alloying elements in the Nb_{ss} in the bulk microstructure were similar to those in the cast one and thus higher compared to the Nb_{ss} in the oxygen diffusion zone, as seen in Tables 9.4 and 9.5. This would suggest that all the elements of the Nb_{ss} in the DZ had contributed to the formation of the oxides in the scale, which is consistent with the Nb_{ss} being the Achilles heel of Nb silicide based alloys. The WDS analysis was also applied to the two oxides type in the scale and the data is shown in Table 9.6. The light grey oxide in Figure 9.20b was Nb rich, while the dark contrast oxide was Nb-Si rich.

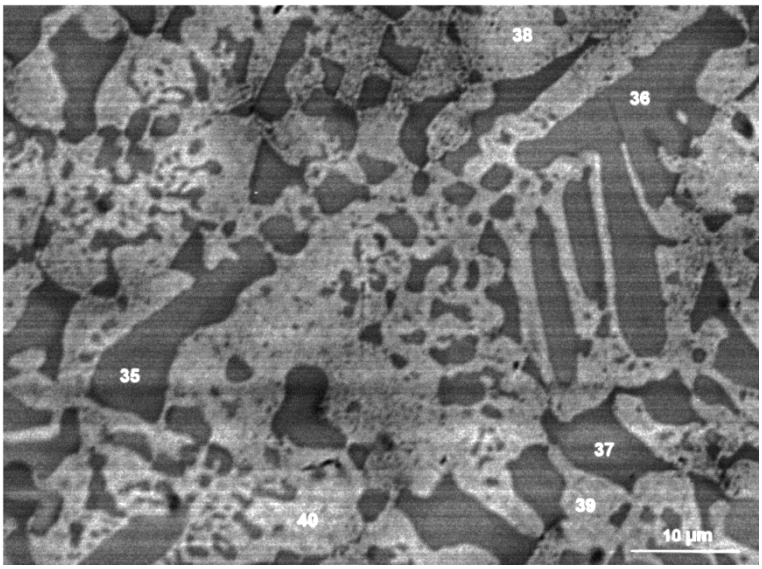


Figure 9.22 BSE image of the bulk microstructure of the oxidised alloy ZX7 at 800 °C showing the numbers of spot WDS analyses of phases.

Table 9.5 The WDS analysis of the phases in the bulk area of the oxidised alloy ZX7.

	Nb	Ti	Si	Cr	Al	Sn	O
Spot 35	44.21	16.82	30.47	1.05	3.69	1.04	2.72
Spot 36	43.43	16.98	28.87	1.08	3.80	1.19	4.65
Spot 37	43.85	16.65	29.40	1.04	3.67	1.04	4.35
Spot 38	49.15	25.68	1.34	8.36	6.49	3.32	5.66
Spot 39	52.03	28.79	1.06	4.12	5.00	2.49	6.51
Spot 40	51.72	28.44	1.30	6.04	4.07	1.88	6.55

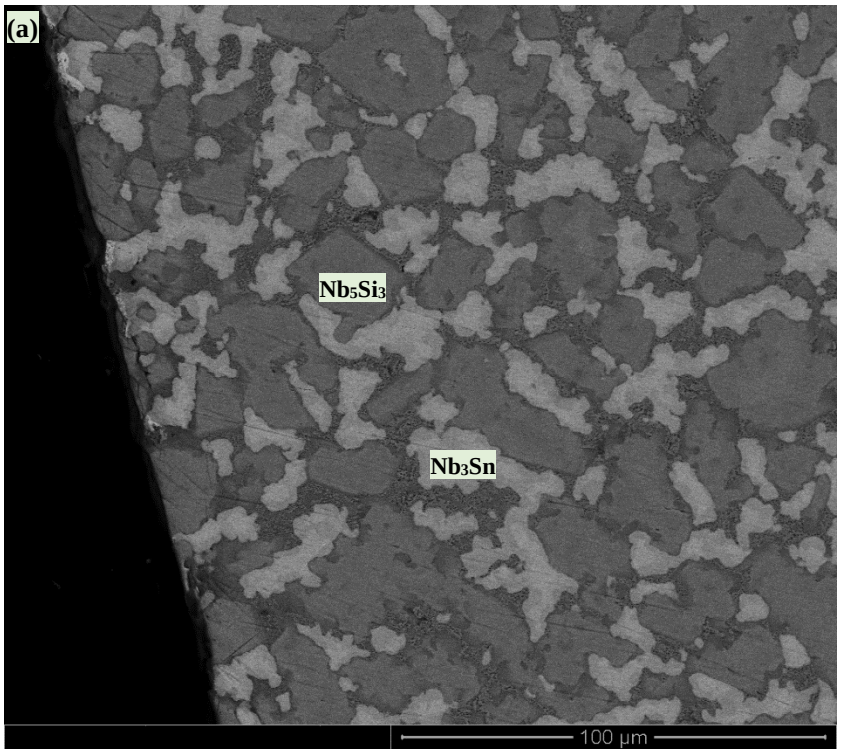
Table 9.6 WDS results of the oxides presented in alloy ZX7 at 800°C.

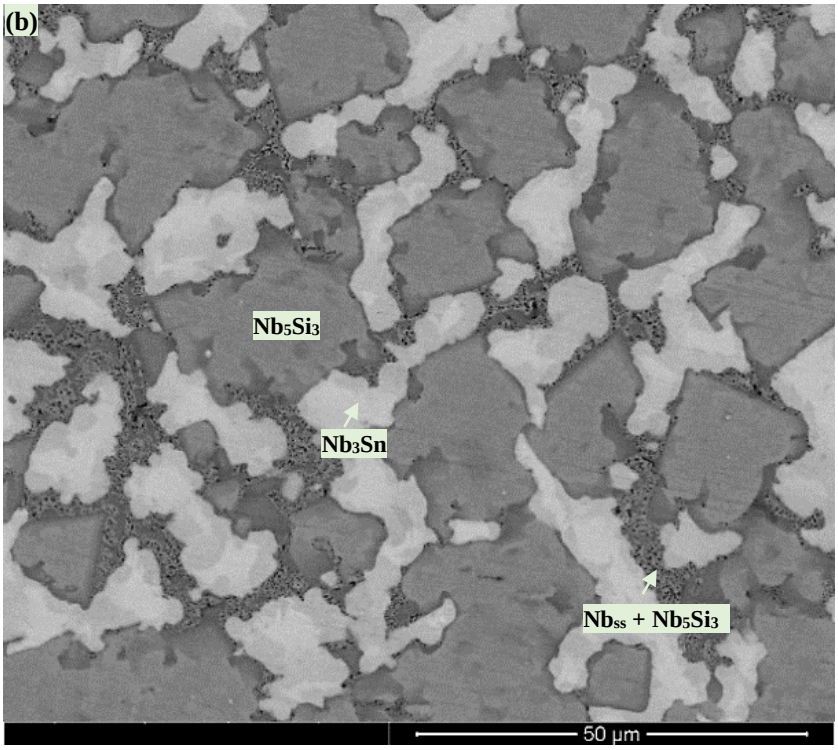
	Nb	Ti	Si	Cr	Al	Sn	O
Nb rich oxide	14.24	9.78	1.32	2.81	0.76	1.07	70.02
Nb-Si rich oxide	16.11	5.00	11.80	0.25	0.89	0.27	65.68

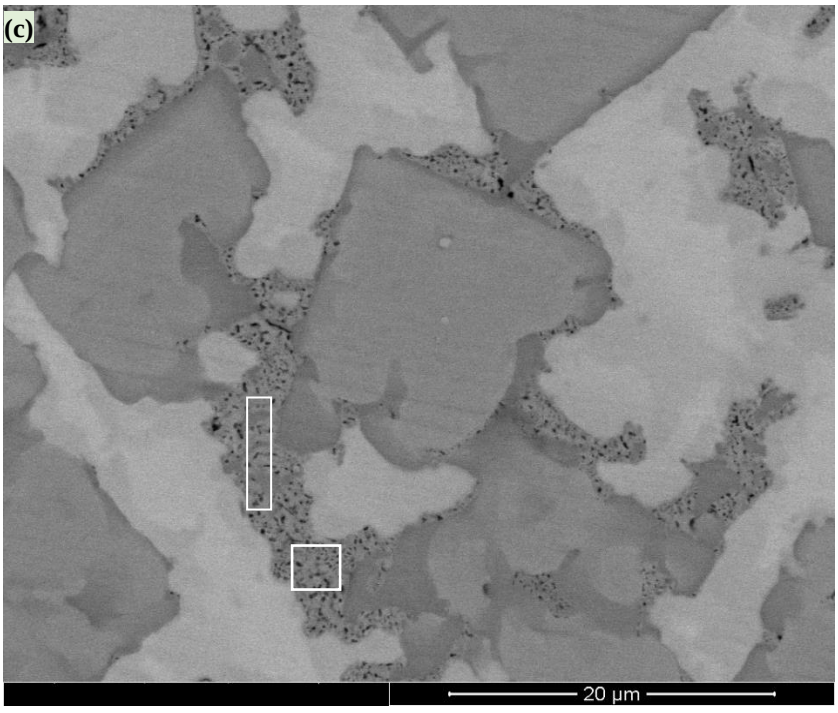
The cross section microstructure of the oxidised alloy ZX8 at 800 °C is shown in Figure 9.23. A very thin (Figure 24a) and porous (Figure 25) oxide scale was formed on the surface of the oxidised specimen. Similar to the alloy ZX7, the scale was composed of two oxides of different contrasts (see Figure 9.24). The oxygen diffusion zone in the alloy was also very thin (~10 µm) The Nb_3Sn and Nb_5Si_3 had micro-cracks in this area. A Sn rich area was found between the scale and Nb_3Sn in the oxygen diffusion zone which agrees with the alloys ZX4 and ZX6. As shown in Figure 9.23,

the bulk microstructure had been contaminated. This is believed to be linked with the formation of Nb_{ss} in the microstructure in areas where (as we shall see below) the Si + Al + Sn content was close to the composition of the Nb-Si binary, in other words it is believed that during the exposure to 800 °C a lamellar Nb_{ss} + Nb_5Si_3 formed, where the Nb_{ss} was contaminated by oxygen. Thus, it is suggested that a structure consisting of Nb_{ss} + Nb_5Si_3 was formed at 800 °C were the Nb_{ss} was oxidised (see rectangular in Figure 9.23c and d).

The Nb_5Si_3 in the bulk had Ti rich areas that exhibited darker contrast Figure 9.23b and c. This is also believed to have been the case for the Nb_3Sn phase which was also enriched in Ti at the edge of grains and showed a slightly darker contrast, as seen in Figure 9.23c.




(b)
Nb5Si3
Nb3Sn
Nbss + Nb5Si3
50 μm


(c)
20 μm

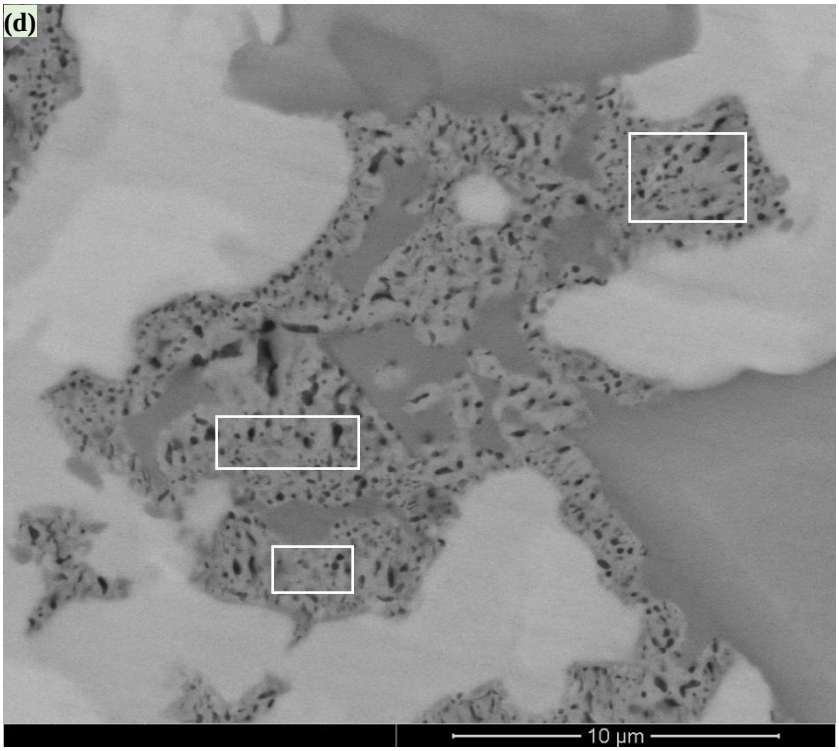


Figure 9.24 BSE images of the microstructure of the oxidised alloy ZX8 at 800 °C, (a) low magnification, (b) bulk area, (c) high magnification of the bulk area, (d) details of Nb_{ss}+Nb_5Si_3 eutectic.

The two oxide types were analysed by WDS, and the analysis data is given in Table 9.7. Similar to that of the alloy ZX7, the light grey oxide was Nb rich, and the darker contrast oxide was Nb-Si rich.

Table 9.7 The WDS analysis (at.%) of the oxides in the scale formed on the alloy ZX8 at 800 °C.

Phase	Nb	Ti	Si	Cr	Al	Sn	O
Nb rich oxide	19.66	8.83	0.62	4.67	1.46	0.17	64.59
Nb-Si rich oxide	15.33	6.92	10.72	0.66	1.55	0.18	64.64

As seen in Table 9.8, the oxygen concentration in the Nb_5Si_3 and Nb_3Sn phases in the diffusion zone was low compared with that in the Nb_{ss} in the DZ in the alloy ZX7 (Table 9.4) with the exception of Cr, the other alloying elements showed similar compositions with the Nb_5Si_3 and Nb_3Sn phases in the same area of the oxidised alloy ZX6 (see Table 8.21).

Table 9.8 The WDS analysis (at.%) of the phases in the oxygen diffusion zone of the alloys ZX8 at 800 °C.

Phase	Nb	Ti	Si	Cr	Al	Sn	O
Nb_5Si_3	44.76	15.68	28.08	1.18	4.69	2.06	3.55
Nb_3Sn	52.04	19.54	3.16	3.78	3.55	8.94	8.99

The WDS analysis of the phases in the bulk microstructure is shown in Table 9.9. In what was suggested to be a contaminated fine Nb_{ss} + Nb_5Si_3 microstructure (see above), the Si + Al + Sn concentration was around 17 at.%, which is close to the Nb_{ss} + Nb_5Si_3 microstructure in the bulk area of the oxidised alloy ZX6 (~ 18 at.%). The Si + Al + Sn concentration in the Nb_3Sn phase in the oxidised alloy ZX8 is around 16 at.% which is also very similar to that of the Nb_3Sn in the oxidised alloy ZX6 (~ 17 at.%). The Cr rich Laves phase which was observed in the cast and heat treated microstructure of the alloy ZX8 was present in the bulk of the oxidised alloy. Due to its similar contrast to the Nb_5Si_3 and its small size, it was not possible hard to apply spot WDS analysis of the Laves phase. X-ray elemental maps in Figure 9.25 showed Cr rich areas, which were attributed to the Laves phase.

Table 9.9 The WDS analysis (at.%) of the phases in the bulk microstructure of the alloy ZX8 at 800 °C.

Phase	Nb	Ti	Si	Cr	Al	Sn	O
Nb_5Si_3	40.94	19.73	32.30	1.23	0.87	1.02	3.91
Nb_3Sn	54.49	19.59	2.44	3.83	5.17	8.32	6.16
Nb_{ss} + Nb_5Si_3	37.22	29.52	7.73	8.18	6.40	3.04	7.92

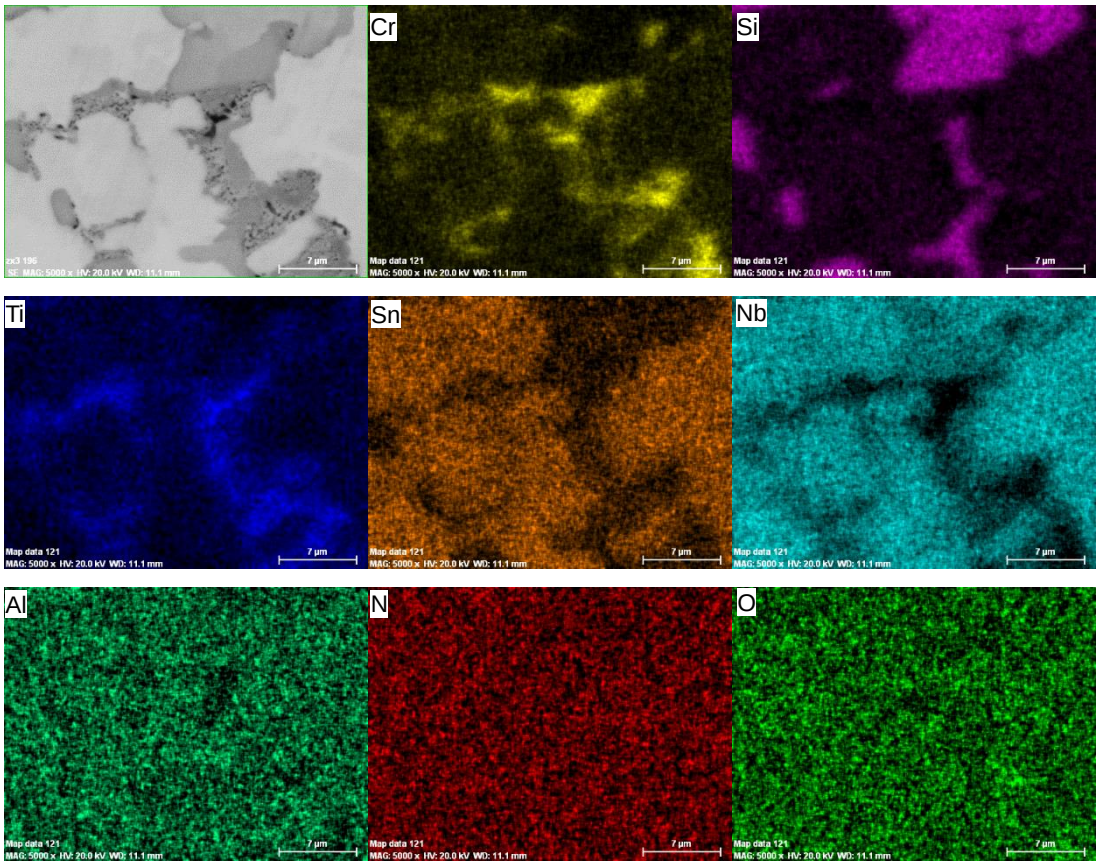
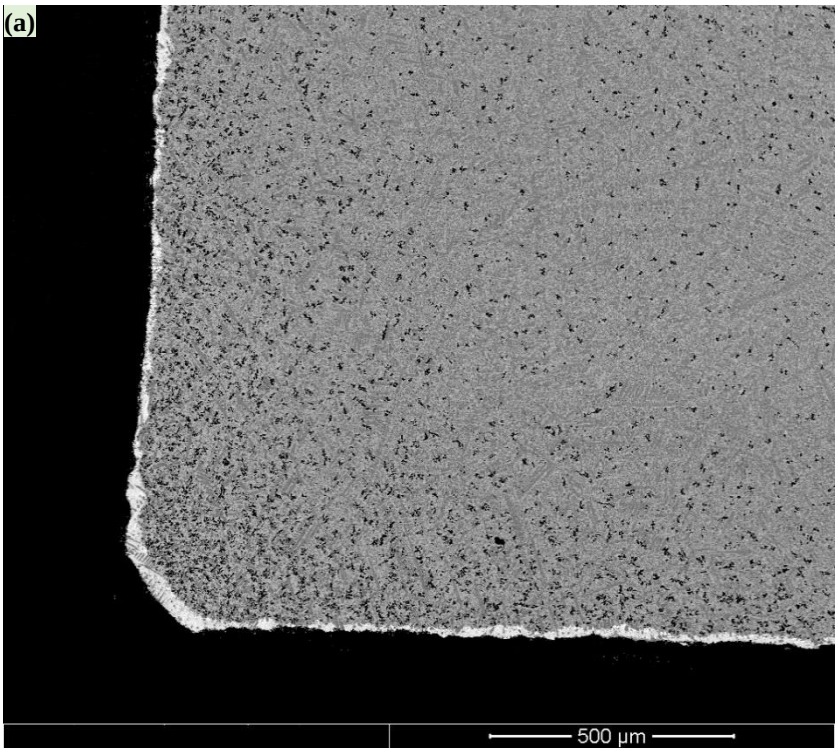
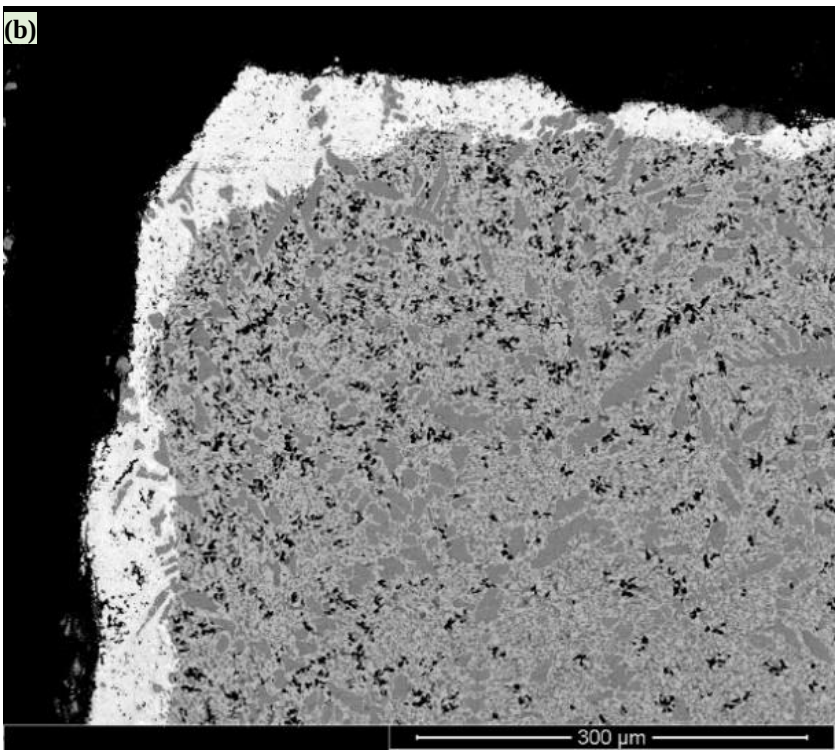


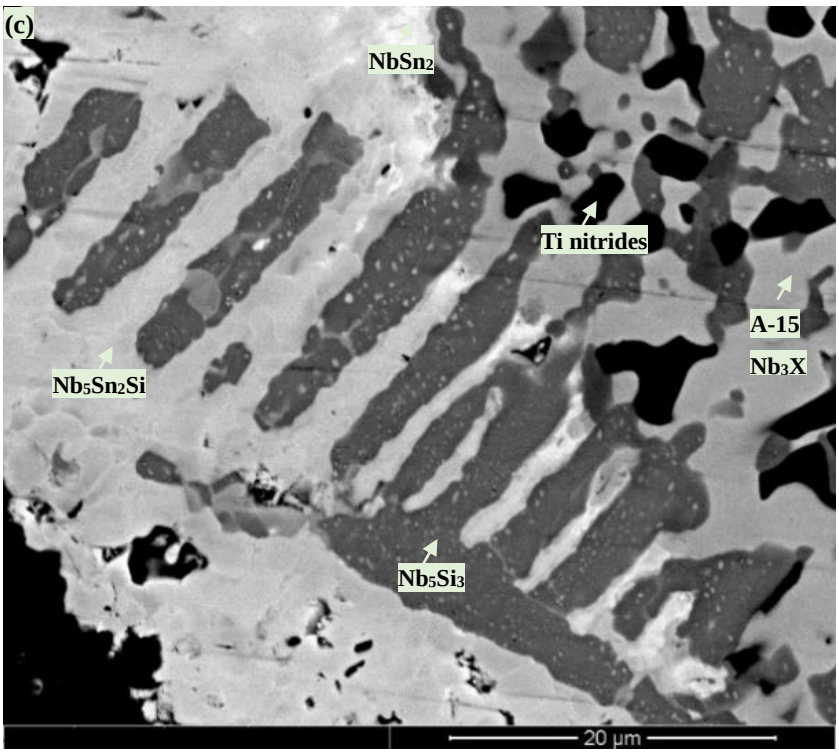
Figure 9.25 X-ray elemental maps showing the Cr rich Laves phase in the microstructure of the oxidised alloy ZX8 at 800 °C.

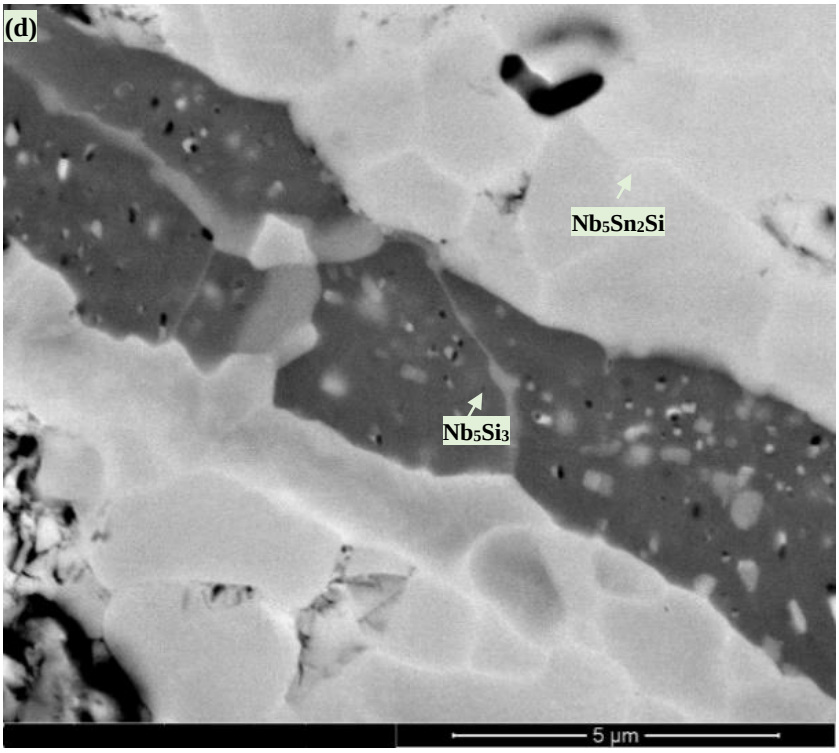
9.3.3 Microstructure of Oxidised alloys ZX7 and ZX8 at 1200 °C

The cross section microstructure of the oxidised alloy ZX7 at 1200 °C is shown in Figure 9.26. A bright contrast continuous layer of varying thickness, particularly near the corner where it was noticeably thicker, was observed on the edge of the oxidised specimen (Figures 9.26a, b and 9.27), similar to the previously discussed alloys. The thickness of the layer was around 30 µm despite the Sn addition in the alloy being only 2 at.%. At the higher magnification image in Figure 9.26c, the Sn rich area is seen with different contrast, indicating higher and lower Sn concentration. There were also changes inside the Nb_5Si_3 (see Figure 9.26d). Similar features were observed inside Nb_5Si_3 grains in the bulk, see Figures 9.26e and f. The X-ray maps in Figure 9.28 show that some of the feature inside the Nb_5Si_3 were Sn rich. The Sn rich area was analysed using WDS and the results are given in Figure 9.29 and Table 9.10.


(a)
500 μm


(b)
300 μm


(c)
NbSn2
Ti nitrides
A-15
Nb3X
Nb5Sn2Si
Nb5Si3
20 μm


(d)
Nb5Sn2Si
Nb5Si3
5 μm

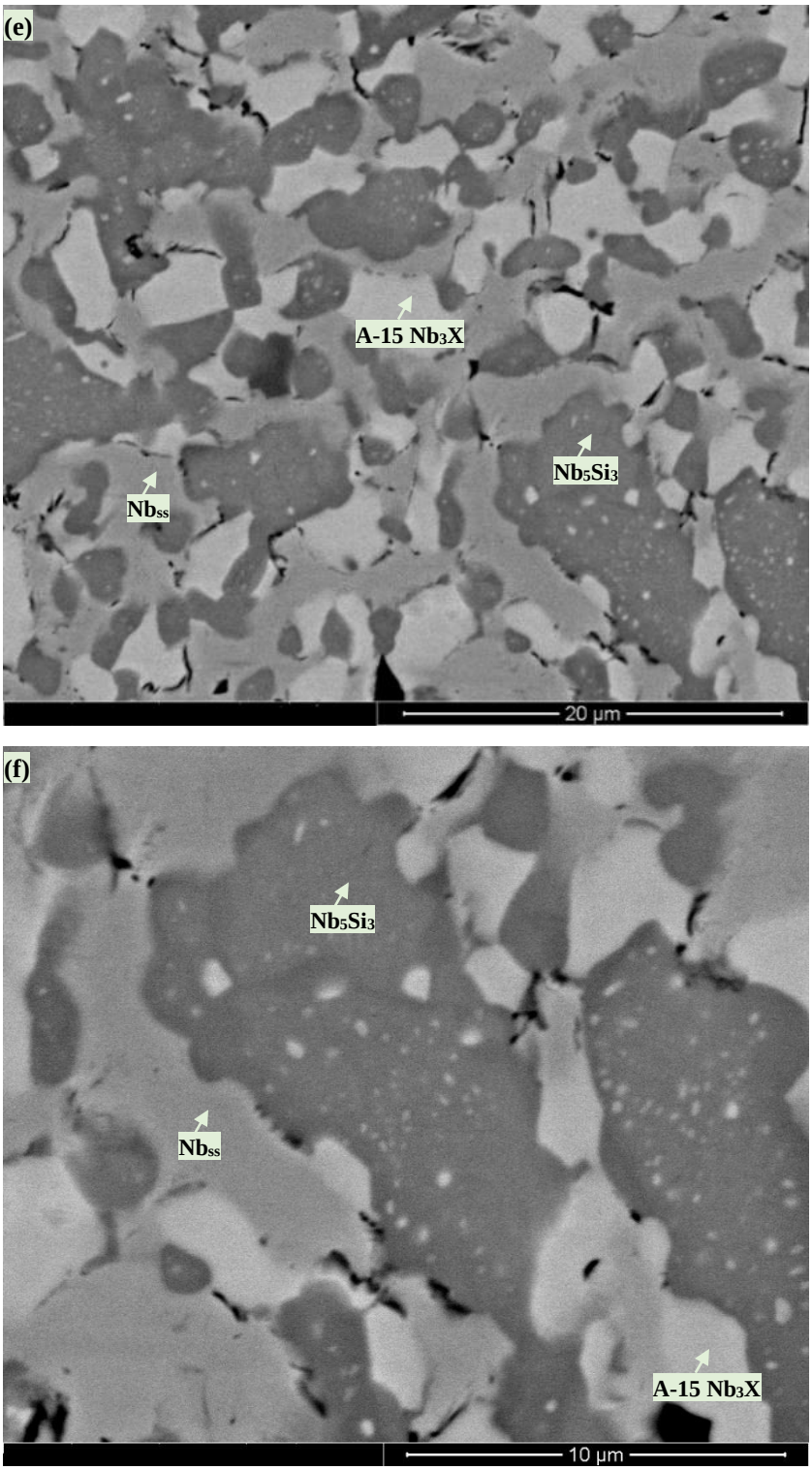


Figure 9.26 BSE images of the microstructure showing (a)(b) the Sn rich area at low magnifications, (c)(d) Phases in the Sn rich area, (e)(f) the microstructure of the bulk of the oxidised ZX7 at 1200 °C.

In the bulk microstructure, the Nb_5Si_3, Nb_3Sn and Nb_{ss} phases were present as well as

some Lave phase. The X-ray maps of the Sn rich area in Figure 9.27 and bulk of the alloy confirmed the presence of Laves phase and areas very rich in Sn (very strong contrast in the Sn map in the Sn rich area).

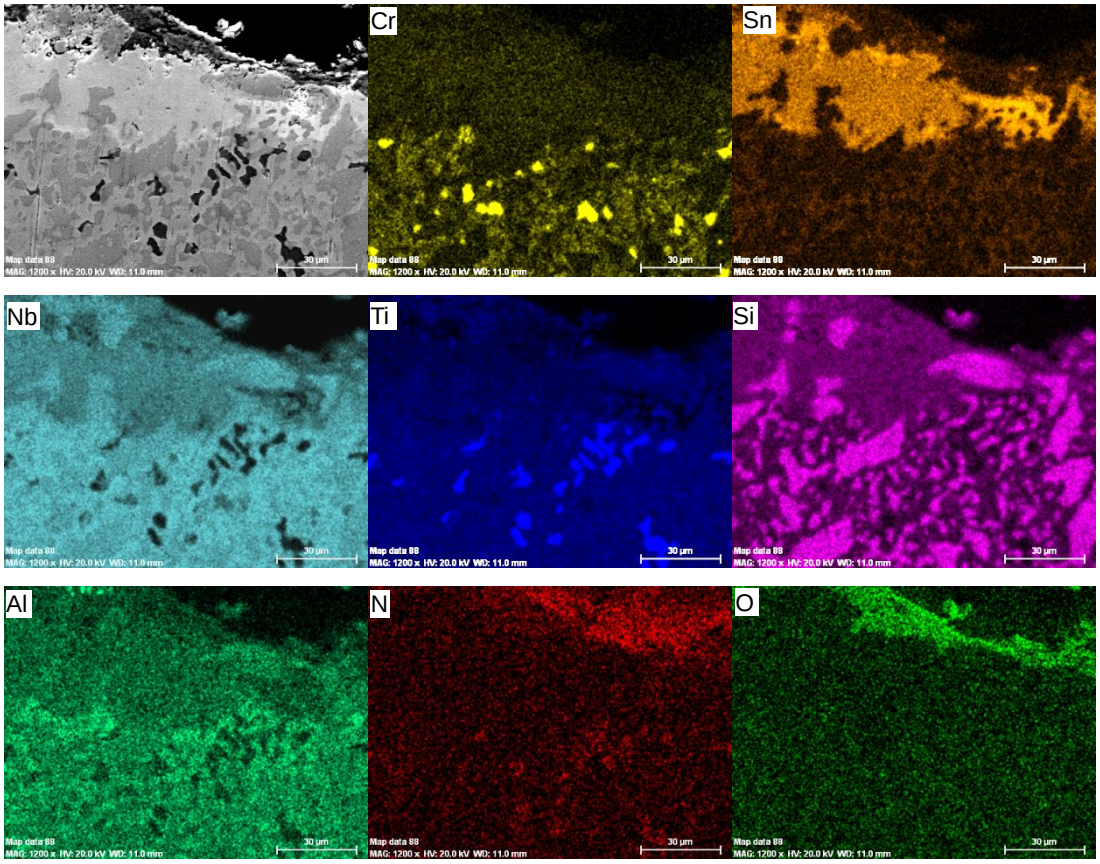


Figure 9.27 X-ray elemental map on the Sn rich region and bulk area of the alloy ZX7 at 1200°C.

The WDS analysis data of the Sn rich area is shown in Table 9.10. Spots 1 and 2 analyse corresponding to the Nb_5Si_3 with average Si + Al + Sn 35.47 at.%. Spot 3 analysis was from the extremely bright contrast phase in the Sn rich area, with around 61 at.% Sn. This high Sn content phase could be the $NbSn_2$ compound, with 9.3at.% Ti substituting for Nb. The concentration of Si, Cr and Al were very low in this compound. The Spot 4 analysis was from a Sn rich phase with 22 at.% Sn and 10 at.% Si, which is believed to be the oxidised Nb_5Sn_2Si compound.

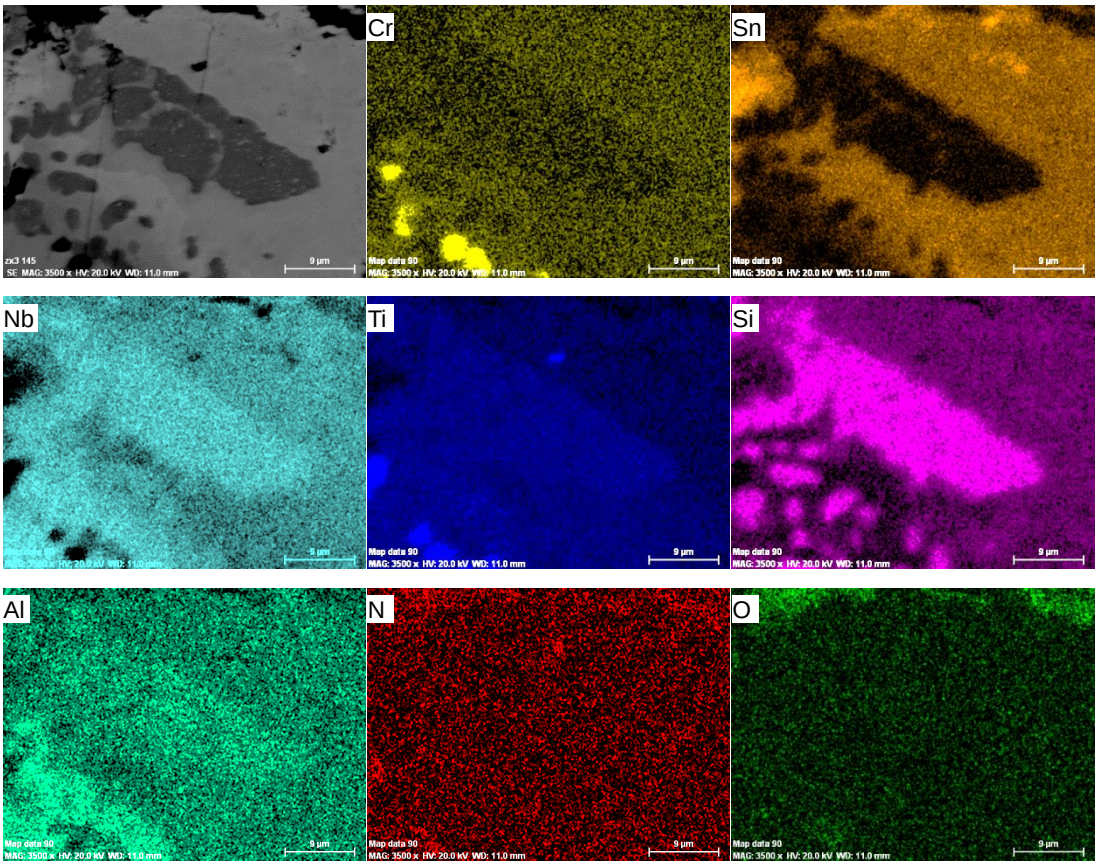


Figure 9.28 X-ray elemental map on the Sn rich area of the alloy ZX7 at 1200°C.

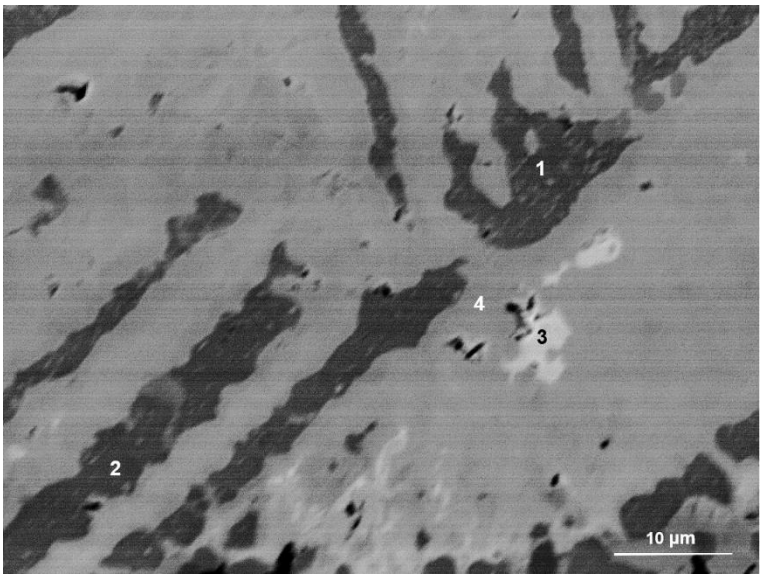


Figure 9.29 The microstructure of Sn rich area in the alloy ZX7.

Table 9.10 WDS analysis (at.%) of the phases in the Sn rich region of the alloy ZX7 at 1200 °C. For the spot number see Figure 9.29.

	Nb	Ti	Si	Cr	Al	Sn	O
Spot 1	43.38	15.94	29.95	0.89	3.43	1.59	4.82
Spot 2	43.94	16.19	31.35	0.49	3.28	1.12	3.63
Spot 3	23.43	9.24	0.40	0.39	0.04	**60.86**	5.63
Spot 4	41.75	15.93	10.69	2.47	2.10	22.48	4.58

The transition from the Sn rich area to bulk area of the oxidised alloy was studied using WDS analysis. As seen in Figure 9.30 and Table 9.11, some spot analyses were done on the Nb_5Si_3 in the Sn rich area. Comparing the data of the spot 7, 8, 9 and 10 shows that all correspond to the normal Nb_5Si_3 in the Sn rich area with Si + Al + Sn in the range 35.1 to 36.7 at.%, very close to the stoichiometric Si content of unalloyed Nb_5Si_3. The Sn rich Nb_5Si_3 from spot analysis 10 is consistent with the formation of Sn rich area inside the Nb_5Si_3, as seen in Figures 9.26 and 9.28 and would suggest that in the case of the alloy ZX7, the 5-3 silicide contributed to the formation of the Sn rich area. The Nb_5Si_3 grains from spot analyses 7 and 9 provide further evidence for the formation of Sn rich areas inside the Nb_5Si_3, some kind of partitioning of the Nb_5Si_3 grain in subgrains with Sn rich subgrain "boundary areas", see also Figure 9.28.

The data of spots 11 and 12 analyses would suggest the presence of oxidised Nb_5Sn_2Si. Spots 13 and 14 are closer to the interface (dashed line between the two areas) and are richer in Sn with Sn: (Si+ Al) ratio close to 2:1, and could also be oxidised Nb_5Sn_2Si since Nb_5Sn_2Si and Nb_5Sn_2Al have the same structure.

Below the Sn rich area, the Nb_5Si_3 (spot 15) and Al rich A15 intermetallic Nb_3Al (spots 16 and 17) were analysed. The Al concentration in the latter phase was around 10 at.% and the Al + Si + Sn was 18 at.%. The Laves phase was also detected in this area (spot 18) and contained 49.8 at.% Cr, and Cr + Al + Si + Sn = 57.9 at.%.

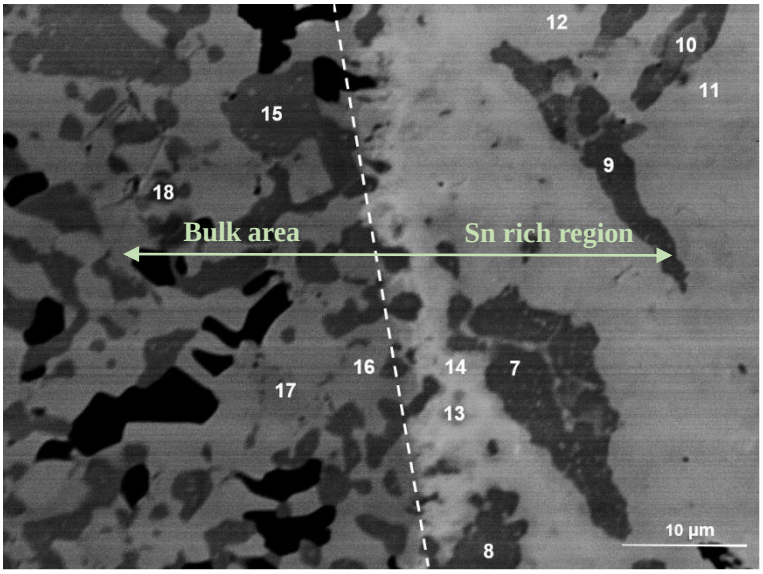


Figure 9.30 The microstructure of the transition area between the bulk and Sn rich area in the alloy ZX7 after oxidation at 1200 °C.

Table 9.11 WDS spot analysis (at.%) of the phases in the oxygen diffusion zone in the alloy ZX7 oxidised at 1200 °C.

Nb_5Si_3	Nb	Ti	Si	Cr	Al	Sn	O
Spot 7	43.07	16.02	30.58	0.56	3.30	1.23	5.24
Spot 8	43.18	16.66	32.11	0.29	2.69	1.02	4.05
Spot 9	43.79	16.31	31.23	0.49	2.99	1.52	3.67
Spot 10	45.96	10.85	28.90	0.82	0.76	6.99	5.72
Spot 15	41.91	17.99	33.07	0.30	1.36	0.43	4.94
Nb_5Si_2Sn	Nb	Ti	Si	Cr	Al	Sn	O
Spot 11	42.86	13.39	11.99	2.76	1.78	19.91	7.31
Spot 12	42.40	14.67	12.79	3.02	1.74	19.81	5.57
Spot 13	45.57	13.24	6.50	1.18	5.90	21.27	6.34
Spot 14	41.32	16.57	7.50	1.72	5.13	21.63	6.13
A15 Nb_3X	Nb	Ti	Si	Cr	Al	Sn	O
Spot 16	55.65	17.28	2.73	4.60	10.05	3.58	6.11
Spot 17	54.79	18.83	2.05	4.68	9.00	3.27	7.38
Laves Phase	Nb	Ti	Si	Cr	Al	Sn	O
Spot 18	28.42	9.96	5.82	**49.81**	2.00	0.31	3.68

The oxides forming the scale were three types, as indicated in Figure 9.31 and Table 9.12. The oxides were Nb rich, Ti rich and Nb-Si rich according to the WDS data. The oxygen content of all oxides would suggest that they were of the MO_2 type.

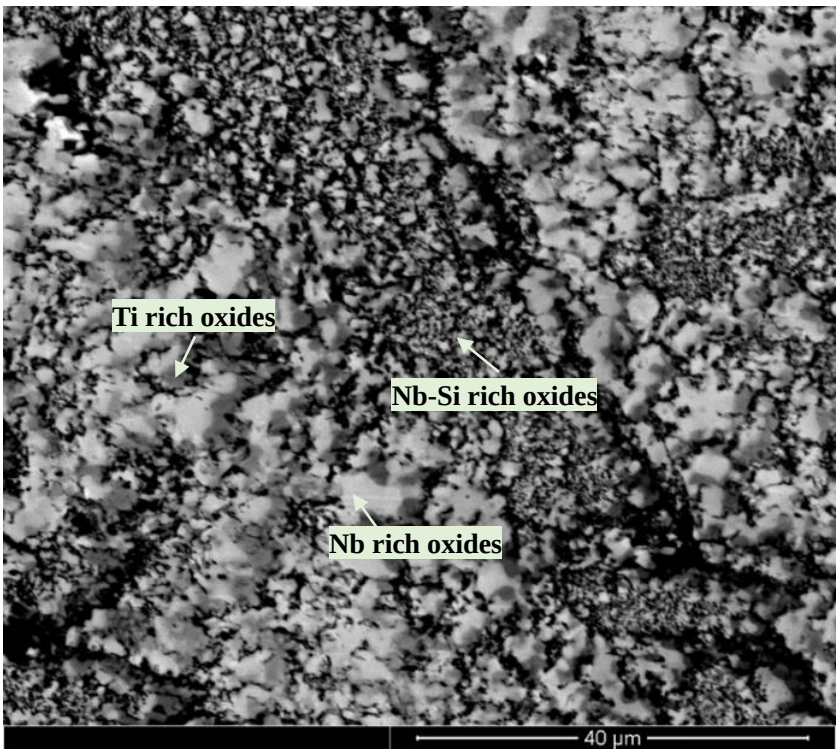
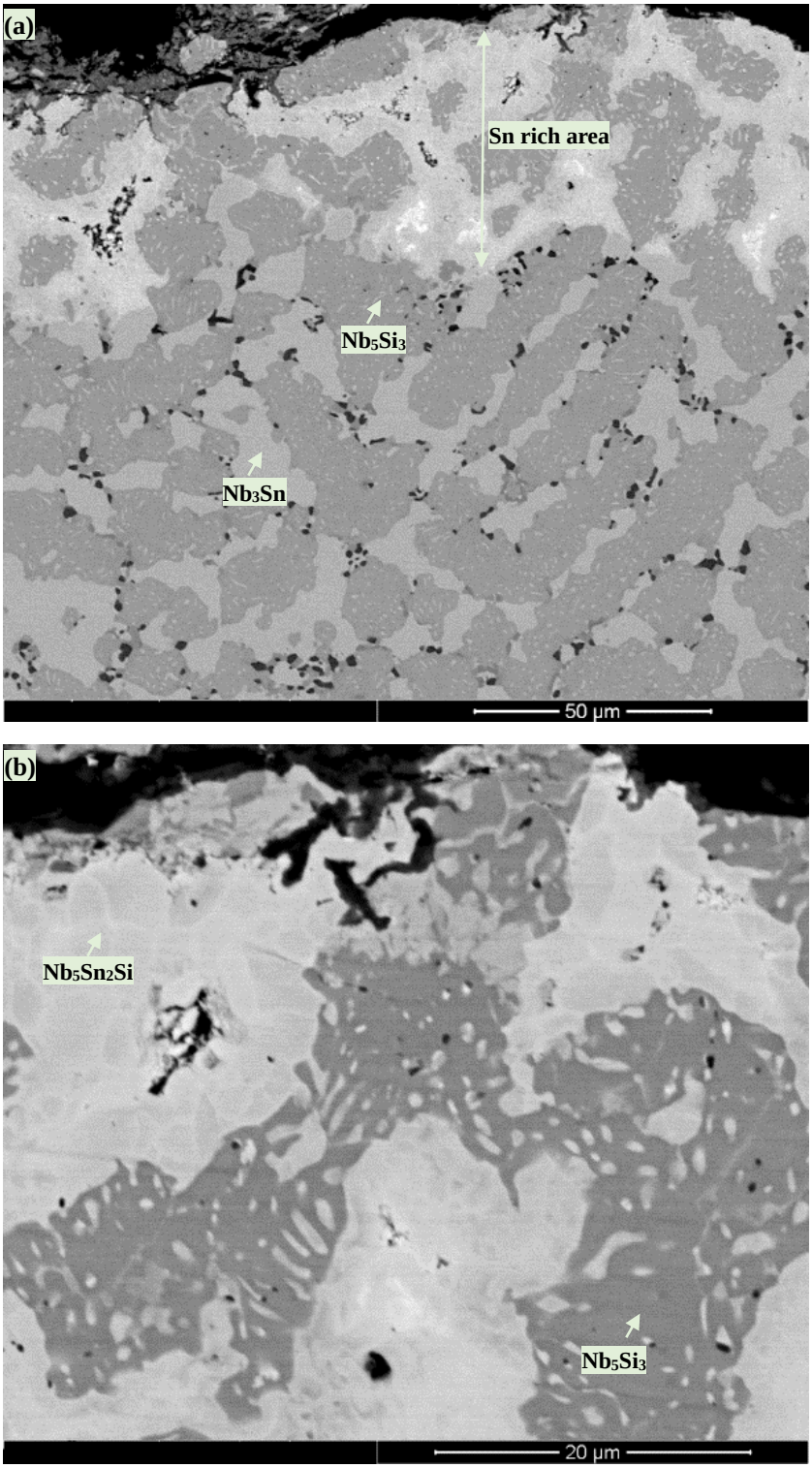


Figure 9.31 Cross section microstructure of the oxide scale formed on the alloy ZX7 at 1200 °C.

Table 9.12 WDS spot analysis data (at.%) of the oxides in the scale of the alloy ZX7.

	Nb	Ti	Si	Cr	Al	Sn	O
Nb rich oxide	23.20	7.05	0.11	0.18	1.36	0.01	68.09
Nb rich oxide	26.79	4.81	0.05	0.17	0.29	0.01	67.88
Ti rich oxide	8.26	15.98	1.51	4.31	3.14	0.23	66.57
Ti rich oxide	9.12	14.98	1.13	3.56	4.38	0.16	66.67
Nb-Si rich oxide	12.43	4.48	13.36	0.85	1.01	0.02	67.85
Nb-Si rich oxide	14.50	5.30	13.33	0.38	0.79	0.02	65.68
Nb-Si rich oxide	16.19	3.73	11.54	0.15	0.41	0.00	67.98

A cross section of the microstructure of the oxidised alloy ZX8 at 1200 °C is shown in Figure 9.32. The Sn rich area of this alloy was around 50 µm (see Figure 9.32a. Inside the Sn rich area similar features were observed as in the oxidised alloy ZX7 at 1200 °C. The Cr rich Laves phase was observed in the bulk (Figure 9.33) where Ti nitrides were also observed, as seen in Figure 9.32c and d. The line scan in Figure 9.34 shows Sn rich area on either side of Nb_5Si_3. The X-ray maps in Figure 9.35 are of the bulk area and indicate the presence of the Cr rich Laves phase.


(a)
Sn rich area
Nb5Si3
Nb3Sn
50 μm
(b)
Nb5Sn2Si
Nb5Si3
20 μm

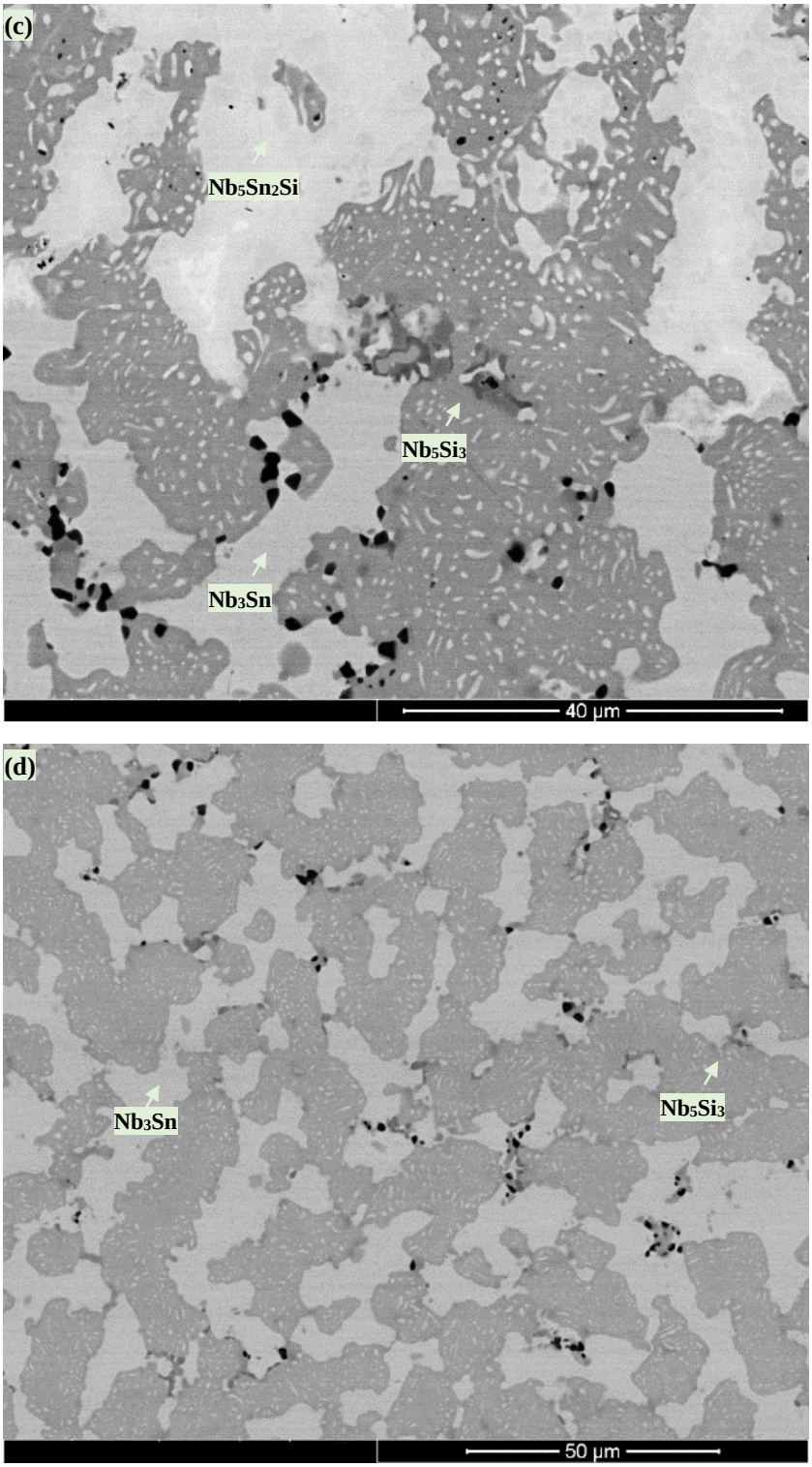


Figure 9.32 Cross section microstructure of the alloy ZX8 at 1200 °C (a) Sn rich area and bulk, (b) high magnification of the Sn rich area, (c) interface of Sn rich area and bulk (d) bulk.

The Sn rich area was studied using WDS analysis. The spot indication see Figure 9.36 and Table 9.13. Spot 10 analysis corresponds to oxidised Nb_5Sn_2Si. Spot 11 and 13

analysis correspond to Nb_5Si_3 and the higher Sn concentration in spot analysis 11 is attributed to the Sn rich area forming in the silicide while in spot 13 (normal Nb_5Si_3) the Sn concentration is around 1 at.% and formation of Sn rich area has not occurred yet. Spot 13 is the normal Nb_5Si_3 phase where Sn concentration is around 1 at.%. Spot 12 analysis shows a very rich in Sn phase with 40 at.% Sn. This phase however is very small and thus caution is required as it is likely that the analysis interfered with the surrounding phase and this must have had an effect on the Sn concentration (the surrounding phase (spot 10) is also rich in Sn). Further towards the bulk, the Nb_3Sn phase was observed (spot 14).

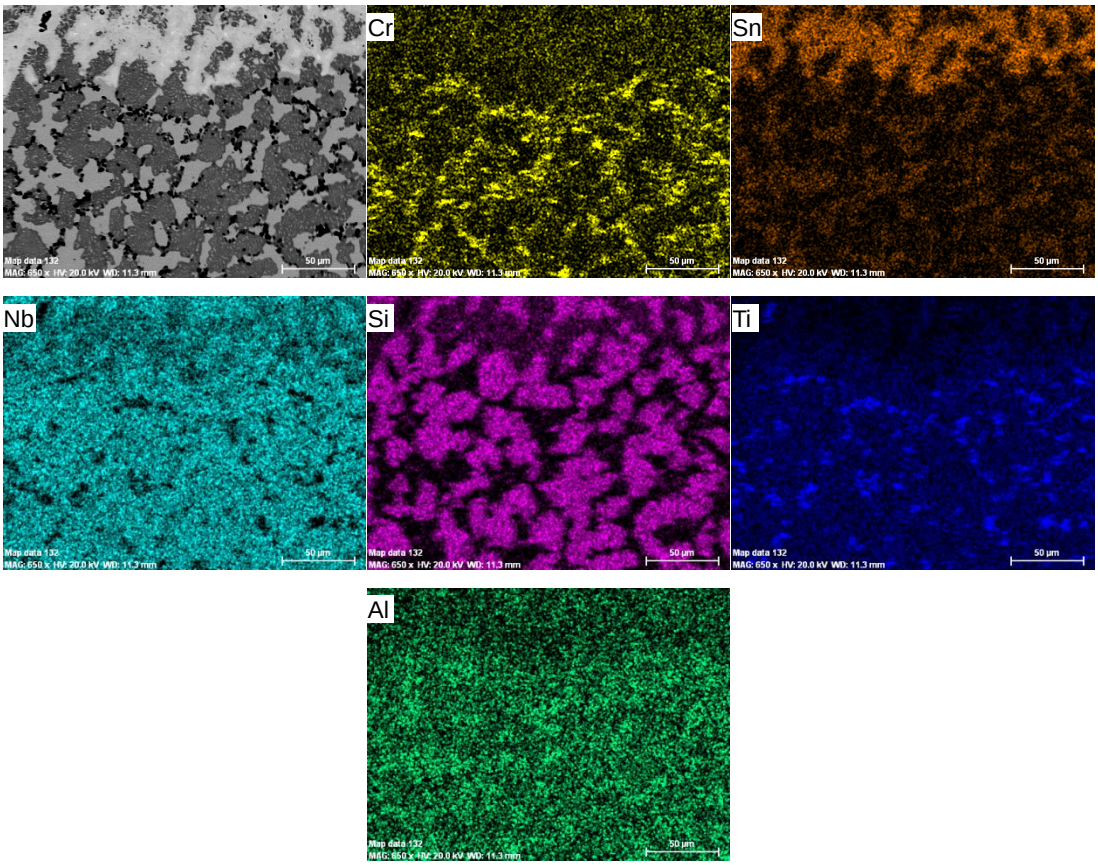


Figure 9.33 BSE image and X-ray elemental maps of the Sn rich area of alloy ZX8 at 1200 °C.

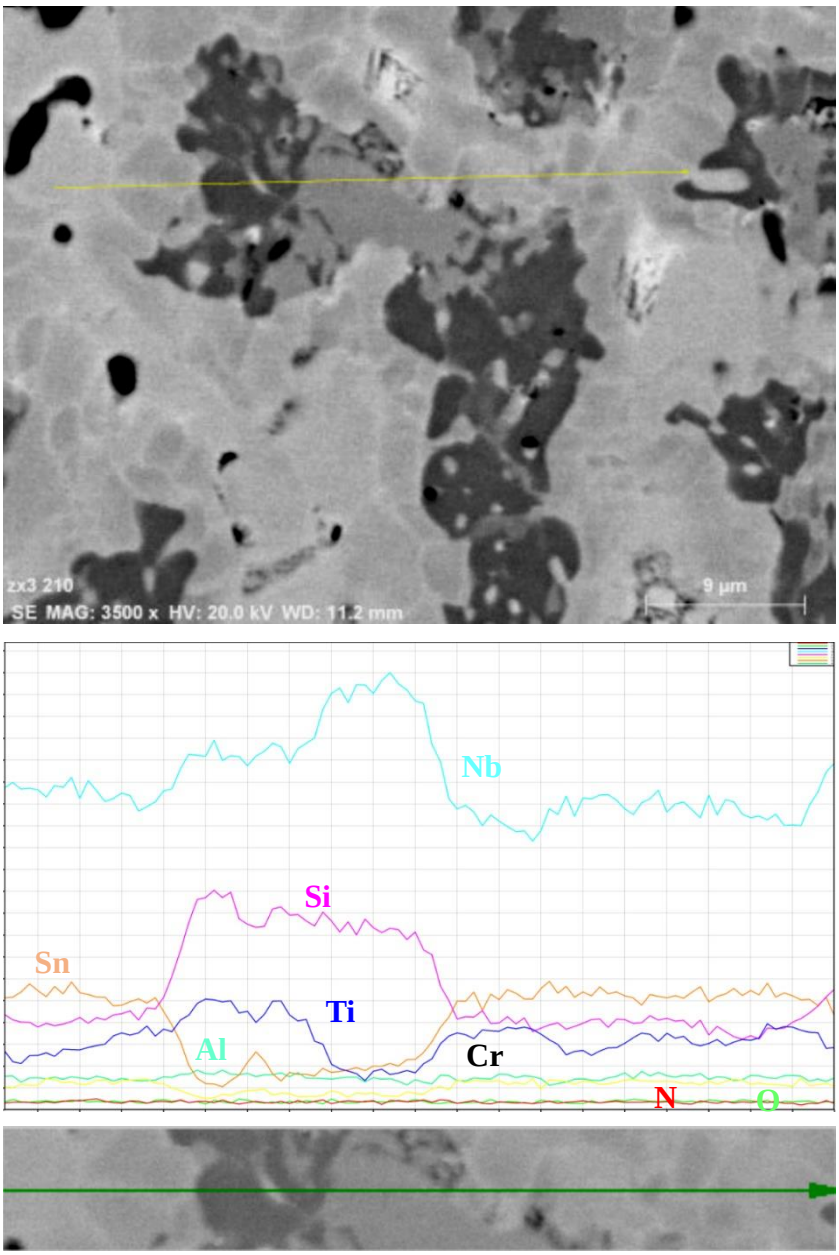


Figure 9.34 BSE image and line scans of indicated elements in Sn rich area formed in the alloy ZX8 after oxidation at 1200 ℃.

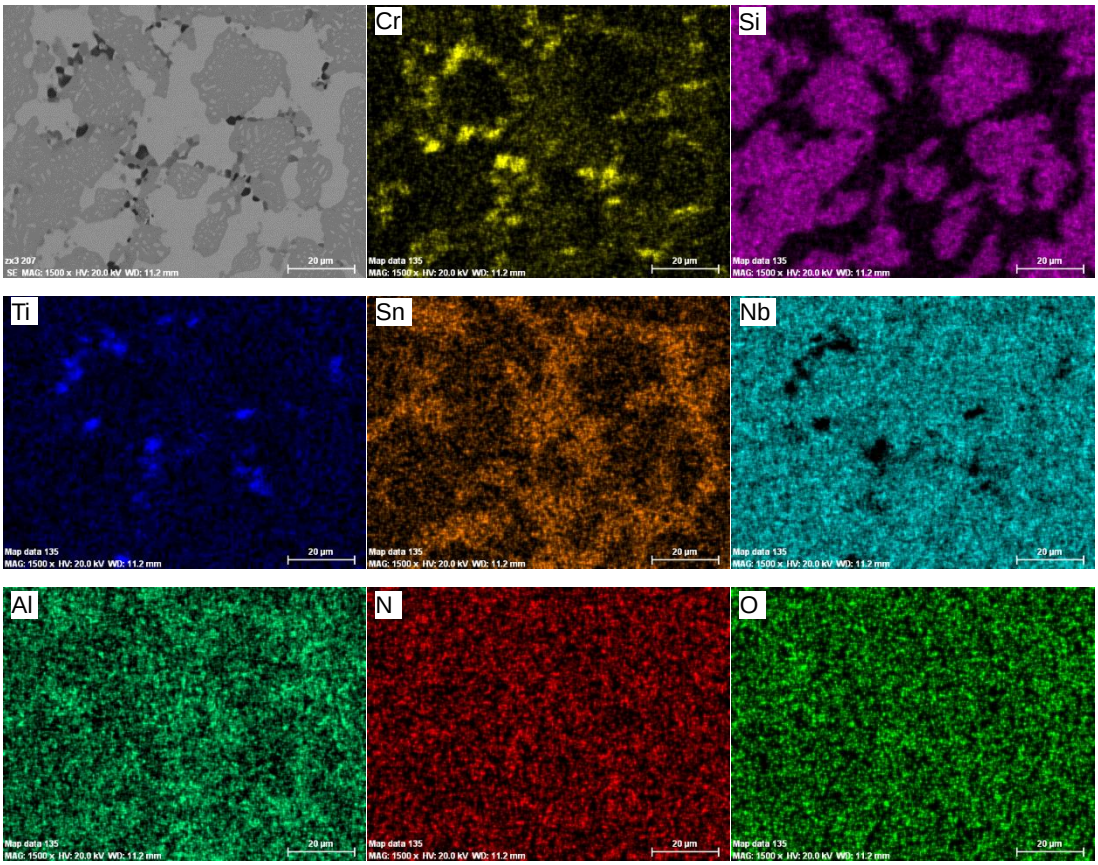


Figure 9.35 X-ray elemental maps of the bulk area of the alloy ZX8 at 1200 °C.

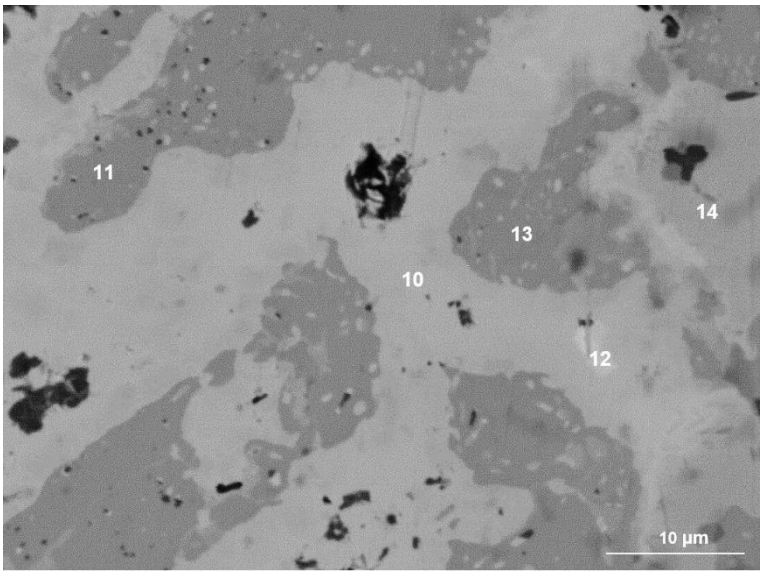


Figure 9.36 BSE image of the microstructure of the Sn rich area of the alloy ZX8 at 1200 °C.

Table 9.13 WDS analysis data (at.%) of the oxygen diffusion zone of the alloy ZX8 at 1200 °C.

	Nb	Ti	Si	Cr	Al	Sn	O
Spot 10	44.28	11.65	8.68	3.02	1.47	25.05	5.85
Spot 11	46.10	13.35	29.80	0.57	1.09	4.44	4.65
Spot 12	35.67	14.16	1.36	3.43	0.06	**40.39**	4.93
Spot 13	42.76	19.08	30.08	0.89	1.64	1.07	4.48
Spot 14	49.26	21.89	1.30	4.68	7.83	9.25	5.77

In the bulk area, the Nb_5Si_3, Nb_3Sn and Laves phase were analysed by WDS, as shown in Table 9.14. It is notice the Lave phase contained 26.2 at.% Cr which is low than the Cr rich lave phase in the oxidised alloy ZX7(49.8 at.% Cr). However, the Si concentration in this feature is close to 15 at.% which is higher than that of the ZX7.

Table 9.14 WDS analysis data (at.%) of the phases in the bulk area of the alloy ZX8 at 1200 °C.

Phase	Nb	Ti	Si	Cr	Al	Sn	O
Nb_5Si_3	42.03	18.95	30.20	0.74	2.84	1.09	4.15
Nb_3Sn	51.75	21.78	1.51	4.34	6.41	8.18	6.03

The microstructure of the scale was similar to that of the ZX7 at 1200 °C (see Figure 9.37). Nb rich, Ti rich and Nb-Si rich oxides were detected, and their compositions were analysed by WDS and are given in Table 9.15. The O concentration of the Nb based oxide was 71 at.%, which could indicate that the oxide was a Niobate. The Ti based oxide was closer to the composition of TiO_2.

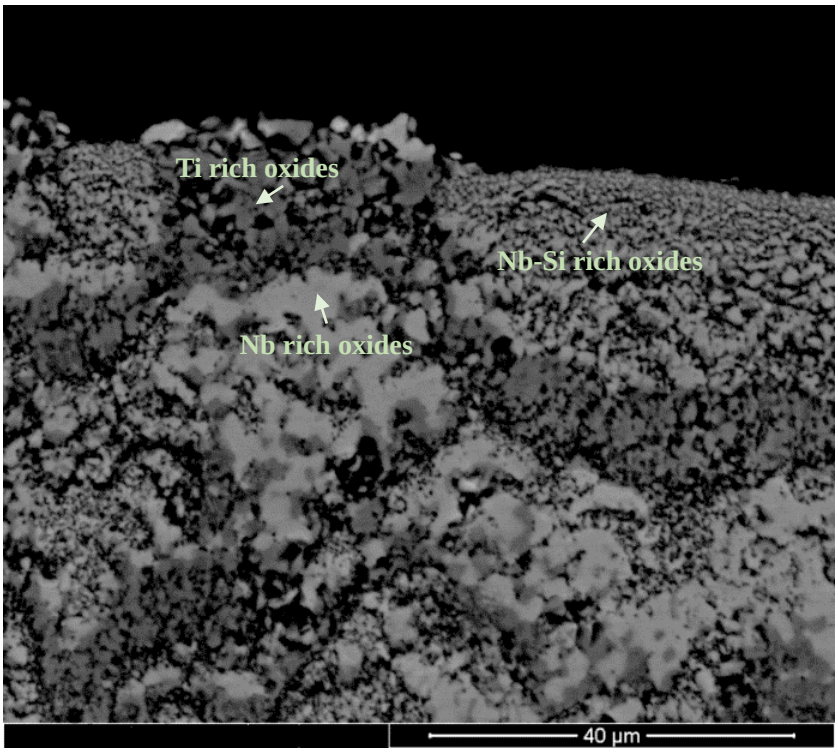


Figure 9.37 BSE image of the microstructure of the oxide scale of the alloy ZX8 at 1200 °C.

Table 9.15 WDS analysis (at.%) of the oxides of the scale of the alloy ZX8 at 1200°C.

	Nb	Ti	Si	Cr	Al	Sn	O
Nb rich oxides	20.62	7.68	0.09	0.22	0.20	0.00	71.19
Ti rich oxides	7.23	17.63	0.15	3.46	1.88	0.35	69.29
Nb-Si rich oxides	14.33	5.40	8.80	0.53	0.53	0.01	70.40

9.4 Discussion

9.4.1 Introduction

Below the results for macrosegregation of Si in the alloys ZX7 and ZX8 are discussed, then phase stability and transformations are considered and finally oxidation behaviour at 800 °C and 1200 °C is studied.

9.4.2 Macrosegregation of Si

In the cast button ingot of the alloy ZX7 there was macrosegregation of Si and in the case of the alloy ZX8 there was macrosegregation of Si and all other alloying elements except Sn. In the alloy ZX8 the macrosegregation of Si was marginally more severe compared with that of Ti in the same alloy (MACS values of 10 and 9.7 at.%, respectively). For both these elements their MACS values were the highest measured among the alloys studied in this thesis. The severe macrosegregation in ZX8 resulted in highly inhomogeneous microstructures, as shown in Figures 9.9 to 9.11.

In the case of the alloy ZX8 the highest MACS values were observed between the bulk (C_{min}^{i}) and top (C_{max}^{i}) of the ingot, with the exception of Si where the opposite was the case i.e., between areas where the melt had experienced different cooling rates. In these two areas of the ingot the cast microstructure of the alloy ZX8 exhibited severe chemical inhomegeneities in the scale of the individual phases (see Figures 9.9 and 9.10), which could explain the high MACS values.

In the case of the alloys ZX7 and ZX8 the macrosegregation of Si was significantly different. In the Table 9.16 the aforementioned parameters of the alloys ZX7 and ZX8 are given and those of the alloy KZ5 (Nb-24Ti-18Si-5Al-5Cr (nominal composition) in [68]) are included for comparison purposes. The Table 9.16 shows (i) that when only the alloys ZX7 and ZX8 are compared the aforementioned trends are followed by the parameters T_m, ΔH_m, T_m^{sd}, and T_m^{sd}/T_m^{sp} , which decreased with increasing

MACS, and T_m^{sp} , which increased with increasing MACS and (ii) that when the alloys ZX7 and ZX8 are compared with the alloy KZ5 then only the parameters T_m and T_m^{sd} follow the aforementioned trends. The (ii) was also the case in the alloys ZX3 and ZX4 when compared with the alloy KZ4 (Nb-24Ti-18Si-5Cr (nominal composition) in [68]), which could be an indication that Cr played a key role in the macrosegretation of elements in the alloy ZX8.

Table 9.16 Alloy parameters for the macrosegregation of Si in the cast alloys ZX7 and ZX8.

alloy	ΔH_m kJ/mol	T_m (K)	$\Delta H_m/T_m$ J/molK	$\Delta H_m^{sd}/\Delta H_m^{sp}$	T_m^{sd} (K)	T_m^{sp} (K)	T_m^{sd}/T_m^{sp}	$[\Delta H_m/T_m]x[\Delta H_m^{sd}/\Delta H_m^{sp}]^{-1}$	MACS (at.%)
ZX8	**26.86**	**2152**	12.48	1.84	**1794**	**358**	**5**	6.78	10
ZX7	**29.45**	**2214**	13.53	1.79	**1889**	**325**	**5.82**	7.56	3
KZ5	27.5	**2239**	12.28	2.05	**1909**	330	5.78	5.99	1.3

However, if the data for the alloy ZX6 (Al present, no Cr) were to be included in the comparison of alloys (the alloy ZX6 contained the A15 intermetallic in its microstructure like the other alloys in Table 9.17) then the ranking shown in the Table 9.17 is destroyed. This could suggest that the parameters used in the Table 9.17 cannot catch how the synergy of Al with Sn and Cr in an alloy affects the macrosegregation of Si. Another reason for this could be that the potency of material parameter changes by a particular element when in synergy with other additions in Nb silicide based alloys is different for Sn and Al and Cr. The potency is strong regarding ΔH_m, $\Delta H_m/T_m$ and T_m^{sp} for Sn and T_m, $\Delta H_m/T_m$, $\Delta H_m^{sd}/\Delta H_m^{sp}$, T_m^{sd}, T_m^{sp} and T_m^{sd}/T_m^{sp} for both Al and Cr but weak for Sn regarding the parameters T_m, T_m^{sd} and T_m^{sd}/T_m^{sp} (see Table 3 in [78]). It is interesting that trends are followed by the latter three parameters in Table 9.17.

The alloys of this study with only 2 at.% Sn addition are compared for their MACS values of Si in the Table 9.18. It is noted that the aforementioned trends are followed by the parameters ΔH_m, $\Delta H_m^{sd}/\Delta H_m^{sp}$, T_m^{sp} and T_m^{sd}/T_m^{sp} but not by the parameter $[\Delta H_m/T_m] \times [\Delta H_m^{sd}/\Delta H_m^{sp}]^{-1}$ that follows the opposite trend, indicated in red in the

Table 9.18.

Table 9.17 Alloy parameters linked with macrosegregation of Si in the alloys ZX8, ZX4, NV6 and NV9.

alloy	ΔH_m kJ/mol	T_m (K)	$\Delta H_m/T_m$ J/molK	$\Delta H_m^{sd}/\Delta H_m^{sp}$	T_m^{sd} (K)	T_m^{sp} (K)	T_m^{sd}/T_m^{sp}	$[\Delta H_m/T_m]\times[\Delta H_m^{sd}/\Delta H_m^{sp}]^{-1}$	MACS (at.%)
ZX8	**26.86**	**2152**	12.48	**1.84**	**1794**	*358*	**5**	6.78	10
ZX4	**27.84**	**2205**	*12.63*	**1.85**	**1862**	*342*	**5.44**	*6.85*	7.3
NV6	**28**	**2241**	*12.49*	**1.98**	**1911**	*330*	**5.79**	*6.31*	5.5
NV9	**30.4**	**2454**	*12.39*	**2.1**	**2112**	342	**6.18**	*5.9*	2.5

Table 9.18 Alloy parameters linked with macrosegregation of Si in the cast alloys ZX3, ZX5, and ZX7.

alloy	ΔH_m kJ/mol	T_m (K)	$\Delta H_m/T_m$ J/molK	$\Delta H_m^{sd}/\Delta H_m^{sp}$	T_m^{sd} (K)	T_m^{sp} (K)	T_m^{sd}/T_m^{sp}	$[\Delta H_m/T_m]\times[\Delta H_m^{sd}/\Delta H_m^{sp}]^{-1}$	MACS (at.%)
ZX5	**28.1**	2215	12.68	**1.74**	1837	**377**	**4.87**	**7.29**	5.5
ZX3	**28.97**	2257	12.84	**1.74**	1896	**361**	**5.25**	**7.39**	3.6
ZX7	**29.45**	2214	13.53	**1.79**	1889	**325**	**5.82**	**7.56**	3

Considering the data in the latter two Tables and in the Tables 8.15 and 8.16, it is suggested that alloy design could consider the macro-segregation of Si in Nb silicide based alloys with Sn and Al and/or Cr via the parameters ΔH_m, $\Delta H_m^{sd}/\Delta H_m^{sp}$ and T_m^{sd}/T_m^{sp} with their trends as discussed in [78].

9.4.3 Phase stability in the alloy Nb-24Ti-18Si-5Al-5Cr-2Sn (ZX7)

The Si + Al + Sn content of the alloy ZX7 was 23 at.%. Considering Si and Al and Sn as equivalent, the alloy was hyper-eutectic according to the Nb-Si binary system. Thus, in the solidification of ZX7 the βNb_5Si_3 was the primary phase. The microstructures in the top and bulk of the cast alloy ZX7 would suggest that the solidification path in these areas of the ingot was $L \rightarrow L + \beta Nb_5Si_3 \rightarrow L + \beta Nb_5Si_3 + Nb_{ss} \rightarrow \beta Nb_5Si_3 + Nb_{ss} + (Nb_{ss} + \beta Nb_5Si_3)_{eutectic}$. As the primary phase formed the surrounding melt became richer in Ti and Cr and possibly in Al and Sn (see Table 9.1) and from this melt formed the Nb_{ss} and the βNb_5Si_3 with the two phases forming the eutectic. Nb_{ss}

haloes (Figure 9.1) formed owing to competitive growth of the Nb_{ss} and βNb_5Si_3 phases from melt of eutectic composition, as was the case in the cast alloy ZX5.

Transitions from lamellar to lamellar + anomalous to anomalous eutectic have been reported for free (un-constrained) solidification of eutectic alloys with increasing melt undercooling (see discussion in chapter 6). The microstructure in the bottom of the ingot of the alloy ZX7 showed areas where lamellar Nb_{ss} + Nb_5Si_3 eutectic or anomalous Nb_{ss} + Nb_5Si_3 eutectic were observed in a ~ 50 μm thick zone formed next to the crucible wall (Figure 9.3a and b) followed by anomalous eutectic (Figure 9.3a) and then the Nb_5Si_3 + $(Nb_{ss} + Nb_5Si_3)_{eutectic}$ microstructure in the bulk (Figures 9.1) and top (Figure 9.2).

Anomalous eutectic was not observed in the cast alloy ZX5 (Al present, no Cr), where the volume fraction of the lamellar Nb_{ss} + Nb_5Si_3 eutectic was higher in the bottom areas of the ingot compared with the bulk and top, but anomalous eutectic was observed in the bottom of the cast alloy ZX3 (Cr present, no Al), where the Laves phase was also formed, as was the case in the anomalous eutectic in the bottom of ZX7 (Figure 9.3a). Thus, it is suggested that near the water cooled crucible wall the aforementioned ~ 50 μm thick zone was formed from Al rich eutectic melt of ZX7 solidifying as lamellar eutectic while Cr rich eutectic melt of ZX7 solidified as anomalous eutectic.

The microstructure in the bottom of the alloy ZX7 (Figure 9.3a, b) and the aforementioned transition in eutectic microstructures with increased melt undercooling would also suggest that the microstructure in the ~ 50 μm thick zone (Figure 9.3b) was formed from melts that solidified under different undercoolings near the crucible wall. Assuming that the temperature of the melt in contact with the crucible wall was $T_{melt}^{crucible}$, and different eutectic temperatures $T_{eutectic}$ for Cr or Al

rich melts the undercooling ΔT varied as follows (see Figure 9.38) $\Delta T_{Al\ rich\ melt} < \Delta T_{Cr\ rich\ melt}$. Assuming that nucleation of solidification occurred first at the lower undercooling (a plausible assumption), as the Nb_{ss} + Nb_5Si_3 lamellar eutectic formed from the Al rich melt the surrounding melt became richer in Si, see Table 9.1 (notice that the Ti, Al, Si and Sn contents of the eutectics in ZX5 and ZX7 were essentially the same, see Table 8.1) and from this richer in Si melt formed the anomalous eutectic at higher melt undercooling (notice that the Ti, Si and Sn contents of the eutectic in ZX3 were essentially the same as in the eutectics in ZX5 and ZX7 but the eutectic in ZX3 was richer in Si and that the eutectic in ZX1 was also richer in Si than those in ZX5 and ZX7, see Table 6.1).

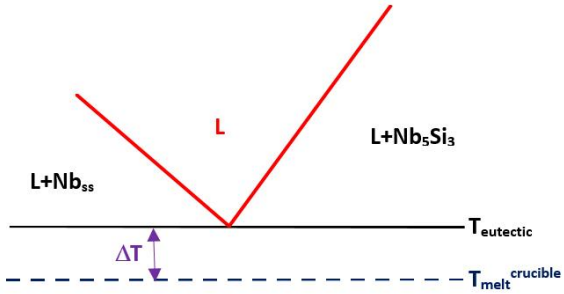


Figure 9.38 Schematic diagram of Nb_{ss} and Nb_5Si_3 eutectic

It is reasonable to assume that the growth velocity $V_{S/L}$ was "constant" during the solidification of the 50 μm zone (growth velocity "imposed" by the conditions near the crucible wall). According to the model of Tiller at el [99] for the S/L interface concentration in solute (C_L*) during the initial transient solidification, the C_L* is proportional to the solute concentration in the melt C_o and the constitutional undercooling ΔT_{CS} during the initial transient is [100]

$$\Delta T_{CS} = m_L [C_o/k_o](1-k_o)[1-\exp(-k_o V_{S/L}^2 t/D_L)][1-\exp(-V_{S/L}x/D_L)] - Gx \qquad (9.1)$$

where t is time, x is distance from S/L interface, D_L is diffusion coefficient in the melt, k_o is the partition coefficient, G is the temperature gradient and m_L is the liquidus slope. In other words as the melt became rich in Si ahead of the lamellar eutectic (i.e., C_o

increased in the above equation) the ΔT_{CS} increased and thus the anomalous eutectic formed. The latter grew over some distance in excess of 50 μm (Figure 9.3a) and eventually the transition to the normal eutectic in the bulk of the ingot occurred, for the same reasons as discussed in chapters 6 and 7.

The A-15 intermetallic was formed in the heat treated microstructure. Aluminium like Sn can form the A 15 Nb_3Al phase and thus it enhances the stability of the A-15 structure intermetallic phase. The heat treated alloy can be considered in the 1500 °C isothermal section proposed by Pan *et al* [49] either by considering Sn and Al as equivalent or Si and Sn as equivalent, see Figure 9.39. In both cases the alloy lies in the three phase field Nb_{ss} – αNb_5Si_3 – A-15 Nb_3Al.

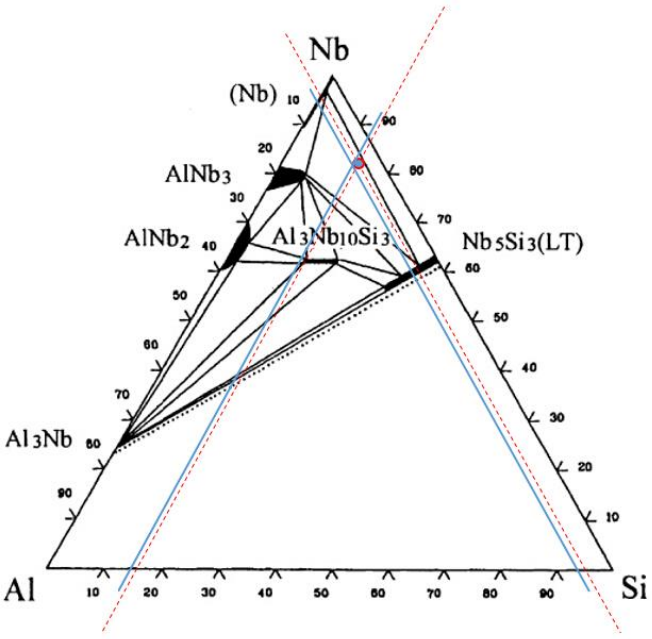


Figure 9.39 Partial 1500 °C isothermal section of the Nb-Si-Al system by Pan *et al*. Red lines, Si and Sn equivalent, blue lines, Al and Sn equivalent.

After the heat treatment the $\beta Nb_5Si_3 \rightarrow \alpha Nb_5Si_3$ transformation had been completed and in some of the 5-3 silicide grains a second phase had precipitated (Figure 9.6). The fine precipitates observed in αNb_5Si_3 grains exhibited contrast similar to that of the Nb_{ss} and Nb_3Sn, and the Si and Sn maps in Figure 9.8 could suggest that the fine

precipitates were Sn rich. However, the A-15 intermetallic phase in the heat treated alloy ZX7 was richer in Al than Sn and the Al map in Figure 9.8 does not provide strong evidence for Al rich areas where the precipitates were (see back scattered electron image in this figure). Thus, this limited evidence is not considered to be strong enough to categorically state the nature of the precipitates. The formation of fine precipitates in αNb_5Si_3 is consistent with the data for the alloys Nb-24Ti-18Si-5Al and Nb-24Ti-18Si-5Al-5Cr (respectively alloys KZ7 and KZ5 in [68]) where it was suggested (based on contrast under BSE imaging) that the fine precipitaes were Nb_{ss} formed via the transformation (not Ti rich) $\beta Nb_5Si_3 \rightarrow Nb_{ss} + \alpha Nb_5Si_3$.

The microstructure of the heat treated alloy showed evidence of contamination of the Nb_{ss} but not of the A-15 phase, see Figure 9.6. The same was the case for the heat treated alloy ZX5. This suggested that the synergy of Al, Cr, Sn and Ti in the three phases in the heat treated microstructure was not sufficient to stop contamination of the bulk during heat treatment in argon atmosphere.

9.4.4 Phase stability in the alloy Nb-24Ti-18Si-5Al-5Cr-5Sn (ZX8)

The Si + Al + Sn content of the alloy ZX8 was 26.6 at.%. Considering Si and Al and Sn as equivalent, the alloy was hyper-eutectic according to the Nb-Si binary system. Thus, in the solidification of the alloy ZX8 the βNb_5Si_3 was the primary phase. The presence of Al in the melt ensured that the $\beta Nb_5Si_3 \rightarrow \alpha Nb_5Si_3$ transformation, which was enhanced by Cr in the alloys ZX3 and ZX4, did not occur. This was also the case in the alloys ZX5, ZX6 and ZX7 (Al containing alloys).

The microstructures in all areas of the cast alloy ZX8 would suggest that the solidification path in ZX8 was $L \rightarrow L + \beta Nb_5Si_3 \rightarrow L + \beta Nb_5Si_3 + Nb_3Sn \rightarrow \beta Nb_5Si_3 + Nb_3Sn$ + Laves $NbCr_2$. The βNb_5Si_3 and Nb_3Sn formed a co-continuous microstructure with the Laves phase forming in some parts in between these two phases. As solidification progressed from the bottom, where the melt was in contact

with the water cooled crucible, to the top the melt became richer in Cr and the ranges of Cr concentration values increased (Table 9.2).

The Nb_{ss} was suppressed during solidification in all parts of the ingot of the alloy ZX8. Thus, the Nb_{ss} + βNb_5Si_3 eutectic was also suppressed. We have already seen that in the alloys ZX4 and ZX6, which had higher Sn content compared with the alloys ZX3 and ZX5, the volume fractions of the eutectic were reduced significantly compared with the lower Sn content alloys. There was no eutectic in the alloy ZX8 even though eutectic was formed in the alloy ZX7 (low Sn content alloy). These facts would suggest that when Al and Cr are present in an alloy individually with higher Sn concentration there is increased tendency to destabilise the eutectic but the eutectic is not completely suppressed, meaning that there is an increasing tendency to destabilise the Nb_{ss} (the βNb_5Si_3 is formed) and when Al and Cr are present in an alloy simultaneously with higher Sn concentration the eutectic is suppressed, meaning the synergy of Al and Cr with high Sn content can suppress the Nb_{ss} during solidification.

As the primary phase (i.e., Nb_5Si_3) formed the surrounding melt became richer in Al, Cr, Sn and Ti and leaner in Si, while the melt next to Ti rich Nb_5Si_3 became richer in Al, Cr and Sn and leaner in Si and Ti (see Table 9.2). In this melt the Nb_3Sn was formed instead of the Nb_{ss} according to the highest interface temperature criterion, see § 6.3.1 and Figure 6.23. With Nb_5Si_3 and Nb_3Sn in the solidifying melt, the growth of the latter phase was kinetically easier owing to its lower entropy of fusion (see § 8.4.3 for the entropies of fusion of Nb_5Si_3, Nb_3Sn and Nb_{ss}). As the Nb_3Sn was formed the surrounding melt became richer in Cr and Si and leaner in Sn and Ti.

From the growth of the Nb_5Si_3, Ti rich Nb_5Si_3 and Nb_3Sn the melt became rich in Al and Cr, both of which stabilise the $NbCr_2$ Laves phase, and in the Si containing and Al and Cr rich melt the C14-$NbCr_2$ Laves phase formed. In the case of the cast alloy ZX4, where the Laves phase was observed only in the bottom of the ingot (with Nb_{ss},

Nb_5Si_3 and Nb_3Sn), the Nb_{ss} formed during solidification and was very rich in Cr (~ 11.3 at.%) and the Laves was absent when the eutectic formed. In this alloy (ZX4) the Cr in the melt was consumed by the formation of the Nb_{ss} (and the Cr rich Laves could not form).

In the cast microstructure of the alloy ZX8 the transition to eutectic shown in Figure 7.36 never occurred because the Nb_{ss} could not form during the solidification owing to the consumption of Cr by the Laves phase (i.e., the Laves starved the melt from the Cr required for the formation of the Nb_{ss}). In the solidification of the alloy ZX8 the highest interface temperature criterion accounts for the nucleation of Nb_3Sn instead of Nb_{ss} in the melt and the Cr starvation argument accounts for the suppression of the formation of the Nb_{ss} during solidification. Thus, Cr was important for co-continuous microstructure architectures in high Sn concentration alloys as it was for the formation of anomalous eutectic (a co-continuous microstructure) in low Sn content alloys.

After the heat treatment at 1450 °C the Laves phase was still present and the Nb_{ss} was formed, which means that the solid solution was stable in this alloy as it was in the heat treated alloy ZX4 (see Table 7.2) but not in the heat treated alloy ZX6 (see Table 8.2). These facts would suggest that Al is the element that controls the stability of the Nb_{ss} in alloys with high Sn content and no Cr and that Cr can challenge on this effect and eliminate the effect of Al.

There was also evidence of fine precipitates inside the αNb_5Si_3 exhibiting contrast similar to that of the Nb_{ss} and Nb_3Sn. However, the X-ray map evidence in this case was not as helpful as in the alloys ZX4 (Figures 7.16, 7.17) and ZX6 (Figure 8.10b) where the evidence pointed to Sn rich precipitates.

9.4.5 Oxidation of the alloys ZX7 and ZX8 at 800 °C

The starting microstructures of both alloys before isothermal oxidation at 800 °C (i.e., the cast microstructures) were different. The Nb_{ss} was present in the starting microstructure of the alloy ZX7 but not in the alloy ZX8. The Achilles' heel in the oxidation of Nb silicide based alloys is the solid solution, in which the solubility of oxygen is high (the maximum solid solubility of oxygen in Nb (before NbO can form) is about 9 to 10 at.%).

We saw in the previous chapters that the Nb_5Si_3 and Nb_3Sn phases suffered from micro-cracking close to the scale/substrate interface and are not immune to contamination by oxygen even in the bulk. This was also the case in the alloy ZX8 where as a result of the micro-cracking of the aforementioned phases below the scale and their contamination by oxygen, the contamination of the microstructure by oxygen changed (altered) the phase equilibria, and the oxygen contamination stabilised the Nb_{ss} and a eutectoid Nb_{ss} + Nb_5Si_3 microstructure formed in the bulk with Si + Al + Sn content (~ 17.2 at.%, see Table 9.9). The latter is close to the composition of the eutectic in the Nb-Si binary and also close to the Si + Al + Sn content (18.3 at.%, see Table 8.8) of the Nb_{ss} + Nb_5Si_3 microstructure in the bulk of the alloy ZX6 at 800 °C and with higher oxygen content (owing to the presence of the Nb_{ss}) than the Nb_5Si_3 and Nb_3Sn (Table 9.9) (for the formation of Nb_{ss} in ZX8 at 800 °C because of change in phase equilibria owing to the contamination by oxygen see discussion about the Nb_{ss} in the ZX8 at 1200 °C in the next section). Furthermore Ti rich areas were formed in the Nb_3Sn in the bulk of the oxidised alloy ZX8. Such shift in the phase equilibria as a result of contamination by oxygen has been noticed before in the group for some of the Sn containing Nb silicide based alloys studied by Vellios [88]. Thus, even though the starting microstructures were different at the beginning of isothermal oxidation, the microstructure of the alloy ZX8 evolved to one having essentially the same phases as that of the alloy ZX7. This "delayed" stabilisation of the Nb_{ss} in ZX8

and the formation of a Sn rich area between the scale and Nb_3Sn in the diffusion zone could account for the slightly better oxide scale thickness and diffusion zone thickness in the alloy ZX8 and the less severe contamination of the Nb_{ss} and Nb_5Si_3 in the bulk of the alloy ZX8 compared with the bulk of the alloy ZX7. Apart from this very important microstructural difference, both alloys (i) formed relatively thin non compact scales consisting of two oxides, one Nb rich and the other Nb and Si rich and (ii) below the scale the intermetallic phases exhibited micro-cracking.

In contrast to the alloys with high Sn concentration where the Al and Cr additions were present individually, i.e., the alloys ZX4 and ZX6, the alloys ZX8 followed linear oxidation kinetics with a rate not significantly different compared with that of the alloy ZX7 (Table 9.3). The oxidised specimen of the alloy ZX8 exhibited damage along one edge (Figure 9.17), but otherwise its surfaces were of the same quality, if not better than those of ZX4 (Figure 7.18) and ZX6 (Figure 8.12). For the reasons discussed in § 9.3, it is suggested that the linear oxidation kinetics of ZX8 in Table 9.3 do not represent the oxidation kinetics of the alloy ZX8 at 800 °C.

9.4.6 Oxidation of the alloys ZX7 and ZX8 at 1200 °C.

The starting microstructures of both alloys before isothermal oxidation at 1200 °C (i.e., the cast microstructures) were different. The Nb_{ss} was present only in the microstructure of the alloy ZX7. Both alloys followed linear oxidation kinetics with a slightly better constant for the alloy ZX8 (Table 9.3) and both alloys suffered from spallation of their scales (Figure 9.17), as was the case for all the alloys of this research at 1200 °C.

In both alloys Sn rich areas formed at the scale/substrate interface. In the low Sn content alloy (ZX7) the Sn rich area was noticeably thicker near corners (Figure 9.26a,b) and in the high Sn content alloy (ZX8) the Sn rich area was thicker than that formed in ZX7. In the Sn rich areas in both alloys the Sn content varied. The oxide

scales of both alloys contained three oxide types, namely Nb rich, Ti rich and Nb and Si rich.

In the case of the alloy ZX7 in the Nb_5Si_3 present in the Sn rich areas some of the silicide grains exhibited sub-structure and second phase Sn rich particles (Figures 9.26d, 9.28, Table 9.11 - spot analysis 10). Similar Sn rich features were also observed in the Nb_5Si_3 in the bulk. Sn rich phases in the Sn rich areas formed in both alloys included the intermetallics $NbSn_2$, Nb_5Sn_2Si, Nb_3Sn and these intermetallics were contaminated by oxygen, as was the Nb_5Si_3. In the bulk microstructure the Nb_5Si_3, Nb_3Sn, Nb_{ss} and Laves phase were present. It should be remembered that in the alloy ZX3 (low Sn), which had essentially same behaviour in TG, the $NbSn_2$ was also formed in the Sn rich area, but not in the alloy ZX5 (also low Sn) but better oxidation behaviour in TG compared with ZX3 and ZX7.

In the case of the alloy ZX8 the same phases were observed in the Sn rich area as in the alloy ZX7 with the exception of $NbSn_2$, and also Sn rich areas were formed in the Nb_5Si_3, as was the case in the alloy ZX7. In the bulk microstructure the Nb_5Si_3, Nb_3Sn and Laves phase were present. Thus, contrary to the formation of the Nb_{ss} and Nb_{ss} + Nb_5Si_3 lamellar structure in the oxidised alloy ZX8 at 800 °C, the Nb_{ss} was not stabilised in the microstructure at 1200 °C even though it was present in the heat treated microstructure at 1500 °C, meaning that in the new phase equilibria with oxygen at 1200 °C the solid solution was not stable.

9.5 Summary

Two Nb-24Ti-18Si-5Al-5Cr based alloys with low and high Sn concentrations were studied, namely the alloys Nb-24Ti-18Si-5Al-5Cr-2Sn (ZX7) and Nb-24Ti-18Si-5Al-5Cr-5Sn (ZX8), in the cast and heat treated (1450 °C) conditions and after isothermal oxidation at 800 °C and 1200 °C.

Both alloys were hyper-eutectic with βNb_5Si_3 the primary phase. In both cast alloys there was macrosegregation of Si and macrosegregation of Ti in the alloy with the high Sn concentration (ZX8). The increase in Sn content with Al and Cr being present simultaneously in the alloy was accompanied by more than three times increase in Si macrosegregation compared with the low Sn alloy. In both alloys the Nb_3Si was supressed but the metastable $Nb_{ss} + \beta Nb_5Si_3$ eutectic was formed only in the alloy with low Sn (ZX7). The prior eutectic microstructure was not present after the heat treatment. The Nb_3Sn formed only in the cast alloy with the high Sn content (ZX8) but was stable in both alloys after the heat treatment at 1500 °C. The $NbCr_2$ Laves phase was stable in both alloys. The Nb_{ss} was not formed during solidification of the high Sn alloy (ZX8) but was stable in the microstructures of both alloys after their heat treatments.

In both alloys the transformation of βNb_5Si_3 to αNb_5Si_3 did not start during solidification and was completed at 1500 °C. In the latter condition there was precipitation of second phase(s) in some αNb_5Si_3 grains, the evidence being stronger in the low Sn alloy (ZX7). The Nb_{ss} was destabilised by oxygen contamination in the high Sn concentration ZX8 at 1200 °C (present in the heat treated (1450 °C) microstructure) and stabilised by oxygen contamination at 800 °C (not present in the starting cast microstructure).

Both alloys did not pest during isothermal oxidation at 800 °C (the alloy ZX8 exhibited "catastrophic damage along one edge) and their scales spalled off at 1200 °C.

At 800 °C the scale formed on the alloy ZX7 had constant (uniform) thickness but was not compact, while the scale formed on the alloy ZX8 was thinner. The scales of both alloys consisted of Nb rich and Nb and Si rich oxide. At 1200 °C the scales on both alloys were compact and thicker but not of constant (uniform) thickness and the same oxide types plus Ti rich oxide were formed the scales in both alloys. There was WDS

data for all three oxide types.

In both alloys there was enrichment in Sn of the microstructure below the scale and formation of Sn rich phases in this area and at the scale/substrate interface. In both alloys at 1200 °C the the Sn rich intermetallic Nb_5Sn_2Si was formed and the $NbSn_2$ was formed only in the low Sn alloy (ZX7). In the latter alloy, in the Nb_5Si_3 in the Sn rich area and in the bulk there was precipitation of Sn rich phase(s) and in the former area “Sn rich sub-grains” were also formed.

In both alloys the bulk microstructures were contaminated by oxygen.

Chapter 10

Comparison of the alloys

In this chapter the data for the alloys studied in this research is used to deduce how the increase in Sn concentration in alloys with Al and Cr additions individually and simultaneously affects phase stability and oxidation behaviour.

10.1 Macrosegregation in the alloys

As we discussed in the previous chapters, macrosegregation of an element in Nb silicide based alloys is said to occur when MACS = $C_{max}^{i} - C_{min}^{i} > 2$ at.%, i.e., when the difference between the maximum and minimum concentrations of the element in the alloy exceeds 2 at.%. Macrosegregation is linked with the partitioning of solutes between the phases present in the microstructures of Nb silicide based alloys [78]. Tin has a strong effect on the macrosegregation of Si [78]. In [78] the ranking of alloys in terms of increasing Si macrosegregation indicated that the latter tended to increase in Nb silicide based alloys when the parameters $\Delta H_m/T_m$ ("alloy entropy of fusion"), T_m^{sp} (melting temperature of sp electronic configuration elements) and $[\Delta H_m/T_m][\Delta H_m^{sd}/\Delta H_m^{sp}]^{-1}$ increased and the ratios $\Delta H_m^{sd}/\Delta H_m^{sp}$ and T_m^{sd}/T_m^{sp} and the parameters ΔH_m ("alloy enthalpy of melting"), T_m (alloy melting temperature) and T_m^{sd} (melting temperature of the sd electronic configuration elements) decreased. The data in this paper also indicated that not all parameter trends are followed by all groups of Nb silicide based alloys, or, to put this another way, the data confirmed that different parameters are important for different groups of alloys, depending on the alloying additions.

The macrosegregation of Si in the alloy ZX8 was compared with the alloy ZX4 (Cr present, no Al) and the alloys NV9 (Nb-19Si-4.2Sn) and NV6 (Nb-25.5Ti-18.1Si-4.9Sn) because in all four alloys the Nb_3Sn was present in their microstructures. The data in Table 10.1 shows that trends in parameters studied in [78] are obeyed with the exception of the parameters $\Delta H_m/T_m$, T_m^{sp} and $(\Delta H_m/T_m)/(\Delta H_m^{sd}/T_m^{sd})$, but the former

and the latter two parameters respectively decreased and increased with MACS (numbers in italics in the Table 9.17), which could be another indication that Cr played a key role in the macrosegretation of elements in the alloy ZX8.

Table 10.1 Alloy parameters linked with macrosegregation of Si in the alloys ZX8, ZX4, NV6 and NV9

alloy	ΔH_m kJ/mol	T_m (K)	$\Delta H_m/T_m$ J/molK	$\Delta H_m^{sd}/\Delta H_m^{sp}$	T_m^{sd} (K)	T_m^{sp} (K)	T_m^{sd}/T_m^{sp}	$[\Delta H_m/T_m] \times [\Delta H_m^{sd}/\Delta H_m^{sp}]^{-1}$	MACS (at.%)
ZX8	**26.86**	**2152**	12.48	**1.84**	**1794**	*358*	**5**	6.78	10
ZX4	**27.84**	**2205**	*12.63*	**1.85**	**1862**	*342*	**5.44**	*6.85*	7.3
NV6	**28**	**2241**	*12.49*	**1.98**	**1911**	*330*	**5.79**	*6.31*	5.5
NV9	**30.4**	**2454**	*12.39*	**2.1**	**2112**	342	**6.18**	*5.9*	2.5

However, if the data for the alloy ZX6 (Al present, no Cr) were to be included in the comparison of alloys (the alloy ZX6 contained the A-15 intermetallic in its microstructure like the other alloys in Table 10.1) then the ranking shown in Table 10.1 is destroyed. This could suggest that the parameters used in Table 10.1 cannot catch how the synergy of Al with Sn and Cr in an alloy affects the macrosegregation of Si. Another reason for this could be that the potency of material parameter changes caused by a particular element when in synergy with other additions in Nb silicide based alloys is different for Sn and Al and Cr. The potency is strong regarding ΔH_m, $\Delta H_m/T_m$ and T_m^{sp} for Sn and T_m, $\Delta H_m/T_m$, $\Delta H_m^{sd}/\Delta H_m^{sp}$, T_m^{sd}, T_m^{sp} and T_m^{sd}/T_m^{sp} for both Al and Cr but weak for Sn regarding the parameters T_m, T_m^{sd} and T_m^{sd}/T_m^{sp} (see Table 3 in [78]). It is interesting that trends are followed by the latter three parameters in Table 10.1.

The alloys of this study with only 2 at.% Sn addition are compared for their MACS values of Si in the Table 10.2. It is noted that the aforementioned trends are followed by the parameters ΔH_m, $\Delta H_m^{sd}/\Delta H_m^{sp}$, T_m^{sp} and T_m^{sd}/T_m^{sp} but not by the parameter $[\Delta H_m/T_m] \times [\Delta H_m^{sd}/\Delta H_m^{sp}]^{-1}$ that follows the opposite trend, indicated in red in Table 10.2.

Considering the data in Tables 10.1 and 10.2 and in Tables 8.15 and 8.16, it is suggested that alloy design could consider the macrosegregation of Si in Nb silicide

based alloys with Sn and Al and/or Cr via the parameters ΔH_m, $\Delta H_m^{sd}/\Delta H_m^{sp}$ and T_m^{sd}/T_m^{sp} with their trends as discussed in [78].

Table 10.2 Alloy parameters linked with macrosegregation of Si in the cast alloys ZX3, ZX5, and ZX7

alloy	ΔH_m kJ/mol	T_m (K)	$\Delta H_m/T_m$ J/molK	$\Delta H_m^{sd}/\Delta H_m^{sp}$	T_m^{sd} (K)	T_m^{sp} (K)	T_m^{sd}/T_m^{sp}	$[\Delta H_m/T_m] \times [\Delta H_m^{sd}/\Delta H_m^{sp}]^{-1}$	MACS (at.%)
ZX5	**28.1**	2215	12.68	**1.74**	1837	**377**	**4.87**	**7.29**	5.5
ZX3	**28.97**	2257	12.84	**1.74**	1896	**361**	**5.25**	**7.39**	3.6
ZX7	**29.45**	2214	13.53	**1.79**	1889	**325**	**5.82**	**7.56**	3

10.2 Phase stability and transformations in the alloys with low Sn concentration

The phases present in the alloys with low Sn concentration in the cast and heat treated conditions, i.e., the alloys ZX1, ZX3, ZX5 and ZX7 of this research, are summarised in Table 10.3. The compositions of the Nb_{ss}, and the Nb_5Si_3 and A-15 intermetallic phases and Nb_{ss} + Nb_5Si_3 eutectics are compared in Table 10.4, where the alloy ZX1 is also included for comparison purposes, even though its Sn content was slightly higher (≈ 3 at.%) than the other three alloys (≈ 2 at.%).

The microstructures in the bottom areas of the ingots of the alloys ZX1, ZX3, ZX5 and ZX7 would suggest (i) that Cr has a strong effect (promotes, stabilises) on the anomalous to lamellar eutectic transition (that can occur in low Sn content Nb-Si melts (alloy ZX1, see Figure 6.4f) with decreased melt undercooling), (ii) that Al does not promote (stabilise) the aforementioned transition and (iii) that it is possible to have a co-continuous Nb_{ss} and Nb_5Si_3 microstructure formed from deeply undercooled Cr containing eutectic melts, even in the presence of Al.

The additions of Al and Cr individually or simultaneously in the alloys did not destabilise the Nb_{ss} in all the alloys with low Sn content and did not suppress the partitioning of Ti in the Nb_{ss}. Indeed, Ti rich areas in the Nb_{ss} (i.e, partitioning of Ti in Nb_{ss}) were observed in all cast alloys but not in the Nb_5Si_3.

Table 10.3 Comparison of phases present in the cast and heat treated alloys of this research

	As cast	Heat treated	
		1200 °C	1500 °C
ZX1	Nb_{ss}, βNb_5Si_3, $(Nb_{ss}+Nb_5Si_3)_{eutectic}$	Nb_{ss}, $(Nb_{ss}+Nb_5Si_3)_{lamellar}$ αNb_5Si_3, βNb_5Si_3	Nb_{ss}, αNb_5Si_3, $(Nb_{ss}+Nb_5Si_3)_{lamellar}$ Nb_3Sn
ZX2	Nb_{ss}, Nb_3Sn, βNb_5Si_3, $(Nb_{ss}+Nb_5Si_3)_{eutectic}$	Nb_3Sn, Nb_{ss}, αNb_5Si_3, $(Nb_{ss}+Nb_5Si_3)_{lamellar}$	Nb_3Sn, Nb_{ss}, αNb_5Si_3 $(Nb_{ss}+Nb_5Si_3)_{lamellar}$
		1500 °C	
ZX3	αNb_5Si_3, βNb_5Si_3, Nb_{ss}, $(Nb_{ss}+Nb_5Si_3)_{eutectic}$, Laves phase	Nb_{ss}, αNb_5Si_3	
ZX4	αNb_5Si_3, βNb_5Si_3, Nb_3Sn, Nb_{ss}, $(Nb_{ss}+Nb_5Si_3)_{eutectic}$, Laves phase	αNb_5Si_3, Nb_3Sn, $Nb_{ss,}$ Laves phase	
ZX5	βNb_5Si_3, Nb_{ss}, $(Nb_{ss}+Nb_5Si_3)_{eutectic}$	αNb_5Si_3, Nb_3Sn, Nb_{ss}, Laves phase	
ZX6	βNb_5Si_3, Nb_3Sn, Nb_{ss}, $(Nb_{ss}+Nb_5Si_3)_{eutectic}$	αNb_5Si_3, Nb_3Sn	
		1450 °C	
ZX7	βNb_5Si_3, Nb_{ss}, $(Nb_{ss}+Nb_5Si_3)_{eutectic}$, Laves phase	αNb_5Si_3, Nb_3Sn, Nb_{ss}, Laves phase	
ZX8	βNb_5Si_3, Nb_3Sn, Laves phase	αNb_5Si_3, Nb_3Sn, Nb_{ss}, Laves phase	

The additions of Al and Cr individually or simultaneously in the alloys also did not destabilise the Nb_{ss} + βNb_5Si_3 eutectic in all alloys with low Sn content. The lamellar microstructure of the eutectic was stable up to 1500 °C in the absence of Al and Cr in the alloys, or in other words, Al and Cr individually or simultaneously destabilised the lamellar Nb_{ss} and Nb_5Si_3 microstructure at 1500 °C.

Only Cr on its own promoted the βNb_5Si_3 to αNb_5Si_3 transformation during solidification and Al destabilised this effect of Cr. In all alloys the αNb_5Si_3 was the stable 5-3 silicide at high (≥ 1200 °C) temperatures. The addition of Al in the alloys ZX5 and ZX7 promoted the precipitation of a second phase in the αNb_5Si_3 after the heat treatment at 1500 °C. This is consistent with the data in [68, 101]) for Al containing alloys, see the discussion of the results for the alloy ZX8 regarding the identity (Nb_{ss} or Nb_3Sn) of second phase precipitates in αNb_5Si_3.

The addition of Cr could suppress the formation of (i.e., destabilise) Nb_3Sn, but this was possible only when Al was not present in the alloys. The A-15 intermetallic was stable at 1500 °C even in the "simple" ternary alloy ZX1, in which the lamellar

microstructure of the Nb_{ss} + βNb_5Si_3 eutectic was stable (at least) up to 100 h at 1500 °C. Whether this would be the case in the alloys where Al and Cr were present individually or simultaneously cannot be deduced from the results of this research. Tin and Al did not destabilise the $NbCr_2$ Laves phase in ZX7. However, formation of the latter was dependent on solidification conditions and in the alloy ZX3 (no Al present) it is likely that the Laves phase participated in a ternary eutectic.

Cr and Al had opposite effects on the solubilities of Si and Sn in the Nb_{ss} which were decreased when Al was present in the alloy (compare data for the Nb_{ss} in Tables 6.1 and 7.1 with Tables 8.1 and 9.1) but the Si/Sn ratio was not affected (Table 10.4). In the alloys with Al the concentration of the simple elements in the Nb_{ss} was constant and increased slightly in the Ti rich Nb_{ss} when Al and Cr were simultaneously present in the alloy, see Table 10.4.

In the cast alloys the additions of Al and Cr individually or simultaneously did not affect the solubility of Sn in the Nb_5Si_3. Al substituted Si in the Nb_5Si_3 and in the Al containing alloys the simple element concentration of the Nb_5Si_3 was slightly lower than the lower value of the Si concentration range of the unalloyed Nb_5Si_3 (36.5 at.%). This effect of Al on the Nb_5Si_3 has been reported before for the non Sn containing alloy Nb-24Ti-5Al-5Cr (alloy KZ5 in [68]).

The additions of Cr and Al individually or simultaneously did not affect the solubility of Sn in the eutectic (see Tables 6.1, 7.1, 8.1 and 9.1) but Cr and Al respectively had weak and strong effect on the solubility of Si in the eutectic, the effect of Al arising from its effect on the Si concentration in Nb_5Si_3 (see Si + Sn and Si + Sn + Al data for the eutectic in the Table 10.4). In the cast alloys containing Al the eutectic composition was in the range of values reported for the metastable Nb_{ss} + βNb_5Si_3 eutectic, but in the alloys ZX1 and ZX3 (no Al present) the eutectic composition was in the range of compositions reported for the stable eutectic in the Nb-Si binary.

In the heat treated alloys the addition of Cr did not affect the solubility of Sn in the Nb_{ss} (see Tables 6.1 and 7.1) but the addition of Al in the alloys caused a small

reduction (Tables 8.1 and 9.1). In all the heat treated alloys at 1500 °C the solubility of Si in the Nb_{ss} was reduced compared with the cast condition, which is in agreement with the literature, and as a result the Si/Sn ratio and the Si + Sn + Al sum were reduced to about 0.3 and 9 at.%, respectively (see Table 10.4).

The additions of Al and Cr individually or simultaneously in the alloys destabilised the lamellar Nb_{ss} + Nb_5Si_3 microstructure after heat treatment at 1500 °C even though the latter was stable at T ≥ 1200 °C in the alloy ZX1 (Table 10.3). The Si + Sn content of the lamellar Nb_{ss} + Nb_5Si_3 microstructure in the heat treated alloy ZX1 had shifted towards the value reported for the lamellar Nb_{ss} + Nb_5Si_3 metastable eutectic, see Table 10.4.

The A-15 Nb_3Sn formed in the heat treated alloys with low Sn concentration and no Cr, the alloys ZX1, ZX5 and ZX7. In the latter two alloys, where EDS analysis of this phase was possible, the Si + Sn, Si + Sn + Al and Si/Sn were ≈ 10 at.%, ≈ 18.7 at.% and 0.9, respectively, see Table 10.4.

Table 10.4. Comparison of Nb_{ss}, Ti rich Nb_{ss}, Nb_5Si_3, Nb_{ss} + Nb_5Si_3 eutectic and A15 phases in the alloys ZX1, ZX3, ZX5 and ZX7 in terms of their Si + Sn, Si + Sn + Al (at.%) and Si/Sn ratio. Numbers rounded up to first decimal point.

Alloy and Condition	Si + Sn					Si + Sn + Al					Si/Sn		
	Nb_{ss}	Ti rich Nb_{ss}	eutectic	Nb_5Si_3	A15	Nb_{ss}	Ti rich Nb_{ss}	eutectic	Nb_5Si_3	A15	Nb_{ss}	Ti rich Nb_{ss}	A-15
ZX3-AC	6.5	6.1	17.5	36.7							0.9	1.1	
ZX5-AC	5.2	5.2	14.7	31.7		11.1	11.1	19.8	35.4		1	0.9	
ZX7-AC	5.1	6.2	14.6	31.1		11	12.3	19.8	35.4		0.8	1.3	
ZX1-AC	7.3		18.4	37.4							0.9		
ZX3-HT15	4.1			37							0.2		
ZX5-HT15	2.6			34.5	10.4	9.1			36.8	18.8	0.3		0.9
ZX7-HT15	2.4			35.2	9.7	9.2			36.9	18.6	0.3		0.9
ZX1-HT15	4.5		20.3*	36.7							0.4		

* Prior eutectic area at 1500 °C, at 1200 °C the Si + Sn value was 19.4 at.%

10.3 Phase stability and transformations in the alloys with high Sn concentration

The phases present in the alloys with high Sn concentration in the cast and heat treated conditions, i.e., the alloys ZX2, ZX4, ZX6 and ZX8 of this research, are summarised in Table 10.3. The compositions of the Nb_{ss}, and the Nb_5Si_3 and A15 intermetallic phases and Nb_{ss} + Nb_5Si_3 eutectics are compared in Table 10.5, where the alloys NV9 and NV6 are also included for comparison purposes, because of their similar Sn content.

The additions of Al and Cr individually did not destabilise the Nb_{ss} in the cast alloys with high Sn content but suppressed the partitioning of Ti in the Nb_{ss}. Indeed, no Ti rich areas in the Nb_{ss} (i.e, partitioning of Ti in Nb_{ss}) were observed in the cast alloys but Ti rich areas were observed in the Nb_5Si_3.

The additions of Al and Cr individually did not destabilise the Nb_{ss} + βNb_5Si_3 eutectic in the cast alloys with high Sn content but when Al and Cr were simultaneously present in the alloy the eutectic was destabilised owing to the effect of the synergy of the two elements with high Sn content on the stability of the Nb_{ss} (see above). The lamellar microstructure of the eutectic, however, was stable up to 1500 °C in the absence of Al and Cr in the alloy.

Only Cr on its own promoted the βNb_5Si_3 to αNb_5Si_3 transformation during solidification and Al destabilised this effect of Cr. In all alloys the αNb_5Si_3 was the stable 5-3 silicide at high (≥ 1200 °C) temperatures.

The addition of Al and Cr individually or simultaneously in alloys with high Sn content led to the precipitation of a second phase in the αNb_5Si_3 after the heat treatment at 1500 °C. These precipitates were Sn rich when the Al and Cr were present individually in the alloys ZX4 and ZX6. The evidence for ZX8 was not conclusive. Such precipitation was not observed in the alloys NV9 (no Ti) and NV6 (Ti present) [56].

Precipitation in Nb_5Si_3 has been reported in [68, 101] for Al containing Nb-24Ti-18Si silicide based alloys without Sn after heat treatment at 1500 °C, in Ti rich Nb_5Si_3 in heat treated (1200 °C) Al free and Sn containing Nb-24Ti-18Si-5Fe-5Sn (alloy NV8 in [69] and in the Nb_5Si_3 in the heat treated (1200 °C) Nb-24Ti-18Si-5Cr-5Fe-5Sn (alloy NV5 in [70]), where the precipitates were the Nb_3Sn intermetallic phase. The available evidence would thus suggest that precipitation of second phase in the 5-3 silicide after heat treatment is not necessarily linked with the presence of Al in the alloy and that such precipitates can be the A2 (bcc) Nb_{ss} or the A-15 Nb_3Sn, the latter having been observed in Sn rich Nb-24Ti-18Si silicide based alloys.

The addition of Al and Cr individually or simultaneously in the cast alloys with high Sn content did not destabilise the Nb_3Sn whose Si + Sn content was significantly reduced in the alloys with Al, in which the Si + Al + Sn was "constant" at about 20 at.%, see Table 10.5, and confirmed that Al, Si and Sn occupy the X position in A15-Nb_3X. The Nb_3Sn in the cast alloys NV9 and NV6 had Si + Sn about 18 at.% [56]. The A15 intermetallic was stable at 1500 °C in all alloys with its Si + Sn content slightly reduced and Si + Sn + Al ≈ 20 at.%. In all cast alloys the Si/Sn ratio in the A-15 was in the range 0.6 to 1 and was reduced to about 0.6 after the heat treatment.

The simultaneous addition of Cr and Al in ZX8 did not destabilise the $NbCr_2$ Laves phase. However, formation of the latter was dependent on solidification conditions in the alloy ZX4 where it is likely that it participated in a ternary eutectic, as was the case in the alloy ZX3.

The addition of Al and Cr individually in the cast alloys ZX4 and ZX6 increased the solubilities of Si in the Nb_{ss} but had no effect on the solubility of Sn compared with the cast alloys NV9 and NV6 [56] and thus the Si/Sn ratio was double that in the latter two alloys (Table 10.5).

Table 10.5. Comparison of Nb_{ss}, Nb_5Si_3, Ti rich Nb_5Si_3, Nb_{ss} + Nb_5Si_3 eutectic and A-15 phases in the alloys ZX4, ZX6, ZX8 and NV9 and NV6 in terms of their Si + Sn, Si + Sn + Al (at.%) and Si/Sn ratio. Numbers rounded up to first decimal point

Alloy and Condition	Si + Sn					Si + Sn + Al				Si/Sn	
	Nb_{ss}	eutectic	Nb_5Si_3	Ti rich Nb_5Si_3	A-15	Nb_{ss}	Nb_5Si_3	Ti rich Nb_5Si_3	A-15	Nb_{ss}	A-15
ZX4-AC	9.2		36.7	34.9	19.4					0.7	0.6
ZX6-AC	7.6		34.3	32.9	15.3	13.4	37.3	36.9	21.3	0.6	0.8
ZX8-AC			33.7	31	14.9		36.3	34.7	20.1		0.6
NV9-AC	5.7	20.7	36.2		17.8					0.3	1
NV6-AC	7.7	20.5	36.8	36.2	18.2					0.3	0.7
ZX4-HT15	5.6		37.1		18.9					0.1	0.4
ZX6-HT15			34.6	35.1	12.9		36.8	36.9	19.9		0.6
ZX8-HT15	2.4		35.4	32.8	13.5	8.4	36.9	36	19.3	0.3	0.6
NV9-HT15	3.4		36.7		17.7					0.1	0.6
NV6-HT12	4.3		36.5	35.7	16.3					0.1	0.5

In the cast alloys the additions of Al and Cr individually or simultaneously did not affect the solubility of Sn in the Nb_5Si_3 but increased it slightly compared with the Nb_5Si_3 in the alloy NV9. Al substituted Si in the Nb_5Si_3 and in the Al containing alloys the simple element concentration of the Nb_5Si_3 was essentially the same as the lower value of the Si concentration range of the un-alloyed Nb_5Si_3 (36.5 at.%), see Table 10.5. This effect of Al on the Nb_5Si_3 has been reported before for the non Sn containing alloy Nb-24Ti-5Al-5Cr (alloy KZ5 in [68]).

The addition of Cr in ZX4 did not have an effect on the solubility of Sn in the Nb_{ss} after the heat treatment. The solubility of Sn in the Nb_{ss} was slightly reduced as was the case in the heat treated alloys NV9 and NV6. In all the heat treated alloys at 1500 °C (1450 °C for the alloy ZX8), the solubility of Si in the Nb_{ss} was reduced compared with the cast condition, which is in agreement with the literature, and as a result the Si/Sn ratio was reduced to ≤ 0.3 (see Table 10.5).

The additions of Al and Cr individually in the alloys destabilised the lamellar Nb_{ss} + Nb_5Si_3 microstructure after heat treatment at 1500 °C even though the latter was stable at 1500 °C in the alloy ZX2 (Table 10.3).

10.4 Segregation of Sn in the scale/substrate interface

A common feature of the oxidised alloys of this research has been the formation of Sn rich areas at the scale/substrate interface the thickness and continuity of which increased with Sn content in the alloy and oxidation temperature, making the analysis of Sn rich phases possible mainly in the alloys oxidised at 1200 °C. In the Sn rich areas different Sn rich intermetallics were formed at the scale/substrate interface which indicated that phase selection depended on the concentration of Sn. These intermetallics were the $NbSn_2$, Nb_5Sn_2Si, Nb_3Sn, the former two with Ti, Al and Cr and the latter with Ti, Cr, Al and Si in their composition and were contaminated by oxygen (Figures 7.30, 7.33a, Tables 8.12, 9.11, 9.13).

Surface segregation of solute elements in an alloy was predicted by Gibbs [103] who stated that the equilibrium chemical composition of the surface of an alloy should not

necessarily be the same as its bulk chemical composition. Experimental research has confirmed surface segregation. Almost all the research has concentrated on binary systems. There is limited research on ternary systems.

The research on binary systems confirmed that the segregation of a species to the surface depends (i) on the bulk composition, (ii) on temperature, (iii) on surface orientation and (iv) on the presence of grain boundaries in a polycrystalline alloy. From (iii) and (iv) above it follows that since the grains near the surface would be of different orientations, differences in the extent (magnitude) of surface segregation should be expected between different grains.

Research on ternary systems with at least two surface active solute elements has also indicated (v) co-segregation (meaning synergistic segregation) which was observed in systems with strong attractive interaction of the solutes or (vi) site competition which was observed when the surface became saturated by surface active solutes and occurred when the surface active solutes attracted or repelled each other [102].

If we take the surface segregation of Sn for granted, then the observations referred to in the previous paragraph do not contradict any of (i) to (v) above. But why does Sn segregate to a surface?

Gibbs [103] showed that the enrichment of a surface in a solute (i.e., the excess surface concentration of a solute) element over its bulk concentration depends on the composition dependence of the surface tension and that a solute element should segregate to the surface if the surface tension decreases with increasing concentration of the solute. Such data about the surface tension is not available for most alloys.

Given the difficulty of applying Gibbs theory to calculate the excess surface concentration because of the lack of data, different “theories” have been proposed to account for surface segregation of solutes. These include (a) an approach based on the heat of segregation according to which the solute of the alloy with lower heat of sublimation should segregate to the surface (we shall call this “theory A”) [104], (b)

an approach based on elastic strain energy according to which the larger the solute atom relative to the solvent the higher the degree of surface segregation (we shall call this "theory B") [105] (c) an approach based on bulk alloy phase diagrams [106] according to which the surface segregation is related with the partitioning of solute to the melt of the alloy and surface segregation should occur when owing to distribution (partitioning) of solute the melt is richer in solute than the solid (we shall call this "theory C"), (d) an approach based on surface energy according to which the element with the lower surface energy segregates [107] (we shall call this "theory D").

In addition to the "theories" A to D electronic theory and computer simulations have been used to predict surface segregation of solutes in different solvents, particularly for transition metal - transition metal binary alloys, e.g., see references [102, 107-111]. We shall refer to the results of electronic theory calculations and computer simulations as "theory E".

Considering "theory A", the heat of sublimation (kJ/mol) of solvent and solute elements of binary Nb-X alloys with X the solutes of this research is as follows: Nb – 689.9, Ti – 425, Si – 359, Cr – 339.5, Sn (white) – 296.1 and Al – 284. Thus, according to "theory A" all the solutes in the alloys of this research should segregate to the surface of Nb-X alloys.

Considering "theory B", the atomic size (Å) of solvent and solute elements of binary Nb-X alloys with X the solutes of this research is as follows: Nb – 1.429, Ti – 1.462, Si – 1.153, Cr – 1.249, Al – 1.432, and Sn – 1.620. Thus, according to "theory B" the solutes Ti, Al and Sn should segregate to the surface of Nb-X alloys.

Considering "theory C", surface segregation should be expected for the binaries Nb-Si, Nb-Sn and Nb-Cr (because of small freezing range) but not for Nb-Ti and Nb-Al.

Considering "theory D", the surface energy (F_S) data (erg/cm^2) from Murr [112] gives F_s values Nb – 2100 (for T = 2250 °C), Cr – 2300, Al – 980 and Sn – 685, and thus predicts "strong" surface segregation for Al and Sn. If we were to use the equation F_s

(erg/cm^2) = 1.2 γ_{LV} + 0.45 (T_m – T) in Murr [112] with T_m – T = 223 K (T_m^{Nb} = 2473 C and T = 2250 °C) and γ_{LV} data from Table 3.4 in Murr [112] we calculate F_s values Nb – 2380, Ti – 2080, Si – 976, Cr – 2008, Al – 1140 and Sn – 760 and according to "theory D" the solutes Ti, Si, Al, Cr and Sn should segregate to the surface, with "strong" segregation for Sn, Si and Al. These conclusions are also supported by the calculation in [107]. Furthermore, data about surface energies from [113] would also predict (according to "theory D") surface segregation for Ti, Si, Al, Cr and Sn, with "strong" segregation for Sn, Si and Al (surface energies (erg/cm^2) Nb – 2700, Ti – 2050, Si – 1290, Cr – 2400, Al – 1200, Sn – 710). The equation 10 and data from Table 1 in [113] show that the surface concentration of Sn in Nb-5Sn would be 6.4 at.%.

Considering "theory E" Ruban *et al* [111] predict surface segregation of Ti in Nb-Ti, while Mukherjee and Moran-Lopez [109] predict surface segregation of Ti and Cr but Christensen *et al* [110] do not predict surface segregation of Ti.

The elements predicted to segregate to the surface of binary Nb-X alloys are summarised in Table 10.6.

Table 10.6: Solutes in Nb-X segregating to the surface

Theory	Surface segregating element				
A	Al	Cr	Si	Sn	Ti
B	Al			Sn	Ti
C		Cr	Si	Sn	
D	Al	Cr	Si	Sn	Ti
E*		Cr			Ti?

*for transition metal-transition metal binary alloys (see text)

All proposed approaches for surface segregation confirm that Sn should segregate to the surface, and would suggest that the other solute elements in the alloys of this study could also segregate to the surface.

Opila [114] showed (1) that the surface segregation of Sn in a polycrystalline dilute Pd-Sn alloy was enhanced in the presence of oxidising atmosphere and (2) that the surface segregation near grain boundaries was also enhanced.

The predictions of the available theories for surface segregation (Table 10.6), the experimental results of Opila, the fact that Al, Si and Sn can form equilibrium A-15 (Nb_3Al, Nb_3Sn) and metastable A-15 (Nb_3Si) compounds and that Nb_5Sn_2X can form with X = Al, Si, can explain:

- the formation of Sn rich areas at the scale/substrate interface the thickness and continuity of which increased with Sn content in the alloy and oxidation temperature,
- the formation of different Sn rich intermetallics at the scale/substrate interface depending on the surface concentration of Sn and other solute(s) and
- that these intermetallics were the $NbSn_2$, Nb_5Sn_2Si, Nb_3Sn the former two with Ti, Al and Cr and the latter with Ti, Cr, Al and Si in their composition and all contaminated by oxygen.

10.5 Comparison of the oxidation of the alloys at 800 °C

The starting (cast) microstructures of the alloys were summarised in Table 10.3. The TGA weight change data of the alloys, shown separately in the Figures 7.20a, 8.14a and 9.19a is compared in Figure 10.1. The oxidation kinetics data is summarised in Table 10.7 and the oxides forming the scale, and the phases in the oxygen diffusion zone and the bulk microstructures of the oxidised alloys are summarised in Table 10.8. The chemical compositions of the Nb rich and Nb and Si rich oxides formed in the scales of the three alloys are compared in Tables 10.9a, b and Tables 10.10a, b and the chemical compositions of the Nb_{ss}, Nb_5Si_3 and Nb_3Sn in the bulk microstructures of the oxidised alloys are compared in Tables 10.11a, b, Tables 10.12a, b and Table 10.13.

For the low Sn content alloys the TGA data suggested that break-away oxidation was more common in the alloys ZX5 and ZX7, i.e., the Al containing alloys, even though the latter alloy had lower linear oxidation rate constant compared with the alloy ZX3. The weight gain of the alloy ZX5 up to about 3000 mins at 800 °C was the highest of the three alloys and after that time it followed closely the weight change of the alloy ZX3.

For the high Sn content alloys the TGA data showed less breakaway oxidation for the alloys ZX4 and ZX6, with the strongest evidence of breakaway oxidation for the alloy ZX8. Up to about 1250 mins the weight gain of the latter exhibited essentially the same behaviour as the alloy ZX4, but after that time the weight change of the former alloy (ZX8) accelerated relative to the latter and after about 5250 mins it was equal to the weight change of the alloy ZX6 and exceeded that weight over longer times. However, the data for the alloy ZX8 must be considered with care for the reasons discussed in § 9.3.1. The lowest weight gain was exhibited by the alloy ZX4, see Figure 10.1, which also had the lowest parabolic rate constant, see Table 10.7. It should be noted that in the starting microstructure of the alloy ZX4 the Laves phase was present (Table 10.3) but was not observed after the oxidation at 800 °C (Table 10.8), which would suggest that the contamination of the ZX4 with oxygen altered the phase equilibria making the Laves phase unstable.

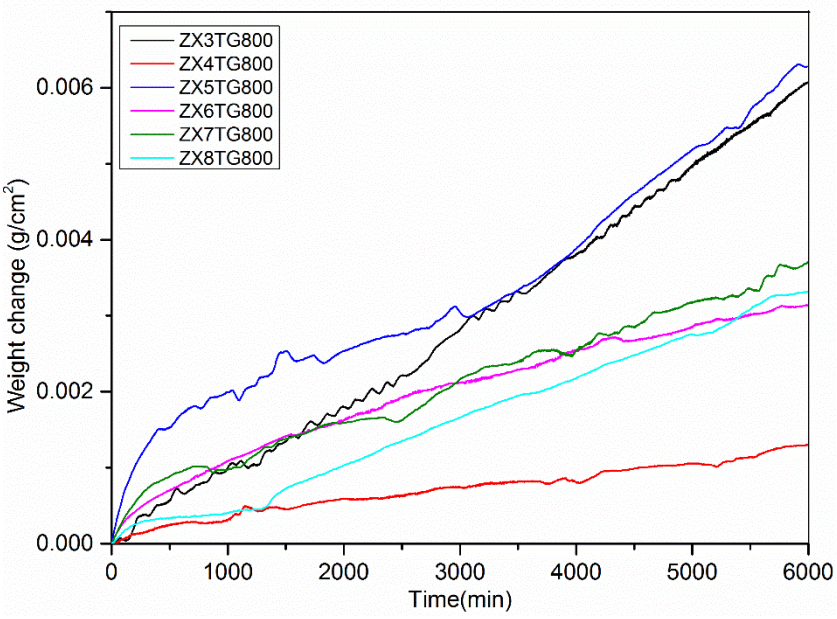


Figure 10.1 Comparison of the TGA data for the alloys of this research at 800 °C.

The weight change of the alloy ZX7 was lower than that of the other two alloys with low Sn content and up to about 4500 mins it followed closely the weight change of the alloy ZX6 at 800 °C. This could suggest that in the early stages of oxidation at 800 °C the same behaviour could be achieved with the simultaneous presence of about 5 at.% Al, 5 at.% Cr and 2 at.% Sn in the alloy (ZX7) as with about 5 at.% Al and 5 at.% Sn

in the alloy (ZX6). In the alloy ZX7 no Sn rich area was observed below the scale. This was not the case for the alloy ZX6. Both alloys exhibited parabolic oxidation in the early stages and linear oxidation after that. The significantly higher linear oxidation kinetic rate constant of the alloy ZX7 could be attributed to the absence of an Sn rich area below the scale. This effect of Sn probably was via the formation of the Sn rich layer below the scale of ZX6 but not in the case of the alloy ZX7, see Table 10.8.

Table 10.7 Oxidation kinetic rate constants of the alloys of this research at 800 °C and 1200 °C, linear rate constant k_l ($g \cdot cm^{-2} \cdot s^{-1}$), parabolic rate constant k_p ($g^2 \cdot cm^{-4} \cdot s^{-1}$)

Alloy	800 °C	1200 °C
ZX3	$k_l = 1.69 \times 10^{-8}$	$k_p = 4.54 \times 10^{-9}$ ($t \leq 1000$ mins)
		$k_l = 1.42 \times 10^{-7}$ ($t > 1000$ mins)
ZX4	$k_p = 4.69 \times 10^{-12}$	$k_p = 1.65 \times 10^{-9}$ ($t \leq 1000$ mins)
		$k_l = 1.00 \times 10^{-7}$ ($t > 1000$ mins)
ZX5	$k_p = 5.16 \times 10^{-11}$ ($t \leq 3000$ mins)	$k_p = 1.15 \times 10^{-9}$ ($t \leq 1300$ mins)
	$k_l = 1.80 \times 10^{-8}$ ($t > 3000$ mins)	$k_l = 6.70 \times 10^{-8}$ ($t > 1300$ mins)
ZX6	$k_p = 2.22 \times 10^{-11}$ ($t \leq 1500$ mins)	$k_l = 7.31 \times 10^{-8}$
	$k_l = 6.40 \times 10^{-9}$ ($t > 1500$ mins)	
ZX7	$k_p = 1.76 \times 10^{-11}$ ($t \leq 2500$ mins)	$k_p = 5.91 \times 10^{-9}$ ($t \leq 2200$ mins)
	$k_l = 9.94 \times 10^{-9}$ ($t > 2500$ mins)	$k_l = 1.42 \times 10^{-7}$ ($t > 2200$ mins)
ZX8	$k_p = 2.81 \times 10^{-12}$ ($t \leq 1320$ mins)	$k_l = 1.07 \times 10^{-7}$
	$k_l = 1.01 \times 10^{-8}$ ($t > 1320$ mins)	

The same oxides were formed in the scales of all the alloys at 800 °C (Table 10.8). Regarding the Nb rich oxide in the scales (see Tables 10.9a and b), as the Sn content in the alloys increased (Table 10.9b) the concentrations of Al and Cr in the oxide increased when the latter two elements were present in the alloy simultaneously (alloy ZX8). In the alloys with high Sn content (Table 10.9b) in which the Al and Cr were present individually the ratios (Nb + Ti)/Si, (Nb + Ti)/(Si + Sn), and (Nb + Ti)/(Si + Al + Sn) did not differ significantly. The concentrations of Sn and Cr decreased and Al increased in the Nb rich oxide when Al and Cr were present in the Sn rich alloys individually compared with the low Sn content alloys. (Tables 10.9a and b).

In the "best" alloy at 800 °C (alloy ZX4) the Nb rich oxide had the lowest (Nb + Ti)/Si and highest (Nb + Ti)/(Al + Cr + Sn) ratios (17.9 and 12.6 respectively) and the lowest Sn and highest Si concentrations and the highest Nb + Ti ratio of all the studied alloys.

In the Nb rich oxide on the alloys ZX7 and ZX6, whose weight changes were similar up to 4500 mins at 800 °C, the Si concentration was the same and the (Nb + Ti)/(Al + Si + Sn) and Nb/Ti ratios were similar (Tables 10.9a and b).

Table 10.8 Comparison of scales, diffusion zones and bulk microstructures in the oxidised alloys of this research at 800 °C.

Alloy	Oxide Scale		Enrichment in Sn and Sn rich phase(s) formation	Oxygen diffusion zone		Bulk microstructure
	Thickness (μm)	Oxides		Thickness (μm)	Phases	Phases
ZX3	15	Nb rich, Nb and Si rich	Yes	40	Nb_5Si_3, oxidised Nb_{ss}	Nb_5Si_3, Nb_{ss}
ZX4	10	Nb rich, Nb and Si rich, Ti rich$^+$	Yes	20	Nb_5Si_3, Nb_3Sn, oxidised Nb_{ss}	Nb_5Si_3, Nb_3Sn, Nb_{ss}
ZX5	10-15	Nb rich, Nb and Si rich	Yes	50	Nb_5Si_3, oxidised Nb_{ss}	Nb_5Si_3, Nb_{ss}
ZX6	10	Nb rich, Nb and Si rich	Yes	30	Nb_5Si_3, Nb_3Sn, (Nb_5Si_3 + Nb_{ss})*	Nb_5Si_3, Nb_3Sn, (Nb_5Si_3 + Nb_{ss})
ZX7	10	Nb rich, Nb and Si rich	Not observed	40	Nb_5Si_3, oxidised Nb_{ss}	Nb_5Si_3, Nb_{ss}
ZX8	5	Nb rich, Nb and Si rich	Yes	10	Nb_5Si_3, Nb_3Sn	Nb_5Si_3, Nb_{ss}, Nb3Sn, Laves (Nb_5Si_3 + Nb_{ss})

*oxidised structure
+ no WDS data for this oxide type

Regarding the Nb and Si rich oxide, when the Al and Cr were present individually or simultaneously in the high Sn content alloys the Al and Cr concentrations in the oxide increased and the concentration of Sn decreased (Table 10.10b). In the low and high Sn content alloys the Nb/Ti ratios were essentially constant at 3.2 and 2.2 respectively, Tables 10.10a and b.

In the “best” alloy at 800 °C (alloy ZX4) the Nb and Si rich oxide had the highest Si and Si + Sn, and the lowest Sn and (Nb + Ti)/Si of all the studied alloys. The “worst” alloy at 800 °C (alloy ZX5) had the lowest Al and (Nb + Ti)/(Al + Si + Sn) ratio of all the studied alloys, see Tables 10.10a and b.

Table 10.9a Comparison of the Nb rich oxides formed in the scales of the low Sn content alloys of this research at 800 °C

Alloy	Nb	Ti	Si	Cr	Al	Sn	O	Nb+Ti	[Nb+Ti]/Si	Si+Sn	Si+Sn+Al	[Nb+Ti]/ [Si+Sn]	[Nb+Ti]/ [Si+Al+Sn]	Al+Cr+Sn	[Nb+Ti]/ [Al+Cr+Sn]	Nb/Ti
ZX3	15.97	9.02	0.34	3.66		0.29	70.72	24.99	73.5	0.63		39.7		3.95	6.33	1.77
ZX5	20.15	8.44	1.48		1.78	1.27	66.88	28.59	19.3	2.75	4.53	10.4	6.3	3.05	9.37	2.39
ZX7	14.24	9.78	1.32	2.81	0.76	1.07	70.02	24.02	18.2	2.39	3.15	10	7.6	4.64	3.92	1.46

Table 10.9b Comparison of the Nb rich oxides formed in the scales of the high Sn content alloys of this research at 800 °C

Alloy	Nb	Ti	Si	Cr	Al	Sn	O	Nb+Ti	[Nb+Ti]/Si	Si+Sn	Si+Sn+Al	[Nb+Ti]/ [Si+Sn]	[Nb+Ti]/ [Si+Al+Sn]	Al+Cr+Sn	[Nb+Ti]/ [Al+Cr+Sn]	Nb/Ti
ZX4	18.40	10.99	1.64	2.99		0.08	65.91	29.39	17.92	1.72		17.1		3.07	12.64	1.67
ZX6	17.52	10.78	1.35		2.26	0.55	67.54	28.3	20.97	1.9	4.16	14.9	6.8	2.81	10.1	1.62
ZX8	19.66	8.83	0.62	4.67	1.46	0.17	64.59	28.49	45.95	0.79	2.25	36.06	12.7	6.3	10.8	2.22

Table 10.10a Comparison of the Nb and Si rich oxides formed in the scales of the low Sn content alloys of this research at 800 °C

Alloy	Nb	Ti	Si	Cr	Al	Sn	O	Nb+Ti	[Nb+Ti]/ Si	Si+Sn	Si+Sn+Al	[Nb+Ti]/ [Si+Sn]	[Nb+Ti]/ [Si+Al+Sn]	Al+Cr+Sn	[Nb+Ti]/ [Al+Cr+Sn]	Nb/Ti
ZX3	13.85	4.33	11.84	0.28		0.28	69.42	18.18	1.54	12.12		1.5		0.56	32.5	3.2
ZX5	15.50	4.94	12.75		0.54	0.19	66.08	20.44	1.6	12.94	13.48	1.58	1.52	0.73	28	3.14
ZX7	16.11	5	11.80	0.25	0.89	0.27	65.68	21.11	1.8	12.07	12.96	1.75	1.63	1.41	14.97	3.2

Table 10.10b Comparison of the Nb and Si rich oxides formed in the scales of the high Sn content alloys of this research at 800 °C

Alloy	Nb	Ti	Si	Cr	Al	Sn	O	Nb+Ti	[Nb+Ti]/ Si	Si+Sn	Si+Sn+Al	[Nb+Ti]/ [Si+Sn]	[Nb+Ti]/ [Si+Al+Sn]	Al+Cr+Sn	[Nb+Ti]/ [Al+Cr+Sn]	Nb/Ti
ZX4	14.21	5.83	13.30	0.54		0.15	65.97	20.04	1.51	13.45		1.5		0.69	29.73	2.44
ZX6	15.11	7.59	9.41		1.13	0.48	66.28	22.7	2.41	9.89	11.02	2.3	2.06	1.61	14.1	1.99
ZX8	15.33	6.92	10.72	0.66	1.55	0.18	64.63	22.25	2.08	10.9	12.45	2.04	1.79	2.39	11.7	2.2

Table 10.11a Comparison of the compositions of the Nbss in the bulk of the oxidised low Sn content alloys of this research at 800 °C

Alloy	Nb	Ti	Si	Cr	Al	Sn	O	Ti/(Si+Sn+Cr+Al)	Si+Sn	Si+Sn+Al	Si/Sn	Al+Cr+Sn	Nb/Ti	Ti+Si+Sn+Al+Cr
ZX3	56.7	25.9	1.7	7.2		2.7	5.8	2.2	4.4		0.63	9.9	2.2	37.5
ZX5	54.4	31.8	1.5		4.2	2.6	5.5	3.8	4.1	8.3	0.58	6.8	1.7	40.1
ZX7	51.3	27.6	1.2	6.2	5.2	2.2	6.3	1.9	3.4	8.6	0.55	13.6	1.9	42.4

Table 10.11b Comparison of the compositions of the Nbss in the bulk of the oxidised high Sn content alloys of this research at 800 °C, no data for the alloys ZX6, ZX8

Alloy	Nb	Ti	Si	Cr	Sn	O	Ti/(Si+Sn+Cr+Al)	Si+Sn	Si/Sn	Nb/Ti	Ti+Si+Sn+Al+Cr
ZX4	46.7	29.4	2.7	9.2	4.8	7.2	1.76	7.5	0.56	1.6	46.1

Table 10.12a Comparison of the compositions of the Nb_5Si_3 in the bulk of the oxidised low Sn content alloys of this research at 800 °C

Alloy	Nb	Ti	Si	Cr	Al	Sn	O	Si+Sn	Si+Sn+Al	Nb/Ti
ZX3	42.2	16.1	35.8	1		0.7	4.2	36.5		2.6
ZX5	44.6	15	35		1.8	0.6	3	35.6	37.4	3
ZX7	44.7	16.8	29.6	1.1	3.7	1.1	3	30.7	34.4	2.7

Table 10.12b Comparison of the compositions of the Nb_5Si_3 in the bulk of the oxidised high Sn content alloys of this research at 800 °C

Alloy	Nb	Ti	Si	Cr	Al	Sn	O	Si+Sn	Si+Sn+Al	Nb/Ti
ZX4	43.7	15.6	34	1		1.5	4.2	35.5		2.8
ZX6	42.9	16.5	33.7		2.5	2	2.4		38.2	2.6
ZX8	41	19.7	32.3	1.2	0.9	1	3.9		34.2	2.1

The contamination by oxygen of the Nb_{ss} in the bulk of the oxidised alloys at 800 °C seemed to increase with the Sn concentration in the alloy (Tables 10.11a and b). However, in all the studied alloys the Si/Sn ratio for the Nb_{ss} in the bulk was essentially the same, about 0.57. In the "best" alloy at 800 °C (alloy ZX4) the Cr and Sn concentrations in the Nb_{ss} were the highest of all studied alloys and the Nb_{ss} of this alloy had the lowest Ti/(Al + Cr + Si + Sn) and Nb/Ti ratios and the highest Si + Sn and Ti + Si + Sn + Al + Cr concentrations. In the "worst" alloy at 800 °C (ZX5) the Nb_{ss} had the highest Ti/(Al + Cr + Si + Sn) ratio (Tables 10.11a and b).

Table 10.13 Comparison of the compositions of the Nb3Sn in the bulk of the oxidised high Sn content alloys of this research at 800 °C

Alloy	Nb	Ti	Si	Cr	Al	Sn	O	Si+Sn	Si+Sn+Al	Nb/Ti
ZX4	55	20.5	5.9	2.9		9.4	6.3	15.3		2.7
ZX6	53.4	22	5.1		4.6	8.6	6.3	13.7	18.3	2.4
ZX8	54.5	19.6	2.4	3.8	5.2	8.3	6.2	10.7	15.9	2.8

There was contamination by oxygen of the Nb_5Si_3 in the bulk of all the studied alloys after oxidation at 800 °C and this seemed to be higher for the 5-3 silicide in the "best" alloy (ZX4), see Tables 10.12a and b. The increase of Sn concentration in the alloy caused a slight increase in the Sn concentration in the Nb_5Si_3 and did not have any strong effects on the composition of Nb_5Si_3 in the bulk. The Nb_3Sn in the bulk of the high Sn content alloys was also contaminated by oxygen but the concentration of the latter was the same (~ 6 at.%) regardless of whether the Al and Cr were present individually or simultaneously in the alloys (Table 10.13). In the "best" alloy at 800 °C

(alloy ZX4) the Nb_3Sn had the highest Si and Sn concentrations and thus the highest Si + Sn concentration.

10.6 Comparison of the oxidation of the alloys at 1200 °C

The starting (cast) microstructures of the alloys were summarised in Table 10.3. The TGA weight change data of the alloys, shown separately in Figures 7.20b, 8.14b and 9.19b, is compared in Figure 10.2. The oxidation kinetics data is summarised in Table 10.7 and the oxides forming the scale, and the phases in the Sn rich area zone and the bulk microstructures of the oxidised alloys are summarised in Table 10.14. The chemical compositions of the Nb rich, Nb and Si rich and Ti rich oxides formed in the scales of the three alloys are compared respectively in Tables 10.15a, b, Tables 10.16a, b and Tables 10.17a, b and the chemical compositions of the Nb_{ss}, Nb_5Si_3 and Nb_3Sn in the bulk microstructures of the oxidised alloys are compared respectively in Tables 10.18a, b, Tables 10.19a, b and Tables 10.20a, b. All alloys of this research suffered from spallation of their scale at 1200 °C.

Table 10.14 Comparison of the alloys of this research in terms of the scale thickness, oxides in the scale, thickness of Sn rich area, Sn rich intermetallics forming in the latter and phases in the bulk microstructure after oxidation at 1200 °C.

Alloy	Scale		Sn rich area		Bulk
	Thickness (μm)	Oxides	Thickness (μm)	Sn rich intermetallics	Phases
ZX3	450	Nb rich, Nb and Si rich, Ti rich	25	Nb_5Si_3, Nb_3Sn, Nb_5Sn_2Si, $NbSn_2$	Nb_5Si_3, Nb_{ss}, Laves phase
ZX4	500	Nb rich*, Nb and Si rich*, Ti rich*	55	Nb_5Si_3, Nb_3Sn, Nb_5Sn_2Si, $NbSn_2$	Nb_5Si_3, Nb_{ss}, Nb_3Sn, Laves phase
ZX5	300	Nb rich, Nb and Si rich,	10	Nb_5Si_3, Nb_3Sn, Nb_5Sn_2Si	Nb_5Si_3, Nb_{ss}, A15-Nb_3X,
ZX6	300	Nb rich, Nb and Si rich, Ti rich	50	Nb_5Si_3, Nb_3Sn, Nb_5Sn_2Si	Nb_5Si_3, Nb_3Sn
ZX7	400	Nb rich, Nb and Si rich, Ti rich	35	Nb_5Si_3, $NbSn_2$, Nb_5Sn_2Si	Nb_5Si_3, Nb_{ss}, A15-Nb_3X, Laves phase
ZX8	250	Nb rich, Nb and Si rich, Ti rich	50	Nb_5Si_3, Nb_3Sn, Nb_5Sn_2Si	Nb_5Si_3, Nb_3Sn, Laves phase

*no WDS data for this oxide is available

The low Sn content alloys had Nb_{ss} in their (as cast) microstructures at the start and end of oxidation at 1200 °C. These alloys did not show breakaway oxidation, Figures

7.20b, 8.14b and 9.19b and Figure 10.2. The weight changes of the alloys ZX3 and ZX7 were essentially the same, as were the thicknesses of their scales (Table 10.14) and their linear oxidation rate constants (Table 10.7), and all three (i.e., weight change, scale thickness and rate constant) were higher than those of the alloy ZX5. In the scales of the alloys ZX3 and ZX7 the Nb rich, Nb and Si rich and Ti rich oxides were present but the latter oxide was not present in the scale of the alloy ZX5 (see Tables 10.15a, 10.16a, 10.17a). Furthermore, the thickness of the Sn rich area formed at the scale/substrate interface was lower in the alloy ZX5 (no Cr) and highest in the alloy ZX7 (both Al and Cr present). The $NbSn_2$ was formed in the Sn rich areas of the alloys ZX3 and ZX7 but not in ZX5.

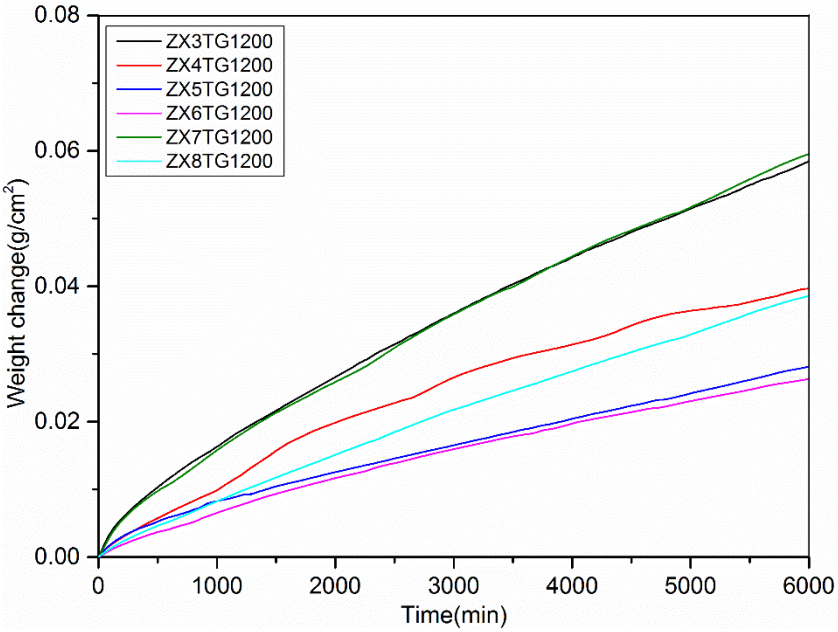


Figure 10.2 Comparison of the TGA data for the alloys of this research at 1200 °C.

The above results for the low Sn content alloys would suggest (i) that the surface segregation of Sn was less severe when Al was only present in the alloy, (ii) that Nb_5Sn_2Si and Nb_3Sn in the Sn rich area were "beneficial" for oxidation resistance, (iii) that the Laves phase did not "benefit" oxidation at 1200 °C, (iv) that the synergy of Al and Cr with low Sn concentration in the alloy was detrimental to oxidation at 1200 °C and therefore (v) that Al was most important for oxidation at 1200 °C (while as we show Cr was most important for oxidation at 800 °C, Figure 10.1).

Table 10.15a Comparison of the Nb rich oxides formed in the scales of the low Sn content alloys of this research at 1200 °C

Alloy	Nb	Ti	Si	Cr	Al	Sn	O	Nb+Ti	[Nb+Ti]/ Si	Si+Sn	Si+Sn+Al	[Nb+Ti]/ Si+Sn	[Nb+Ti]/ Si+Al+Sn	Al+Cr+Sn	[Nb+Ti] /Al+Cr+Sn	Nb/Ti
ZX3	18.34	5.87	4.46	0.41		0.04	70.88	24.21	5.43	4.5		5.38		0.45	53.8	3.12
ZX5	20.70	9.78	0.47		1.83	0.16	67.06	30.48	64.85	0.63	2.46	48.38	12.39	1.99	15.32	2.12
ZX7	25	5.93	0.08	0.17	0.82	0.01	67.99	30.93	386.6	0.09	0.91	343.67	33.99	1	30.93	4.22

Table 10.15b Comparison of the Nb rich oxides formed in the scales of the high Sn content alloys of this research at 1200 °C (No data for the alloy ZX4)

Alloy	Nb	Ti	Si	Cr	Al	Sn	O	Nb+Ti	[Nb+Ti]/ Si	Si+Sn	Si+Sn+Al	[Nb+Ti]/ Si+Sn	[Nb+Ti]/ Si+Al+Sn	Al+Cr+Sn	[Nb+Ti]/ Al+Cr+Sn	Nb/Ti
ZX6	24.3	7.8	0.04		1.27	0	66.57	32.11	802.8	0.04	1.31	802.8	24.5	1.27	25.28	3.1
ZX8	20.62	7.68	0.086	0.22	0.20	0	71.19	28.3	329	0.086	1.08	329	26.2	0.42	67.38	2.7

Table 10.16a Comparison of the Nb and Si rich oxides formed in the scales of the low Sn content alloys of this research at 1200 °C

Alloy	Nb	Ti	Si	Cr	Al	Sn	O	Nb+Ti	[Nb+Ti]/ Si	Si+Sn	Si+Sn+Al	[Nb+Ti]/ Si+Sn	[Nb+Ti]/ Si+Al+Sn	Al+Cr+Sn	[Nb+Ti]/ Al+Cr+Sn	Nb/Ti
ZX3	13.08	5.53	9.31	0.26		0.03	71.79	18.61	2	9.34		2		0.29	64.2	3.36
ZX5	16.26	4.87	10.83		0.52	0.15	67.38	21.13	1.95	10.98	11.5	1.92	1.84	0.67	31.5	3.34
ZX7	14.37	4.5	12.74	0.46	0.74	0.01	67.18	18.87	1.48	12.75	13.49	1.48	1.4	1.21	15.6	3.2

Table 10.16b Comparison of the Nb and Si rich oxides formed in the scales of the high Sn content alloys of this research at 1200 C (No data for the alloy ZX4)

Alloy	Nb	Ti	Si	Cr	Al	Sn	O	Nb+Ti	[Nb+Ti]/ Si	Si+Sn	Si+Sn+Al	[Nb+Ti]/ Si+Sn	[Nb+Ti]/ Si+Al+Sn	Al+Cr+Sn	[Nb+Ti]/ Al+Cr+Sn	Nb/Ti
ZX6	14.7	5.64	13.55		0.48	0	65.62	20.34	1.5	13.55	14.04	1.5	1.45	0.48	42.38	2.6
ZX8	14.33	5.40	8.8	0.53	0.53	0.013	70.39	19.7	2.2	8.8	9.34	2.2	2.1	1.07	18.4	2.6

Table 10.17a Comparison of the Ti rich oxides formed in the scales of the low Sn content alloys of this research at 1200 °C (not observed in the alloy ZX5)

Alloy	Nb	Ti	Si	Cr	Al	Sn	O	Nb+Ti	[Nb+Ti]/ Si	Si+Sn	Si+Sn+Al	[Nb+Ti]/ Si+Sn	[Nb+Ti]/ Si+Al+Sn	Al+Cr+Sn	[Nb+Ti]/ Al+Cr+Sn	Nb/Ti
ZX3	6.10	17.49	0.16	6.01		0.24	70.00	23.59	147.4	0.4		59		6.25	3.77	0.35
ZX7	8.69	15.48	1.32	3.93	3.76	0.19	66.63	24.17	18.3	1.51	5.27	16	4.7	7.9	10.9	0.56

Table 10.17b Comparison of the Ti rich oxides formed in the scales of the high Sn content alloys of this research at 1200 °C (no data for the alloy ZX4)

Alloy	Nb	Ti	Si	Cr	Al	Sn	O	Nb+Ti	[Nb+Ti]/ Si	Si+Sn	Si+Sn+Al	[Nb+Ti]/ Si+Sn	[Nb+Ti]/ Si+Al+Sn	Al+Cr+Sn	[Nb+Ti]/ Al+Cr+Sn	Nb/Ti
ZX6	6.57	21.11	0.14		5.5	0.06	66.6	27.69	197.8	0.20	5.7	138.45	4.86	5.56	5	0.3
ZX8	7.23	17.63	0.15	3.46	1.88	0.351	69.31	24.86	165.7	0.5	2.38	49.7	10.45	5.69	4.37	0.4

The high Sn content alloys started oxidation at 1200 °C with only the alloy ZX8 not having the Nb_{ss} in its microstructure. The contamination of the microstructure of the latter alloy by oxygen did not stabilise the Nb_{ss} during oxidation at 1200 °C. However, in the alloy ZX6 the Nb_{ss} was not stable after the heat treatment at 1500 °C (see chapter 8) and the Nb_{ss} was not observed in the oxidised alloy ZX6. Therefore, the Nb_{ss} was not present in both the oxidised alloys ZX6 and ZX8, of which the former was the "best" in terms of its oxidation behaviour at 1200 °C.

For the three high Sn content alloys the TGA data suggested break-away oxidation only for the alloy ZX4, i.e., the Cr containing alloy, even though the latter alloy had almost the same linear oxidation rate constant compared with the alloy ZX8. These two alloys, contained the Laves phase in their starting microstructures and after oxidation at 1200 °C, had gained the same weight in the early stages of oxidation (up to about 500 mins) and after about 6000 mins, see Figure 10.2. But in between these times the weight gain of the former increased, owing to the breakaway oxidation, which would suggest that the simultaneous presence of Al and Cr in the latter alloy had improved the mechanical behaviour of the scale when the Sn content had increased. This phenomenon must be attributed to Al, as the weight gains of the two Al containing alloys ZX5 and ZX6 were essentially not significantly different but the oxidation of the alloy ZX6 (high Sn content) was linear throughout while that of ZX5 was initially parabolic followed by linear behaviour with a linear rate constant slightly lower than ZX6. This would suggest that with Al in the alloy 2 at% Sn is good enough for oxidation at 1200°C. However, as we show for the oxidation at 800°C, the higher Sn content of ZX6 compared to ZX5 was beneficial for pest oxidation.

We have no WDS data for the oxides in the scale of the alloy ZX4 (only Cr present). Figure 7.32 shows that three oxides were present in its scale. The "best" alloy in terms of its oxidation behaviour at 1200 °C was the alloy ZX6 (see Figure 10.2 and Table 10.14). The scales formed on the alloys ZX4, ZX6 and ZX8 contained Nb rich, Nb and Ti rich and Ti rich oxides. Therefore, as the Sn content of the alloy increased the Ti rich oxide formed in the scale of ZX6 (was not observed in the scale of the alloy ZX5).

The increase in Sn content in the alloys was accompanied with thicker Sn rich areas at the scale/substrate interface (Table 10.14), which is consistent with the surface segregation of a solute element being dependent on the bulk concentration (see section 10.4) but in the three alloys ZX4, ZX6 and ZX8 the thickness of this area was essentially the same (≈ 50 μm) while it varied between the low Sn content alloys (Table 10.14). The same Sn rich intermetallic phases were formed in the Sn rich areas of the alloys with the exception of $NbSn_2$ that was formed only in the alloy ZX4, which exhibited the "worst" oxidation of the three high Sn content alloys of this study (Table 10.14 and Figure 10.2). This observation and the data for the low Sn content alloys, where the $NbSn_2$ was not formed in the Sn rich area of the alloy ZX5 but was formed in the alloy ZX7, would suggest that the formation of $NbSn_2$ in the microstructure at the scale/substrate interface was detrimental to oxidation at 1200 °C.

The TGA data for all the alloys of this research thus supports conclusions (ii) and (v) above (see discussion of low Sn content alloys, third paragraph of this section) and would also suggest (a) that high Sn (i.e., about 5 at.% Sn) content in the alloy and the presence of Laves phase are not essential requirements for achieving "best" oxidation behaviour at 1200 °C and (b) that with only Sn as the alloying addition improving oxidation resistance, the spallation of the scale cannot be avoided, even though the synergy of Al and Cr with Sn seems to (might) have some effect on the mechanical behaviour of the scales.

The Nb rich oxide formed in the scale of the alloys, considering the errors in WDS analysis, essentially did not contain Al, Cr, Si and Sn (Tables 10.15a, b) and compared with the same oxide type formed at 800 °C had the same Nb + Ti but higher Nb/Ti ratio.

The concentrations of Al, Cr and Sn in the Nb and Si rich oxide formed in the scale of the alloys were essentially zero (Tables 10.16a, b) with similar Nb + Ti, (Nb + Ti)/Si and lower Nb/Ti ratios as the Sn content in the alloys increased. Very low were the concentrations of the same elements in the Nb and Si rich oxides formed at 800 °C. At 1200 °C the Nb/Ti ratio was about 3.3 in the low Sn alloys and 2.6 in the high Sn

alloys, the same ratio (3.2) as in the low Sn alloys at 800 °C and slightly higher than the ratio (2.2) in the high Sn alloys. The Nb + Ti content of the Nb and Si rich oxide formed in the scales of the low Sn content alloys at 800 °C and 1200 °C was essentially the same. The alloys at 800 °C (ZX4) and 1200 °C (ZX6) had the same values for Nb/Ti, Nb + Ti, (Nb + Ti)/Si, (Nb + Ti)/(Si + Sn).

Ti rich oxide was observed only at 1200 °C and the concentrations of Al and Cr in the oxide were low but not zero and comparable with those in the Nb rich oxide formed at 800 °C. The Nb + Ti content of the Ti rich oxide was between those of the other two oxides formed at 1200 °C, and like the Nb rich oxide it was essentially free of Si and Sn. The Nb/Ti ratio did not change significantly as the Sn content in the alloy increased (Tables 10.17a, b).

Table 10.18a Comparison of the compositions of the Nb_{ss} in the bulk of the oxidised low Sn content alloys of this research at 1200 °C, no data for the Nb_{ss} in the alloy ZX7

Alloy	Nb	Ti	Si	Cr	Al	Sn	O	Si + Sn	Si/Sn	Nb/Ti
ZX3	56.8	23.5	0.2	7.5		3.3	8.7	3.5	0.06	2.4
ZX5	58.8	28	0.3		3.4	1.4	8.1	3.7	0.09	2.1

Table 10.18b Comparison of the compositions of the Nb_{ss} in the bulk of the oxidised high Sn content alloys of this research at 1200 °C, no Nb_{ss} in the alloys ZX6, ZX8

Alloy	Nb	Ti	Si	Cr	Sn	O	Si + Sn	Si/Sn	Nb/Ti
ZX4	54.8	26.4	2.9	6.4	3.1	6.4	6	0.94	2.1

It is suggested (1) that the parameters Nb + Ti and Nb/Ti "controlled" the oxide types in the scales of the alloys of this study, (2) that the Al and/or Cr participated in (stabilised?) the Ti rich oxide possibly as the Nb rich oxide approached its "equilibrium" composition at 1200 °C making Al and Cr available for the Ti rich oxide and (3) that Al and Cr do not play a key role in the formation of the Nb and Si rich oxide (their concentrations were very low at 800 °C and essentially zero at 1200 °C). The solubility of oxygen in the Nb_{ss} in the bulk decreased with increase in the Sn content of the alloy ZX4. Compared with the Si content of the Nb_{ss} in the heat treated alloy ZX4, the Si content in the bulk of the alloy after oxidation at 1200 °C was very high and out of step with other data from the group. It is therefore proposed that it is highly likely that the Si concentration in Table 10.18b is wrong, probably due to

analysis error. If we were to accept this then in the Nb_{ss} the parameters Si + Sn, Si/Sn and Nb/Ti did not change significantly with increase of the Sn content of the alloy. If we were not to accept the above proposition then only the ratio Nb/Ti did not change significantly with increase of the Sn content of the alloy.

Table 10.19a Comparison of the compositions of the Nb_5Si_3 in the bulk of the oxidised low Sn content alloys of this research at 1200 °C

Alloy	Nb	Ti	Si	Cr	Al	Sn	O	Si + Sn	Si + Sn + Al	Nb/Ti
ZX3	43.8	16.6	34.3	0.9		0.7	3.7	35		2.6
ZX5	44.2	14.9	34.6		1.7	0.6	4	35.2	36.9	3
ZX7	41.9	18	33.1	0.3	1.4	0.4	4.9	33.5	34.9	2.3

Table 10.19b Comparison of the compositions of the Nb_5Si_3 in the bulk of the oxidised high Sn content alloys of this research at 1200 °C

Alloy	Nb	Ti	Si	Cr	Al	Sn	O	Si + Sn	Si + Sn + Al	Nb/Ti
ZX4	43.6	15.4	34.9	0.9		1.6	3.6	36.5		2.8
ZX6	43.1	15.6	33.9		1.5	1.4	4.5	35.3	36.8	2.8
ZX8	42	19	30.2	0.7	2.8	1.1	4.2	31.3	34.1	2.2

The solubility of oxygen and the parameters Si + Sn, Si + Sn + Al and Nb/Ti in the Nb_5Si_3 in the bulk of the alloys at 1200 °C did not change as the Sn content of the alloys increased but the Sn concentration in the silicide increased (Table 10.19a and b).

In the A15 intermetallic phase the oxygen solubility was the same as in the Nb_{ss} of the alloy ZX4 (Tables 10.20a, b and 10.18b) and the A15 phase at 800 °C (Table 10.13) and did not change with increasing Sn in the alloys, but the Sn concentration increased. At 1200 °C the Nb/Ti ratio did not change significantly compared with 800 °C (Tables 10.13 and 10.20a, b) and with increasing Sn content in the alloy (Table 10.20a, b).

Table 10.20a Comparison of the compositions of the Nb_3Sn in the bulk of the oxidised low Sn content alloys of this research at 1200 °C

Alloy	Nb	Ti	Si	Cr	Al	Sn	O	Si + Sn	Si+Sn+Al	Nb/Ti
ZX5	56.8	22	3.1		7.2	5.1	5.8	8.2	15.4	2.6
ZX7	51.5	18.1	2.4	4.7	9.6	6.9	6.8	9.3	18.9	2.8

Table 10.20b Comparison of the compositions of the Nb_3Sn in the bulk of the oxidised high Sn content alloys of this research at 1200 °C.

Alloy	Nb	Ti	Si	Cr	Al	Sn	O	Si + Sn	Si + Sn + Al	Nb/Ti
ZX4	48.8	26.4	2.9	3.8		12.4	5.7	15.3		1.85
ZX6	54.2	23.5	3.1		5	8.6	5.6	11.7	16.7	2.3
ZX8	51.8	21.8	1.5	4.3	6.4	8.2	6	9.7	16.1	2.4

Chapter 11
Conclusions and Suggestions for future work

11.1 Conclusions

In this research Nb-Si ternary alloys with low and high concentrations of Sn and higher order Nb-24Ti-18Si based alloys with 5 at.% of both Al and Cr added individually and simultaneously were studied in the cast and heat treated conditions (100 h at 1200 °C, 1500 °C or 1450 °C depending on alloy) to understand how Sn on it's own and in synergy with Al and Cr individually and simultaneously affects the stability (i) of Nb_3Sn in the alloys and (ii) of Nb_{ss}, Nb_3Sn, βNb_5Si_3 and αNb_5Si_3 and Laves phase in the higher order alloys.

The role played by Sn in the isothermal oxidation behaviour of the latter alloys was also studied at 800 °C and 1200 °C.

The studied alloys had nominal compositions (at.%) Nb-14Si-3Sn (ZX1), Nb-12.5Si-7.5Sn (ZX2), Nb-24Ti-18Si-5Cr-2Sn (ZX3), Nb-24Ti-18Si-5Cr-5Sn (ZX4), Nb-24Ti-18Si-5Al-2Sn (ZX5), Nb-24Ti-18Si-5Al-5Sn (ZX6), Nb-24Ti-18Si-5Cr-5Al-2Sn (ZX7) and Nb-24Ti-18Si-5Cr-5Al-5Sn (ZX8).

Cast and heat treated alloys

Alloy making: Special clean melting technique(s) are required for preparing Nb-Si based alloys with specific alloy chemistries containing low and high Sn concentrations, owing to the low melting point and high vapour pressure of Sn.

Macrosegregation of Si: The macrosegregation of Si was more severe in the high Sn content alloys with Al and Cr added individually or simultaneously, with Al having

the weakest effect and Al + Cr having the strongest effect (MACS values 10 (ZX8), 7.3 (ZX4), 5.5 (ZX6)). The opposite was the case in the low Sn content alloys (MACS values 5.5 (ZX5), 3.6 (ZX3), 3 (ZX7)).

Nb_{ss}: In the presence of Sn regardless of the concentration, Cr on its own or together with Al stabilised the Nb_{ss} in the heat treated microstructure. However, the stability of Nb_{ss} depended on the Sn concentration in the alloy when only Al was present; the Nb_{ss} was destabilised by the high Sn concentration in the alloy ZX6. Indeed, in this alloy the Nb_{ss} was formed during solidification and was destabilised after the heat treatment at 1500 °C. In the alloy ZX8, where Al and Cr were present simultaneously, the Nb_{ss} was stabilised after the heat treatment even though it was not formed in the cast microstructure.

Ti rich areas were formed in the Nb_{ss} in the low Sn content alloys in the cast microstructures. In the latter alloys the Si/Sn ratio and the Si + Sn concentration were essentially the same (≈ 1 and 5.5) for the Nb_{ss} and Ti rich Nb_{ss}. The Si/Sn ratio and the Si + Sn concentration respectively decreased (≈ 0.65) and increased in the Nb_{ss} in the high Sn content alloys. In all alloys the Si/Sn ratio and the Si + Sn concentration in the Nb_{ss} decreased after heat treatment, consistent with the reduced Si solubility in the Nb_{ss} after heat treatment.

Nb_3Si: The equilibrium (tetragonal tP32) Nb_3Si was not stable in any of the studied alloys with low or high Sn concentration. The destabilising effect of Sn concentration in the ternary alloys ZX1 and ZX2 was not mitigated by the addition of 24 at.% Ti or by the additions of 5 at.% each of Cr or Al individually or simultaneously in the higher order alloys.

βNb_5Si_3: The high temperature tetragonal Nb_5Si_3 was the (primary) phase formed during the solidification of all the studied alloys regardless of their Sn content. Only in the alloys with Cr and no Al (ZX3, ZX4), did the addition of Cr promote the transformation of βNb_5Si_3 to αNb_5Si_3 during solidification, in other words (a) Cr destabilised the high temperature tetragonal Nb_5Si_3 during solidification and (b) Al reduced this effect of Cr on the high temperature tetragonal Nb5Si3 during solidification (ZX7, ZX8).

αNb_5Si_3: The low temperature silicide was stable in all the heat treated alloys regardless of their Sn content, including the "simple" ternary alloys ZX1 and ZX2. At high (≥ 1200 °C) temperatures Sn promoted the formation of αNb_5Si_3 in the microstructures of the studied Nb silicide based alloys and Al and Sn individually and Al and Cr simultaneously promoted the $\beta Nb_5Si_3 \rightarrow \alpha Nb_5Si_3$ transformation at 1200 °C (ZX2), 1450 °C (ZX7, ZX8) or 1500 °C (ZX5, ZX6).

Chemistry of Nb_5Si_3: In the alloys with Al (ZX5, ZX6, ZX7, ZX8) the Al substituted for Si in the βNb_5Si_3. The Si + Sn content of the βNb_5Si_3 changed after the heat treatment in the αNb_5Si_3 in both the low and high Sn content alloys, but this increase was larger in the low Sn alloys. The Si + Sn + Al content of the Nb_5Si_3 did not change with alloy condition.

In the alloys with only Cr (ZX3, ZX4) the Si + Sn was essentially the same before and after heat treatment.

Nb_{ss} + βNb_5Si_3 eutectic: The suppression of Nb_3Si by Sn allows the metastable Nb_{ss} + βNb_5Si_3 eutectic to form during solidification. This was indeed the case in the two ternary alloys in which the lamellar eutectic microstructure was stable to up to 1500 °C in the absence of other additions. The additions of Al and Cr simultaneously

destabilised the Nb_{ss} + βNb_5Si_3 eutectic only in the cast high Sn content alloy ZX8. Al and Cr individually in the low and high Sn alloys and simultaneously in the low Sn alloy ZX7 destabilised the lamellar microstructure at 1500 °C.

The eutectic composition was analysed only in the low Sn alloys where the Si + Sn and Si + Al + Sn concentrations were in the range of values reported for the metastable eutectic.

A-15 Nb_3X: Only Cr could suppress the formation of (i.e., destabilise) Nb_3Sn in the low (2 at.%) Sn content alloys of this research, but this effect of Cr was possible only when it was not present with Al simultaneously in the alloy. The A15 intermetallic was stable at 1500 °C even in the "simple" ternary alloy ZX1. The results of this research would thus suggest that the A15 phase can be stable (meaning stable in microstructures exposed to high temperatures (> 1200 °C)) in Nb silicide based alloys with low Sn content (≤ 3 at.%).

In the high Sn cast alloys the Si + Sn and Si + Al + Sn concentrations were about 20 at.% and the Si/Sn ratio about 0.7, both did not change significantly after the heat treatment at 1500 °C. In the low Sn alloys, where the A15 phase formed in the heat treated microstructure, the Si + Al + Sn and the Si/Sn ratio were slightly lower (19 at.%) and higher (0.9), respectively.

C14-$NbCr_2$ Laves phase: Tin and Al did not destabilise the $NbCr_2$ Laves phase in the alloys with low and high Sn content. Formation of the Laves phase was dependent on solidification conditions and in the alloys without Al it is likely that it participated in a ternary eutectic. In the Laves the Cr was substituted by Al, Si and Sn and the Al + Cr + Si + Sn concentration shifted closer to the stoichiometric composition of the alloy after the heat treatment.

Isothermal oxidation at 800 °C

Weight gain and oxidation rate constants: At low Sn content, Al individually and simultaneously with Cr (alloys ZX5, ZX7), and at high Sn content simultaneously with Cr (alloy ZX8) encouraged break-away oxidation. Addition of Cr individually with high Sn content in the alloy ZX4 gave the lowest weight gain and the lowest parabolic rate constant.

Surface enrichment in Sn: Tin rich area was formed below the scale/substrate interface in the alloys with low and high Sn concentration with the exception of the alloy ZX7, i.e., the low Sn alloy with Al and Cr being present simultaneously in its microstructure.

Oxides in scale: The same oxides, namely Nb rich and Nb and Si rich oxides, were formed in the scales of all the alloys at 800 °C.

In the "best" alloy at 800 °C (alloy ZX4) the Nb rich oxide had the lowest (Nb+Ti)/Si and highest (Nb+Ti)/(Al+Cr+Sn) ratios (17.9 and 12.6 respectively) and the lowest Sn and highest Si concentrations and the highest Nb+Ti ratio of all the studied alloys.

In the "best" alloy at 800 °C (alloy ZX4) the Nb and Si rich oxide had the highest Si and Si+Sn, and the lowest Sn and (Nb+Ti)/Si of all the studied alloys.

The "worst" alloy at 800 °C (alloy ZX5) had the lowest Al and (Nb+Ti)/(Al+Si+Sn) ratio of all the studied alloys

Contamination by oxygen and bulk microstructure: In all the alloys all phases in the diffusion zone and bulk were contaminated by oxygen. In the diffusion zone the effect was very severe for the Nb_{ss}. In the starting microstructure of the "best" alloy

(ZX4) at 800 °C the Laves phase was present but was not observed after the oxidation at 800 °C. Thus, the contamination of the alloy ZX4 with oxygen altered the phase equilibria making the Laves phase unstable.

The contamination by oxygen of the Nb_{ss} in the bulk of the oxidised alloys at 800 °C seemed to increase with the Sn concentration in the alloy. The contamination of the bulk by oxygen in ZX8 caused a shift in phase equilibria at 800 °C and the formation of Nb_{ss} and Nb_{ss} + Nb_5Si_3 lamellar microstructure (the Nb_{ss} was absent in the cast alloy).

In all the alloys the Si/Sn ratio for the Nb_{ss} in the bulk was about 0.57. In the "best" alloy at 800 °C (alloy ZX4) the Cr and Sn concentrations in the Nb_{ss} were the highest of all studied alloys and the Nb_{ss} of this alloy had the lowest Ti/(Cr+Si+Sn) and Nb/Ti ratios and the highest Si + Sn and Ti + Si + Sn + Cr concentrations. In the "worst" alloy at 800 °C (ZX5) the Nb_{ss} had the highest Ti/(Al + Si + Sn) ratio.

Contamination by oxygen of the Nb_5Si_3 was higher in the "best" alloy (ZX4).

The Nb_3Sn in the bulk of the alloys was contaminated by oxygen whose concentration was the same (~ 6 at.%) regardless of whether the Al and Cr were present individually or simultaneously in the alloys. In the "best" alloy (alloy ZX4) the Nb_3Sn had the highest Si and Sn concentrations and thus the highest Si + Sn concentration.

Isothermal oxidation at 1200 °C

Weight gain and oxidation rate constants: The low Sn content alloys did not show breakaway oxidation while in the high Sn content alloys break-away oxidation was observed only in the alloy ZX4 (Cr, no Al).

Only the alloys ZX6 and ZX8 followed linear oxidation throughout the oxidation experiments. The other alloys of this study followed parabolic oxidation at the early stages and linear oxidation after that the "best" low Sn alloy was the ZX5 (no Cr) and the lowest linear rate constant for all alloys was for the high Sn alloy where Al was added individually (ZX6).

The Laves phase did not "benefit" oxidation at 1200 °C, the synergy of Al and Cr with low or high Sn concentration in the alloy did not have a significant effect on oxidation at 1200 °C.

Al was the most important alloying addition regarding oxidation behaviour at 1200 °C.

Surface enrichment in Sn: Tin rich area was formed below the scale/substrate interface in all the alloys regardless of the amount of Sn concentration. In the low Sn content alloys the surface segregation of Sn was less severe when Al was only present in the alloy (ZX5).

In the low Sn alloys the thickness of the Sn rich area was smaller in the alloy ZX5 (no Cr) and highest in the alloy ZX7 (both Al and Cr present). The increase in Sn content in the alloys was accompanied with thicker Sn rich areas at the scale/substrate interface and in the three alloys ZX4, ZX6 and ZX8. The thickness of the Sn rich area in these alloys was essentially the same (≈ 50 μm).

In all the low and high Sn alloys the Sn rich intermetallics Nb_3Sn and Nb_5Sn_2Si were formed in the Sn rich area below the scale and the $NbSn_2$ was also formed in the low and high Sn alloys with Cr (ZX3, ZX4) and the low Sn alloy with Al and Cr (ZX7). In other words, the $NbSn_2$ was not formed in the alloy ZX5 (the "best" low Sn alloy).

The formation of $NbSn_2$ in the microstructure of the Sn rich area at the scale/substrate interface was detrimental to oxidation at 1200 °C.

Enrichment of the interface below the scale in Sn and formation of Sn rich intermetallics such as Nb_5Sn_2X (X=Si, Al), which is isomorphous with Nb_5Si_3, i.e., with βNb_5Si_3, is advantageous for oxidation because it tends to stabilise the latter silicide, meaning the loss of Si to the scale does not lead to formation of Nb_3Si. Such intermetallics have low toughness, and their formation could have an adverse effect on the mechanical behaviour of the alloy/scale interface. The formation of dense adherent scales after isothermal oxidation would suggest that the latter might not be as serious as one could expect.

Oxides in scale: In the scales of the alloys the Nb rich, Nb and Si rich and Ti rich oxides were present but the latter oxide was not present in the scale of the alloy ZX5. As the Sn content of the alloy increased the Ti rich oxide formed in the scale of ZX6 (was not observed in the scale of the alloy ZX5).

The parameters Nb + Ti and Nb/Ti "controlled" the oxide types in the scales of the alloys and Al and Cr did not play a key role in the formation of the Nb rich and Nb and Si rich oxides, of which the former did not contain Si and Sn and the latter Sn.
The Ti rich oxide formed in the scale of the alloys did not contain Si and Sn.

Contamination by oxygen and bulk microstructure: In all the alloys all phases in the diffusion zone and bulk were contaminated by oxygen. In the diffusion zone the effect was very severe for the Nb_{ss}. The contamination of the bulk of ZX8 by oxygen caused a shift in phase equilibria at 1200 °C and led to the destabilisation of the Nb_{ss} in the microstructure.

The solubility of oxygen in the Nb_{ss} in the bulk decreased with increase in the Sn content of the alloy ZX4.

In the Nb_{ss} the parameters Si + Sn, Si/Sn and Nb/Ti did not change significantly with increase of the Sn content of the alloy.

The solubility of oxygen and the parameters Si + Sn, Si + Sn + Al and Nb/Ti in the Nb_5Si_3 in the bulk of the alloys at 1200 °C did not change as the Sn content of the alloys increased but the Sn concentration in the silicide increased.

In the A-15 intermetallic phase the oxygen solubility did not change with increasing Sn in the alloys, but the Sn concentration increased

11.2 Suggestions for future work

This research helped improve our understanding of how the addition of Sn affects phase stability and oxidation at 800 °C and 1200 °C in Nb-24Ti-18Si based alloys with 5 at.% each of Al and Cr added individually or simultaneously. It shows that on its own Sn cannot "sort out" the scale spallation at 1200 °C. Germanium additions in the same family of base alloys as those of this research, like Sn, improve oxidation at 800 °C (supress pest oxidation) but spallation still occurs at 1200 °C. Boron on the other hand has been shown to "do a better job" regarding oxidation at 1200 °C, where spallation of the scale can be avoided, but its effect on phase stability is not the desirable one. Thus, it is suggested that future research could attempt to understand the effects of Sn and B on phase stability and oxidation when Sn and B and Ge, Sn and B are present simultaneously in Nb-24Ti-18Si based alloys.

References

[1] B. P. Bewlay, M. R. Jackson, P. R. Subramanian, and J. C. Zhao, “A review of very-high-temperature Nb-silicide-based composites,” *Metall. Mater. Trans. A*, vol. 34, no. October, pp. 2043–2052, 2003.

[2] T. M. Pollock and S. Tin, “Nickel-Based Superalloys for Advanced Turbine Engines: Chemistry, Microstructure and Properties,” *J. Propuls. Power*, vol. 22, no. 2, pp. 361–374, 2006.

[3] J. D. Venables, “High temperature structural materials,” *Life Support Systems (EOLSS)*. .

[4] J. A. DiCaro, “Andvances in SiC/SiC Matrix Composites for Aero-Propulsion,” in *Ceramic Matrix Composites: Materials, Modelling adn Technology*, M. P. Bansal and J. Lamon, Eds. New Jersey, 2014, p. 217.

[5] D. A. Lewis, M. T. Hogan, J. McMahon, and S. Kinney, “Applicaition of uncooled ceramic matrix composite power turbine blades for performance improvement of advanced turboshaft engines,” in *64th American Helicopter Society International Annual Forum*, 2008, pp. 961–966.

[6] M. Mecham, “Out of the lab,” *Aviation Week*, p. 13, 2012.

[7] P. Pontiller and M. Willert-Porada, “High Temperature Behavior of Si3N4 and Yb2SiO5 Coated Carbon Fibers for Silicon-Nitride CMC,” *Adv. Eng. Mater.*, vol. 16, no. 556–564, 2014.

[8] D. M. Shah and D. L. Anton, “Evaluation of refractory intermetallics with A15 structure for high temperature structural applications,” *Mater. Sci. Eng. A*, vol. 153, no. 1–2, pp. 402–409, May 1992.

[9] D. L. Anton and D. M. Shah, “High temperature evaluation of topologically close packed intermetallics,” *Mater. Sci. Eng. A*, vol. 153, no. 1–2, pp. 410–415, May 1992.

[10] T. B. Massalski, H. Okamoto, and P. R. Subramanian, “Binary alloy phase diagrams,” *ASM Int.*, vol. 3, p. 1485, 1990.

[11] W. B. Pearson, *Handbook of Lattice Spacing and Structure of Metals*. Oxford, 1967.

[12] J. D. Livingston, "Refractory and Silicide Laves Phases," in *MRS Proceedings*, 1993, vol. 322, p. 395.

[13] J. J. Petrovic and A. K. Vasudevan, "Key developments in high temperature structural silicides," *Mater. Sci. Eng. A*, vol. 261, pp. 1–5, 1999.

[14] P. Peralta, S. A. Maloy, F. Chu, J. J. Petrovic, and T. E. Mitchell, "Mechanical properties of monocrystalline C11b MoSi2 with small aluminum addtion," *Scr. Mater.*, vol. 37, no. 10, pp. 1599–1604, 1997.

[15] M. K. Meyer and M. Akinc, "Isothermal Oxidation Behavior of Mo-Si-B Intermetallics at 1450°C," *J. Am. Ceram. Soc.*, vol. 79, no. 10, pp. 2763–2766, 1996.

[16] P. R. Subramanian, M. G. Mendiratta, D. M. Dimiduk, and M. A. Stucke, "Advanced intermetallic alloys—beyond gamma titanium aluminides," *Mater. Sci. Eng. A*, vol. 239–240, pp. 1–13, 1997.

[17] B. P. Bewlay, M. R. Jackson, and M. F. X. Gigliotti, "Niobium Silicide High Temperature In Situ Composites," *Intermet. Compd.*, vol. 3, 2002.

[18] J. H. Schneibel, M. J. Kramer, Ö. Ünal, and R. N. Wright, "Processing and mechanical properties of a molybdenum silicide with the composition Mo-12Si-8.5B (at.%)," *Intermetallics*, vol. 9, no. 1, pp. 25–31, 2001.

[19] M. G. Mendiratta and D. M. Dimiduk, "Strength and toughness of a Nb/Nb5Si3 composite," *Metall. Trans. A*, vol. 24A, pp. 501–504, 1993.

[20] D. M. Shah, D. L. Anton, D. P. Pope, and S. Chin, "In-situ refractory intermetallic-based composites," *Mater. Sci. Eng. A*, vol. 192–193, pp. 658–672, 1995.

[21] R. G. Rowe and D. W. Skelly, "The Synthesis and Evaluation of Nb3Al-Nb Laminated Composites," *MRS Proc.*, vol. 273, pp. 411–416, 1992.

[22] R. G. Rowe, D. W. Skelly, M. Larsen, J. Heathcote, G. Lucas, and G. R. Odette, "Properties of microlaminated intermetallic-refractory metal composites," *Mat. Res. Soc. Symp. Proc.*, no. 322, pp. 461–472, 1994.

[23] B. P. Bewlay, H. A. Lipsitt, W. J. Reeder, M. R. Jackson, and J. A. Sutliff, "Toughening Mechanisms in Directionally Solidified Nb-Si In-Situ Composites," in *Processing and Fabrication ofAdvanced Materials for High*

Temperature Applications III, 1994, pp. 547– 565.

[24] B. P. Bewlay, M. R. Jackson, W. J. Reeder, and H. A. Lipsitt, "Microstructures and Properties of DS inSitu Composites of Nb-Ti-Si Alloys," *MRS Proc.*, vol. 364, pp. 943–948, 1995.

[25] I. Weiss, M. Thirukkonda, and R. Srinivasan, "Effect of Deformation Processing on Mechanical Properties of Nb-10 a/o Si In-Situ Composite," *MRS Proc.*, vol. 322, p. 377, 1993.

[26] D. P. Pope, D. M. Shah, W. Romanow, and Huntley.M., "Directional Solidification of Refractory Intermetallics: Single Crystals and Composites," *MRS Proc.*, vol. 322, p. 353, 1993.

[27] M. E. Schlesinger, H. Okamoto, A. B. Gokhale, and R. Abbaschian, "The Nb-Si (Niobium-Silicon) system," *J. Phase Equilibria*, vol. 14, no. 4, pp. 502–509, 1993.

[28] C. Zhao, B. P. Bewlay, M. R. Jackson, and L. a. Peluso, "Alloying and phase stability in niobium silicide in-situ composites," in *Proceedings of the 3rd international symposium on structural intermetallics*, 2001, p. 483.

[29] Z. Sun, X. Guo, and C. Zhang, "Thermodynamic modeling of the Nb-rich corner in the Nb-Si-Sn system," *Calphad Comput. Coupling Phase Diagrams Thermochem.*, vol. 36, pp. 82–88, 2012.

[30] W.-K. Wang, C. J. Lobb, and F. Spaepen, "Formation of metastable Nb-Si phases by picosecond and nanosecond pulsed laser quenching," *Mater. Sci. Eng.*, vol. 98, pp. 325–328, 1988.

[31] M. G. Mendiratta and D. M. Dimiduk, "Microstructures and Mechanical Behavior of Two-Phase Niobium Silicide-Niobium Alloys," *MRS Proc.*, vol. 133, p. 441, 1988.

[32] J. L. Murray, "The Nb−Ti (Niobium-Titanium) system," *Bull. Alloy Phase Diagrams*, vol. 2, no. 1, pp. 55–61, 1981.

[33] D. L. Moffat and U. R. Kattner, "The stable and metastable Ti-Nb phase diagrams," *Metall. Trans. A*, vol. 19, no. 10, pp. 2389–2397, 1988.

[34] J. L. Murray, "Phase Diagrams of Binary Titanium Alloys," *ASM Int.*, pp. 197–211, 1987.

[35] B. P. Bewlay, M. R. Jackson, and R. R. Bishop, "The Nb-Ti-Si ternary phase diagram: Determination of solid-state phase equilibria in Nb- and Ti-rich alloys," *J. Phase Equilibria*, vol. 19, no. 6, pp. 577–586, 1998.

[36] B. P. Bewlay, M. R. Jackson, and H. A. Lipsitt, "The Nb-Ti-Si ternary phase diagram: Evaluation of liquid- solid phase equilibria in Nb-and Ti-rich alloys," *J. Phase Equilibria*, vol. 18, no. 3, pp. 264–278, 1997.

[37] J.-C. Zhao, B. P. Bewlay, and M. R. Jackson, "Determination of Nb-Hf-Si phase equilibria," *Intermetallics*, vol. 9, pp. 681–689, 2001.

[38] J.-C. Zhao, M. R. Jackson, and L. A. Peluso, "Determination of the Nb-Cr-Si phase diagram using diffusion multiples," *Acta Mater.*, vol. 51, no. 20, pp. 6395–6405, Dec. 2003.

[39] C. T. Liu, J. H. Zhu, M. P. Brady, C. G. McKamey, and L. M. Pike, "Physical metallurgy and mechanical properties of transition- metal Laves phase alloys," *Intermetallics*, vol. 8, pp. 1119–1129, 2000.

[40] M. Venkatraman and J. P. Neumann, "The Cr−Nb (Chromium-Niobium) system," *Bull. Alloy Phase Diagrams*, vol. 7, no. 5, pp. 462–466, 1986.

[41] A. B. Gokhale and G. J. Abbaschian, "The Cr−Si (Chromium-Silicon) system," *J. Phase Equilibria*, vol. 8, no. 5, pp. 474–484, 1987.

[42] J. L. Murray, "The Cr−Ti (chromium-titanium) system," *Bull. Alloy Phase Diagrams*, vol. 2, no. 2, pp. 174–181, 1981.

[43] H. J. Goldschmidt and J. A. Brand, "The Constitution of the Chromium-Niobium-Silicon System," *J Less Common Met.*, vol. 3, pp. 34–43, 1961.

[44] J. Geng, G. Shao, and P. Tsakiropoulos, "Study of three-phase equilibrium in the Nb-rich corner of Nb-Si-Cr system," *Intermetallics*, vol. 14, pp. 832–837, 2006.

[45] B. P. Bewlay, Y. Yang, R. L. Casey, M. R. Jackson, and Y. a. Chang, "Experimental study of the liquid-solid phase equilibria at the metal-rich region of the Nb-Cr-Si system," *Intermetallics*, vol. 17, pp. 120–127, 2009.

[46] U. R. Kattner and W. J. Boettinger, "Thermodynamic calculation of the ternary Ti-Al-Nb system," *Mater. Sci. Eng. A*, vol. 152, no. 1–2, pp. 9–17, 1992.

[47] J. L. Murray and A. J. McAlister, "The Al-Si (Aluminum-Silicon) system," *Bull.*

Alloy Phase Diagrams, vol. 5, no. 1, pp. 74–84, 1984.

[48] C. Brukl, H. Nowotny, and F. Benesovsky, "Investigations into the three-component systems: V-Al-Si, Nb-Al-Si, Cr-Al-Si, Al-Si-Mo and Cr(Mo)-Al-Si," *Monatsh Chemie*, vol. 92, no. 5, pp. 967–980, 1961.

[49] V. M. Pan, V. I. Latysheva, O. G. Kulik, A. G. Popov, and E. N. Litvinenko, "The Al3Nb-Nb-Nb5Si3 Phase Diagram," *Russ.Metall.*, vol. 4, pp. 233–235, 1984.

[50] J.-C. Zhao, L. Peluso, M. Jackson, and L. Tan, "Phase diagram of the Nb–Al–Si ternary system," *J. Alloys Compd.*, vol. 360, no. 1–2, pp. 183–188, Oct. 2003.

[51] J. Geng and P. Tsakiropoulos, "A study of the microstructures and oxidation of Nb-Si-Cr-Al-Mo in situ composites alloyed with Ti, Hf and Sn," *Intermetallics*, vol. 15, no. 3, pp. 382–395, Mar. 2007.

[52] F. A. Shunk, *Constitution of Binary Alloys*, Second Sup. New York: McGraw-Hill Book Company, 1969.

[53] C. Toffolon, C. Servant, J. C. Gachon, and B. Sundman, "Reassessment of the Nb-Sn system," *J. Phase Equilibria*, vol. 23, no. 2, pp. 134–139, 2002.

[54] R. W. Olesinski and G. J. Abbaschian, "The Si−Sn (Silicon−Tin) system," *Bull. Alloy Phase Diagrams*, vol. 5, no. 3, pp. 273–276, 1984.

[55] R. M. Waterstrat and J. Müller, "Ternary A15-phase regions in the Nb-Sn-Si and Nb-Sn-As systems," *J. Less Common Met.*, vol. 52, no. 2, pp. 271–277, Apr. 1977.

[56] N. Vellios and P. Tsakiropoulos, "The role of Sn and Ti additions in the microstructure of Nb-18Si base alloys," *Intermetallics*, vol. 15, no. 12, pp. 1518–1528, 2007.

[57] R. Smith, "The development of oxidation-resistance niobium alloys," *Less Common Met.*, vol. 2, pp. 191–206, 1960.

[58] P. Y. Hou, "Oxidation of Metals and Alloys," in *Shreir's Corrosion*, Elsevier, 2010, pp. 195–239.

[59] E. M. Lyutyi, O. I. Eliseeva, V. I. Stepanyshyn, and S. Y. Romanko, "Mechanism and regularities of oxidation in Nb-Ti and Nb-Ti-Si systems," *Mater. Sci.*, vol. 31, no. 1, pp. 105–111, 1996.

[60] H. Hindam and D. P. Whittle, "Microstructure, adhesion and growth kinetics of protective scales on metals and alloys," *Oxid. Met.*, vol. 18, no. 5–6, pp. 245–284, 1982.

[61] G. H. Meier, "A review of advances in high-temperature corrosion," *Mater. Sci. Eng. A*, vol. 120–121, pp. 1–11, 1989.

[62] E. S. K. Menon and M. G. Mendiratta, "High Temperature Oxidation in Multicomponent Nb Alloys," *Mater. Sci. Forum*, vol. 475–479, pp. 717–720, 2005.

[63] B. P. Bewlay, P. W. Whiting, A. W. Davis, and C. L. Briant, "Creep Mechanisms in Niobium-Silicide Based In-Situ Composites," *Mat. Res. Soc. Symp. Proc.*, vol. 552, pp. 3–8, 1999.

[64] K. S. Chan, "Alloying effects on fracture mechanisms in Nb-based intermetallic in-situ composites," *Mater. Sci. Eng. A*, vol. 329–331, pp. 513–522, 2002.

[65] R. T. Begley, "Evolution of Refractory Metals and Alloys," in *TMS*, 1994, pp. 29–48.

[66] K. S. Chan and D. L. Davidson, "Effects of Ti addition on cleavage fracture in Nb-Cr-Ti solid-solution alloys," *Metall. Mater. Trans. A*, vol. 30, no. 4, pp. 925–939, 1999.

[67] A. L. Bendersky, F. S. Biancaniello, W. J. Boettinger, and J. H. Perepezko, "Microstructural Characterization of Rapidly Solidified Nb-Si Alloys," *Mater. Sci. Eng.*, vol. 87, pp. 151–159, 1987.

[68] K. Zelenitsas and P. Tsakiropoulos, "Study of the role of Al and Cr additions in the microstructure of Nb-Ti-Si in situ composites," *Intermetallics*, vol. 13, no. 10, pp. 1079–1095, 2005.

[69] N. Vellios and P. Tsakiropoulos, "The role of Fe and Ti additions in the microstructure of Nb–18Si–5Sn silicide-based alloys," *Intermetallics*, vol. 15, no. 12, pp. 1529–1537, Dec. 2007.

[70] N. Vellios and P. Tsakiropoulos, "Study of the role of Fe and Sn additions in the microstructure of Nb–24Ti–18Si–5Cr silicide based alloys," *Intermetallics*, vol. 18, no. 9, pp. 1729–1736, Sep. 2010.

[71] E. Zacharis, *PhD Thesis*. University of Sheffield, 2013.

[72] N. David, Y. Cartigny, T. Belmonte, J. M. Fiorani, and M. Vilasi, "Thermodynamic description of the Cr-Nb-Si isothermal section at 1473 K," *Intermetallics*, vol. 14, no. 4, pp. 464–473, 2006.

[73] H. Dbiloni and W. J. Boettinger, *Physical Metallurgy, Volume 1*, 4th ed. North Holland, 1996.

[74] X. J. Han and B. Wei, "Microstructural characteristics of Ni-Sb eutectic alloys under substantial undercooling and containerless solidification conditions," *Metall. Mater. Trans. A*, vol. 33, no. 4, pp. 1221–1228, 2002.

[75] A. M. Mullis, C. R. Clopet, and R. F. Cochrane, "Determination of the Origin of Anomalous Eutectic Structures from In-situ Observation of Recalescence Behaviour," *Mater. Sci. Forum*, vol. 790–79, pp. 349–354, 2014.

[76] M. Li, K. Nagashio, and K. Kuribayashi, "Reexamination of the solidification behavior of undercooled Ni-Sn eutectic melts," *Acta Mater.*, vol. 50, pp. 3239–3250, 2002.

[77] M. Li and K. Kuribayashi, "Nucleation controlled microstructures and anomalous eutectic formation in undercooled Co-Sn and Ni-Si eutectic melts," *Metall. Mater. Trans. A*, vol. 34A, pp. 2999–3008, 2003.

[78] P. Tsakiropoulos, "On the macrosegregation of silicon in niobium silicide based alloys," *Intermetallics*, vol. 55, pp. 95–101, Dec. 2014.

[79] K. Zelenitsas, *PhD Thesis*. University of Sheffield, 2005.

[80] A. Tweddle, *PhD Thesis*. University of Sheffield, 2015.

[81] P. Tsakiropoulos, "Priate Communication."

[82] M. G. Mendiratta and D. M. Dimiduk, "Phase relations and transformation kinetics in the high Nb region of the Nb-Si system," *Scr. Metall. Mater.*, vol. 25, no. 1, pp. 237–242, 1991.

[83] Z. F. Li and P. Tsakiropoulos, "Study of the effects of Ge addition on the microstructure of Nb-18Si in situ composites," *Intermetallics*, vol. 18, no. 5, pp. 1072–1078, 2010.

[84] C. Utton and P. Tsakiropoulos, "Private Communication," 2015.

[85] Y. Yang, B. P. Bewlay, S.-L. Chen, and Y. A. Chang, "Application of phase diagram calculations to development of new ultra-high temperature structural

materials," *Trans. Nonferrous Met. Soc. China*, vol. 17, no. 6, pp. 1396–1404, 2007.

[86] J. Geng, P. Tsakiropoulos, and G. Shao, "A thermo-gravimetric and microstructural study of the oxidation of Nbss/Nb5Si3-based in situ composites with Sn addition," *Intermetallics*, vol. 15, pp. 270–281, 2007.

[87] S. Knittel, S. Mathieu, L. Portebois, and M. Vilasi, "Effect of tin addition on Nb–Si-based in situ composites. Part II: Oxidation behaviour," *Intermetallics*, vol. 47, pp. 43–52, 2014.

[88] N. Vellios, *PhD Thesis*. University of Surrey, 2007.

[89] P. Tsakiropoulos, K. Zelenitsas, and N. Vellios, "Study of the effect of Al, Cr and Sn additions on the microstructure and properties of Nb silicide based alloys," *MRS Proc.*, vol. 1295, pp. 367–372, 2011.

[90] J. Geng, P. Tsakiropoulos, and G. Shao, "Oxidation of Nb-Si-Cr-Al in situ composites with Mo, Ti and Hf additions," *Mater. Sci. Eng. A*, vol. 441, pp. 26–38, 2006.

[91] I. Papadimitriou, C. Utton, A. Scott, and P. Tsakiropoulos, "Ab initio study of the intermetallics in Nb–Si binary system," *Intermetallics*, vol. 54, pp. 125–132, Nov. 2014.

[92] I. Papadimitriou, C. Utton, and P. Tsakiropoulos, "Ab initio investigation of the intermetallics in the Nb–Sn binary system," *Acta Mater.*, vol. 86, pp. 23–33, Mar. 2015.

[93] M. Hojo, T. Matsuoka, M. Hashimoto, M. Tanaka, M. Sugano, S. Ochiai, and K. Miyashita, "Direct measurement of elastic modulus of Nb3Sn using extracted filaments from superconducting composite wire and resin impregnation method," *Phys. C Supercond. its Appl.*, vol. 445–448, pp. 814–818, Oct. 2006.

[94] M. Sundareswari, S. Ramasubramanian, and M. Rajagopalan, "Elastic and thermodynamical properties of A15 Nb3X (X = Al, Ga, In, Sn and Sb) compounds — First principles DFT study," *Solid State Commun.*, vol. 150, no. 41–42, pp. 2057–2060, Nov. 2010.

[95] B. C. Collins, *PhD Thesis*. Berkley: University of California, 2013.

[96] I. Papadimitriou, C. Utton, A. Scott, and P. Tsakiropoulos, “On the Nb-Ge Binary System,” *Metall. Mater. Trans. A*, vol. 46, no. 12, pp. 5526–5536, 2015.

[97] G. Fujii, M. A. Ranney, and A. F. Clark, “Thermal Expansion of Multifilamentary Nb3Sn and V3Ga Superconductive Cables and Fiberglass-Epoxy and Cotton-Phenolic Composite Materials,” *Japnese J. Appl. Phyisics*, vol. 20, no. 4, pp. 267–270, 1981.

[98] A. V. Emyashev, “Gas-Phase Metallurgy of Refractory Compounds,” in *Metallurgiya*, Moscow, 1987.

[99] W. A. Tiller, K. A. Jackson, J. W. Rutter, and B. Chalmers, “The redistribution of solute atoms during the solidification of metals,” *Acta Metall.*, vol. 1, pp. 435–438, 1953.

[100] X. Yao, A. K. Dahle, C. J. Davidson, and D. H. StJohn, “Effect of solute on the growth rate and the constitutional undercooling ahead of the advancing interface during solidification of an alloy and the implications for nucleation,” *J Mater.Res*, vol. 21, no. 10, pp. 2470–2479, 2006.

[101] J. Geng, P. Tsakiropoulos, and G. Shao, “The effects of Ti and Mo additions on the microstructure of Nb-silicide based in situ composites,” *Intermetallics*, vol. 227–235, 2006.

[102] P. Wynblatt and A. Landa, “Computer simulation of surface segregation in ternary alloys,” *Comput. Mater. Sci.*, vol. 15, no. 2, pp. 250–263, Jun. 1999.

[103] J. W. Gibbs, *The Collected Works of J W Gibbs*, vol. 1. New Haven, Connecticut: Yale University Press, 1948.

[104] F. L. Williams and D. Nason, *Surface Science*. 1970.

[105] D. McLean, *Grain Boundaries in Metals*. Oxford: Clarendon Press, 1957.

[106] J. J. Burton and E. S. Machlin, “Prediction of Segregation to Alloy Surfaces from Bulk Phase Diagrams,” *Phys Rev Let.*, vol. 37, no. 21, pp. 1433–1436, 1976.

[107] G. Treglia, B. Legrand, and F. Ducastelle, “Segregation and Ordering at Surfaces of Transition Metal Alloys: The Tight-Binding Ising Model,” *Europhys. Lett.*, vol. 7, pp. 575–580, 1988.

[108] R. N. Barnett, U. Landman, and C L Cleveland, “Multilayer lattice relaxation

at metal surfaces: A total-energy minimization," *Phys Rev B*, vol. 28, pp. 6647–6658, 1983.

[109] S. Mukherjee and J. L. Moran-Lopez, "Theory of surface segregation in transition-metal alloys," *Surf. Sci.*, vol. 188, no. 3, pp. L742–L748, 1987.

[110] A. Christensen, A. V Ruban, P. Stoltze, K. W. Jacobsen, H. L. Skriver, J. K. Norskov, and F. Besenbacher, "Phase diagrams for surface alloys," *Phys.Rev B*, vol. 56, pp. 5822–5834, 1997.

[111] A. V. Ruban, H. L. Skriver, and J. K. Norskov, "Surface segregation energies in transition-metal alloys," *Phys. Rev. B*, vol. 59, no. 24, pp. 15990–16000, 1999.

[112] L. E. Murr, *Interfacial Phenomena in Metals and Alloys*. Canada: Addison-Wesley Publishing Company, 1975.

[113] A. R. Miedema, P. F. de Châtel, and F. R. de Boer, "Cohesion in alloys — fundamentals of a semi-empirical model," *Phys. B+C*, vol. 100, no. 1, pp. 1–28, Apr. 1980.

[114] R. L. Opila, "The role of grain boundaries in the surface segregation of tin in tin-lead alloys," *J.Vac. Sci. Technol. A*, vol. 4, pp. 173–178, 1986.